Universidade Estadual Paulista
"Júlio de Mesquita Filho"
Programa Interunidades

unesp

Doutorado

Engenharia Civil e Ambiental

Jhaber Dahsan Yacoub

Study of hydraulic conductivity and pollutant transport parameters in a municipal solid waste disposal area

Bauru
2024

Jhaber Dahsan Yacoub

Study of hydraulic conductivity and pollutant transport parameters in a municipal solid waste disposal area

Thesis submitted to the São Paulo State University – Unesp, Engineering College at Bauru as a partial fulfillment of the requirements for obtaining the degree of Doctor in Civil and Environmental Engineering.

Dr. Roger Augusto Rodrigues
Advisor
Dr. Heraldo Luiz Giacheti
Co – Advisor

Bauru
2024

Y12s

Yacoub, Jhaber Dahsan
Study of hydraulic conductivity and pollutant transport parameters in a municipal solid waste disposal area / Jhaber Dahsan Yacoub. -- Bauru, 2024
457 f. : il., tabs.

Tese (doutorado) - Universidade Estadual Paulista (UNESP), Faculdade de Engenharia, Bauru
Orientador: Roger Augusto Rodrigues
Coorientador: Heraldo Luiz Giacheti

1. Bauru's MSW disposal site. 2. Weathered sandstone. 3. Tropical soil. 4. Contaminant transport. 5. Numerical simulations. I. Título.

Sistema de geração automática de fichas catalográficas da Unesp. Dados fornecidos pelo autor(a).

UNIVERSIDADE ESTADUAL PAULISTA

Câmpus de Bauru

ATA DA DEFESA PÚBLICA DA TESE DE DOUTORADO DE JHABER DAHSAN YACOUB, DISCENTE DO PROGRAMA DE PÓS-GRADUAÇÃO EM ENGENHARIA CIVIL E AMBIENTAL, DA FACULDADE DE ENGENHARIA - CÂMPUS DE BAURU.

Aos 25 dias do mês de novembro do ano de 2024, às 14:00 horas, por meio de Videoconferência, realizou-se a defesa de TESE DE DOUTORADO de JHABER DAHSAN YACOUB, intitulada **Study of hydraulic conductivity and pollutant transport parameters in a municipal solid waste disposal area.** A Comissão Examinadora foi constituida pelos seguintes membros: Prof. Dr. ROGER AUGUSTO RODRIGUES (Orientador(a) - Participação Presencial) do(a) Departamento de Engenharia Civil e Ambiental / Universidade Estadual Paulista (UNESP) - Faculdade de Engenharia - Câmpus de Bauru , Prof. Dr. MARCOS MUSSO (Participação Virtual) do(a) Ingeniería Geotécnia / Facultad de Ingeniería UdelaR - Uruguay, Profª. Drª. MIRIAM DE FATIMA CARVALHO MACHADO (Participação Virtual) do(a) Departamento de Ciência e Tecnologia dos Materiais - DCTM / UNIVERSIDADE FEDERAL DA BAHIA, Profa. Dra. ANA ELISA SILVA DE ABREU (Participação Virtual) do(a) IG / UNICAMP/Campinas (SP), Prof.ª Dr.ª GIULLIANA MONDELLI (Participação Presencial) do(a) Departamento de Engenharia Civil e Ambiental / Universidade Estadual Paulista (Unesp) - Faculdade de Engenharia - Câmpus Bauru . Após a exposição pelo doutorando e arguição pelos membros da Comissão Examinadora que participaram do ato, de forma presencial e/ou virtual, o discente recebeu o conceito final: aprovado. Nada mais havendo, foi lavrada a presente ata, que após lida e aprovada, foi assinada pelo(a) Presidente(a) da Comissão Examinadora.

Prof. Dr. ROGER AUGUSTO RODRIGUES

List of Figures

List of Tables

Contents

Abstract

Municipal solid waste (MSW) disposal sites play a vital role in waste management but pose significant environmental risks due to the transport of contaminants into soil and groundwater. This work examines these risks through an integrative study comprising experimental, analytical, and numerical analyses. A detailed experimental investigation of the tropical soil profile and weathered sandstone near Brazil's Bauru MSW disposal site revealed key geotechnical and hydraulic properties influencing contaminant transport, including anisotropic permeability and expansive behaviors attributed to clay minerals. Laboratory column tests using the non-reactive tracer NaCl and heavy metals (Mn, Ni, Pb) identified hydraulic conductivity (k), dispersivity (α), hydrodynamic dispersion (Dh), retardation factor (Rd), and partition coefficient (Kd) as critical parameters. Numerical simulations using CODE_BRIGHT evaluated the fate and transport of contaminants in Bauru's MSW disposal site's North-South and East-West profiles over 1, 10, and 100 years under varying leachate heads. Results show that increased leachate head accelerates breakthrough times, with horizontal flow dominating permeable soil horizons. The East-West profile exhibited greater vulnerability to contaminant migration, though sandstone layers provided some attenuation. These findings underscore the importance of integrating field data, laboratory experiments, and modeling to enhance MSW disposal site management strategies, mitigate contamination risks, and safeguard environmental resources.

Keywords: Bauru's MSW disposal site; Weathered sandstone; Tropical soil; Contaminant transport; Numerical simulations.

Introduction

Municipal solid waste disposal sites are integral to modern waste management systems but present significant environmental risks due to the potential for contaminant transport into surrounding soil and groundwater. This issue is particularly pressing in increasing urbanization and growing global waste volumes. The environmental impact of MSW disposal sites is especially concerning when contaminants, such as heavy metals, organic compounds, and gases, migrate through the soil and water systems, posing long-term threats to ecosystems and public health.

There is a growing need to refine and enhance numerical and analytical models that simulate contaminant transport in MSW disposal sites. Different numerical and analytical models are increasingly applied but require continuous improvement to predict long-term contaminant behavior accurately. Furthermore, the interaction of contaminants with different geological formations, e.g., tropical soils and sandstones, introduces complexities in how contaminants migrate. Studies on soil and rock properties, such as strength, stiffness, deformability, and hydraulic conductivity, are essential for understanding contaminant spread.

Long-term contaminant behavior in MSW disposal sites, particularly over 100 years in a natural attenuation context, must be understood more. Contaminants can reach critical levels when there are no interventions, posing long-term environmental risks. Moreover, the integration between laboratory data and modeling efforts is beneficial and necessary to improve predictions' reliability. This interdisciplinary collaboration is vital for managing contaminant transport risks and making informed decisions regarding MSW disposal site operations and remediation efforts.

In this context, this work was motivated by the following questions:

1. What are the leading software programs, periods covered, and tracers used to simulate the transport of contaminants in MSW disposal sites?
2. How does weathered sandstone near an MSW disposal site behave regarding strength, deformability, and permeability?
3. What are the primary contaminant transport parameters and their variation in a tropical sandy soil profile and an outcropping sandstone as a function of confinement pressure and depth?
4. Using the previous laboratory parameters, how would the contamination plume spread with different leachate heads in other periods?

Objectives

This thesis aims to advance the study of Bauru's MSW disposal site by determining crucial new laboratory data on the transport of contaminants in tropical sandy soil and the outcropping sandstone around the MSW disposal site, as well as to estimate the sandstone's hydromechanical parameters to support and validate numerical analyses and, through them, extrapolates the MSW disposal site's behavior concerning the natural attenuation of the contamination plume.

Thesis presentation

The thesis has been divided into four main chapters to address these concerns.

Recent research has focused on improving the accuracy and reliability of contaminant transport models in MSW disposal sites. Chapter 1 reviews advancements in modeling approaches and presents widely used tools like COMSOL Multiphysics, MODFLOW, and POLLUTE. These models simulate contaminants' spatial and temporal distribution, providing

critical insights into the dynamics of heavy metals, inorganic tracers, and organic compounds in MSW disposal site environments. Integrating field and laboratory data with numerical models is crucial to refining our understanding of MSW disposal site behavior and mitigating potential environmental risks.

In addition to the challenge of modeling contaminant transport, the mechanical and hydraulic behavior of soils and rock formations surrounding MSW disposal sites plays a crucial role in determining how contaminants move through these environments. Chapter 2 investigates the properties of weathered sandstone in tropical regions, highlighting the outcome of uniaxial compressive strength and Young's modulus and underscoring the differences in permeability and shear strength between gray and brown sandstones. The influence of mineral composition, consolidation pressures, and anisotropy on water flow through these formations offers essential insights into their capacity to contain or allow the spread of contaminants.

Chapter 3 explores MSW disposal site-related contamination by examining the hydraulic properties of tropical soils and bedrock near Bauru's MSW disposal site in Brazil. By studying key transport parameters, such as hydraulic conductivity, dispersivity, hydrodynamic dispersion, partition coefficient, and retardation factors, this chapter provides an understanding of how NaCl, as a non-reactive tracer, migrates through soil profiles and bedrock under varying stresses and depths. Furthermore, it also presents the transport of Mn, Ni, and Pb in unconsolidated sandstones to assess the sandstone's ability to retain these critical contaminants. These findings offer essential data for future numerical modeling and decision-making in Bauru's MSW disposal site.

Lastly, Chapter 4 focuses on numerical simulations of contaminant transport from Bauru's MSW disposal site in Brazil, using NaCl to project the long-term environmental impact over 100 years. The study underscores the significance of hydraulic leachate heads in accelerating breakthrough times, particularly in heterogeneous geological formations like tropical soil and sandstone. The findings stress the need for intervention to prevent critical contamination levels from threatening local water resources and ecosystems long term.

Chapter 1

Analysis of the current scenario of contaminant transport in municipal solid waste disposal sites

Abstract

Municipal solid waste (MSW) disposal sites are essential components of waste management systems, but they pose significant environmental risks due to the potential for contaminant transport through soil and groundwater. This paper analyzes the state of contaminant transport in MSW disposal sites, focusing on studies published between 2019 and January 2022, focusing on state-of-the-art modeling approaches and the most frequently studied contaminants. The review emphasizes the application of advanced numerical and analytical modeling techniques. COMSOL Multiphysics was used in 26% of the analyzed studies, MODFLOW in 23%, and POLLUTE in 13%, reflecting their growing importance in simulating complex contaminant transport phenomena in MSW disposal sites. The findings highlight the primary use of these models for simulating the spatial distribution of contaminants over varying time frames, with 100, 10, and 20-year periods being the most frequently employed by authors. Heavy metals, comprising 41% of all tracers, were the most commonly studied contaminants, with lead (Pb), copper (Cu), chromium (Cr), cadmium (Cd), and zinc (Zn) being the most prevalent. Inorganic tracers, such as chlorine (Cl), chlorides, and ammonium (NH_4), along with non-heavy metals, accounted for 26%, while organic compounds like toluene, dichloromethane, and benzene comprised 24% of the tracers. Methane (CH_4) was the primary gas tracer, representing 9% of the simulation tracers. This study emphasizes the importance of integrating field and laboratory data with numerical and analytical models to improve the accuracy and reliability of predictions. It calls for continuous refinement of these models, considering the inherent complexities of MSW disposal sites, to manage contaminant transport risks better and contribute to developing more sustainable waste management practices.

Keywords: MSW disposal sites; Analytical and numerical modeling; Contaminant transport; Organic and inorganic tracers; Heavy metals.

1.1 Introduction

Efforts towards waste reduction, reuse, and recycling are primarily directed at preventing it from being immediately considered final waste and transported to MSW disposal sites without undergoing prior stages of treatment. The goal is to extract or add value to the waste, reducing the overall waste volume in MSW disposal sites, especially in regions with limited disposal capacity, such as large urban centers. This approach is crucial in mitigating the environmental impact of waste and promoting sustainable waste management practices (Daniel, 1993; Malusis & Shackelford, 2004; Varank et al., 2011).

Despite concerted efforts, MSW continues to be widely disposed of in sanitary landfills, controlled landfills, and dumps, making them one of the leading sources of environmental pollution and a significant risk to human health (Rowe & Barakat, 2021; Shackelford & Jefferis, 2018). In addition, MSW in countries with less economic capacity is often mixed with hazardous waste, such as Health Services Waste (HSW) and Industrial Waste (IW), leading to increased waste volume and improper disposal methods that exacerbate the environmental and health impacts (Mondelli et al., 2007, 2012; Samadder et al., 2017).

The typical result of these cases is a gradient of pollutant concentration in the physical environment, with the highest concentrations close to the polluting sources. Flora, fauna, and human beings can be exposed to and contaminated by heavy metals by consuming them in food or water (Hamer, 2003; Bakis & Tuncan, 2011; Gworek et al., 2016). Chronic exposure to heavy metals is associated with severe damage to human health, such as exposure to lead (kidney and brain damage, anemia, insomnia, irritability, concentration, and learning disorders), cadmium (damage to kidneys, lungs, and bones), mercury (damage to the nervous system, lungs, and development of fetuses) and arsenic (disorders of the central nervous and cardiovascular systems, polyneuropathy, increased risk of cancer) (Järup, 2003).

Thus, many studies on contaminant transport have been centered around heavy metals, frequently found in the leachate produced by MSW (Dong et al., 2020; Garg et al., 2020; Sun et al., 2020; He et al., 2022; Yong et al., 2022). Nevertheless, researchers have also focused on other organic and inorganic pollutants, pharmaceuticals, and personal care

products. Each of these substances has unique migration profile trends and a range of transport parameters (Chen et al., 2019; Divya et al., 2020; Lin & Yeh, 2020; Ding et al., 2021; Peng et al., 2021; Wu et al., 2021; Yu et al., 2021; Yan et al., 2022).

It is important to note that applying engineering techniques to prevent or contain soil and water contamination, such as using liners and clay to create a barrier against transport by advection, does not entirely prevent the transport of contaminants by molecular diffusion. Factors such as the composition of the waste and the leachate, the water content in the soils, the position of the water table, the stage of decomposition of the waste, the degradation of geomembranes, the heterogeneity of the physical environment, climatic factors, the gases generation, and the consolidation of the mass of waste, among others, suggest a complex flow behavior in porous media. Therefore, it is necessary to consider these factors while implementing any remediation strategy (Feng et al., 2019; Ozelim et al., 2021; Yu et al., 2021).

Another critical phenomenon inside MWS disposal sites due to biochemical reactions is the accumulation and diffusion of heat generated. Wang et al. (2017) comment that the internal temperature of MWS disposal sites can reach 55°C to 60°C, affecting geomembranes, hydraulic conductivity, and sorption of clays.

Given the aforementioned complexity, one way to evaluate the behavior and fate of contaminants in soil, rock, air, and water is through laboratory and field tests aimed at determining parameters that help interpret and obtain analytical and numerical models that can describe this behavior and predict the performance of MWS disposal sites over time.

Therefore, this work aims to investigate cases reported in the literature that provide enlightenment on analytical and numerical modeling and better analyze the primary pollutants/tracers to understand the migration of contamination plumes in MWS disposal sites.

1.2 Material and Methods

1.2.1 Information sources

This study conducted a literature review following the modified Preferred Reporting Items for Systematic Reviews and Meta-Analyses (PRISMA) report for systematic reviews by Page et al. (2021a,b). The construction and visualization of bibliometric networks employing VOSviewer software version 1.6.18.

In January 2022, a literature search was carried out utilizing the Web of Science, Scopus, and SciELO databases. The search strategy involved the following keywords: "contaminant transport" AND "landfill" OR "landfills" AND "municipal solid waste" OR "MSW." For the Brazilian SciELO database, the search incorporated the Portuguese keywords: "transporte de contaminantes" E "aterro" OU "aterros" E "resíduos sólidos urbanos" OU "RSU."

1.2.2 Search strategy and selection process

After identifying the documents in the databases, filters were made using the databases' automation tools: (i) year of publication, (ii) book chapters, and conferences. Duplicate studies were then removed using Zotero 6.0.1 software. Finally, the papers were screened to determine their adherence to the review's objective. This screening process involved three stages: title, abstract, and full text. The analysis was conducted following the inclusion and exclusion eligibility criteria.

1.2.3 Eligibility criteria

The selected studies were limited to papers published between 2019 and 2022 that reported on the transportation of contaminants in MSW disposal sites, specifically in English or Portuguese. To ensure the quality and relevance of the studies, exclusion criteria were applied for conference papers, systematic literature reviews, book chapters, duplicate papers, studies unrelated to the transportation of contaminants in landfills, and documents in languages other than English or Portuguese, as exemplified by Figure 1.1.

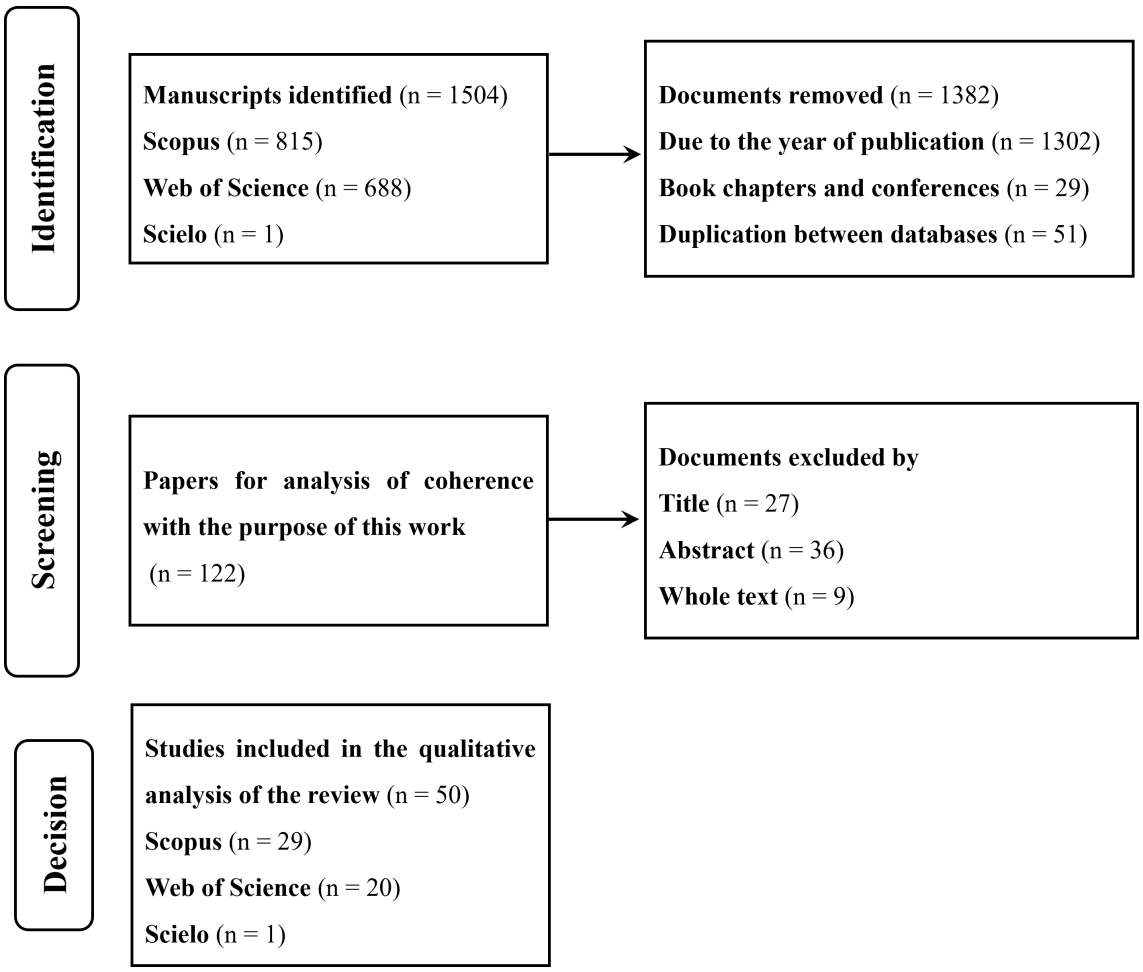

Figure 1.1: Identification of studies through databases.

1.3 Results and Discussion

1.3.1 Database

The literature search returned 1504 documents that were screened for eligibility. Of these, 1331 were excluded during the filters in the databases themselves, followed by 51 papers due to duplicate documents between the databases. After screening the titles and abstracts and reading the complete text, 72 papers were subtracted, resulting in 50 studies, as shown in Figure 1.1. The authors with the highest number of citations during the period under review are detailed in Table 1.1.

Table 1.1: Authors with the highest number of citations until March 2022.

Scopus		Web of Science	
Reference	Citations	Reference	Citations
Sun et al. (2020)	43	Sun et al. (2020)	40
Nika et al. (2020)	24	Chen et al. (2019)	25
Abbas et al. (2019)	19	Divya et al. (2020)	15
Feng et al. (2019)	16	Jarsjö et al. (2020)	15
Garg et al. (2020)	15	Abbas et al. (2019)	15

1.3.2 Bibliometric analysis

Figure 1.2 depicts that of the 50 papers reported in the period analyzed, 37.5% were from China, 10.7% from the UK, 7.1% from Brazil and India, and 5.4% from Canada, while Egypt, Italy, and Sweden 3.6% each. Notably, China had the highest contribution and the most authors with multiple institutional affiliations, with four double citations. The United Kingdom and the Kingdom of Saudi Arabia followed, each mentioned by the primary author once.

Figure 1.3 shows the connections related to each cluster of keywords. The keywords can be classified into four clusters: blue for "diffusion", red for "transport", green for "soil", and yellow for "contaminant transport". All the above start from "landfill".

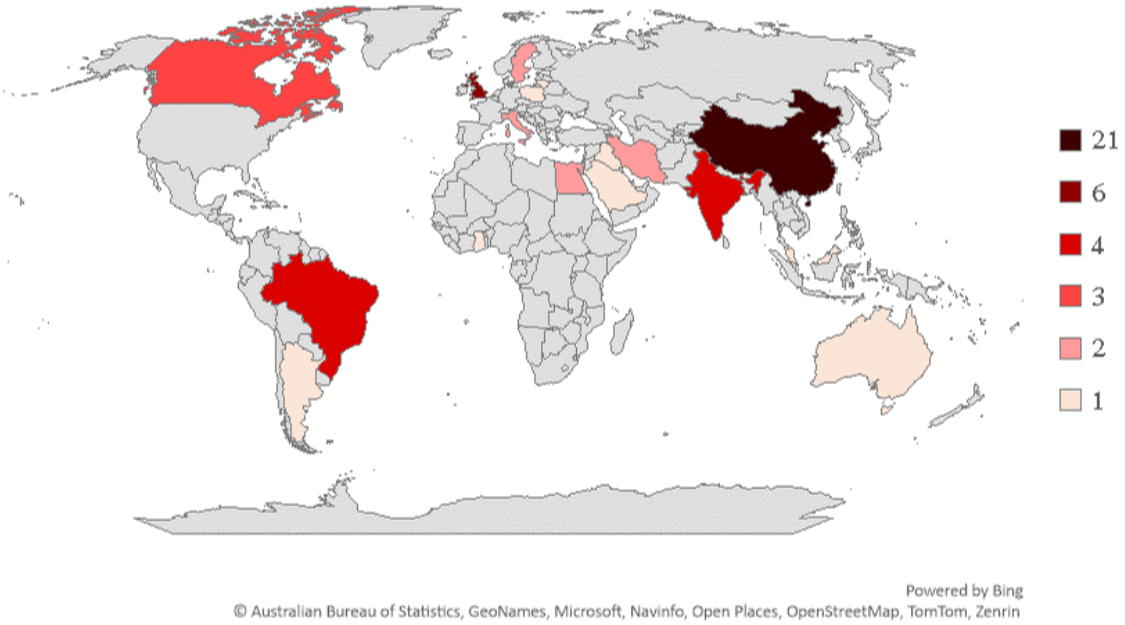

Figure 1.2: Number of publications by country involving the terms searched and the authors selected between 2019 and 2022.

The words "landfill" and "diffusion" are highlighted in blue. As mentioned above, transport by diffusion is widely studied in MSW disposal sites since attempts to reduce advection by installing low-permeability liners do not prevent transport by diffusion. Thinking of a landfill with protective liners, not surprisingly, the words "geomembrane" and "composite liner" also belong to the blue cluster. Other critical words highlighted are "porous media", "advection", "consolidation", and "analytical solution". All are closely related, but the last one stands out, in which authors have sought to update analytical solutions for contaminant transport already established in the literature that incorporate different parameters for different engineering solutions.

The yellow "contaminant transport" cluster features "municipal solid waste" and performance more prominently and "adsorption" less prominently. Perhaps because the keywords "transport" and "diffusion" exemplify different transport mechanisms or because of the complexity involved in the transport of contaminants, the keywords remained more general in the yellow cluster, as there is no doubt that the transport of pollutants in municipal solid waste depends on its performance. And its performance relies on a series of factors

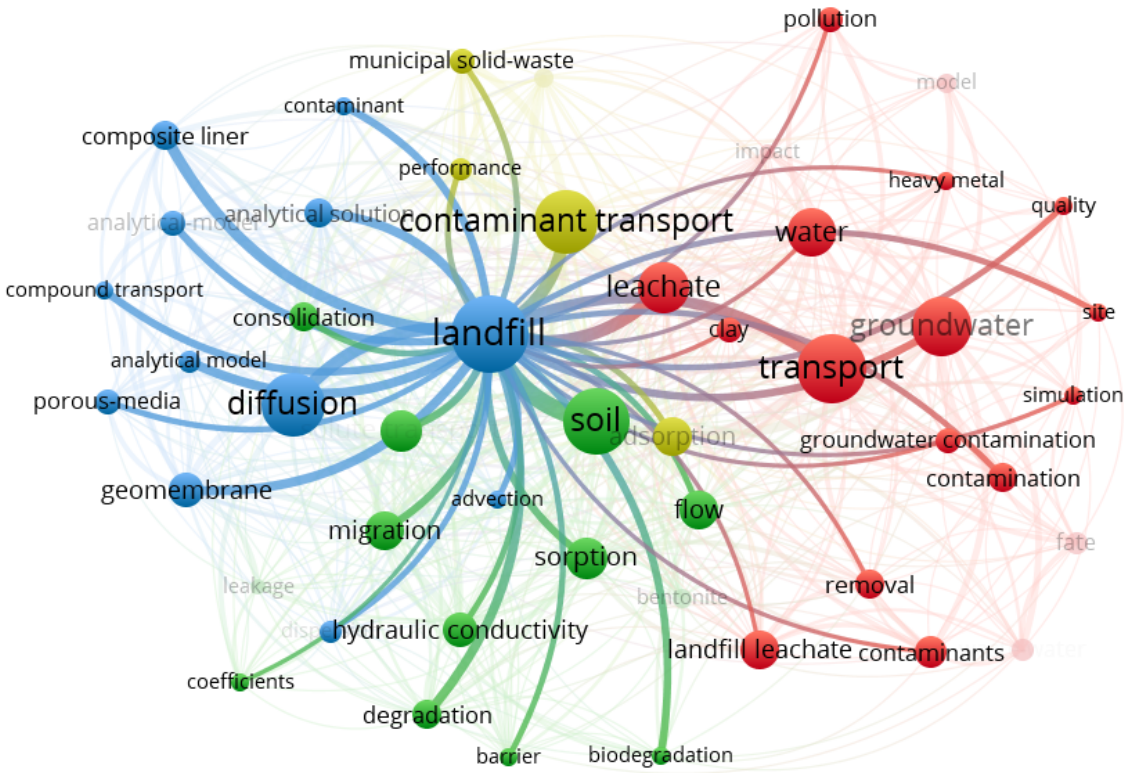

Figure 1.3: Division into clusters with the predominant keywords identified in the databases from the works previously selected.

such as "leachate", "flow", "hydraulic conductivity", "sorption", "advection", "diffusion", and "composite liner", among others that were part of other clusters, but which are also related to "contaminant transport", "performance" and "municipal solid waste", perhaps only summarized by the keyword "performance" in the yellow cluster.

The presence of the keywords "migration", "flow", "coefficients", and "hydraulic conductivity" in the green set "soil" is noticeable in almost all of the papers dealing with the migration of contaminants in porous media, both in manuscripts dealing with more conservative situations that do not involve chemical and attenuation processes, and those involving various other factors such as those dealt with by the other keywords "sorption", "degradation", and "biodegradation". This shows how wide-ranging the situations linked to the transport of contaminants through the soil and the considerations that authors need to make, with various factors acting concurrently, whether in the definition of parameters, which

transport mechanism can be considered dominant in a given situation, and which can be disregarded, whether there is chemical, biological, of retardation, attenuation or transport. These previous factors explain the challenges facing contaminant transport and attenuation mechanisms in the physical environment.

Finally, the red with the main keyword "transportation" focuses on the impacts generated on the physical environment due to the various transportation mechanisms, particularly on water resources, exemplified by the keywords "water" and "groundwater". The keywords related to the impact on water resources include "leachate", "landfill leachate", "contaminants", "contamination", "groundwater contamination", "quality", "heavy metal" and "pollution". These words illuminate the authors' concerns about surface and groundwater contamination. "Quality" can refer to both leachate and water quality. "Heavy metal" also stands out as one of the main components targeted by the research. This set of keywords also includes "clay", site, simulation, and removal, which can be related to managing and/or remediation of contaminated areas.

In short, keywords can be grouped into:

- Blue set: diffusion, containment barriers and analytical solutions;
- Yellow set: an overview of contaminant transport;
- Green set: transport mechanisms and soil attenuation;
- Red set: impact of contaminants on water resources.

Tables 1.2 to 1.19 contain information on the 50 papers analyzed within the specified period. The tables present details regarding the computer programs utilized for simulating contaminant transport, as well as for validating the models put forth by the respective authors. Additionally, the tables outline the tracers under investigation, their initial concentrations, and the simulation durations as reported in the papers.

Table 1.2: General characteristics of the studies selected between 2019 and 2022.

Reference	Computational Program	Pollutant/Target Tracer	Tracer Concentration	Simulation Time
Ahmed et al. (2019)	MODFLOW	Pb, Cr, Cu, and Ni	Pb: 0.305 mg/L Cr: 1.840 mg/L Cu: 0.602 mg/L Ni: 1.225 mg/L	From 30 days to 1 year
Bortone et al. (2019)	COMSOL Multiphysics	Benzene Toluene	Benzene: 9 µg/L Toluene: 60 µg/L	5, 15, 20, and 100 years
Chen et al. (2019)	Development of an analytical solution, validated through the HYDRUS-1D program	Acetone	100 µg/L	2, 5, and 10 years for model verification with experimental 50 years for model verification with HYDRUS 1D. Up to 1000 years for behavior prediction
de Oliveira et al. (2019)	MPHMTP (Multiphase Heat and Mass Transfer Program)	TiO_2, SiO_2, CuO, and ZnO	250, 500, 750, 1000, 1500, 2000, 4000, 6000, and 8000 mg/L	700 min
Dominijanni & Manassero (2019)	Development of analytical solutions	Toluene	The authors do not inform the initial value of the concentration, they used the relative concentration	Authors' focus was spatial rather than temporal, involving various configurations for landfill liners
Feng & Jin (2019)	MODFLOW (2000)	Sulfate ions	5000 mg/L	16 years. From January 2015 to December 2030

Table 1.3: The general characteristics of the studies selected between 2019 and 2022 (continuation).

Reference	**Computational Program**	**Pollutant/Target Tracer**	**Tracer Concentration**	**Simulation Time**
Feng et al. (2019)	Authors present analytical solution for the transport of organic contaminants in different engineering liner configurations	Toluene	1 mg/L	Up to 1000 years (time needed to reach the breakthrough curve)
Fonseca et al. (2019)	Use of semi-analytical solution in pure diffusion and sorption tests	Cl, K, Na, and NH_4	Cl: 4157.8 mg/L K: 1525 mg/L Na: 2625 mg/L NH4: 357.06 mg/L	1.06, 2.01, and 3.07 days
Naveen et al. (2019)	fluidyn-Pollusol	Iron	100 mg/L	From 25 hours to 60 days
Rowe & Abdelrazek (2019)	SEEP/W CTRAN/W POLLUTE	Chloride	1500 mg/L (for 150,000 t/ha) and 2500 mg/L (for 250,000 t/ha)	250 years
Samad et al. (2019)	MODFLOW	Cd, Cr, Hg, Pb, and Zn	Not mentioned	Investigated the spatial distribution
Shu et al. (2019)	Proposal of a method to calculate the analytical breakthrough time. Validated with Dtransu 2D software	Chemical Oxygen Demand (COD)	20 mg/L	50 years

Table 1.4: The general characteristics of the studies selected between 2019 and 2022 (continuation).

Reference	**Computational Program**	**Pollutant/Target Tracer**	**Tracer Concentration**	**Simulation Time**
Slavinskienė et al. (2019)	Microsoft Excel add-in module XLSTAT for statistical analysis	NH_4, Fe, K, and Cl	Not reported	Focus was on attenuation distance in different aquifers
Uddh Söderberg et al. (2019)	Visual MINTEQ	As, Cd, Pb, and Sb	The authors used various average concentrations depending on the depth sampled. The highest concentrations were found in the 0 to 1.5 m depth interval, reported here: As: 140 mg/kg Cd: 13 mg/kg Pb:1700 mg/kg Sb: 38 mg/kg	100 years
Xie et al. (2019)	COMSOL Multiphysics, used to compare with the proposed analytical solution	Methane gas	Not available	The focus of the work was depth, but there was a simulation with 10 days in order to ascertain the time to reach the steady-state

Table 1.5: The general characteristics of the studies selected between 2019 and 2022 (continuation).

Reference	Computational Program	Pollutant/Target Tracer	Tracer Concentration	Simulation Time
Balbarini et al. (2020)	COMSOL Multiphysics	13 key pharmaceuticals (mainly sulfonamides, barbiturates, and ethyl urethane)	The authors noted that not enough data was available to conduct numerical simulations. Therefore, they opted to simulate the local hydrogeology and investigate groundwater flow combined with statistical analyses of pharmaceutical contaminant concentrations	The work centered on the particular distribution of the contamination plume towards the Grindsted stream
Ding et al. (2020)	Development of two analytical models with cutoff walls. COMSOL Multiphysics to validate the model	Toluene	1 mg/L to validate the model. A function that varies with depth (z) was used for the simulations: $C=C_{in,max} \times \exp(-(z-\mu)/2\sigma^2)$. The authors assigned a maximum concentration of 10 mg/L ($C_{in,max}$) and a breakthrough concentration of 1 mg/L ($C_{cw,max}$). The breakthrough time was set at the ratio $C_{cw,max}/C_{in,max}=0.1$	2 years to validate with analytical model and 100 years to validate with COMSOL Multiphysics. 200 years of simulation implementing analytical models

Table 1.6: The general characteristics of the studies selected between 2019 and 2022 (continuation).

Reference	**Computational Program**	**Pollutant/Target Tracer**	**Tracer Concentration**	**Simulation Time**
Divya et al. (2020)	MODFLOW	Chloride	100 mg/L	1 year (2017–2018)
Dong et al. (2020)	Development of own framework	Chromium	30.65 mg/m^3 for the source and 10 mg/m^3 for other areas	6 years. From 2010 to 2015
Faisal et al. (2020)	COMSOL multiphysics	Cd	50 mg/L	100 years
Fandiño et al. (2020)	MODFLOW	Cr, Cu, Pb, and Zn	Cr (mg/L) RL 0.64, ET $<$ 0.05; Cu (mg/L) RL 0.65, ET $<$ 0.03 RT; Pb (mg/L) RL 0.40, ET 0.20; Zn (mg/L) RL 2.80, ET 0.05. RL: the concentration of raw leachate. ET: the concentration of effluent treatment system.	50 years
Feng et al. (2020)	Study of an analytical model with experimental data	Multicomponent gas (CH_4, O_2, CO_2, and N_2)	The authors considered the concentration of each component at the landfill gas source: CH_4: 20.72 mol/m^3 O_2: 0 mol/m^3 CO_2: 20.72 mol/m^3 N_2: 0 mol/m^3	The authors analyzed contamination by depth

Table 1.7: The general characteristics of the studies selected between 2019 and 2022 (continuation).

Reference	Computational Program	Pollutant/Target Tracer	Tracer Concentration	Simulation Time
Francisca & Glatstein (2020)	The authors developed two transport models: high and low permeability liners	The paper does not specify the metals used in the proposed analytical solution, but uses experimental results for Cd, Cu and Pb for the modeling	1 mg/L	Modeling of reactive filters and permeable reactive barriers: 150 years. Modeling of bottom liners in landfills: 1400 years to evaluate different hydraulic conductivities. 250 years for the same hydraulic conductivity and different hydraulic heads (leaching heights)
Garg et al. (2020)	MATLAB	Chlorides, Zn, Fe, Pb, and Cu	Chloride: 4000 ppm Zn: 3.2 ppm Fe: 73.6 ppm Pb: 19.4 ppm Cu: 62.6 ppm	100 years
Guarena et al. (2020)	Proposal for an analytical solution	NaCl	The work only reports the zero concentration downstream of the simulated landfill	The authors do not verify the variation over time. They compared the relative concentrations of the leachate pond with the contamination downstream of the landfill, using various combinations of materials as landfill liners

Table 1.8: The general characteristics of the studies selected between 2019 and 2022 (continuation).

Reference	Computational Program	Pollutant/Target Tracer	Tracer Concentration	Simulation Time
Hagan & Darko (2020)	MODFLOW	There was no specific study of a pollutant but a hydrogeological study. The flow velocity was investigated and associated with the potential transport of contaminants	The authors did not investigate a specific pollutant	From 7 to 833 years
Hassanzadeh et al. (2020)	Development of a computer model using UFV (upwind finite-volume)	Cl^-, Na^-, K^+, and Total Organic Carbon (TOC)	The authors mention the concentrations in the leachate, but do not specify those used in the simulations. Na: 2541 mg/L K: 5166 mg/L Cl: 3456 mg/L TOC: 1783 mg/L	Work focuses on the vertical and horizontal spread of the contamination plume
Jarsjö et al. (2020)	MODFLOW	Pb and As	Concentration in soil: Pb: 780 mg/kg As: 2300 mg/kg Concentration in water: Pb:0.0781 and 0.0071 g/m^3 As (V): 3.4 g/m^3 As (III): 77.0 g/m^3	41 years

Table 1.9: The general characteristics of the studies selected between 2019 and 2022 (continuation).

Reference	Computational Program	Pollutant/Target Tracer	Tracer Concentration	Simulation Time
Lin & Yeh (2020)	The authors developed an analytical model. They compared it with a finite difference solution and other existing models. However, they suggest using MATLAB or Mathematica software to implement the model presented	The research was validated by two studies. For the first one, the work does not specify the tracer when validating with the research by Chen et al. (2019). When validating with the work of Park et al. (2012), it uses 5 VOCs (volatile organic compounds): dichloromethane, methyl tertiary-butyl ether, trichloroethylene, toluene, and chlorobenzene with constant concentration co: 0.1 kg/m^3	The authors used relative C/Cpeak concentration when validating with the work of Chen et al. (2019). VOCs: 0.1 kg/m^3	1, 5, and 10 years to validate with Chen et al. (2019), with 100 years for parameter sensitivity analysis. 400 days to compare with Park et al. (2012)

Table 1.10: The general characteristics of the studies selected between 2019 and 2022 (continuation).

Reference	Computational Program	Pollutant/Target Tracer	Tracer Concentration	Simulation Time
Mahallei & Badv (2020)	POLLUTE	Chlorine	The authors used different mixtures of sand and bentonite. In the validation stage, each test was carried out in duplicate with different initial concentrations: 3% bentonite and 97% sand: 1825 mg/L and 2085 mg/L 6% bentonite and 94% sand: 1975 and 1900 mg/L 3% brick clay, 12% bentonite and 85% sand: 10200 mg/L for both No information on the initial concentration in the simulation by depth	45 s to validate with the numerical solution provided by POLLUTE. After validation, the authors aimed to simulate the variation in concentration by depth along the soil profile

Table 1.11: The general characteristics of the studies selected between 2019 and 2022 (continuation).

Reference	Computational Program	Pollutant/Target Tracer	Tracer Concentration	Simulation Time
McWatters et al. (2020)	POLLUTE	Aroclor - PCB (polychlorinated biphenyl)	Several situations to validate the modeling Situation 1 (Influence of leachate concentration): Different concentrations were analyzed to adjust the modeling, up to the limit value of 240 ug/L Situation 2: (Influence of variable Darcy velocity and leachate collected) co:8 ug/L (specimen A) and co:50 ug/L (specimen B) provided the most reasonable comparison between the model and the concentrations observed in the CCL Situation 3: Influence of increasing leachate heads For cell 1, based on the insights from the modeling in scenarios 1 and 2, the modeling of scenario 3 was based on co:8 ug/L (sample A) and 50 ug/L (sample B). *	Up to 25 years for parameter fitting and model validation Up to 6000 years in simulations

Table 1.12: The general characteristics of the studies selected between 2019 and 2022 (continuation).

Reference	Computational Program	Pollutant/Target Tracer	Tracer Concentration	Simulation Time
McWatters et al. (2020) - continuation			*Concentrations used in the modeling of each cell: 3 ug/L; 8 ug/L; 50 ug/L; 60 ug/L; 160 ug/L; 192 ug/L.	
Podlasek et al. (2020)	HELP (Hydrologic Evaluation of Landfill Performance) for modeling the unsaturated area MODFLOW 2005 and MT3DMS for modeling the saturated region and contaminant transport	Ammonium and nitrate ions	80 kg N/ha (kg of nutrient per hectare)	5 years for the hydrological balance Up to 20 years for simulation
Pu et al. (2020)	Developing an analytical solution. CST3 and POLLUTE to check the analytical solution	Benzene	100 ug/L	Up to 100 years to validate the analytical solution Between 200, 300, and 1000 years, depending on the simulated boundary condition

Table 1.13: The general characteristics of the studies selected between 2019 and 2022 (continuation).

Reference	Computational Program	Pollutant/Target Tracer	Tracer Concentration	Simulation Time
Ding et al. (2021)	Development of an analytical model COMSOL to compare with the proposed analytical solution	The authors simulate four scenarios. For each one, they exemplify a type of pollutant, but they don't make it clear whether they use them in the simulations Scenario 1. Finite pulse injection to simulate pesticides Scenario 2. Describe sewage leaking from tanks and/or pipes Scenario 3. Simulating the decay of radioactive contaminants Scenario 4. Coupled with the situation of instant contaminant injection with leakage	Authors have varied the rate of contaminant injection and the number of injection points as pollutant sources	From 1000 to 1500 days depending on the simulated condition

Table 1.14: The general characteristics of the studies selected between 2019 and 2022 (continuation).

Reference	Computational Program	Pollutant/Target Tracer	Tracer Concentration	Simulation Time
El-Mathana et al. (2021)	The Groundwater Modeling System (GMS) and MODFLOW	Total Dissolved Solids (TDS) Lead, Boron, Nitrate, Manganese, and Chemical Oxygen Demand (COD)	*	20 years to calibrate the model and 100 years of simulation

*** Tracer Concentration**

Study area (mg/L)	Pond (mg/L)	IsmailiaCanal (mg/L)	Dumpsite (mg/L)
TDS: 200	500	300	30000
COD: 2	2	10	10000
Nitrate: 0.5	0.5	1.5	2
Manganese: 0.2	0.5	0.25	1
Boron: 0	0	0.28	2
Lead: 0	0	0.065	0.02

Table 1.15: The general characteristics of the studies selected between 2019 and 2022 (continuation).

Reference	Computational Program	Pollutant/Target Tracer	Tracer Concentration	Simulation Time
Ma et al. (2021)	MATLAB	Dissolved organic matter (DOM)	There was no initial concentration Samples were collected from monitoring wells at 12 landfills and analyzed by fluorescence	The simulations focused on identifying the spread of DOM in different origins
Ozelim et al. (2021)	Development of an analytical solution using Python	Copper and zinc	The authors use various initial concentrations for validation. In the result called "properly modeling the sorption isotherm" by the authors, the initial concentration was 800 mg/L	10^4 hours
Peng et al. (2021)	New analytical model for organic contaminant transport. COMSOL Multiphysics for model validation	Toluene	0.054 mol/m^3	1000 years

Table 1.16: The general characteristics of the studies selected between 2019 and 2022 (continuation).

Reference	Computational Program	Pollutant/Target Tracer	Tracer Concentration	Simulation Time
Rowe & Barakat (2021)	Two approaches: using the POLLUTE V7 analytical model and the SEEP/W and CTRAN/W finite element numerical solutions	Perfluorooctane sulfonate (PFOS)	Case study I - varying transmissivity: co:4800 ng/L Case study II - varying the initial concentration co (mg/L): 4800, 160, 740, 1670	Case I (years): 220, 215, 135, and 170 Case II A (years): 220, 510, 345, 280 Case II B (years): 135, 245, 185, 160
Singh & Rajput (2021)	Application of the analytical solution in three case studies. No computer program was provided	Not reported	Case 1: background concentration: 0.1 mg/L pollutant concentration: 1 mg/L Case 2: background concentration: 0.1 mg/L for the first layer, and 0.001 mg/L for the second one pollutant concentration: 1 mg/L Case 3 background concentration: 0.1 mg/L for the first layer, and 0.001 mg/L for the second and third layers pollutant concentration: 1 mg/L	Case 1: 2 and 3 years Case 2: from 1 to 5 years Case 3: 2 years

Table 1.17: The general characteristics of the studies selected between 2019 and 2022 (continuation).

Reference	Computational Program	Pollutant/Target Tracer	Tracer Concentration	Simulation Time
Yan et al. (2021a)	Proposed analytical solution for non-isothermal diffusion in an unsaturated composite liner. COMSOL Multiphysics to validate the analytical solution	Cl^- and DCM (Dichloromethane) to validate the simulations Benzene used in the simulations	Cl^-: 0.1 M DCM: 1 mg/L Benzene: 1 mg/L	10 and 20 years
Yan et al. (2021d)	Analytical model for contaminant transport coupled with consolidation settlement in a clay liner under transient conditions. COMSOL Multiphysics to validate the analytical solution	Not informed to validate results with COMSOL software Br^- to validate with experimental data Not mentioned for simulations	Validation: 1 mg/L Br: 961.6 mg/L	10, 20, and 50 years to validate the model Up to 100 years for simulations

Table 1.18: The general characteristics of the studies selected between 2019 and 2022 (continuation).

Reference	Computational Program	Pollutant/Target Tracer	Tracer Concentration	Simulation Time
Yan et al. (2021b)	Development of an analytical model for organic contaminant transport coupling consolidation and diffusion COMSOL Multiphysics to validate the proposed model	Not informed for validation with experimental results Dichloromethane (DCM) to validate with COMSOL	Validation with experimental: 100 mg/L Validation with COMSOL: 1 mg/L	2 years to validate with experimental 10 years to validate with COMSOL Up to 200 years in simulations
Yan et al. (2021c)	2D analytical solution for contaminant transport through cutoff walls	Toluene (TOL)	10 mg/L	50, 200, and 250 years
Zhang et al. (2021)	Use of existing analytical solutions	Chloride and ammonia-nitrogen for model validation	NH_4−N: 200-250 mg/L Chloride: 750-808 mg/L	18000 days
He et al. (2022)	MODFLOW	Cu_2^+	0.014 mg/L	From 1 to 10 years

Table 1.19: The general characteristics of the studies selected between 2019 and 2022 (continuation).

Reference	Computational Program	Pollutant/Target Tracer	Tracer Concentration	Simulation Time
Wang et al. (2022)	COMSOL Multiphysics to validate the model	Potassium bromide (KBr)	For validation: Br^-: 1672 mg/L K^+: 259 mg/L In the simulations: Br^-: 10 mol/m^3 = 799 mg/L K^+: 10 mol/m^3 = 391 mg/L	18 days
Yan et al. (2022)	Proposed analytical solution	Toluene (TOL) and Dichloromethane (DCM)	1 mg/L	Analyzed in terms of depth
Yong et al. (2022)	HYDRUS-1D	Cadmium (Cd), copper (Cu), lead (Pb), and zinc (Zn)	Cd: 1 mg/L Cu: 2.3 mg/L Pb: 2.8 Zn: 7 mg/L	120, 150, and 180 days for results validation 10, 20, 30, 40, 50, and 100 years applied in the simulations

The computer programs used in the works analyzed are depicted in Figure 1.4. Notably, COMSOL Multiphysics accounted for 26% of the programs, MODFLOW for 23%, and POLLUTE for 13%. These software solutions employ distinct methodologies for solving the equations governing contaminant transport, with COMSOL Multiphysics utilizing the finite-element method, POLLUTE, produced by Rowe & Booker (1984) employing the finite-layer method, and MODFLOW relying on the finite-difference method. It is worth noting that COMSOL Multiphysics and POLLUTE are commercial software, while the U.S. Geological Survey (USGS) is the developer of MODFLOW.

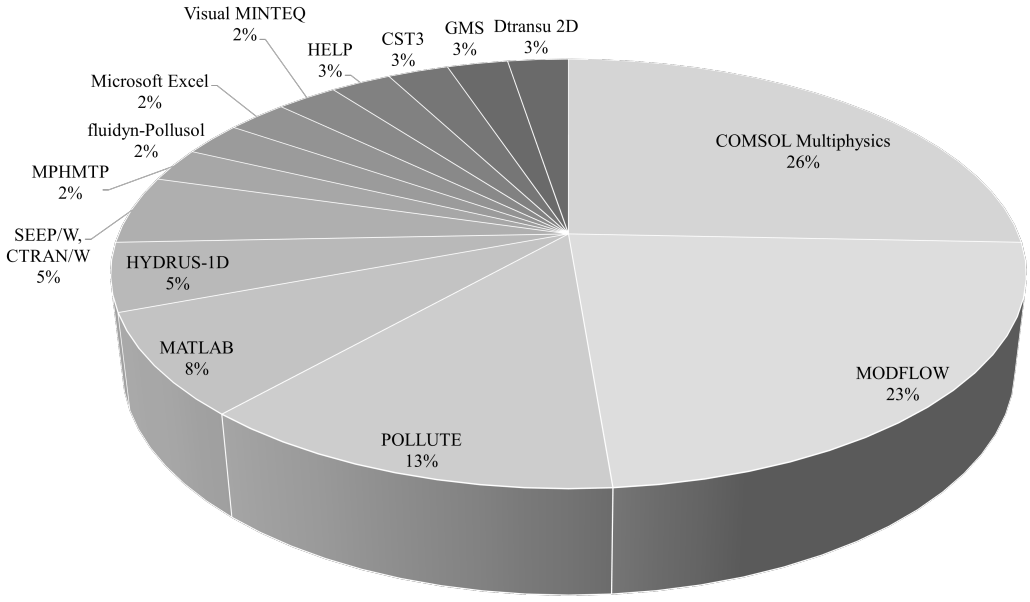

Figure 1.4: Programs used for the simulations or validation of simulations involving the transport of contaminants from the works selected between 2019 and 2022.

MSW disposal sites are complex systems that generate leachate and gas, iterate with the physical environment, and depend on local climatic conditions such as temperature and rainfall. These factors affect many phenomena and parameters to be considered in the simulations, leading to challenging numerical solutions with high computational demands and greater complexity in validating the results. Therefore, choosing representative pollutants and understanding the main transport phenomena associated with the contaminant and the

physical environment in which transport occurs is essential. The same considerations apply to the selection of software, the choice of which depends on the complexity of the problem.

COMSOL Multiphysics is a highly robust program widely recognized for its ability to analyze unsaturated materials and can couple different phenomena to the contaminant transport such as settlement, reactive pollutants (organic and inorganic), gas, and heat generation, among others, in addition to allowing complex geometries and different boundary conditions. On the other hand, it requires a significant licensing investment, high computational demand, and user training (Bortone et al., 2019; COMSOL Multiphysics, 2019; Xie et al., 2019).

MODFLOW is a free groundwater flow tool capable of simulating large areas. Widely used by industry and academia, when coupled with MT3DMS, it is able to simulate the contaminant transport. Aimed at the saturated zone of the physical environment, it is also capable of estimating pumping parameters, which are often used to validate the simulations with data from monitoring wells. This is also a limitation since it is not possible to simulate unsaturated zones, and it is not possible to couple different physical phenomena such as gas generation, heat, and geomechanics (Harbaugh, 2005; Bear & Cheng, 2010; Ebrahim et al., 2019).

Unlike its predecessors, POLLUTE is geared towards 1D simulations, especially for the flow and fate of contaminants in MSW disposal site layers. It can handle steady-state and transient flow simulations at a low computational cost. The software can assess the performance of flow barriers, the efficiency of geomembranes, as well as the combined use of different solutions, including remediation. However, due to its simplicity, it cannot simulate unsaturated conditions, extensive areas, or intricate environments that necessitate integrated analysis involving gas generation, heat, and geomechanical considerations (Shackelford et al., 1989; Shackelford & Daniel, 1991; Rowe & Booker, 2004).

The most reported tracers in the period analyzed are illustrated in Figure 1.5 and the group to which they belong in Figure 1.6. With 41% of the papers, the use of heavy metals was notable, including Pb, Cu, Cr, Cd, and Zn with 30% of the elements cited. Among the inorganic and non-heavy metals, chlorides stood out, with 9% of use being over 26% of the surveyed period. They were followed by organic elements, which accounted for 24% of

the total. Toluene and dichloromethane accounted for 13% of the total and were the most prevalent organic elements. The use of gases as tracers was lower, with 9% of the total, and methane stood out with 3% of the target tracers.

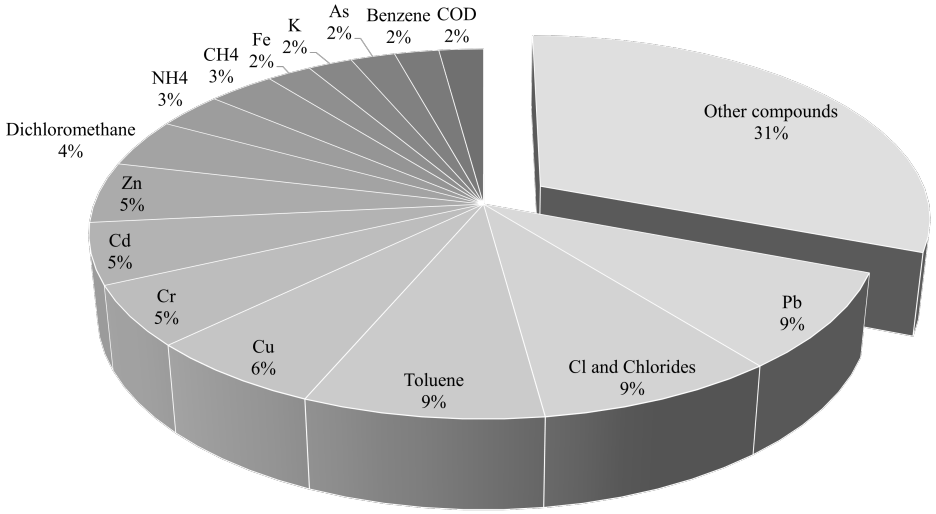

Figure 1.5: Main tracers used by the authors of the papers picked between 2019 and 2022.

Given the heterogeneity of the generated leachate and the challenges associated with working with it in natura, using a wide variety of tracers has proved common. The 41% of studies that used heavy metals as target pollutants show how important and damaging they are to the environment. Additionally, organic contaminants were the subject of nearly a quarter of the studies. While the use of gases as tracers is currently limited, substantial potential exists for further exploration in this area.

It should be noted that specific authors have employed multiple tracers with varying characteristics. For instance, one tracer may have been utilized to validate the simulations, while another was used to conduct them (Yan et al., 2021; Yan et al., 2021a). This practice may stem from the challenges associated with handling heavy metals and organic tracers, which often necessitate the recurrent use of conservative tracers due to their inert nature and

limited affinity for sorption and chemical reactions (Morita & Wendland, 2019; Divya et al., 2020; Hassanzadeh et al., 2020).

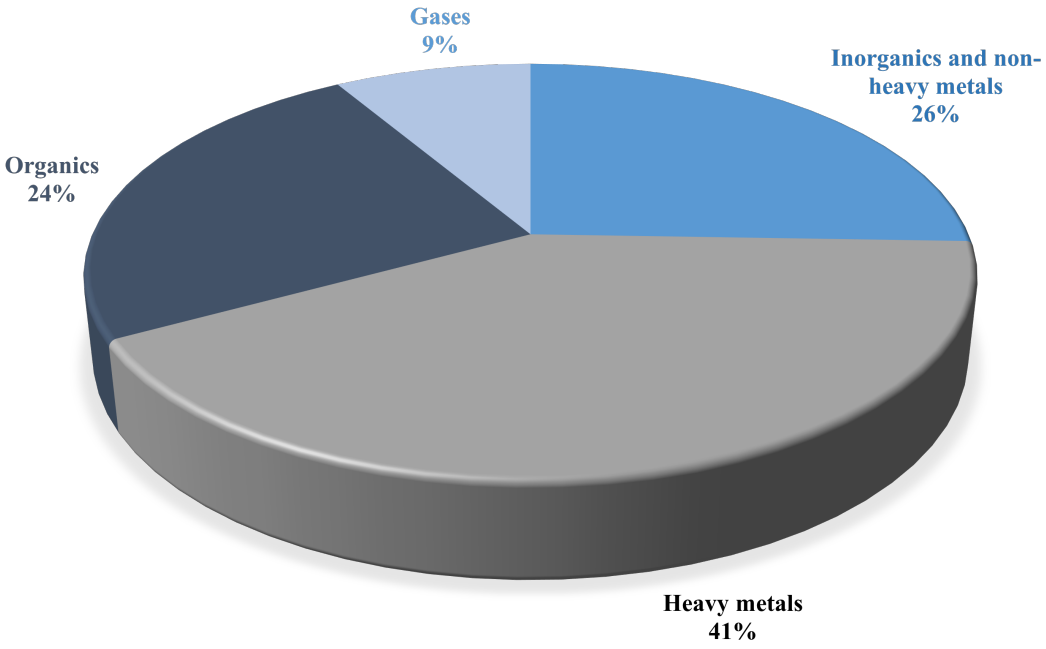

Figure 1.6: Predominant group of chemical compounds utilized in the period under review.

Heavy metals are persistent in the environment and bioaccumulate in the food chain. A carcinogen and highly toxic even at low concentrations, lead has been the central heavy metal targeted in research. Due to its low mobility and susceptibility to sorption, precipitation, and pH-dependent behavior, using lead as a tracer presents significant challenges. It is typically used in research involving reactive conditions and long-term contamination, especially near polluting sources. Pb is most susceptible to the adverse effects of exposure in children and pregnant women and is found in batteries, cigarettes, industrial waste from iron and steel production, paints, and waste incineration. In children it is associated with neurological damage, attention deficit disorder and aggression, in pregnant women it can lead to problems in the fetus such as malformations, stillbirth, and premature birth (Lanphear et al., 2005; WHO, 2019; National Institutes of Health, 2021).

As widely used as Pb, chlorine and its derivatives are conservative tracers not subject to chemical and biological reactions, and with high mobility, they are generally used in

advective-dispersive transport. However, they have also been utilized in works involving diffusion, as evidenced by Mahallei & Badv (2020), which endorse chlorides as tracers to avoid cation exchange in the soil. Widely used as a disinfectant in water treatment, as a household cleaner, and in bleaches, chlorine is not reported to be carcinogenic, and there are no studies on the consequences of its exposure on fetuses, children, or during pregnancy. The commonly reported consequences of short-term exposure are related to irritation of the eyes, skin, and respiratory system, while long-term exposure can cause severe lung damage (US EPA, 1994; ATSDR, 2010).

Volatile organic compounds (VOCs) accounted for most of the organic components cited in the studies, with toluene, dichloromethane, and benzene accounting for 15% of the total chemical substances reported in the studied period. Widely used by industry as a solvent, toluene is little affected by the sorption effect, proving to be mobile in the liquid and gas phases. It is recurrent in studies aimed at natural attenuation because it is biodegradable under anaerobic conditions. Dichloromethane is also widely used in industrial processes as a degreasing agent and in the pharmaceutical industry. Because it has a low Kow (octanol-water partition), is very soluble in water, and has a high vapor pressure, it spreads quickly through saturated and unsaturated zones, making it a critical tracer in situations involving high mobility, e.g., MSW disposal sites with a high hydraulic head or gas emission studies. Carcinogenic and widely found in petroleum products, benzene can move through the liquid and gaseous phases and is persistent in the environment. It is suitable for long-term simulations, poses a high risk to human health, and is resistant to anaerobic biodegradation conditions, making it a particular target for investigations in low-oxygen environments such as landfills (Roberts et al., 1986; Banzhaf & Hebig, 2016; Bright et al., 2000).

As noted above, VOCs are toxic and carcinogenic substances and can migrate in the aqueous and gaseous phases. Toluene is non-carcinogenic and can cause neurological, respiratory, and skin problems in acute exposures. In contrast, chronic exposures can lead to reduced cognitive capacity, liver and kidney damage, and interfere with the development of fetuses, with consequent developmental problems in children (US EPA, 2005; ATSDR, 2017). Acute exposure to dichloromethane can lead to damage to the central nervous system,

irritation to the eyes, skin, and respiratory system, and intoxication when processed by the liver, consequences that worsen with long-term exposure and add to cardiovascular problems (ATSDR, 2000; US EPA, 2011). Short-term exposure to benzene leads to effects similar to those caused by toluene, with the aggravating factor of causing a drastic reduction in red blood cells, which can develop into anemia when exposure is very high, in addition to being a known carcinogen of leukemia, chronic exposure can also lead to severe damage to the bone marrow, as well as developmental problems in fetuses and children (US EPA, 2003; ATSDR, 2007).

In addition to the organic substances mentioned above, methane (CH_4) was the most recurrent gas during the period studied. This primary gas, produced during the anaerobic digestion of organic matter, is not very soluble in water and is highly mobile in the vadose zone. One of the leading gases generated in MSW disposal sites and one of those responsible for the greenhouse effect, it has high environmental and economic appeal, as it can be captured to produce energy.

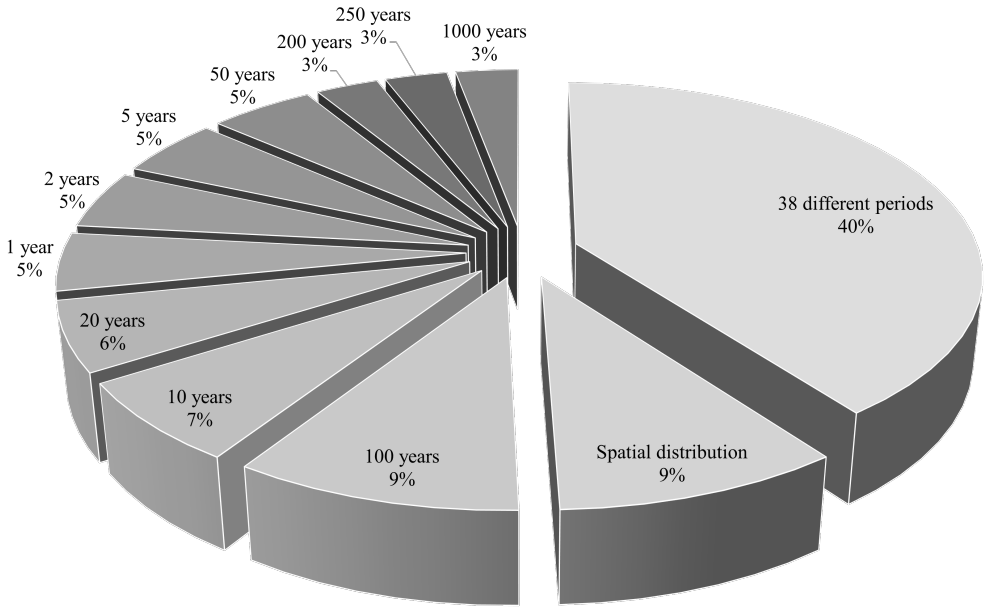

Figure 1.7: Different simulation times applied by the authors.

Concerning time intervals in Figure 1.7, a century was the period most adopted by the authors, with 9% of the total, followed by 10 and 20 years, with 7% and 6% of the approaches, respectively. The studies that aimed to determine the plume's path in the horizontal and vertical directions achieved the same 9%. Another 40% had different simulation intervals, ranging from 45 seconds (Mahallei & Badv, 2020) to six millennia (McWatters et al., 2020). It should be noted that several studies simulated different years and, in some cases, together with analyses of the spatial spread of the contamination plume, such as the studies by Xie et al. (2019) and Ding et al. (2020).

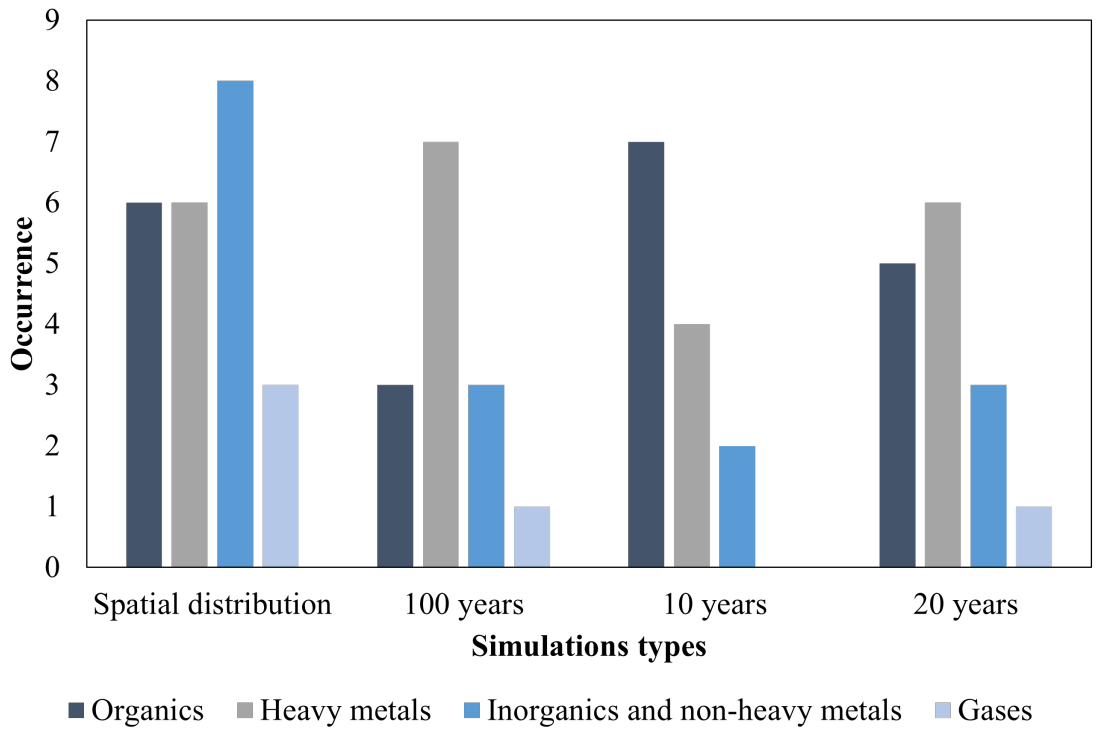

Figure 1.8: Tracer groups' occurrences in the most frequently reported types of simulations during the analyzed period.

The commonly utilized tracers during prevailing periods, as well as their use in the spatial distribution of contaminants, are shown in Figure 1.8. Tracers were widely applicable across all categories of pollutants, including organic compounds, heavy metals, inorganic and non-heavy metals, and gases, except for gases in 10-year simulations. The spatial distribution analysis revealed the highest frequency of occurrences for inorganic tracers and non-heavy

metals (eight occurrences), followed by organic tracers and heavy metals (six occurrences) and gases (three occurrences). When predicting behavior over 100 years, heavy metals were the predominantly used tracers, with seven occurrences, matching the usage frequency of organic tracers in 10-year simulations. At 20 years, occurrences were less frequent but more evenly distributed, with six occurrences of heavy metals, five of organic tracers, three of inorganic non-heavy metals, and one occurrence of gas tracers.

Naturally, gases would be less reported since they were a minority among the tracers used, and the same reasoning applies to the other tracers. Heavy metals have been preferred in 100-year simulations, likely due to their persistent nature and accumulation in the trophic chain, posing significant risks to fauna and flora. However, as explained above, all tracers have been widely used. Selecting the appropriate tracer or tracers is a critical and challenging consideration, as each possesses unique peculiarities, such as different mobilities, physicochemical properties, and reactions with the environment, being governed by various physical, chemical, and biological phenomena, with their use depending on the objective of the authors and, as Rosqvist & Bendz (1999), citeWoodman2015 and Woodman et al. (2017) show, the choice of tracer type is fundamental to the success of research involving contaminant transport, not only in analytical and numerical analyses but also in field and laboratory tests, which subsidize the parameters of the simulations.

The number of studies returned by the keywords showed that MSW disposal sites are still one of the predominant destinations for municipal solid waste, garnering significant attention from several researchers in situations ranging from engineering liners to MSW disposal sites without protective layers. The analysis indicates a notable emphasis on developing analytical solutions in different configurations of protective liners that comply with various environmental legislations, such as the work by Rowe & Barakat (2021) that addresses the legislations of the American states of Texas, California, Michigan, and New York, the provinces of British Columbia and Ontario in Canada, as well as Australia and Europe. Of the 50 articles analyzed, 24 focused on developing analytical solutions.

The studies also elucidated that understanding the transport phenomena associated with them and their interaction with the environment is crucial in addition to the choice of

tracers. For example, Rowe & Abdelrazek (2019), endorsed by Giroud & Morel (1992) and Chappel et al. (2012), warn about the importance of advection transport. Neglecting this aspect would mean an unattainable rigor in executing the MSW disposal site. The authors illustrate the example of geomembranes, which ideally should only result in transport by diffusion. However, due to their construction, they may have wrinkles and holes, inevitably leading to percolation by advection in these places. Podlasek et al. (2020) points out that success in predicting the contamination plume only occurs when the main transport mechanisms are well-defined.

The authors addressed several crucial points during the study period, including the consideration of unsaturated layers (Chen et al., 2019; Yan et al., 2021a), thermodiffusion (Jones & Rowe, 2016; McWatters et al., 2016; Peng et al., 2021), and advection induced by consolidation (Meric et al., 2017; Wang et al., 2022; Yan et al., 2022), as well as emerging contaminants such as pharmaceutical and personal care products (Yu et al., 2021; Dai et al., 2020).

Understanding the seepage of the contamination plume in MSW disposal sites is complex, depending on the characteristics of the physical environment, the contaminants involved, the layers of protection (or lack thereof), and the execution and maintenance of the MSW disposal sites. The authors' efforts have focused on understanding the application possibilities and limitations of both the software and the analytical models used, whether for use in projects, evaluating the behavior of MSW disposal sites in operation or closed down, or even remediating them.

1.4 Conclusions

This study aimed to enlighten the frontiers of knowledge regarding the transport of contaminants involving MSW disposal sites using analytical and numerical modeling, as well as both of them. The following key findings were observed:

(i) The most widely used programs for numerical analysis and validation of analytical solutions were COMSOL Multiphysics, MODFLOW, and POLLUTE.

(ii) Researchers primarily focused on heavy metals as tracers, followed by inorganic and non-heavy metals, organics, and gases.

(iii) Lead, chloride, chlorides, and toluene were the most commonly used tracers.

(iv) The predominant analysis periods were 100, 10, and 20 years and spatial analysis. The joint tracer-simulation time analysis revealed heavy metals as the primary focus of the 100-year simulations, organic tracers in the 1-decade simulations, and a similar distribution of tracers in the 2-decade simulations and those with spatial distribution as their target.

References

Ahmed, A. T., Alluqmani, A. E., & Shafiquzzaman, M. (2019). Impacts of landfill leachate on groundwater quality in desert climate regions. *International Journal of Environmental Science and Technology*, 16(11), 6753–6762.

ATSDR (2000). Public health statement - Methylene Chloride. *US Department of Health and Human Services. Agency for Toxic Substances and Disease Registry-ATSDR*, (pp. 1–12).

ATSDR (2007). Public Health Statement for Benzene. *US Department of Health and Human Services. Agency for Toxic Substances and Disease Registry-ATSDR*, (pp.$\tilde{7}$).

ATSDR (2010). Public health statement for chlorine. *US Department of Health and Human Services. Agency for Toxic Substances and Disease Registry-ATSDR*, (November).

ATSDR (2017). Public health statement for toluene. *US Department of Health and Human Services. Agency for Toxic Substances and Disease Registry-ATSDR*, (pp.$\tilde{8}$).

Bakis, R. & Tuncan, A. (2011). An investigation of heavy metal and migration through groundwater from the landfill area of Eskisehir in Turkey. *Environmental Monitoring and Assessment*, 176(1-4), 87–98.

Balbarini, N., Frederiksen, M., Rønde, V., Møller, I., Sonne, A. T., McKnight, U. S., Pedersen, J. K., Binning, P. J., & Bjerg, P. L. (2020). Assessing the Transport of Pharmaceutical Compounds in a Layered Aquifer Discharging to a Stream. *Groundwater*, 58(2), 208–223.

Banzhaf, S. & Hebig, K. H. (2016). Use of column experiments to investigate the fate of organic micropollutants – a review. *Hydrology and Earth System Sciences*, 20(9), 3719–3737.

Bear, J. & Cheng, A. H.-D. (2010). *Modeling groundwater flow and contaminant transport*. Springer Science & Business Media.

Bortone, I., Chianese, S., Erto, A., Di Nardo, A., De Crescenzo, C., Karatza, D., Santonastaso, G. F., & Musmarra, D. (2019). An optimized configuration of adsorptive wells for the

remediation of an aquifer contaminated by multiple aromatic hydrocarbon pollutants. *Science of the Total Environment*, 696, 133731.

Bright, M. I., Thornton, S. F., Lerner, D. N., & Tellam, J. H. (2000). Attenuation of landfill leachate by clay liner materials in laboratory columns, 1. Experimental procedures and behaviour of organic contaminants. *Waste Management and Research*, 18(3), 198–214.

Chappel, M. J., Rowe, R. K., Brachman, R. W., & Take, W. A. (2012). A comparison of geomembrane wrinkles for nine field cases. *Geosynthetics International*, 19(6), 453–469.

Chen, R., Ge, Y., Chen, Z., Liu, J., Zhao, Y., & Li, Z. (2019). Analytical solution for one-dimensional contaminant diffusion through unsaturated soils beneath geomembrane. *Journal of Hydrology*, 568(October 2018), 260–274.

COMSOL Multiphysics (2019). Introduction to COMSOL Multiphysics.

Dai, Y., Zhuang, J., & Chen, X. (2020). Synergistic effects of unsaturated flow and soil organic matter on retention and transport of PPCPs in soils. *Environmental Research*, 191(August), 110135.

Daniel, D. E. (1993). Landfills and impoundments. In D. E. Daniel (Ed.), *Geotechnical Practice for Waste Disposal* chapter 5, (pp. 97–112). Boston, MA: Springer US.

de Oliveira, E. M., do Carmo Paresque, M. C., Ferreira, I. L., Garcia, A., & de Castro, J. A. (2019). Modeling the transport of hazardous colloidal suspensions of nanoparticles within soil of landfill layers considering multicomponent interactions. *Journal of Sustainable Metallurgy*, 5(4), 581–593.

Ding, X. H., Feng, S. J., & Zheng, Q. T. (2021). A two-dimensional analytical model for contaminant transport in a finite domain subjected to multiple arbitrary time-dependent point injection sources. *Journal of Hydrology*, 597(March), 126318.

Ding, X.-H., Feng, S.-J., Zheng, Q.-T., & Peng, C.-H. (2020). A two-dimensional analytical

model for organic contaminants transport in a transition layer-cutoff wall-aquifer system. *Computers and Geotechnics*, 128(May), 103816.

Divya, A., Shrihari, S., & Ramesh, H. (2020). Predictive simulation of leachate transport in a coastal lateritic aquifer when remediated with reactive barrier of nano iron. *Groundwater for Sustainable Development*, 11(March), 100382.

Dominijanni, A. & Manassero, M. (2019). Steady-state analysis of pollutant transport to assess landfill liner performance. *Environmental Geotechnics*, 8(7), 480–494.

Dong, J., Chen, Z., Han, Y., Guo, J., & Wang, K. (2020). 2DNEMM: a numerical environmental multimedia modeling method for landfill case study. *International Journal of Environmental Science and Technology*, 17(8), 3595–3606.

Ebrahim, M. N., Man, H. C., Zawawi, M. A. M., & Hamzah, M. H. (2019). Prediction of groundwater contaminants from cattle farm using visual MODFLOW. *Pertanika Journal of Science and Technology*, 27(4), 2265–2279.

El-Mathana, M. E., Mostafa, N. G., Galal, M. M., & Elawwad, A. (2021). Assessment and simulation of a solid waste dumpsite impact on the surrounding water resources: a case study in Abu Zaabal, Egypt. *Heliyon*, 7(11), e08421.

Faisal, A. A., Ibreesam, M. M., Al-Ansari, N., Naji, L. A., Naushad, M., & Ahamad, T. (2020). COMSOL multiphysics 3.5a package for simulating the cadmium transport in the sand bed-bentonite low permeable barrier. *Journal of King Saud University - Science*, 32(3), 1944–1952.

Fandiño, J. S. M., Nagalli, A., & Moro filho, R. C. (2020). Modeling of the dispersion of pollutants in porous media: case of a landfill in Brazil. *Journal of Environmental Chemical Engineering*, 8(6), 104400.

Feng, S. J., Peng, M. Q., Chen, Z. L., & Chen, H. X. (2019). Transient analytical solution for one-dimensional transport of organic contaminants through GM/GCL/SL composite liner. *Science of the Total Environment*, 650, 479–492.

Feng, S.-J., Zhu, Z.-W., Chen, Z.-L., & Chen, H.-X. (2020). Analytical model for multicomponent landfill gas migration through four-layer landfill biocover with capillary barrier. *International Journal of Geomechanics*, 20(3), 04020001.

Feng, Y. & Jin, X. (2019). Studies on effects of traffic tunnels on the migration of the contaminants under landfill sites. *Environmental Science and Pollution Research*, 26(34), 34801–34817.

Fonseca, M. C., Ritter, E., & Cavalcante, A. L. B. (2019). Aplicação de solução semianalítica para modelagem de ensaios de sorção e difusão pura com lixiviado. *Engenharia Sanitaria e Ambiental*, 24(5), 965–973.

Francisca, F. M. & Glatstein, D. A. (2020). Environmental application of basic oxygen furnace slag for the removal of heavy metals from leachates. *Journal of Hazardous Materials*, 384(September 2019), 121294.

Garg, A., Reddy, N. G., Huang, H., Buragohain, P., & Kushvaha, V. (2020). Modelling contaminant transport in fly ash–bentonite composite landfill liner: mechanism of different types of ions. *Scientific Reports*, 10(1), 1–8.

Giroud, J. & Morel, N. (1992). Analysis of geomembrane wrinkles. *Geotextiles and Geomembranes*, 11(3), 255–276.

Guarena, N., Dominijanni, A., & Manassero, M. (2020). From the design of bottom landfill liner systems to the impact assessment of contaminants on underlying aquifers. *Innovative Infrastructure Solutions*, 5(1), 1–13.

Gworek, B., Dmuchowski, W., Koda, E., Marecka, M., Baczewska, A., Brągoszewska, P., Sieczka, A., & Osiński, P. (2016). Impact of the municipal solid waste Łubna landfill on wnvironmental pollution by heavy metals. *Water*, 8(10), 470.

Hagan, G. B. & Darko, E. (2020). Stochastic analysis of the groundwater velocity field and implications for contaminant transport within the Ga East and Adentan municipalities, Ghana. *Journal of African Earth Sciences*, 170(May), 103929.

Hamer, G. (2003). Solid waste treatment and disposal: effects on public health and environmental safety. *Biotechnology Advances*, 22(1-2), 71–79.

Harbaugh, A. (2005). Derivation of the finite-difference equation. In *The U.S. Geological Survey Modular Ground- Water Model (MODFLOW)* chapter 2, (pp. 6–A16). U.S. Geological Survey Techniques and Methods.

Hassanzadeh, Y., Marofi, S., & Vahabian, M. (2020). Three-Dimensional Modeling of Contaminant Transport in Subsurface Soil Media Using UFV Approach. *International Journal of Geomechanics*, 20(4), 1–15.

He, Y., Hu, G., Wu, D.-y., Zhu, K.-f., & Zhang, K.-n. (2022). Contaminant migration and the retention behavior of a laterite–bentonite mixture engineered barrier in a landfill. *Journal of Environmental Management*, 304(932), 114338.

Jarsjö, J., Andersson-Sköld, Y., Fröberg, M., Pietroń, J., Borgström, R., Löv, Å., & Kleja, D. B. (2020). Projecting impacts of climate change on metal mobilization at contaminated sites: controls by the groundwater level. *Science of the Total Environment*, 712.

Järup, L. (2003). Hazards of heavy metal contamination. *British Medical Bulletin*, 68(1), 167–182.

Jones, D. D. & Rowe, R. K. (2016). BTEX Migration through various geomembranes and vapor barriers. *Journal of Geotechnical and Geoenvironmental Engineering*, 142(10).

Lanphear, B. P., Hornung, R., Khoury, J., Yolton, K., Baghurst, P., Bellinger, D. C., Canfield, R. L., Dietrich, K. N., Bornschein, R., Greene, T., Rothenberg, S. J., Needleman, H. L., Schnaas, L., Wasserman, G., Graziano, J., & Roberts, R. (2005). Low-level environmental lead exposure and children's intellectual function: an international pooled analysis. *Environmental Health Perspectives*, 113(7), 894–899.

Lin, Y. C. & Yeh, H. D. (2020). A simple analytical solution for organic contaminant diffusion through a geomembrane to unsaturated soil liner: considering the sorption effect and Robin-type boundary. *Journal of Hydrology*, 586(March), 124873.

Ma, Y., Liu, Z. H., Xi, B. D., Li, W. T., Xu, Y. Q., Zhao, H. Z., Chen, Z. Q., He, X. S., & Xing, B. (2021). Molecular structure and evolution characteristics of dissolved organic matter in groundwater near landfill: implications of the identification of leachate leakage. *Science of the Total Environment*, 787, 147649.

Mahallei, H. & Badv, K. (2020). The study of diffusion characteristics of soil bentonite to control contaminant transport. *World Journal of Engineering*, 18(3), 379–388.

Malusis, M. A. & Shackelford, C. D. (2004). Predicting solute flux through a clay membrane barrier. *Journal of Geotechnical and Geoenvironmental Engineering*, 130(5), 477–487.

McWatters, R. S., Jones, D. D., Rowe, R. K., & Markle, J. M. (2020). Investigation of a decommissioned landfill barrier system containing polychlorinated biphenyl (PCB) waste after 25 years in service. *Canadian Geotechnical Journal*, 57(6), 882–902.

McWatters, R. S., Rutter, A., & Rowe, R. K. (2016). Geomembrane applications for controlling diffusive migration of petroleum hydrocarbons in cold region environments. *Journal of Environmental Management*, 181, 80–94.

Meric, D., Hellweger, F., Alshawabkeh, A. N., & Sheahan, T. C. (2017). Nonlinear nonequilibrium one-dimensional large-strain consolidation-coupled contaminant transport model of capped sediments. *Journal of Geotechnical and Geoenvironmental Engineering*, 143(8), 1–9.

Mondelli, G., Giacheti, H. L., Boscov, M. E. G., Elis, V. R., & Hamada, J. (2007). Geoenvironmental site investigation using different techniques in a municipal solid waste disposal site in Brazil. *Environmental Geology*, 52(5), 871–887.

Mondelli, G., Luiz, H., & Roberto, V. (2012). Geo-environmental site investigation for municipal solid waste disposal sites. *Municipal and Industrial Waste Disposal*, (May 2014).

Morita, A. K. M. & Wendland, E. C. (2019). Caracterização hidrogeoquímica de área impactada por depósito de resíduos desativado em zona de recarga do aquífero guarani. *Geosciences = Geociências*, 38(4), 1017–1028.

National Institutes of Health (2021). Lead and your health. *U.S. Department and Human Services*, (pp.2̃).

Naveen, B. P., Sumalatha, J., & Malik, R. K. (2019). Numerical modelling of leachate transport into water bodies at a landfill site. *Journal of Environmental Engineering and Science*, 15(1), 6–15.

Ozelim, L. C. d. S. M., Paz, Y. P. L., da Cunha, L. S., & Cavalcante, A. L. B. (2021). Enhanced landfill's characterization by using an alternative analytical model for diffusion tests. *Environmental Monitoring and Assessment*, 193(11).

Page, M. J., McKenzie, J. E., Bossuyt, P. M., Boutron, I., Hoffmann, T. C., Mulrow, C. D., Shamseer, L., Tetzlaff, J. M., Akl, E. A., Brennan, S. E., Chou, R., Glanville, J., Grimshaw, J. M., Hróbjartsson, A., Lalu, M. M., Li, T., Loder, E. W., Mayo-Wilson, E., McDonald, S., McGuinness, L. A., Stewart, L. A., Thomas, J., Tricco, A. C., Welch, V. A., Whiting, P., & Moher, D. (2021a). The PRISMA 2020 statement: An updated guideline for reporting systematic reviews. *The BMJ*, 372.

Page, M. J., McKenzie, J. E., Bossuyt, P. M., Boutron, I., Hoffmann, T. C., Mulrow, C. D., Shamseer, L., Tetzlaff, J. M., & Moher, D. (2021b). Updating guidance for reporting systematic reviews: development of the PRISMA 2020 statement. *Journal of Clinical Epidemiology*, 134, 103–112.

Park, M.-G., Edil, T. B., & Benson, C. H. (2012). Modeling Volatile Organic Compound Transport in Composite Liners. *Journal of Geotechnical and Geoenvironmental Engineering*, 138(6), 641–657.

Peng, M. Q., Feng, S. J., Chen, H. X., Chen, Z. L., & Xie, H. J. (2021). Analytical model for organic contaminant transport through GMB/CCL composite liner with finite thickness considering adsorption, diffusion and thermodiffusion. *Waste Management*, 120, 448–458.

Podlasek, A., Bujakowski, F., & Koda, E. (2020). The spread of nitrogen compounds in

an active groundwater exchange zone within a valuable natural ecosystem. *Ecological Engineering*, 146(January), 105746.

Pu, H., Qiu, J., Zhang, R., & Zheng, J. (2020). Analytical solutions for organic contaminant diffusion in triple-layer composite liner system considering the effect of degradation. *Acta Geotechnica*, 15(4), 907–921.

Roberts, P. V., Goltz, M. N., & Mackay, D. M. (1986). A natural gradient experiment on solute transport in a sand aquifer: 3. Retardation estimates and mass balances for organic solutes. *Water Resources Research*, 22(13), 2047–2058.

Rosqvist, H. & Bendz, D. (1999). An experimental evaluation of the solute transport volume in biodegraded municipal solid waste. *Hydrology and Earth System Sciences*, 3(3), 429–438.

Rowe, R. K. & Abdelrazek, A. Y. (2019). Effect of interface transmissivity and hydraulic conductivity on contaminant migration through composite liners with wrinkles or failed seams. *Canadian Geotechnical Journal*, 56(11), 1650–1667.

Rowe, R. K. & Barakat, F. B. (2021). Modelling the transport of PFOS from single lined municipal solid waste landfill. *Computers and Geotechnics*, 137(June), 104280.

Rowe, R. K. & Booker, J. R. (1984). The analysis of pollutant migration in a non-homogeneous soil. *Géotechnique*, 34(4), 601–612.

Rowe, R. K. & Booker, J. R. (2004). POLLUTEv7 Reference Guide.

Samad, M. S. A., Padippingal, A., Varghese, G. K., & Alappat, B. J. (2019). An environmental forensic investigation at a bio-medical waste treatment and disposal facility in Kerala, India. *Environmental Forensics*, 20(2), 162–170.

Samadder, S., Prabhakar, R., Khan, D., Kishan, D., & Chauhan, M. (2017). Analysis of the contaminants released from municipal solid waste landfill site: a case study. *Science of The Total Environment*, 580, 593–601.

Shackelford, C. D. & Daniel, D. E. (1991). Diffusion in saturated soil. II: results for compacted clay. *Journal of Geotechnical Engineering*, 117(3), 485–506.

Shackelford, C. D., Daniel, D. E., & Liljestrand, H. M. (1989). Diffusion of inorganic chemical species in compacted clay soil. *Journal of Contaminant Hydrology*, 4(3), 241–273.

Shackelford, C. D. & Jefferis, S. A. (2018). Geoenvironmental engineering for in situ remediation. In *ISRM International Symposium 2000, IS 2000* (pp.6̃5).

Shu, S., Zhu, W., & Shi, J. (2019). A new simplified method to calculate breakthrough time of municipal solid waste landfill liners. *Journal of Cleaner Production*, 219, 649–654.

Singh, M. K. & Rajput, S. (2021). Study of pollutant dispersion in finite layers of semi-infinite geological formation. *Pollution*, 7(2), 257–274.

Slavinskienė, G., Jurevičius, A., Satkūnas, J., & Šimanauskienė, R. (2019). Landfill leachate quantity and attenuation distance of inorganic contaminants in the groundwater of different hydrogeological systems: A case study of Lithuania. *Baltica*, 32(2), 127–138.

Sun, Y., Chen, S. S., Lau, A. Y., Tsang, D. C., Mohanty, S. K., Bhatnagar, A., Rinklebe, J., Lin, K. Y. A., & Ok, Y. S. (2020). Waste-derived compost and biochar amendments for stormwater treatment in bioretention column: Co-transport of metals and colloids. *Journal of Hazardous Materials*, 383(September 2019), 121243.

Uddh Söderberg, T., Berggren Kleja, D., Åström, M., Jarsjö, J., Fröberg, M., Svensson, A., & Augustsson, A. (2019). Metal solubility and transport at a contaminated landfill site – From the source zone into the groundwater. *Science of the Total Environment*, 668, 1064–1076.

US EPA (1994). Drinking water criteria document for chlorine, hypochlorous acid and hypochlorite ion (draft). *US EPA - United States Environmental Protection Agency*, (pp. 166).

US EPA (2003). Integrated Risk Information System (IRIS) on Benzene. *US EPA - United States Environmental Protection Agency*, (pp.4̃3).

US EPA (2005). Integrated Risk Information System (IRIS) on Toluene. *US EPA - United States Environmental Protection Agency*, (pp.3̃3).

US EPA (2011). Integrated Risk Information System (IRIS) on Methylene Chloride. *US EPA - United States Environmental Protection Agency*, (pp.4̃5).

Varank, G., Demir, A., Yetilmezsoy, K., Bilgili, M. S., Top, S., & Sekman, E. (2011). Estimation of transport parameters of phenolic compounds and inorganic contaminants through composite landfill liners using one-dimensional mass transport model. *Waste Management*, 31(11), 2263–2274.

Wang, C., Liu, S., Shi, X., Cui, G., Wang, H., Jin, X., Fan, K., & Hu, S. (2022). Numerical modeling of contaminant advection impact on hydrodynamic diffusion in a deformable medium. *Journal of Rock Mechanics and Geotechnical Engineering*, 14(3), 994–1004.

Wang, S., Zhu, W., Qian, X., Xu, H., & Fan, X. (2017). Temperature effects on non-Darcy flow of compacted clay. *Applied Clay Science*, 135, 521–525.

WHO (2019). Exposure to lead: a major public health concern. *World Healh Organization*, (pp.6̃).

Woodman, N. D., Rees-White, T. C., Beaven, R. P., Stringfellow, A. M., & Barker, J. A. (2017). Doublet tracer tests to determine the contaminant flushing properties of a municipal solid waste landfill. *Journal of Contaminant Hydrology*, 203(May), 38–50.

Wu, L., Zhan, L., Lan, J., Chen, Y., Zhang, S., Li, J., & Liao, G. (2021). Leachate migration investigation at an unlined landfill locattensão ed in granite region using borehole groundwater TDS profiles. *Engineering Geology*, 292(June), 106259.

Xie, H., Wang, Q., Wu, J., & Chen, Y. (2019). Analytical model for methane migration through fractured unsaturated landfill cover soil. *Engineering Geology*, 255(May 2018), 69–79.

Yan, H., Sedighi, M., Ding, H., Sun, Z., & Xie, H. (2021a). Analytical model for non-isothermal diffusion of contaminants in unsaturated composite liner. *Journal of Hydrology*, 603(PA), 126848.

Yan, H., Wu, J., Thomas, H. R., Ding, H., Zhan, L., & Xie, H. (2021b). Analytical model for coupled consolidation and diffusion of organic contaminant transport in triple landfill liners. *Geotextiles and Geomembranes*, 49(2), 489–499.

Yan, H., Xie, H., Ding, H., Yang, D., Chen, C., Chen, Y., & Chen, Y. (2022). Analytical solution for one-dimensional steady-state contaminant transport through a geomembrane layer (GMBL)/compacted clay layer (CCL)/attenuation layer (AL) composite liner considering consolidation. *International Journal for Numerical and Analytical Methods in Geomechanics*, 46(6), 1046–1063.

Yan, H., Xie, H., Wang, S., & Zheng, Z. (2021c). A two-dimensional analytical model for organic contaminant transport in cutoff wall and aquifer system. *International Journal for Numerical and Analytical Methods in Geomechanics*, 45(5), 631–647.

Yan, H., Xie, H., Wu, J., Ding, H., Qiu, Z., & Sun, Z. (2021d). Analytical model for transient coupled consolidation and contaminant transport in landfill liner system. *Computers and Geotechnics*, 138(March), 104345.

Yong, L. L., Anggraini, V., Taha, M. R., & Raghunandan, M. E. (2022). Short- and long-term transports of heavy metals through earthen liners: physical and numerical modeling. *Bulletin of Engineering Geology and the Environment*, 81(1), 1–20.

Yu, X., Sui, Q., Lyu, S., Zhao, W., Wu, D., Yu, G., & Barcelo, D. (2021). Rainfall influences occurrence of pharmaceutical and personal care products in landfill leachates: evidence from seasonal variations and extreme rainfall episodes. *Environmental Science and Technology*, 55(8), 4822–4830.

Zhang, J., min Zhang, J., Xing, B., dong Liu, G., & Liang, Y. (2021). Study on the effect of municipal solid landfills on groundwater by combining the models of variable leakage

rate, leachate concentration, and contaminant solute transport. *Journal of Environmental Management*, 292(May), 112815.

Chapter 2

Hydraulic and geomechanical characteristics of tropical sandstone: a laboratory approach

Abstract

This study investigates a weathered sandstone outcrop's mechanical and hydraulic behavior in a tropical region, focusing on specimens distinguished by their predominant colors - gray and brown. We evaluated the compressibility, shear strength, and permeability under dry and saturated conditions. The presence of clay minerals from the smectite group was identified, contributing to the sandstone's expansive properties, with expansion pressures of 55 kPa and 65 kPa for gray and brown sandstone, respectively. The uniaxial compressive strength for dry sandstone was 8.31 MPa, with Young's modulus of 3.99 GPa. Tensile strength by diametrical compression ranged between 0.78 and 0.88 MPa. Under saturated conditions, shear strength exhibited cohesion values between 70 and 110 kPa and friction angles from 44° to 55°. The compressibility differences between the gray and brown sandstone were minimal, with pre-consolidation stresses of 21 kPa (gray) and 14.5 kPa (brown). Permeability tests revealed significant anisotropy. The brown sandstone demonstrated one to two orders of magnitude higher permeability than the gray sandstone, particularly in the horizontal direction. In the gray sandstone, vertical permeability ranged from 7.50×10^{-9} m/s (unconsolidated) to 3.41×10^{-10} m/s (consolidated at 320 kPa), while horizontal permeability ranged from 3.38×10^{-9} m/s to 7.68×10^{-11} m/s under the same conditions. The brown sandstone exhibited vertical permeability values between 1.01×10^{-8} m/s and 1.40×10^{-9} m/s, with horizontal permeability ranging from 2.45×10^{-8} m/s to 4.85×10^{-9} m/s. These findings highlight the influence of mineralogical composition and consolidation pressure on the sandstone's behavior, with implications for its mechanical performance and water flow characteristics.

Keywords: Tropical sandstone; Weathered sandstone; UCS; Compressibility; Young's modulus; Shear strength; Brazilian test; Hydraulic conductivity; Anisotropy.

2.1 Introduction

Understanding rock strength, deformability, and permeability is crucial for many science fields, including geology, geotechnical, and environmental engineering. These parameters play a significant role in characterizing the behavior of rock formations and are essential for various applications, most notably mining (Meng et al., 2016; Ranjith et al., 2017; Zhu et al., 2019; Sotoudeh et al., 2020; Kassymkanova et al., 2023), petroleum engineering (Abay et al., 2017; Liu et al., 2021; Wang & Tang, 2024), civil engineering (Wang et al., 2020; Zhu et al., 2023; Huang et al., 2024), and environmental science (Ma et al., 2017; Hu et al., 2019; Shaojie et al., 2021; Li et al., 2022; Miao et al., 2023; Zhang et al., 2023).

Such parameters are closely related. Changes in pore pressure resulting from a fluid flow can influence deformability and potentially alter the rock's mechanical behavior. As a rock undergoes compression or shearing, pore spaces may become compressed or distorted, changing the rock's permeability.

Sedimentary rocks, such as sandstone, hold immense geological, economic, and environmental significance due to their unique characteristics and wide–ranging applications. They are often used to identify the location of oil and gas reserves and serve as essential building materials. Additionally, sedimentary rocks can provide valuable insight into the history of the earth and its various processes, including plate tectonics, erosion, and weathering. Sedimentary rocks are also highly significant for their unique properties, which include porosity and permeability. These characteristics make them indispensable in groundwater management and environmental remediation initiatives.

Especially in tropical environments, rock formations are exposed to vigorous weathering, including chemical weathering, erosion, and biological activity. Moreover, the inadequacy of water treatment and supply in developing countries is a well–known fact, and therefore, sedimentary rocks play a pivotal role in current and future water supply. They are responsible for recharging and storing aquifers such as the Guarani, spanning south-central Brazil, Paraguay, Argentina, and Uruguay.

In the São Paulo State, Brazil, sandstone aquifers supply groundwater for drinking,

irrigation, and industrial use. The municipality of Bauru uses artesian wells to supply water to the population and has aquifer recharge areas, such as outcropping rocks. These are often exposed to the risk of contamination, as in Bauru's municipal solid waste (MSW) disposal site, where the waste pit at the MSW disposal site lacks an engineering liner and is close to the water table and the sandstone formation, exposing both to the risk of contamination.

Analyzing tropical sandstone outcrops' mechanical and hydraulic properties and investigating the effects of anisotropy and heterogeneity would significantly contribute to a more comprehensive understanding of their behavior. This paper presents a laboratory examination of these properties. It aims to contribute to understanding the hydrogeological features of sandstone aquifers to ensure the sustainable management of water resources and the protection of groundwater reserves.

2.2 Materials and Methods

2.2.1 Studied area and sampling

Bauru is located in the midwest region of the São Paulo State, around 300 km away from the state capital. The city experiences a tropical climate with distinct wet and dry seasons. During summers (December to February), temperatures often reach 30–35°C with high humidity and frequent rainfall. The average annual rainfall is between 1200 and 1400 mm. In winter (June to August), temperatures range between 15–25°C.

The geological formations present in the region of Bauru are consistent with those found in the western part of the São Paulo State. These formations, known as the Bauru Group, were formed during the Cretaceous period and comprised the Adamantina, Caiuá, Marília, and Santo Anastácio Formations.

The Adamantina and Marília Formation represent diverse sedimentary environments, including fluvial, lacustrine, and aeolian settings. The sediments of these Formations were deposited in a dynamic landscape. The Adamantina Formation comprises sandstones with a thin to medium grain size distribution, argillites, and conglomerates. On the other hand, the Marília Formation has a granulometry ranging from thin to coarse and features conglomerates, laminites, and carbonaceous cement, according to the Ferreira et al. (1993) report.

Their mineralogy mainly includes silicates (quartz), carbonates (calcite and ankerite), and clay minerals (kaolinite, montmorillonite, smectite, and palygorskite) (Dal' Bó et al., 2010; Basilici et al., 2016; Silva et al., 2019).

For this study, sandstone samples were collected from the rock outcrop shown in Figure 2.1 near Bauru's MSW disposal site (22°15'S 49°08'W). Figure 2.2 shows the stratigraphy of the Bauru Basin formed in the Upper Cretaceous.

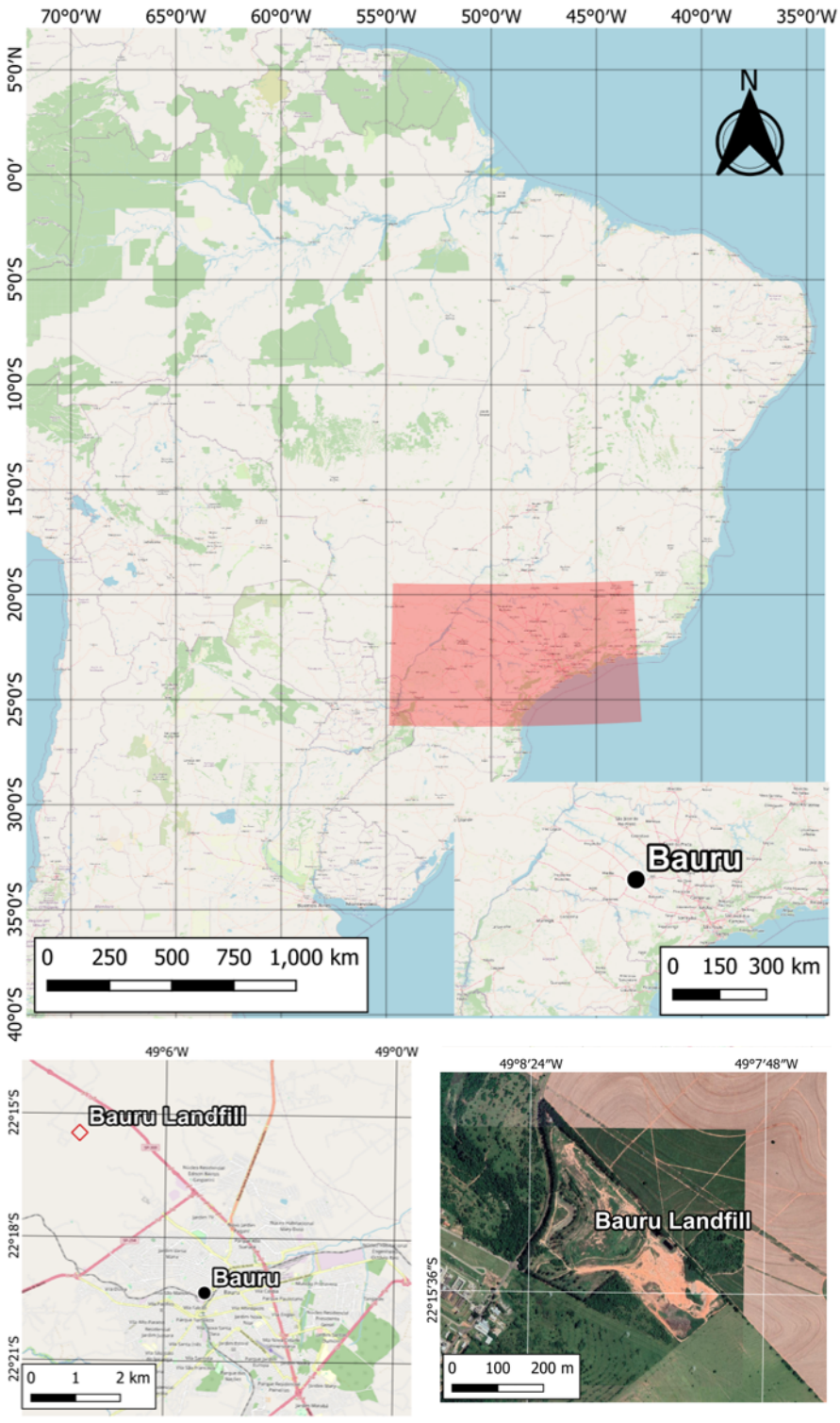

Figure 2.1: Location of the municipality of Bauru, Brazil. Study area and collection of sandstone samples at the Bauru's MSW disposal site.

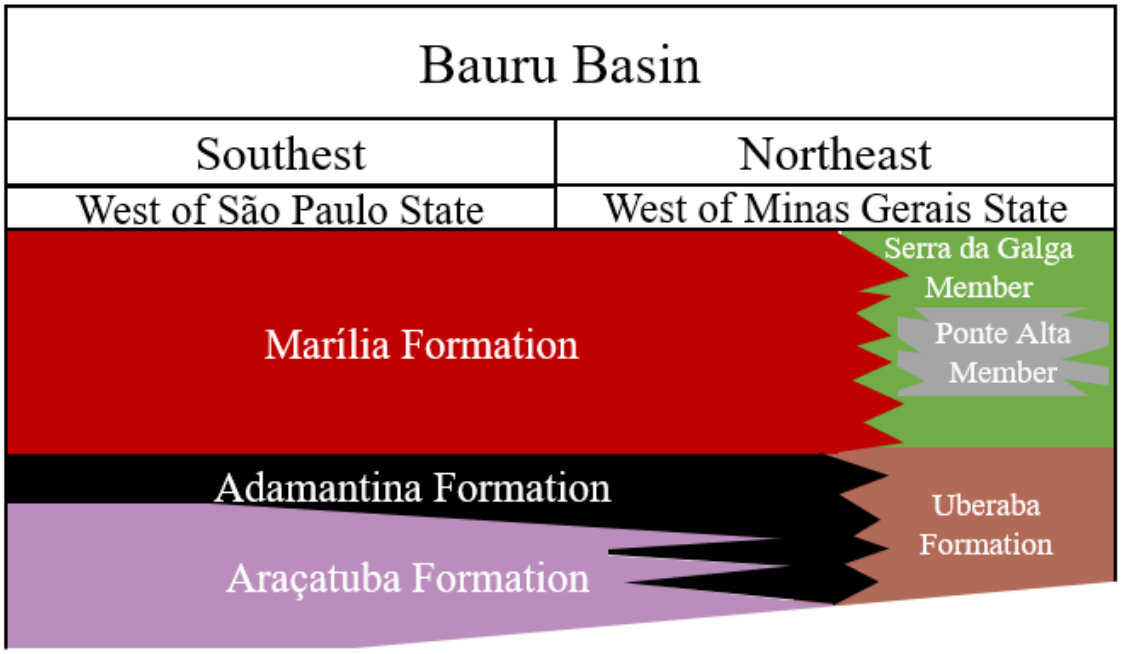

Figure 2.2: Upper Cretaceous stratigraphy of the Bauru basin in southern Brazil (adapted from Batezelli, 2017).

The sandstone samples were collected using a crawler bulldozer (Figure 2.3), which removed blocks of outcropping rock around Bauru's MSW disposal site. The samples were marked top and bottom and, as depicted in Figure 2.4, transported to the laboratory where they were stored. Figure 2.5 illustrates an outcropping sandstone profile on the MSW disposal site. Once in the laboratory, the samples were segregated based on color, i.e., gray and brown, for characterization and to prepare the specimens used in the strength, deformability, and permeability tests.

Standard soil mechanics tests were employed, as the material undergoes considerable disaggregation and demonstrates characteristics similar to those of soil when exposed to water. In other words, it can be excavated without the necessity of explosives.

Figure 2.3: Crawler bulldozer supporting the collection of sandstone samples.

Figure 2.4: Sandstone removed and identified.

Figure 2.5: Sandstone outcrop profile.

2.2.2 Characterization

Grain size distribution

The sandstone's color variation is depicted in Figure 2.6, while its separation is displayed in Figure 2.7 for the granulometry tests with and without deflocculant (Figures 2.8 and 2.9), consistency limits (Figure 2.10), and methylene blue (Figure 2.11). Table 2.1 summarizes the characterization tests and the standards utilized to determine them.

Figure 2.6: Detail of a sandstone sample composed of two predominant colors.

Figure 2.7: Preparation of the samples selected by predominant color for the particle size test.

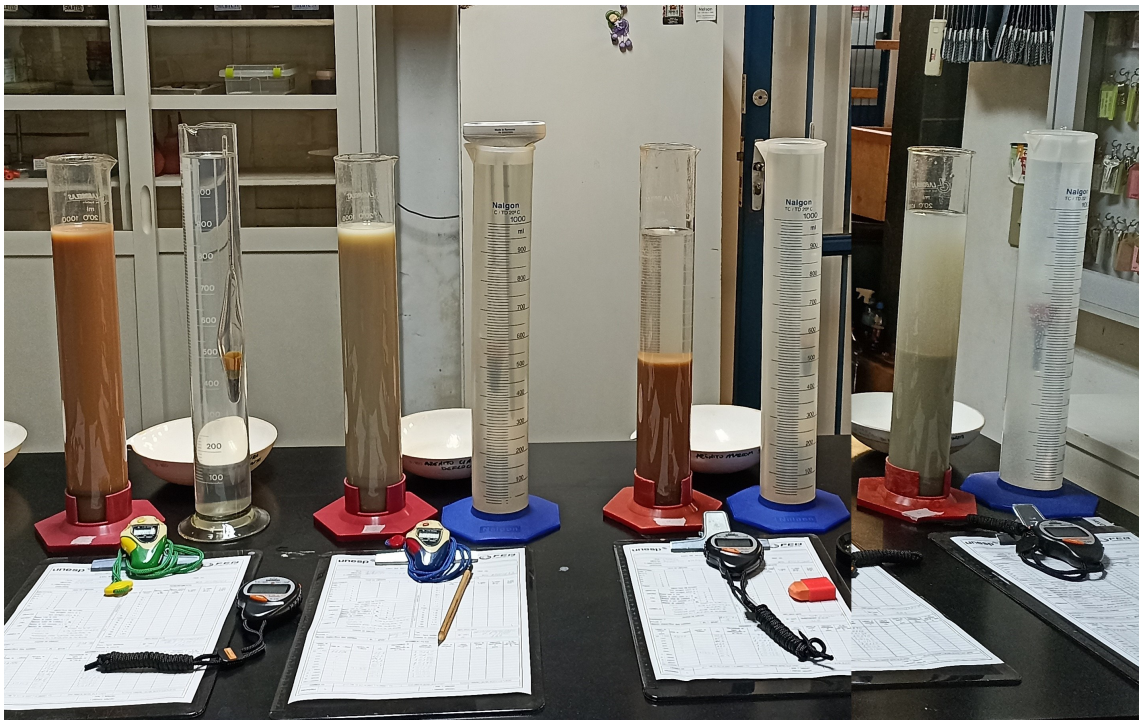

Figure 2.8: Sedimentation (hydrometer) stage with and without the use of deflocculant.

Table 2.1: Sandstone characterization tests.

Test	Reference
Particle-size distribution	ASTM D7928-17 (2017) ASTM D6913/D6913M (2017)
Atterberg limits	ASTM D4318 (2017)
Methylene blue	Pejon (1992)

Figure 2.9: Washing the material to be sieved. Despite having few fines, the sandstone could retain water on the 0.075 mm sieve.

Atterberg limits and Methylene blue test

Figure 2.10: Liquidity and plasticity limits exemplified by the brown sandstone sample

Figure 2.11: Methylene blue test to identify the activity of the clay fraction present in the sandstone under study.

2.2.3 Cylindrical specimen molding process

The cylindrical specimens were fabricated in stages. The initial one, depicted in Figure 2.12, used a diamond hollow with a 70 mm diameter but with a reduced length. However, the extraction of the sample using a grinding wheel was found to be inadequate.

As a new attempt, a 70 mm diameter by 15 cm long hole saw was manufactured and attached to a bench drill. The equipment proved useful. However, the bench drill's low spindle stroke compromised the complete removal of the specimens. The abovementioned attempt is illustrated in Figures 2.13 and 2.14.

The latest configuration, depicted in Figures 2.15 and 2.16, was developed by modifying the diamond hollow to ensure sufficient stroke for complete extraction of the sandstone specimens. Once this last configuration was achieved, the samples were also tested to assess potential anisotropy. The tests were performed on molded specimens in both the transverse and longitudinal directions, as illustrated by Figure 2.17.

Additionally, Figure 2.18 illustrates the progression of specimen extraction before the completion of the top and bottom, which are presented in Figure 2.19, after the removal of the coarsest layer and polishing, as shown in Figure 2.20. The final design for removing the cores followed the recommendations of the ASTM D4543 (2019).

The cylindrical specimens, identified, separated by color, and ready for the uniaxial compressive strength (UCS), modulus of elasticity, permeability, column tests (Chapter 3), and diametrical compression (Brazilian test) tests are depicted in Figure 2.21. The Brazilian test involved the analysis of specimens with varying lengths, which will be further discussed below.

Figure 2.12: First attempt at molding the specimen.

Figure 2.13: Sample being prepared for trial with a bench drill.

Figure 2.14: Bench drill proved helpful, but there was a short spindle stroke when removing the specimens.

Figure 2.15: Cutting the samples with a circular saw to prepare them for another configuration with enough spindle stroke to remove the specimens.

Figure 2.16: Final setting with a diamond hollow core drill adapted to have enough stroke to remove the sandstone specimens.

Figure 2.17: Longitudinal and transverse core samples.

Figure 2.18: Evolution of the rock core extracted using the several techniques presented above.

Figure 2.19: Specimen's top and bottom preparation by removing the coarse layer.

Figure 2.20: Fine polishing of sandstone rock sample using the specimen grinding machine.

Figure 2.21: Sandstone specimens completed and identified for testing.

2.2.4 Uniaxial compression strength and Young's modulus

Upon completion of the molding process for the cylindrical specimens, they underwent preparation for uniaxial compressive strength and Young's modulus tests. This procedure involved subjecting the specimens to drying in an oven at 60 ºC until they achieved a constant mass, as depicted in Figure 2.22. Subsequently, the samples were removed from the oven and allowed to cool to room temperature in dissectors containing silica gel to prevent moisture absorption, as illustrated in Figure 2.23.

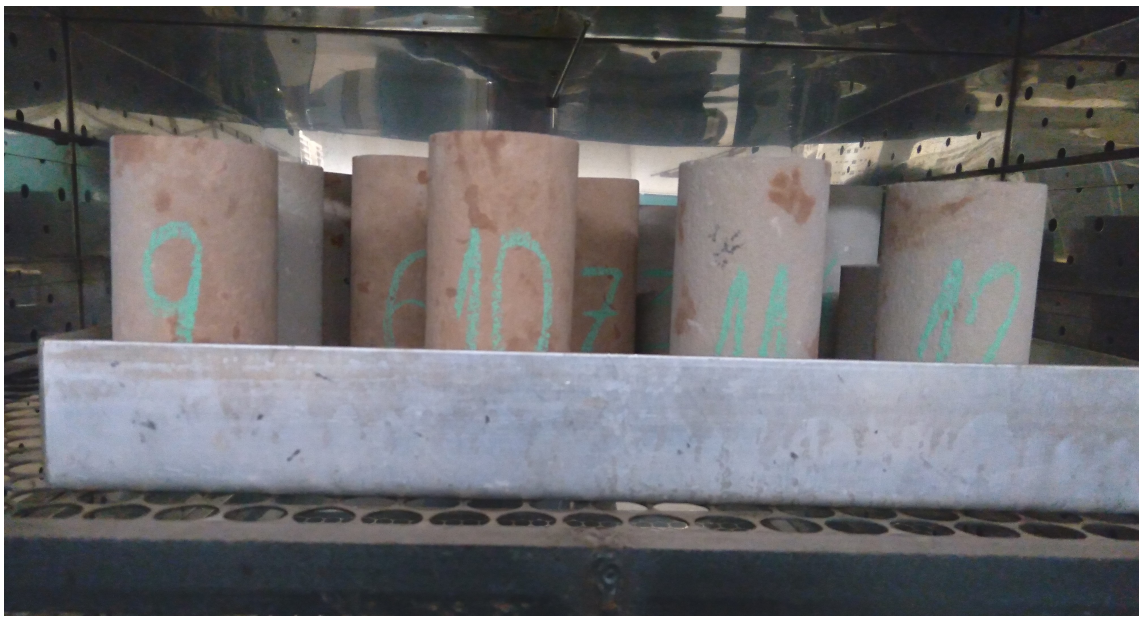

Figure 2.22: Pre-drying the specimens in the oven.

The unconfined compressive strength (UCS) was determined based on the modulus of elasticity test results, in which the specimen is brought to failure in its final stage. The testing adhered to the standards outlined in ASTM C170/C170M (2017) and ASTM D7012 (2014) method C, using seven specimens with a length-to-diameter ratio of 2:1. A 300 kN EMIC universal compression press was employed to collect force and axial displacement data through a data acquisition system, from which the UCS was derived.

As previously explained, Young's modulus was determined using the same equipment on 5 of the seven aforementioned samples. This was achieved by affixing strain gauges to the

specimen's sides and measuring the lateral displacements in loading and unloading cycles until the specimen failed. The methods adhered to the standards of ASTM D7012 (2014) method D and ABNT NBR 8522-1 (2021) methodology A, as illustrated in Figure 2.24.

Figure 2.23: Cooling the specimens to room temperature in a desiccator.

Initially, two specimens underwent testing until failure, and the average UCS of both determined the maximum load, which was set at 30% of the UCS. This load was applied in 4 loading and unloading cycles with 60-second breaks in between. The data from the last loading cycle was used to calculate the modulus of elasticity. Following this cycle, the strain gauges were removed, and the specimen was subjected to failure, providing the necessary data to estimate the other UCS. Young's modulus in GPa was calculated by

$$E = \frac{\sigma_b - \sigma_a}{\epsilon_b - \epsilon_a} 10^{-3} \tag{2.1}$$

Where σ_b is the stress reading at the moment it reaches 30% of the compressive strength, σ_a is the stress referring to the second-to-last pause before the sample fails, after loading and unloading cycles, ϵ_b the deformation referring to σ_b, and ϵ_a the deformation referring to σ_a.

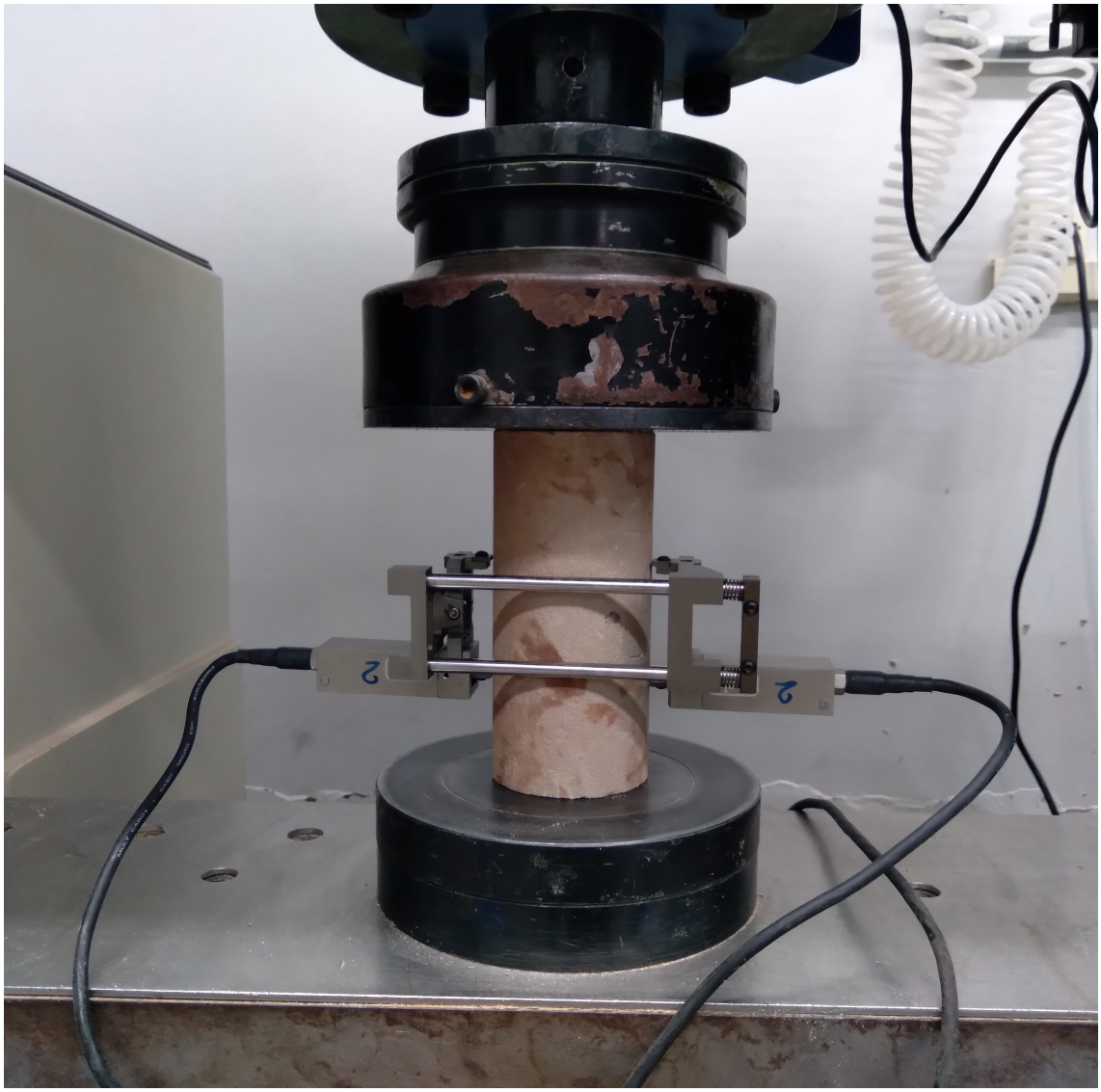

Figure 2.24: Test layout to obtain Young's modulus.

2.2.5 Diametral compression

The tensile strength was assessed using a diametral compression test on specimens with two length/diameter ratios. The first test, depicted in Figure 2.25, utilized a 2:1 ratio per the guidelines of ASTM C496/C496M (2017), and six samples were tested. The second test was conducted following the specifications of ASTM D3967 (2016) using 13 core samples with a thickness/diameter ratio 0.5, as illustrated in Figure 2.26. Similar to the UCS and Young's modulus determinations, the samples were initially placed in an oven at 60^{o} C until a constant mass was achieved and then cooled to room temperature in desiccators.

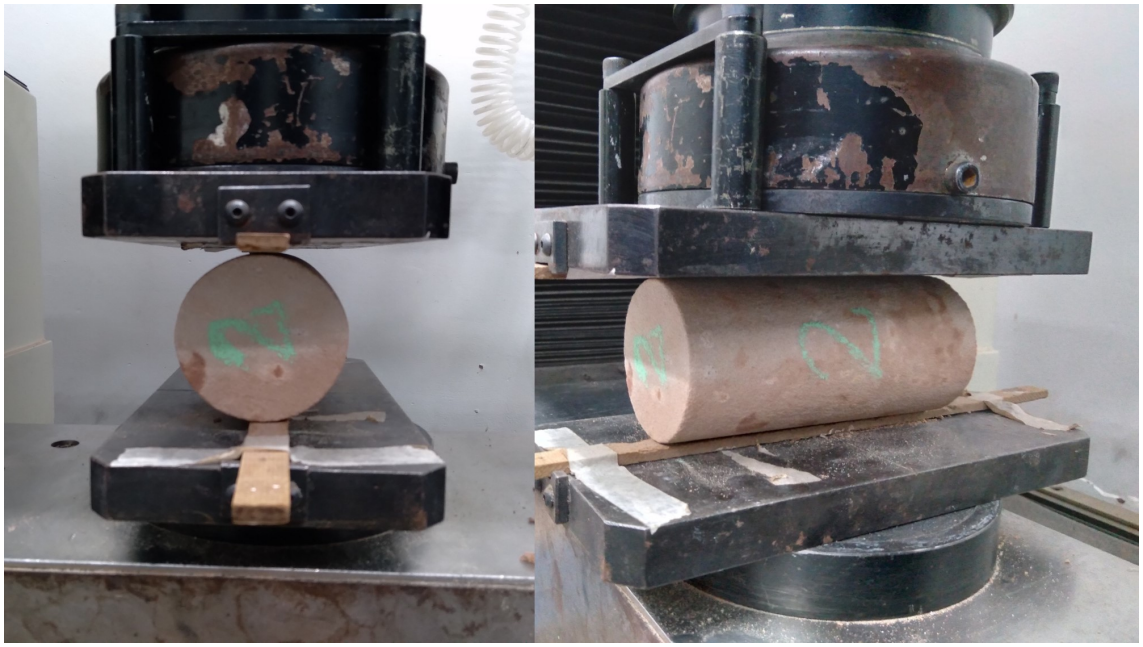

Figure 2.25: Tensile strength in diametrical compression according to the ASTM C496/C496M (2017) standard.

The samples were subjected to diametrical compression until failure using the EMIC 300 kN press. The data acquisition system collected force and displacement data, and the tensile strength by diametrical compression was determined. Given the configuration of the equipment and the layout of the samples, the stresses for both standards were calculated by

$$\sigma_t = \frac{2P}{\pi t D} \tag{2.2}$$

Where σ_t is the tensile strength, P is the maximum load applied, t is the thickness of the specimen, and D is the diameter of the specimen.

Figure 2.26: Specimens suitable for the diametral compression test as recommended by ASTM D3967 (2016).

2.2.6 Direct shear

The direct shear tests followed the standard ASTM D5607 (2016), focusing on evaluating the shear resistance and strength envelope of gray and brown sandstone.

Unlike cylindrical samples, a box specimen cutter could remove test specimens from the sandstone. For this purpose, smaller samples were manually cut to approximate dimensions of the samplers and then shaped until they penetrated the samplers. Figures 2.27 and 2.28 detailed this process.

The top and base of the test specimens were finished using the samplers as a reference, with approximate dimensions of 60 mm in height and 60 mm in length by 50 mm in thickness. They were then moved to the direct shear chamber illustrated in Figure 2.29 and positioned. The samples were taken to the direct shear machine shown in Figure 2.30 with a data acquisition system for the saturation, consolidation, and shearing stages.

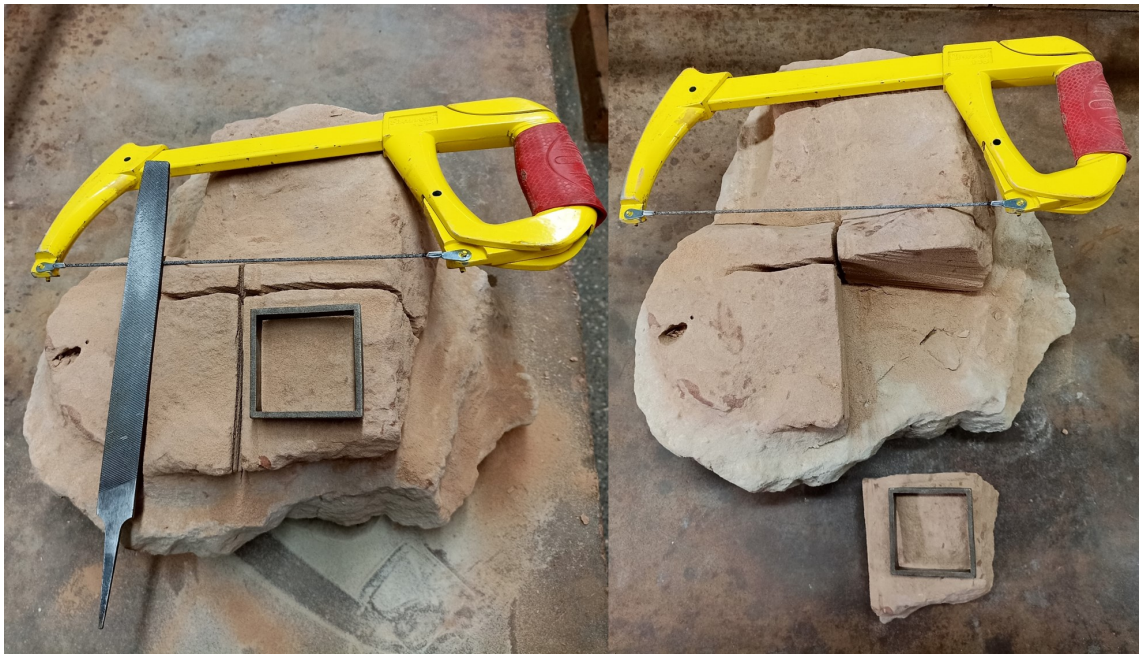

Figure 2.27: Molding of the specimens for the direct shear tests.

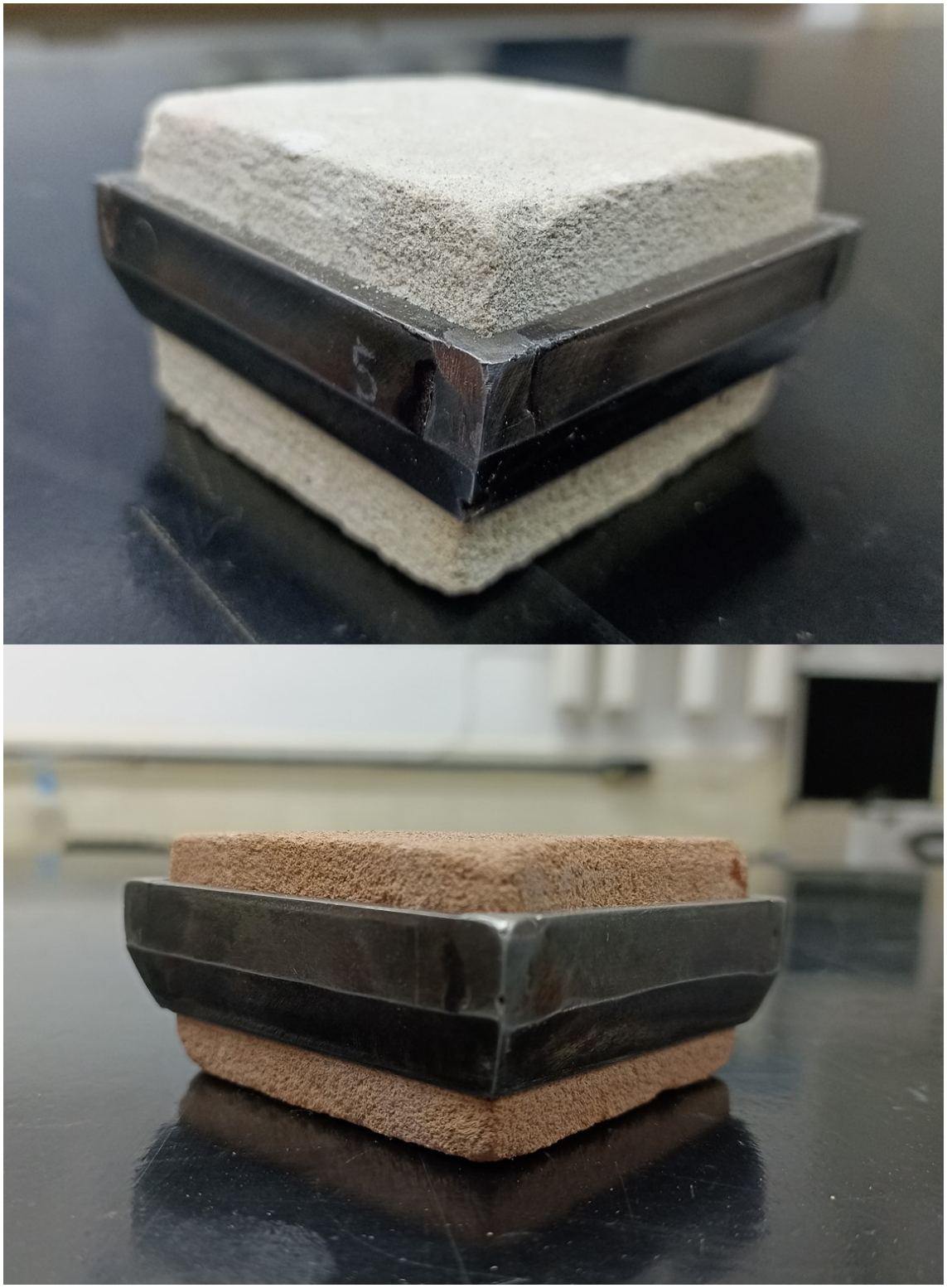

Figure 2.28: Gray and brown sandstone samples in the molds for direct shear testing before grinding the top and bottom.

To investigate the saturated behavior of the sandstone, which proved fragile in the presence of water as it disintegrated and showed cracks characterizing the material's expansion when saturated by capillarity, we decided to use saturated resistance envelopes.

Four gray and four brown specimens were used to obtain the envelopes. Following a 24-hour immersion in deionized water and the collection of height variation data, each sample underwent the consolidation process. The gray specimens were consolidated at 29, 57, 112, and 233 kPa, while the brown specimens were subjected to stresses of 28, 57, 114, and 224 kPa. The slight stress differences were due to the irregular shape of the core samples during the molding process.

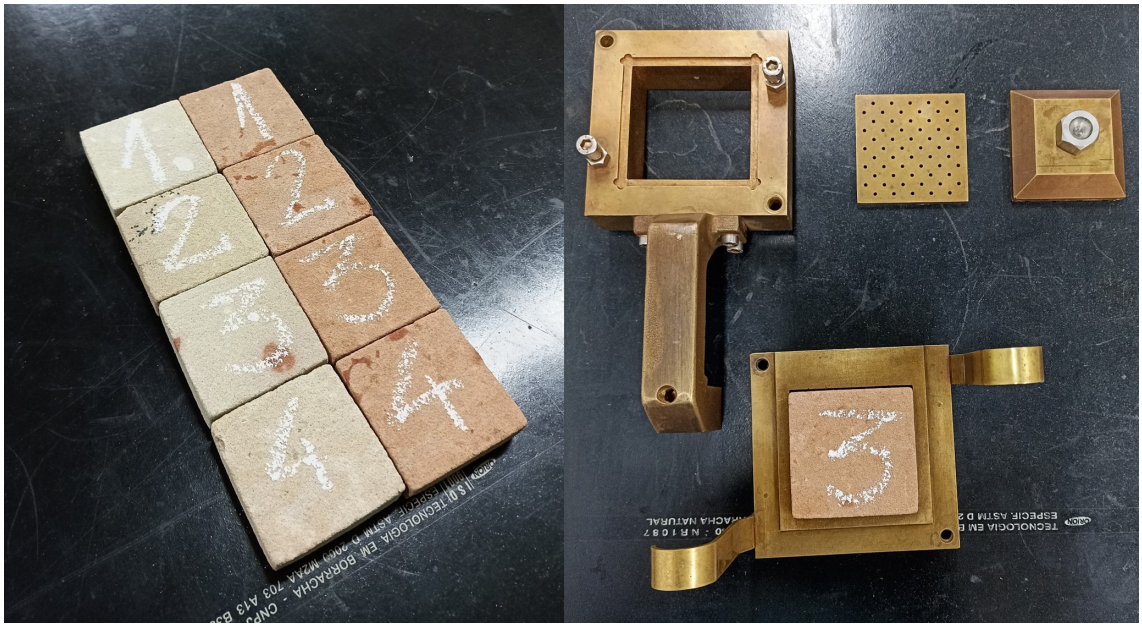

Figure 2.29: Samples used to obtain the envelope. Apparatus for the direct shear test.

Upon stabilizing the deformations resulting from the applied normal stresses, the corresponding samples underwent shearing until they achieved an approximate deformation of 10% of their initial length, equivalent to 6 mm. Based on the force, displacement, and normal stress data, the shear strength envelopes of gray and brown sandstone were determined.

Figure 2.30: Direct shear machine and data acquisition system.

2.2.7 Compressebility – oedometer test

Motivated by the peculiar behavior of sandstone when exposed to water, and following the guidelines of the standards ASTM D2435/D2435M (2011) and ASTM D4546 (2014) method C, we conducted tests to measure the compressibility and potential expansion of the material. These tests included saturated compressibility tests and natural condition tests.

Exemplified by Figures 2.31 and 2.31 and, similarly to the direct shear test, the gray and brown sandstone specimens were molded with the help of cutting ring, with the top and base finished using the cutting rings themselves as guides. At the end of the molding process, the samples were placed in the odometric chamber, and for those tested under natural conditions, the loading stages commenced. In contrast, those subjected to saturation were initially flooded, with their height variation monitored until stable values were reached, followed by the start of the loading process. Figure 2.33 depicts the sample in the odometric cell, as well as the flooding process with deionized water.

Both the saturated and natural conditions went through stages of approximate stresses of 3, 6, 12.5, 25, 50, 100, 200, 400, and 800 kPa during loading and 400, 100, and 25 kPa during unloading.

Figure 2.31: Gray and brown sandstone samples in the molds for oedometer testing before grinding the top and bottom.

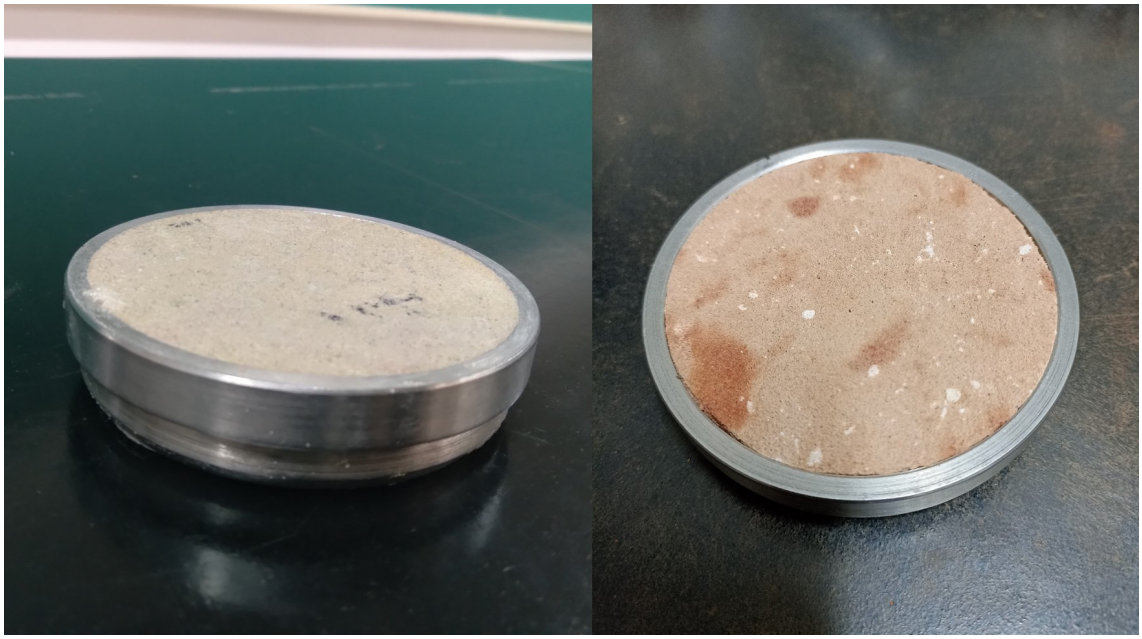

Figure 2.32: Gray and brown sandstone ready for the oedometer test

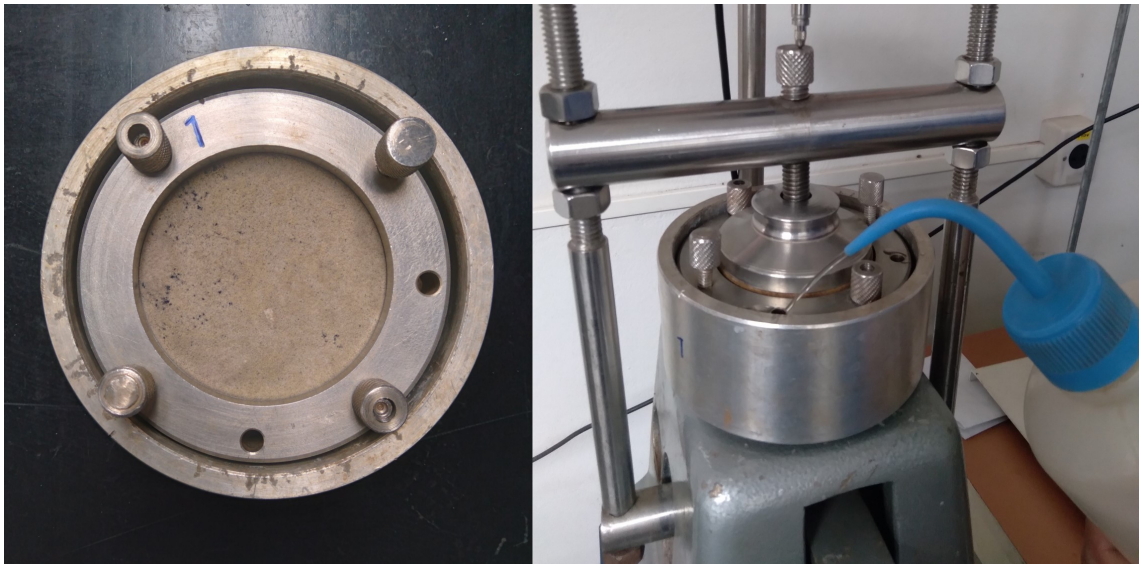

Figure 2.33: Sandstone positioned in the oedometer test camera. Pre-wetting process of the sample.

2.2.8 Permeability

Hydraulic conductivity was determined using a Triflex 2 flexible wall permeameter. Cylindrical specimens previously molded were positioned in the test chamber, as illustrated in Figure 2.34, maintaining the original top and bottom positions of their sampling, which were protected by glass microfiber filters and porous stones. Latex membranes were added to prevent lateral flow and attached to the base cap and top cap with o-rings. The arrangement described above is shown in Figure 2.35.

The core samples underwent the saturation, consolidation, and permeability testing stages. Saturation was conducted in accordance with the guidelines outlined from Skempton (1954) until parameter B reached 0.95 or higher. Consolidation occurred with an increase in confining pressure to the desired value and the release of excess pore pressure until deformations stabilized. The confining pressure values used were 20, 40, 80, 160, and 320 kPa, with a hydraulic gradient of 20 applied to the consolidated specimens up to 160 kPa. At 320 kPa of confining stress, some tests were conducted to reduce testing time, verify potential distortions at elevated gradients, as well as assess the influence of flow direction. Thus, tests with hydraulic gradients of 25, 50, 100, 200, and 400 were applied in various ways: keeping the pressure at the base constant while reducing the pressure at the top, distributing the pressures between the top and the base, and maintaining the pressure at the top constant while increasing the pressure at the base. In the latter case, achieving the gradient of 400 was impossible, as the increase in pressure at the base would exceed the applied confining pressure.

In addition to tests with different gradients, the possible occurrence of anisotropy in the sandstone was investigated by conducting permeability tests on samples molded in the horizontal direction (see Figure 2.17). In these tests, the sandstone samples were subjected to the same conditions previously described, i.e., consolidated with effective stress of 20, 40, 80, 160, and 320 kPa, with an applied hydraulic gradient during the permeability stage of 20 for samples with confining pressure of up to 160 kPa and 25 for 320 kPa.

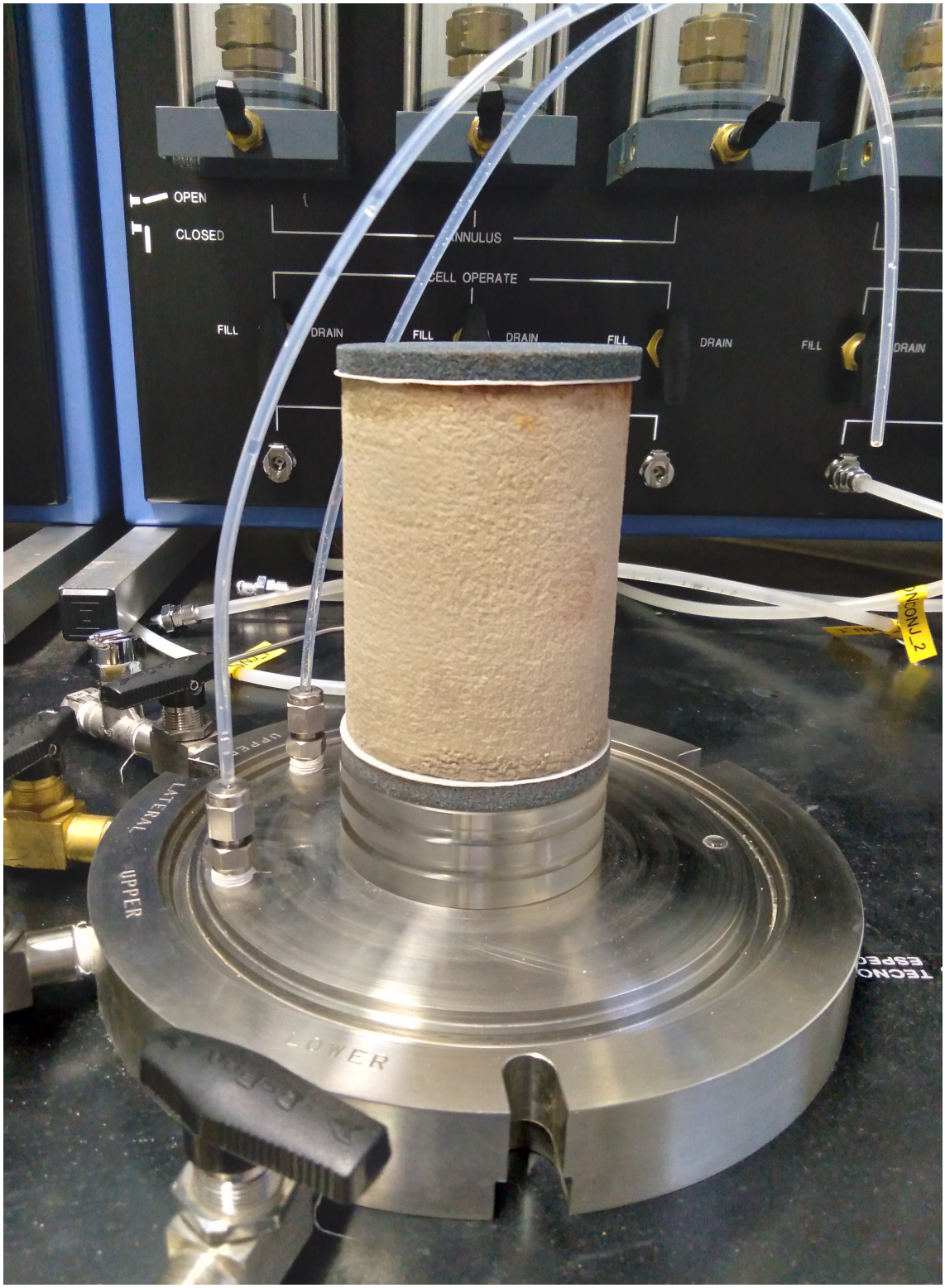

Figure 2.34: Cylindrical specimen positioned in the permeability test chamber.

Following the recommendations of ASTM D5084 (2016) for constant head testing and upward flow, except for the 320 kPa confinement of the sample taken in the vertical direction as previously justified, hydraulic conductivity was determined according to Darcy's law.

$$\mathrm{k} = \frac{Q}{i \times A} \tag{2.3}$$

where Q is the volume flow, i hydraulic gradient, and A the cross-sectional area.

As commented below, the estimation of unsaturated permeability for the sandstone was conducted in addition to the assessment of saturated permeability.

Figure 2.35: Flexible wall permeameter running three tests.

Unsaturated permeability

The unsaturated hydraulic conductivity was estimated using the Soil Water Retention Curve (SWRC) through the drying process using filter paper (Whatman 42) and Haines' funnel, as shown in Figures 2.36, and 2.37. Equations 2.4 and 2.5 proposed by van Genuchten (1980) were used to fit the SWRC and estimate the unsaturated hydraulic conductivity.

$$w(s) = w_r + (w_s - w_r)\left\{\frac{1}{[1 + (as)^n]^m}\right\} \tag{2.4}$$

where $w(s)$ is the water content in the suction function, w_r is the residual water content, w_s is the saturation water content, s is the suction, a, n, and m are the fitting parameters.

$$\mathrm{k(s)} = \mathrm{k_s}\sqrt{\frac{w(s) - w_r}{w_s - w_r}}\left\{1 - \left[1 - \left(\frac{w - w_r}{w_s - w_r}\right)^{\frac{1}{m}}\right]^m\right\}^2 \tag{2.5}$$

where k(s) is the unsaturated hydraulic conductivity, and $\mathrm{k_s}$ is the saturated hydraulic conductivity

(a) Specimen saturation

(b) Drying process

Figure 2.36: Sandstone samples during the capillary saturation and air-drying stages for the soil water retention curve.

Table 2.2 displays the tests that were carried out along with their corresponding standards.

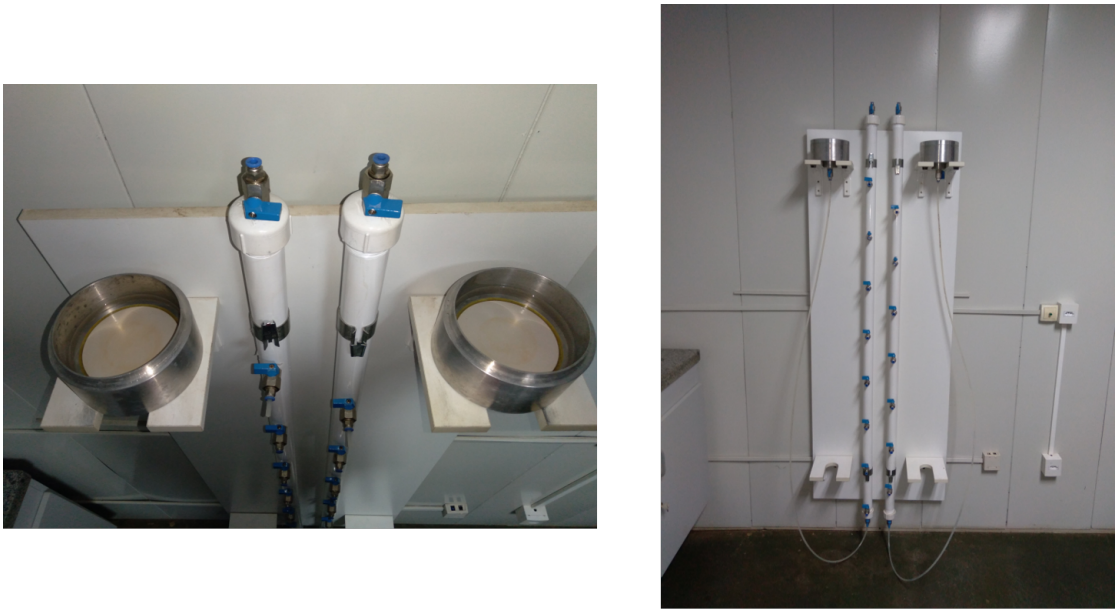

(a) Porous stone saturation

(b) Haines' funnel

Figure 2.37: Saturation of porous stones with high air intake. Haines' funnel with test in progress.

Table 2.2: Technological tests employed to obtain the UCS, elastic modulus, tensile strength by diametrical compression, direct shear, and hydraulic conductivity.

Test	**Reference**
Uniaxial compressive strength	ASTM C170/C170M (2017) ASTM D7012 (2014) - method C
Young's modulus	ASTM D7012 (2014) - method D ABNT NBR 8522-1 (2021) - method A
Brasilian test	ASTM C496/C496M (2017) ASTM D3967 (2016)
Direct shear	ASTM D5607 (2016)
Oedometer	ASTM D2435/D2435M (2011) ASTM D4546 (2014) - method C
Permeability	ASTM D5084 (2016) - constant head

2.3 Results and Discussion

2.3.1 Characterization

Particle size distribution and Atterberg limits

The granulometric curve of the gray and brown sandstones, as well as the percentages of each fraction, the consistency limits, and their classification according to ASTM D2487-17 (2017) are respectively presented in Figure 2.38 and Tables 2.3 and 2.4.

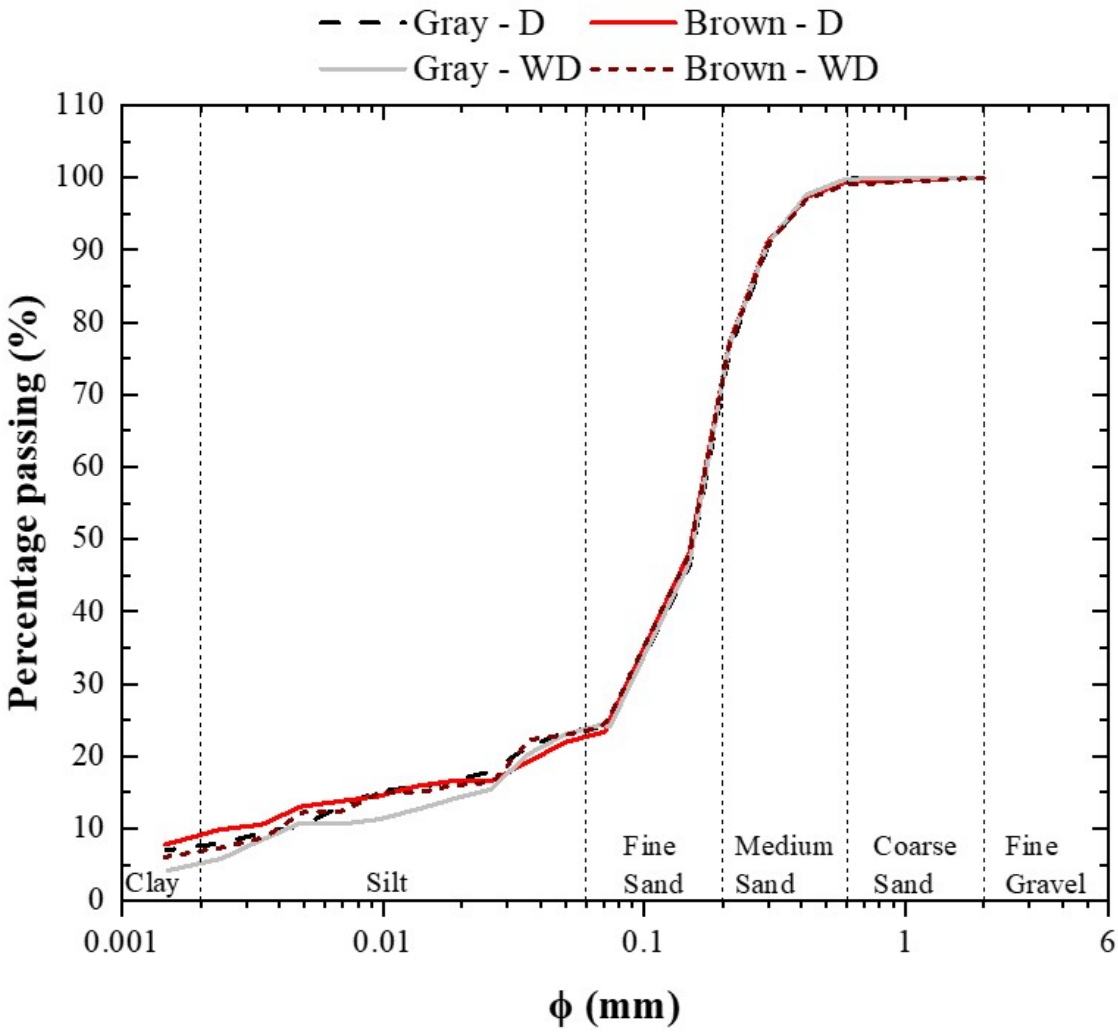

Figure 2.38: Particle size distribution of gray and brown sandstones with and without deflocculant.

Considering the fine sieving in the grain size distribution, it was found that there was no difference between the materials, with minor differences in the data obtained from the hydrometer stage. It is noteworthy that the granulometric curve of the brown sandstone without deflocculant differs drastically from the others at the interface between sieving and sedimentation (0.075 mm). At the time of data collection, the hydrometer bottom scale was exceeded, and the maximum value was adopted. The result remained consistent despite repeating the test with a material reduction from 60 to 40g. This observation is depicted in Figure 2.8, where almost all the brown material settled right at the beginning of the test, making it challenging to obtain conclusive data about it.

Table 2.3: Distribution of medium and fine sand, silt, and clay percentages in gray and brown sandstones.

Sandstone	**Medium Sand (%)**	**Fine sand (%)**	**Silt (%)**	**Clay (%)**
Gray - D	24	53	15	8
Gray - WD	24	53	18	5
Brown - D	24	53	13	10
Brown - WD	24	53	16	7

Table 2.4: Results of the Atterberg limits and the unified soil classification system for both sandstones.

Sandstone	**LL**	**PI**	**USCS**
Gray	38	20	SC
Brown	44	23	SC

The behavior observed in the brown sandstone was due to the absence of a deflocculant, which led to the agglomeration of fine particles into a larger grain that rapidly sedimented. This phenomenon was not observed in the gray sandstone.

The Atterberg limits indicate that the sandstone fines exhibit plasticity, with slightly higher values for the brown sandstone than the gray sandstone. Both demonstrate behavior akin to slightly compressible clay, classified under the USCS as clayey sand. These findings, along with the methylene blue data presented in Table 2.5, suggest that the plasticity of the

sandstone aligns with clays from the smectite group, as also reported by Jesus et al. (2013) and elaborated below.

Methylene blue and scanning electron microscope

Observing the sandstone's distinct behavior in the presence of water, further tests were conducted to confirm the presence of clay minerals, particularly expansive ones.

Figures 2.39 and 2.40 indicate the presence of clay platelets on a more prominent grain, possibly quartz. These platelets' energy-dispersive X-ray spectroscopy (EDS) results reveal the elements commonly found in clay minerals (O, Fe, Mg, Al, and Si). The combination of hydrometer data, EDS results, and the methylene blue technique suggests the presence of clay minerals from the smectite group in the sandstone. Direct shear tests and oedometer compression will further support these findings during saturation. These findings were confirmed by Mondelli (2008), who identified the presence of phyllosilicates (palygorskite and sepiolite) as well as beidellite from the smectite group in sandstone from the Bauru landfill through X-ray diffraction tests.

Table 2.5: Results of the methylene blue test, including cation exchange capacity (CEC), specific surface area (SA), value of methylene blue adsorbed (BV), and activity index of the clay fraction (Acb).

Parameter	Gray	Brown
CEC (meq/100g)	127	90
SA (m^2/g)	79.36	70.19
BV (g/100g de solo)	3.24	2.87
Acb (g/100g de solo)	0.43	0.32

Similar results to those observed here using SEM and EDS have also been verified by Jing et al. (2018), Ueda et al. (2019), Bolarinwa et al. (2019), Bakhshi Ardakani & Rajabi (2021), and Rajabi & Hamrahi (2021).

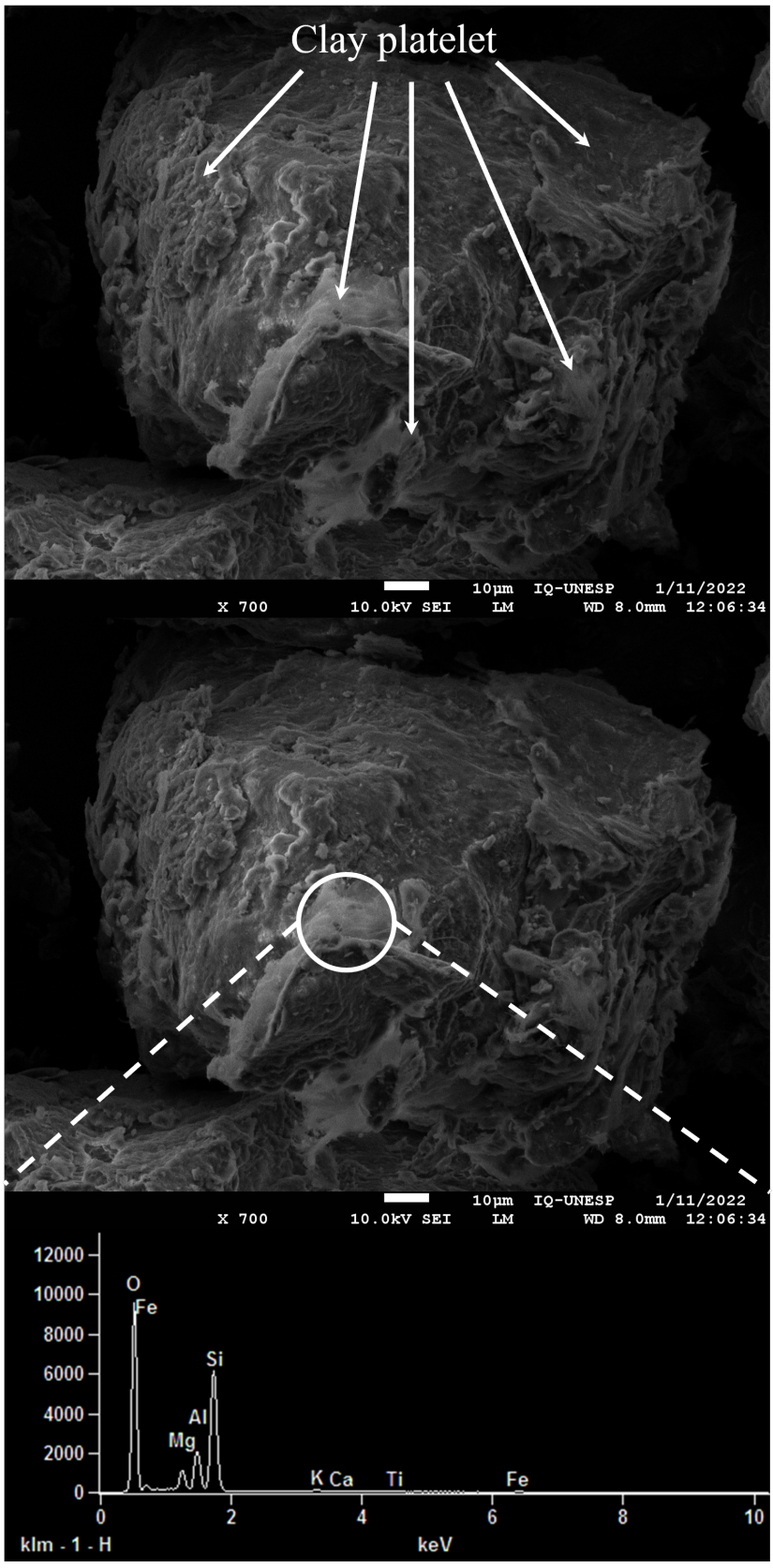

Figure 2.39: Scanning electron microscopy (SEM) of the gray sample in combination with energy-dispersive X-ray spectroscopy (EDS).

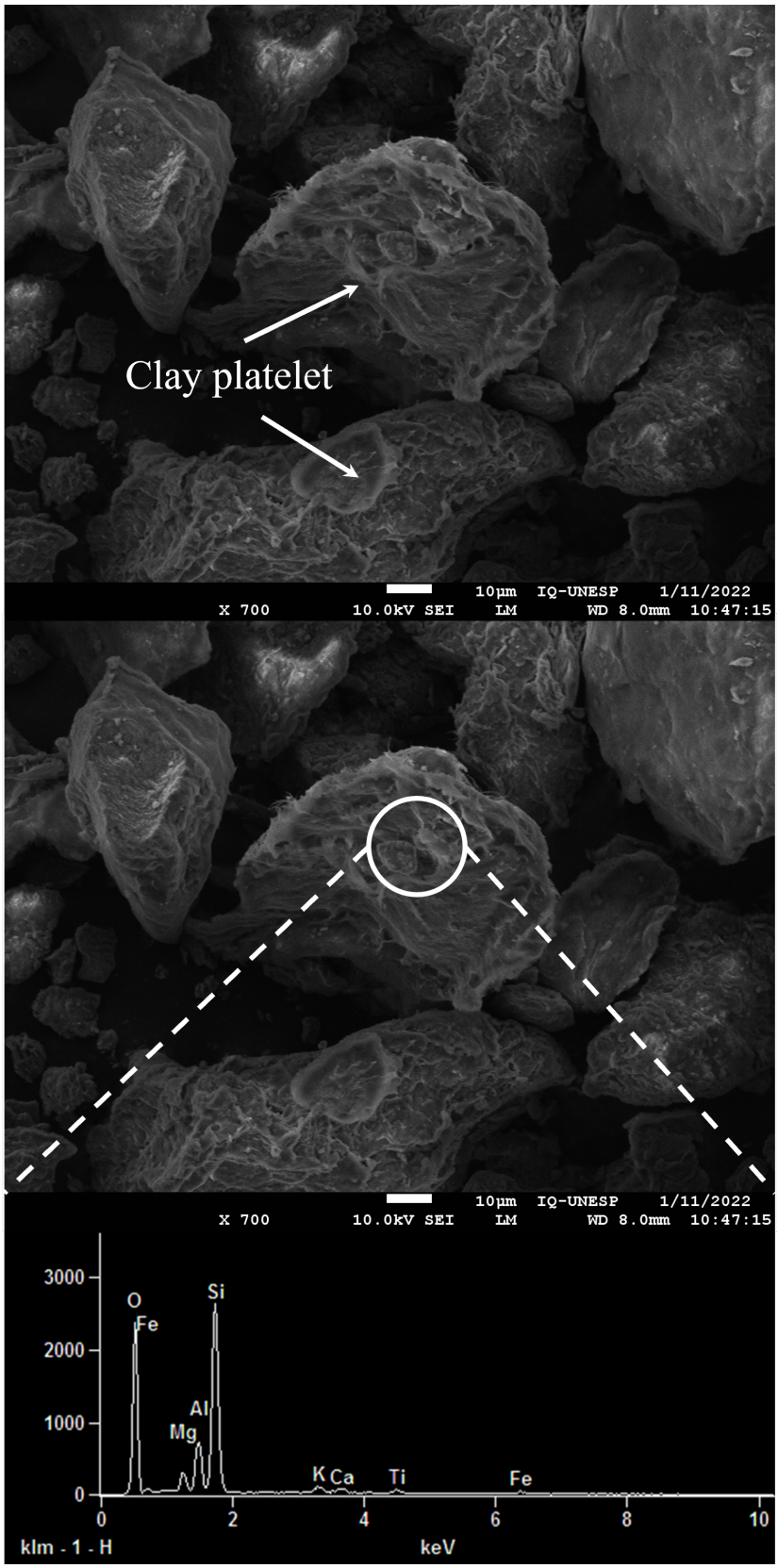

Figure 2.40: Scanning electron microscopy (SEM) of the brown sample in combination with energy-dispersive X-ray spectroscopy (EDS).

2.3.2 Strength

Uniaxial compressive strength

A uniaxial compressive strength (UCS) was obtained from two test specimens to define the maximum load to be applied during the elasticity modulus test, along with another five taken to failure at the end of the test to determine Young's modulus. The UCS was defined by values that did not deviate more than 20% from the average. Since the core samples used to determine the modulus of elasticity also provided data on uniaxial compressive strength, those that did not meet the criteria for calculating Young's modulus were disregarded for the UCS determination. Thus, Table 2.6 depicts the initial sandstone's index properties used in Young's modulus and UCS tests, and Table 2.7 presents the data from all seven tests, emphasizing test specimen 11, which did not meet the standard criteria ABNT NBR 8522-1 (2021) for determining the modulus of elasticity. Therefore, Table 2.8 presents the average values, standard deviation (sd), and coefficient of variation (cv) for the valid UCS data.

With an average value of 8.31 MPa, the uniaxial compressive strength refers to a weathered brittle sandstone, with the gray and brown varieties showing no significant differences.

Table 2.6: Initial index properties of the sandstone used to determine the Young's modulus and UCS.

Sandstone	Specimen	wi (%)	ρs (g/cm³)	ei	ρd (cm³)	ni (%)
Brown	1	1.49	2.676	0.403	1.907	28.75
Brown	6	1.54	2.676	0.441	1.857	30.60
Brown	8	1.49	2.676	0.446	1.851	30.84
Brown	9	1.48	2.676	0.389	1.927	27.98
Gray	11	1.67	2.628	0.292	2.034	22.59
Gray	12	1.86	2.628	0.300	2.022	23.05
Gray	13	1.86	2.628	0.304	2.015	23.34

Where wi is the initial water content, ρs is the grain density, ei is the initial void ratio, ρd is the dry density, and ni is the initial porosity.

Table 2.7: Uniaxial compressive strength of the specimens used to get Young's modulus.

Specimen	UCS (MPa)	Sandstone
1	8.48	Brown
6	8.91	Brown
8	7.77	Brown
9	8.62	Brown
11	6.43	Gray
12	7.88	Gray
13	8.21	Gray
mean	8.04	
sd	0.82	
cv (%)	10.15	

Table 2.8: Uniaxial compressive strength considering the specimens used to get the Young's modulus, within the range of ± 20% of the mean.

Specimen	UCS (MPa)	Sandstone
1	8.48	Brown
6	8.91	Brown
8	7.77	Brown
9	8.62	Brown
12	7.88	Gray
13	8.21	Gray
mean	8.31	
sd	0.44	
cv (%)	5.30	

Diametral compression

The assessment of tensile strength through diametrical compression for a core sample, as per ASTM D3967 (2016), before and after failure, is depicted in Figure 2.41, as well as Table 2.9 describes the initial index proprieties from the sandstone applied in the Brazilian test. Additionally, Figure 2.42 presents all test specimens after the completion of the test. The stress-strain data displayed in Figures 2.43, 2.44, and 2.45 indicates the brittle failure of the material, with no significant differences observed between the gray sandstone and the brown sandstone, as detailed in Table 2.10, which provides the results of the 13 test specimens, 9 of which yielded usable results. The valid results and the average, standard deviation, and coefficient of variation are presented in Table 2.11.

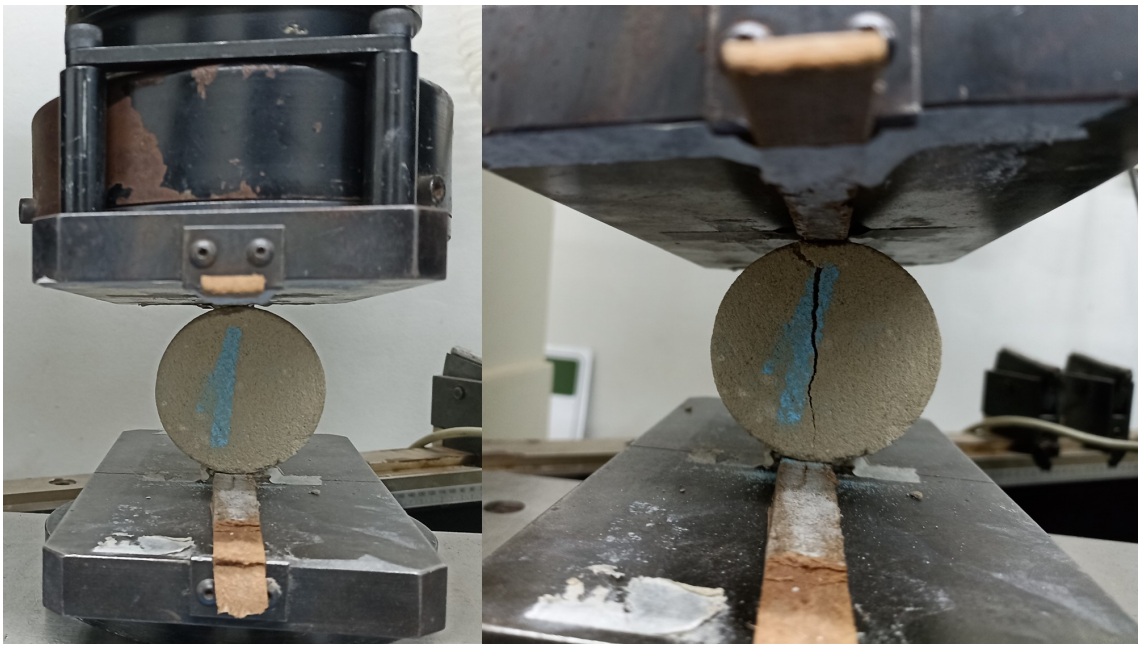

Figure 2.41: Specimen before and after the diametral compression test following the recommendations of ASTM D3967 (2016).

Table 2.9: Initial index properties of the sandstone used to determined the tensile strength by diametral compression.

Sandstone	Specimen	wi (%)	ρs (g/cm³)	ei	ρd (cm³)	ni (%)
Brown	2	1.43	2.676	0.368	1.956	26.91
Gray	3	1.81	2.628	0.302	2.019	23.17
Gray	4	1.67	2.628	0.273	2.064	21.44
Gray	5	1.76	2.628	0.299	2.023	23.03
Brown	7	1.42	2.676	0.402	1.908	28.68
Brown	10	1.48	2.676	0.439	1.860	30.49

Figure 2.42: Core samples after failure by tensile by diametral compression.

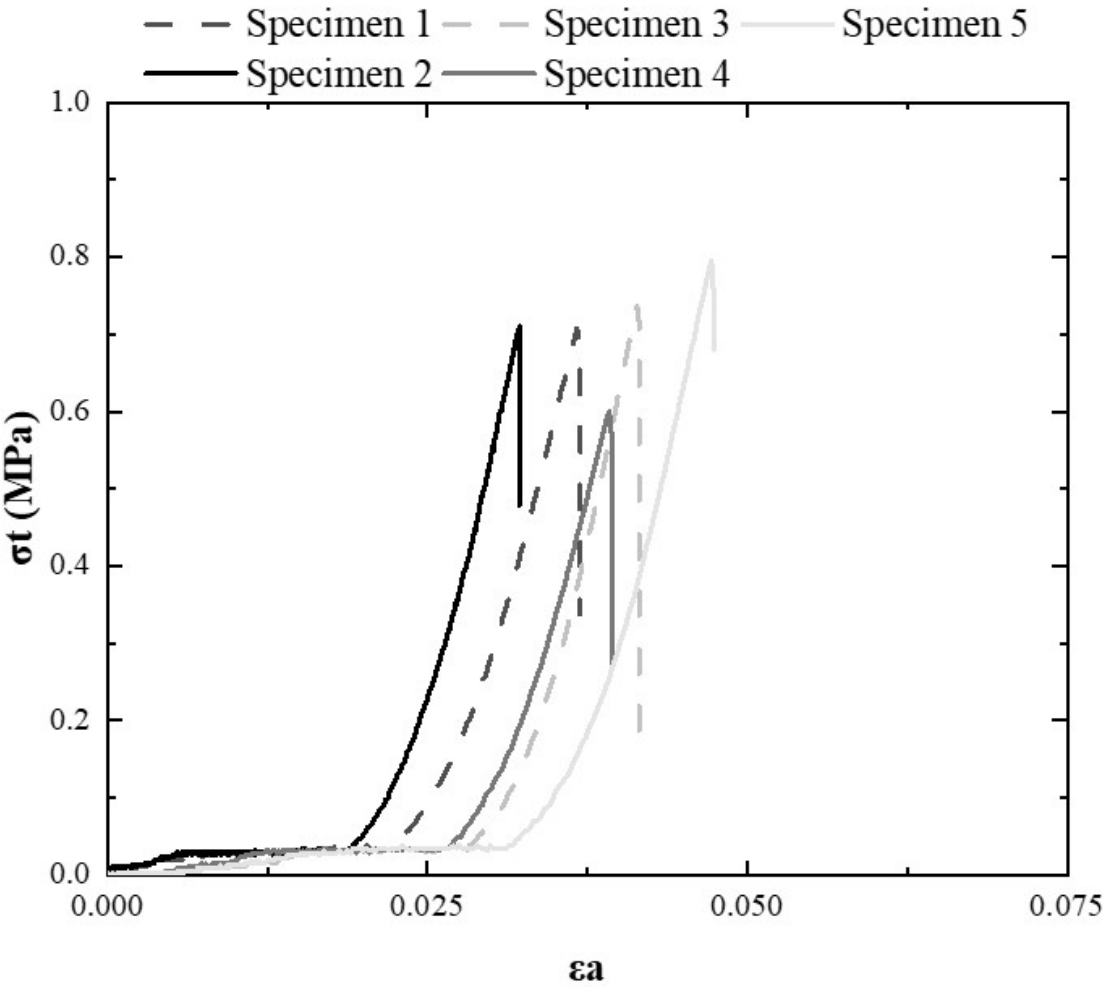

Figure 2.43: Stress-strain curve used to calculate the diametral compressive tensile strength according to the ASTM D3967 (2016) standard.

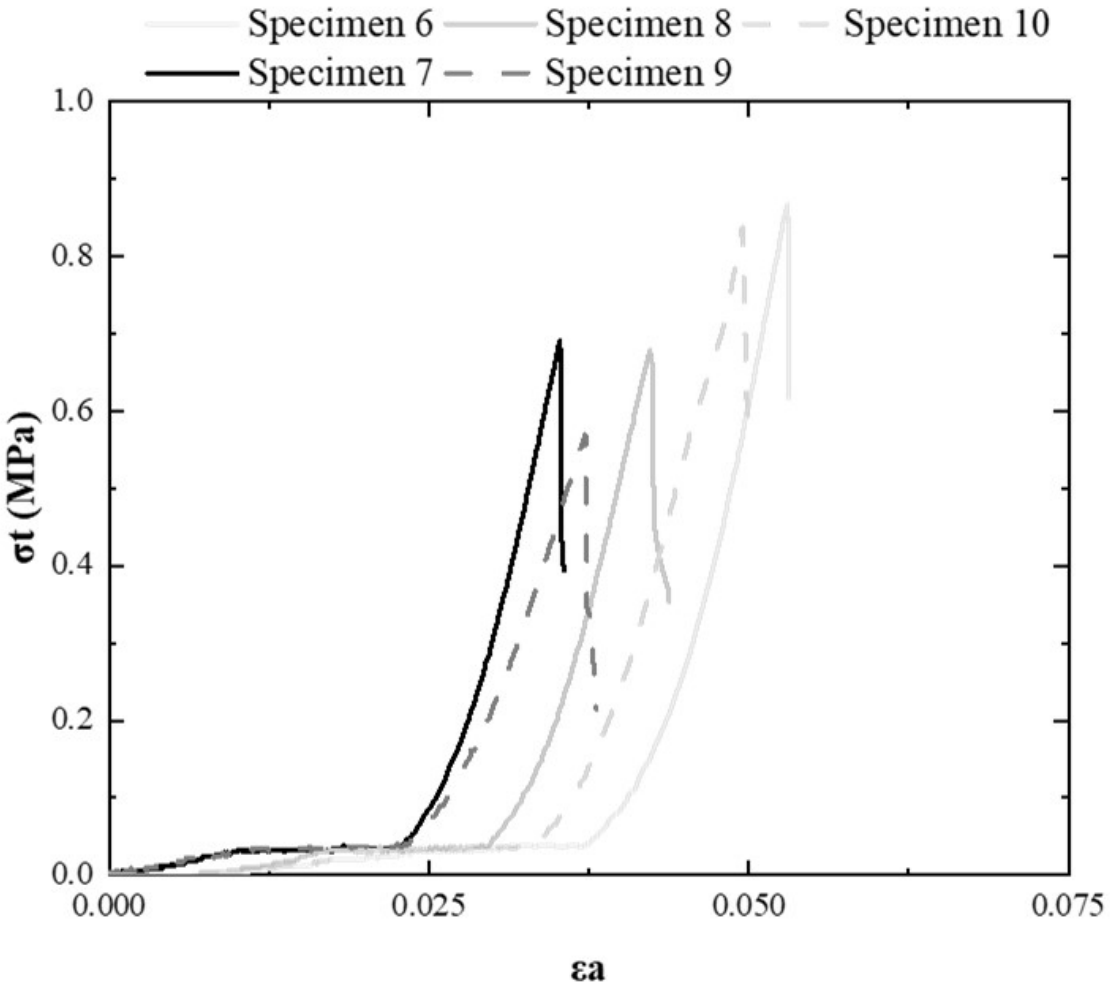

Figure 2.44: Stress-strain curve used to calculate the diametral compressive tensile strength according to the ASTM D3967 (2016) standard (continuation).

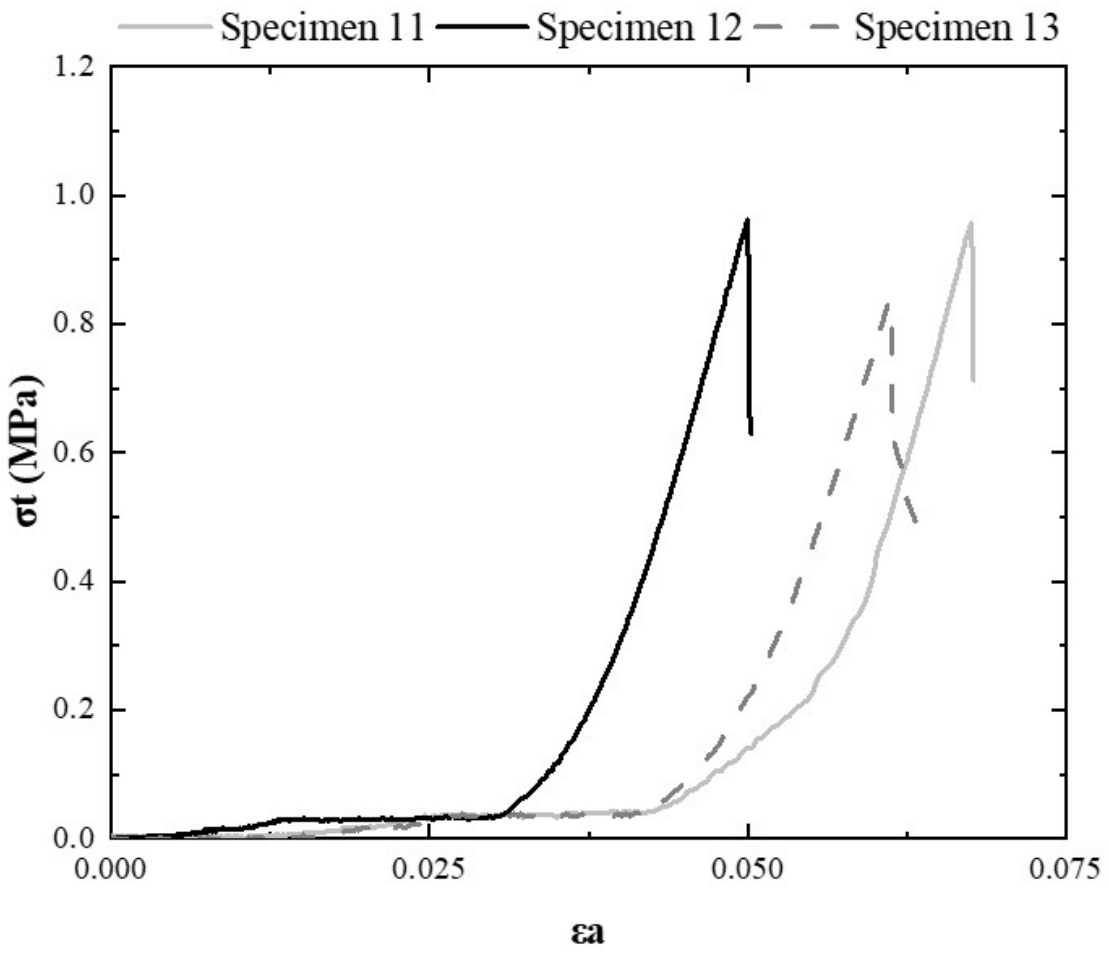

Figure 2.45: Stress-strain curve used to calculate the diametral compressive tensile strength according to the ASTM D3967 (2016) standard (continuation).

Table 2.10: Results for tensile strength in diametrical compression (σ_t), thickness/diameter ratio (t/φ), and compressive strength (σ_c) according to the ASTM D3967 (2016) standard.

Specimen	Strength-σ_t (MPa)	t/φ	Strength-σ_c (MPa)	Sandstone
1	0.71	0.51	2.12	Gray
2	0.71	0.51	2.13	Gray
3	0.74	0.47	2.21	Gray
4	0.60	0.48	1.80	Gray
5	0.79	0.47	2.38	Brown
6	0.87	0.52	2.60	Brown
7	0.86	0.48	2.57	Gray
8	0.68	0.47	2.04	Gray
9	0.58	0.47	1.75	Brown
10	0.84	0.50	2.51	Brown
11	0.96	0.45	2.87	Brown
12	0.96	0.52	2.89	Gray
13	0.84	0.45	2.51	Gray
mean	0.78	0.49	2.34	
sd	0.12	0.03	0.36	
cv (%)	15.59	5.58	15.59	

Table 2.11: Data reported by Table 2.10 considering valid results.

Specimen	Strength-σ_t (MPa)	t/φ	Strength-σ_c (MPa)	Sandstone
1	0.71	0.51	2.12	Gray
2	0.71	0.51	2.13	Gray
3	0.74	0.47	2.21	Gray
5	0.60	0.48	1.80	Brown
6	0.87	0.52	2.60	Brown
7	0.86	0.48	2.57	Gray
8	0.68	0.47	2.04	Gray
10	0.84	0.50	2.51	Brown
13	0.84	0.45	2.51	Gray
mean	0.78	0.49	2.34	
sd	0.07	0.03	0.22	
cv (%)	9.29	5.30	9.29	

Furthermore, adhering to the guidelines outlined in ASTM C496/C496M (2017) for the Brazilian test, the results obtained from 6 cylindrical test specimens, with a length/diameter ratio of 2:1, are provided in Table 2.12, while Table 2.13 displays the valid results. The stress-strain curves are illustrated in Figure 2.46.

The analysis of the valid results for both standards reveals a slight variation in the average values of tensile strength by diametral compression, with 0.78 MPa following ASTM D3967 (2016) and 0.88 MPa considering ASTM C496/C496M (2017). The results of around 10% of the UCS are consistent with what the literature indicates Broch & Franklin (1972); Fjær et al. (2008).

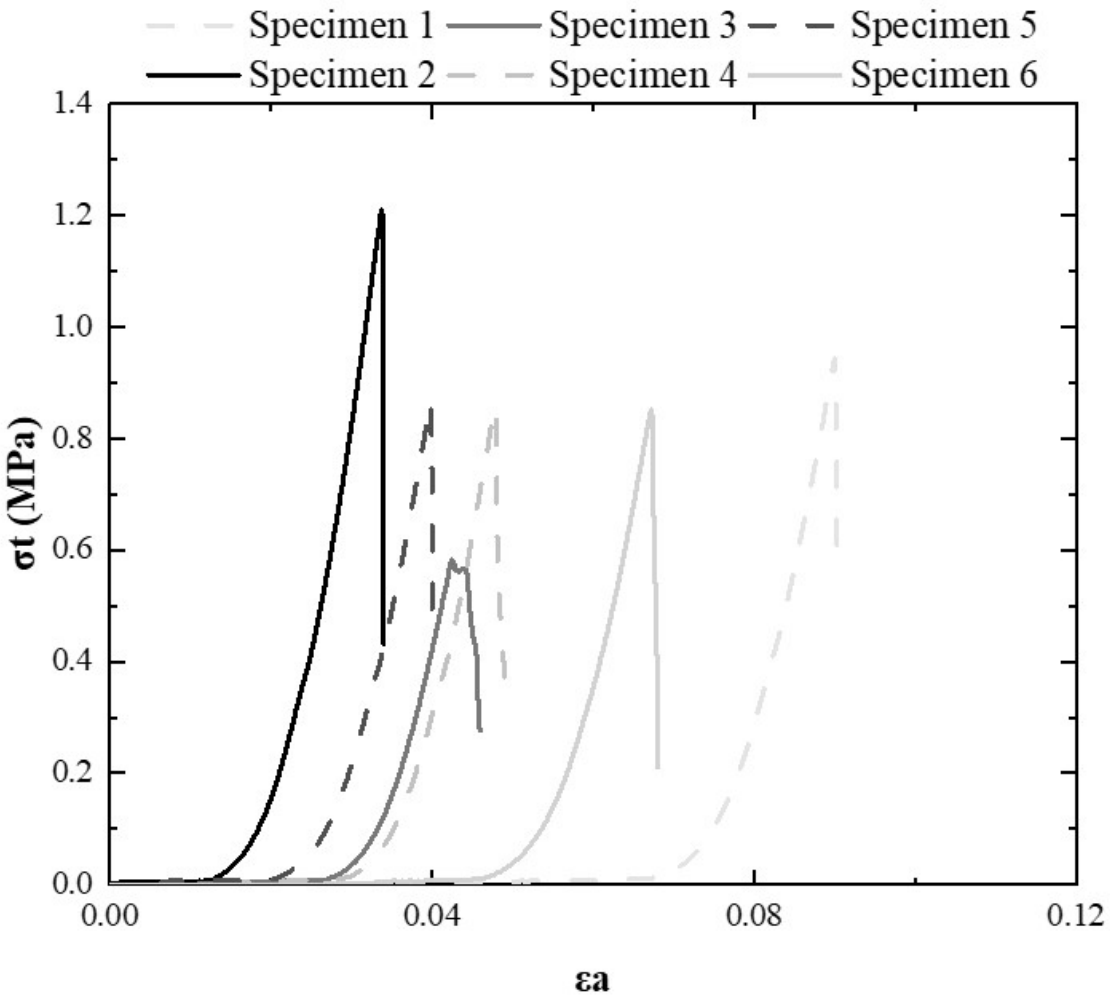

Figure 2.46: Stress-strain curve used to calculate the diametral compressive tensile strength according to the standard ASTM C496/C496M (2017).

Following both standards, the compressive strength values obtained from the diametral compression test illustrate the compressive efforts throughout the specimen during the test. The samples failed due to tension because the tensile strength represented one-third of the compressive strength.

Although the core samples prepared with lengths equal to or greater than double the diameter showed slightly improved outcomes, the change in scale did not demonstrate significant differences. Considering it is a natural material that is difficult to extract and prepare, making samples using a thickness/diameter ratio 0.5 represents a considerable material saving without compromising quality. Thus, the standard aimed at rocks is endorsed

for Brazilian testing.

Despite its brittle nature, the sandstone's performance under the previously tested conditions meets the minimum requirements outlined in the literature for geoenvironmental use as a liner for sanitary landfills, which indicates a minimum unconfined compressive strength of 0.2 MPa (Buragohain et al., 2018; Garg et al., 2020).

Table 2.12: Results for tensile strength in diametrical compression (σ_t), length/diameter ratio (L/φ), and compressive strength (σ_c) according to the ASTM C496/C496M (2017) standard.

Specimen	Strength–σ_t (MPa)	L/φ	Strength–σ_c (MPa)	Sandstone
2	1.21	2.18	3.63	Brown
3	0.58	2.00	1.75	Gray
4	0.86	2.23	2.57	Gray
5	0.87	2.15	2.60	Gray
7	0.94	2.39	2.83	Brown
10	0.85	2.29	2.56	Brown
mean	0.89	2.21	2.66	
sd	0.20	0.13	0.60	
cv (%)	22.71	6.01	22.71	

Table 2.13: Data reported by Table 2.12 considering valid results.

Specimen	Strength–σ_t (MPa)	L/φ	Strength–σ_c (MPa)	Sandstone
4	0.94	2.39	2.83	Gray
5	0.86	2.23	2.57	Gray
7	0.87	2.15	2.60	Brown
10	0.85	2.29	2.56	Brown
mean	0.88	2.27	2.64	
sd	0.04	0.10	0.13	
cv (%)	4.88	4.37	4.88	

Regarding the tensile strength reported in the literature, Huang et al. (2010) evaluated it through a diametral compression test on dry and saturated Longyou sandstone samples with different loading rates. For the dry condition, the values ranged from 2.8 to 5.3 MPa for

loading rates of 10^{-4} and 58 GPa/s. The saturated samples had a maximum value of 3.01 MPa at 50 GPa/s and a minimum of 0.38 MPa at 10^{-4} GPa/s.

Yuan & Shen (2017) simulated and tested different types of rocks with contact conditions with and without a cushion. The results for tensile strength without a cushion and with a cushion, elasticity modulus, and compression from the diametral compression test on a gritstone were 6.3 MPa, 7.0 MPa, 14.1 GPa, and 89.9 MPa, respectively. For the mid-grain sandstone, the values were 7.9 MPa, 9.6 MPa, 23.8 GPa, and 116.8 MPa, respectively.

Liu et al. (2022) examined the mechanical behavior of fine-grained homogeneous sandstone subjected to freeze-thaw treatment. The mechanical properties reported during diametral compression testing were compressive strength of 62.5 MPa, tensile strength of 7.0 MPa, and elastic modulus of 6.7 GPa.

Wang et al. (2022) conducted tensile-shear tests on red sandstone, obtaining the mechanical properties of unconfined compressive strength (UCS) of 68.89 MPa, tensile strength of 5.88 MPa, and Young's modulus of 7.44 GPa.

UCS values of 61 MPa and diametral tensile strength of 7 MPa with an elastic modulus of 6.7 GPa were reported by You et al. (2022) for Neijiang sandstone.

Direct shear

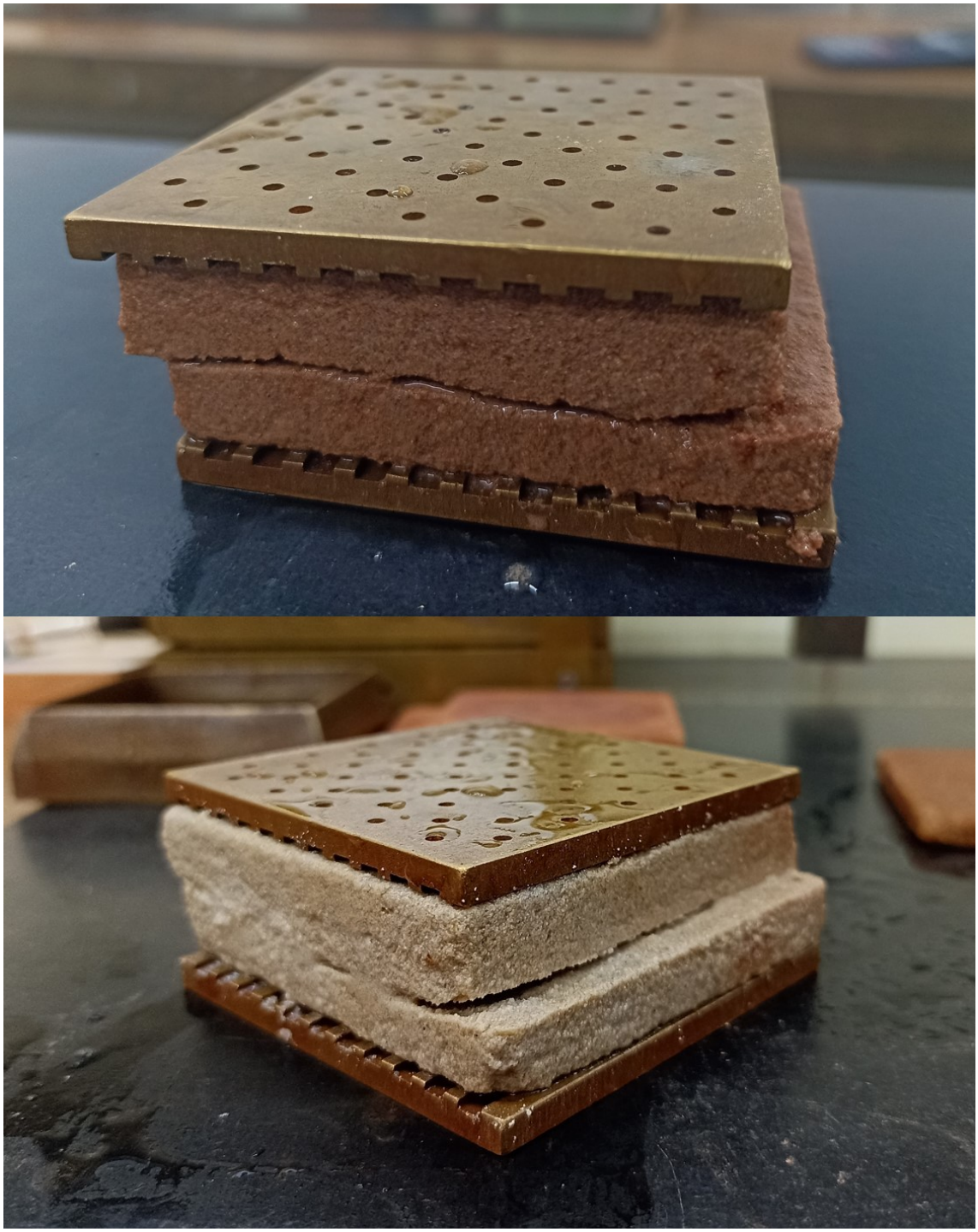

Figure 2.47: Brown and gray sandstone after failure when subjected to the direct shear test.

Gray sandstone

Direct shear tests were conducted to evaluate the shear resistance of gray and brown sandstone. Table 2.14 displays the preliminary index properties of the direct shear specimens employed in the testing procedure. Figure 2.47 illustrates an image of each sheared specimen.

The outcomes of the saturation, consolidation, and shearing phases of the gray sample are presented in Figures 2.48, 2.49, 2.50, and 2.51 correspondingly.

From the saturation phase, it can be inferred that the samples underwent expansion, ranging from 0.7 to 1.13% in the volume of the specimen. As anticipated, during the consolidation process, the percentage reduction of the samples was directly proportional to the applied loads, specifically 0.91, 1.25, 2.25, and 5.50% for 29, 57, 112, and 233 kPa, respectively.

Table 2.14: Initial index properties of the gray sandstone used to determine the shear strength.

Sandstone	**σ (kPa)**	**wi (%)**	**ei**	**ρd (cm³)**	**ni (%)**
Gray	29	1.50	0.398	1.880	28.45
	57	2.50	0.386	1.896	27.85
	112	1.40	0.447	1.817	30.871
	233	1.65	0.409	1.865	29.044

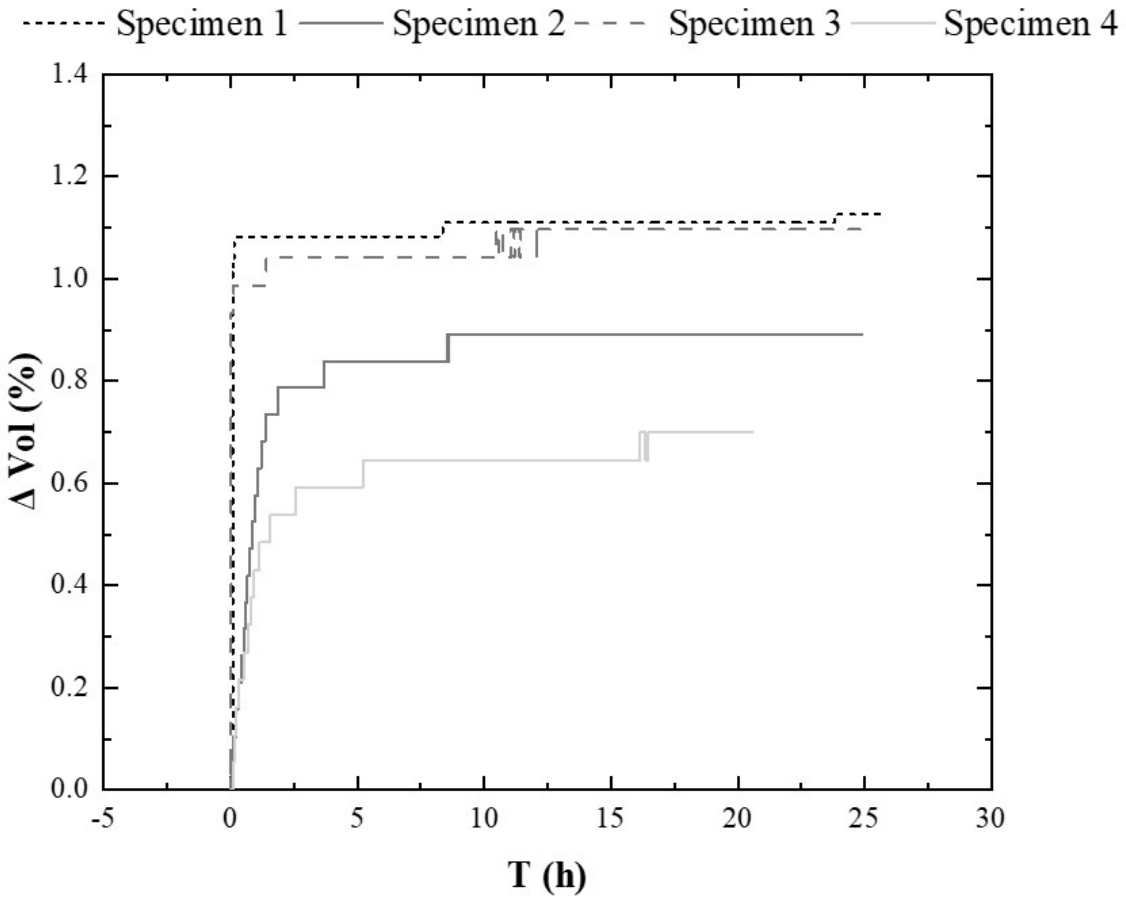

Figure 2.48: Volumetric variation of gray sandstone samples in the saturation stage.

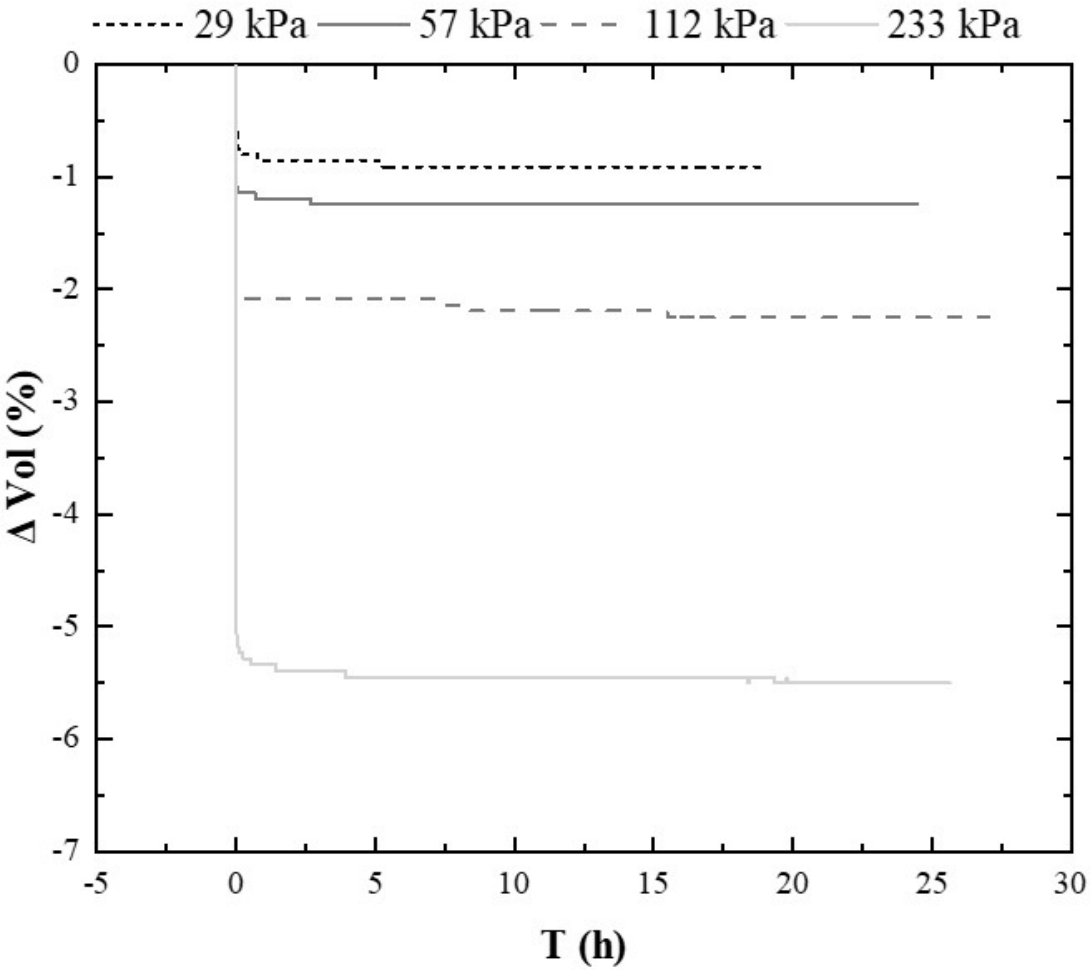

Figure 2.49: Volumetric variation of gray sandstone samples in the consolidation stage.

Figures 2.50 and 2.51 explain the shearing stage. The first illustrates the relationship between vertical and horizontal displacements, while the second presents the shear stress variation with horizontal displacement.

From the joint analysis, it was possible to verify that the sample with lower consolidation initiated the shearing process more quickly, exhibiting expansion from the start of the test. However, with 3% vertical displacement, the sample ceased its vertical deformations.

The consolidated specimen with a pressure of 57 kPa did not exhibit vertical deformation at the start of the test. Nevertheless, it showed the most significant expansion (2.79% of the initial height) by the end of the shearing stage among the four specimens used

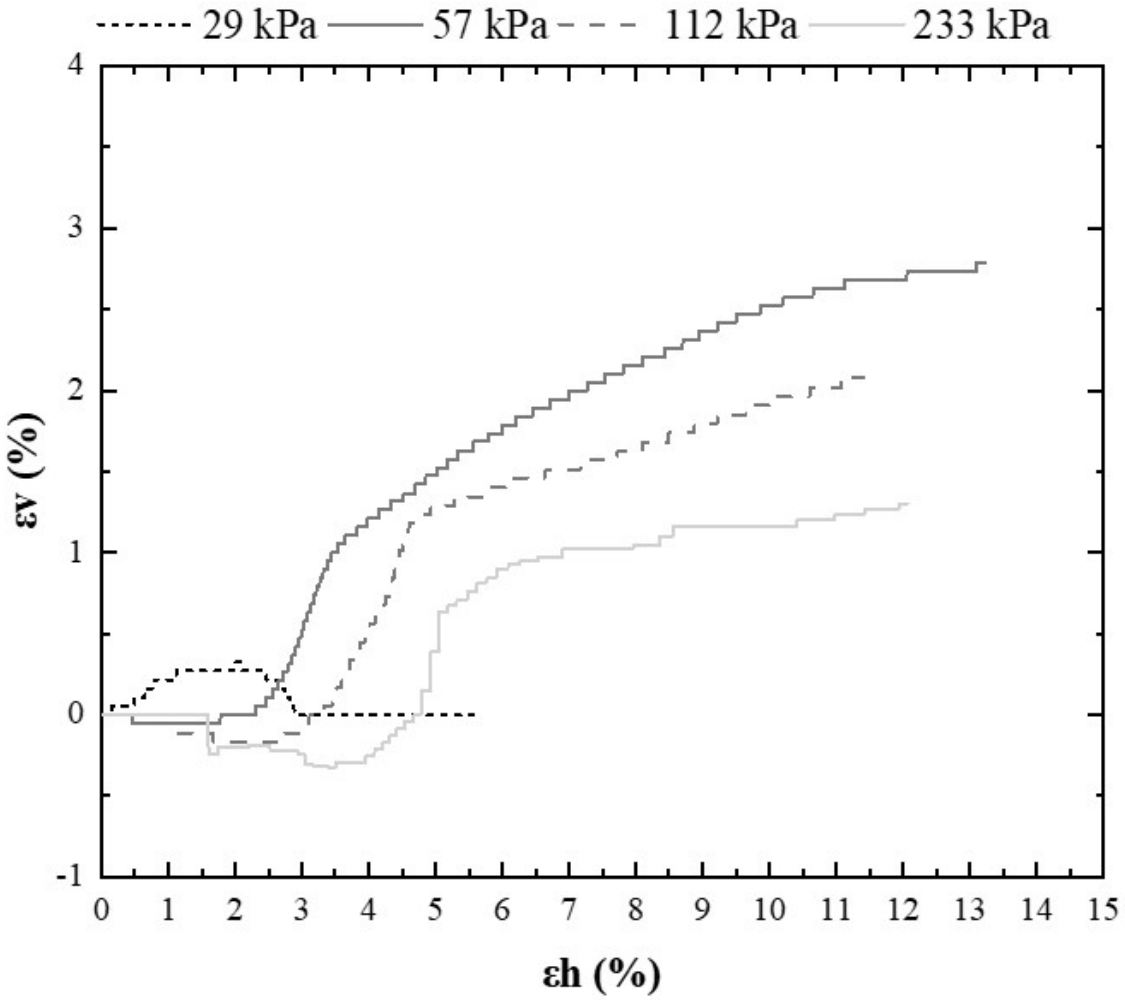

Figure 2.50: Vertical and horizontal deformations of gray sandstone samples under shear stage conditions.

to establish the envelope.

The core samples consolidated at 114 and 234 kPa behaved similarly regarding vertical expansion. Initially, they compressed and expanded with 3% vertical displacement for the first sample and 4% for the second. In general, the gray sandstone exhibited peak and residual strength; the samples followed the expected behavior, i.e., an increase in shear strength with an increase in normal stress, displaying a characteristic similar to compact sandy materials, expanding when failure occurred due to shearing.

The shear strength envelope illustrated in Figure 2.52 was established with the peak

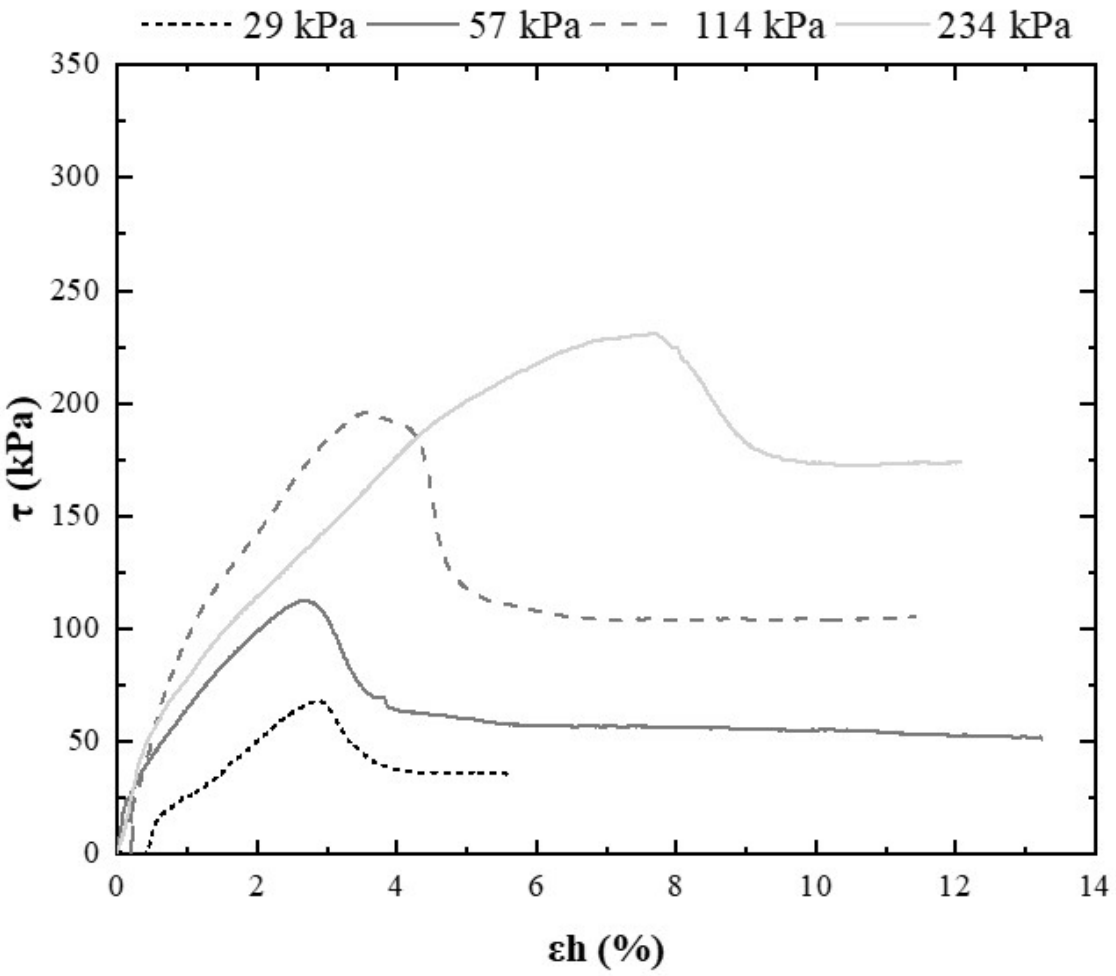

Figure 2.51: Stress-strain behavior of the gray sandstone cores required to establish the strength envelope.

shear strength and its associated normal stress. From this, values of 44° for the friction angle and 69 kPa for the cohesion intercept were obtained.

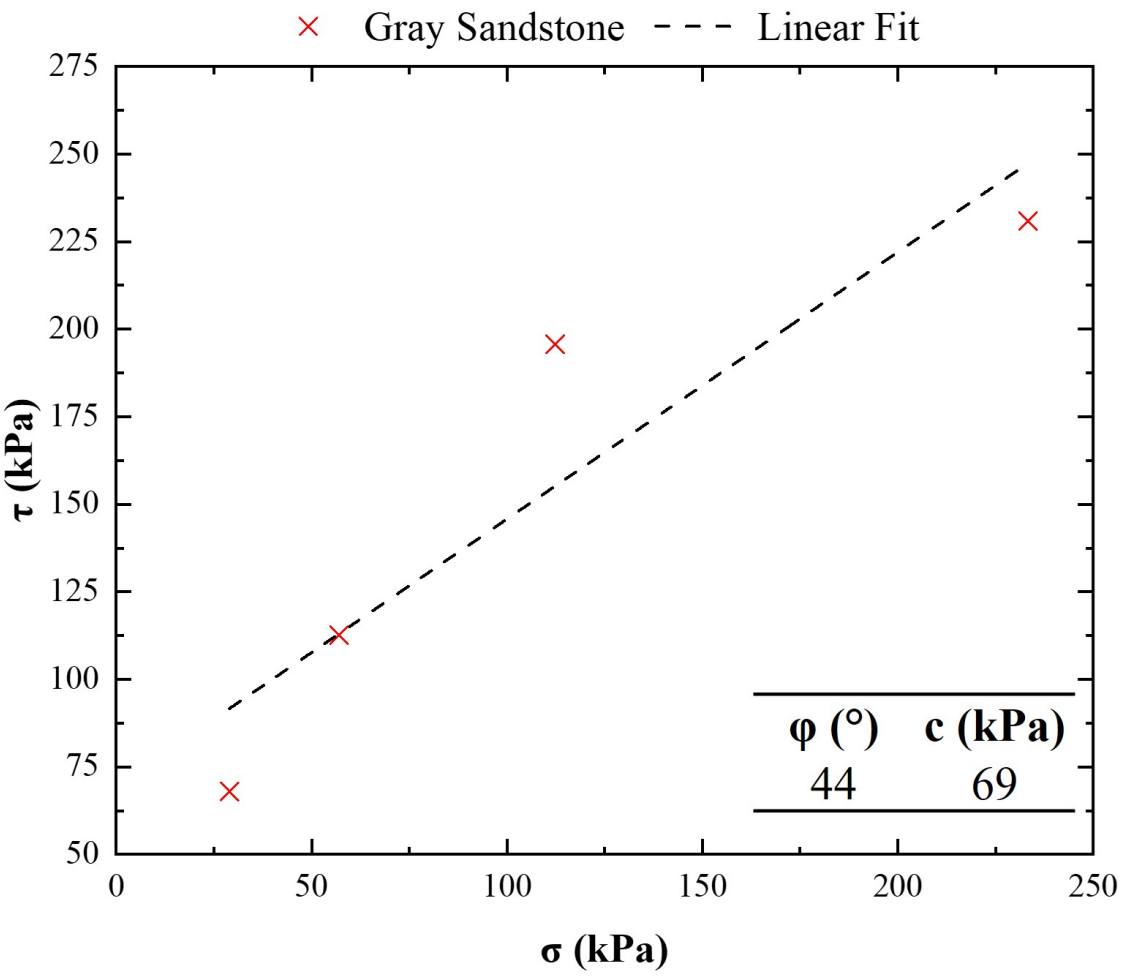

Figure 2.52: Strength envelope of gray sandstone based on the Mohr-Coulomb criterion.

Brown sandstone

Analogous to the gray sandstone, brown sandstone displayed similar behavior, as evidenced by Table 2.15, and Figures 2.53 to 2.56, which clarify the saturation, consolidation, and shearing stages. As depicted in Figure 2.53, the volumetric deformation of brown sandstone illustrates an expansion ranging between 0.49% and 0.93% concerning the initial volume. This expansion was slightly lower than that of gray sandstone.

Table 2.15: Initial index properties of the brown sandstone used to determine the shear strength.

Sandstone	**σ (kPa)**	**wi (%)**	**ei**	**ρd (cm³)**	**ni (%)**
Brown	28	1.20	0.458	1.836	31.40
	57	2.10	0.462	1.830	31.62
	114	1.80	0.457	1.837	31.37
	224	1.85	0.478	1.811	32.34

In the consolidation phase, the vertical deformations were proportional to the applied loads, as seen in Figure 2.54. The percentage reduction in the volume of the test specimens related to the loads of 28, 57, 114, and 234 kPa was respectively 1.03%, 1.14%, 2.17%, and 3.07%. Similar to the expansion, the consolidation of the brown material was lower than that of the gray sandstone, except for the consolidation resulting from the first load, which was slightly higher, that is, 0.91% for the gray compared to 1.03% for the brown.

These percentage values of volumetric variation for the gray and brown test specimens are summarized in Table 2.16. The normal stress related to saturation indicates which sample the vertical displacement refers to, with no stress applied in that stage. In contrast, the vertical displacement during consolidation occurred precisely due to applying normal stress.

As shown in Figures 2.55 and 2.56, the shearing of the brown samples occurred similarly. All test specimens were compressed at the beginning and underwent expansion at the end of the shearing process. The increase in normal stress required horizontal displacement in the same order as the gray core samples, both to initiate the expansion process (between 3 and 4.5%) and to reach the peak shear stress (between 3 and 5%), which was naturally higher

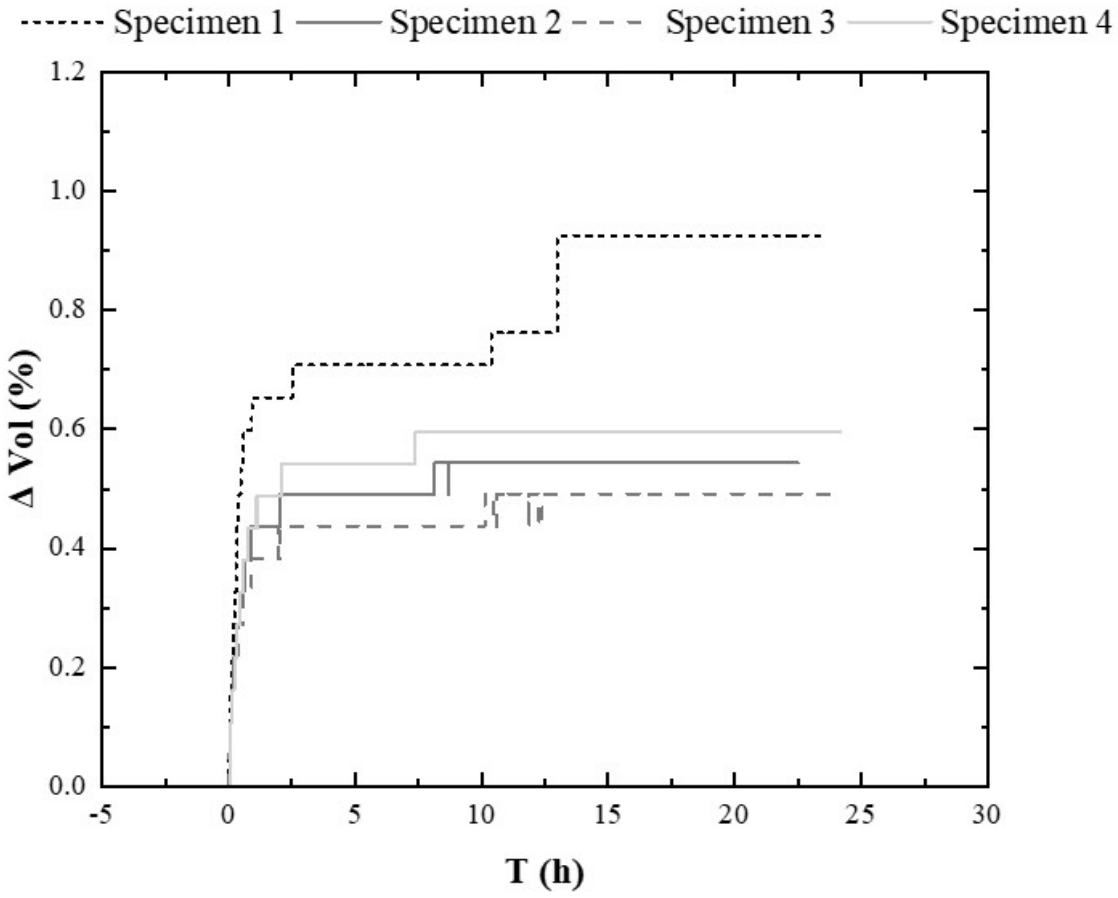

Figure 2.53: Volumetric variation of brown sandstone samples in the saturation stage.

for more significant vertical stresses and, like the gray sandstone, also exhibited residual shear strength.

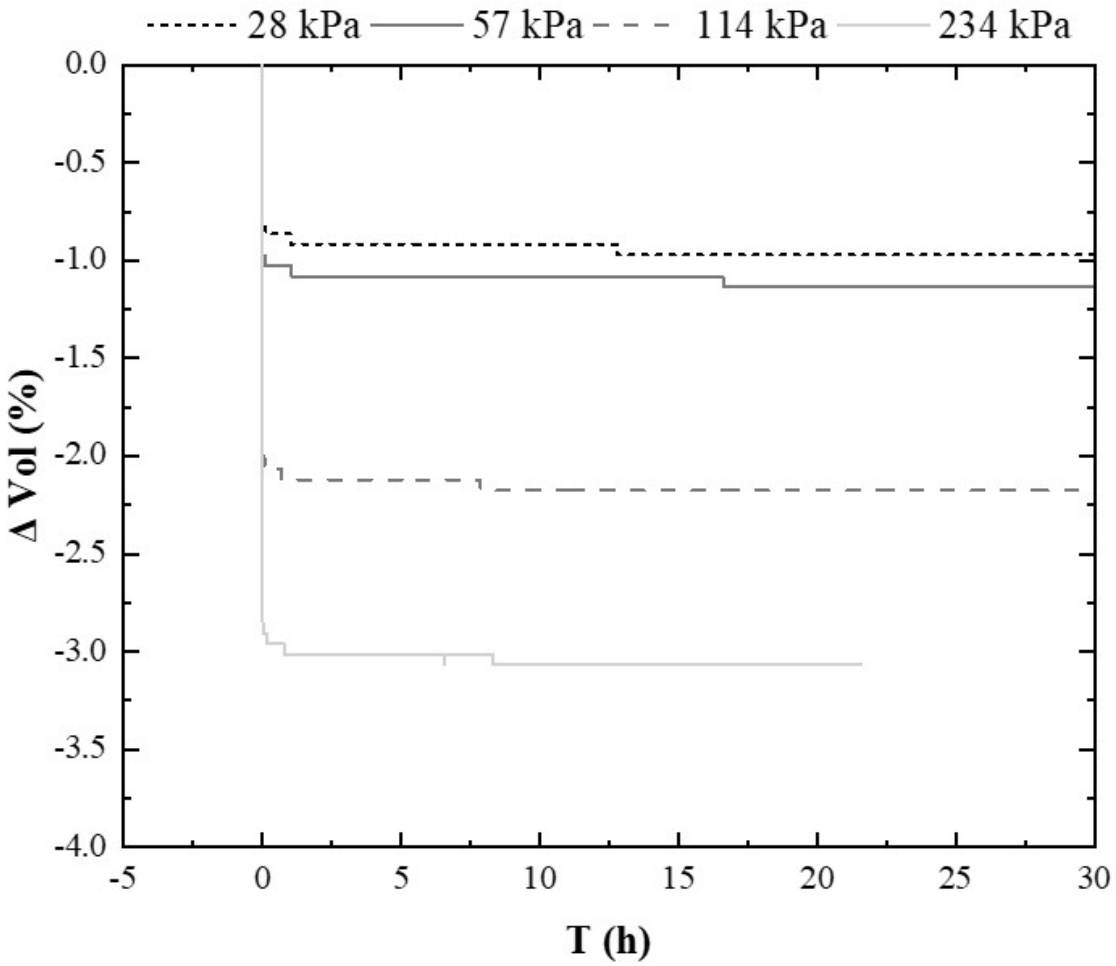

Figure 2.54: Volumetric variation of brown sandstone samples in the consolidation stage.

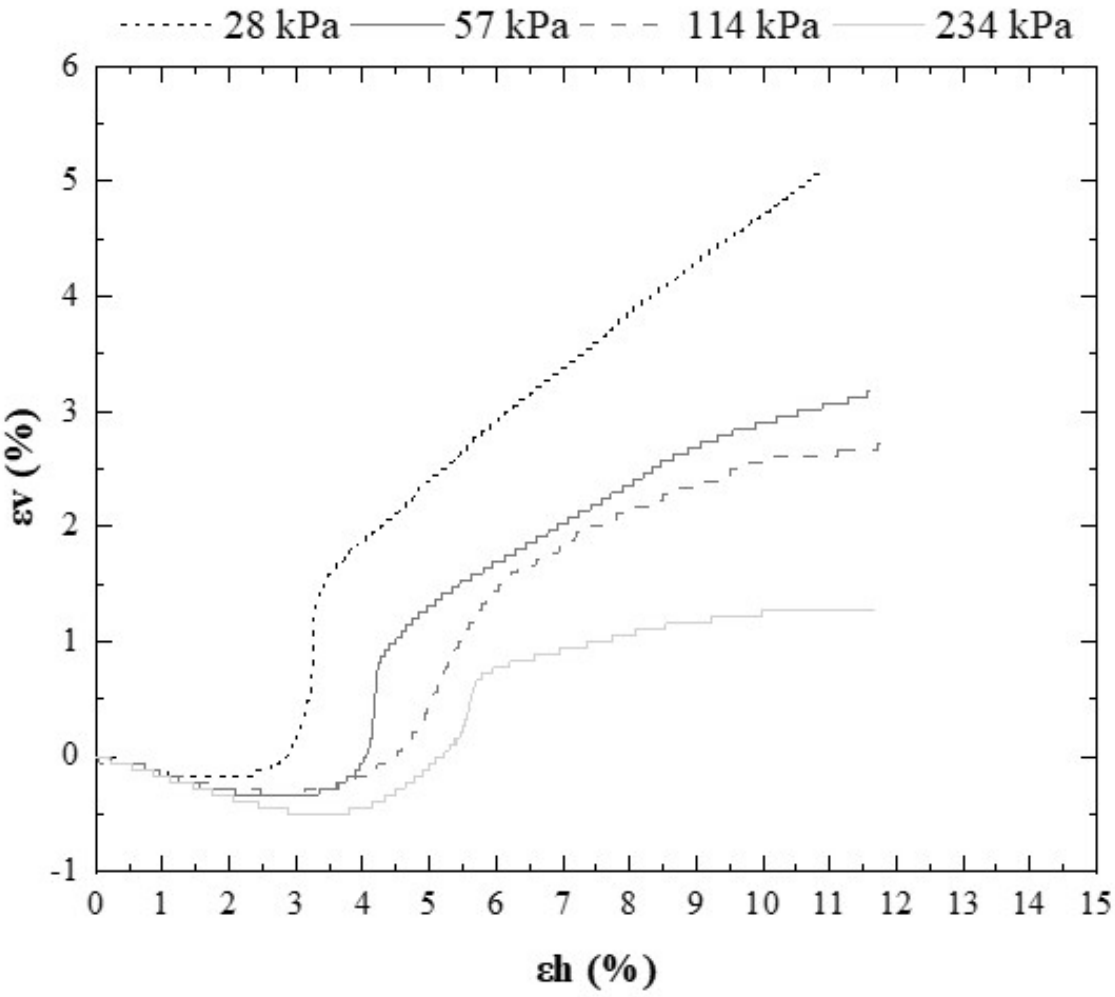

Figure 2.55: Vertical and horizontal deformations of brown sandstone samples under shear stage conditions.

The brown samples proved to be more resistant, with a friction angle of 54° and a cohesion intercept of 113 kPa, as illustrated in Figure 2.57. The normal and peak shear stresses, residual stresses, and resistance parameters for both envelopes are shown in Table 2.17, indicating higher parameters for the brown sandstone compared to the gray sandstone. However, the gray sandstone proportionally showed less loss in shear resistance after reaching the peak value, as clarified by the $\tau r/\tau p$ ratio.

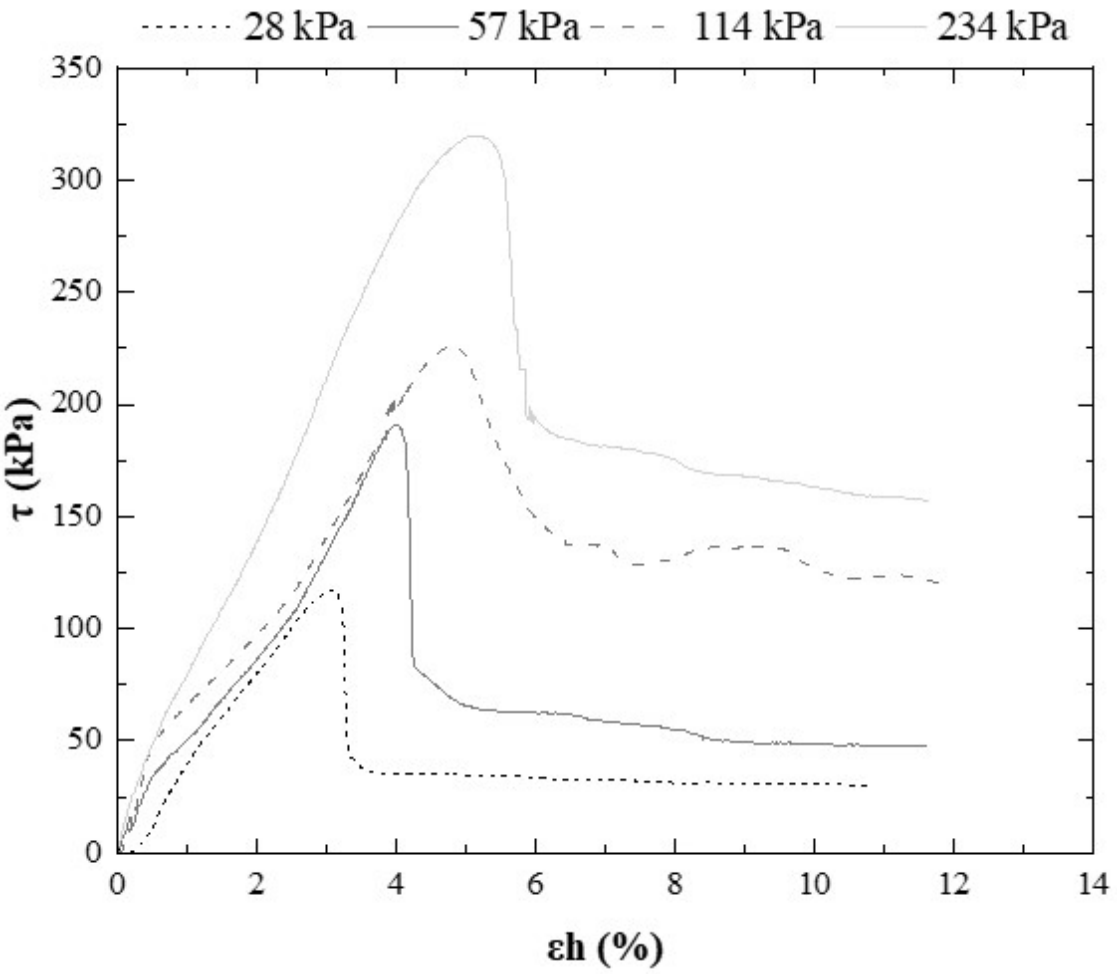

Figure 2.56: Stress-strain behavior of the brown sandstone cores required to establish the strength envelope.

The gray sandstone exhibited a residual shear strength of 74% of its peak strength when subjected to 233 kPa of normal stress, while the brown sandstone maintained ap-

proximately half of its peak strength under 224 kPa of vertical stress. However, the brown sandstone only retained a quarter of its peak strength under 28 and 57 kPa of normal stress. Notably, samples subjected to 112 kPa (gray) and 114 kPa (brown) of normal stress retained 53% of their peak strength in the residual state.

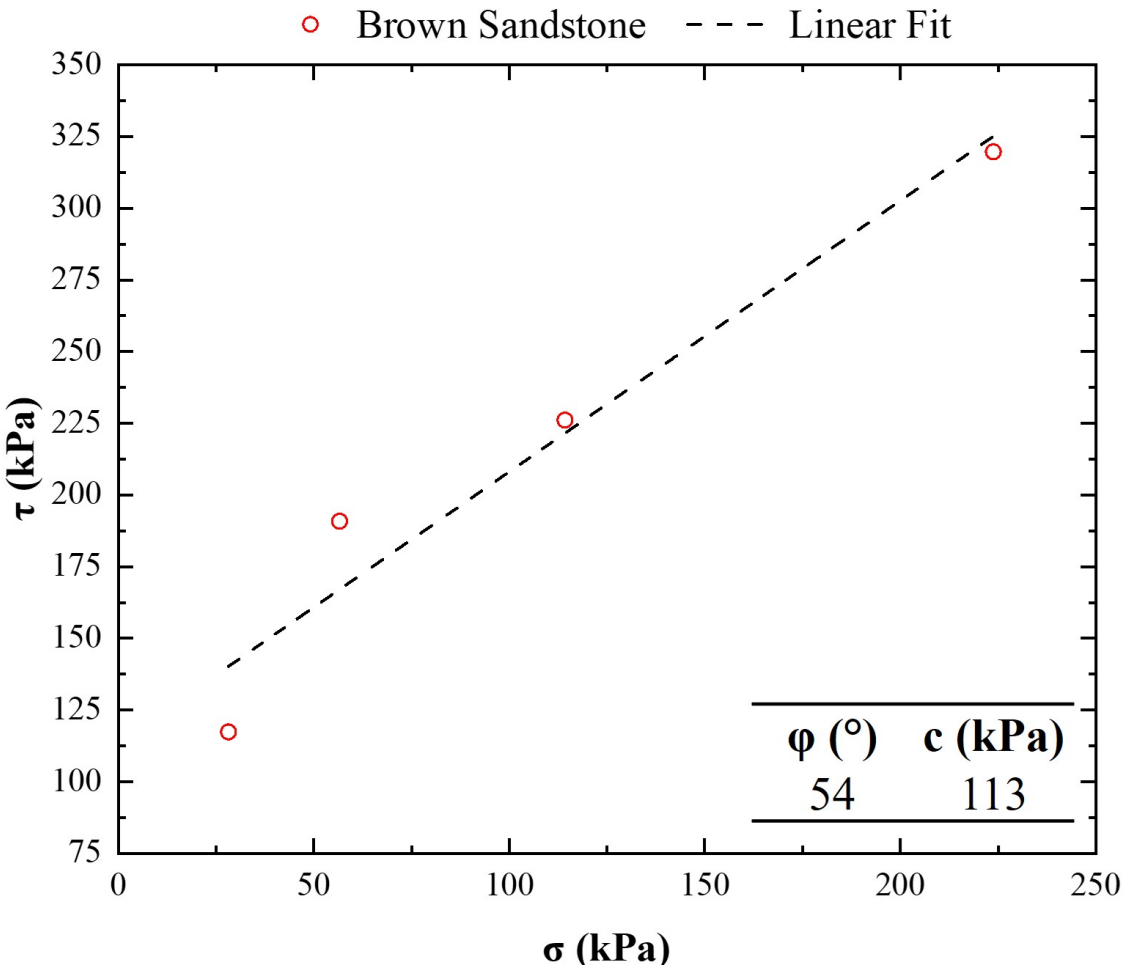

Figure 2.57: Strength envelope of brown sandstone based on the Mohr-Coulomb criterion.

Yang (2016) conducted triaxial tests on intact sandstones and artificially hollow sandstones, the former obtaining a strength envelope according to the Mohr-Coulomb criterion with internal angle parameters of 45.7° and cohesion of 30.58 MPa, with USC of 150.19 MPa, in dry samples at room temperature.

Compared to strength envelopes from direct shear tests, Huang et al. (2020) per-

formed on sandstone under different conditions and loading rates. The strength parameters according to the Mohr-Coulomb criterion for loading rates of 0.2, 1, 5, and 10 mm/min concerning the friction angle were all approximately 55.1°, 56.6°, 59.7°, 61.2°, and regarding cohesion, the values were around 5.589, 6.321, 7.155, 7.647 MPa.

Zhao et al. (2022) conducted a series of experiments on undisturbed and reconstructed samples examining the mechanical properties of swelling soft rocks at various initial moisture levels and immersion times. Considering the lowest moisture content tested by the authors (20%), after 24 hours of immersion, the cohesion, friction angle, and expansion rate were 32.18 kPa, 7.82°, and 19.45%.

Table 2.16: Summary of volumetric variations due to the saturation and consolidation stages of the gray and brown sandstones.

Sandstone	**Stage**	**σ (kPa)**	**ΔVol (%)**
Gray	Saturation	29	1.13
		57	0.89
		114	1.10
		234	0.70
	Consolidation	29	-0.91
		57	-1.25
		114	-2.25
		234	-5.50
Brown	Saturation	28	0.93
		57	0.54
		114	0.49
		234	0.60
	Consolidation	28	-1.03
		57	-1.14
		114	-2.17
		234	-3.07

Table 2.17: Values of normal stress (σ), peak shear strength (τ_p), residual shear strength (τ_r), ratio between the two, friction angle (φ) and cohesion (c) of the gray and brown specimens.

Sandstone	**σ (kPa)**	**τ_p (kPa)**	**τ_r (kPa)**	**τ_r/τ_p (%)**	**φ (°)**	**c (kPa)**
Gray	29	68	36	53	44	69
	57	113	52	46		
	112	196	104	53		
	233	231	172	74		
Brown	28	117	31	26	54	113
	57	191	47	25		
	114	226	120	53		
	224	320	157	49		

2.3.3 Stiffness and deformability

Modulus

Figure 2.58 depicted the stress-strain behavior during the compression and decompression cycles of the 5 test specimens used to determine Young's modulus, whose values are presented in Table 2.18. As previously noted, the core samples that did not meet the standard criteria were excluded from the calculation of Young's modulus, for instance, the highlighted test specimen 11. Therefore, Table 2.19 displays the valid values from the test.

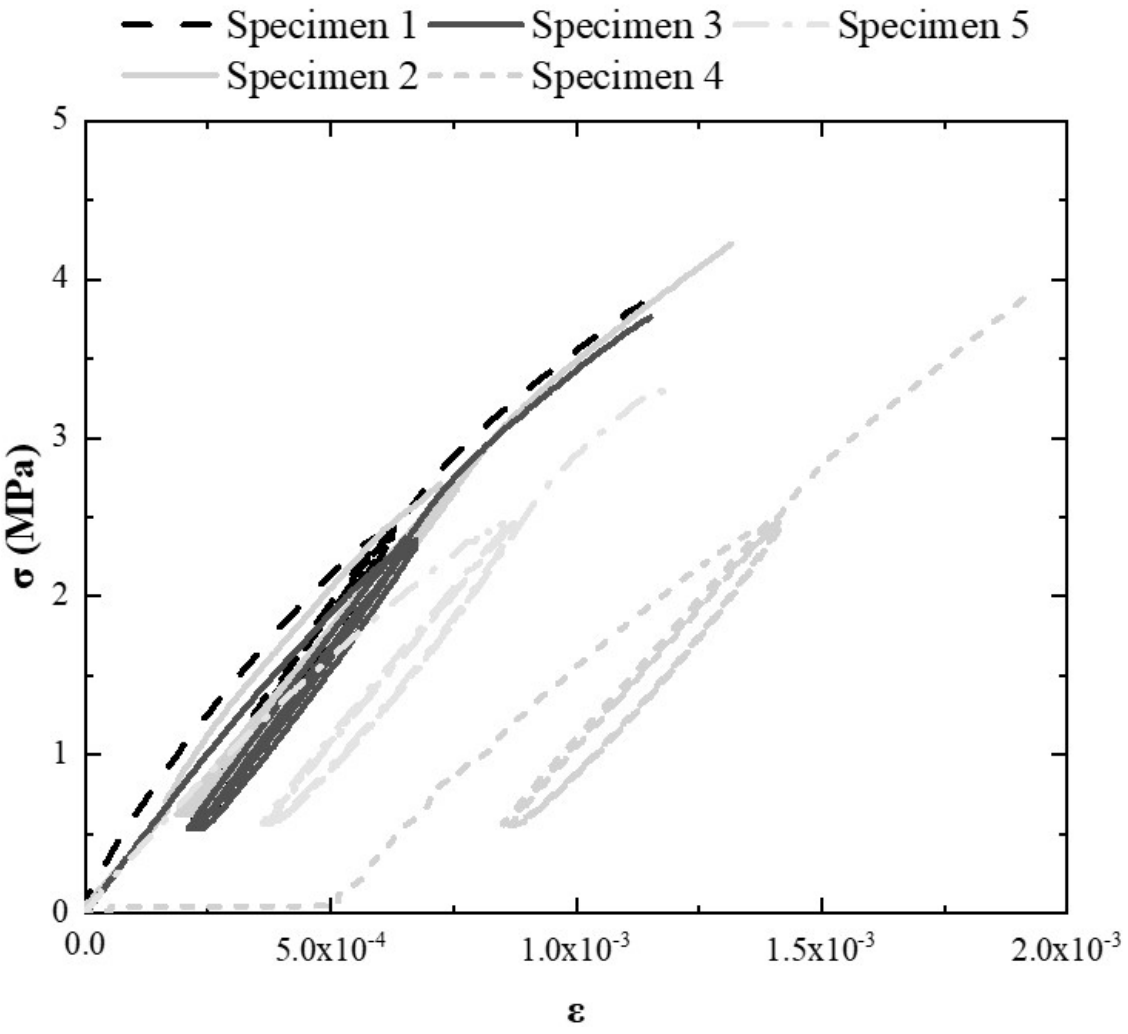

Figure 2.58: Compression-decompression cycles of the specimens to determine Young's modulus.

Table 2.18: Results of the five core samples used to determine Young's modulus and UCS from the same test.

Specimen	Modulus (GPa)	UCS (MPa)	Sandstone
1	4.59	8.48	Brown
6	3.63	8.91	Brown
9	4.07	8.62	Brown
11	3.43	6.43	Gray
12	3.68	7.88	Gray
mean	3.88	8.06	
sd	0.46	0.99	
cv (%)	11.86	12.23	

Table 2.19: Valid Young's modulus and UCS values reported by Table 2.18.

Specimen	Modulus (GPa)	UCS (MPa)	Sandstone
1	4.59	8.48	Brown
6	3.63	8.91	Brown
9	4.07	8.62	Brown
12	3.68	7.88	Gray
mean	3.99	8.47	
sd	0.44	0.43	
cv (%)	11.11	5.10	

The sandstone in question exhibits an average modulus of elasticity of 3.99 GPa and an unconfined compressive strength (UCS) of 8.47 MPa. This classification places the rock as having low unconfined compressive strength, with Young's modulus falling near the intermediate and high boundary. The graphical representation of this classification can be observed in Figure 2.59.

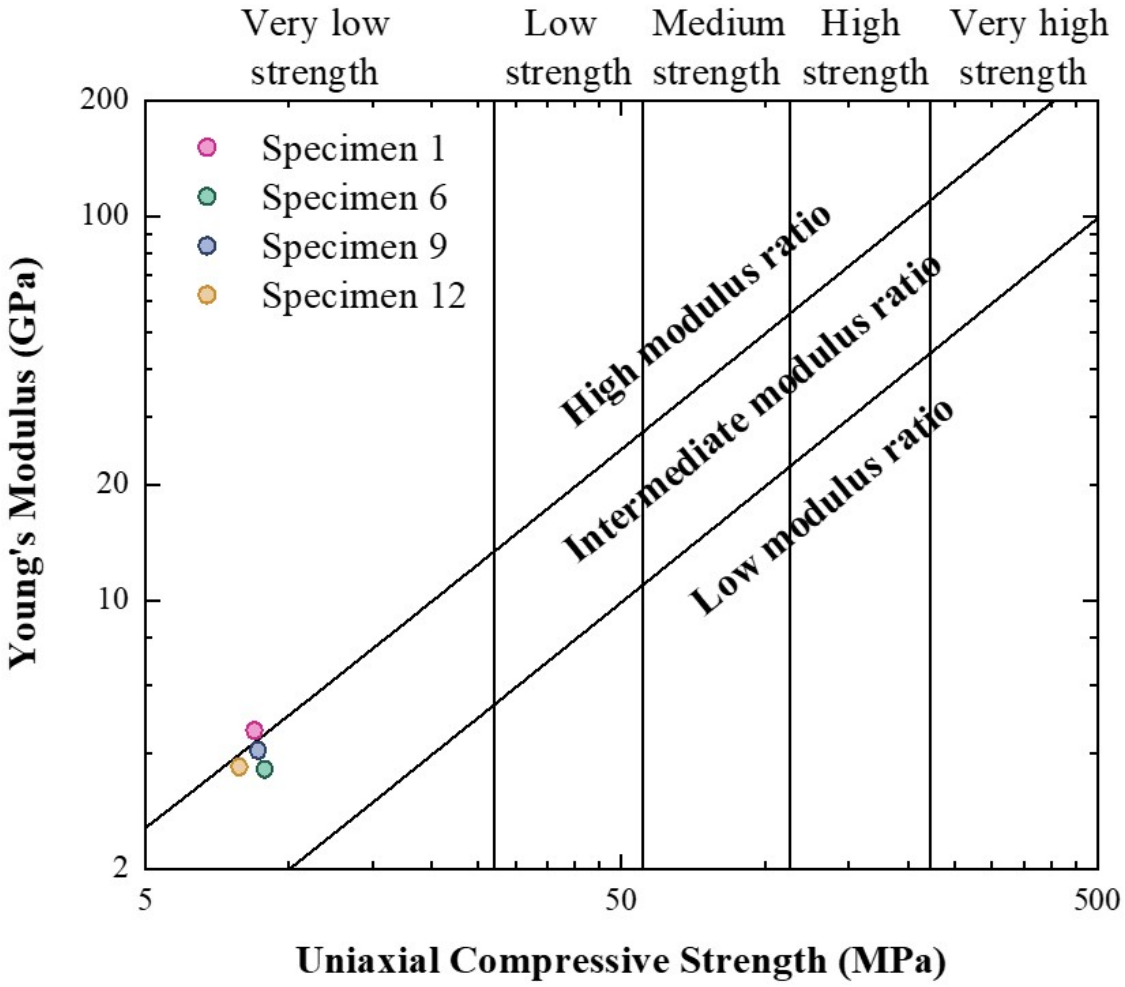

Figure 2.59: Relationship between UCS and elastic modulus.

Compressibility

Regarding compressibility, Figure 2.60 illustrates the oedometer test results, depicting the relationship between the normalized void ratio and the applied vertical stress. Notably, the tests conducted under natural and saturated conditions revealed significant differences, particularly in the saturation of the gray and brown sandstones. The saturated samples showed expansion, as evidenced by the increase in the void ratio from the loading of 0.1 to 1 kPa, with the loading starting at 3.15 kPa. This expansion is solely attributed to the increase in sample volume.

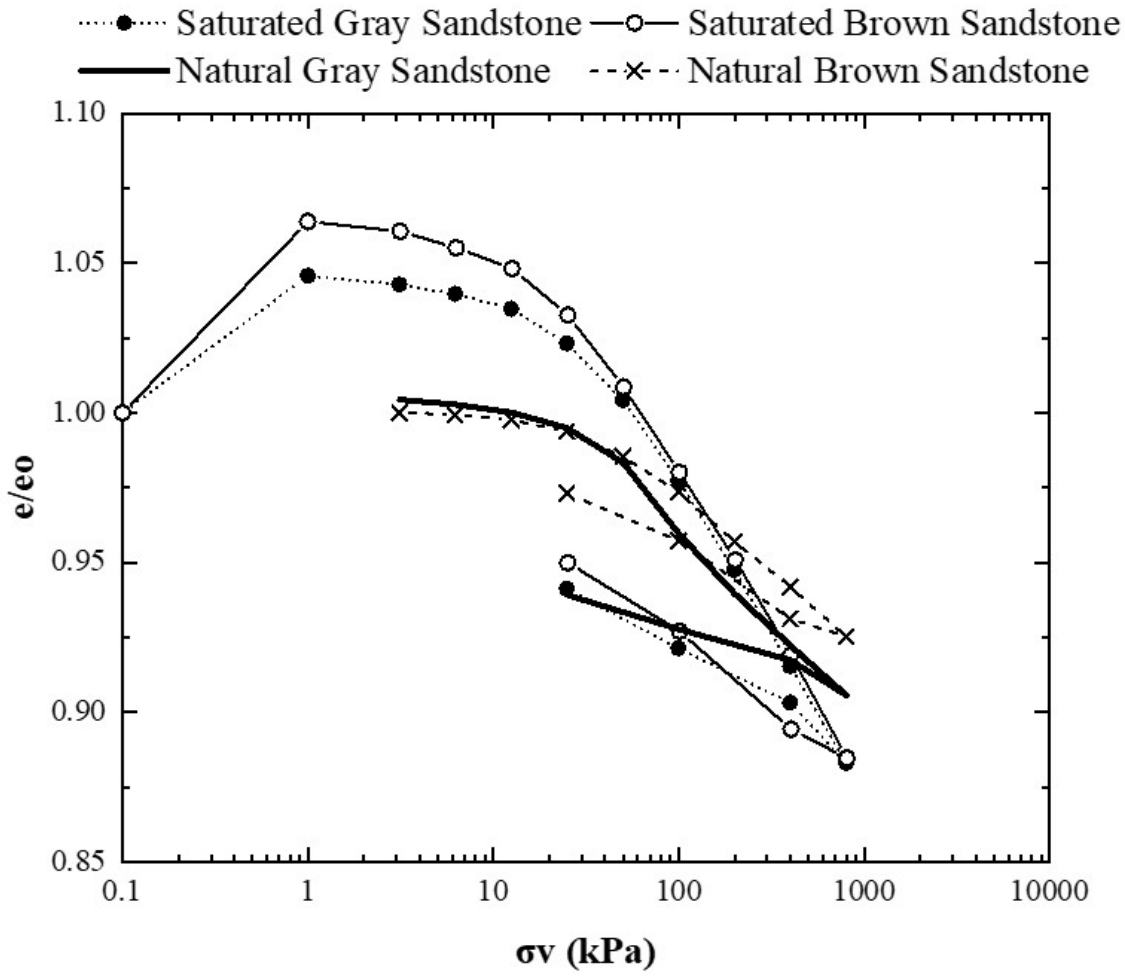

Figure 2.60: Normalized void ratio *versus* vertical stress curves applied to brown and grey sandstone in natural and saturated conditions.

The virgin compression curve for both types of sandstone could not be determined in their natural state. However, the preconsolidation stresses for the saturated gray and brown sandstones were 21 and 14.5 kPa, respectively. The findings indicate the low compressibility of the material in its natural state, consistent with the modulus of elasticity at the boundary between intermediate and high. Under saturated conditions, the results suggest higher compressibility and deformability of the gray sandstone than the brown sandstone. This contradicts the results of the consolidation phase of the direct shear test, where the brown sandstone experienced less volumetric deformation. This comparison extends to isotropic consolidation, which will be further addressed.

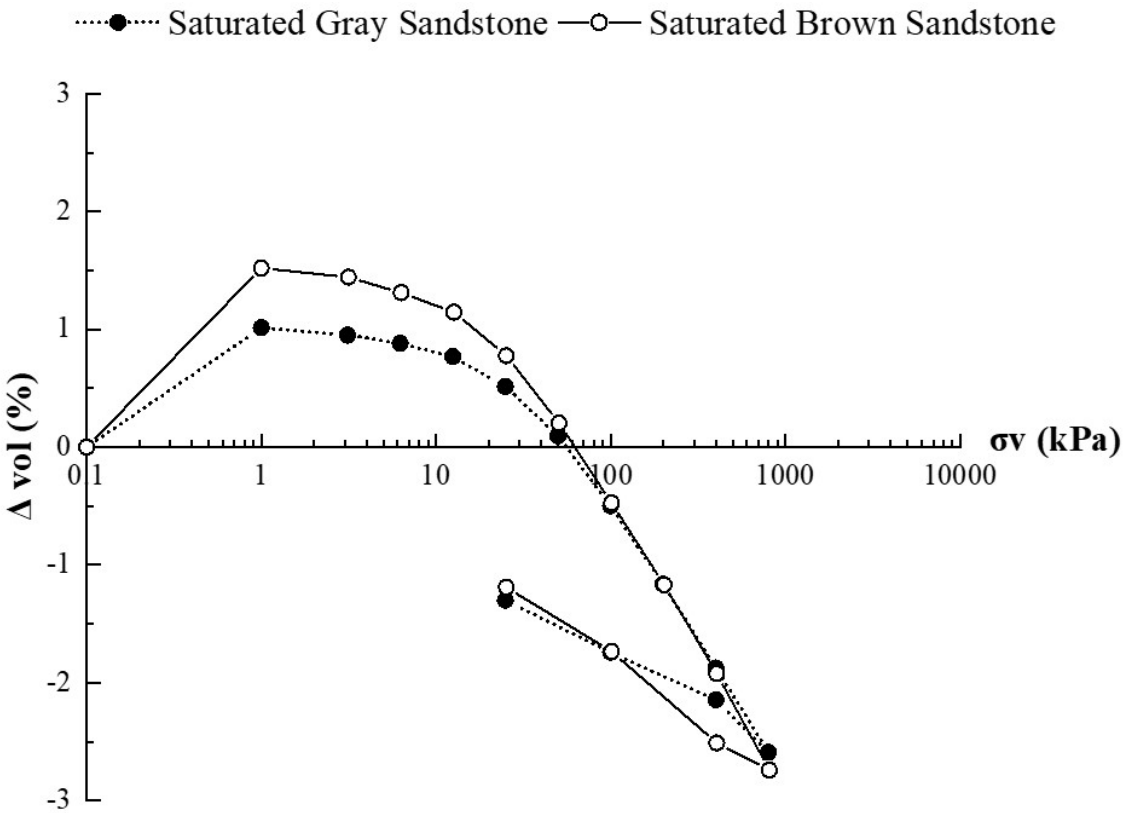

Figure 2.61: Determination of the expansion pressure of gray and brown sandstones using the saturated oedometer test.

Figure 2.61 emphasizes the expansion of both materials, which exhibited similar expansion pressure, with the gray sandstone at 55 kPa and the brown at 65 kPa. Figure 2.62 shows the opening of a fracture approximately 1 mm thick in a specimen when saturated by capillarity due to the expansion of the material.

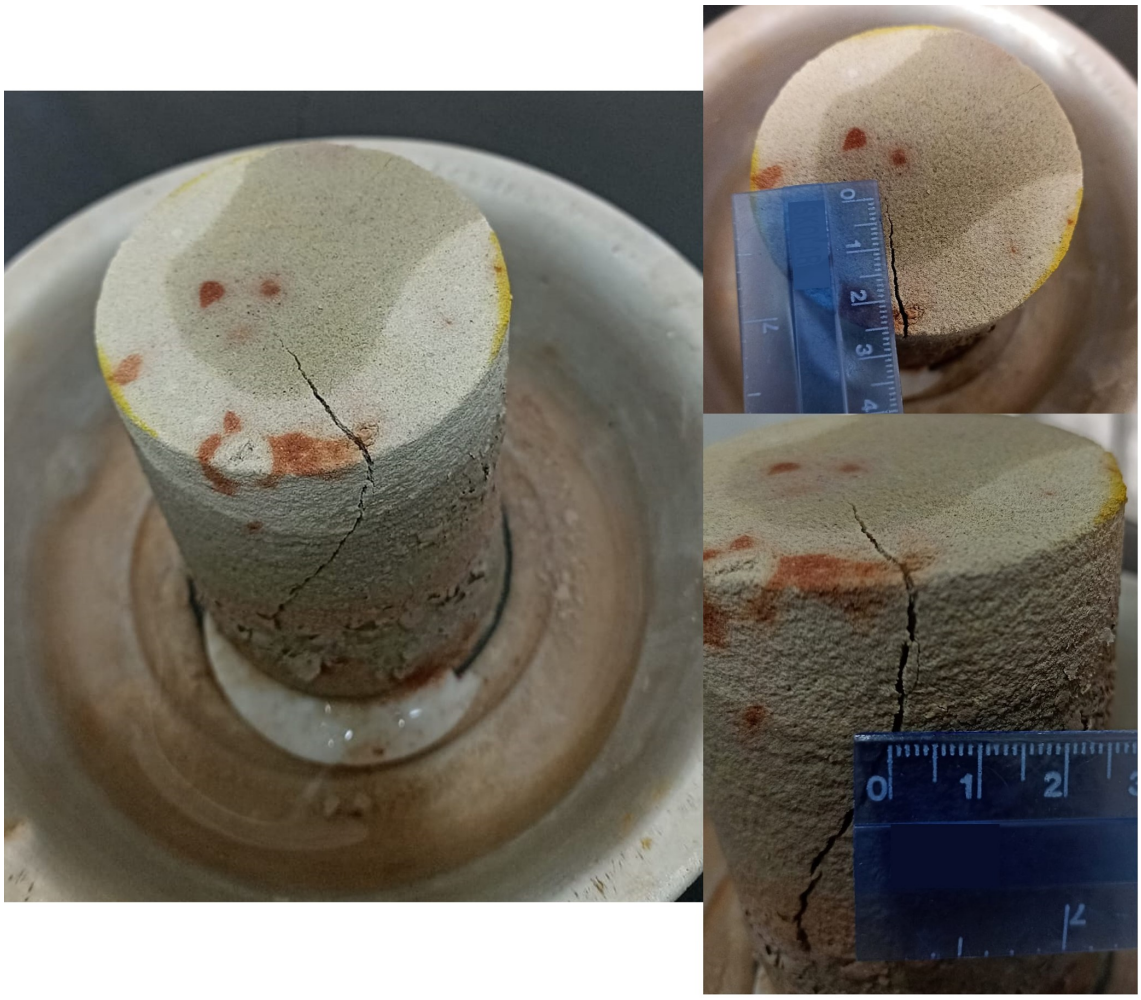

Figure 2.62: Fracture in a gray sandstone sample caused by the expansion of the material exposed to saturation by capillarity.

Huang et al. (2023) explain that the formation of cracks in rocks due to expansion occurs due to the induction of stresses between particles that exceed the shear strength. Once the rock's expansion process and subsequent cracking begin, the opening becomes a preferential path for water, increasing its absorption and contribution to the deformation of

the material, especially when subjected to low stresses. However, under high stresses, the rock matrix undergoes a "self-sealing" process, mitigating deformations caused by expansion. Depending on the level of confining stress, the stresses induced by expansion may not surpass the shear strength.

From the above, it was notable from the results that the presence of water altered the behavior of the sandstone and, as discussed by Tiennot et al. (2019), some factors are crucial in the rock-water interaction, such as texture, porosity, and mineralogy. Franzen & Mirwald (2004) and Wangler & Scherer (2008) complement the importance of clay minerals in rocks based on their quantity, nature, and distribution due to their sensitivity to the presence of water.

Other researchers' findings align with these results, as exemplified by Tables 2.20 and 2.21, which present the results in sandstones about UCS, Young's modulus, and tensile strength (TS) via diametral compression, while Table 2.22 provides strength parameters according to the Mohr-Coulomb criterion in triaxial and direct shear tests.

It is observed that there is a significant variation in values, and as previously discussed, the moisture content greatly influences the results. For instance, Zhang et al. (2020) subjected samples of red sandstone to wetting and drying cycles aimed at the weathering process of the rock. The determination of UCS under natural, dry, and saturated conditions resulted in values of 10.3 MPa for the first condition, 20.4 MPa for the dry sample, and 4.7 MPa for the saturated condition.

Since it is a natural material, the cited values exhibit substantial variability even under similar conditions. Tang (2018) obtained an average UCS value of 124.64 MPa in dry black sandstones, while Liu et al. (2023) conducted tests on soft sandstones at different moisture contents, yielding a UCS result of 10.17 MPa in the dry condition.

It is not uncommon for the UCS values reported in textbooks to be broad, constituting a range from 10 to 220 MPa (Sanjay et al., 2013; Small, 2016), extending to the modulus of elasticity, tensile strength, and shear strength parameters. Therefore, it is crucial to report the conditions under which the relevant data were collected, particularly the moisture and/or degree of saturation.

Table 2.20: Results of the different authors' UCS, E, and TS. Blank spaces refer to the absence of information.

Reference	Sandstone	Sandstone condition	UCS (MPa)	E (GPa)	TS (MPa)
This work	Gray and Brown	Dry	8.31	3.99	0.78-0.88
Huang et al. (2010)	Longyou	Dry			2.8-5.3
		Saturated			0.38-3.01
Yuan & Shen (2017)	Gritstone	Without cushion	87.90	14.10	6.30
		With cushion			7.00
	Mid-grain sandstone	Without cushion	116.80	23.80	7.90
		With cushion			9.60
Liu et al. (2022)	Fine-grained homogeneous	Before freeze-thaw treatment	62.50	6.70	7.00
Wang et al. (2022)	Red		68.89	7.44	5.88
You et al. (2022)	Neijiang		61.00	6.70	7.00
Yang (2016)	Hollow	Intact - air dry	150.19		
		Hollow - 15 mm	161.80		
		Hollow - 26 mm	147.38		
Zhang et al. (2020)	Red	Dry	20.40		
		Natural	10.30		
		Saturated	4.70		

Table 2.21: Results of the different authors' UCS, E, and TS. Blank spaces refer to the absence of information (continued).

Reference	Sandstone	Sandstone condition	USC (MPa)	E (Gpa)	TS (MPa)
Feng et al. (2018)	Red Erdos		47.79	6.38	
Cai et al. (2020)	Linyi	Unsaturated - length/diameter 1:1	102.30		
		Saturated - length/diameter 1:1	88.00		
		Unsaturated - length/diameter 2:1	95.70		
		Saturated - length/diameter 2:1	79.90		
Tang (2018)	Black	Dry	124.64	20.18	
		960 hours wetting	61.25	12.25	
Tiennot et al. (2019)	Thüringer	Dry - $E_{\perp}$		13.20	
		Humidification - W:33% - $E_{\perp}$		13.00	
		Humidification - W:65% - $E_{\perp}$		11.90	
		Humidification - W:97% - $E_{\perp}$		5.20	
		Drying - W:65% - $E_{\perp}$		13.70	
		Drying - W:33% - $E_{\perp}$		13.40	
		Dry - $E_{\parallel}$		14.40	
		Humidification - W:33% - $E_{\parallel}$		13.10	
		Humidification - W:65% - $E_{\parallel}$		10.60	
		Humidification - W:97% - $E_{\parallel}$		6.33	
		Drying - W:65% - $E_{\parallel}$		11.40	
		Drying - W:33% - $E_{\parallel}$		13.00	
Liu et al. (2023)	Soft	Dry	10.17	0.89	
		Water immersion	2.90	0.27	
Zhao et al. (2024)	Sichuan Province		45.79	4.70	
	Zigong City		44.60	4.53	
	Rong County		36.88	4.21	
			58.15	6.55	

Table 2.22: Results of the different authors' c and φ. Blank spaces refer to the absence of information.

Reference	Sandstone	Sandstone condition	Test	c (MPa)	φ (°)
This work	Gray	Saturated	Direct shear	0.07	44.00
	Brown	Saturated		0.11	54.00
Yang et al. (2014)	Red	Dry	Triaxial	23.10	45.50
		Saturated		13.05	49.30
Yang (2016)	Hollow	Intact - air dry	Triaxial	30.58	45.70
		Hollow - 15 mm		37.97	39.70
		Hollow - 26 mm		38.52	34.80
Huang et al. (2020)		0.2 mm/ min	Direct shear	5.59	55.10
		1 mm/ min		6.32	56.60
		5 mm/min		7.16	59.70
		10 mm/min		7.65	61.20

2.3.4 Hydraulic conductivity

The hydraulic conductivity of the gray and brown sandstone was determined to encompass possible field situations and reduce laboratory testing time. This means different confinements and hydraulic gradients, in addition to the direction of sampling (anisotropy). In particular, the gray sandstone consolidated at 320 kPa underwent various tests to determine future column tests and transport parameters, a topic discussed in Chapter 3.

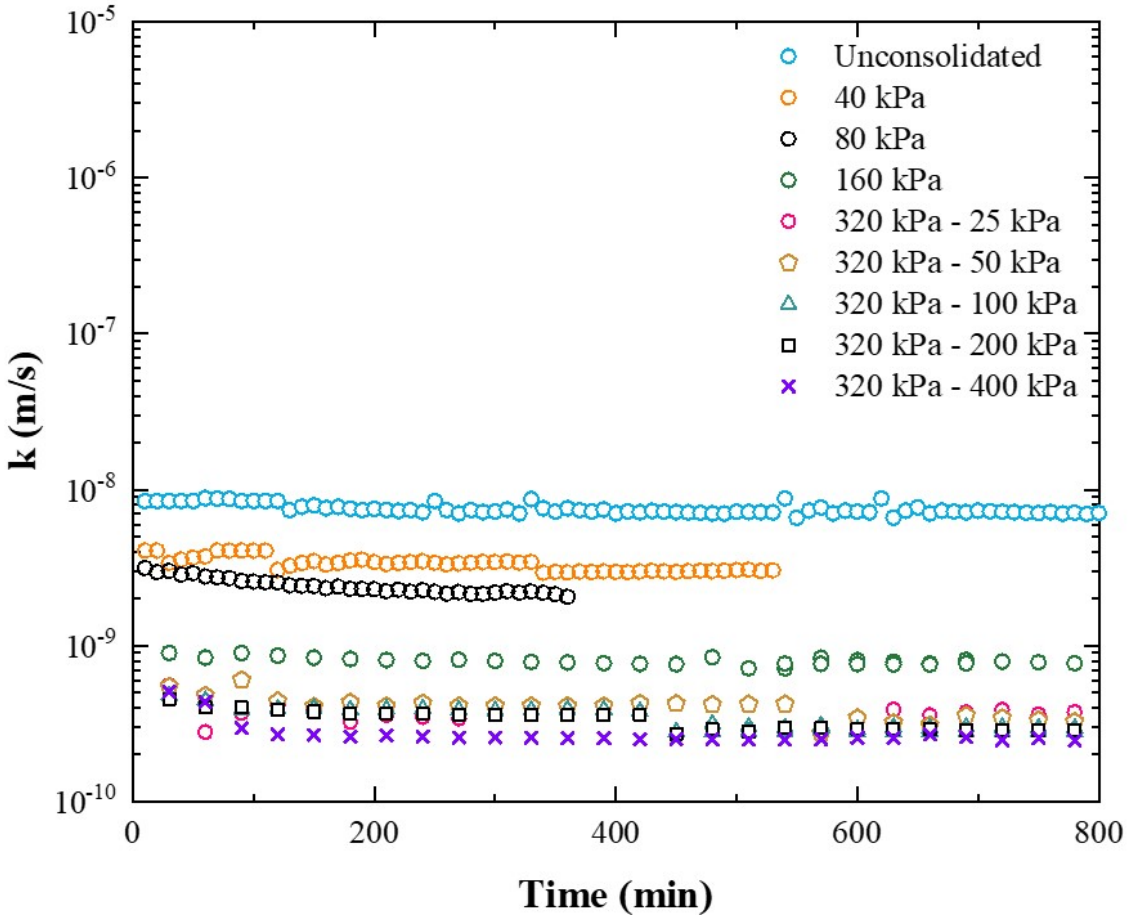

Figure 2.63: Hydraulic conductivity obtained with constant pressure at the bottom of the specimens in unconsolidated and consolidated gray sandstone samples at 40, 80, 160, and 320 kPa.

In line with the standard configuration detailed earlier, Figures 2.63 and 2.64 present the hydraulic conductivity results for the gray and brown sandstone samples. These tests were conducted under constant pressure at the base and subjected to confinements of 10 kPa

(unconsolidated), 40, 80, 160, and 320 kPa. The hydraulic conductivity data for the gray sample confined at 20 kPa were not included in the plots, as this pressure level did not lead to the consolidation of the specimen.

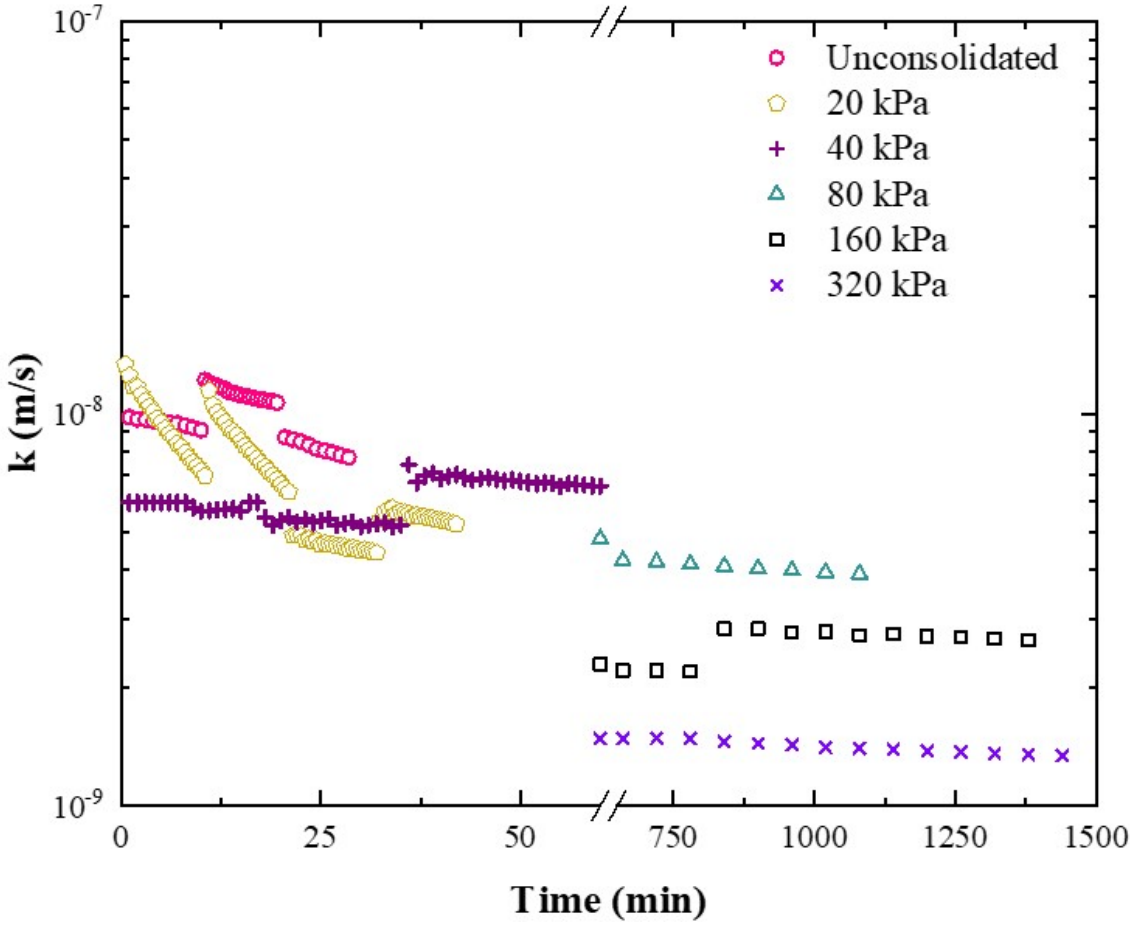

Figure 2.64: Hydraulic conductivity obtained with constant pressure at the bottom of the specimens in unconsolidated and consolidated brown sandstone samples at 20, 40, 80, 160, and 320 kPa.

As expected, confinement reduced hydraulic conductivity; the average k values for the gray sandstone in the unconsolidated situation and at 40, 80, 160, and 320 kPa were 7.50×10^{-9}, 3.35×10^{-9}, 2.41×10^{-9}, 7.88×10^{-10}, and 3.41×10^{-10} m/s, respectively, representing a percentage reduction compared to the unconsolidated sample of 55, 68, 89, and 95%. On the other hand, the reduction in void ratio caused by the increase in confinement was 1.1, 3.0, 5.7, and 8.3% for the same stresses as the initial specimen configuration. Thus, the reduction

in hydraulic conductivity was more pronounced compared to the decrease in void ratio.

Similar to the gray sandstone, the brown sample showed a reduction in hydraulic conductivity when consolidated, with hydraulic conductivity values higher than those obtained for the gray sample, namely, 1.01×10^{-8}, 6.98×10^{-9}, 6.08×10^{-9}, 4.35×10^{-9}, 2.46×10^{-9}, and 1.40×10^{-9}, under the unconsolidated condition (10 kPa), 20 kPa, 40 kPa, 80 kPa, 160 kPa, and 320 kPa.

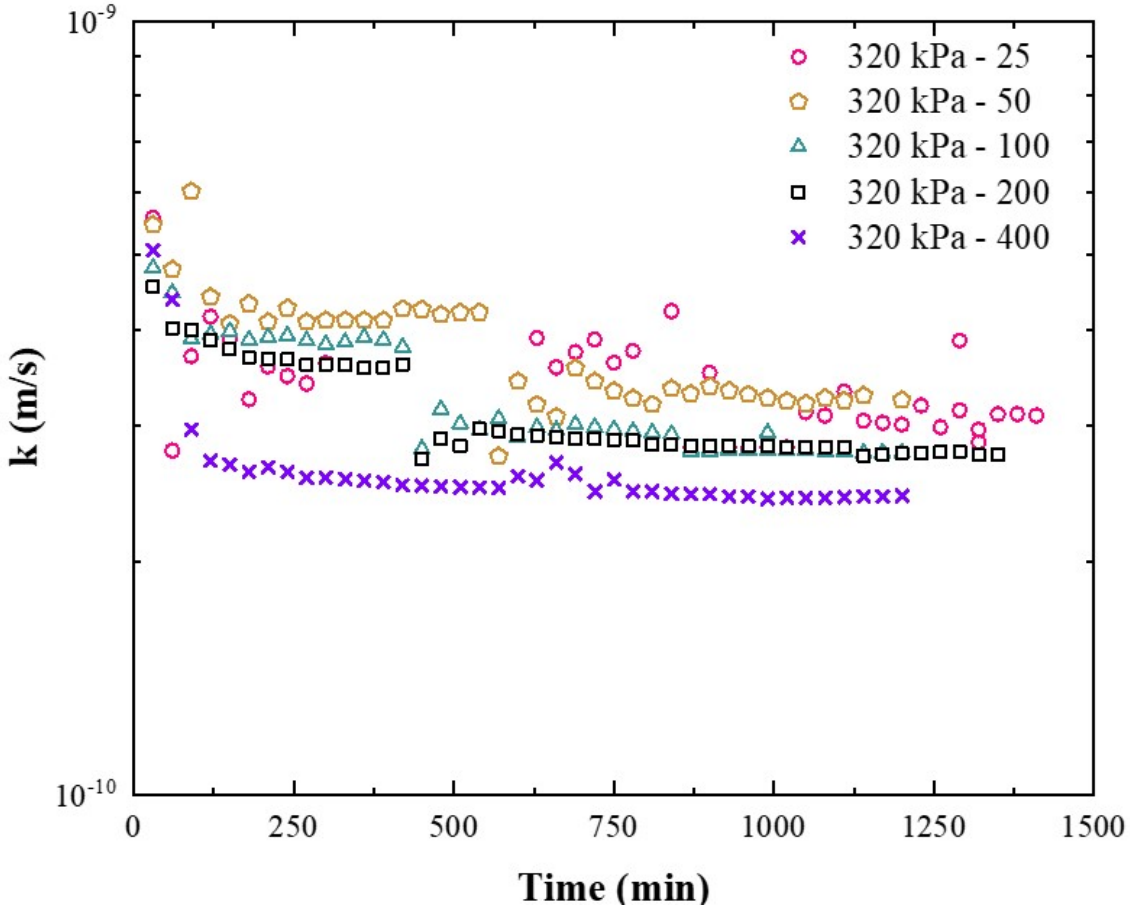

Figure 2.65: Hydraulic conductivity values of the consolidated gray sample at 320 kPa with gradients of 25, 50, 100, 200, and 400.

The gray sandstone exhibited lower permeability, with a 25% reduction in k compared to the unconsolidated brown sandstone, 45% at 40 and 80 kPa confinement, 68% with 160 kPa confining stress, and a 76% reduction with 320 kPa of consolidation. These findings suggest

that increased confinement significantly decreased hydraulic conductivity in the gray sample and accentuated the differences between the gray and brown values, highlighting preferential flow through the brown sandstone over the gray.

Figures 2.65, 2.66, and 2.65 present the results of tests conducted on gray sandstone subjected to 320 kPa of confining stress using different hydraulic gradients and different imposition methods. From there, it can be inferred that the increase in hydraulic gradient did not significantly alter k, which remained close to 3×10^{-10} m/s in all configurations adopted.

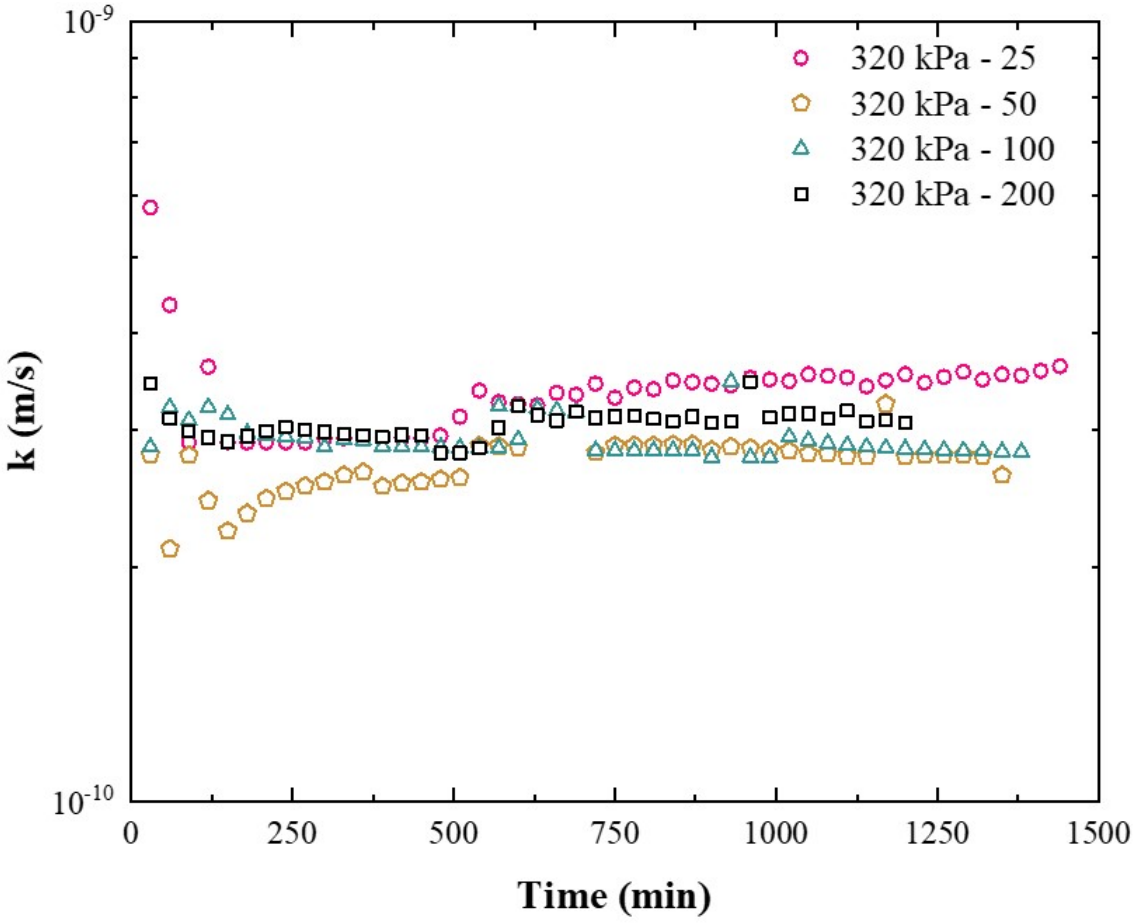

Figure 2.66: Hydraulic conductivity determined with constant pressure at the top of the gray sample consolidated at 320 kPa for gradients of 25, 50, 100 and 200.

The average values considering respectively the application of the gradient with constant base pressures, constant top, and divided between top and base were 3.16×10^{-10}, 3.00×10^{-10}, and 2.92×10^{-10} m/s. For the same gradients, the average k values for 25, 50,

100, 200, and 400 were 3.39×10^{-10}, 3.09×10^{-10}, 2.98×10^{-10}, 2.95×10^{-10}, and 2.61×10^{-10} m/s, respectively. It should be pointed out that the determination for the gradient of 400 used configurations with constant base pressure and divided pressure.

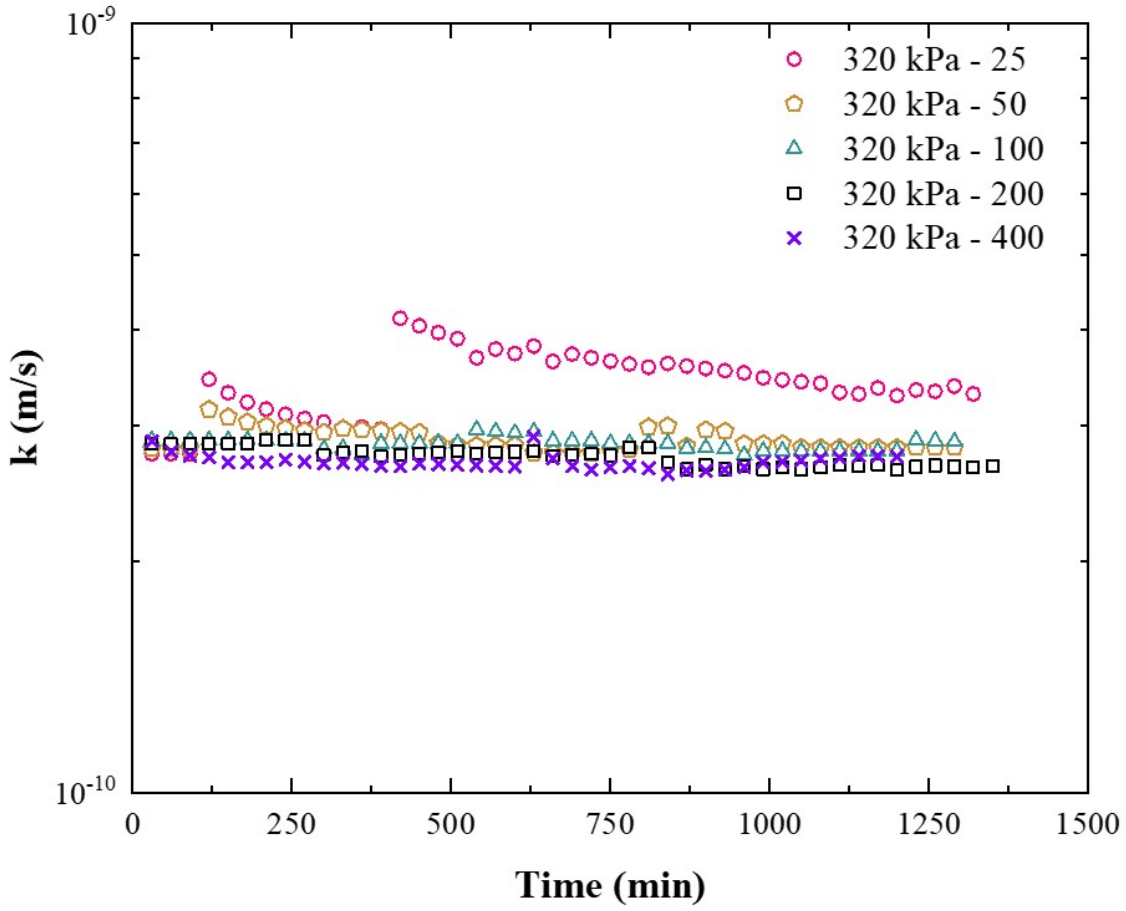

Figure 2.67: Hydraulic conductivity obtained by dividing the pressure between the top and bottom of the specimen for consolidated gray sandstone at 320 kPa for gradients of 25, 50, 100, 200, and 400.

Regarding variability, the coefficient of variation (CV) for the imposed conditions of constant pressure at the base, at the top, and divided pressures were 13.8%, 8.2%, and 10.7%, respectively. Grouping the tests by the same hydraulic gradient, CVs of 2.6%, 16.8%, 5.5%, 6.1%, and 4.79% were determined for 25, 50, 100, 200, and 400. Notably, the CVs were reduced, with extreme values of 2.6% for the gradient of 25 and 16.8% for that of 50. The difference in pressure application for flow occurrence resulted in the most minor variability for constant top pressure (8.2%) and the greatest for constant base pressure (13.8%).

The test configurations evaluated did not show significant changes from the above, indicating that the highest gradient applied for the material under study can reduce the testing time without affecting data quality. Thus, the test with pressure divided between the top and bottom is presented as the most suitable option, with a coefficient of variation of 10.7%. Furthermore, applying a 400 gradient resulted in a coefficient of variation of 4.8%.

Even though ASTM D5084 (2016) does not recommend the aforementioned option, its use is endorsed for future studies involving the sandstone evaluated here. In addition to the previous explanations, the material can undergo critical variations in effective pressure at high gradients. By imposing the gradient through divided pressures, the variations in effective stresses on the sample are reduced, preventing excessive consolidation or expansion due to increased or decreased effective stress. This situation is especially important in the presence of active clay minerals. Further details on the variation of effective stress due to the imposition of hydraulic gradient in flexible wall permeameters can be consulted in Kodikara & Rahman (2002).

Anisotropy

The hydraulic conductivity concerning anisotropy was assessed by comparing the values obtained from samples extracted in the horizontal and vertical directions. Table 2.23 depicts the initial index properties of the gray and brown sandstones extracted in the horizontal direction. Figures 2.68 and 2.69 display the data collected to determine the hydraulic conductivity in the horizontal direction of the gray and brown samples under the same consolidation conditions as the specimens molded vertically.

From the previous data and those obtained in the vertical direction, the variation of hydraulic conductivity and void ratio with the respective effective stresses applied to the core samples are presented in Figures 2.70 and 2.71.

The results for k in the horizontal direction demonstrate that the brown sandstone is one to two orders of magnitude more permeable than the gray sandstone, as indicated by the results in the unconsolidated condition of the gray sample at 3.38×10^{-9} m/s com-

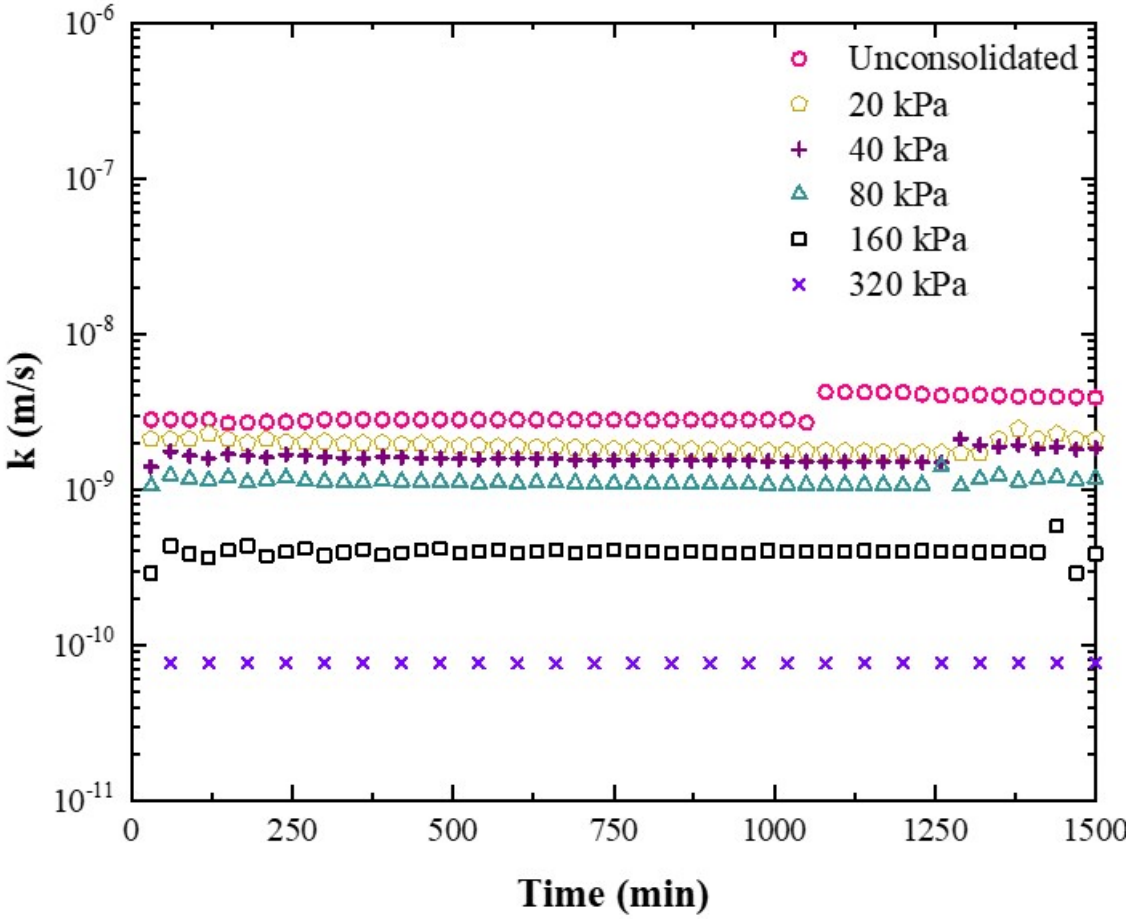

Figure 2.68: Hydraulic conductivity of the gray sandstone sample taken horizontally under the confining pressures of 20, 40, 80, 260, and 320 kPa, following the standard methodology adopted here.

pared to 2.45×10^{-8} m/s for the brown sample, and in the consolidated sample at 320 kPa with 7.68×10^{-11} m/s compared to 4.85×10^{-9} m/s for the gray and brown samples, respectively.

Table 2.23: Initial index properties of the sandstones used for the anisotropy test.

Sandstone	wi (%)	ρs (g/cm³)	ei	ρd (cm³)	n (%)
Gray	2.00	2.628	0.309	2.008	23.58
Brown	1.64	2.676	0.410	1.898	29.06

The hydraulic conductivity results revealed distinct anisotropic conditions. The gray sandstone exhibited lower permeability in the horizontal direction, with kh/kv ratios ranging from 0.23 at 320 kPa confinement to 0.50 at 40 kPa confining stress.

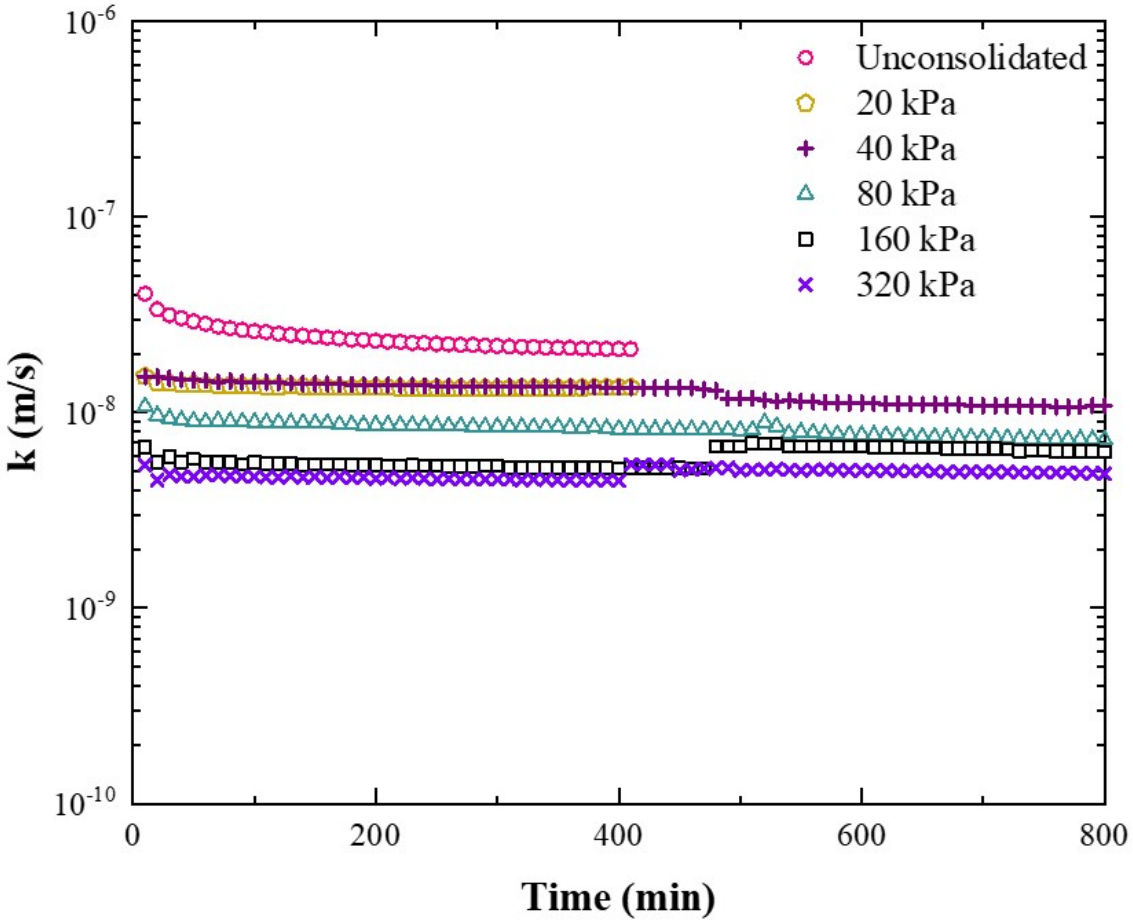

Figure 2.69: Hydraulic conductivity of the brown sandstone sample taken horizontally under the confining pressures of 20, 40, 80, 260, and 320 kPa, following the standard methodology adopted here.

On the other hand, the permeability of the brown sandstone in the horizontal direction was higher than its permeability in the vertical direction. The minimum and maximum values of kh/kv were 1.85 and 2.43 for the conditions of the unconsolidated and consolidated test specimens at 80 kPa. Table 2.24 summarizes the hydraulic conductivity data in the vertical and horizontal directions, as well as the relationship between both and their percentage variation.

As previously illustrated by Figures 2.70 and 2.71, and summarized by Table 2.25, the void ratios of the brown sample were higher than those of the gray ones. When comparing the test specimens of the same color, the gray core sample extracted in the horizontal direction

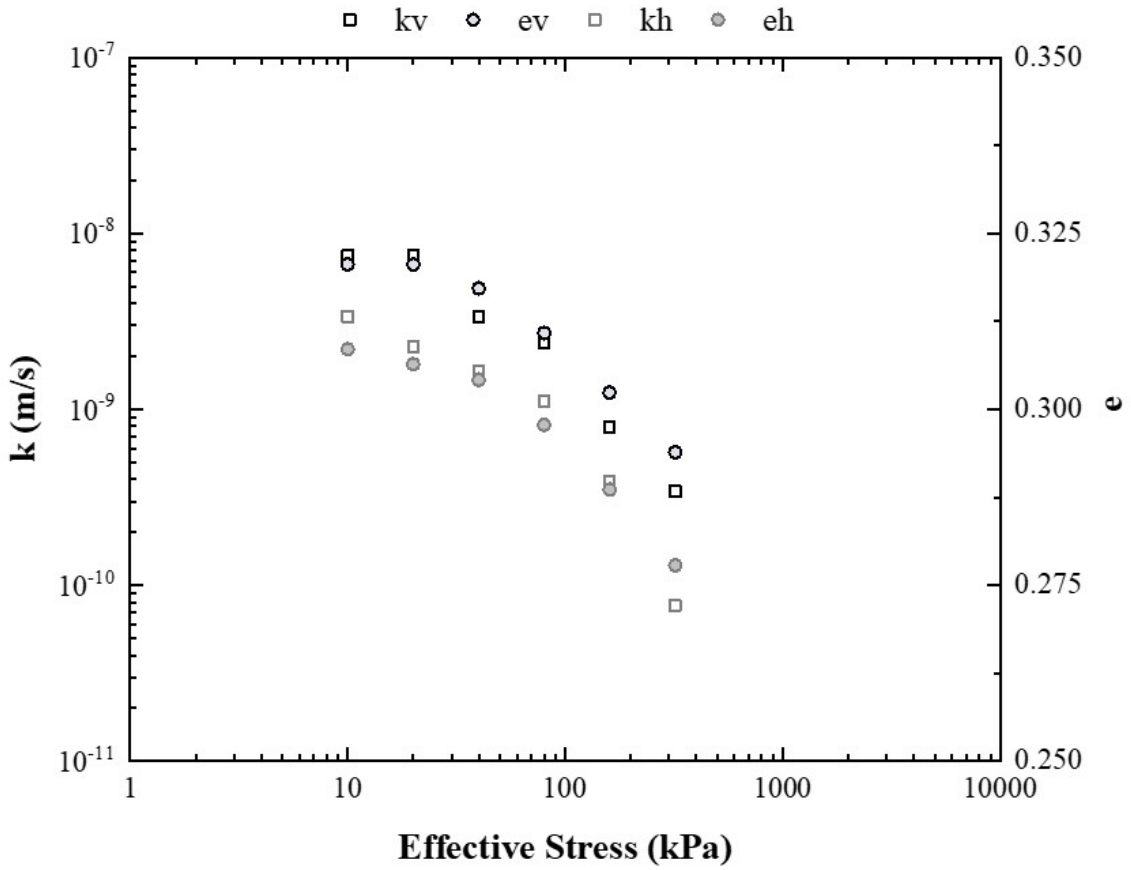

Figure 2.70: Variation in hydraulic conductivity, void ratio, and effective stresses of gray sandstone.

had lower void ratios than in the vertical direction. In contrast, the brown test specimen extracted in the horizontal direction showed higher void ratios than in the vertical direction.

From the above, the permeability of the brown sandstone was higher than that of the gray sandstone in both directions, particularly in the horizontal direction. Since the hydraulic conductivity and porosity of the material are intrinsically related, the increase in the void ratio of the brown samples, and consequently in porosity, explains the increase in permeability and the resulting reflection on anisotropy.

An analogous aspect to the inversion of anisotropy was also highlighted by Tiennot et al. (2019) in the wetting and drying cycles of a Thüringer sandstone, aiming to obtain the modulus in the directions parallel and perpendicular to the material's bedding plane. The authors noted that during the drying cycle, there was an inversion of the anisotropy with a higher Young's modulus in the direction perpendicular to the natural bedding plane compared

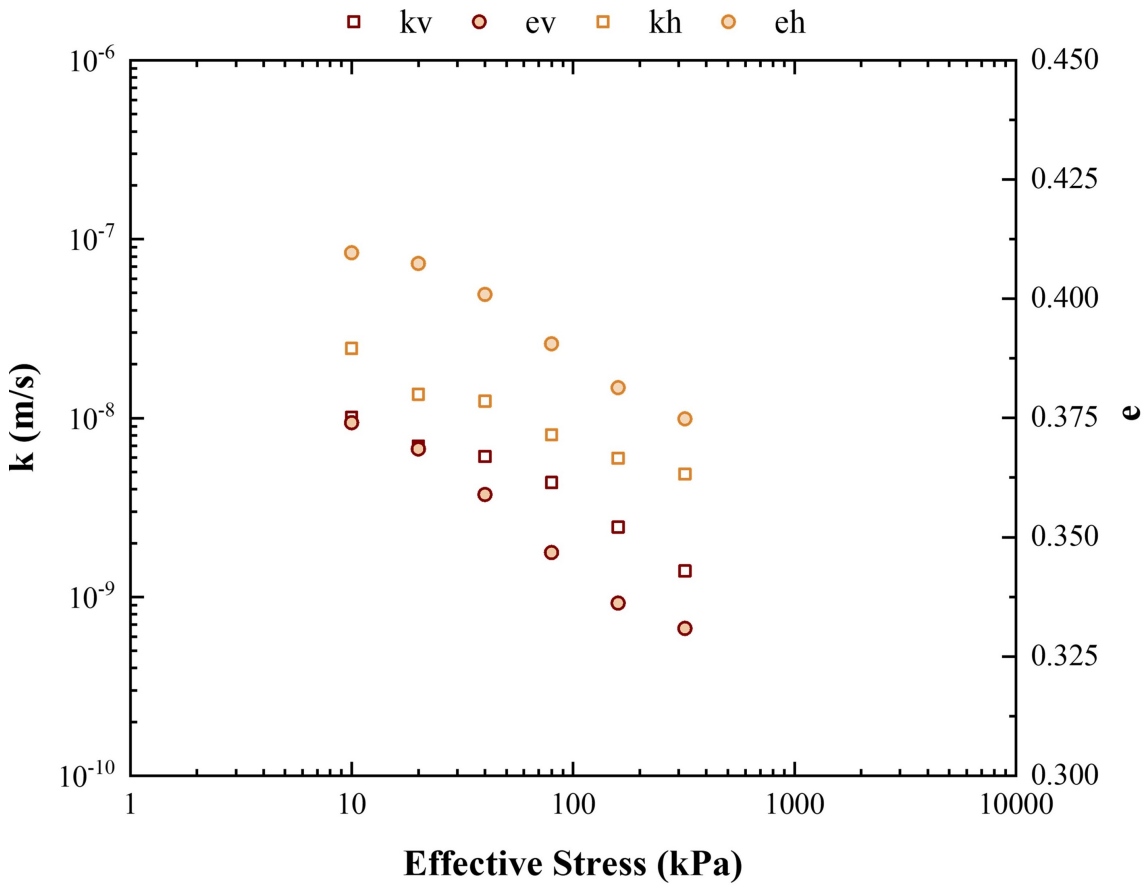

Figure 2.71: Variation in hydraulic conductivity, void ratio, and effective stresses of brown sandstone.

to the samples in the direction parallel to the natural bedding plane.

Table 2.24: Gray and brown sandstone average hydraulic conductivities in the vertical (kv) and horizontal (kh) directions and its percentage variation (Δ) concerning the unconsolidated condition.

Sandstone	**Consolidation (kPa)**	**kv (m/s)**	**kh (m/s)**	**kh/kv**	**Δ kv (%)**	**Δ kh (%)**
Gray	10	7.50×10^{-9}	3.38×10^{-9}	0.45	0	0
	20*	7.50×10^{-9}	2.28×10^{-9}	0.30	0	-33
	40	3.35×10^{-9}	1.66×10^{-9}	0.50	-55	-51
	80	2.41×10^{-9}	1.11×10^{-9}	0.46	-68	-67
	160	7.88×10^{-10}	3.87×10^{-10}	0.49	-89	-89
	320	3.41×10^{-10}	7.68×10^{-11}	0.23	-95	-98
Brown	10	1.01×10^{-8}	2.45×10^{-8}	2.43	0	0
	20	6.96×10^{-9}	1.36×10^{-8}	1.95	-31	-45
	40	6.08×10^{-9}	1.24×10^{-8}	2.04	-40	-49
	80	4.35×10^{-9}	8.04×10^{-9}	1.85	-57	-67
	160	2.46×10^{-9}	5.94×10^{-9}	2.42	-76	-76
	320	1.40×10^{-9}	4.85×10^{-9}	3.48	-86	-80

* The same kv value was used for 10 and 20 kPa effective pressure since there was no volumetric variation in the consolidation process.

Table 2.25: Overview of the void ratio of the gray and brown sandstone samples in the vertical (ev) and horizontal (eh) directions, as well as their percentage variation (Δ) about the unconsolidated sample.

Sandstone	**Consolidation (kPa)**	**ev**	**eh**	**Δ ev (%)**	**Δ eh (%)**	**Δ evh (%)**
Gray	10	0.321	0.309	0.0	0.0	-3.8
	20*	0.321	0.306	0.0	-0.7	-4.4
	40	0.317	0.304	-1.1	-1.4	-4.1
	80	0.311	0.298	-3.0	-3.5	-4.2
	160	0.302	0.289	-5.7	-6.5	-4.6
	320	0.294	0.278	-8.3	-10.0	-5.5
Brown	10	0.374	0.410	0.0	0.0	9.5
	20	0.369	0.407	-1.5	-0.5	10.6
	40	0.359	0.401	-4.0	-2.1	11.7
	80	0.347	0.391	-7.3	-4.7	12.6
	160	0.336	0.381	-10.1	-6.9	13.4
	320	0.331	0.375	-11.5	-8.5	13.3

* The same ev value was used for 10 and 20 kPa effective pressure since there was no volumetric variation in the consolidation process.

Unsaturated hydraulic permeability

The unsaturated hydraulic conductivity was estimated through the soil water retention curve (SWRC) with the parameters derived from the proposal by van Genuchten (1980). The experimental data collected via the filter paper technique, along with the analytical fit from van Genuchten (1980), as well as the estimate of unsaturated hydraulic conductivity, are exemplified in Figure 2.72, which reports the values of the unconfined gray and brown sandstones. Given that the saturated permeability of the brown sandstone was higher than that of the gray sandstone, the estimate of unsaturated values was also higher. The values of k for the unsaturated condition are presented up to $\times 10^{-15}$ relative to moisture near zero, as lower suction values do not align with the expected in situ behavior, even when the sandstone is outcropping. The parameter values from the analytical solution of van Genuchten (1980) are shown in Table 2.26, which, in conjunction with the previously determined saturated hydraulic conductivity values, made it possible to estimate k for the unsaturated condition.

Table 2.27 presents the outcomes of saturated hydraulic conductivity of some sandstones determined by different methods. The results demonstrate a notable variability, as evidenced by Chen et al. (2009), who conducted permeability tests in a triaxial apparatus similar to the one used here, with the maximum and minimum results reported by the authors for intrinsic permeability of a porous sandstone without deviatoric stress of 5.2×10^{-11} m^2 and with deviatoric stress of 108.6 MPa of 5.7×10^{-18} m^2 (ranging from 5.2×10^{-7} m/s to 5.7×10^{-11} m/s considering the dynamic viscosity of water at 10^{-3} Pa.s and the specific weight of 10 kN/m^3). Additionally, the authors analyzed anisotropy concerning the permeability of shaly siltstone by conducting tests on samples in different directions. They pointed out that the bedding distribution controlled the flow and, therefore, the anisotropy.

This work observed that the decrease in saturated hydraulic conductivity was more significant than the reduction in void ratio caused by the applied confining stress. This phenomenon was linked to the effective porosity of the sandstone. Bohnsack et al. (2021) assert that well-connected pores are less affected by increased effective stress, with stiffer materials being less susceptible to changes in stress state. Thus, the pores in the sandstone

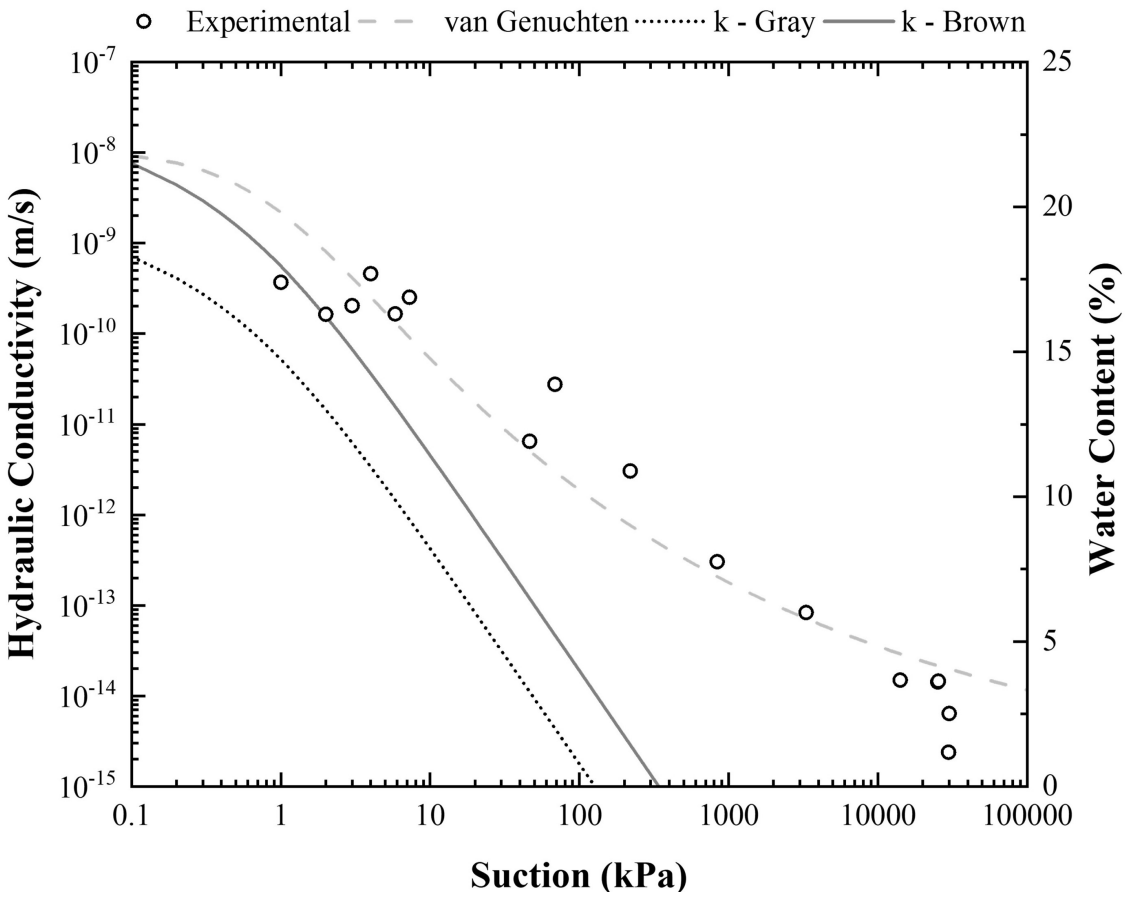

Figure 2.72: Soil water retention curve (SWRC) of sandstone and the estimation of unsaturated hydraulic conductivity of gray and brown sandstones.

appeared to be poorly connected, and a small reduction in porosity significantly affected permeability, as the flow lines depended on a few interconnected pores. Francisca & Glatstein (2020) noted a similar scenario and commented on the significance of interconnected voids and, once obstructed—in this case by the presence of microorganisms filling the voids—permeability was considerably reduced.

Similarly, Selvadurai & Selvadurai (2007) point out that the primary mechanisms for reducing permeability under isotropic confinement are the degree of saturation, reduction of voids, clogging of pores, and collapse of the channels that form the connection between pores.

Quigley & Thompson (1966) present fundamental factors for reducing hydraulic conductivity in materials containing clay minerals, which, in addition to the obstruction of voids, when hydrated, lead to an increase of the double layer due to fluid sorption present in

Table 2.26: SWRC parameters

Parameter	Value
α	1.104
n	1.163
m	0.140
wr (%)	0.0
ws (%)	22.0

the voids and a consequent reduction of these voids, along with the reorientation of particles imposed by the flow, resulting in increased tortuosity and changes in flow lines.

Huggett & Uwins (1994) reinforce the importance of understanding the clay minerals present in rocks, especially illites and smectites, which can form a gel when in contact with water that fills the voids of the rock matrix and consequently reduces permeability.

The results presented here likely draw parallels with the presence of clay minerals from the smectite group and suggest a relationship between the expansion observed in the oedometer and direct shear tests during the saturation stages of the samples and hydraulic conductivity. However, expansion and hydraulic conductivity are not commonly related, despite both being a function of the quantity and type of clay mineral, as noted by Xu et al. (2020).

In this way, the sandstone exhibited unique characteristics, primarily with the presence of water. That is, it underwent disaggregation when placed in water and cracking when saturated by capillarity. Baker et al. (1993) observed the same behavior in sandstones containing illite and smectite, which belong to the same group of clay minerals elucidated here through methylene blue tests and SEM. In this context, the brown sandstone demonstrated strong agglomeration of fines without a deflocculant in the combined grain size tests. Although the material was classified as clayey sand, the results of direct shear on the saturated sandstone did not indicate typical resistance envelopes of soil, with apparent cohesion values above 50 kPa, nor did the uniaxial compression results with the oven-dried material indicate typical rock resistance, with values below the minimum commonly reported in the literature (see Tables 2.20 and 2.21), demonstrating that it is weathered sandstone.

The contrasting behavior of the brown sandstone did not reflect in the strength, stiffness, and compressibility results. The UCS and Young's modulus values were similar, with the strength envelope of the brown sandstone above that of the gray sandstone and the expansion pressures very close. The discrepancy between the sandstones was again noted in the determination of permeability, where the brown sandstone proved to be more permeable and exhibited anisotropy opposite to that of the gray sandstone. In other words, the hydraulic conductivity of the brown sandstone in the vertical direction was lower than that in the horizontal direction, such that the flow was preferential in the brown sandstone, mainly in the horizontal direction.

Sebastián et al. (2008) observed behaviors similar to those reported here regarding gray and brown sandstones with fracture formation when saturated by capillarity. However, the results with brown sandstone were more contrasting, showing lower mechanical resistance and more significant expansion compared to the gray sandstone researched by the authors, who, through optical microscopy and ultrasound, identified that the phyllosilicates in the brown sandstone had orientation in the same direction as their basal planes parallel to the original sedimentation. This type of orientation made the brown sandstones more fragile by forming weaker planes, making them more susceptible to expansion. The bedding planes' orientation indicated pronounced anisotropy with higher water absorption in the direction perpendicular to the stratification.

In order to enhance the understanding of the sandstone's mechanical behavior in the presence of water, we propose conducting UCS tests under saturated conditions and strength envelopes under dry conditions.

The results of this research reflected very complex material to work with. The complexity of the material was evident throughout the research process, from collection through molding to the execution of technological tests. Notably, no distinct standard behavior of sandstone based on color was observed, indicating that all specimens constitute a singular material. Moreover, the possibility of in situ material expansion leading to fracture formation significantly impacts the mechanical and hydraulic behavior of the sandstone, adding to the complexity of drawing accurate conclusions about the material.

Table 2.27: Saturated hydraulic conductivity values reported by other authors, determined by different methods.

Reference	**Sandstone**	**Test**	**k (m/s)**
Bishop et al. (1993)	Coventry	Laboratory in situ pumping	1.15×10^{-7} 1.74×10^{-6}
Schulze-Makuch (1997)	Dane County lower aquifer	New permeameter designed	2×10^{-7}
Boving & Grathwohl (2001)	Buntsandstein Upper Keuper Middle Keuper	Constant head permeameter	4.3×10^{-10} - 5.5×10^{-9} 3.20×10^{-8} 7.8×10^{-10} - 1.3×10^{-8}
Shepherd et al. (2002)	Birmingham Triassic	Falling head permeameter	2.31×10^{-7} - 5.90×10^{-5}
Chen et al. (2009)	Porous	Triaxial	5.2×10^{-7} - 5.7×10^{-11}
Wei et al. (2011)	Zhuxianzhuang coal mine	Triaxial	6.39×10^{-11} - 6.69×10^{-11}
Neukum et al. (2014)	Herzogenrather Obernkirchner Solling	Constant head permeameter	1.53×10^{-6} - 2.2×10^{-10}

2.4 Conclusions

This paper aims to provide insights into the hydraulic and mechanical behaviors of weathered sandstone outcroppings in a tropical region. The key findings are as follows:

(i) There are indications of clay minerals from the smectite group that give the sandstone expansive characteristics.

(ii) Gray and brown sandstones exhibit similar properties in UCS, Young's modulus, and shear strength, indicating brittle failure with low resistance and intermediate to high modulus.

(iii) The materials display distinct compressibility and expansion pressure behaviors under dry and saturated conditions.

(iv) The sandstone exhibited anisotropy concerning permeability, with the brown sandstone being one to two orders of magnitude more permeable than the gray sandstone and preferentially horizontal flow. In contrast, the gray sandstone demonstrated higher permeability in the vertical direction.

References

Abay, T. B., Karlsen, D. A., Lerch, B., Olaussen, S., Pedersen, J. H., & Backer-Owe, K. (2017). Migrated petroleum in outcropping mesozoic sedimentary rocks in spitsbergen: organic geochemical characterization and implications for regional exploration. *Journal of Petroleum Geology*, 40(1), 5–36.

ABNT NBR 8522-1 (2021). Concreto endurecido – Determinação dos módulos de elasticidade e de deformação. Parte 1: módulos estáticos à compressão. *ABNT - Associação Brasileira de Normas Técnicas, Rio de Janeiro, RJ*, (pp. 1–20).

ASTM C170/C170M (2017). Standard test method for compressive strength of dimension stone. *ASTM International, West Conshohocken, PA*, (pp. 1–4).

ASTM C496/C496M (2017). Standard test method for splitting tensile strength of cylindrical concrete specimens. *ASTM International, West Conshohocken, PA*, (pp. 1–5).

ASTM D2435/D2435M (2011). Standard test methods for one-dimensional consolidation properties of soils using incremental loading. *ASTM International, West Conshohocken, PA*, (pp. 1–15).

ASTM D2487-17 (2017). ASTM D2487-17, Standard practice for classification of aoils for engineering purposes (unified soil classification system). *ASTM International, West Conshohocken, PA*, (pp. 1–10).

ASTM D3967 (2016). Standard test method for splitting tensile strength of intact rock core specimens. *ASTM International, West Conshohocken, PA*, (pp. 1–5).

ASTM D4318 (2017). Standard test methods for liquid limit, plastic limit, and plasticity index of soils. *ASTM International, West Conshohocken, PA*, (pp. 1–20).

ASTM D4543 (2019). Standard practices for preparing rock core as cylindrical test specimens and verifying conformance to dimensional and shape tolerances. *ASTM International, West Conshohocken, PA*, (pp. 1–13).

ASTM D4546 (2014). Standard test methods for one-dimensional swell or collapse of soils. *ASTM International, West Conshohocken, PA*, (pp. 1–10).

ASTM D5084 (2016). Standard test methods for measurement of hydraulic conductivity of saturated porous materials using a flexible wall permeameter. *ASTM International, West Conshohocken, PA*, (pp. 1–24).

ASTM D5607 (2016). Standard test method for performing laboratory direct shear strength tests of rock specimens under constant normal force. *ASTM International, West Conshohocken, PA*, (pp. 1–9).

ASTM D6913/D6913M (2017). Standard test methods for particle-size distribution (gradation) of soils using sieve analysis. *ASTM International, West Conshohocken, PA*, (2017), 1–34.

ASTM D7012 (2014). Standard test method for compressive strength and elastic moduli of intact rock core specimens under varying states of stress and temperatures. *ASTM International, West Conshohocken, PA*, (pp. 1–9).

ASTM D7928-17 (2017). Standard test method for particle-size distribution (gradation) of fine-grained soils using the sedimentation (hydrometer) analysis. *ASTM International, West Conshohocken, PA.*, (pp. 1–25).

Baker, J. C., Uwins, P. J., & Mackinnon, I. D. (1993). ESEM study of illite/smectite freshwater sensitivity in sandstone reservoirs. *Journal of Petroleum Science and Engineering*, 9(2), 83–94.

Bakhshi Ardakani, S. & Rajabi, A. M. (2021). Laboratory investigation of clayey soils improvement using sepiolite as an additive; engineering performances and micro-scale analysis. *Engineering Geology*, 293(April 2020), 106328.

Basilici, G., Bo, P. F. D., & de Oliveira, E. F. (2016). Distribution of palaeosols and deposits in the temporal evolution of a semiarid fluvial distributary system (Bauru Group, Upper Cretaceous, SE Brazil). *Sedimentary Geology*, 341, 245–264.

Batezelli, A. (2017). Continental systems tracts of the Brazilian Cretaceous Bauru Basin and their relationship with the tectonic and climatic evolution of South America. *Basin Research*, 29, 1–25.

Bishop, P. K., Jakobsen, R., Gosk, E., Lerner, D. N., & Burston, M. W. (1993). Investigation of a solvent polluted industrial site on a deep sandstone-mudstone sequence in the UK. Part 1. Site description and groundwater flow. *Journal of Hydrology*, 149(1-4), 209–229.

Bohnsack, D., Potten, M., Freitag, S., Einsiedl, F., & Zosseder, K. (2021). Stress sensitivity of porosity and permeability under varying hydrostatic stress conditions for different carbonate rock types of the geothermal Malm reservoir in Southern Germany. *Geothermal Energy*, 9(1), 15.

Bolarinwa, A. T., Idakwo, S. O., & Bish, D. L. (2019). Paleo-environmental conditions, paleoclimatic significance and effects of weathering on clay deposits in the Lower Benue Trough, Nigeria. Mineralogical approach. *Journal of Environmental and Earth Sciences*, 1(2), 18–30.

Boving, T. B. & Grathwohl, P. (2001). Tracer diffusion coefficients in sedimentary rocks: correlation to porosity and hydraulic conductivity. *Journal of Contaminant Hydrology*, 53, 85–100.

Broch, E. & Franklin, J. A. (1972). The point-load strength test. *International Journal of Rock Mechanics and Mining Sciences and*, 9(6), 669–676.

Buragohain, P., Garg, A., Lin, P., Hong, M., Yi, Z., & Sreedeep, S. (2018). Exploring potential of fly ash bentonite mix as a liner material in waste containment systems under concept of sponge city. *Advances in Civil Engineering Materials*, 7(1), 46–70.

Cai, X., Zhou, Z., & Du, X. (2020). Water-induced variations in dynamic behavior and failure characteristics of sandstone subjected to simulated geo-stress. *International Journal of Rock Mechanics and Mining Sciences*, 130(March), 104339.

Chen, T.-M. N., Zhu, W., Wong, T.-f., & Song, S.-R. (2009). Laboratory characterization of permeability and its anisotropy of Chelungpu fault rocks. *Pure and Applied Geophysics*, 166(5-7), 1011–1036.

Dal' Bó, P. F. F., Basilici, G., & Angélica, R. S. (2010). Factors of paleosol formation in a Late Cretaceous eolian sand sheet paleoenvironment, Marília Formation, Southeastern Brazil. *Palaeogeography, Palaeoclimatology, Palaeoecology*, 292(1-2), 349–365.

Feng, M., Wu, J., Ma, D., Ni, X., Yu, B., & Chen, Z. (2018). Experimental investigation on the seepage property of saturated broken red sandstone of continuous gradation. *Bulletin of Engineering Geology and the Environment*, 77(3), 1167–1178.

Ferreira, A. A., Negro Jr, A., Albieiro, J. H., & Cintra, J. C. A. (1993). *Soils of the Interior of São Paulo (in Portuguese)*. ABMS & USP - São Carlos.

Fjær, E., Holt, R., Horsrud, P., Raaen, A., & Risnes, R. (2008). Mechanical properties and stress data from laboratory analysis. In *Developments in Petroleum Science*, volume 53 chapter 7, (pp. 251–287).

Francisca, F. M. & Glatstein, D. A. (2020). Environmental application of basic oxygen furnace slag for the removal of heavy metals from leachates. *Journal of Hazardous Materials*, 384(September 2019), 121294.

Franzen, C. & Mirwald, P. (2004). Moisture content of natural stone: static and dynamic equilibrium with atmospheric humidity. *Environmental Geology*, 46(3-4), 391–401.

Garg, A., Reddy, N. G., Huang, H., Buragohain, P., & Kushvaha, V. (2020). Modelling contaminant transport in fly ash–bentonite composite landfill liner: mechanism of different types of ions. *Scientific Reports*, 10(1), 1–8.

Hu, S., Xiao, C., Liang, X., Cao, Y., Wang, X., & Li, M. (2019). The influence of oil shale in situ mining on groundwater environment: A water-rock interaction study. *Chemosphere*, 228, 384–389.

Huang, D., Cen, D., & Song, Y. (2020). Comparative Investigation on the Compression–Shear and Tension–Shear Behaviour of Sandstone at Different Shearing Rates. *Rock Mechanics and Rock Engineering*, 53(7), 3111–3131.

Huang, K., Dai, Z., Yan, C., Yu, F., Zhang, W., & Chen, S. (2023). Swelling behaviors of heterogeneous red-bed mudstone subjected to different vertical stresses. *Journal of Rock Mechanics and Geotechnical Engineering*, 16(5), 1847–1863.

Huang, S., Xia, K., Yan, F., & Feng, X. (2010). An experimental study of the rate dependence of tensile strength softening of longyou sandstone. *Rock Mechanics and Rock Engineering*, 43(6), 677–683.

Huang, Y.-H., Wu, S.-Y., & Yang, C. (2024). Experimental study on the failure behaviors of sandstone specimens with two fissures under triaxial loading and unloading conditions. *Engineering Fracture Mechanics*, 298, 109933.

Huggett, J. M. & Uwins, P. J. (1994). Observations of water-clay reactions in water-sensitive sandstone and mudrocks using an environmental scanning electron microscope. *Journal of Petroleum Science and Engineering*, 10(3), 211–222.

Jesus, L. S., Fernandes, J. B., & Giacheti, H. L. (2013). Investigação da condutividade hidráulica dos solos de uma área de aterro de resíduos sólidos urbanos através de ensaios de campo e laboratório. *Ciencia y Engenharia/ Science and Engineering Journal*, 22(1), 21–28.

Jing, X., Yang, Z., Tong, Y., Wang, H., & Xu, Y. (2018). Identification of multiple magnetizations of the Ediacaran strata in South China. *Geophysical Journal International*, 212(1), 54–75.

Kassymkanova, K. K., Rysbekov, K. B., Nurpeissova, M. B., Kyrgizbayeva, G. M., Amralinova, B. B., Soltabaeva, S. T., Salkynov, A., & Jangulova, G. (2023). Geophysical Studies of Rock Distortion in Mining Operations in Complex Geological Conditions. In *International*

Archives of the Photogrammetry, Remote Sensing and Spatial Information Sciences - ISPRS Archives, volume 48 (pp. 57–62).

Kodikara, J. K. & Rahman, F. (2002). Effects of specimen consolidation on the laboratory hydraulic conductivity measurement. *Canadian Geotechnical Journal*, 39(4), 908–923.

Li, E., Chen, H., Huang, F., Zhou, L., & Yu, Z. (2022). Waste rocks from the industrial mining process: hazard metals stabilization behavior evaluating and reusing as construction materials. *International Journal of Environmental Science and Technology*, 19(5), 3685–3700.

Liu, D., Su, J., Gu, Z., Qi, Y., Yang, F., Tian, T., & Ye, F. (2021). Geochemical Properties and Pore Structure Control on Oil Extraction of Shale. *Lithosphere*, 2021(SpecialIssue-1), 1–17.

Liu, H. D., Liu, S., Liu, H. N., Chen, J. X., Xia, Z. G., Zhai, J. Y., & Fu, Y. Y. (2023). Mechanical deterioration effect and damage evolution characteristics of soft sandstone with different water-immersed heights under uniaxial compression. *Bulletin of Engineering Geology and the Environment*, 82(4).

Liu, X., Liu, Y., Dai, F., & Yan, Z. (2022). Tensile mechanical behavior and fracture characteristics of sandstone exposed to freeze-thaw treatment and dynamic loading. *International Journal of Mechanical Sciences*, 226(February), 107405.

Ma, D., Rezania, M., Yu, H. S., & Bai, H. B. (2017). Variations of hydraulic properties of granular sandstones during water inrush: effect of small particle migration. *Engineering Geology*, 217, 61–70.

Meng, Z., Shi, X., & Li, G. (2016). Deformation, failure and permeability of coal-bearing strata during longwall mining. *Engineering Geology*, 208, 69–80.

Miao, K., Tu, S., Wang, Y., Li, J., Zhao, H., & Guo, B. (2023). Utilization of broken rock in shallow gobs for mitigating mining-induced water inrush disaster risks and environmental

damage: Experimental study and permeability model. *Science of the Total Environment*, 903(August), 166812.

Mondelli, G. (2008). *Integração de diferentes técnicas de investigação para avaliação da poluição e contaminação de uma área de disposição de resíduos sólidos urbanos*. Tese (doutorado), Escola de Engenharia de São Carlos - Universidade de São Paulo (USP).

Neukum, C., Braun, A., & Azzam, R. (2014). Transport of stabilized engineered silver (Ag) nanoparticles through porous sandstones. *Journal of Contaminant Hydrology*, 158, 1–13.

Pejon, O. J. (1992). *Mapeamento geotécnico da folha de Piracicaba-SP (escala 1:100000): estudo de aspectos metodológicos, de caracterização e de apresentação dos atributos*. PhD thesis, Escola de Engenharia de São Carlos - Universidade de São Paulo (USP).

Quigley, R. M. & Thompson, C. D. (1966). The fabric of anisotropically consolidated sensitive marine clay. *Canadian Geotechnical Journal*, 3(2), 61–73.

Rajabi, A. M. & Hamrahi, Z. (2021). An experimental study on the influence of metakaolin on mechanical properties of a clayey sand. *Bulletin of Engineering Geology and the Environment*, 80(10), 7921–7932.

Ranjith, P. G., Zhao, J., Ju, M., De Silva, R. V., Rathnaweera, T. D., & Bandara, A. K. (2017). Opportunities and challenges in deep mining: a brief review. *Engineering*, 3(4), 546–551.

Sanjay, N. S., Shukla, K., & Das, B. M. (2013). *Rock mechanics an introduction*. CRC Press.

Schulze-Makuch, D. (1997). A permeameter designed to measure both hydraulic conductivity and dispersivity of consolidated rocks. *Canadian Geotechnical Journal*, 34(4), 615–620.

Sebastián, E., Cultrone, G., Benavente, D., Linares Fernandez, L., Elert, K., & Rodriguez-Navarro, C. (2008). Swelling damage in clay-rich sandstones used in the church of San Mateo in Tarifa (Spain). *Journal of Cultural Heritage*, 9(1), 66–76.

Selvadurai, P. A. & Selvadurai, A. P. (2007). On cavity flow permeability testing of a sandstone. *Ground Water*, 45(1), 93–97.

Shaojie, F., Chen, G., & Wenbo, L. (2021). Study on failure law of rock mass and slope stability by open-pit combined mining. *E3S Web of Conferences*, 248, 0–4.

Shepherd, K. A., Rivett, M. O., & Mitchener, R. G. (2002). Organic contaminant sorption in Triassic sandstone deposits, Birmingham, UK. *IAHS-AISH Publication*, (275), 193–198.

Silva, M. L., Batezelli, A., & Ladeira, F. S. B. (2019). Genesis and evolution of paleosols of the Marília Formation, Maastrichtian of the Bauru Basin, Brazil. *CATENA*, 182(October 2018), 104108.

Skempton, A. W. (1954). The pore-pressure coefficients A and B. *Geotechnique*, 4(4), 143–147.

Small, J. C. (2016). *Geomechanics in soil, rock, and environmental engineering*.

Sotoudeh, F., Nehring, M., Kizil, M., & Knights, P. (2020). Integrated underground mining and pre-concentration systems; a critical review of technical concepts and developments. *International Journal of Mining, Reclamation and Environment*, 00(00), 1–30.

Tang, S. (2018). The effects of water on the strength of black sandstone in a brittle regime. *Engineering Geology*, 239(March), 167–178.

Tiennot, M., Mertz, J. D., & Bourgès, A. (2019). Influence of clay minerals nature on the hydromechanical and fracture behaviour of stones. *Rock Mechanics and Rock Engineering*, 52(6), 1599–1611.

Ueda, K., Matsui, R., Ziauddin, M., Teng, L. K., & Wang, W. K. (2019). Acid selection for volcanic tuffaceous sandstone with high analcime contents: a laboratory study in Kita-akita oil field, northern Japan. *SPE Production and Operations*, (January), 26–28.

van Genuchten, M. T. (1980). A closed-form equation for predicting the hydraulic conductivity of unsaturated soils. *Soil Science Society of America Journal*, 44(5), 892–898.

Wang, C., Zhao, Y., He, C., & Bi, J. (2022). Study on the tensile-shear mechanical behavior of sandstone using a simple auxiliary apparatus. *Theoretical and Applied Fracture Mechanics*, 122(October), 103608.

Wang, H., Jiang, C., Zheng, P., Li, N., & Zhan, Y. (2020). Deformation and failure mechanism of surrounding rocks in crossed-roadway and its support strategy. *Engineering Failure Analysis*, 116(May), 104743.

Wang, R. & Tang, Y. (2024). Study on the rock physical mechanical properties evaluation of tight oil reservoir in Chang 7 member, Longdong area, Ordos Basin, China. *Frontiers in Earth Science*, 12(February), 1–15.

Wangler, T. & Scherer, G. W. (2008). Clay swelling mechanism in clay-bearing sandstones. *Environmental Geology*, 56(3-4), 529–534.

Wei, L., Yue-ping, Q., Miao-miao, Z., Cui-xia, W., & Ya-ru, W. (2011). Test study on permeability properties of the sandstone specimen under triaxial stress condition. *Procedia Engineering*, 26, 173–178.

Xu, X., Liu, X., Oh, M., & Park, J. (2020). Development of a novel base liner material for offshore final disposal sites and the assessment of its hydraulic conductivity. *Waste Management*, 102, 190–197.

Yang, S. Q. (2016). Experimental study on deformation, peak strength and crack damage behavior of hollow sandstone under conventional triaxial compression. *Engineering Geology*, 213, 11–24.

Yang, S. Q., Jing, H. W., & Cheng, L. (2014). Influences of pore pressure on short-term and creep mechanical behavior of red sandstone. *Engineering Geology*, 179, 10–23.

You, W., Dai, F., Liu, Y., & Li, Y. (2022). Dynamic mechanical responses and failure characteristics of fractured rocks with hydrostatic confining pressures: An experimental study. *Theoretical and Applied Fracture Mechanics*, 122(April), 103570.

Yuan, R. & Shen, B. (2017). Numerical modelling of the contact condition of a Brazilian disk test and its influence on the tensile strength of rock. *International Journal of Rock Mechanics and Mining Sciences*, 93(December 2015), 54–65.

Zhang, C., Bai, Q., & Han, P. (2023). A review of water rock interaction in underground coal mining: problems and analysis. *Bulletin of Engineering Geology and the Environment*, 82(5), 1–22.

Zhang, Z., Gao, W., Huang, J., Ouyang, S., & Zhang, Z. (2020). Swelling characteristics of red sandstone under cyclic wetting and drying. *Geotechnical and Geological Engineering*, 38(4), 4289–4306.

Zhao, R., Wu, X., Zhu, G., Wang, X., Mei, A., & Zhang, X. (2022). Experimental study on mechanical properties of highly swelling soft rocks in the Yanji basin, northern China. *Rock Mechanics and Rock Engineering*, 55(3), 1125–1141.

Zhao, Y., Qin, W., Jin, A., Wu, H., & Chen, Z. (2024). Research and analysis of the impact of the pore structure on the mechanical properties and fracture mechanism of sandstone. *Materials Today Communications*, 38(November 2023), 107753.

Zhu, Q., Li, D., Han, Z., Li, X., & Zhou, Z. (2019). Mechanical properties and fracture evolution of sandstone specimens containing different inclusions under uniaxial compression. *International Journal of Rock Mechanics and Mining Sciences*, 115(August 2018), 33–47.

Zhu, Q., Li, T., Wang, B., Li, C., Ran, J., & Zhang, H. (2023). A case study on the deformation and failure mechanism of a soft rock mining roadway in the Xin'Shang'Hai No. 1 coal mine, China. *Engineering Failure Analysis*, 146(December 2022), 107136.

Chapter 3

Laboratory investigation of hydraulic and contaminant transport parameters from a municipal solid waste disposal site

Abstract

Disposing of municipal solid waste (MSW) in large urban centers, particularly in developing nations, primarily involves MSW disposal sites. In Bauru, Brazil, the MSW disposal site has led to contamination that could jeopardize future water supplies. Understanding the contamination plume's behavior involves studying hydraulic parameters and contaminant transport. In this context, we investigated a tropical sandy soil profile and its bedrock to determine the saturated and unsaturated hydraulic conductivity (k), dispersivity (α), hydrodynamic dispersion (Dh), partition coefficient (Kd), retardation factor (Rd), and arrival times through column and leaching tests. Undisturbed and disturbed samples were collected in the experimental field at Unesp-Bauru at 1, 4, 7, 11, 13, and 16 m depth. Sandstone samples were collected from a rock outcrop on the outskirts of Bauru's MSW disposal site. Column tests used NaCl as the target tracer, and metals Mn, Ni, and Pb were found in concentrations above the Brazilian environmental agency permitted in the monitoring wells. The tests were carried out with a flexible wall permeameter under confining stresses of 20, 40, 80, 160, and 320 kPa, representing those in situ. The results show that hydraulic conductivity decreased with increasing confinement and depth, while α and Dh decreased with increasing Péclet number (Pe). Rd and Kd indicate low sorption contribution by soil and sandstone. The behavior was consistent across different soil horizons at 1-7 m and 11-16 m. This paper brings a range of values concerning transport contaminant parameters for future decision-making and numerical or analytical modeling involving Bauru's MSW disposal site.

Keywords: MSW disposal site; Subsoil investigation; Weathered sandstone; Hydraulic conductivity; Contaminant transport parameters; Flexible wall permeameter.

3.1 Introduction

The population growth and the subsequent increase in consumption and industrial demand have led to a rise in waste production, which poses a significant challenge for its proper disposal on a global scale. Even though MSW disposal sites present environmental risks, require large areas, and have high installation and maintenance costs, they are still widely used as the final destination for MSW. The decomposition of waste generates leachate, a complex mixture whose composition depends on various factors such as climate and economy. Leachate typically contains harmful substances, including heavy metals, which pose a significant threat to soil and groundwater quality and, consequently, human health (Kjeldsen et al., 2002; Kulikowska & Klimiuk, 2008; Mondelli et al., 2010; Gworek et al., 2016; Moody & Townsend, 2017; Mishra et al., 2018; Abunama et al., 2021).

Brazil disposed of 77.1 million tons of municipal solid waste last year (ABREMA, 2023). Among the final disposal sites is the Bauru's MSW disposal site, where monitoring wells installed in its surroundings indicated the presence of heavy metals in concentrations above the maximum established by the Brazilian environmental agencies CONAMA 420/09 (2009) and CETESB (2014), demonstrating that the contamination plume from leachate generation reached the soil and groundwater.

The hydraulic conductivity is affected by confinement, which involves the advection–dispersion transport parameters. Therefore, simulating this condition in the laboratory is crucial for the results to represent in situ behavior. The flexible wall permeameter provides different boundary conditions, simulating various situations in the field, making it an essential tool for research, especially into parameters that are difficult to measure in situ, such as dispersivity (Rowe et al., 2004; Christensen et al., 2001; Dafalla et al., 2015; Yu et al., 2021).

Chlorides are still widely used as tracers for contaminant transport simulations. Due to their non-reactive nature, they are unaffected by sorption or precipitation. They are controlled by the advection-dispersion process, which is highly suitable for sandy soils, such as Bauru's MSW disposal site (van Breukelen et al., 2004; Rowe & Abdelrazek, 2019; Santos et al., 2019; Slavinskienė et al., 2019; Divya et al., 2020; Puranik & Patil, 2021; Thu et al.,

2023).

In light of the field monitoring, despite the fact that chlorides do not have a significant impact from the point of view of risk to human health or environmental damage, the chlorides detected in situ are indicative of the direction of the plume. They can provide an initial reference for the sample collection and a more detailed analysis of other chemical substances of interest (Feng & Jin, 2019).

Since advection–dispersion transport mechanisms prevail in sandy soils, column and leaching tests are appropriate for determining dispersivity and hydrodynamic dispersion parameters. Various authors have long used both tests.

Column test parameters are more representative in situations that involve verifying or monitoring the spread of the contamination plume. On the other hand, when the aim is to extract the pollutant to remediate a previously intercepted plume, leaching data is indicated.

Even in closed MSW disposal sites such as Bauru, soil and water contamination persist for decades, putting local fauna and flora at risk. Understanding the predominant transportation process and the parameters involved in plume migration is fundamental for future mitigation interventions.

In this context, the main goal of this research is to investigate the hydraulic conductivity and transport parameters of tropical sandy soil and its rock outcrop (sandstone) using NaCl as the tracer in column and leaching tests. Although previous research by Jesus et al. (2013), Mondelli et al. (2007), and Mondelli et al. (2010) contemplated the hydraulic parameters of Bauru's MSW disposal site, little emphasis was placed on the behavior of the sandstone. Therefore, the heavy metals Mn, Ni, and Pb, previously identified by Faria & Mondelli (2018) with concentrations above those permitted by Brazilian environmental agencies, were also used as tracers in the tests involving the sandstone, given that it is close to the waste mass.

Complementing, thus, the hydraulic and pollutant transport parameters of previous work, in which will help in decision-making not only for Bauru's MSW disposal site but also for other locations with similar geological-geotechnical characteristics but with a limited range of data.

3.2 Material and Methods

3.2.1 Studied sites and sampling

Managed by the Bauru Urban and Rural Development Company (EMDURB), Bauru's MSW disposal site received waste from 1993 to 2016. It covers an area of around 270000 m^2 and has a height of 15 m. The MSW disposal site was built with a protective asphalt emulsion slurry and clay liner over the soil. However, these actions were not enough to prevent the leachate migration. Monitoring data from the MSW disposal site indicates that the contamination plume is spreading, confirmed in previous research (Jesus et al., 2013; Mondelli et al., 2007; Faria & Mondelli, 2017, 2018).

Undisturbed soil samples were collected from the experimental field at Unesp Bauru at 1, 4, 7, 13, and 16 m depths to study the soil's hydraulic and transport parameters. Classified as an SM-SC soil by the Unified Classification and an A-2-4 by AASHTO, the soil in the experimental field consists of a fine red clayey sand that has been investigated in detail (Giacheti et al., 2019; Fernandes et al., 2022; Saab et al., 2023).

The sandstone was extracted from outcropping rocks near Bauru's MSW disposal site. As shown in Chapter 2, sandstone can be classified as SC using the Unified Soil Classification System, with clay minerals from the smectite group. The sampling locations are illustrated in Figure 3.1, and a summarized history of the soil profile is shown in Figure 3.2.

Both sites belong to the same stratigraphic profile. Formed in the Upper Cretaceous, the Adamantina and Marília formations belonging to the Bauru Group constitute the sedimentary deposits of the Bauru Basin, where sedimentary rocks predominate. Brownish red to grayish, the sandstones prevail in the upper stratigraphic portion. Their mineralogy mainly includes silicates (quartz), carbonates (calcite and ankerite), and clay minerals (kaolinite, montmorillonite, smectite, and palygorskite) (Dal' Bó et al., 2010; Basilici et al., 2016; Silva et al., 2019). Therefore, the soil from the Unesp Bauru experimental field can be considered representative of Bauru's MSW disposal site.

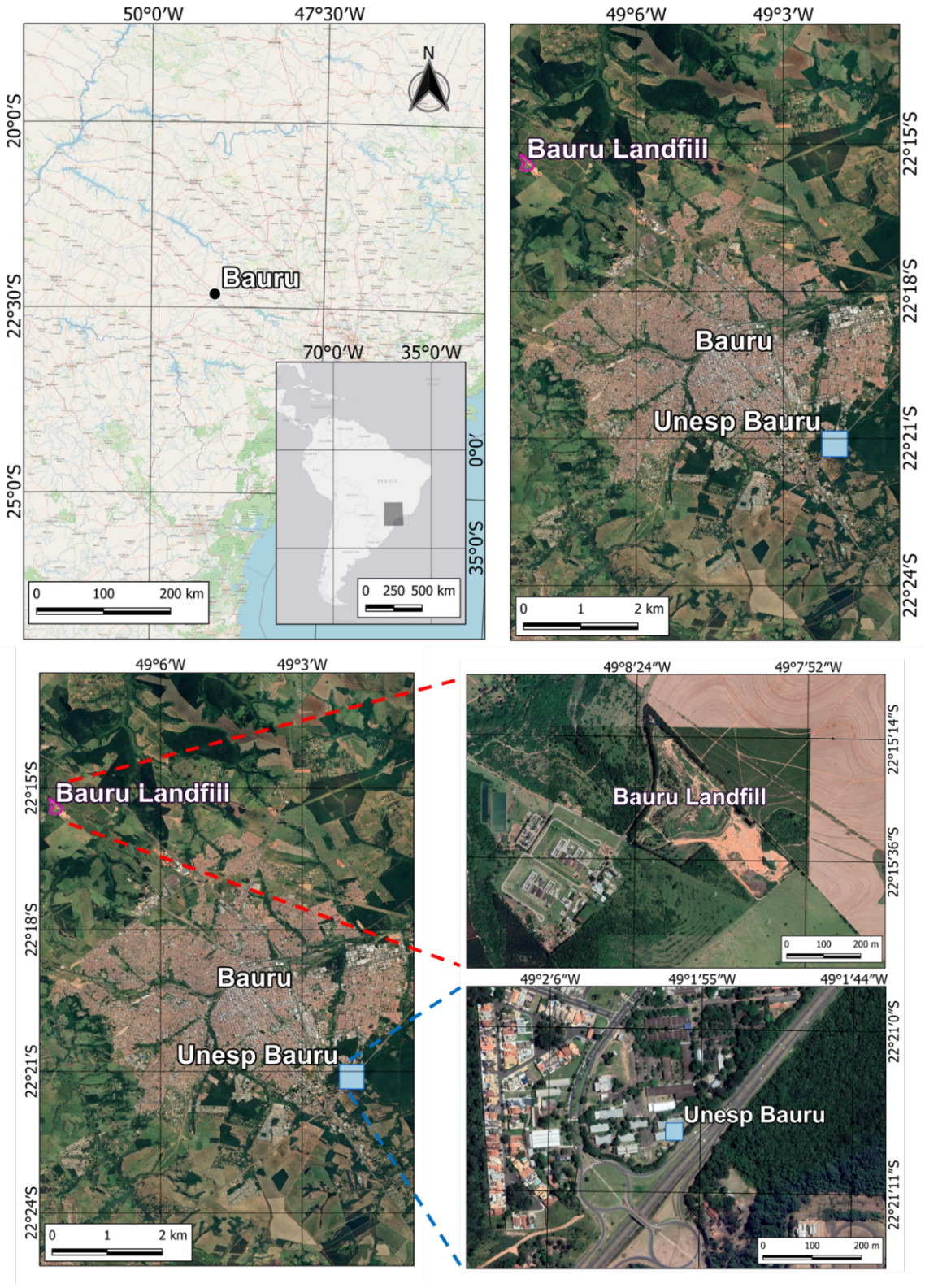

Figure 3.1: Location of the municipality of Bauru in the center-west of the State of São Paulo. Soil (Unesp Bauru) and rock (Bauru's MSW disposal site) sample sites.

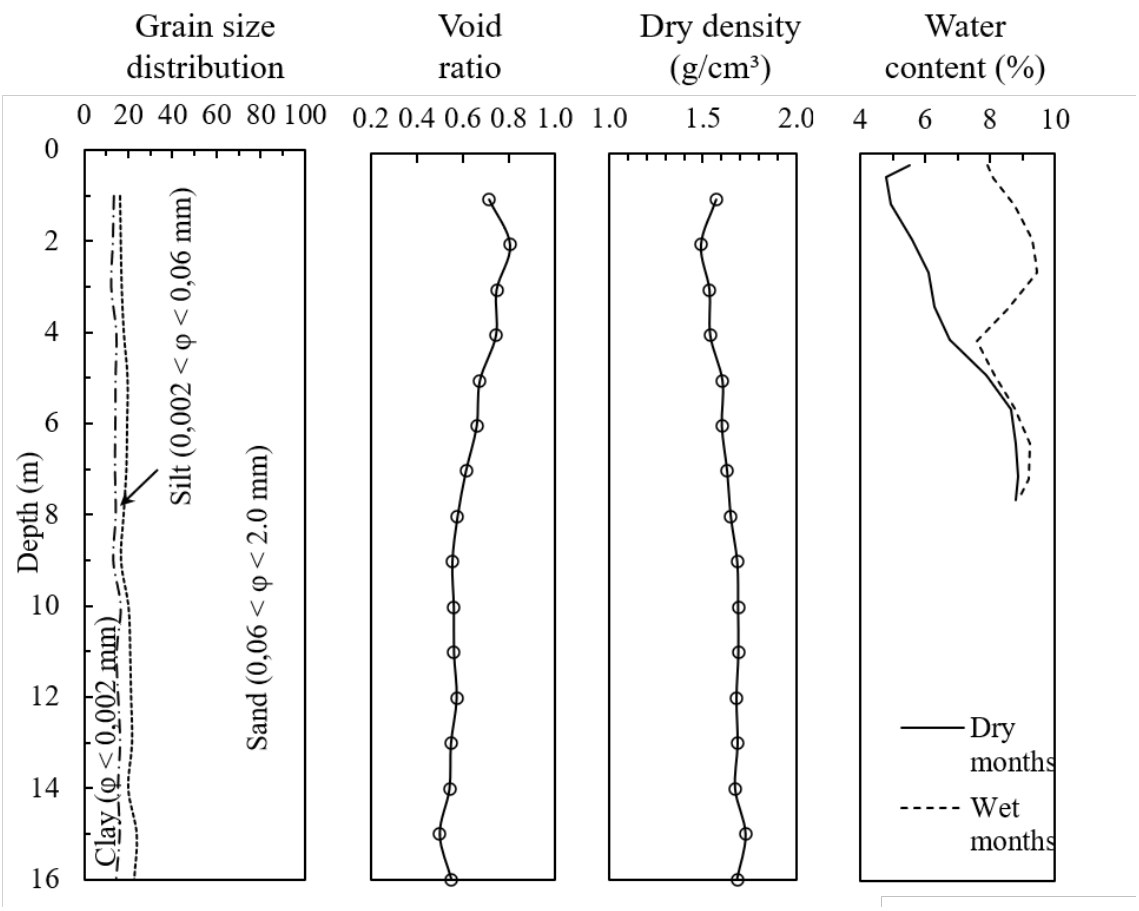

Figure 3.2: Grain size distribution and soil index properties with depth for the Unesp Bauru site (adapted from Fernandes et al., 2022).

3.2.2 Specimens preparation

Soil samples

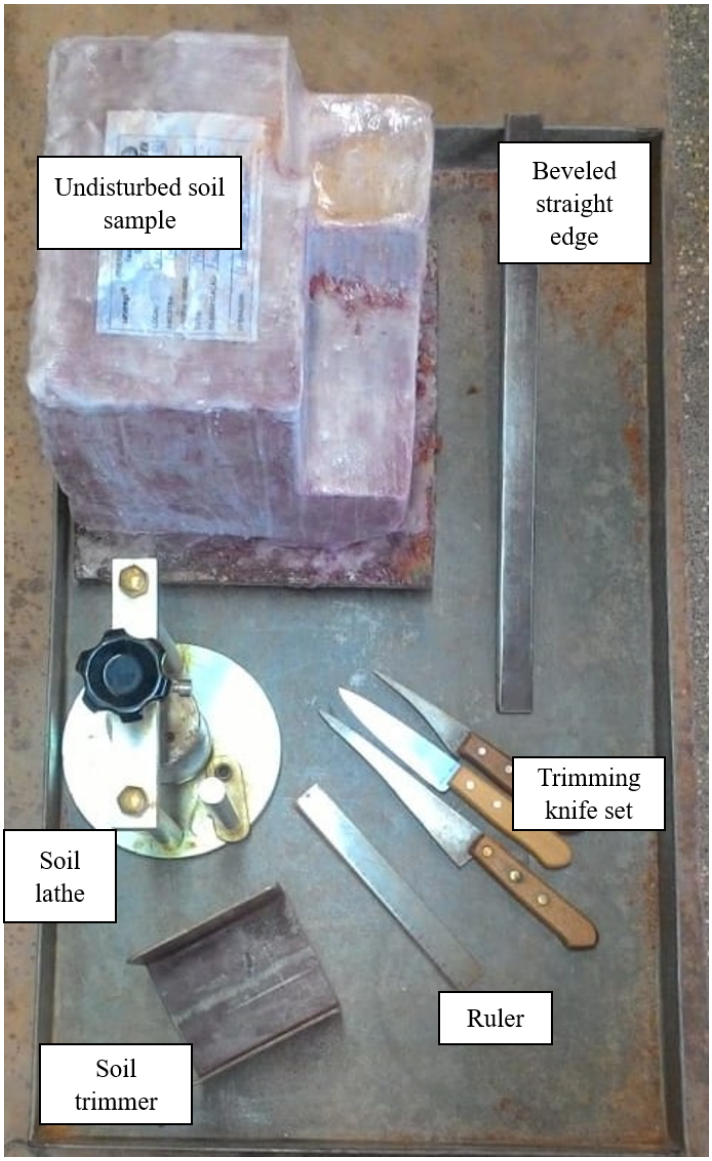

Figure 3.3: Set used for molding the soil specimens.

To determine the material's index properties, the laboratory utilized adequately stored undeformed samples to shape cylindrical test specimens with a diameter and height of 70 mm. Figure 3.3 presents the materials used for the molding process. In contrast, Figure 3.4 demonstrates the procedure for shaping the top and base of the sample (a) and finishing on the lathe (b). Additionally, Figure 3.5 illustrates the positioning of the soil core in the testing chamber before receiving the rubber membrane.

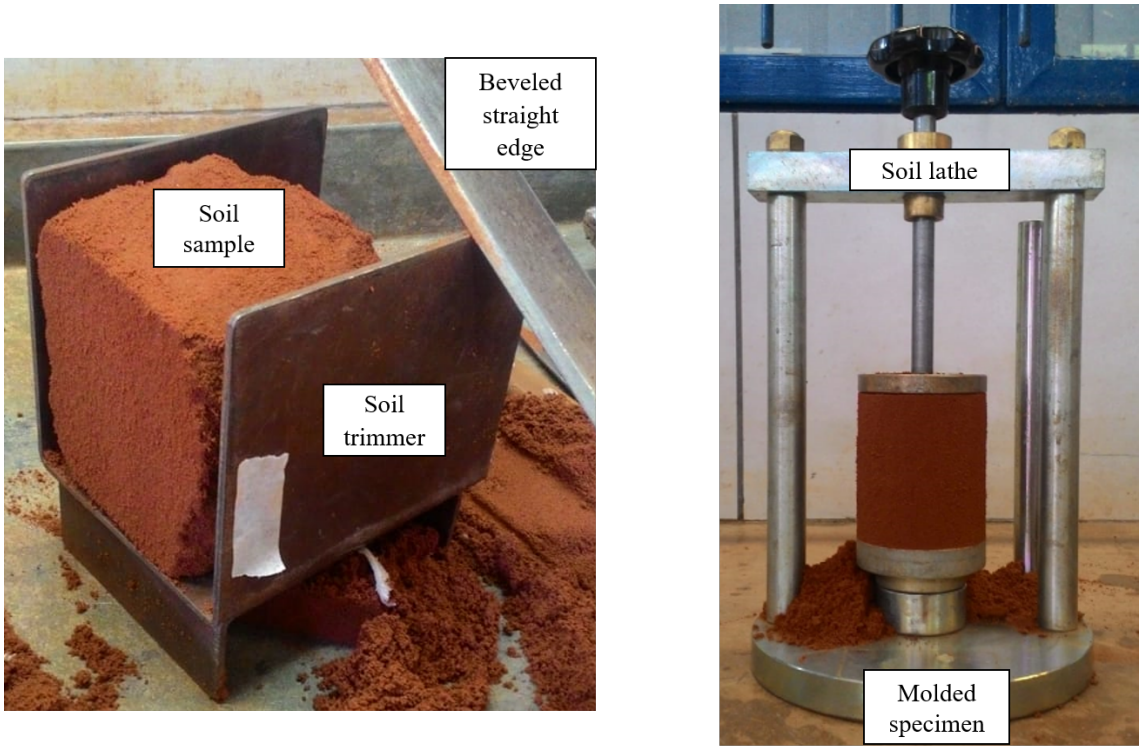

(a) Carving the sample

(b) Specimen on the lathe

Figure 3.4: Trimming devices used to molded the soil specimens.

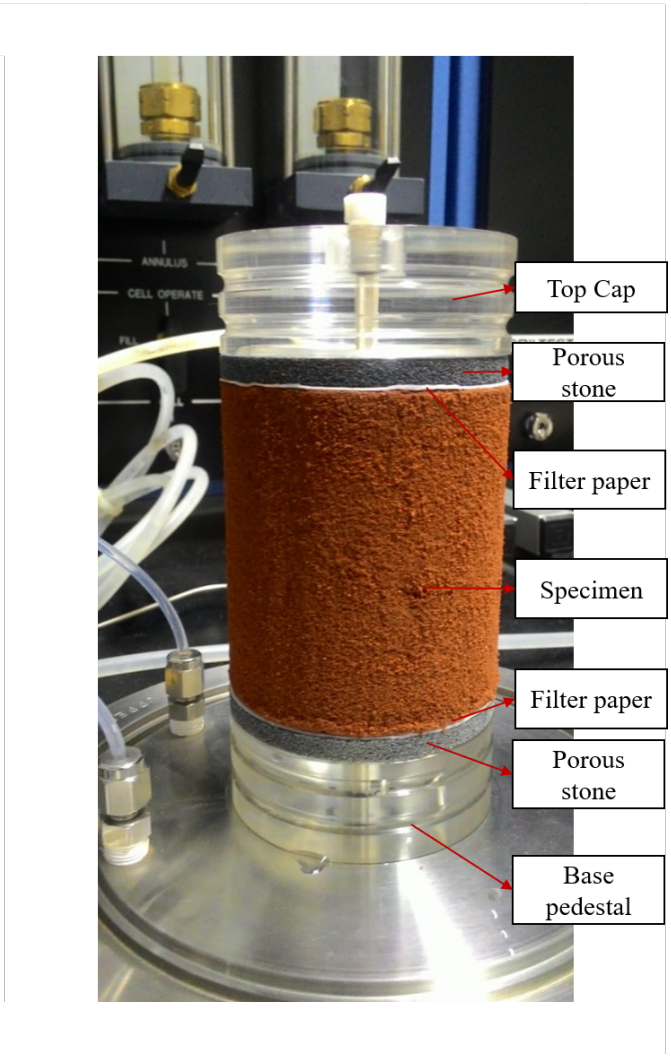

Figure 3.5: Arrangement of the specimen for the tests.

Sandstone samples

Figure 3.6: Sandstone sample cutting process.

The conception of the test specimens in sandstone followed the same steps presented in Chapter 2, which can also be consulted for more detailed information about the process exemplified by Figures 3.6 to 3.8. These figures illustrate the previously established final arrangement. The first one shows the rock-cutting process with a circular saw that allowed the samples collected in the field to be reduced. Figure 3.7 shows the removal of the test specimens using a diamond hollow drill, and the finishing of their top and base is demonstrated by Figure 3.8.

Figure 3.7: Assembly of the diamond hollow core drill used to remove cylindrical rock samples.

Figure 3.9 shows the test specimens of sandstone completed with various height/diameter ratios, depending on the tests discussed in Chapter 2. The specimens with a height and diameter of 70 mm are prepared for permeability, column, and leaching tests. Additionally, Figure 3.10 illustrates the placement of a core sample inside the testing chamber. In contrast, Figure 3.11 depicts the final setup of the test specimen before the chamber is sealed, enclosed by a rubber membrane, and fitted with top and base O-rings. This final configuration was also utilized for the tests involving soil. The materials employed for the samples tested in the flexible wall permeameter are presented in Figure 3.12.

Figure 3.8: The specimen grinding machine polishes the top and bottom of sandstone samples.

Figure 3.9: Specimens ready for testing.

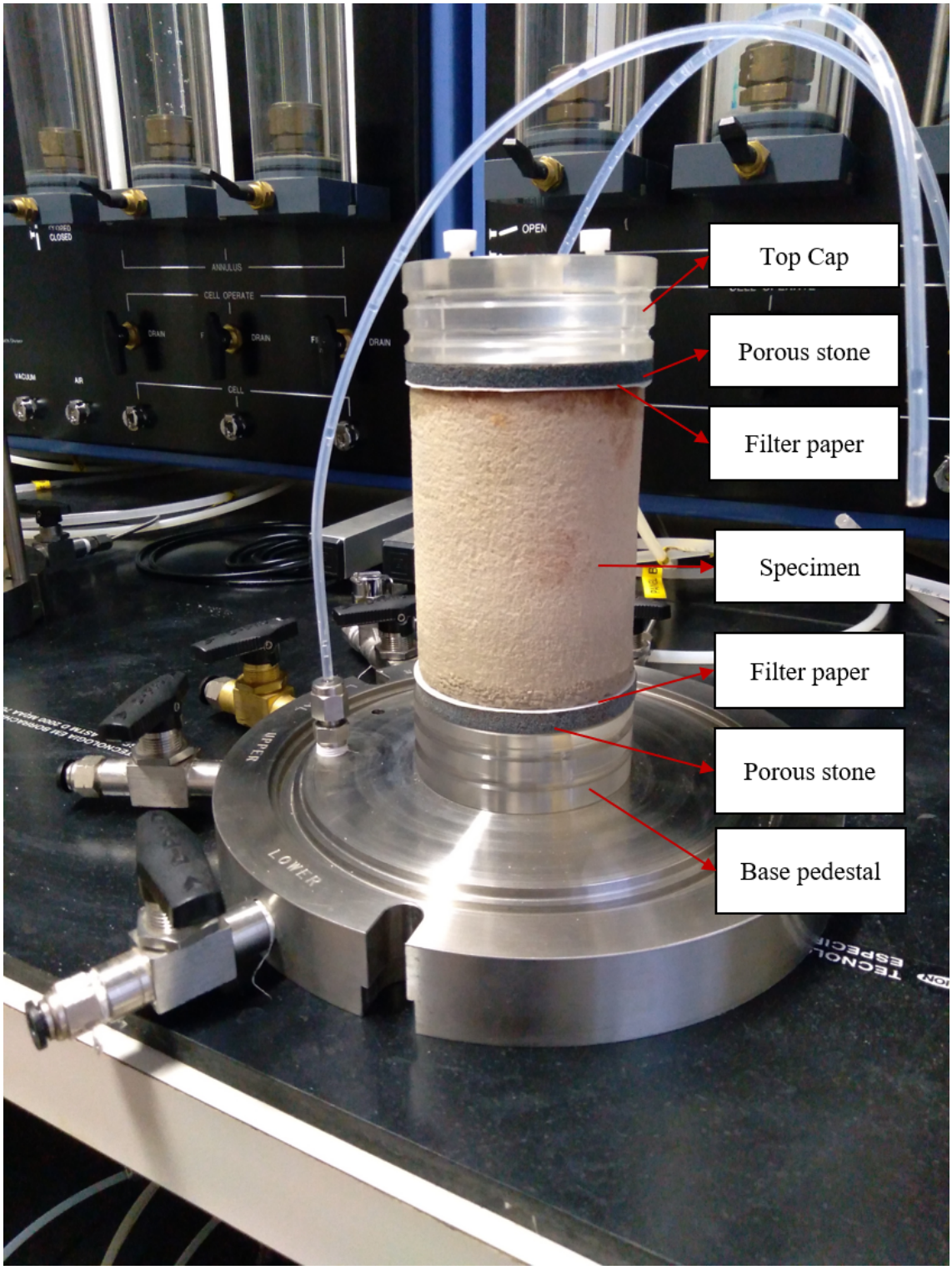

Figure 3.10: Sandstone specimen in the test chamber.

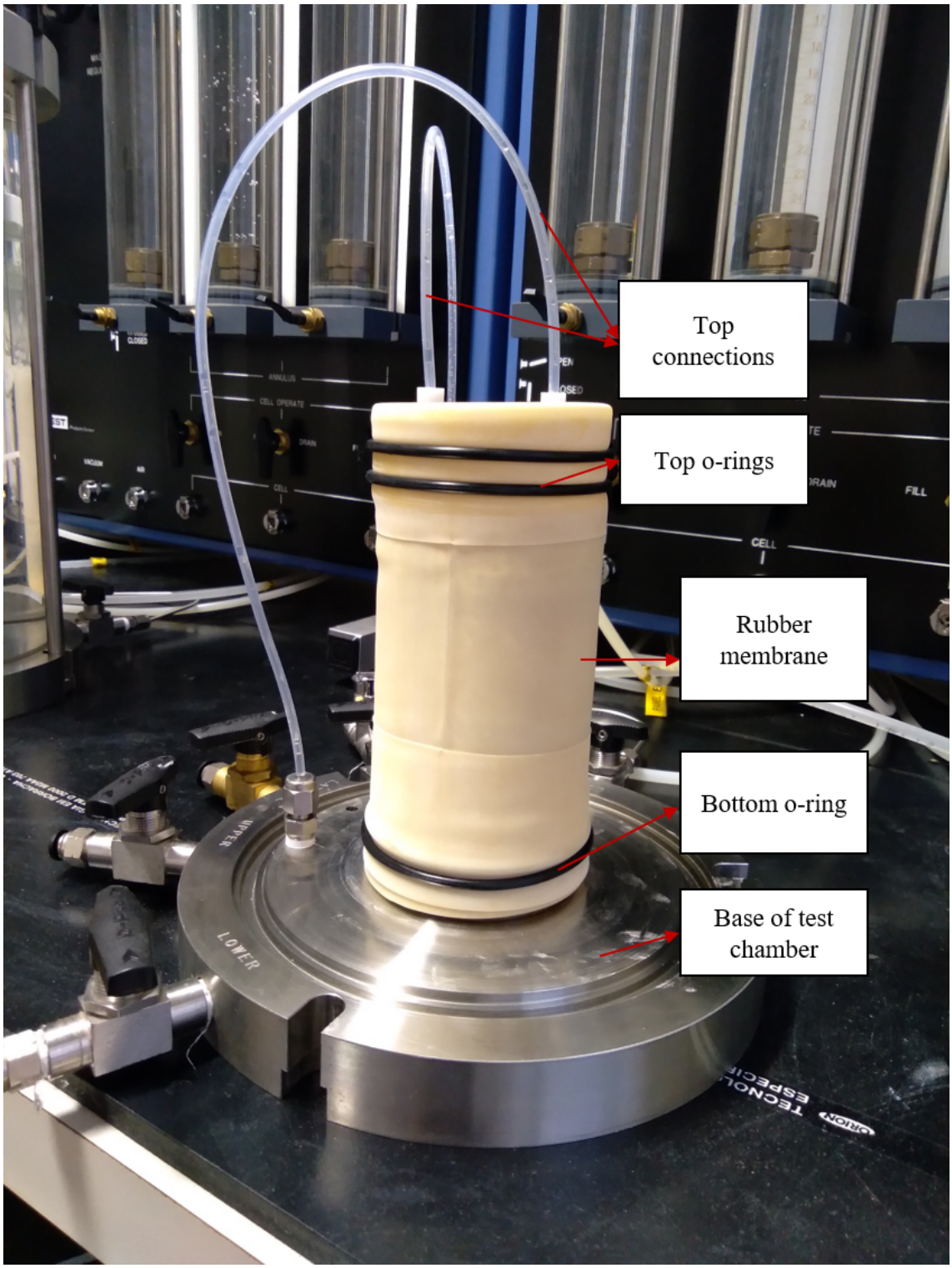

Figure 3.11: Sandstone core sample setup for testing.

Figure 3.12: Materials used to prepare the specimens for the permeability, column and leaching tests.

3.2.3 Permeability tests

After preparing the specimens, they were positioned in the test chambers and saturated by back pressure (Skempton, 1954; Head, 1994). The hydraulic conductivity of the soil and sandstone was determined by upward flow and constant head in accordance with ASTM D5084 (2016), as well as the Chapuis (2012) recommendations.

In order to simulate a range of in situ conditions, varying average isotropic stresses were imposed on the specimens. Specifically, pressures of 20, 40, 80, 160, and 320 kPa were applied to the sandstone and soil samples at depths of 1 and 4 m, 80 and 160 kPa at a depth of 7 m, and 160 and 320 kPa at depths of 11, 13, and 16 m. These stress levels were selected based on the in situ geostatic pressure. After stabilizing the stresses, the permeability test was repeated, and the hydraulic conductivity was calculated using Darcy's law.

$$\mathrm{k} = \frac{Q}{i \times A} \tag{3.1}$$

where Q is the volume flow, i hydraulic gradient, and A the cross-sectional area.

The hydraulic gradient for all tests was assumed in view of the performance of the flexible wall permeameter, which performs better at high hydraulic gradients since it was developed for materials with low permeability, as well as reducing the test time. Thus, gradients of 10 were adopted for the soil and 400 for the sandstone. The latter was also motivated by the results presented in Chapter 2.

The tests were conducted by taking into account the required hypotheses of Darcy's law. The resulting laminar flow was verified by Reynolds number (Re) as shown by Equation 3.2, where Re<1 indicates steady-state and validates Darcy's law (Bear & Cheng, 2010).

$$\mathrm{Re} = \frac{v\ \mathrm{K}\sqrt{n\tau}}{\nu} \tag{3.2}$$

where Re is the Reynolds number, v seepage velocity, K intrinsic permeability, n porosity, τ tortuosity, and ν kinematic viscosity.

Figure 3.13 shows the flexible wall permeameter along with the panels, reservoir, and data acquisition system. Figure 3.14 presents a schematic drawing of the flexible wall permeameter.

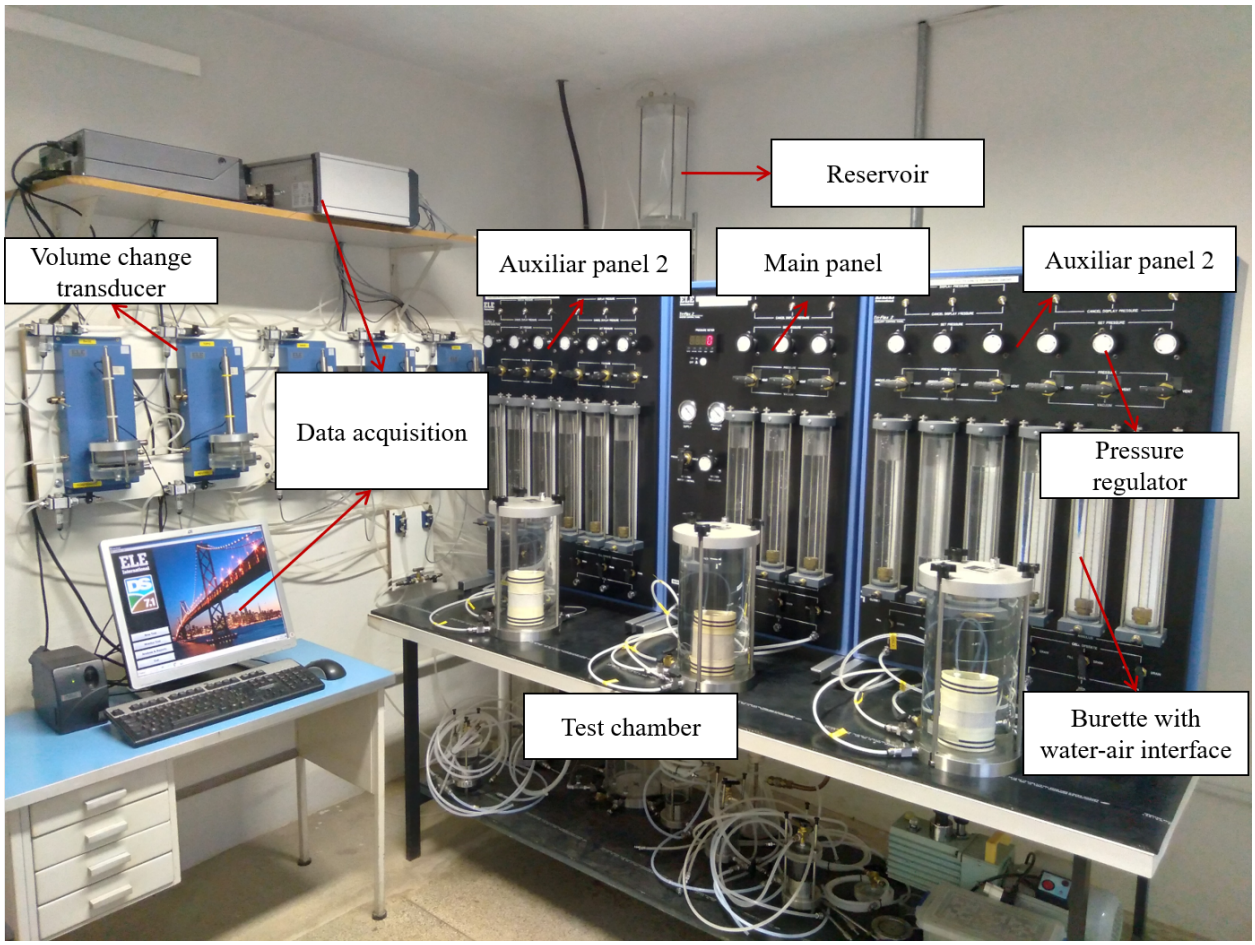

Figure 3.13: The flexible wall permeameter consists of the data acquisition system, main and secondary panels, reservoir, and test chambers.

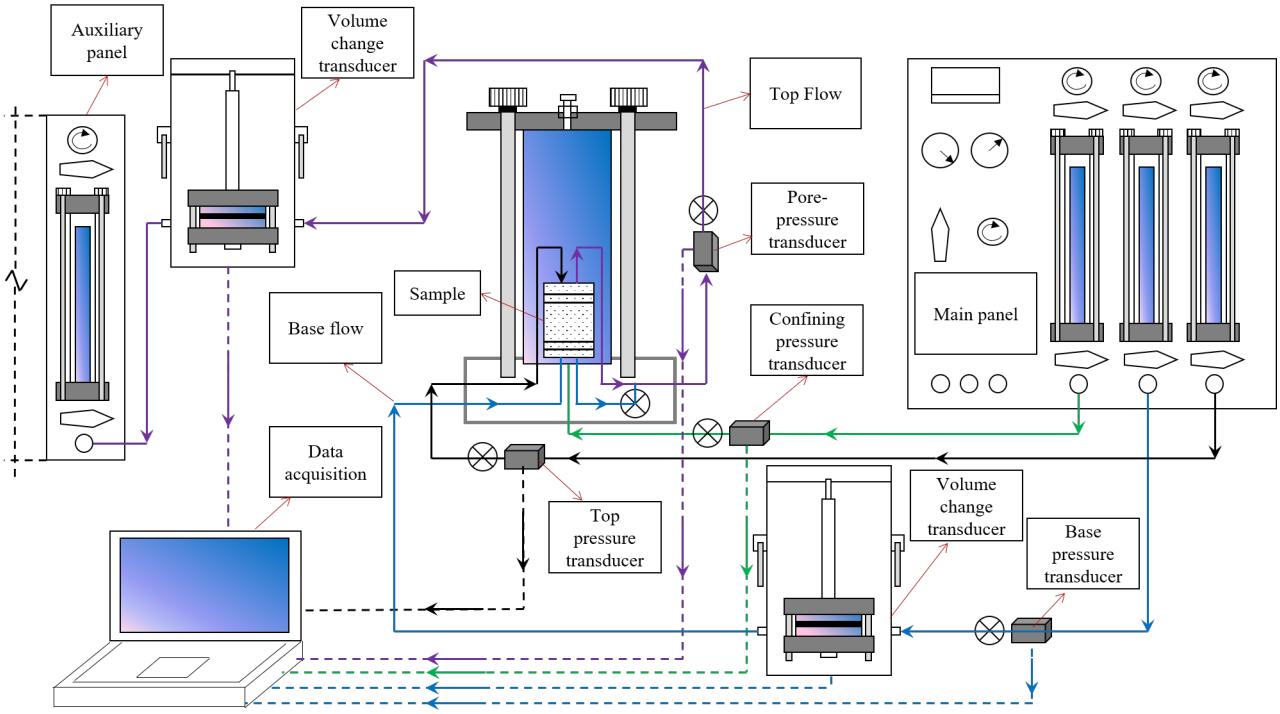

Figure 3.14: Permeability test schematic drawing.

3.2.4 Column tests

A saline tracer was used to estimate the transport parameters for soil and rock materials, while the multi-ionic solution was used only for sandstone. The solutions were prepared in deionized water until the target tracer concentration was achieved. To simulate MSW disposal site leachate, a multi-ionic solution containing the metals Pb, Ni, and Mn was prepared at a concentration of 0.05 mg/L, based on the minimum detection capacity of the mass spectrometer, i.e., 30 µg for Pb; 5 µg for Ni, and 0.4 µg for Mn. These metals were found to be present in concentrations higher than what is tolerated by Brazilian environmental agencies CONAMA 420/09 (2009) e CETESB (2014), as shown by Faria & Mondelli (2018). The saline solution was prepared with 1000 mg/L sodium chloride, and both solutions were adjusted to a pH of 8 ± 0.5, similar to the leachate from Bauru's MSW disposal site.

One pressure interface was set up upstream (bottom) and the other downstream (top) of the test chamber. These interfaces allowed the tracer to be percolated through the chamber at a known concentration. The effluent was collected every 0.3 pore volume for future analysis. The pH, salt solution concentration, and electrical conductivity were measured using a pHmeter and conductivity meter. To detect and measure the concentration of heavy metals, the effluent solution had its pH adjusted to 1.5 ± 0.5 trough HNO_3 and was preserved in a refrigerator until it was submitted to an ICP-OES (Inductively Coupled Plasma – Optical Emission Spectrometry), as suggested in the literature (Shackelford, 1995; Naka et al., 2016; US EPA Method 1314, 2017; ASTM D7100, 2011).

Figure 3.15 illustrates a schematic drawing of the column test with the upstream and downstream interfaces. Figure 3.16 depicts the specimen with the effluent collected from the outlet interface during the test.

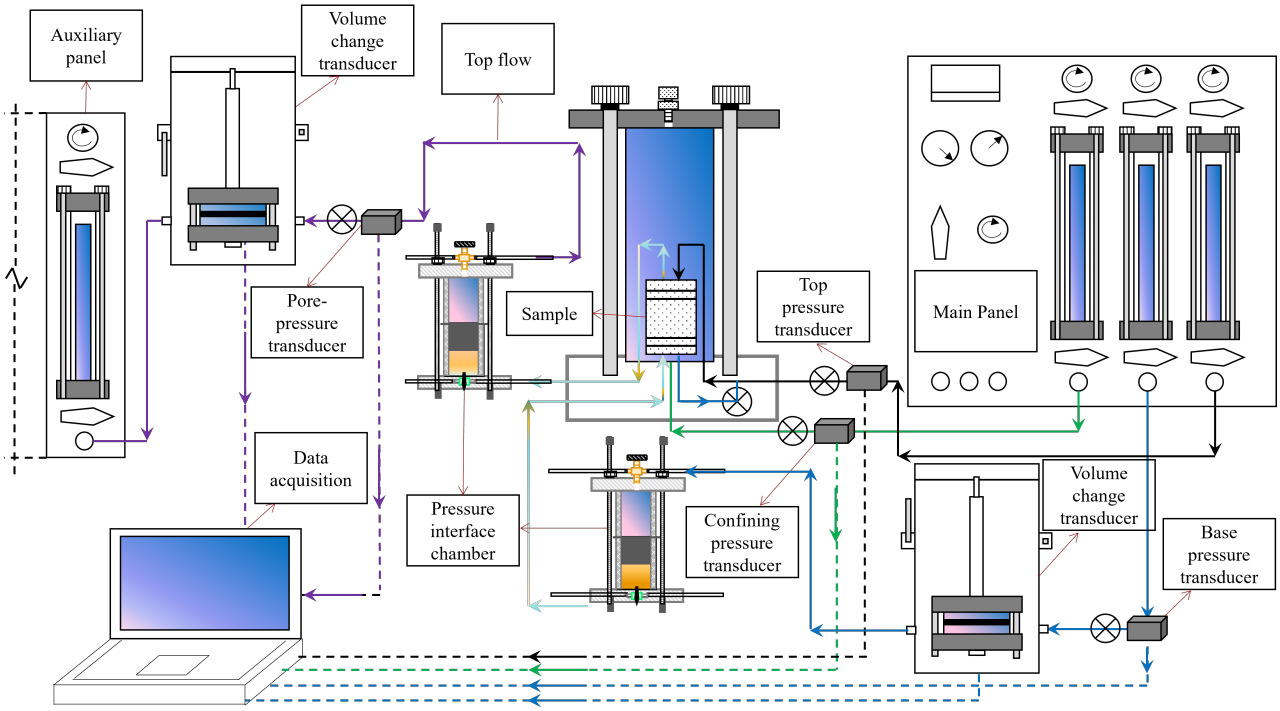

Figure 3.15: Column test schematic drawing.

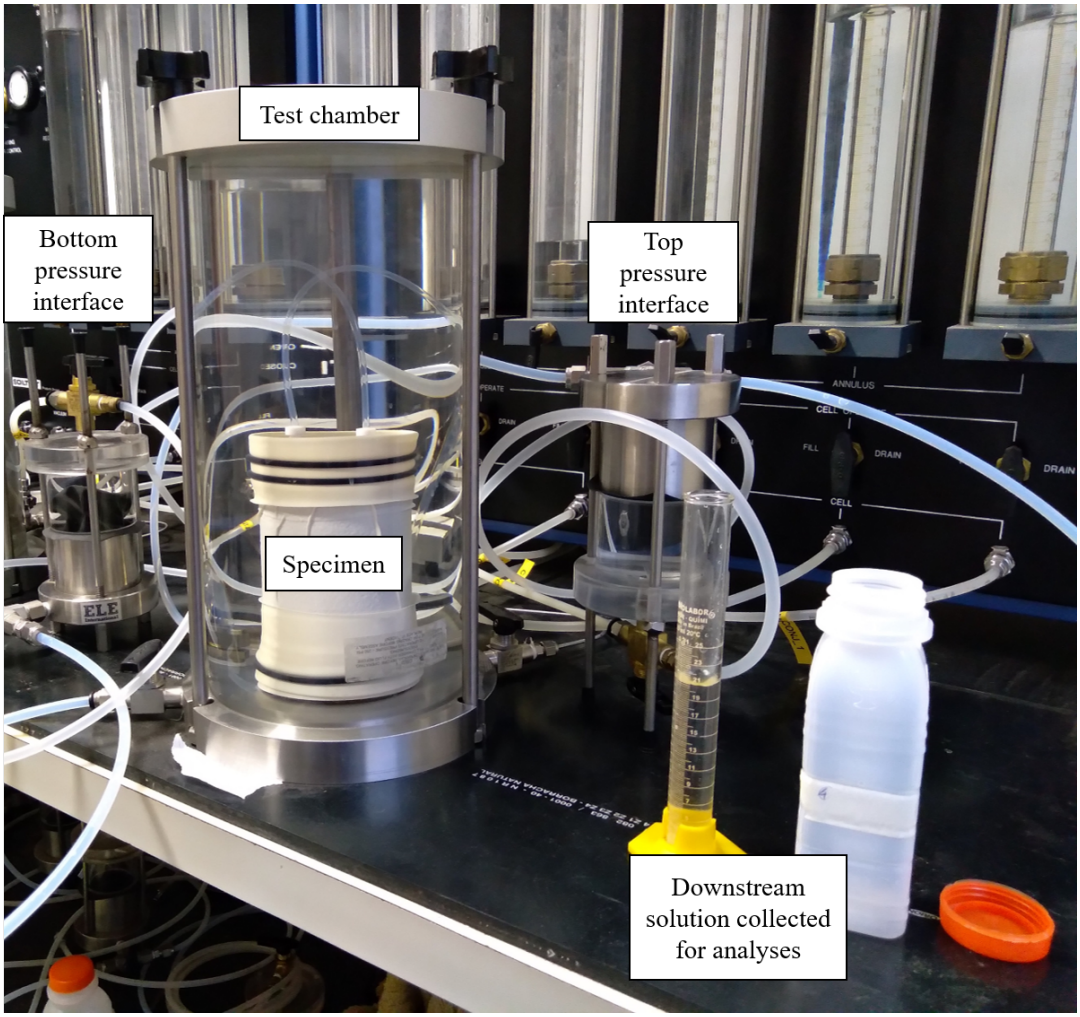

Figure 3.16: Arrangement of the test chamber in the center with the upstream (left) and downstream (right) pressure interfaces, as well as the solution gathered for analysis.

3.2.5 Leaching tests

Once the column test was completed and the medium was thoroughly saturated with the tracer, the leaching test was initiated, following the guidelines in the literature (US EPA, 2008; ASTM D4874, 2014). However, the leaching test could only be conducted on samples that NaCl percolated, as the multi-ionic solution did not reach the maximum relative concentration, i.e., $c/c_0 = 1$. This particular aspect will be discussed later on.

Except for the upstream pressure interface, the test setup was identical to the one outlined in the Column Test section. In this case, direct percolation with deionized water was used instead. The fluid collected by the top pressure interface was analyzed for concentration, electrical conductivity, and pH.

The transport parameters were estimated through column and leaching tests for the same materials in test specimens with specified configurations and isotropic stresses based on the in situ geostatic pressure. Thus, using a saline solution, the first meter of soil was confined to 20 kPa. At a depth of 4 m, stresses of 40 and 80 kPa were applied. The confinement at 7 m depth was 80 and 160 kPa, while at 11, 13, and 16 m depth, the effective stresses were 160 and 320 kPa. The latter was also applied to the sandstone, which did not undergo the consolidation process when tested with a solution containing Pb, Ni, and Mn.

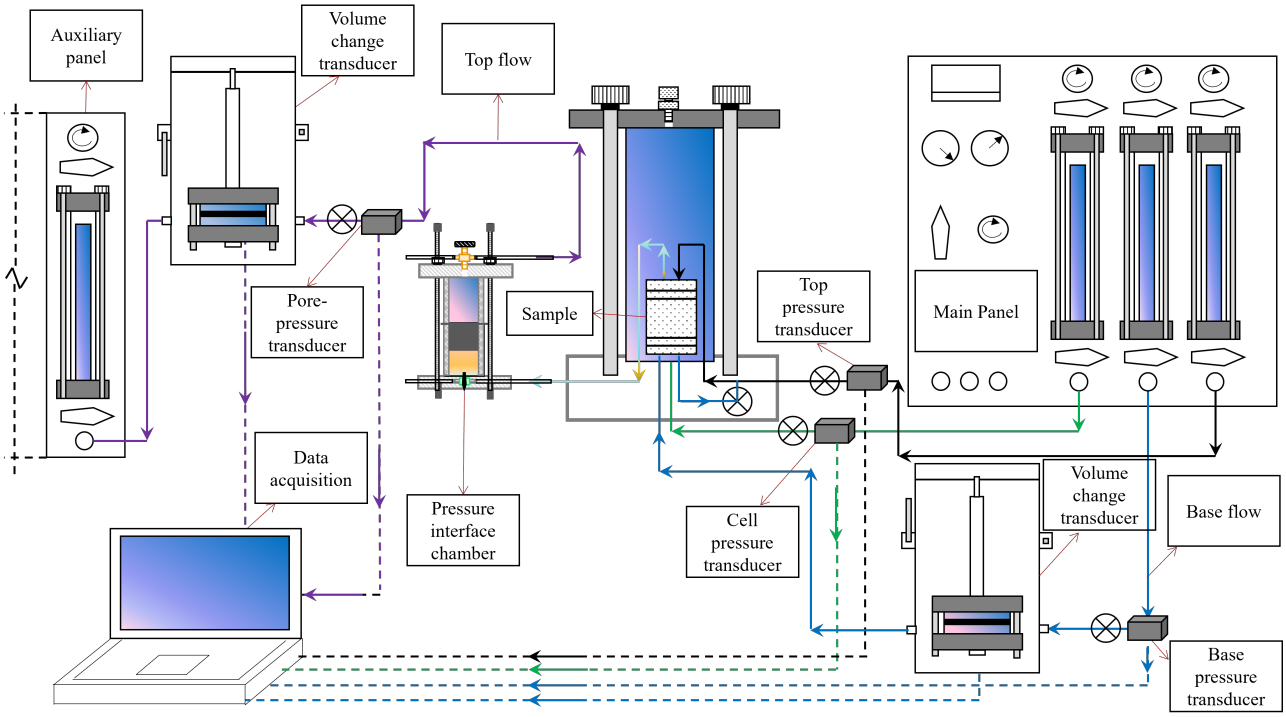

Figure 3.17: Leaching test schematic drawing.

3.2.6 Contaminant transport parameters

Based on the column and leaching data, experimental c/c_0 vs time breakthrough curves (BTC) were fitted using the analytical solution proposed by Ogata & Banks (1961) and Lapidus & Amundson (1952) for the advection–dispersion (equation 3.3), which governs flow in saturated porous media.

$$R_d \frac{\partial c}{\partial t} = D_h \frac{\partial^2 c}{\partial z^2} - v \frac{\partial c}{\partial z} \tag{3.3}$$

where R_d is the retardation factor, c is the concentration, t time, D_h the hydrodynamic dispersion, z the distance, and v the average linear velocity.

The Ogata & Banks (1961) and Lapidus & Amundson (1952) analytical solution (see 3.4) depends on the initial and the boundary conditions.

$$\begin{aligned} \mathrm{c}(z \geq 0, t = 0) &\rightarrow c = 0 \\ \mathrm{c}(z \leq 0, t \geq 0) &\rightarrow c = c_0 \\ \mathrm{c}(z = \infty, t \geq 0) &\rightarrow c = 0 \end{aligned}$$

$$\frac{c}{c_0} = \frac{1}{2}\left[\mathrm{erfc}\,\frac{R_d L - vt}{2\sqrt{D_h R_d t}} + \frac{1}{2}\exp\left(\frac{vL}{D_h}\right)\mathrm{erfc}\,\frac{R_d L + vt}{2\sqrt{D_h R_d t}}\right] \tag{3.4}$$

where c/c_0 is the relative concentration, erfc the complementary error function, and L the length of the column.

The analytical curve fit for the experimental leaching data applied the analytical solution complementary to that implemented by Ogata & Banks (1961) and Lapidus & Amundson (1952), as suggested by Rixey et al. (1999) and Huesemann et al. (2005).

$$\frac{c}{c_0} = 1 - \left\{\frac{1}{2}\left[\mathrm{erfc}\,\frac{R_d L - vt}{2\sqrt{D_h R_d t}} + \frac{1}{2}\exp\left(\frac{vL}{D_h}\right)\mathrm{erfc}\,\frac{R_d L + vt}{2\sqrt{D_h R_d t}}\right]\right\} \tag{3.5}$$

From the analytical fit, it was possible to estimate the dispersivity (α), hydrodynamic dispersion (Dh), retardation factor (R_d), partition coefficient (K_d) and Péclet number (Pe) indicated below.

$$\mathrm{Pe} = \frac{vL}{D_h} \tag{3.6}$$

$$Dh = \alpha \times v \tag{3.7}$$

$$R_d = 1 + \frac{\rho_d K_d}{n} \tag{3.8}$$

Additionally, the retardation factor was determined using three other methods outlined by Fetter et al. (2017), Freeze & Cherry (1979), and van Genuchten & Parker (1984).

(i) Fetter et al. (2017): relate the average linear velocity of the fluid to the velocity of the center of mass of the tracer, i.e., the velocity for a relative concentration equals 0.5.

(ii) Freeze & Cherry (1979): the value of the pore volume at the instant $c/c_0 = 0.5$.

(iii) van Genuchten & Parker (1984): area above the breakthrough curve for the column test and below the curve for the leaching test.

This work used the following definitions to collect information on the breakthrough curves from the column and leaching tests.

Column test:

(i) Arrival time (At): when the tracer concentration was first measured at the pickup point.

(ii) Pick time (Pt): the maximum concentration has been reached.

(iii) Breakthrough time (BTt) is defined as the moment when the system fails (Shackelford, 1990). It establishes the instant at which the concentration of a given pollutant under study exceeds the threshold.

Similarly, for the leaching test:

(i) First leaching time (FLt): the moment when the first tracer concentration reduction was noticed at the sampling point.

(ii) Leaching time (Lt): minimum concentration reached.

(iii) Leaching breakthrough time (LBTt): the time required to reduce the tracer concentration to the established minimum.

Figures 3.18 and 3.19 illustrate the definitions explained above. This research used the breakthrough time for $c/c_0 = 0.2$, equivalent to 200 mg/L of sodium, a value considered to be above that permitted by Brazilian environmental agencies.

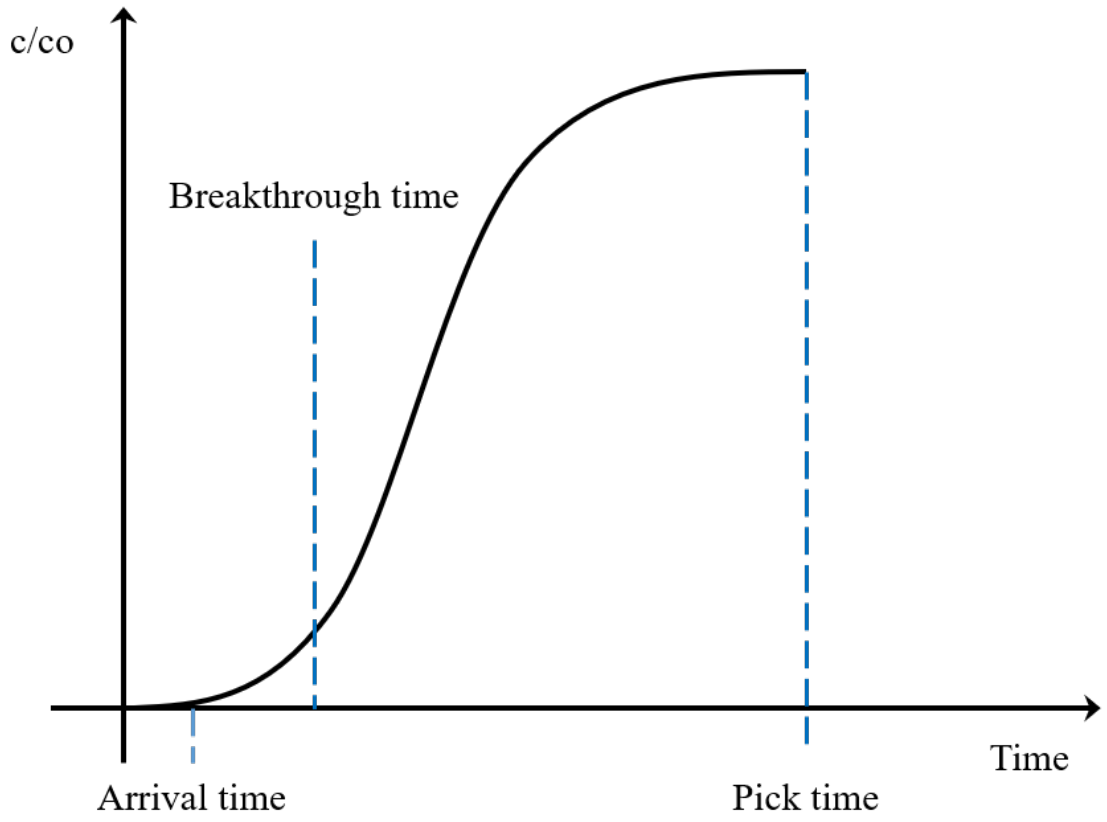

Figure 3.18: Characteristic breakthrough curve of the column test (adapted from Thu et al., 2023).

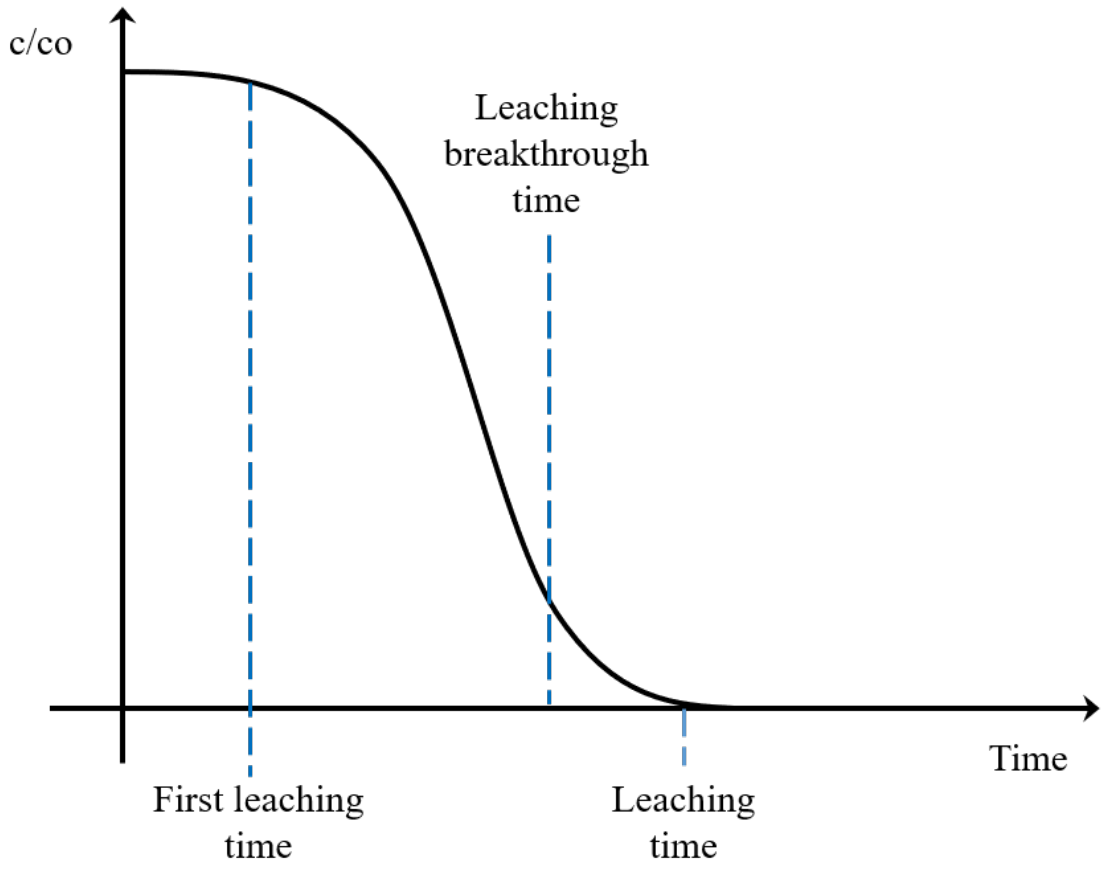

Figure 3.19: Characteristic leaching breakthrough curve of the leaching test (adapted from Thu et al., 2023).

3.3 Results and Discussion

This chapter will focus on the definition of transport parameters for contaminants in sandstone, accompanied by observations on the hydraulic outcomes of the test samples utilized in the assessments about contaminant transport. Chapter 2 presents a more comprehensive discussion of hydraulic characteristics.

Table 3.1: Initial index properties of the soil at the depths tested.

Depth (m)	wi (%)	ρs (g/cm³)	ei	ρd (cm³)	ni (%)
1	4.58	2.696	0.742	1.548	42.6
4	2.20	2.687	0.689	1.591	40.8
7	6.79	2.634	0.685	1.563	40.7
11	9.65	2.645	0.567	1.688	36.2
13	10.58	2.616	0.519	1.722	34.2
16	10.59	2.614	0.511	1.730	33.8

Where wi is the initial water content, ρs is the grain density, ei is the initial void ratio, ρd is the dry density, and ni is the initial porosity.

Figure 3.20 illustrates the variation in soil hydraulic conductivity with confinement. The shallowest soils, i.e., 1 and 4 m, were confined at 20, 40, 80, 160, and 320 kPa. From the seventh meter onward, the samples were subjected to conditions close to the mean geostatic pressure. The 7 m sample was confined at 80 and 160 kPa, while the specimens representing the 11, 13, and 16 m depths were confined at 160 and 320 kPa. Table 3.2 describes the sandstone's initial index properties.

Table 3.2: Initial index properties of the gray and brown sandstone.

Sandstone	wi (%)	ρs (g/cm³)	ei	ρd (cm³)	n (%)
Gray	2.32	2.628	0.321	1.990	24.28
Brown	1.89	2.676	0.374	1.948	27.20

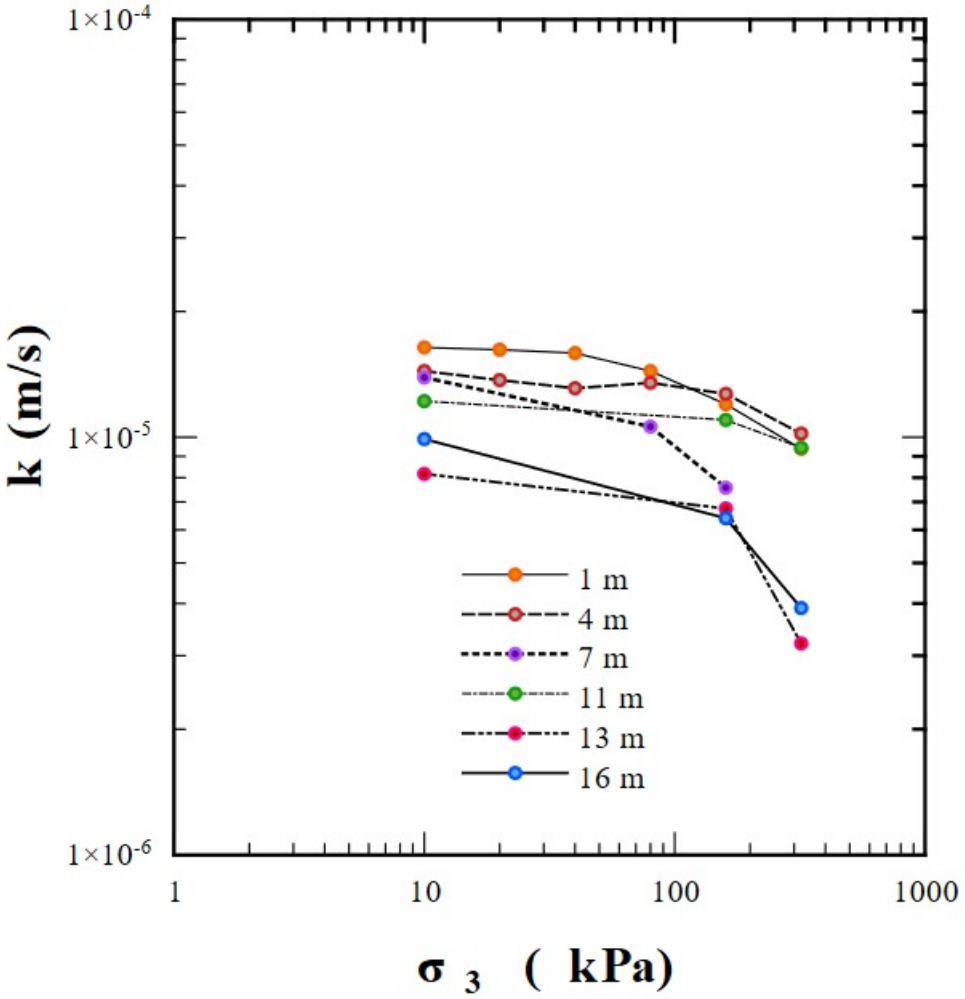

Figure 3.20: Variation in hydraulic conductivity with soil confinement at the depths under study.

As expected, the hydraulic conductivity decreased with increasing confinement, with more pronounced reductions after 80 kPa of confinement, especially for the 7, 13, and 16 m depth samples. Similarly, the sandstone results (Figure 3.21) reduced hydraulic conductivity for tensions above 80 kPa. This decrease in hydraulic conductivity may be related to the preconsolidation pressure of the soil and sandstone in the saturated condition. As mentioned in Chapter 2, the determination of the preconsolidation pressure is unclear for sandstone.

About the soil at 1 and 4 m depth, there was no more significant reduction in hydraulic conductivity values for higher tensions (above 80 kPa). Giacheti et al. (2019) and Fernandes et al. (2022) show that the preconsolidation pressure of the soil under study

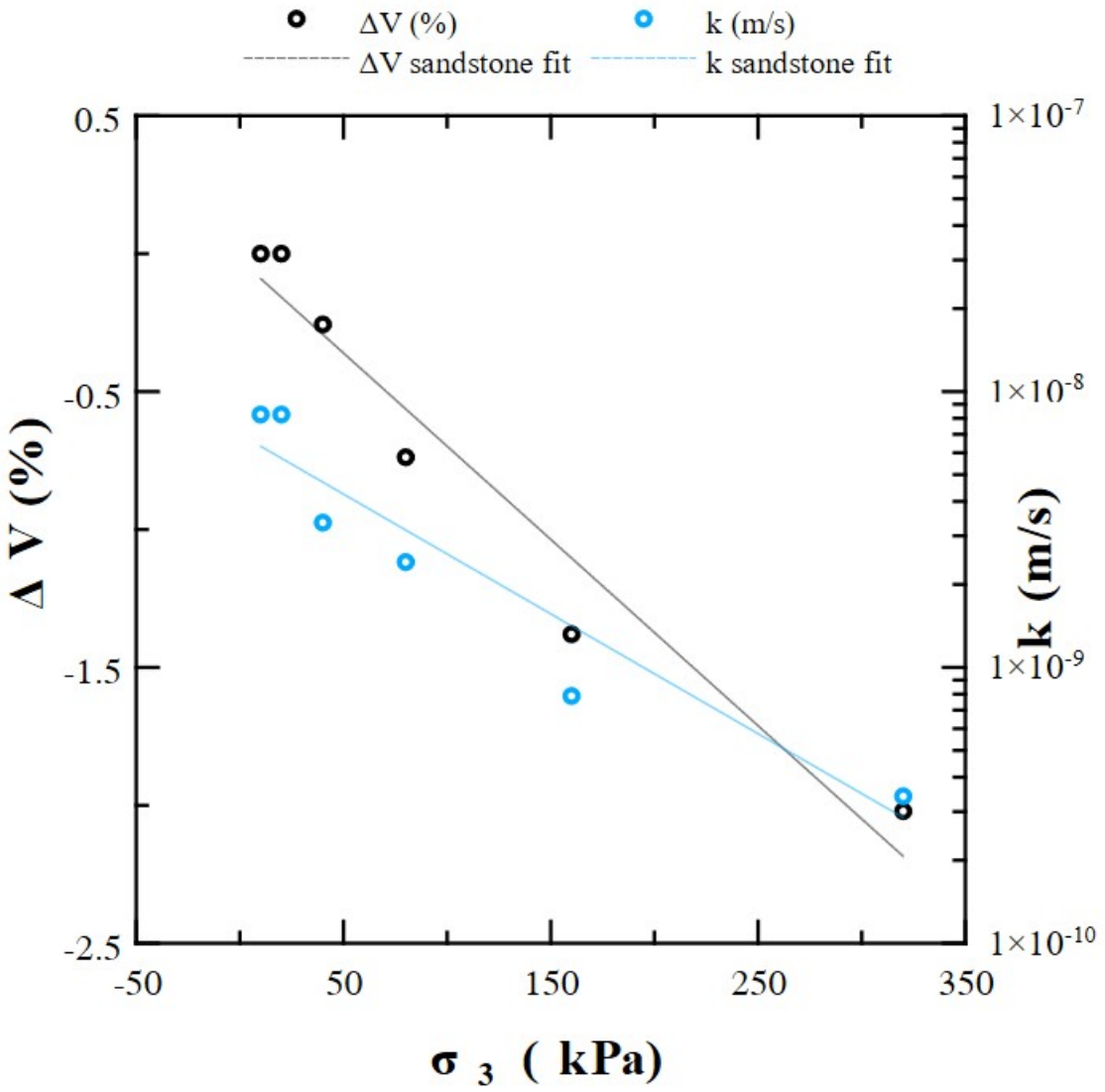

Figure 3.21: Sandstone's hydraulic conductivity values and volume variation as a function of applied confinement.

increases with depth. Therefore, shallower soils are subject to more significant deformations with increased confining stress, which leads to a more substantial reduction in the void ratio and, consequently, in hydraulic conductivity. However, the opposite effect was observed. Increasing depth led to more significant reductions in hydraulic conductivity.

By comparison, the variation in hydraulic conductivity and void ratio with the confining stress of the soil at 1 m and the sandstone are plotted together in Figure 3.22.

The results with a confining stress of 320 kPa show that the more significant

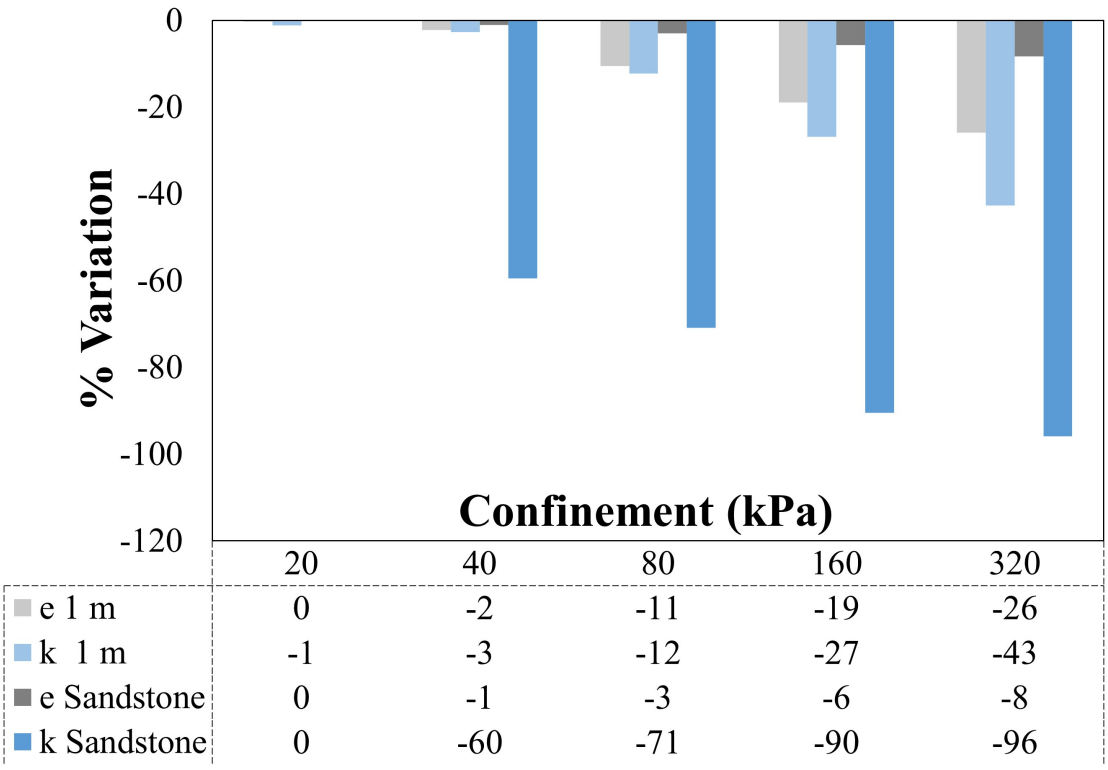

	20	40	80	160	320
e 1 m	0	-2	-11	-19	-26
k 1 m	-1	-3	-12	-27	-43
e Sandstone	0	-1	-3	-6	-8
k Sandstone	0	-60	-71	-90	-96

Figure 3.22: Variation in the values of hydraulic conductivity and void ratio of the soil at a depth of 1 m and of the sandstone as a function of the confinement applied. Negative values indicate a decrease.

percentage variation in the soil's void ratio of 26% compared to 8% for sandstone did not lead to a more substantial variation in hydraulic conductivity. The sandstone showed a 96% reduction in hydraulic conductivity, while the soil at 1 m reduced this parameter by 43%. The initial void ratio of the samples can explain this effect. More significant deformations in the topsoil were not enough to reduce the void ratio to the values of the deep samples and consequently considerably change the hydraulic conductivity.

Furthermore, even with lower deformations, the decrease in the void ratio of the deep samples and the sandstone may have been enough to alter the interconnectivity of pores, which are fundamental for flow, as described by Horn et al. (1994). Bohnsack et al. (2021) and Rhino et al. (2021) commented on the difficulty in relating flow to variations in the state of stress and that permeability is sensitive to porosity and connectivity between pores, with well-connected pores being less affected by increased stress. Ng & Pang (2000) noted how a slight difference in porosity between similar samples can affect soil water retention curves.

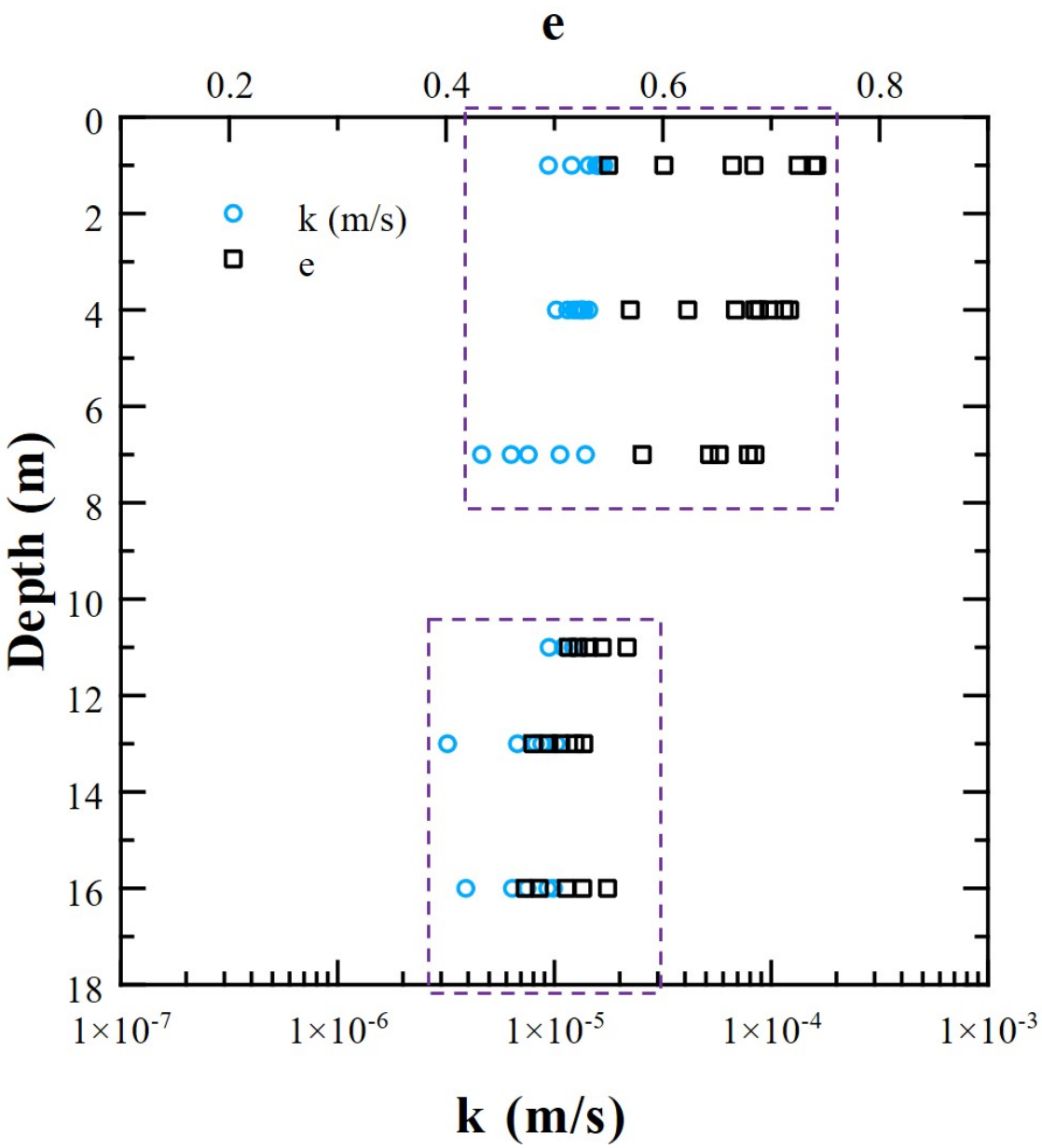

Figure 3.23: Hydraulic conductivity and void ratio of the soil along the depth.

The above observations illustrate the difficulty of inferring flow in porous media. Although the relationships between void ratio, grain size distribution, mineralogical composition, and hydraulic conductivity are well established in classic literature (Hazen, 1911; Terzaghi, 1925; Kozeny, 1927; Taylor, 1948) the materials under study here are not geomaterials textbooks. These observations need to be confirmed in future analyses. More detailed discussions of sandstone can be found in Chapter 2.

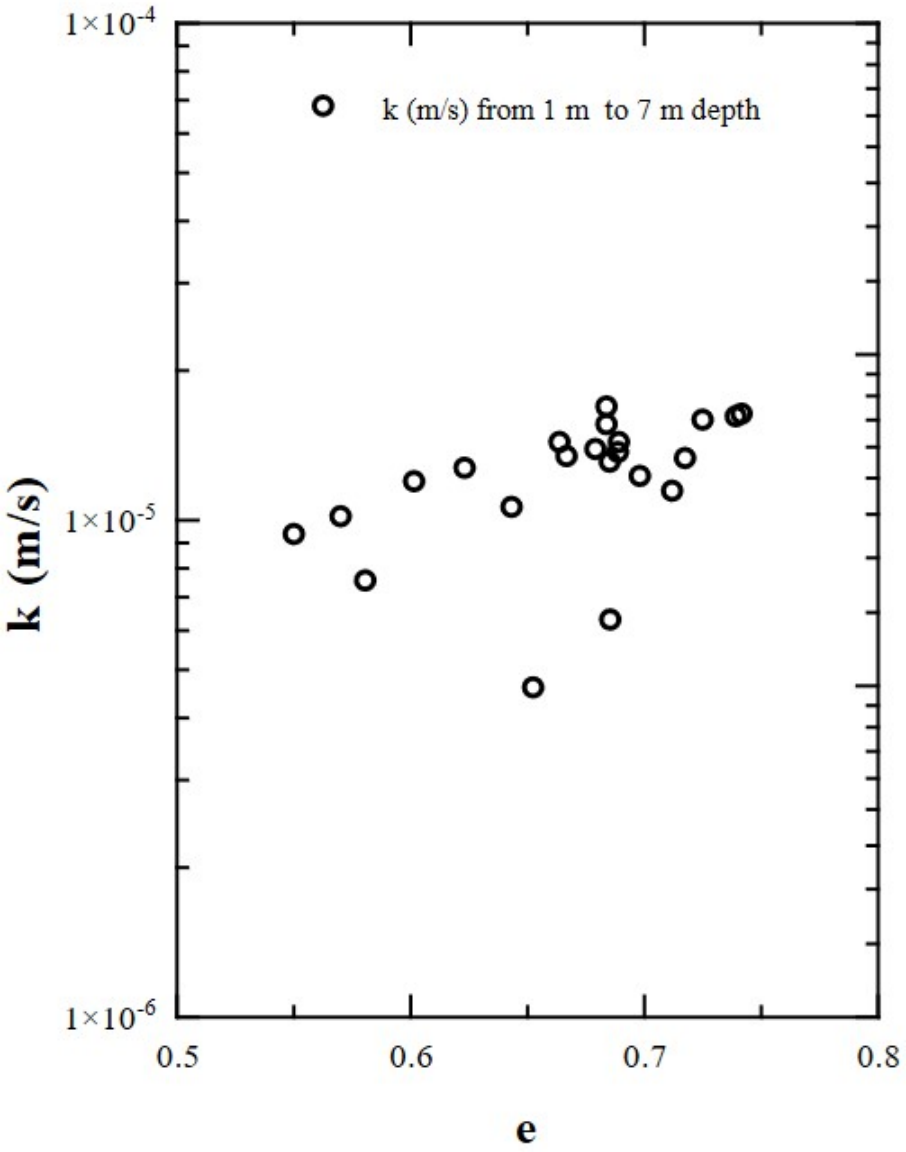

Figure 3.24: Soil hydraulic conductivity of the 1, 4, and 7 m depths.

Figure 3.23 depicts the changes in hydraulic conductivity and void ratio along the soil profile at the previously reported confining stresses. It can be inferred that the relationship between hydraulic conductivity and void ratio can be categorized into two distinct segments: one at depths of 1, 4, and 7 m and another at depths of 11, 13, and 16 m. This separation will delineate the scope and variability of hydraulic conductivity at the specified depths.

Thus, Figure 3.24 illustrates the variation of hydraulic conductivity with the soil's void ratio at depths of 1, 4, and 7 m. Similarly, Figure 3.25 presents the 11, 13, and 16

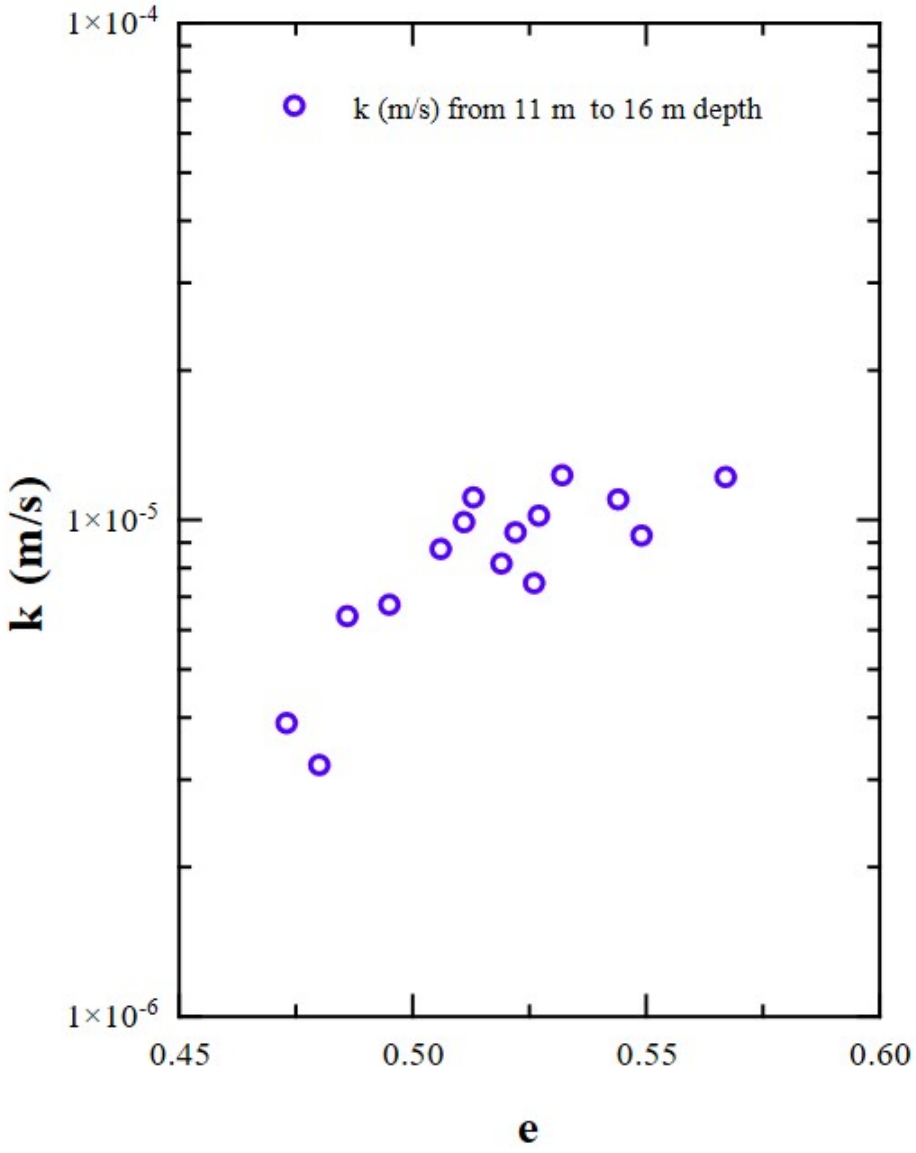

Figure 3.25: Soil hydraulic conductivity of the 11, 13, and 16 m depths.

m depth results. The definition of the range of hydraulic conductivity values indicated in this work was obtained by applying the box plot diagram. The data from the previously mentioned groups were plotted and analyzed together. The recommended range of values for the soil lies within the interquartile distance, represented by the dashed red lines in Figure 3.26.

As previously determined hydraulic conductivity using water, the soil transport parameters could be grouped by depth and/or type of test. This approach resulted in a more

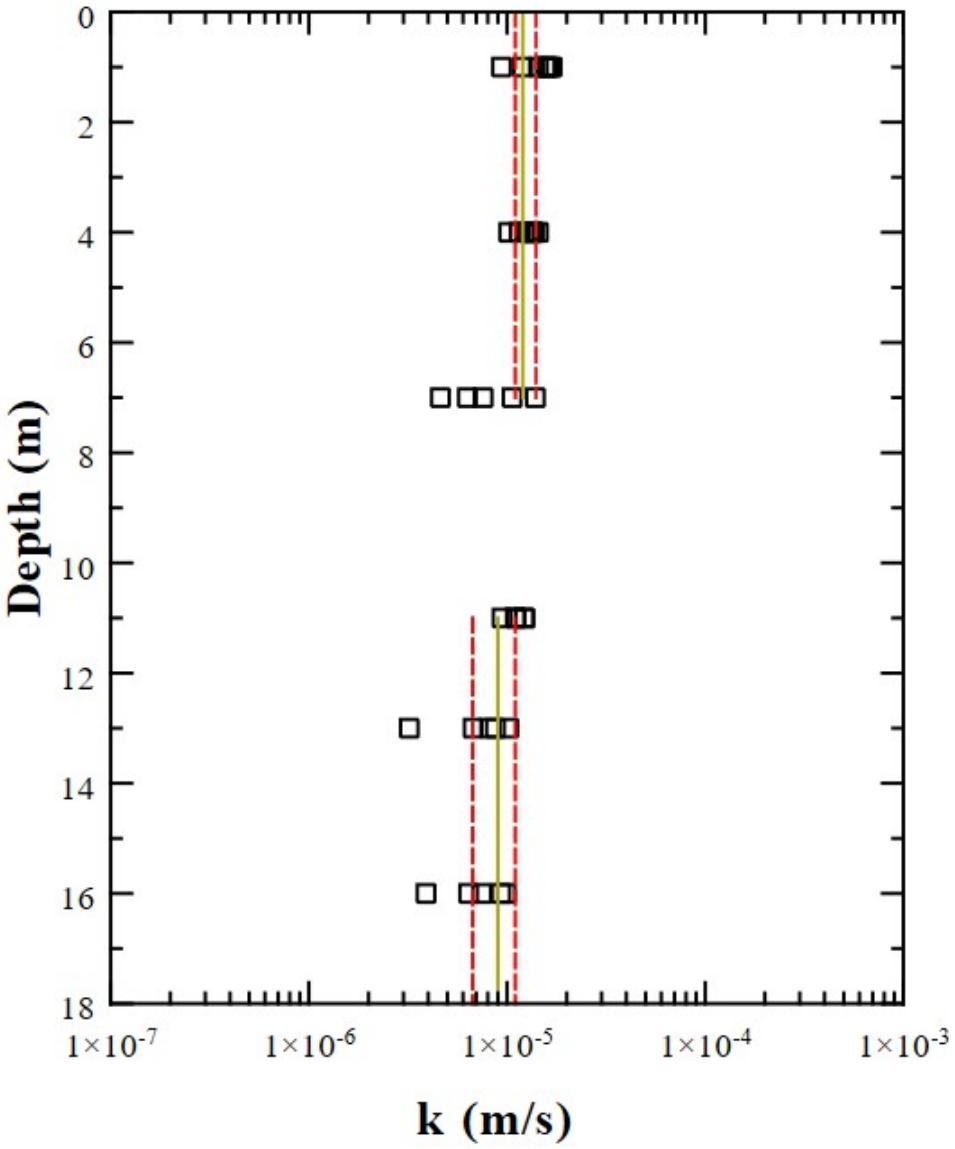

Figure 3.26: Hydraulic conductivity along the soil profile with the defined ranges of values of the mean (golden line), first and third quartiles (dotted red line) for the depths of 1, 4, and 7 m, as well as for 11, 13, and 16 m.

substantial dataset, which was subsequently analyzed using box plot diagrams to establish the value ranges. The diagrams can be referenced in the supplementary material for further details.

Different from the soil, which had a more significant number of data points, the results concerning the sandstone did not meet the statistical criteria for its definition, such as the box plot diagram used for the soil. For the sandstone, the results for k, α, and Dh were

determined directly, the first through the permeability test with the flexible wall permeameter and the others through the fitting of analytical models with the experimental data. For Rd and Kd, the average, maximum, and minimum values were presented since various methods were used to calculate them. However, the data were insufficient for statistical inference.

Following the previous explanations, Figures 3.27 to 3.39 present the experimental results from the column and soil leaching tests at depths of 1, 4, 7, 11, 13, and 16 m, subjected to confinement stresses of 20 kPa (1 m), 40 and 80 kPa (4 m), 80 and 160 kPa (7 m), 160 and 320 kPa (11, 13, and 16 m), and of the sandstone (160 and 320 kPa). As well as the fit of the analytical solutions from Ogata & Banks (1961) and Lapidus & Amundson (1952) for the column tests and Rixey et al. (1999) and Huesemann et al. (2005) for the leaching tests.

Breakthrough curves

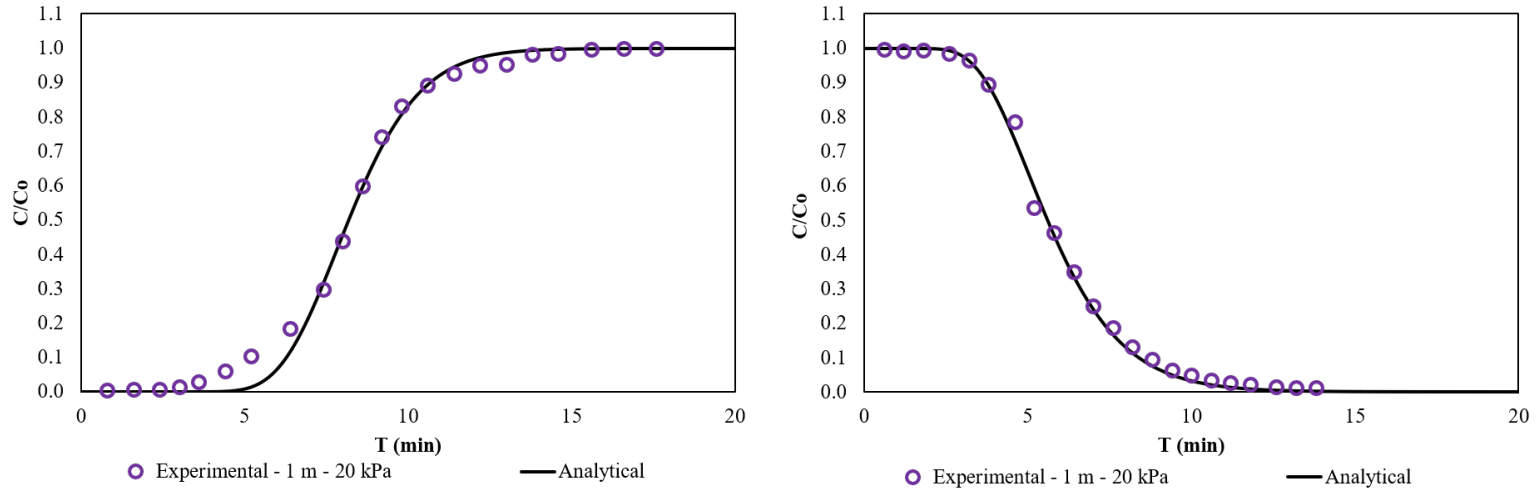

Figure 3.27: Breakthrough curve with experimental results and analytical curve fitting for the column and leaching tests on soil consolidated at 20 kPa and 1 m depth.

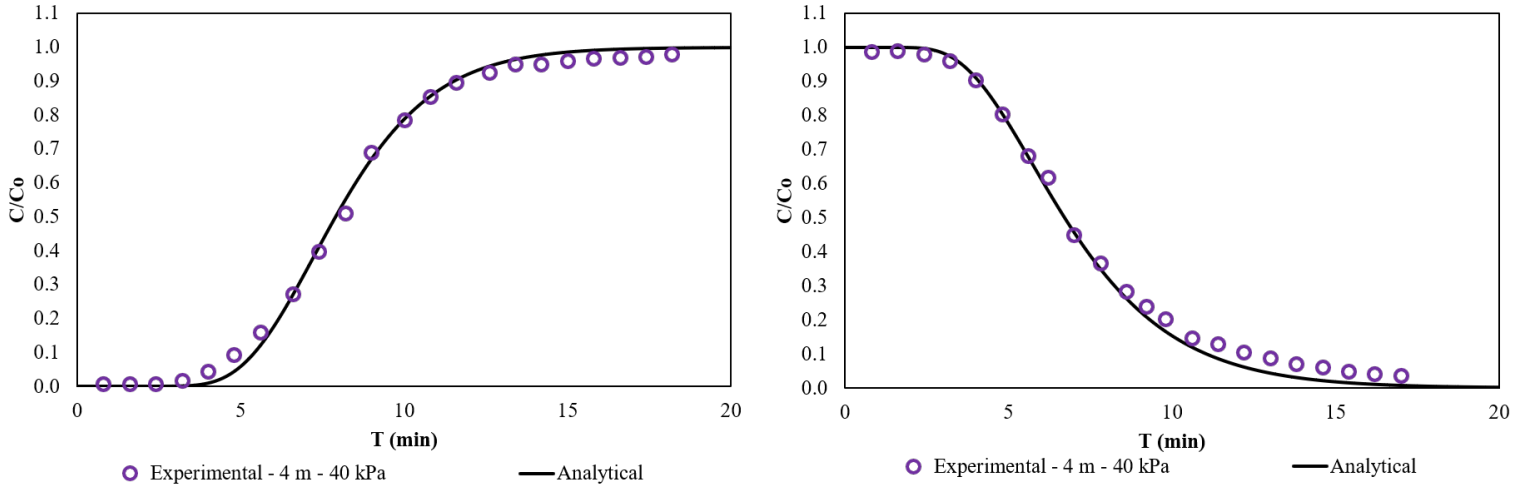

Figure 3.28: Breakthrough curve with experimental results and analytical curve fitting for the column and leaching tests on soil consolidated at 40 kPa and 4 m depth.

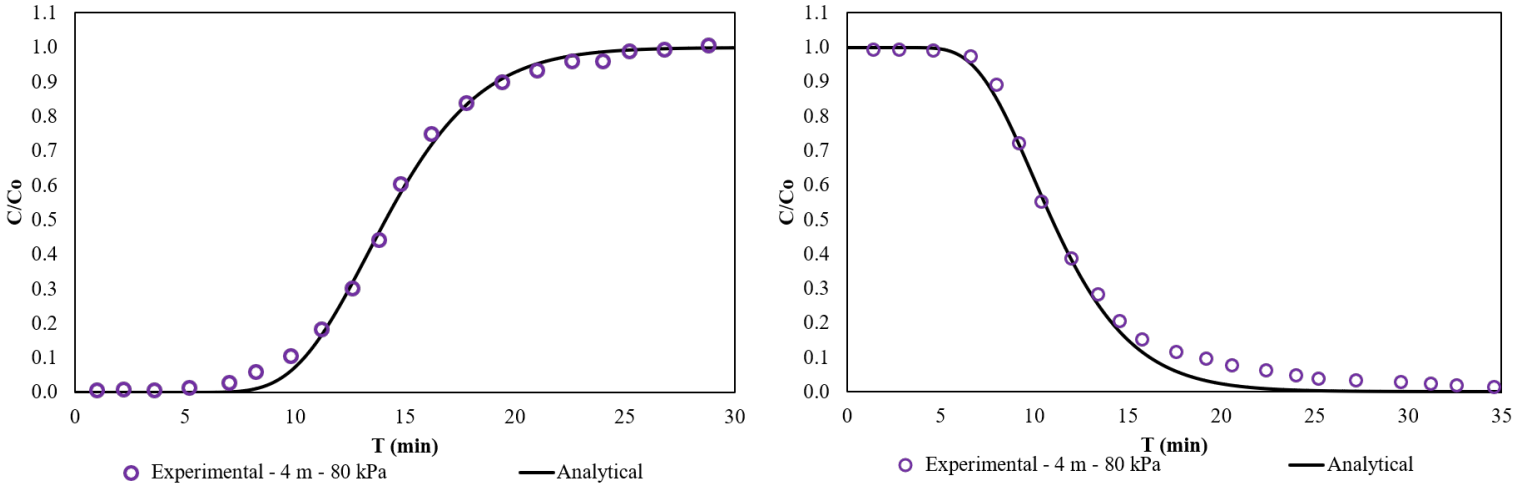

Figure 3.29: Breakthrough curve with experimental results and analytical curve fitting for the column and leaching tests on soil consolidated at 80 kPa and 4 m depth.

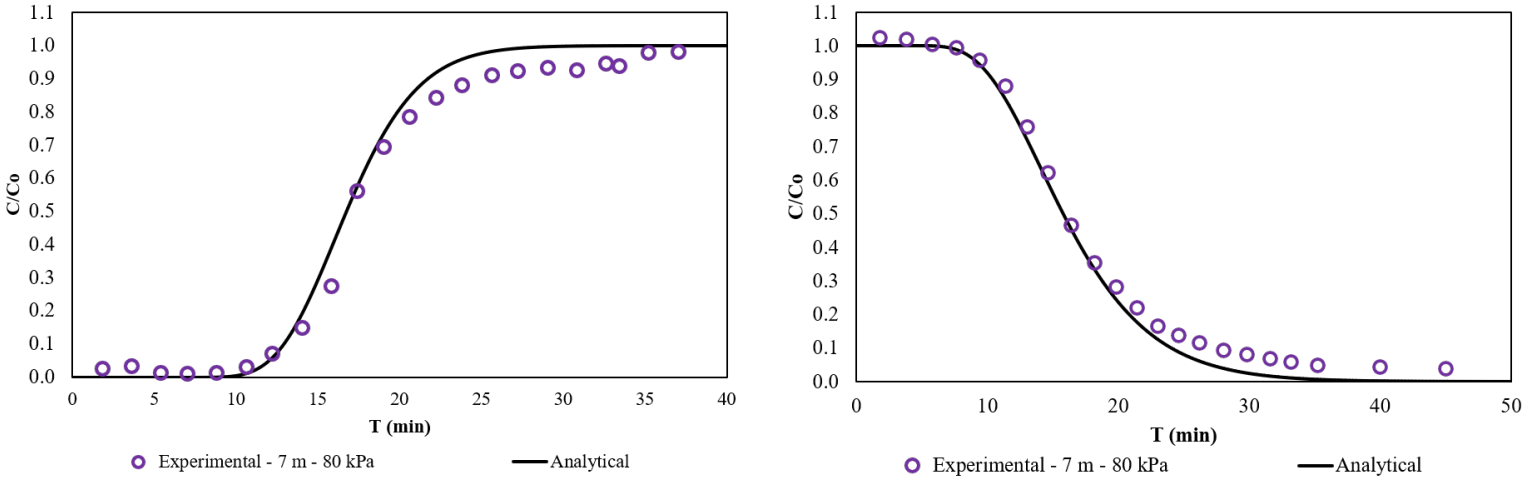

Figure 3.30: Breakthrough curve with experimental results and analytical curve fitting for the column and leaching tests on soil consolidated at 160 kPa and 7 m depth.

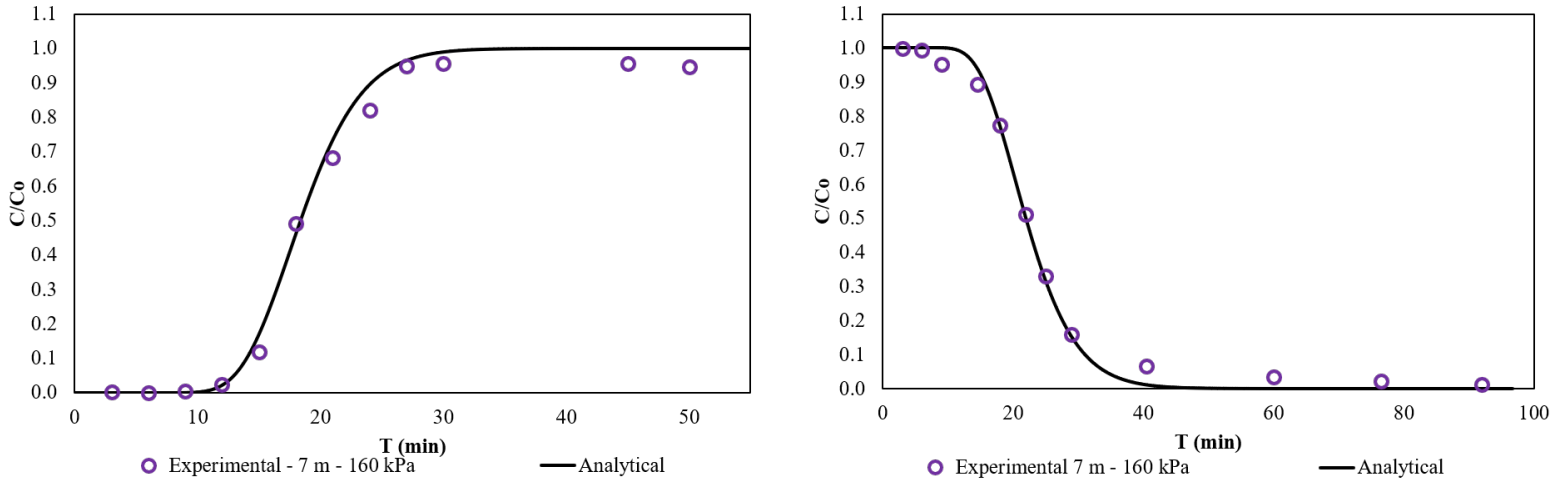

Figure 3.31: Breakthrough curve with experimental results and analytical curve fitting for the column and leaching tests on soil consolidated at 320 kPa and 7 m depth.

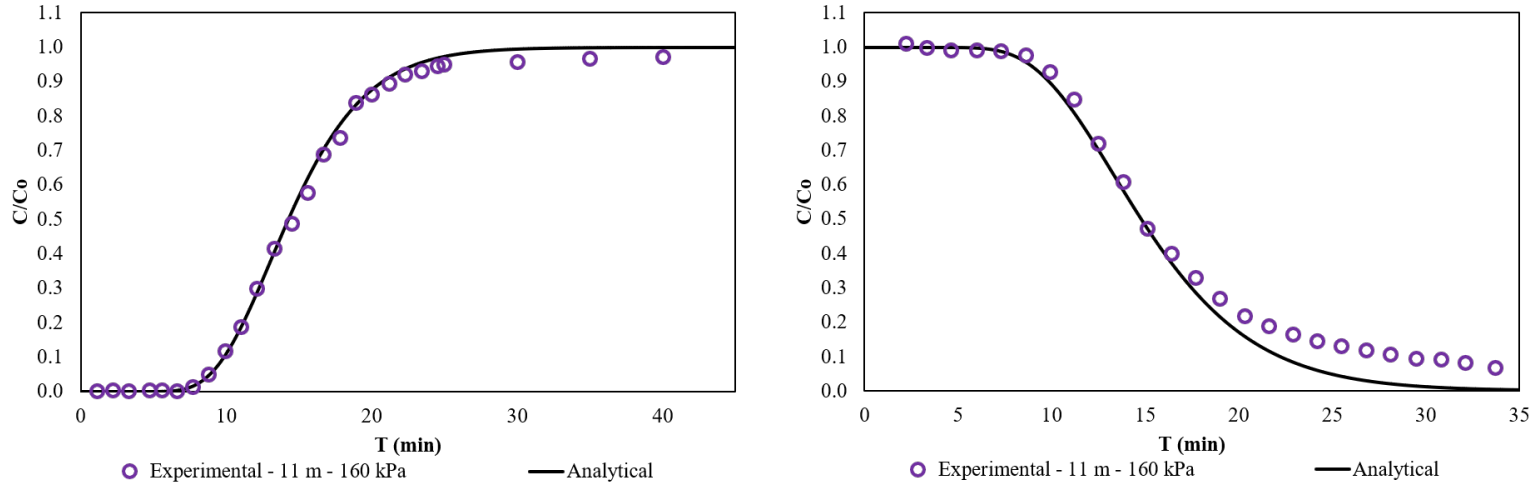

Figure 3.32: Breakthrough curve with experimental results and analytical curve fitting for the column and leaching tests on soil consolidated at 160 kPa and 11 m depth.

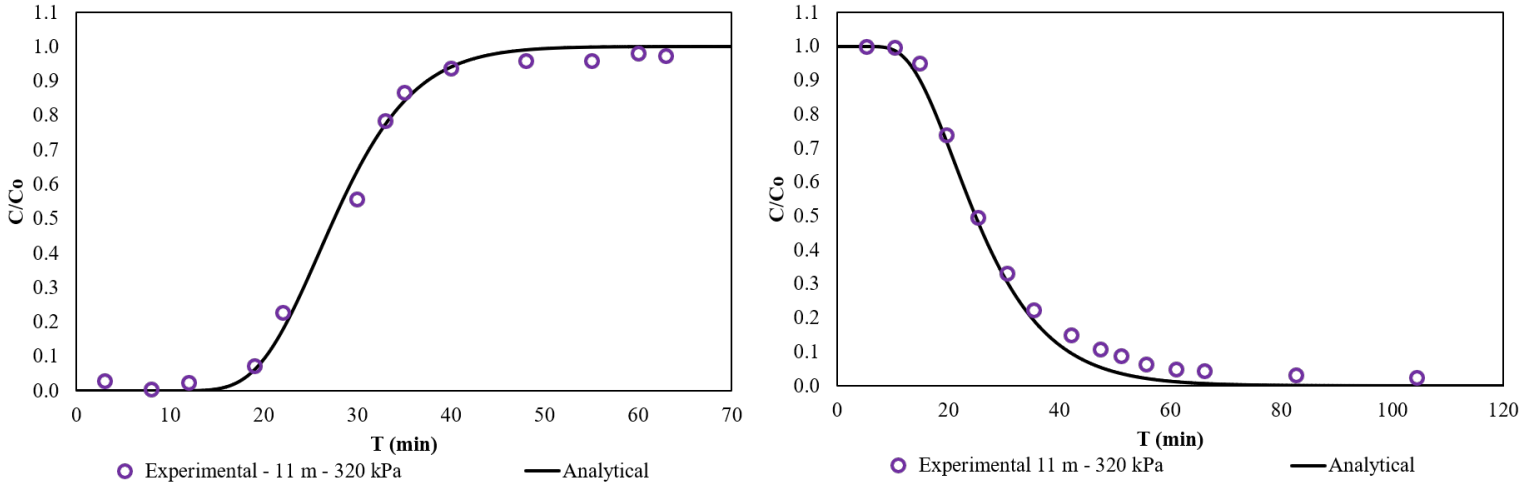

Figure 3.33: Breakthrough curve with experimental results and analytical curve fitting for the column and leaching tests on soil consolidated at 320 kPa and 11 m depth.

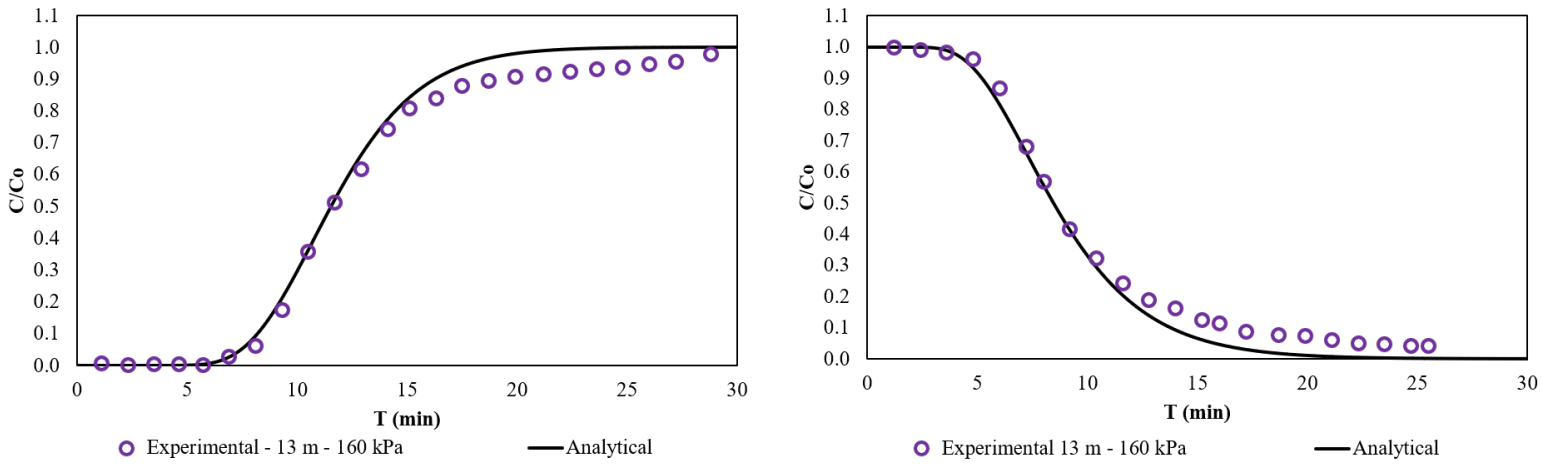

Figure 3.34: Breakthrough curve with experimental results and analytical curve fitting for the column and leaching tests on soil consolidated at 160 kPa and 13 m depth.

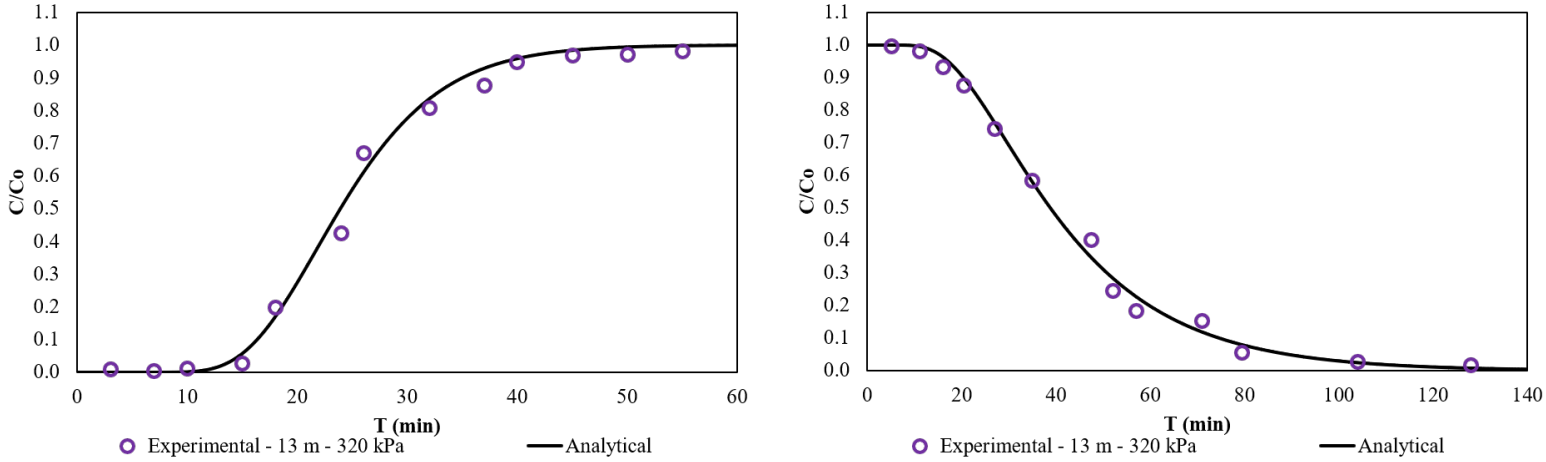

Figure 3.35: Breakthrough curve with experimental results and analytical curve fitting for the column and leaching tests on soil consolidated at 320 kPa and 13 m depth.

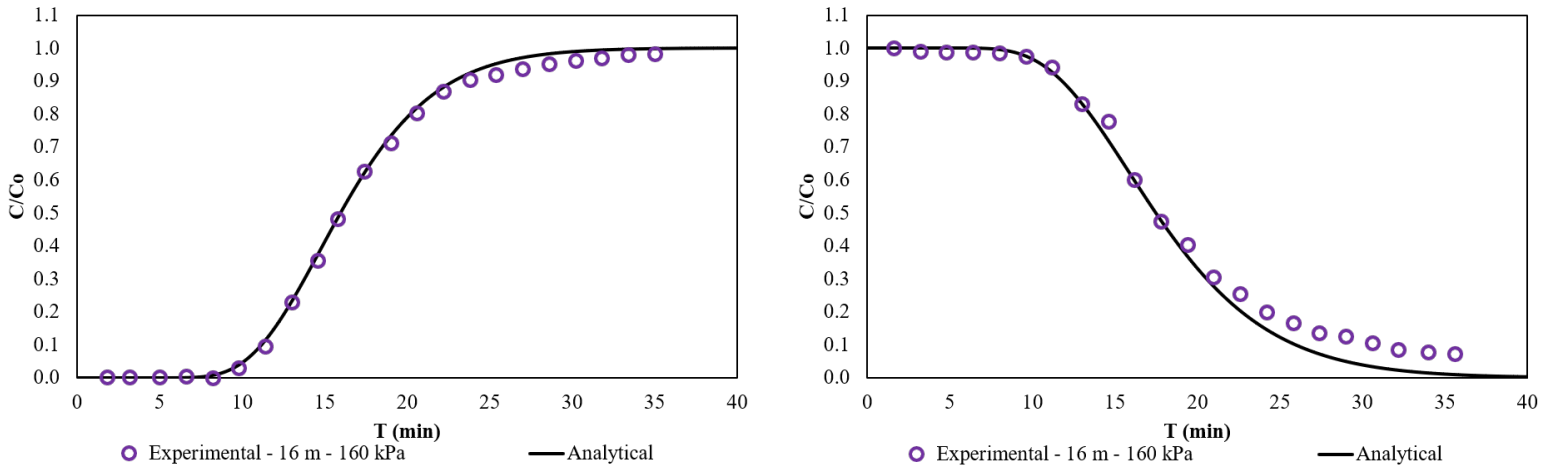

Figure 3.36: Breakthrough curve with experimental results and analytical curve fitting for the column and leaching tests on soil consolidated at 160 kPa and 16 m depth.

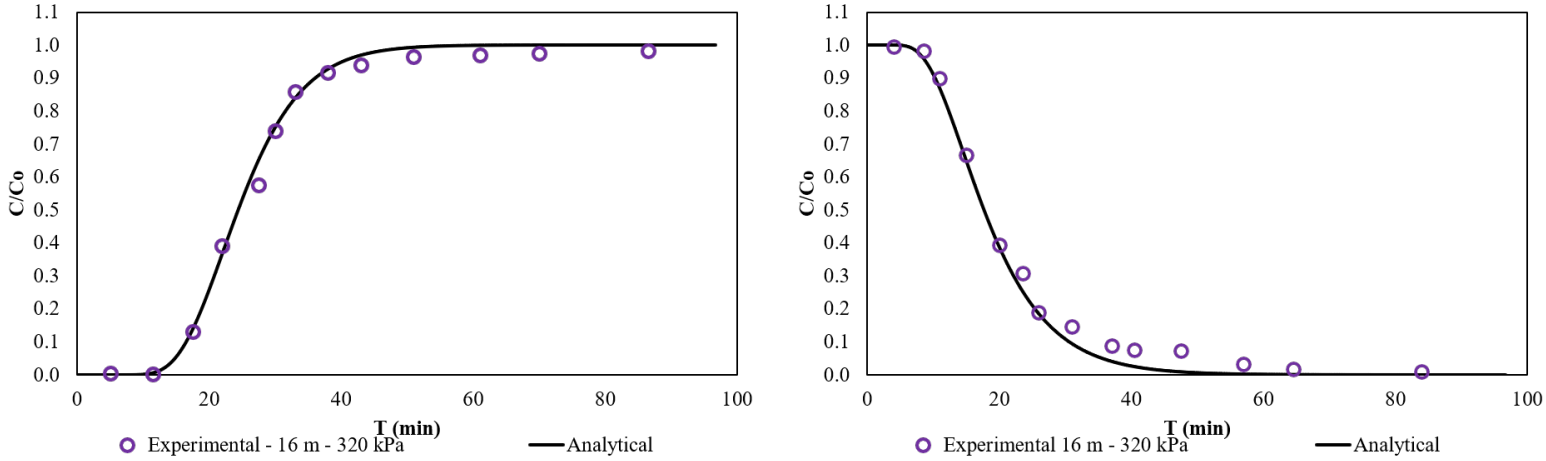

Figure 3.37: Breakthrough curve with experimental results and analytical curve fitting for the column and leaching tests on soil consolidated at 320 kPa and 16 m depth.

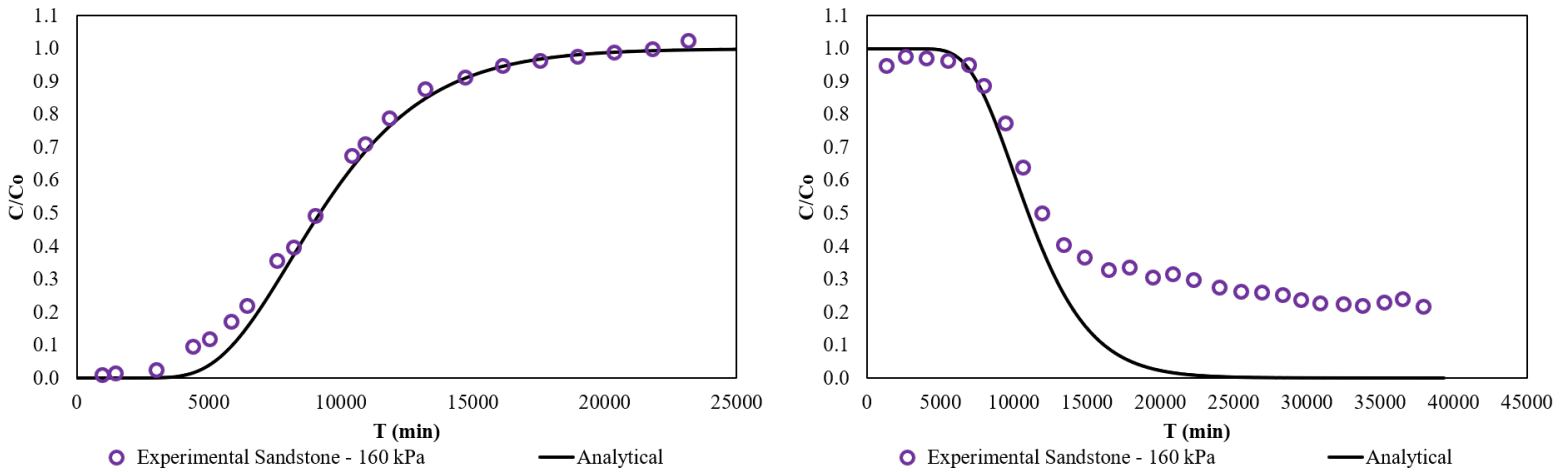

Figure 3.38: Breakthrough curve with experimental results and analytical curve fitting for the column and leaching tests on sandstone consolidated at 160 kPa.

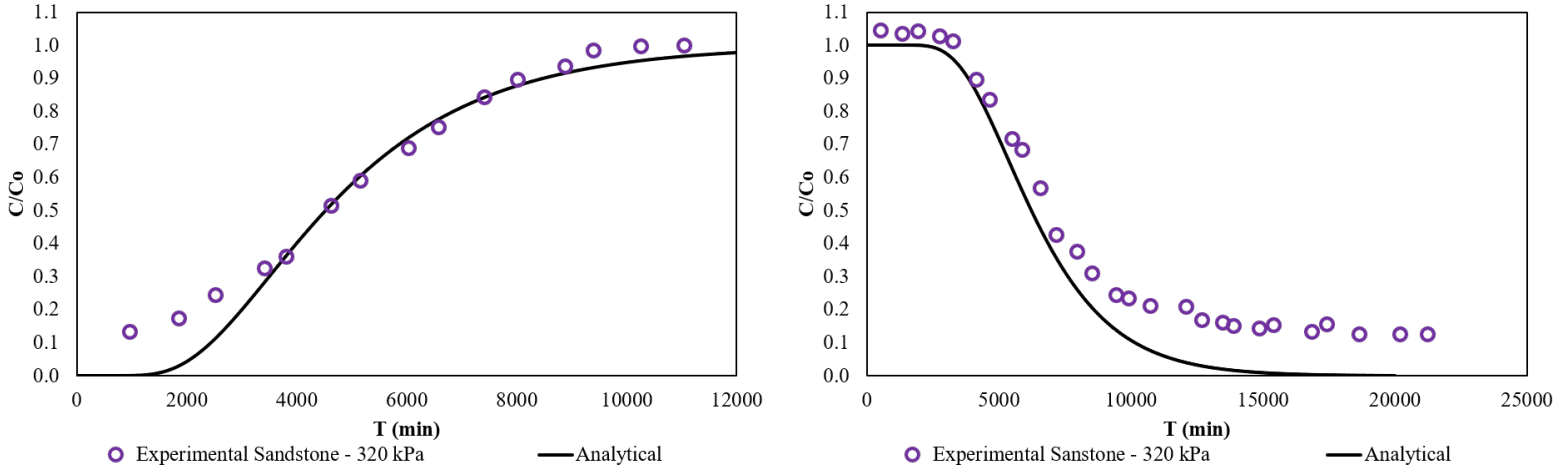

Figure 3.39: Breakthrough curve with experimental results and analytical curve fitting for the column and leaching tests on sandstone consolidated at 320 kPa.

The breakthrough curves obtained from the analytical fits demonstrate a strong correlation with the experimental data, with R^2 values exceeding 0.98 across all tests. The symmetric sigmoid shapes of the curves indicate the presence of linear, reversible sorption isotherms, with advection-dispersion as the primary transport mechanism (Shackelford, 2021). Latrille et al. (2021) state that symmetric breakthrough curves do not exhibit sorption kinetics, while Chotpantarat et al. (2011) suggests that symmetry between column and leaching tests indicates steady state breakthrough curves. However, the steady state is recognized when the relative concentration reaches the maximum plateau (van Genuchten & Parker, 1984; Pearce et al., 1994; Shackelford & Hong, 2020).

As reported by Khayyun (2018), effective porosity plays a fundamental role in contaminant transport, and symmetrical sigmoid BTCs infer that effective porosity is equal to total porosity, with a retardation factor equivalent to the area above the curve or the pore volume at a relative concentration of 0.5 (Shackelford & Hong, 2020). As will be shown below, in addition to the two methods mentioned, the determination of the retardation factor via a linear relationship with the partition coefficient and the ratio between the seepage velocity of the fluid and the seepage velocity of the tracer's center of mass yields similar results.

Hydraulic conductivity through NaCl

The data presented in Figure 3.40 illustrates the variation of void ratio and hydraulic conductivity of the soil as determined by column tests (k-C) and leaching tests (k-L) using sodium chloride as the percolating solution along the profile. The data can be categorized into two regions based on depth: 1, 4, and 7 m, and 11, 13, and 16 m. The relationship between hydraulic conductivity and the void ratio for these depth groupings can be observed in Figures 3.41 and 3.42, where the first relating to depths of 1, 4, and 7 m, and the second to depths of 11, 13, and 16 m.

The range of hydraulic conductivity using sodium chloride is depicted in Figure 3.43, along with the average values and interquartile range. The average values with the NaCl solution from the studied soil profile showed a slight decrease compared to deionized water. However, the order of magnitude of 1×10^{-5} remained consistent. The interquartile range is

recommended to utilize such data.

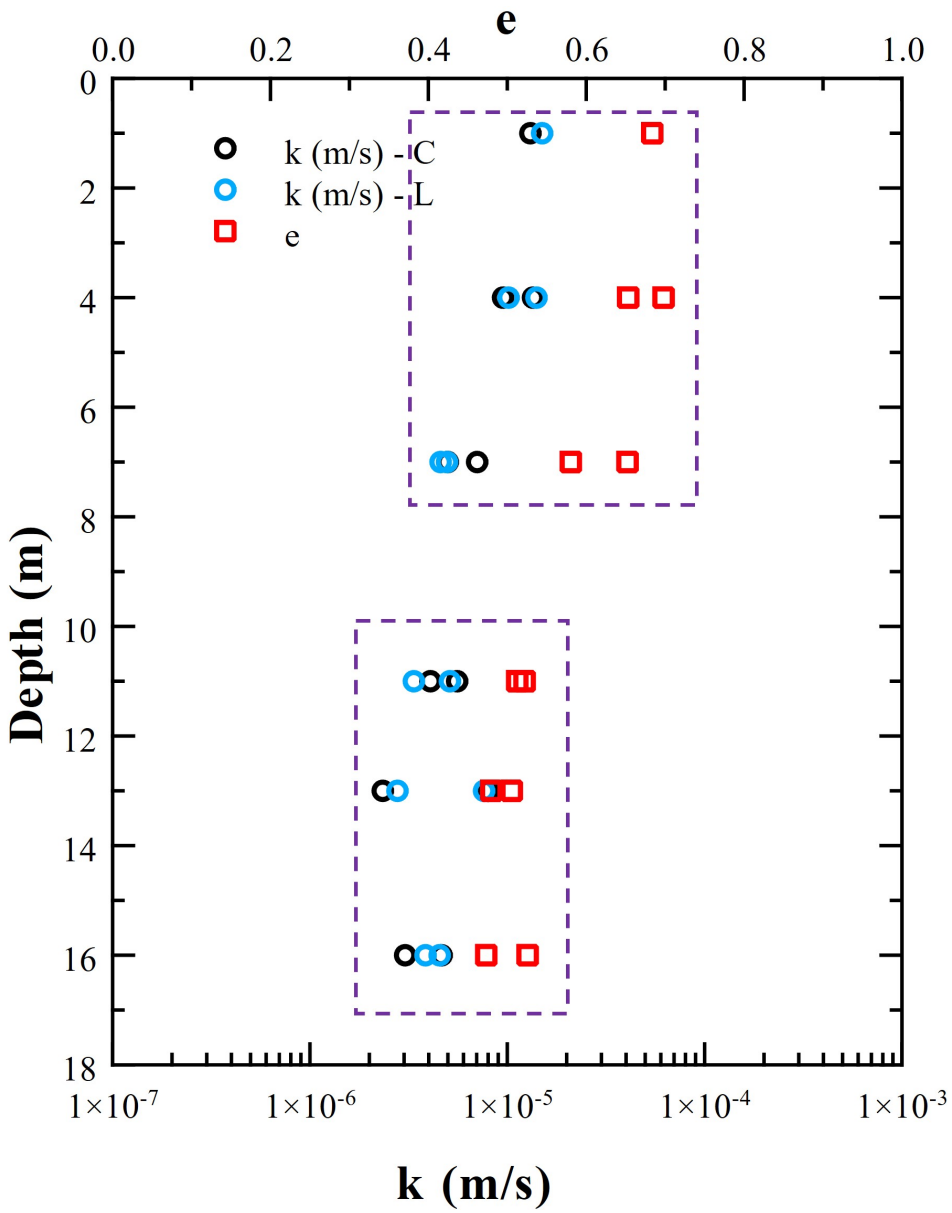

Figure 3.40: Void ratio and hydraulic conductivity using NaCl along the soil profile.

The hydraulic conductivity of sandstone using saline solution determined by the column test was 1.48×10^{-10} m/s with 160 kPa of confinement and 2.49×10^{-10} m/s with 320 kPa of confinement. Through the leaching test, the results were 1.16×10^{-10} and 2.06×10^{-10} m/s for the confinement stresses of 160 and 320 kPa, respectively. Figure 3.44 presents the data used to calculate k of the sandstone at the specified confinement stresses. Due to the

large number of measurements taken in the column and leaching tests, the results are given as a function of the volume of percolated voids or pore volumes (PV).

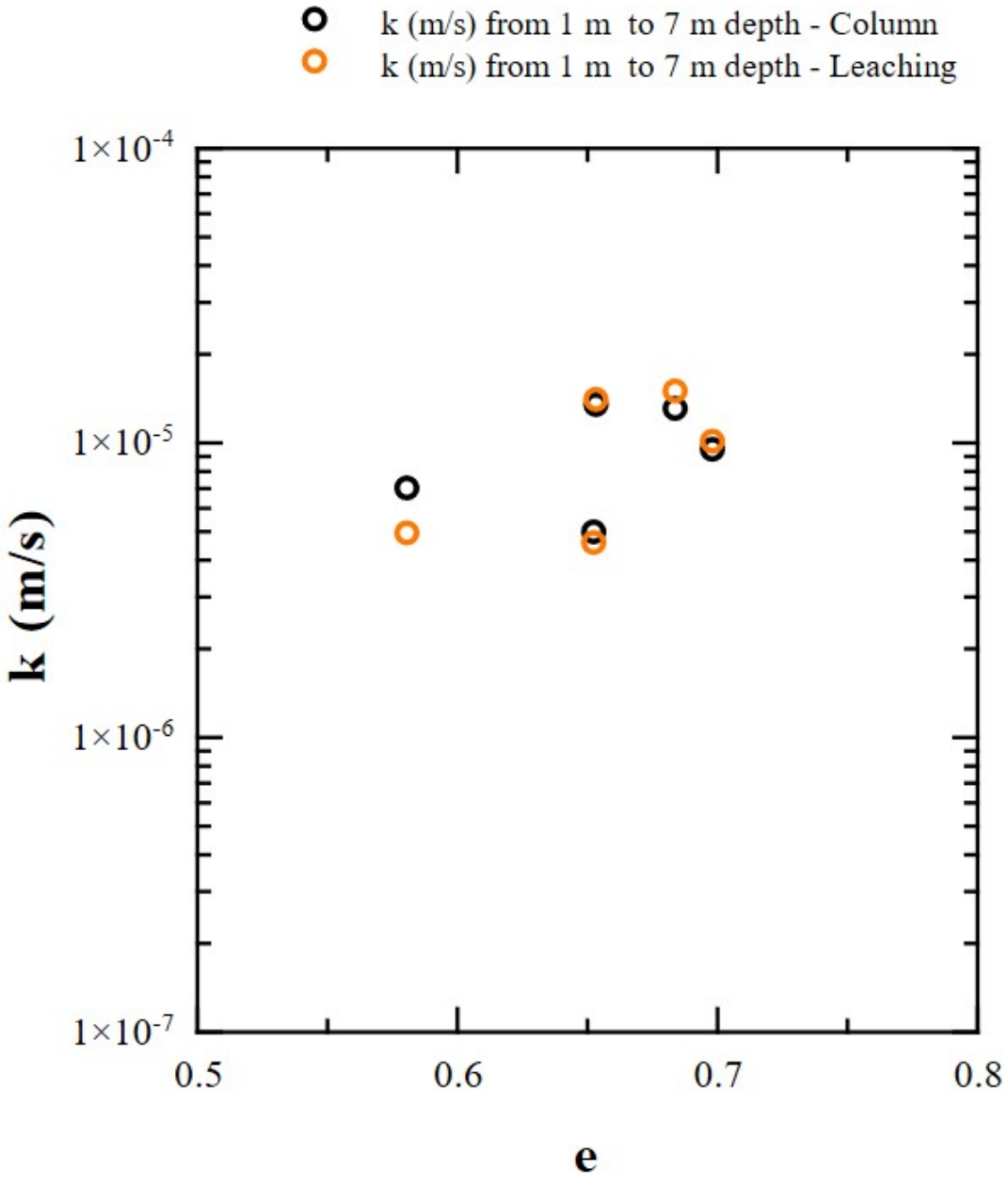

Figure 3.41: Hydraulic conductivity of soil from 1 to 7 m depth as a function of void ratio using column and leaching tests.

As mentioned in Chapter 2, using water as the percolating fluid, the average value of k for the specimen consolidated at 160 kPa was 7.88×10^{-10} m/s and 2.69×10^{-10} m/s for

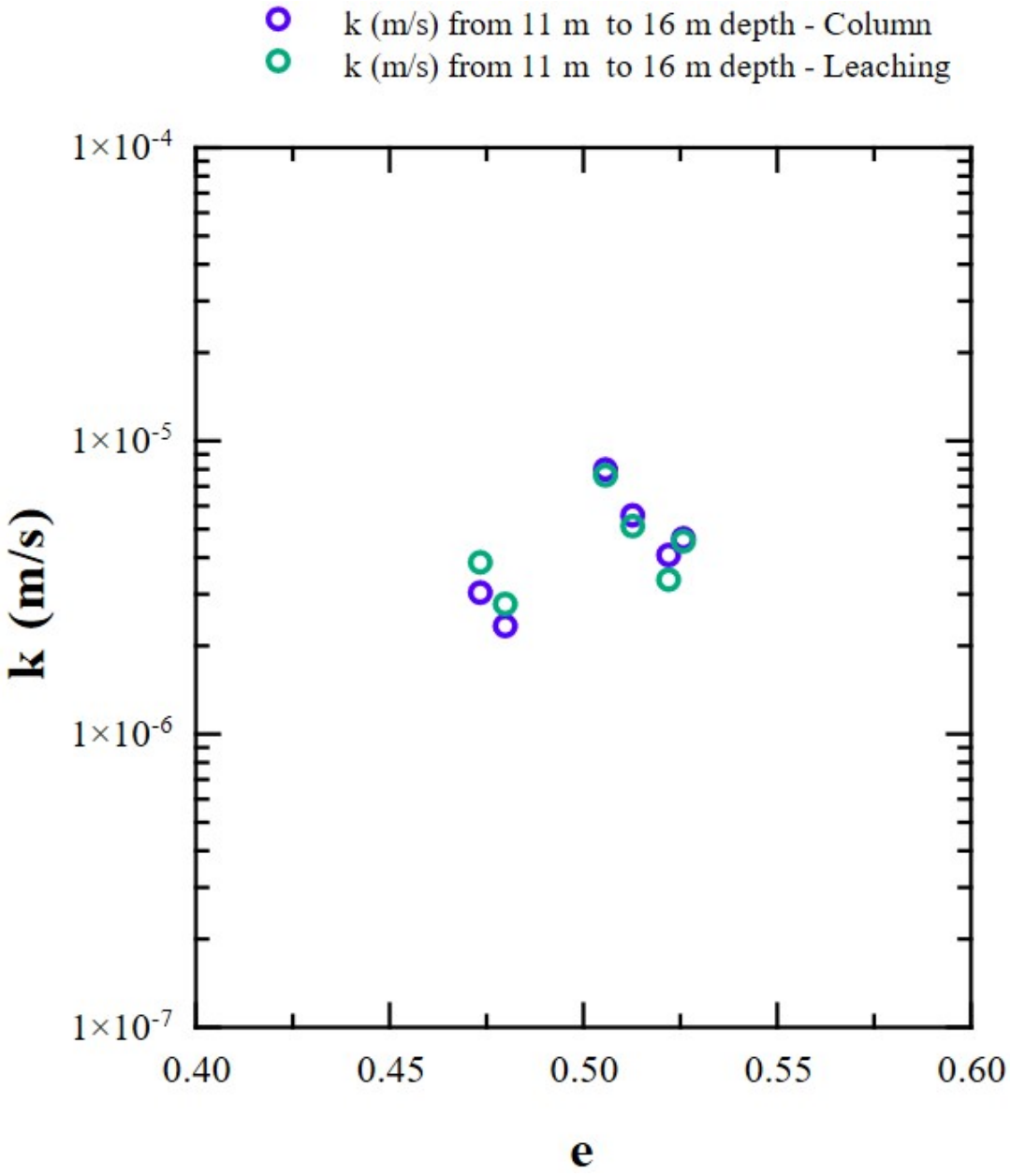

Figure 3.42: Hydraulic conductivity of soil from 11 to 16 m depth as a function of void ratio using column and leaching tests.

320 kPa consolidation, under conditions similar to the saline tracer test, i.e., pressure divided between the top and bottom and a gradient of 20 for 160 kPa confinement and 400 for 320 kPa confinement. During the test, different gradients for the 160 kPa confinement were not evaluated; such a test was conducted for the specimen consolidated at 320 kPa, aiming to observe the outcomes and ascertain the maximum gradient feasible for employment in column

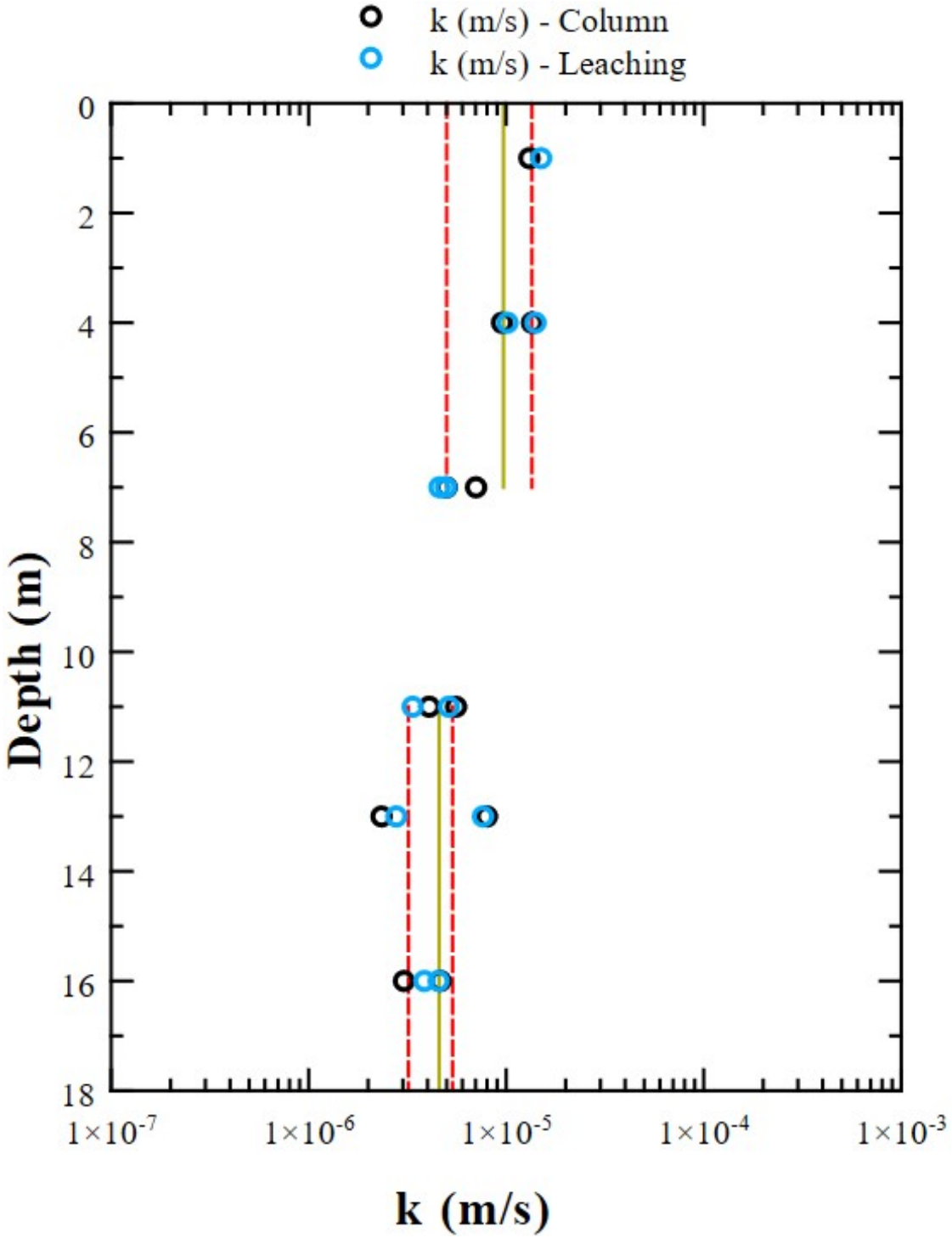

Figure 3.43: Variation in the hydraulic conductivity of the soil subjected to column and leaching tests using NaCl as a tracer. The average value is in golden, and the first and third quartiles are dashed red.

and leaching tests with saline solution, ultimately arriving at a value of 400.

From the results of the column and leaching tests on sandstone using NaCl as a tracer, it can be observed that there is little variation in hydraulic conductivity with a slight reduction in k compared to the use of deionized water. However, the values remained on the order of 1×10^{-10} m/s. This value is recommended for average geostatic pressures exceeding 160 kPa and saline solutions. A value of 1×10^{-8} m/s is suggested for more conservative methods, particularly when determined below 80 kPa of confinement with deionized water.

Tables 3.3 and 3.4 summarize the results of hydraulic conductivity with water and saline tracer in this work. Regarding the hydraulic conductivity values in sandy soils using tracers, the values obtained here are consistent with Freyberg (1986), Jellali et al. (2010), Mondelli et al. (2007), Ojuri & Ola (2010), Lu et al. (2013), Godoy et al. (2018), and Sutton et al. (2022).

Previous studies indicate a more significant saline influence on clays, especially regarding the increased hydraulic conductivity. In sands, the effect was found to be opposite to negligible. The trend of increasing clays' permeability with tracers likely relates to the porosity available for flow. The thickness of the double layer decreases with increasing concentration in the fluid, leading to an increase in the porosity of the clays (Studds, 1998). The hydraulic conductivity of the sandstone determined here is in line with findings reported by Schulze-Makuch (1997), Boving & Grathwohl (2001), and Neukum et al. (2014).

As previously discussed in Chapter 2, the sandstone results may be related to the presence of smectite group clay minerals, although this relationship still needs to be fully understood. As stated by Wilson et al. (2021), pore-clogging in rocks due to the presence of clay minerals, as well as its magnitude and extent, lacks clear understanding, constituting additional uncertainties regarding the transport of contaminants in rocks.

The influence of water-sensitive clay minerals may have had a similar effect on permeability as Ng et al. (2020) reported, where the pores were clogged by the elevated water content that caused the hydration of the biopolymer chains. This characteristic is similar to what is found with the use of bacteria present in the physical medium, which can eventually reduce hydraulic conductivity by clogging the voids (Ng et al., 2019).

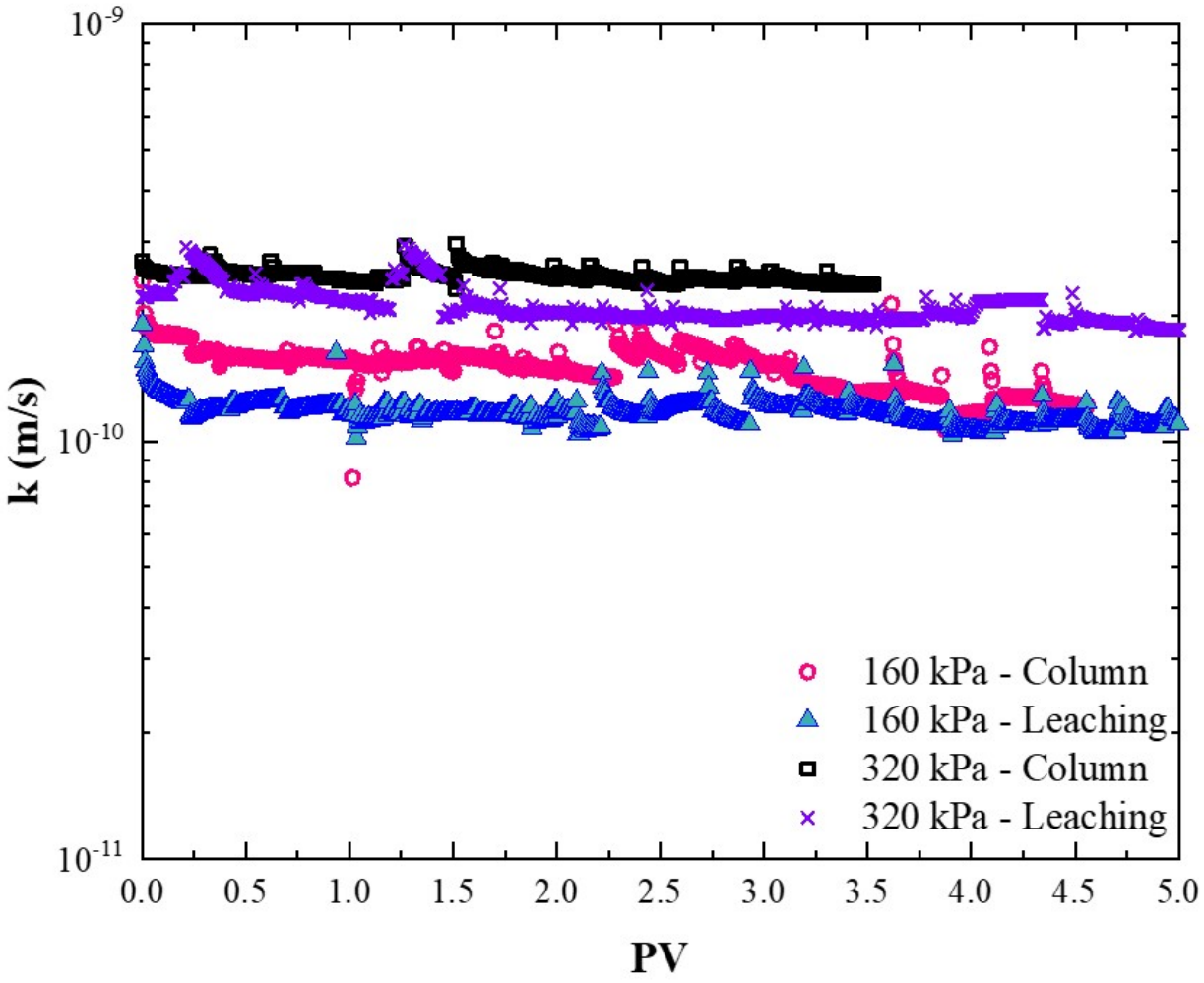

Figure 3.44: Hydraulic conductivity data of sandstone confined at 160 and 320 kPa as a function of pore volumes using NaCl as a tracer.

On the other hand, the presence of salts as tracers may have inhibited the expansion of the clay minerals in the sandstone. Huggett & Uwins (1994) noted the reduction in sandstone expansion after immersion in solutions with KCl. The authors attribute this to the high concentration of electrolytes in the solution. Additionally, Schmittner & Giresse (1999) and Sebastián et al. (2008) noted that NaCl is one of the most effective salts in preventing the expansion of clays, a characteristic also described by Fujii et al. (2020).

In this way, the similar values of hydraulic conductivity of the sandstone with deionized water and sodium chloride under the same confining stresses imply a more significant contribution of confinement and a consequent reduction in effective porosity in the results. For

the previously mentioned reasons, in addition to confinement, the expansion of clay minerals discussed in Chapter 2 indicates little to no interference in the tested conditions, i.e., 160 and 320 kPa of confining stress. The presence of clay minerals and their influence under reduced stresses, especially at values lower than the expansion pressures of around 55 kPa (see Chapter 2), requires further study.

Table 3.3: Summary of the soil's hydraulic conductivity and seepage velocity determined using permeability, column and leaching tests.

Depth	Parameter	Min	1° quartile	Mean	3º quartile	Max	Fluid
1 - 7 m	k (m/s)	4.61×10^{-6}	1.10×10^{-5}	1.20×10^{-5}	1.40×10^{-5}	1.64×10^{-5}	Water
11 - 16 m		3.21×10^{-6}	6.70×10^{-6}	9.00×10^{-6}	1.10×10^{-5}	1.23×10^{-5}	
1 - 7 m	k (m/s)	4.59×10^{-6}	5.00×10^{-6}	9.70×10^{-6}	1.40×10^{-5}	1.50×10^{-5}	NaCl solution
11 - 16 m		2.34×10^{-6}	3.20×10^{-6}	4.60×10^{-6}	5.30×10^{-6}	7.99×10^{-6}	
1 - 7 m	v (m/s)	1.17×10^{-4}	2.80×10^{-4}	3.10×10^{-4}	3.60×10^{-4}	4.17×10^{-4}	Water
11 - 16 m		9.90×10^{-5}	2.00×10^{-4}	2.60×10^{-4}	3.10×10^{-4}	3.56×10^{-4}	
1 - 7 m	v (m/s)	1.22×10^{-4}	1.60×10^{-4}	2.50×10^{-4}	3.40×10^{-4}	3.87×10^{-4}	NaCl solution
11 - 16 m		7.35×10^{-5}	9.80×10^{-5}	1.50×10^{-4}	1.80×10^{-4}	2.75×10^{-4}	

Table 3.4: Sandstone's average values of hydraulic conductivity and seepage velocity with different flowing fluids.

Test	Parameter	Confinement (kPa)	Value	Fluid
Permeability	k (m/s)	160	7.88×10^{-10}	Water
		320	2.69×10^{-10}	
Column Leaching	k (m/s)	160	1.48×10^{-10}	NaCl solution
		160	1.16×10^{-10}	
Column Leaching	k (m/s)	320	2.49×10^{-10}	NaCl solution
		320	2.06×10^{-10}	
Permeability	v (m/s)	160	7.88×10^{-8}	Water
		320	3.41×10^{-8}	
Column Leaching	v (m/s)	160	2.70×10^{-7}	NaCl solution
		160	2.12×10^{-7}	
Column Leaching	v (m/s)	320	4.38×10^{-7}	NaCl solution
		320	3.63×10^{-7}	

Contaminant transport parameters

The contaminant transport parameters: dispersivity (α), hydrodynamic dispersion (Dh), retardation factor (Rd), and partition coefficient (Kd) of the soil and sandstone are presented below as a function of the Péclet number (Pe) to define their variation. The results considered the same confining pressures that defined hydraulic conductivity with a saline tracer. In this work, the dispersivity and hydrodynamic dispersion results are longitudinal, i.e., in the same direction as the flow, and will only be referred to as dispersivity and hydrodynamic dispersion. No transverse value tests or estimates were conducted. In situations requiring the use of transverse parameters, the widely accepted initial value in the literature of $\alpha_L/\alpha_T \sim 10$ (Appelo & Postma, 2004; Rowe et al., 2004; Bear & Cheng, 2010; Fetter et al., 2017) is recommended as the initial value.

Dispersivity

The parameter related to the spread of contaminants through the porous medium, the dispersivity of the soil and sandstone as a function of Pe is shown in Figure 3.45, from which it is inferred that the values obtained from column and leaching tests overlap. Both relate to the Péclet number, which increased with the reduction of dispersivity and showed higher values for the column test. Upon depth analysis, α values can be categorized for the soil at 1 to 7 m and 11 to 16 m for the column and leaching tests, as depicted in Figure 3.46.

From the preceding, Figure 3.47 presents the mean and the interquartile range of the dispersivity calculated for the soil. In this case, the same range of values is recommended for the column and leaching tests, separated by the mentioned depths. Thus, from 1 to 7 m deep, the average value of α was 3×10^{-3} m, with a first quartile of 2×10^{-3} m and a third quartile of 4×10^{-3} m, and the result for the first and third quartiles was 4×10^{-3} and 7×10^{-3} m, respectively.

Regarding the sandstone, the values of α for the column test were 5×10^{-3} m with 160 kPa of confinement and 1.1×10^{-2} m with 320 kPa of confinement. The values obtained from the leaching test were 3.92×10^{-3} and 6.59×10^{-3} m for the confining stresses of 160 and

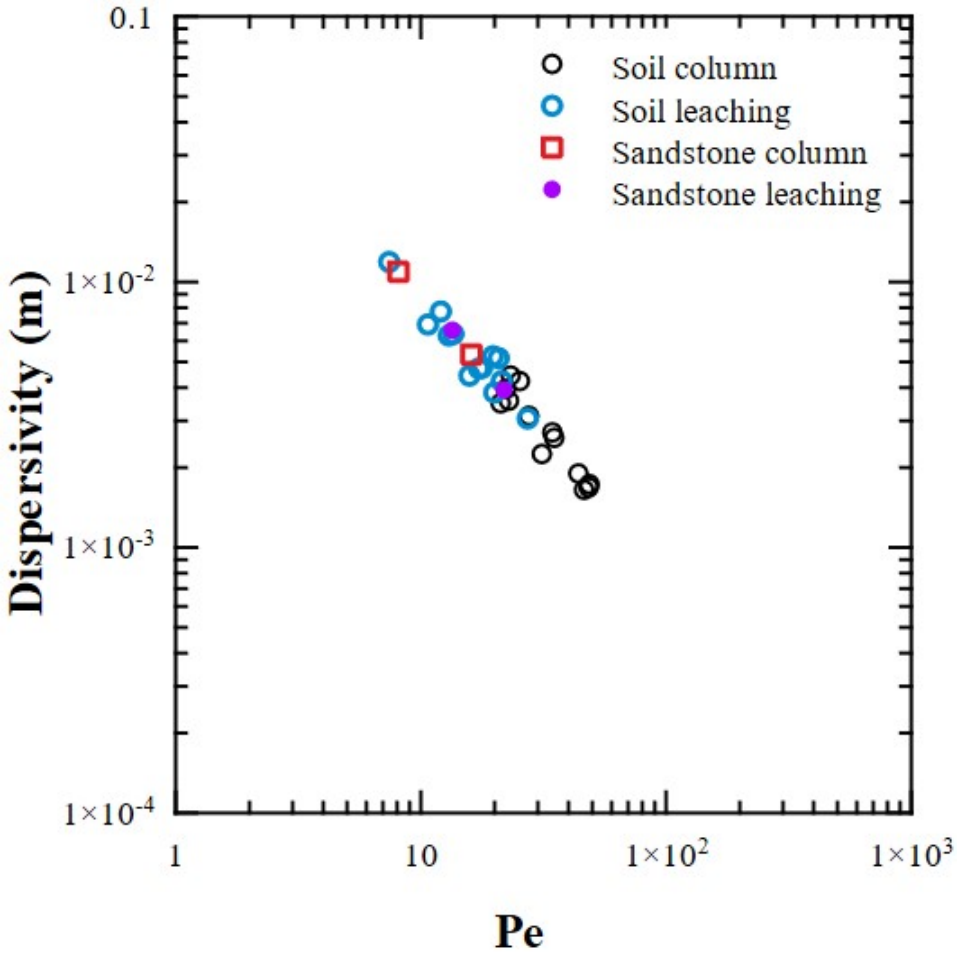

Figure 3.45: Dispersivity as a function of Péclet number from column and leaching tests in soil and sandstone.

320 kPa, respectively.

The results indicate that the dispersivity of soil and sandstone was approximately on the order of 10^{-3} m. The similar magnitude of values in both materials could be attributed to a potential relationship in their determination, as the parameter α was calculated based on hydrodynamic dispersion, neglecting the diffusion component (α=Dh/v). Additionally, the hydrodynamic dispersion, which introduces a parameter for analysis, was determined using the Péclet number derived from the analytical solution (Dh= v×L/Pe). It is worth noting that the seepage velocity is associated with both parameters. Consequently, the decrease in the number of voids available for flow in the sandstone led to proportional reductions in seepage velocity and hydrodynamic dispersion, resulting in similar dispersivity values in both

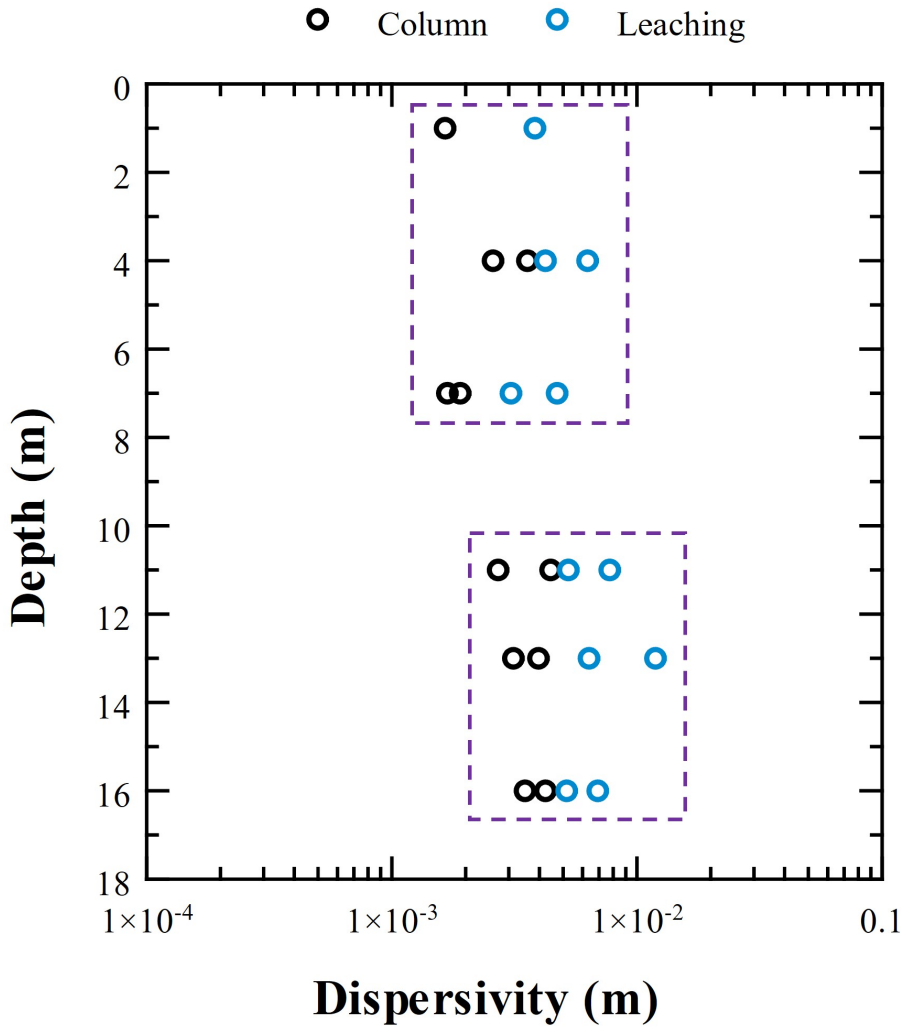

Figure 3.46: Dispersivity values from column and leaching tests along the soil profile.

materials.

Among the factors that influence dispersivity, the flow lines depend on the available voids. A lack of interconnected pores leads to increased tortuosity and both longitudinal and transverse dispersivities (Szecsody et al., 1994). Carey et al. (2018) adds that the distribution of pores can affect dispersivity, such that a broader pore distribution would result in greater dispersivity.

From the discussion about dispersivity, it is noted that the parameter was reduced for both materials. Although dispersivity is classically accepted as a property of the medium (Freeze & Cherry, 1979; Voudrias & Yeh, 1994), it is currently considered that there is a

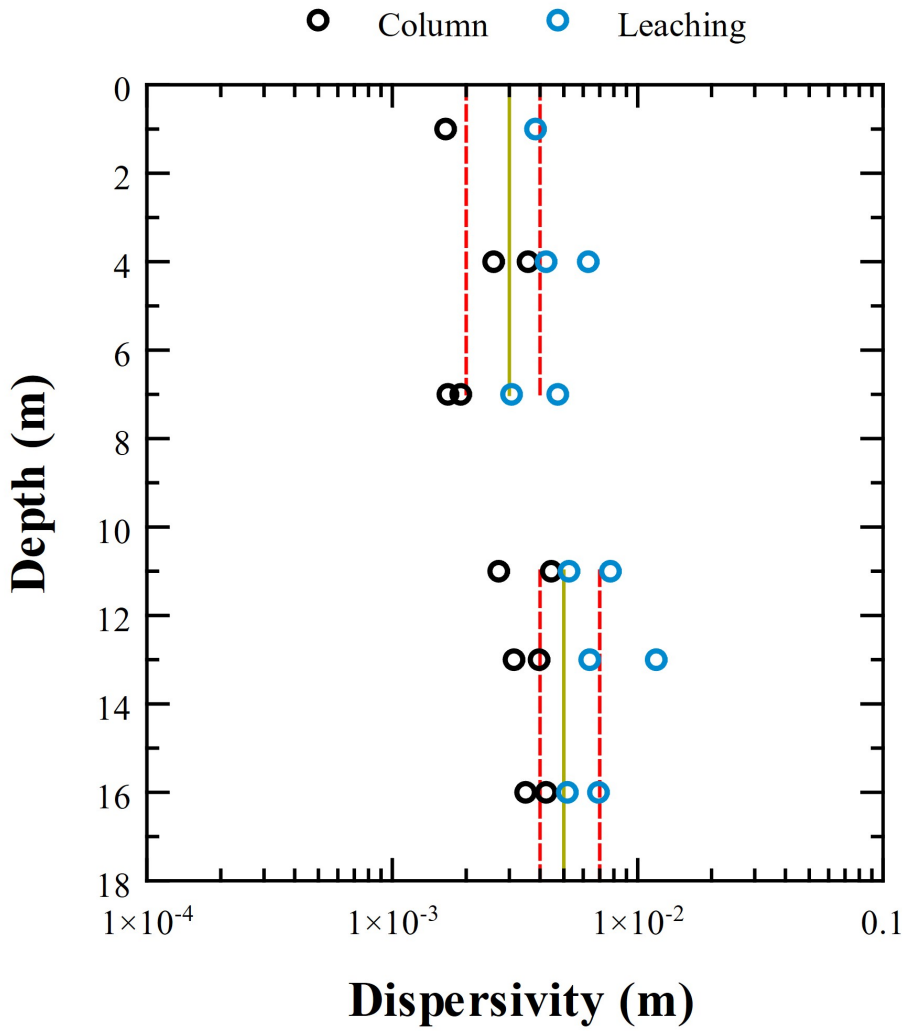

Figure 3.47: Dispersivity along the soil profile with the defined ranges of mean values (golden line), first and third quartiles (dotted red line) for the depths of 1, 4, and 7 m, as well as for 11, 13, and 16 m.

relationship between the scale and the heterogeneity of the porous medium. In situ reported values have been significantly higher than the laboratory's, often for the same material (Levy & Chesters, 1995; Woumeni & Vauclin, 2006; Ojuri & Ola, 2010). Similarly, Freeze & Cherry (1979) point out that the values found in the literature for relatively homogeneous sands under controlled laboratory conditions are generally small and fall within the range of 1×10^{-4} to 1×10^{-2} m.

Hydrodynamic dispersion

The combination of transport through molecular diffusion and mechanical dispersion (Rowe et al., 2004), hydrodynamic dispersion was related to the Péclet number as shown in Figure 3.48. The decrease in the Péclet number with an increase in Dh was consistent with expectations. Particularly the leaching tests demonstrated higher values. However, the result with sandstone differed from that of the soil, in contrast to the behavior of dispersivity. As previously discussed, the distinct values occurred due to the determination of dispersivity, which maintained proportionality even with changes in the seepage velocity. Reiterating, in other words, the reduction in v was proportional to the decrease in Dh, leading to values of α that were close for both materials.

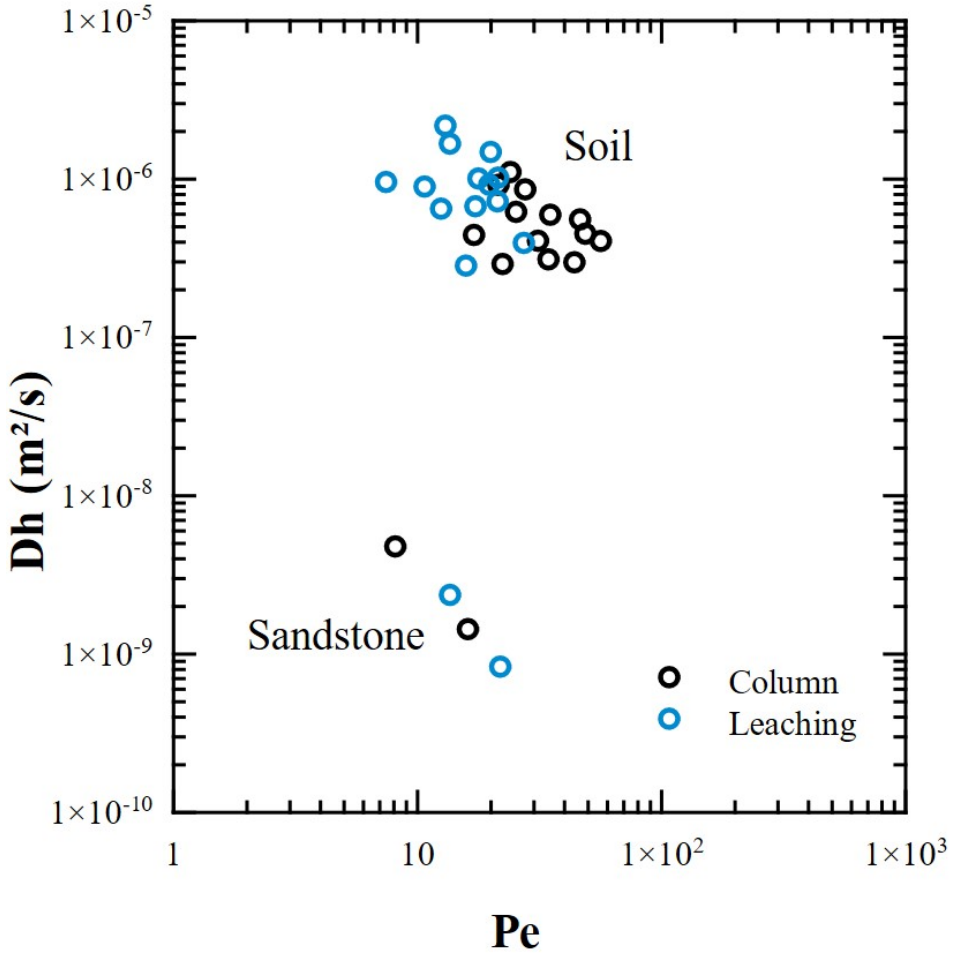

Figure 3.48: Hydrodynamic dispersion of soil and sandstone as a function of Péclet number.

Plotted along the depth, the hydrodynamic dispersion varied based on the type of test, with values being similar by depth (Figure 3.49). Thus, Figures 3.50 and 3.51 show the range of Dh values for the column and leaching test for the soil profile. The values corresponding to a depth of 7 m deviated from the others and were practically disregarded by the box plot diagram. Therefore, the recommended Dh values for the soil profile from the column test were between 3.1×10^{-7} m²/s and 8.5×10^{-7} m²/s, with an average value of 5.7×10^{-7} m²/s. Considering the leaching test, the values ranged between 7.3×10^{-7} and 1.5×10^{-6} m²/s, with an average of 1.1×10^{-6} m²/s.

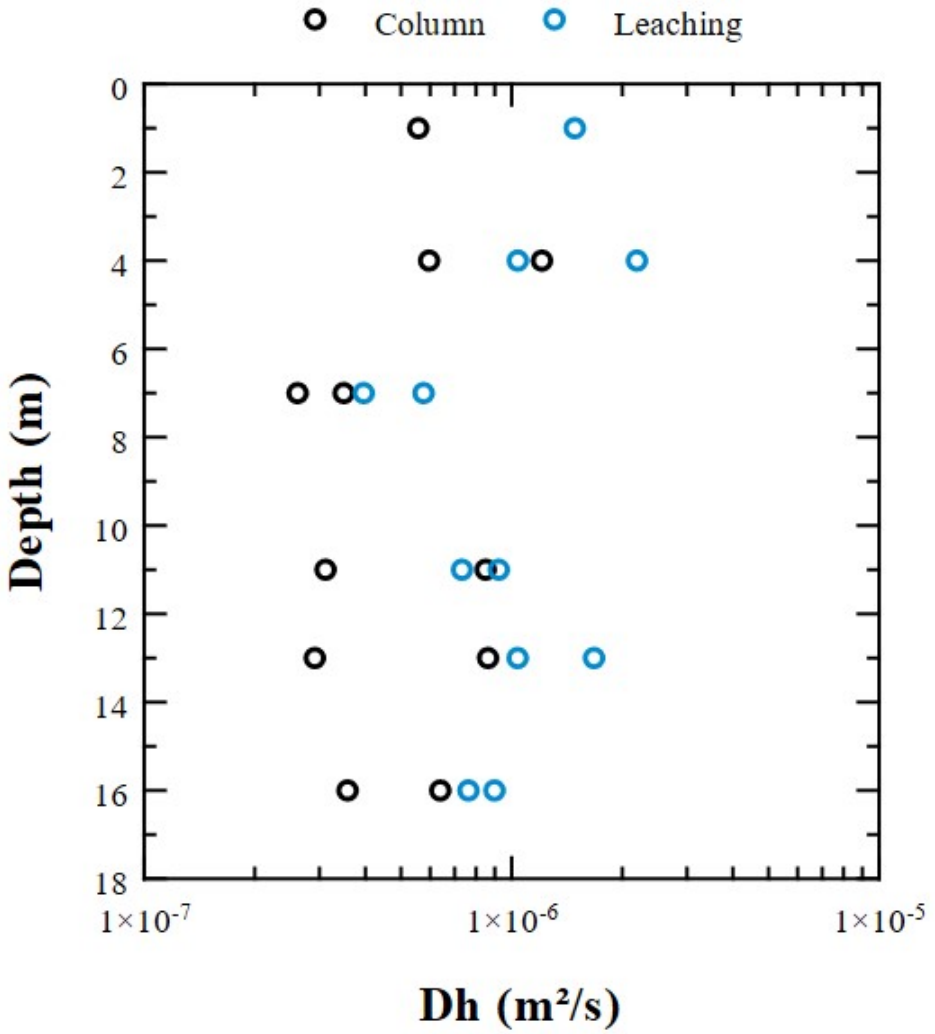

Figure 3.49: Results of hydrodynamic dispersion along the soil profile, as determined by column and leaching tests.

The Dh determined for the sandstone was 1.44×10^{-9} and 4.79×10^{-9} m²/s with 160 and 320 kPa of confining stress, respectively, from the column test. From the leaching test, the results were 8.34×10^{-10} m²/s with 160 kPa of confinement and 2.39×10^{-10} m²/s for 320 kPa of consolidation.

Since dispersivity is one of the terms in hydrodynamic dispersion, the factors that alter both are analogous. Similarly to dispersivity, Dh has an intrinsic relationship with the distribution and connection of pores (Bruderer & Bernabé, 2001), being relevant in the processes of mixing, spreading, and arrival time of contaminants (Whitehead et al., 1985; Theodoropoulou et al., 2003).

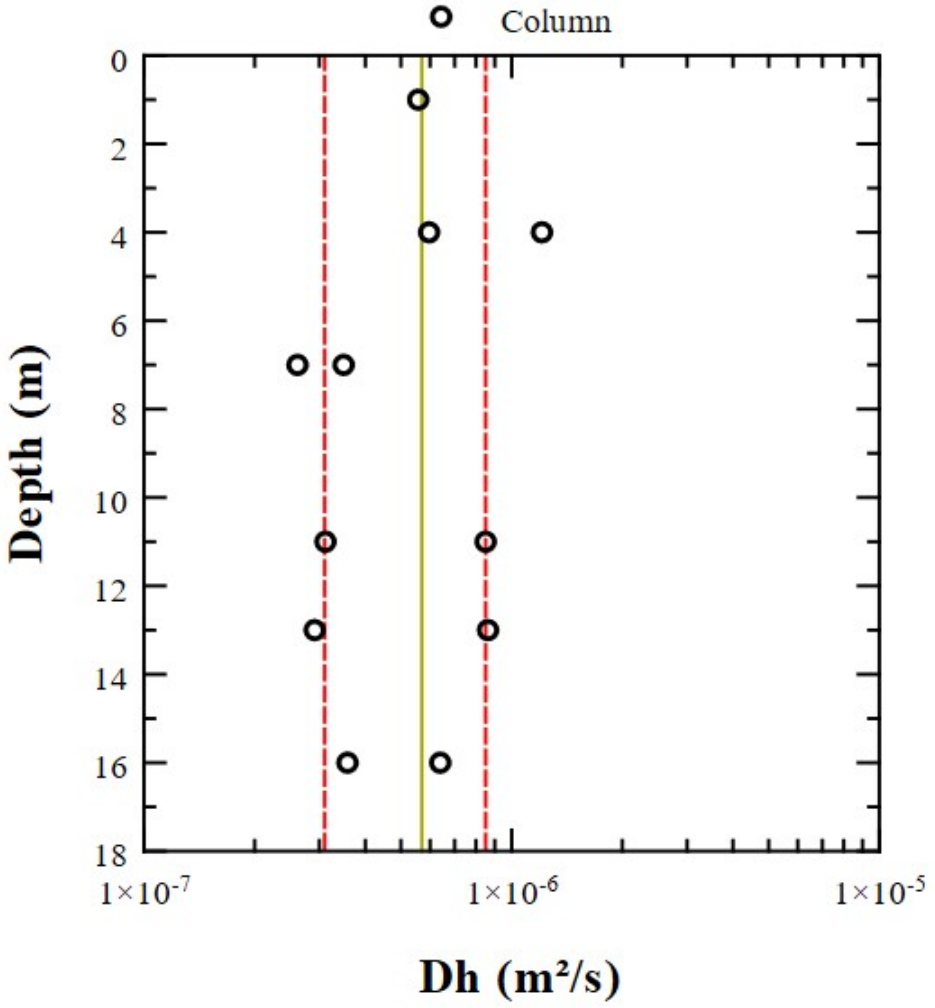

Figure 3.50: Hydrodynamic dispersion along the profile with the mean values (golden line) and first and third quartiles (dashed red line) for the column test.

Rowe et al. (2004) discuss that hydrodynamic dispersion is substantial at seepage velocities above 10^{-9} m/s, at which diffusion can be neglected, and at lower values, mechanical dispersion can be disregarded.

Aral & Liao (1996), Nguyen & Papavassiliou (2020), and Ding et al. (2021) elucidate that despite the studies aimed at determining and applying hydrodynamic dispersion, its understanding is still surrounded by uncertainties.

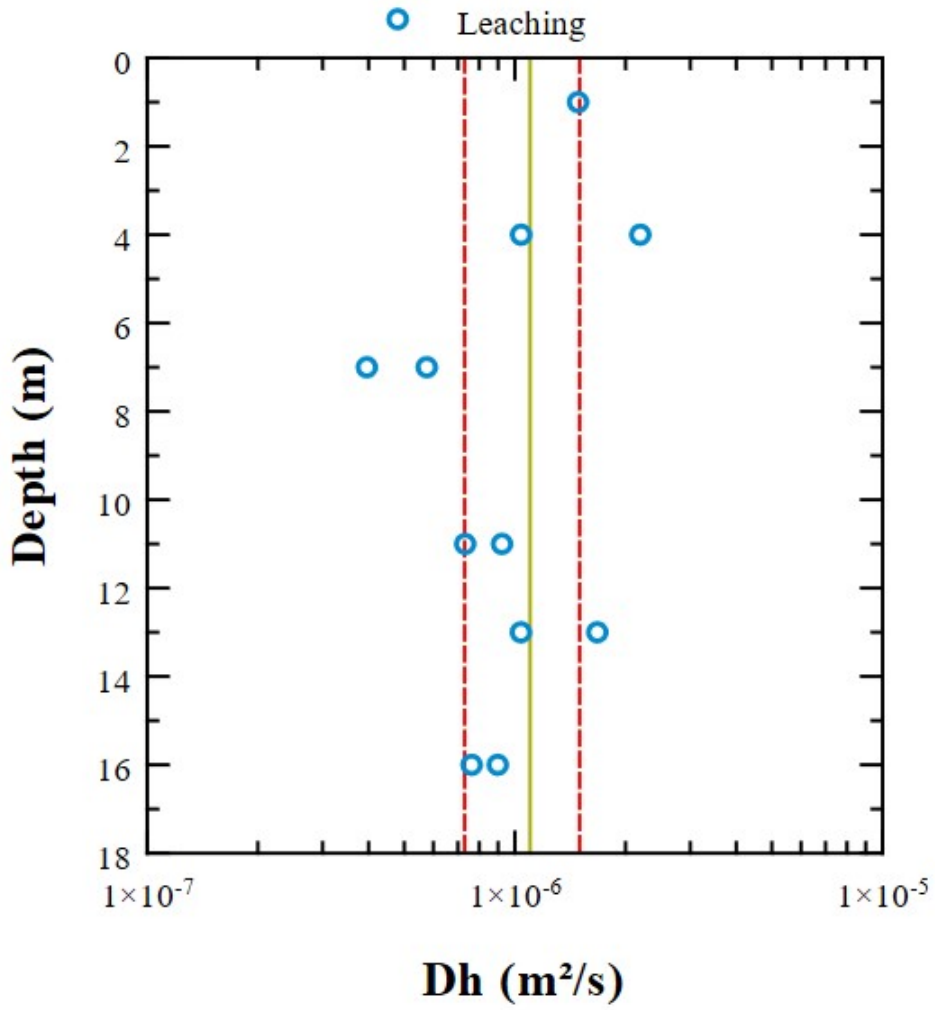

Figure 3.51: Hydrodynamic dispersion along the profile with the mean values (golden line) and first and third quartiles (dashed red line) for the leaching test.

Figure 3.52 represents the Dh/Do versus Péclet number, assuming molecular diffusion equals 10^{-9} m²/s, in which was notable the advective-dispersive behavior was predominant.

The results for sandstone lie below the fitted curve, indicating a less significant hydrodynamic dispersion. In contrast, the results for soil suggest a superior predominance of contaminant transport controlled by advective-dispersive, with similar Péclet numbers for both materials.

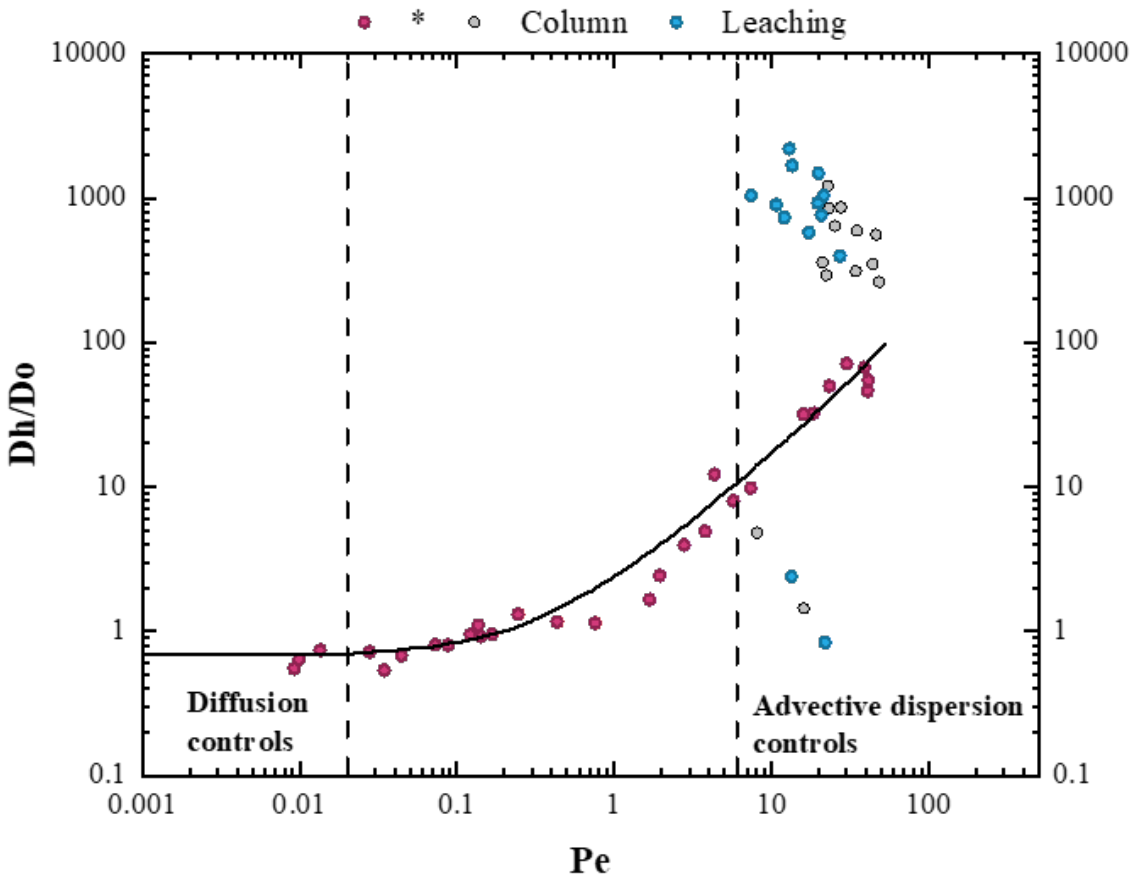

Figure 3.52: Relationship between Dh/Do versus Péclet number (*Data sourced adapted from Von Rosenberg (1956), Carberry & Bretton (1958), Blackwell et al. (1959), and Raimondi et al. (1959) apud Perkins & Johnston (1963) related to uniform sand or beads.)

Retardation factor

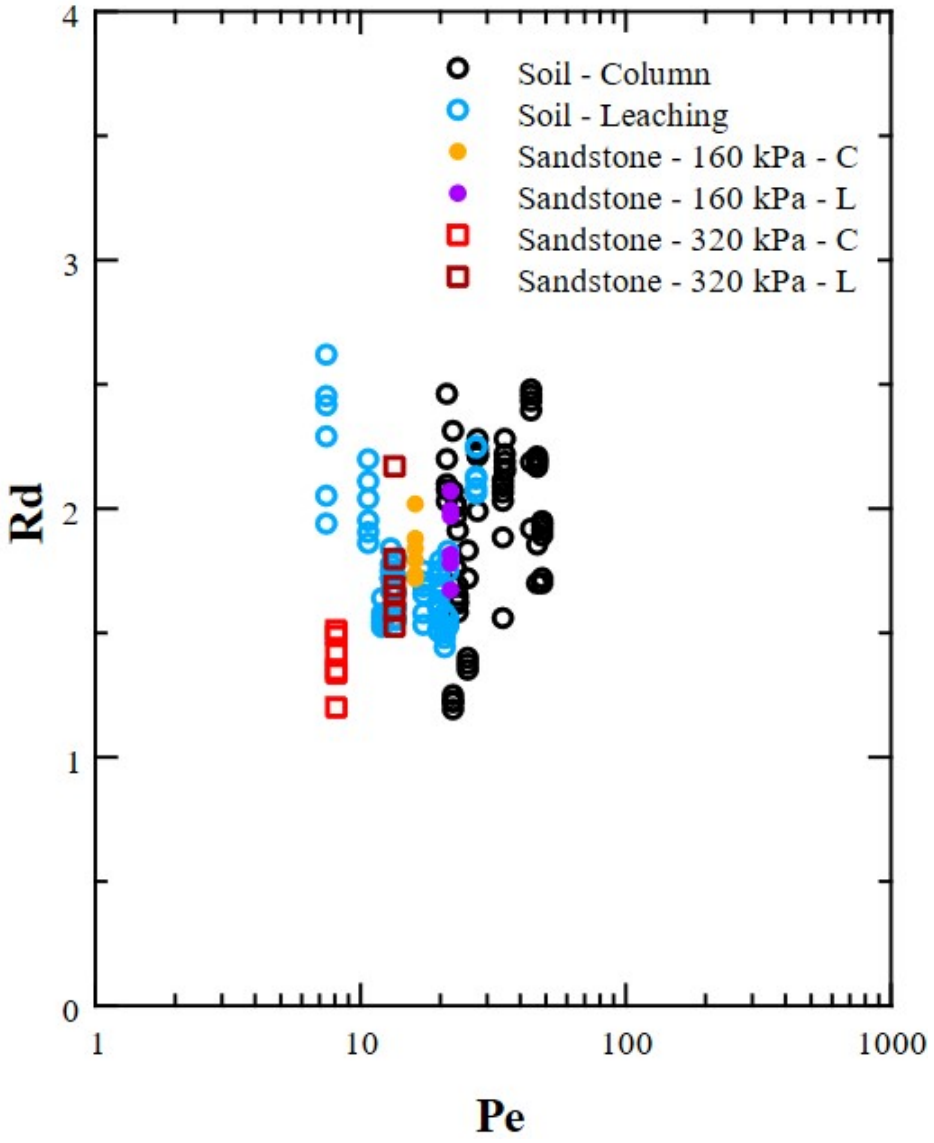

Figure 3.53: Retardation factor of soil and sandstone as a function of the Péclet number for column and leaching tests considering the results of the Lapidus & Amundson (1952) analytical fit.

The retardation factor indicates the sorption effect of the contaminant concerning the medium. Rd $>$ 1 suggests sorption effect, Rd $<$ 1 sorption can be neglected, and Rd $=$ 1 the solute is non-reactive (Shackelford, 1993). The Rd result from the analytical fit of Lapidus & Amundson (1952) to the experimental soil and sandstone data as a function of the Péclet number is shown in Figure 3.53, which shows a distinction between column and

leaching results. Similarly to the previous parameters, higher Péclet values were associated with the column test. As previously described, Rd was calculated in four different ways. The outcomes for the studied soil profile are presented in Figures 3.54 and 3.55 for the column and leaching tests, respectively.

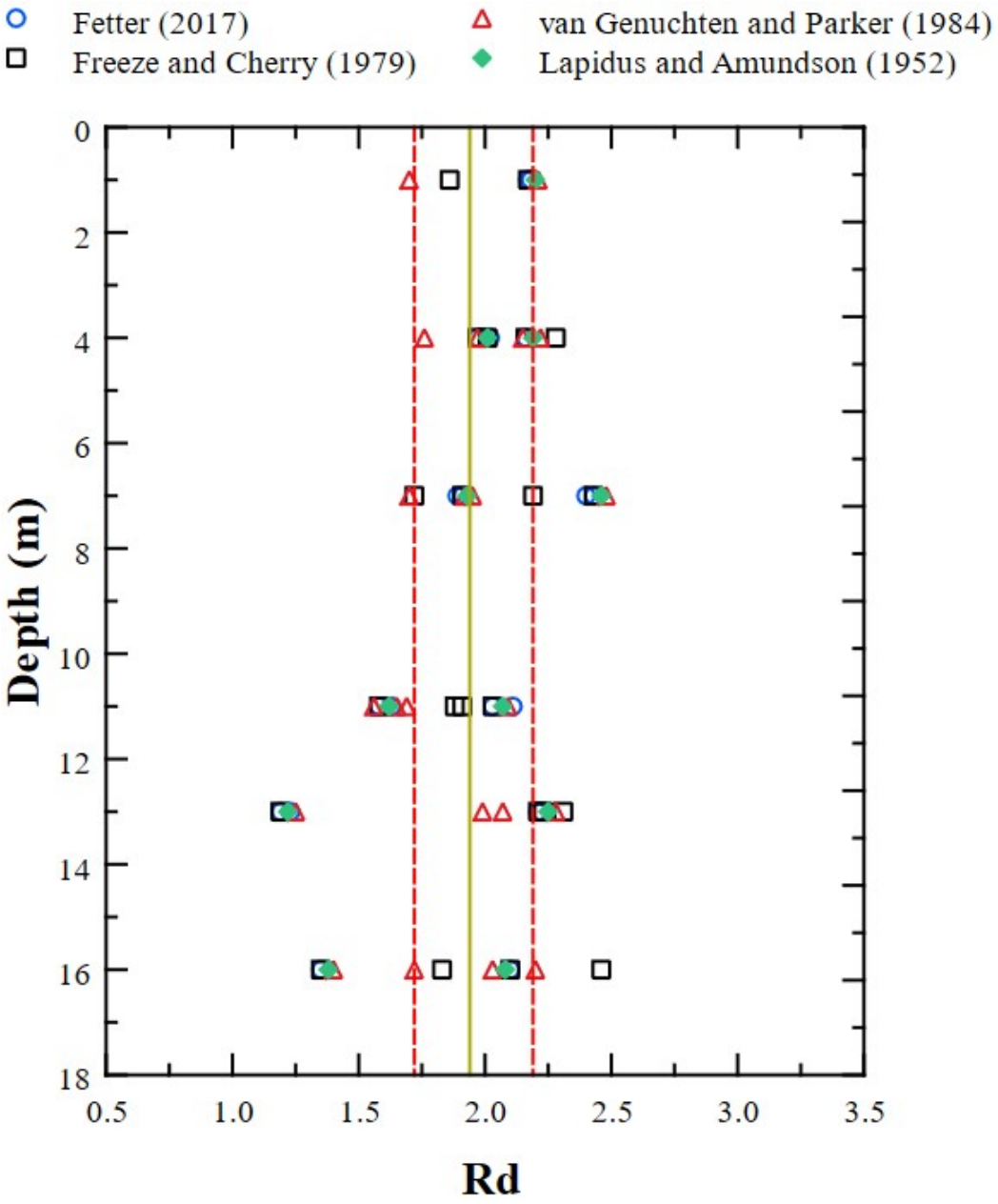

Figure 3.54: Column test retardation factors along the soil profile achieved by different methods, with the average value represented by the golden line and the interquartile range by the red dashed lines.

The values could be organized by column and leaching tests across the soil profile under investigation starting from the four methods. Box plot diagrams, available in the supplementary material, were employed to define the range of values.

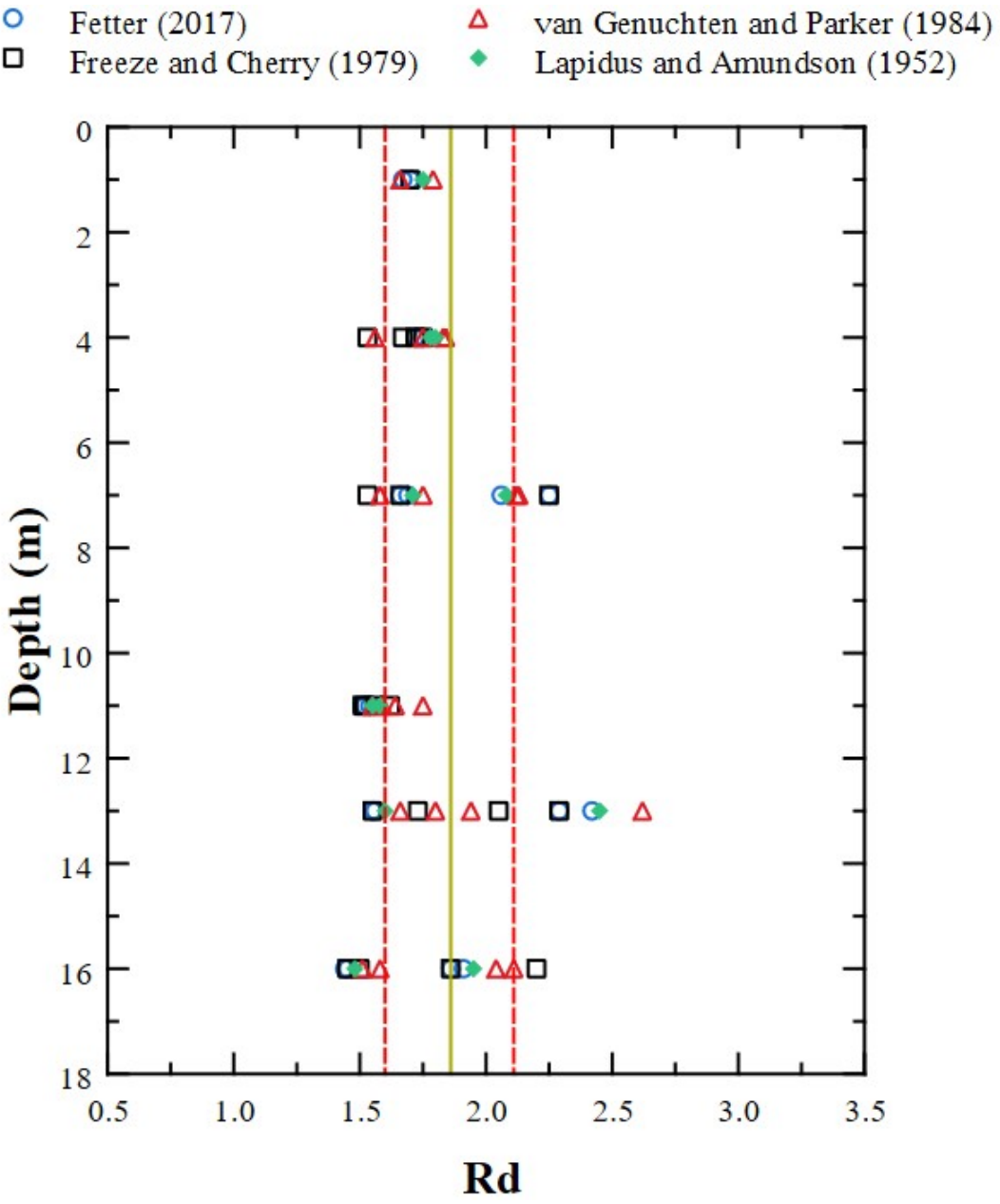

Figure 3.55: Leaching test retardation factors along the soil profile achieved by different methods, with the average value represented by the golden line and the interquartile range by the red dashed lines.

The results from the column test for the first quartile, third quartile, and mean were 1.72, 2.19, and 1.94, respectively. For the leaching test, the interquartile range values were 1.56 and 1.86, with a mean of 1.77. The retardation factor determined for the sandstone showed similar values to that of the soil. With a confining pressure of 160 kPa, the minimum, maximum, and average values were 1.72, 2.02, and 1.82, respectively. When consolidated at 320 kPa, the average value was 1.38, with minimum and maximum results of 1.20 and 1.51.

The Rd values of the soil in both the column and leaching tests indicate a minor sorption contribution. The soil under study is predominantly sandy with a low clay content (<20%), with the presence of kaolinite and iron and aluminum oxides and hydroxides (Giacheti et al., 2019). Indication of sorption in sandy soil can be related to the lateralization of the material, as shown by Fagundes & Zuquette (2011) in a soil similar to the one studied. The authors endorse that the attenuation capacity in materials with theoretically low sorption capacity is significantly more effective at low concentrations and with oxides and hydroxides. About the sandstone, the contribution of the retardation factor, albeit with reduced values, can be explained by the presence of clay minerals, but from the smectite group, as shown in Chapter 2, evidenced by the sandstone's expansion and the clay mineral's detection through the methylene blue technique.

The values of the retardation factor slightly above 1 indicate that the movement of the plume's center of mass is somewhat delayed in relation to the movement of the fluid's center of mass, moving almost together. This slight (practically negligible) delay may be associated with the sorption of sodium alongside the few clay minerals present in the sandstone and the lateralization of the soil.

Kjeidsen & Christensen (1984) state that sodium is mitigated solely by sorption. Shackelford & Redmond (1995) report that Cl^- is generally non-reactive, while Na^+ can be sorbed by kaolinite. However, the authors emphasize that kaolinite's exchange capacity depends on pH. Chlorine tends to be sorbed in solutions with low pH, whereas sodium has a greater affinity for kaolinite at higher pH levels, as observed in this work.

Partition coefficient

Defined as the ratio between the concentration absorbed by the medium and the concentration dissolved in the leachate, the partition coefficient is one of the factors contributing to the delay in the transport of contaminants (Ceazan et al., 1989; Grathwohl & Susset, 2009).

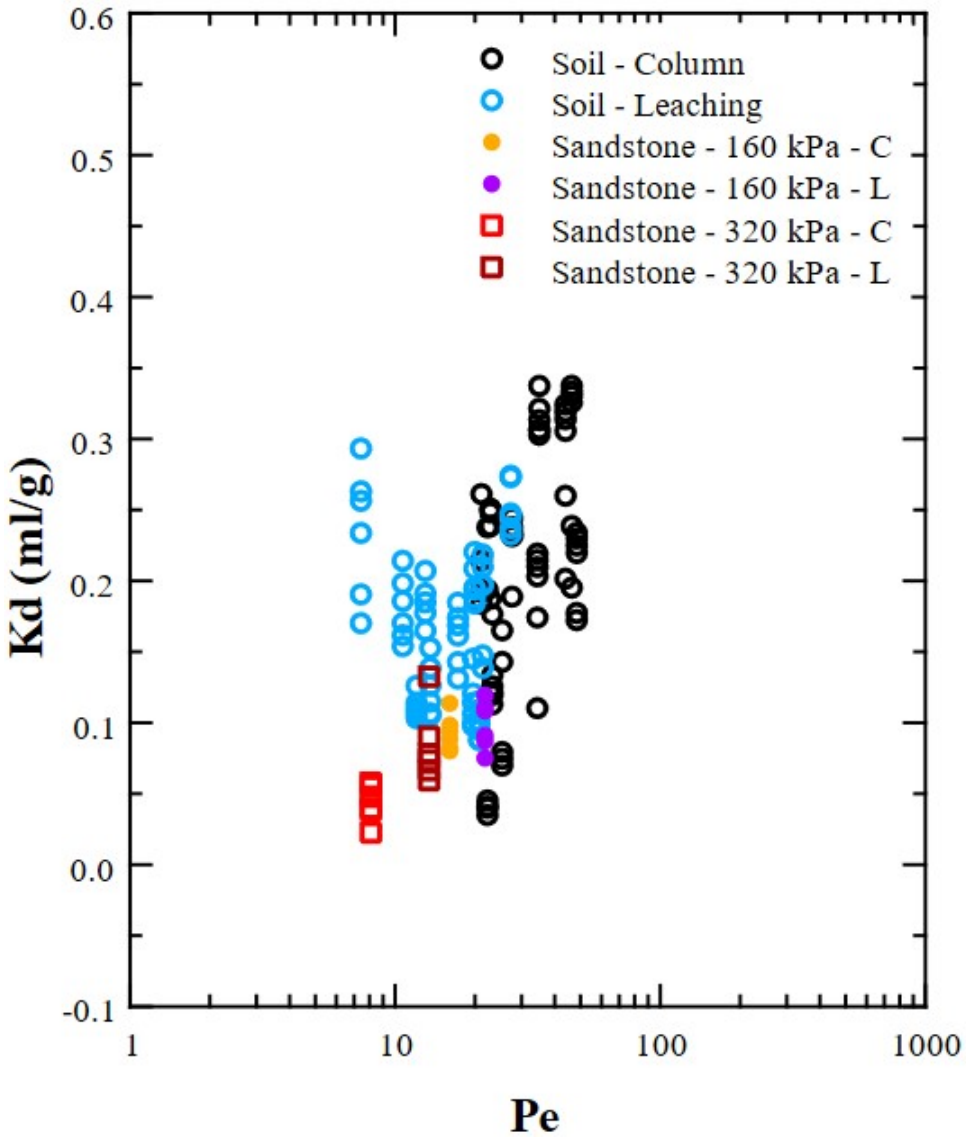

Figure 3.56: Soil and sandstone partition coefficient as a function of the Péclet number based on the analytical fit of Lapidus & Amundson (1952).

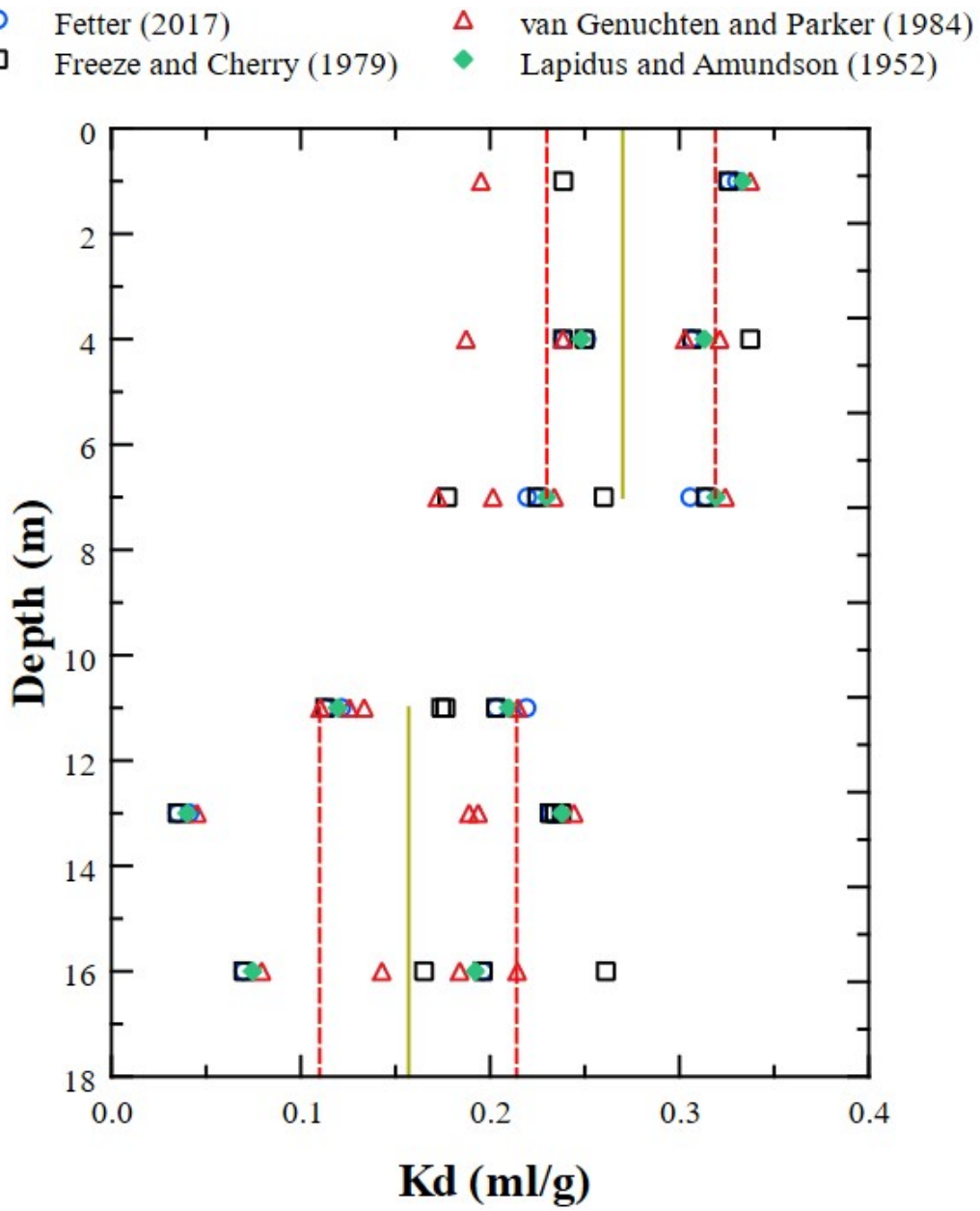

Figure 3.57: Mean column test partition coefficient (golden line) and interquartile distance (red dash lines) along the soil profile achieved by different methods.

Since the partition coefficient is interdependent on retardation factor, Kd was determined based on the four methods used to calculate Rd, considering linear isotherms. The distribution of Kd results as a function of the Péclet number, based on the analytical fitting from Lapidus & Amundson (1952) (see Figure 3.56), appears similar to that of Rd, given that the former was determined from the latter. However, unlike Rd, the partition

coefficient did not show the same trend throughout the profile. This was established for the soil at depths of 1, 4, and 7 m and for 11, 13, and 16 m, as exemplified by Figure 3.57 with results from the column test, and by Figure 3.58 with results from the leaching test.

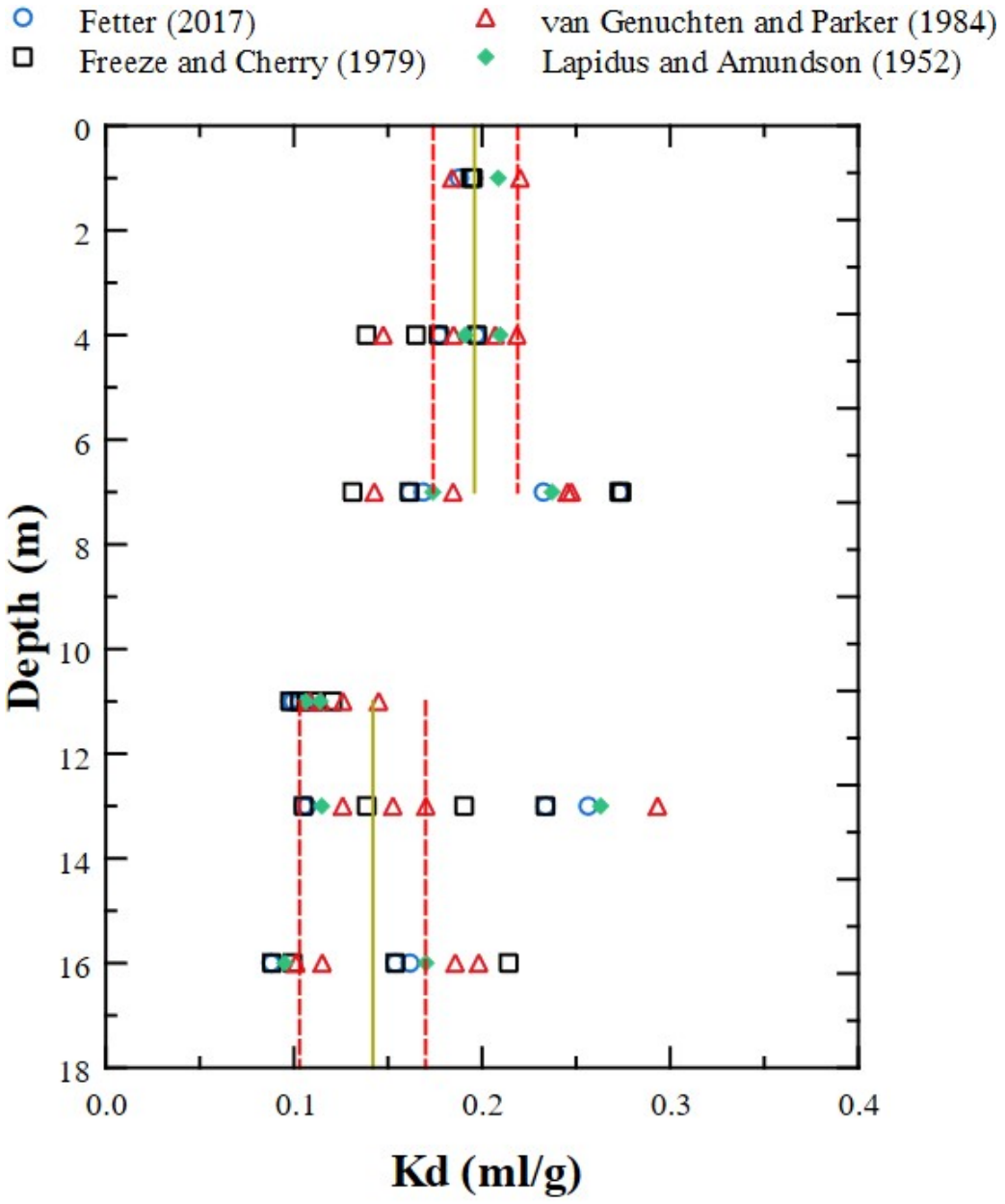

Figure 3.58: Mean leaching test partition coefficient (golden line) and interquartile distance (red dash lines) along the soil profile achieved by different methods.

Considering the column test, the average Kd was 1.94 ml/g, with an interquartile range between 0.23 and 0.32 ml/g for the soil at depths of 1 to 7 m. Conversely, for the same

depths as determined by the leaching test, the first quartile was 0.11 ml/g, the third quartile was 0.21 ml/g, and the average value was 0.16 ml/g.

For the soil between 11 and 16 m deep, the results for the first and third quartiles of Kd from the column test were 0.17 and 0.22 ml/g, respectively, with an average of 0.20 ml/g. For the leaching test, the interquartile values ranged from 0.10 to 0.17 ml/g, with an average of 0.14 ml/g.

For the sandstone, the average, minimum, and maximum values of Kd were determined, which turned out to be minor, like the soil, but with less variation among the data. Considering the column test and the confinement of 160 kPa, Kd had an average of 0.09 ml/g and was between 0.08 and 0.11 ml/g. At 320 kPa of confining stress, Kd was between 0.02 and 0.06 ml/g, with an average value of 0.04 ml/g. The values determined from the leaching test with 160 kPa of confinement ranged between 0.08 and 0.12 ml/g, with an average of 0.10 ml/g. When applying 320 kPa, the minimum, average, and maximum results were 0.06, 0.08, and 0.13 ml/g, respectively. The reduced variability in the sandstone data may be attributed to the smaller dataset processed, potentially leading to better statistical treatment due to the grouping of soil data based on depths.

It is noted that the determined values were low. Therefore, the partition coefficient had little to no influence on the tests. As emphasized by Labrecque & Blanford (2021), when the retardation factor approaches 1, the partition coefficient approaches zero, indicating a small contribution to delaying the transport of pollutants. The small values indicate the substantial importance of transport by advection-dispersion, given that high values of Kd reduce the movement of contaminants, increasing the time for them to reach the receptor (US EPA, 1999), an effect contrary to what is observed here.

A tracer can be considered as mobile as water if Kd $\leq$ 0.1 ml/g and immobile if Kd $\geq$ 10000 ml/g (Amadi & Odedede, 2021). Therefore, the NaCl used in this study is predominantly in solution and experiences minimal sorption by the soil or rock matrix.

The minimum, maximum, average, and interquartile range values of dispersivity, hydrodynamic dispersion, retardation factor, and the partition coefficient determined here are summarized in Table 3.5.

Table 3.5: Summary of the transport parameters determined in this work. The letters *C* and *L* indicate the column and leaching tests. Their absence suggests data for both.

Depth	Parameter	Min	1° quartile	Mean	3º quartile	Max	Fluid
1 - 7 m	α (m)	1.65×10^{-3}	2.00×10^{-3}	3.00×10^{-3}	4.00×10^{-3}	6.29×10^{-3}	NaCl solution
11 - 16 m		2.71×10^{-3}	4.00×10^{-3}	5.00×10^{-3}	7.00×10^{-3}	1.19×10^{-2}	
1 - 16 m C	Dh (m^2/s)	2.61×10^{-7}	3.10×10^{-7}	5.70×10^{-7}	8.50×10^{-7}	1.21×10^{-6}	NaCl solution
1 - 16 m L		3.96×10^{-7}	7.30×10^{-7}	1.10×10^{-6}	1.50×10^{-6}	2.19×10^{-7}	
1 - 16 m C	Rd	1.19	1.72	1.94	2.19	2.48	NaCl solution
1 - 16 m L		1.44	1.56	1.77	1.86	2.62	
1 - 7 m C	Kd (ml/g)	0.17	0.23	0.27	0.32	0.34	NaCl solution
1 - 7 m L		0.13	0.11	0.16	0.21	0.27	
11 - 16 m C	Kd (ml/g)	0.03	0.17	0.20	0.22	0.26	NaCl solution
11 - 16 m L		0.09	0.10	0.14	0.17	0.29	

Arrival times

The experimental and analytical results of arrival time, breakthrough time, and pick time are respectively depicted in Figures 3.59, 3.60, and 3.61 of the soil profile with the confining stresses applied to the representative specimens at the investigated depths. Similarly, the first leaching time, leaching breakthrough time, and leaching time are illustrated in Figures 3.62, 3.63, and 3.64, respectively.

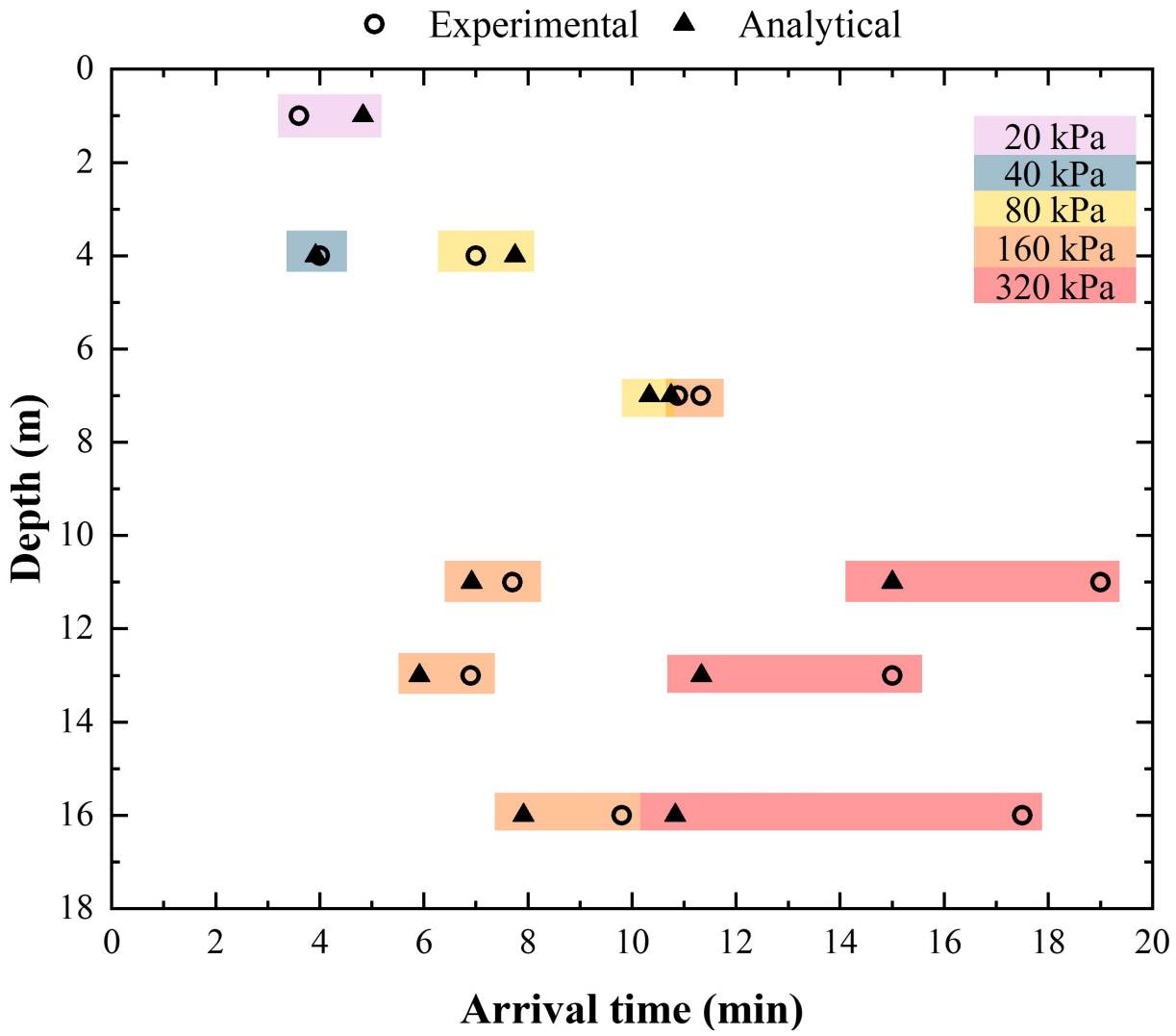

Figure 3.59: Arrival time of NaCl with confinement along the depth of the soil profile studied.

As exemplified by Figure 3.59, the arrival time increased with the increase in con-

finement. The At increased from 2 to 4 min for soil at a depth of 4 m to 5 to 10 min for soil deeper than 11 m with confining stress of 160 kPa and from 10 to 19 min with 320 kPa of confinement. For soil at a depth of 7 m, the arrival time was 10 min.

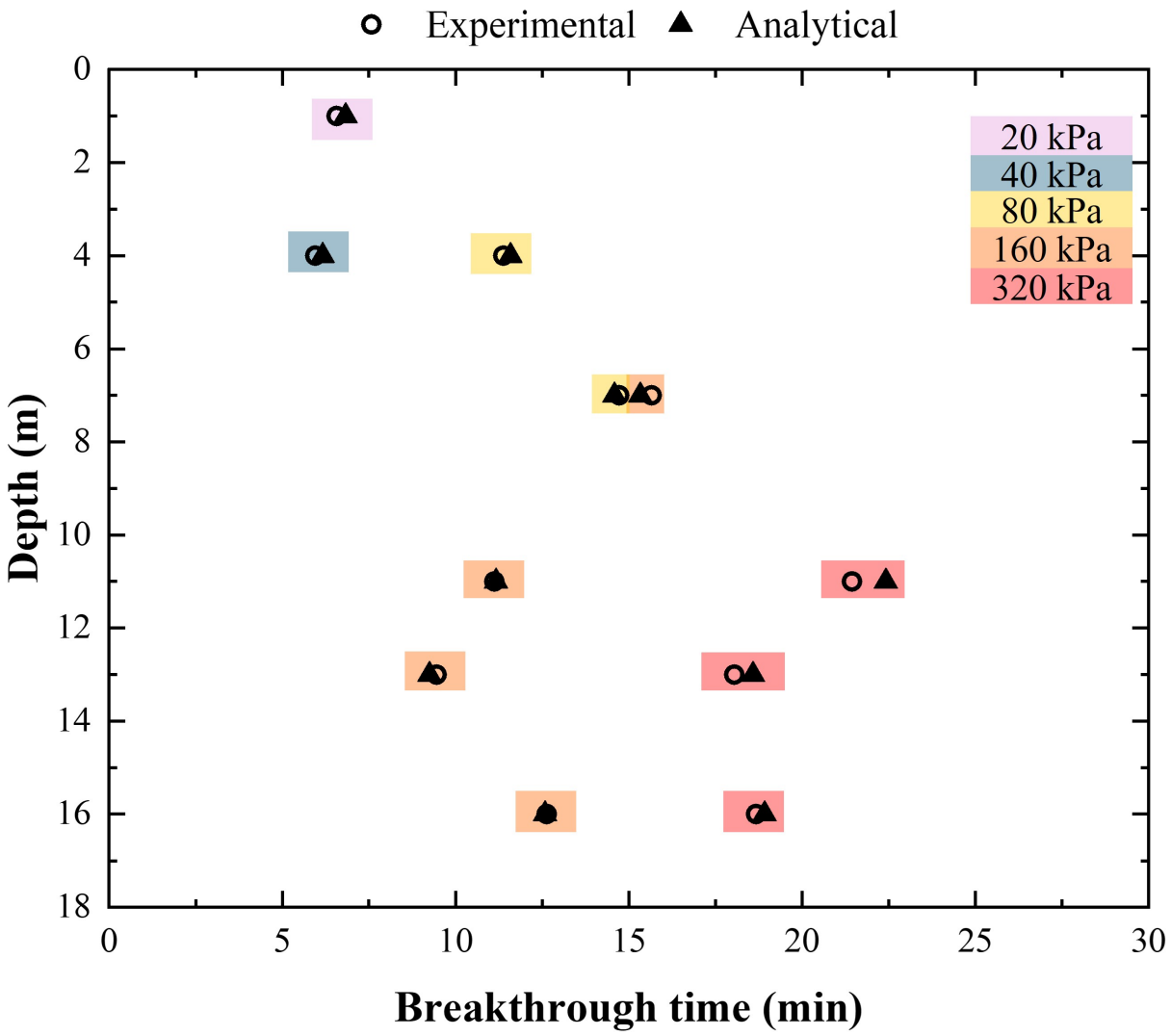

Figure 3.60: Breakthrough time of NaCl with confinement along the depth of the soil profile studied.

The results obtained from the analytical models closely matched the experimental values up to a depth of 7 m. However, they underestimated the experimental results at depths of 11, 13, and 16 m, particularly under higher confinements. This observed deviation can be attributed to the better fit of the analytical curves at shallower depths and with lower

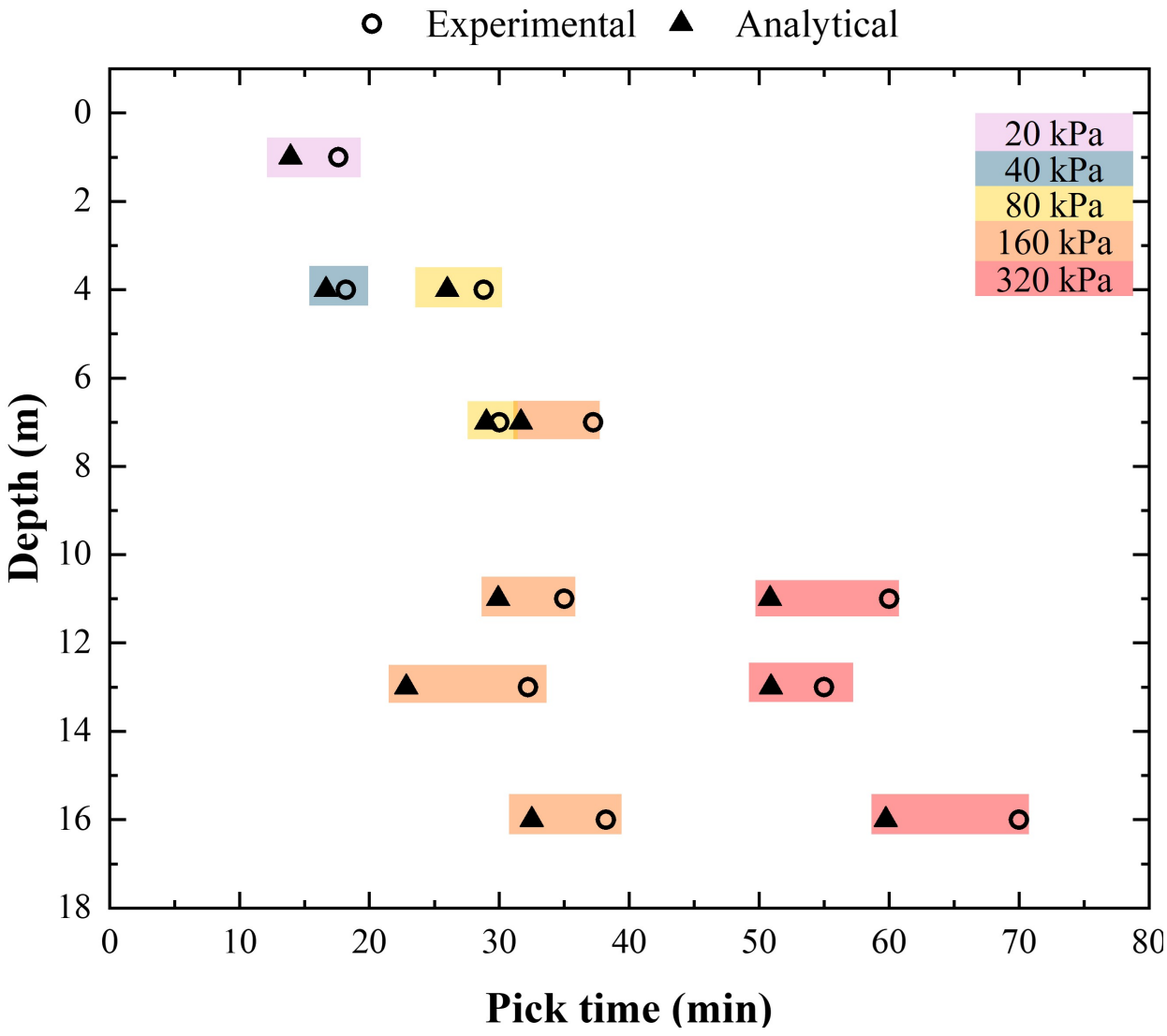

Figure 3.61: Pick time of NaCl with confinement along the depth of the soil profile studied.

confinement, although for all curves, the R^2 was higher than 0.98.

Regarding the breakthrough time illustrated by Figure 3.60, the system failure occurred between 5 and 12 min for soil up to 4 m deep and at 15 min for 7 m deep. Below a depth of 11 m, the breakthrough time was reached between 8 and 12.5 min for a confining stress of 160 kPa and was shown to be between 18 and 23 min for a confinement of 320 kPa. The results clarify that, concerning advective-dispersive flow, the increase in confinement of the samples led the system to fail later. This underscores the significance of reducing permeability to avoid advective-dispersive flow and, consequently, contamination. In the

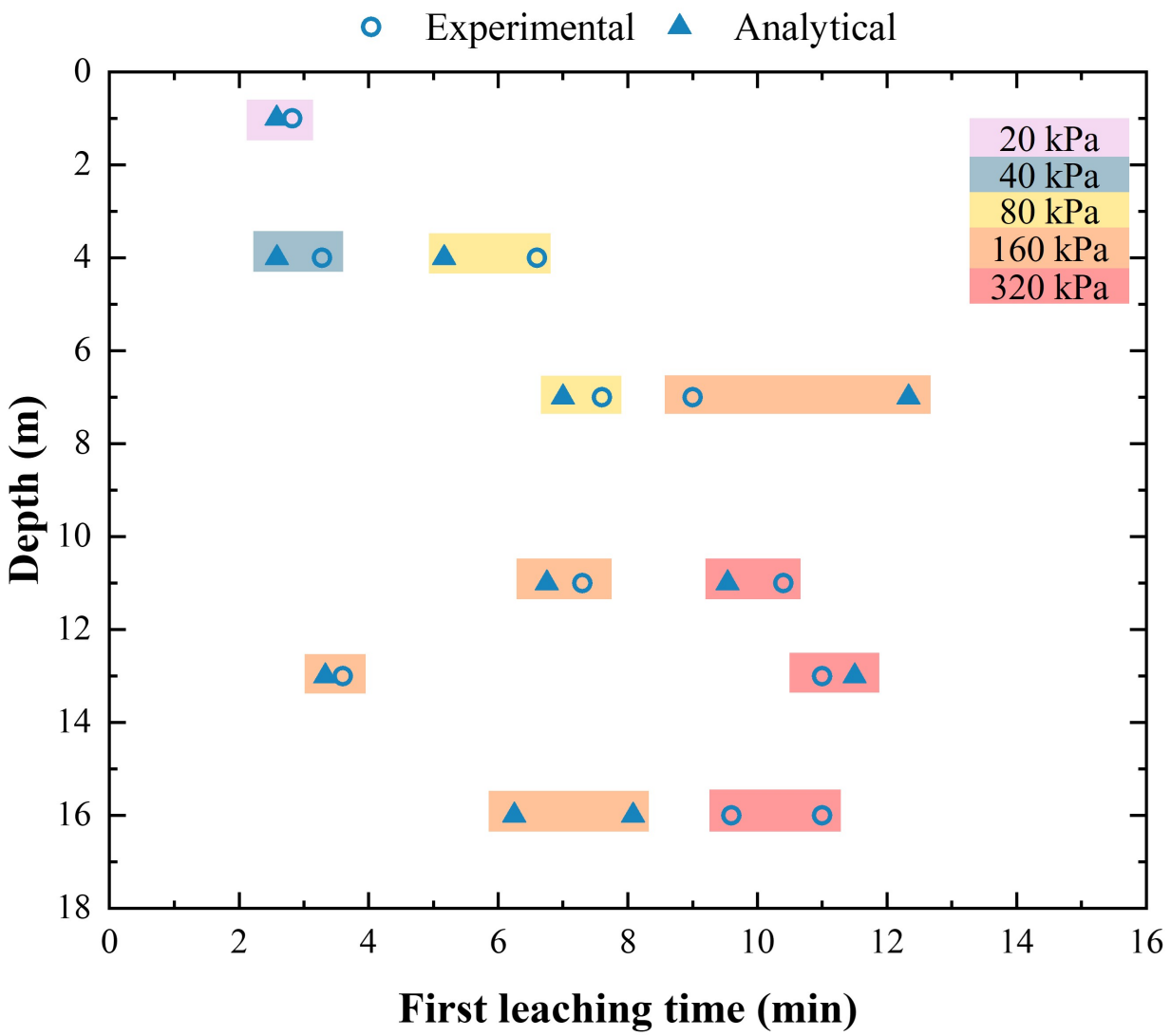

Figure 3.62: First leaching time of NaCl with confinement along the depth of the soil profile studied.

case of sandy soil with a hydraulic conductivity on the order of 1×10^{-5} m/s, undesired concentration was rapidly attained.

The experimental and analytical values in the central region of the breakthrough curves were quite close. However, the beginning and end of the BTCs did not align well with the analytical curves, which was also noted by Hassanzadeh et al. (2020).

Like the arrival time and previous breakthrough time, the peak time value (Figure 3.61) increased with the depth and confinement of the samples, with experimental and analytical data being close to 7 m. At depths of 1 to 4 m, the peak time at the end of the

breakthrough curve ranged from 15 to 30 min, while at depths of 7 m and with 160 kPa of confinement, the peak times were similar, ranging from 22 to 39 min at depths of 11, 13, and 16 m. For a confinement pressure of 320 kPa, peak times at depths of 11, 13, and 16 m ranged from 50 to 70 min.

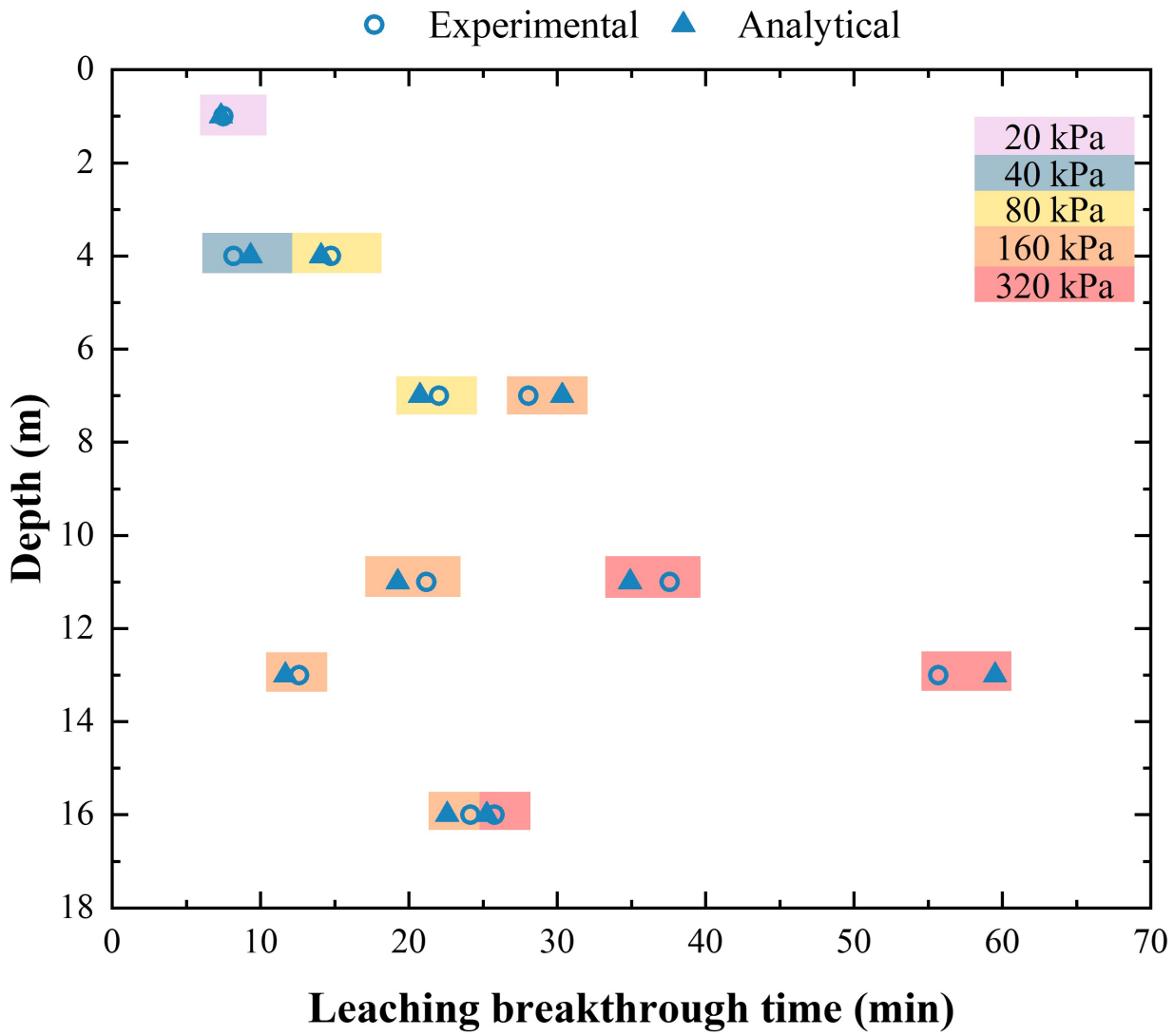

Figure 3.63: Leaching breakthrough time of NaCl with confinement along the depth of the soil profile studied.

In the leaching test, the initial leaching time depicted in Figure 3.62 ranged from 2 to 7 min for the soil up to 4 m deep and 6.5 to 7.5 min for the sample at 7 m depth consolidated

at 80 kPa. For this last depth, with a confinement of 160 kPa, the FLt values varied from 9 to 13 min, a duration exceeding that observed for deeper depths with higher confinement. The samples from depths 11, 13, and 16 exhibited similar behavior. With a confinement of 160 kPa, the FLt ranged from 6 to 8 min, and with 320 kPa of confining stress, the time increased, ranging between 9.5 and 11.5 min, except for the 13-meter sample consolidated at 160 kPa, which displayed an initial reduction in concentration proportionate to the surface soils at 1 and 4 ms deep. The exceptions observed for depths of 7 and 13 ms, and the better analytical fit for the latter and worse for the former, lack a definitive explanation.

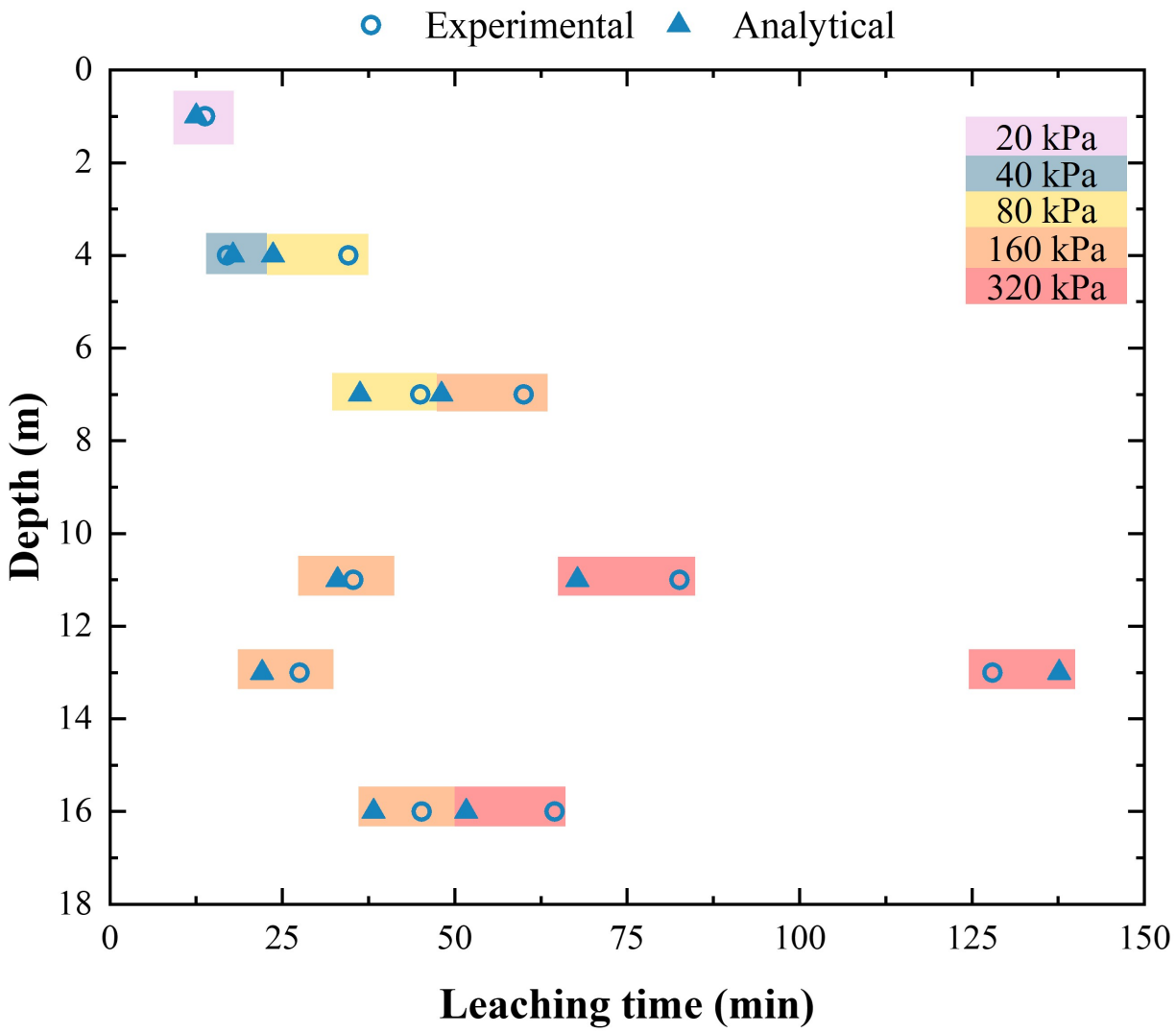

Figure 3.64: Leaching time of NaCl with confinement along the depth of the soil profile studied.

The leaching breakthrough time, defined in this work as the time required to reduce the concentration to the maximum allowable level, is illustrated by Figure 3.63. The comparison between experimental and analytical data revealed a strong agreement. Again, there was an increase in LBTt with depth and confinement. The samples at 1 and 4 m of confinement at 20 and 40 kPa presented similar results, with values between 5 and 9 min. For the 4 m depth sample consolidated at 80 kPa, the LBTt increased to 14 min. The results for depths of 7 m at 80 kPa confinement and 11 and 16 m at 160 kPa ranged between 19 and 24 min. For the confining stress of 160 kPa applied to the test specimen representative of a 13 m depth, the results remained once again close to the soil at 1 and 4 m depths.

Furthermore, when the confining stress was increased to 320 kPa for soils at 11 and 13 m, the breakthrough time increased to 35-38 min and 55-60 min, respectively. On the other hand, the soil at 16 m depth showed little change when increasing the confining stress to 320 kPa, with the LBTt moving to 25 min. The results indicate that the sample corresponding to 16 m depth leached more rapidly, with results like the soil at 7 m depth, even with double the confinement applied. In fact, the values starting from 7 m depth were akin (between 20 and 40 min) except for the sample corresponding to 13 m depth, which had results similar to the soil at 4 m depth for 160 kPa confinement and LBTt values above 55 min for 320 kPa confining stress.

Regarding the total time to leach the soil tracer, the experimental results presented in Figure 3.64 did not reach a relative concentration of zero but instead values on the order of 0.03. Nonetheless, the soil profile's experimental data and analytical curves fit well. The Lt for the first and fourth meter with 20 and 40 kPa of confinement ranged between 12 and 17 min. With a confining stress of 80 kPa applied to the soil sample at the fourth meter, the Lt increased to 24 to 35 min, a value close to the soil at 13 m with 160 kPa of confinement (22 to 28 min).

Analogously, other parameters derived from the breakthrough curve of the leaching test indicated that the values at a depth of 13 m, consolidated at 160 kPa, closely resembled those of the soil at 4 m. In contrast, the values with 320 kPa of confinement at different depths exceeded 125 min. The soil at depths of 7 m, consolidated with 80 kPa, and at 11 and

16 m, consolidated with 160 kPa, yielded results ranging between 29 and 45 min. Similarly, the leaching time of the sample at 7 m depth, subjected to 160 kPa of confinement, ranged between 50 and 62.5 min, aligning closely with the sample at a depth of 16 m under 320 kPa of confinement.

The parameters obtained from the breakthrough curve in the central section of the curve, that is, BTt and LBTt, demonstrated the strongest correlation between experimental and analytical data. As discussed previously, the values of hydraulic conductivity exhibited similar behavior at depths of 1, 4, and 7 m, as well as at 11, 13, and 16 m. This similarity also extended to the contaminant transport parameters, with some exceptions observed, such as the LBTt being approximately 30 min higher for the sample at a depth of 13 m compared to the sample at 16 meters under the same confinement, despite similar hydraulic conductivity values. The results presented here support hydraulic conductivity's crucial role in advection-dispersion parameters.

Overall, the leaching test exhibited a better fit for the analytical model. The reduction of k, directly associated with advective-dispersive flow, resulted in prolonged arrival times. Higher confinements corresponded to more significant reductions in k, thereby influencing the arrival times, as discussed previously.

BTC – Heavy metals

As discussed in the introduction and the materials and methods, the mentioned metals were chosen based on the work of Faria & Mondelli (2018), which found that Mn, Ni, and Pb were detected at concentrations exceeding those permitted by Brazilian environmental authorities CONAMA 420/09 (2009) and CETESB (2014) in monitoring wells around Bauru's MSW disposal site.

In light of the preceding findings and the proximity of sandstone in the waste material, this study opted to examine the most critical scenario: percolating synthetic leachate containing nickel, manganese, and lead through the unconsolidated sandstone. In this way, Table 3.6 presents the initial index properties of the sandstone sample. Figure 3.65 depicts the breakthrough curves for the aforementioned metals in the sandstone over time. Additionally, Figure 3.66 portrays the relative concentration as a function of pore volume.

The flow remained uninterrupted with a constant concentration for 17 days. At this moment, the flow was interrupted for approximately 6 months to verify the occurrence of diffusion as suggested by Brusseau et al. (1989), Brusseau et al. (1997), Appelo & Postma (2004), and Woodman et al. (2015). After the period without flow mentioned, the test was resumed under identical conditions. In the subsequent collection interval, an increase in the relative concentration of Mn from 0.29 to 0.58 and of Ni from 0.12 to 0.34 was observed, demonstrating the presence of pollutant transport by diffusion. The dashed purple line in Figures 3.64 and 3.65 illustrates the pause period of the flow.

Table 3.6: Initial index properties of the sandstone used for the column test with a multi-ionic heavy metals solution.

Sandstone	**wi (%)**	**ρs (g/cm³)**	**ei**	**ρd (cm³)**	**n (%)**
Gray	1.90	2.628	0.396	1.882	28.38

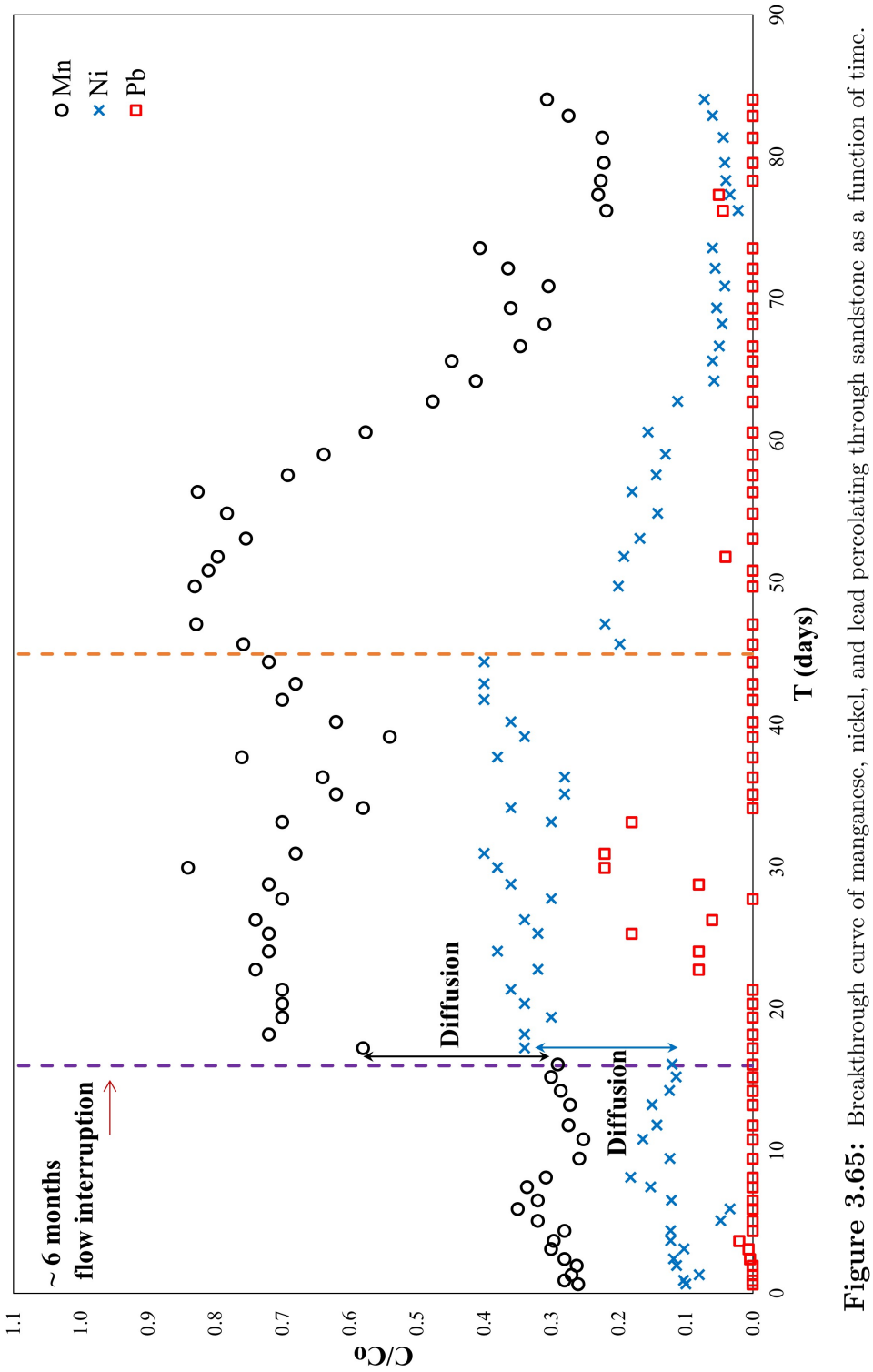

Figure 3.65: Breakthrough curve of manganese, nickel, and lead percolating through sandstone as a function of time.

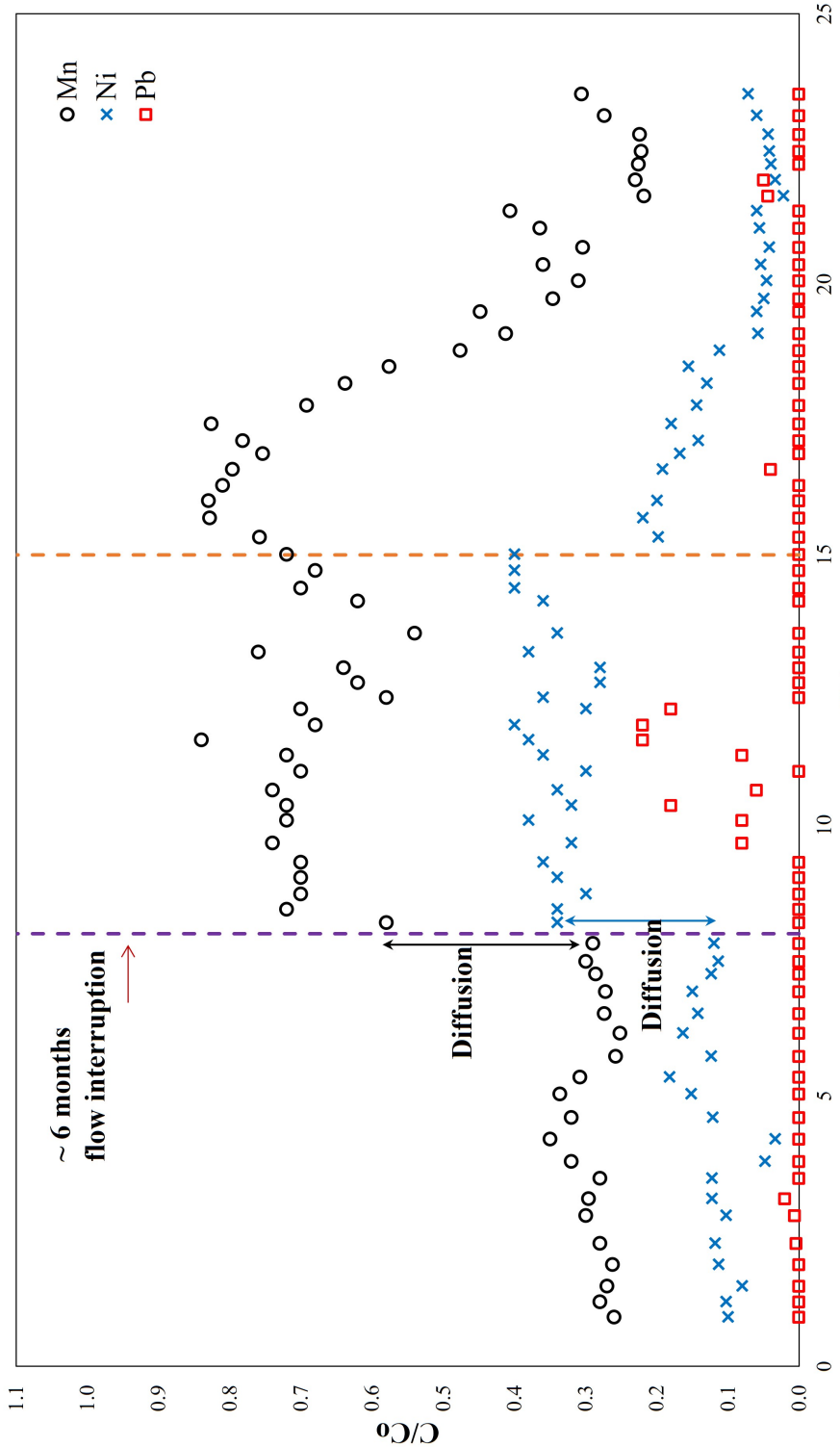

Figure 3.66: Breakthrough curve of manganese, nickel, and lead percolating through sandstone as a function of pore volume.

Utilizing Pb as a reactive tracer presents considerable challenges, particularly at low concentrations in an alkaline medium (pH 8), where lead tends to precipitate (Copenhaver et al., 1993; Francisca & Glatstein, 2020). Furthermore, some authors have reported that lead is preferred in sorption when competing with other metals, and it is difficult to detect in the effluent fluid, leading to an increase in the retardation factor and a reduction in mobility. In contrast, manganese, which tends to remain dissolved, exhibits higher mobility, has a lower retardation factor, and can reach greater distances, as mentioned by Chotpantarat et al. (2011). The authors attribute this preference mainly to the reduced ionic radius of Pb, which favors its binding to the soil surface and limits access to sorption sites by other metals. Therefore, the undetectable concentration of Pb can be attributed to its strong retention in sandstone through sorption and precipitation, resulting in negligible transport.

It is possible to infer from the results that manganese and nickel performed effectively as tracers even in basic environments, representing a greater risk of their dispersion and migration through the sandstone. Both maintained stable concentrations up until the flow interruption. After it resumed, the values remained consistent until the 45th day of the test. At this point, the concentration of both elements dropped to levels comparable to those at the moment of flow interruption, even though the test's unchanged boundary conditions. The test concluded on the 85th day.

Voudrias & Yeh (1994) observed a similar situation with an increase in toluene concentration after stopping the flow for 81 hours. Likewise, in this study, the toluene concentration returned to the same pattern as before the flow interruption. However, unlike the abrupt reduction noted by Voudrias (1994), we observed a gradual decrease occurring approximately 28 days after the flow was restored. Similar observations were also discussed by Koch & Flühler (1993) and Wehrer & Totsche (2008).

Brusseau et al. (1997) noted that if sorption sites are available during the interruption of flow, the concentration determined after the flow is reestablished will be lower. On the other hand, the opposite effect will be noted if there is a limitation on sorption. Considering the reduced Kd values determined in this study for NaCl, the increase in the concentration of Mn and Ni upon cessation of flow aligns with the observations of Brusseau et al. (1997).

Additionally, Reedy et al. (1996) infer that the shape of the BTCs in tests with pauses during their conduction indicates not only diffusion but also the presence of nonlinear physical processes.

Thus, the result of the asymmetric BTC indicates non-linear Rd. Therefore, conducting batch equilibrium tests of the sandstone samples for the mentioned metals of study appears attractive for determining the sorption kinetics of the material. Although Plassard et al. (2000), Pang et al. (2004), Miretzky et al. (2006) and Zhao et al. (2009) recommend column tests to determine Rd as it better reflects field conditions, in situ results have shown to be superior for this parameter, as illustrated in the research by Odling et al. (2007), where the authors attribute this difference to the seepage velocity, aligning with the earlier discussion on dispersivity.

During the 9-month test period, 23 PV percolated through the sample because of the low permeability of the material. The breakthrough time for Mn was 30 days, and for Ni, it was 7 days. In other words, this was the time required for the concentration of Mn to exceed 0.4 mg/L and that of Ni to exceed 0.07 mg/L. Given that the initial concentration of the tracers was 0.5 mg/L, relative concentrations of Mn above 0.8 and Ni above 0.14 indicated the breakthrough time.

The mobility capacity of Mn and Ni highlights the finding from Faria & Mondelli (2018) as two of the metals present in concentrations exceeding the minimum established by the Brazilian environmental agency CONAMA 420/09 (2009) and by the state of São Paulo CETESB (2014). Moreover, Pb, despite its complex migration, was also detected at levels above what is acceptable, given that it has more stringent limits (< 0.01 mg/L) due to being extremely toxic, even at low concentrations (Needleman, 1990; Laidlaw & Taylor, 2011).

It was not possible to determine the arrival time and peak concentration. The data also did not allow for the analytical adjustment proposed by Ogata & Banks (1961) and Lapidus & Amundson (1952). Consequently, the other transport parameters could not be determined.

Tables 3.7 to 3.7 show the results of other authors in determining transport parameters in soils analogous to the soil profile studied here. Similarly, Tables 3.11 to 3.14 present

the results of research on sandstones aimed at determining pollutant transport parameters.

It is noted that the authors present a wide range of values. The determination of complex parameters, such as those related to the transport of contaminants, depends on a series of factors to be considered, including, but not limited to, the use of field or laboratory testing, sampling conditions, the scale used, the tracers employed, the testing methodologies, and the analysis of the results adopted. These factors culminate in a significant number of variables to be considered and, consequently, a high variability of the determined transport parameters.

Table 3.7: Transport parameters ascertained by various researchers using different tracers in similar soils to those utilized in this study.

Reference	Material	Test	Tracer	Parameter	Value
Harleman & Rumer (1963)	Plastic spheres	Column	NaCl	Dh (m^2/s)	2.24×10^{-8} - 8.26×10^{-7}
Wood & Ehrlich (1978)	Sand and gravel	Observation wells	I	α (m)	1.5×10^{-2}
				Transmissivity (m^2/s)	3.2×10^{-3} - 4.4×10^{-3}
Kjeidsen & Christensen (1984)	Sand	Column	Organic matter (COD)	Rd	0.89 - 0.97
			NH_4		0.72 - 0.78
			Na		0.87 - 0.97
			K		0.65 - 0.73
			Ca		1.00
			Mg		0.52 - 0.87
			Fe		0.13 - 0.20
			Mn		0.28 - 0.36
			Zn		0.03
			Cd		0.20 - 0.04
			B		0.20 - 0.7
	Loamy sand	Column	Organic matter (COD)	Rd	0.83 - 0.90
			NH_4		0.30 - 0.45
			Na		0.65 - 0.80
			K		0.23 - 0.43
			Ca		0.87 - 1.00
			Mg		0.48 - 0.56
			Fe		0.11 - 0.15
			Mn		0.20 - 1.00
			Zn		0.02
			Cd		0.02
			B		0.20 - 0.30
	Sand	Leaching	Organic matter (COD)	Rd	0.81 - 0.95
			NH_4		0.54 - 0.76
			Na		0.77 - 0.83
			K		0.55 - 0.67
			Ca		1.00
			Mg		0.27
Batta & Murty (1982)	Alluvial sandy loam	In situ	$CaCl_2$	Dh (m^2/s) - site 1	7.17×10^{-8} - 1.22×10^{-7}
				Dh (m^2/s) - site 2	1.24×10^{-7} - 1.32×10^{-7}
				Dh (m^2/s) - site 3	1.07×10^{-7} - 1.13×10^{-7}
		Column	$CaCl_2$	Dh (m^2/s) - site 1	8.05×10^{-8} - 8.52×10^{-8}
				Dh (m^2/s) - site 2	7.55×10^{-8} - 8.40×10^{-8}
				Dh (m^2/s) - site 3	7.58×10^{-8} - 8.45×10^{-8}

Table 3.8: Transport parameters ascertained by various researchers using different tracers in similar soils to those utilized in this study (continued).

Reference	Material	Test	Tracer	Parameter	Value
Freyberg (1986)	Medium to fine sand	In situ pulse injection	Br and Cl	α (m) k (m/s)	0.49 5.00×10^{-7} - 2.00×10^{-5}
Ceazan et al. (1989)	Sand and gravel	Batch equilibrium	K and NH_4	Kd (ml/g) Rd	0.59 - 0.87 2.00
		In situ tracer		Rd	3.50
Robbins (1989)	Spherical glass beads	Column	Bromide - continuous source	Dh_x (m^2/s) - 1D Dh_x (m^2/s) - 3D Dh_y (m^2/s) - 3D	1.58×10^{-8} - 3.76×10^{-8} 1.15×10^{-8} - 2.58×10^{-8} 3.36×10^{-10} - 1.28×10^{-9}
		Column	Bromide - instantaneous source	Dh_x (m^2/s) - 1D Dh_x (m^2/s) - 3D Dh_y (m^2/s) - 3D	6.93×10^{-9} - 2.3×10^{-8} 4.30×10^{-9} - 1.08×10^{-7} 3.31×10^{-10} - 1.22×10^{-8}
Oostrom et al. (1992)	Homogeneous sand	Column	NaI	α_L (m) α_T (m) Dh_L (m^2/s) Dh_T (m^2/s)	6.30×10^{-4} - 1.20×10^{-3} 3.00×10^{-4} - 4.00×10^{-4} 4.00×10^{-8} 1.39×10^{-8}
		Leaching	NaI	α_L (m)	6.70×10^{-4} - 1.30×10^{-3}
Szecsody et al. (1994)	Fine sand	2-layer system with contrasting hydraulic conductivity	$CaCl_2$ (salt)	α_L (m) Dh_L (m^2/s)	1.10×10^{-3} - 2.90×10^{-3} 3.90×10^{-8} - 1.10×10^{-7}
			Quinoline with 2-Hydroxy-quinoxaline [2-OHQ] (organic)	α_L (m) Dh_L (m^2/s)	2.20×10^{-3} 2.50×10^{-9}
			Salt and organic	α_L (m) Dh_L (m^2/s)	2.10×10^{-3} 2.50×10^{-9}
	Medium sand		Salt	α_L (m) Dh_L (m^2/s)	3.50×10^{-2} - 4.90×10^{-2} 7.20×10^{-6} - 3.00×10^{-5}
			Salt and organic	α_L (m) Dh_L (m^2/s)	3.00×10^{-2} 4.20×10^{-7}
	Fine sand		Salt	α_T (m) Dh_T (m^2/s)	1.70×10^{-4} - 6.30×10^{-4} 5.90×10^{-9} - 2.20×10^{-8}
	Medium sand		Salt	α_T (m) Dh_T (m^2/s)	1.00×10^{-5} - 4.00×10^{-5} 2.70×10^{-8} - 7.90×10^{-8}

Table 3.9: Transport parameters ascertained by various researchers using different tracers in similar soils to those utilized in this study (continued).

Reference	Material	Test	Tracer	Parameter	Value
Seagren et al. (1999)	Artificial porous media - glass beads	Column	Toluene	α (m)	$2.10\times^{-3}$ - 3.00×10^{-3}
Chrysikopoulos et al. (2000)	Sand	Column	Br	Dh (m^2/s) Rd α (m) Kd (ml/g) Pe	2.18×10^{-8} 1.31 2.59×10^{-3} 0.08 2.50
Gaganis et al. (2005)	Artificial porous media - glass-etched pore networks	High-resolution visualization technique	HCl	α (m)	1.50×10^{-3} - 2.50×10^{-3}
Miretzky et al. (2006)	Sandy loam	Column	$NaNO_3$	Dh (m^2/s) Pe α (m)	7.40×10^{-8} - 1.13×10^{-7} 45 - 52 6.70×10^{-5} - 5.80×10^{-4}
Jellali et al. (2010)	Sandy	Column	NH_4	Kd (ml/g) α Pe k (m/s)	0.47 - 0.82 2.00×10^{-3} 500 1.00×10^{-4}
Ojuri & Ola (2010)	Sand	Tank model	Chloride	α (m) Dh (m^2/s) k (m/s)	6.00×10^{-4} - 1.64×10^{-3} 1.60×10^{-6} - 6.90×10^{-6} 5.76×10^{-4}
Lu et al. (2013)	Coarse and fine sands	Column and leaching	Saltwater	k (m/s) α (m)	2.97×10^{-4} - 1.52×10^{-3} 1.82×10^{-3}
Hong & Shackelford (2017)	Backfill (sand, bentonite, zeolite amendment)	Column	Cl^-	Rd Pe Dh (m^2/s)	1.00 - 1.15 0.76 - 8.37 5.00×10^{-10} - 2.09×10^{-9}
		Batch equilibrium	K^+	Kd (ml/g) Rd	0.48 - 5.2 2.65 - 17.9
		Column	K^+	Kd (ml/g) Rd	0.88 - 5.51 4.01 - 18.90
		Batch equilibrium	Zn_2^+	Kd (ml/g) Rd	1.63 - 2.10 6.18 - 7.91
		Column	Zn_2^+	Kd (ml/g) Rd	1.85 - 4.26 6.88 - 15.00

Table 3.10: Transport parameters ascertained by various researchers using different tracers in similar soils to those utilized in this study (continued).

Reference	Material	Test	Tracer	Parameter	Value
Godoy et al. (2018)	Clayey fine sand	Column - small - scale	K	α (m)	$3.00\times^{-3}$ - 1.50
				Kd (ml/g)	4.00×10^{-2} - 16.70
			Cl	α (m)	2.00×10^{-3} - 0.34
				Kd (ml/g)	2.00×10^{-3} - 1.64
			KCl	k (m/s)	4.14×10^{-4}
Podlasek et al. (2020)	Loam	Column	NH_4	Rd	10.50
	Medium sand				3.50
	Silty loam				131.40
	Coarse sand				1.60
	Loam	Column	NO_3	Rd	2.60
	Medium sand				1.00
	Silty loam				11.20
	Coarse sand				1.00
	Medium sand	Batch equilibrium	NH_4	Kd (ml/g)	2.20
	Sandy clayey loam				2.20
	Sandy gravel				1.50
	Gravel				1.10
	Medium sand				2.10
	Clay				5.20
Sousa et al. (2020)	Sand - SM to SP-SM	Column	Organic compounds	Dh (m^2/s)	1.31×10^{-7} - 4.62×10^{-6}
				Rd	1.00×10^{-4} - 1.36×10^{-4}
				α (m) - method 1	5.50×10^{-5} - 1.52×10^{-3}
				α (m) - method 2	$1.00\times^{-4}$ - 3.70×10^{-3}
Sutton et al. (2022)	Tailings sand	Column	Bromide	α (m)	1.50×10^{-3} - 1.30×10^{-2}
				k (m/s)	3.70×10^{-5}

Table 3.11: Transport parameters ascertained by various researchers using different tracers and sandstones.

Reference	Sandstone	Test	Tracer	Parameter	Value
Bourg et al. (1993)	Coventry A	Column	1,1,1- Trichloroethane (TCA)	Rd	1.00 - 1.40
			Trichloroethylene (TCE)	Rd	1.50 - 2.00
			Tetrachloroethylene (TeCE)	Rd	3.00
			NaI	α (m)	9.50×10^{-4}
				Rd	1.20
	Coventry B	Column	KBr	α (m)	4.90×10^{-4}
Mouvet et al. (1993)	Coventry	Batch equilibrium	Trichloroethylene (TCE)	Kd (ml/g)	0.10 - 0.12
			Tetrachloroethylene (TeCE)	Kd (ml/g)	0.27 - 0.34
			TCE and TeCE	Kd (ml/g)	0.13 - 0.30
Schulze-Makuch (1997)	Lower aquifer	Column	KCl	α (m)	1.70×10^{-3}
Thornton et al. (2000a)	Triassic Sherwood	Column	Na	Rd	1.03 - 1.36
			K		1.31 - 2.56
			NH_4		1.28 - 2.52

Table 3.12: Transport parameters ascertained by various researchers using different tracers and sandstones (continued).

Reference	Sandstone	Test	Tracer	Parameter	Value
Thornton et al. (2000b)	Nottingham	Column	Toluene	Rd	1.17
			Trichloroethylene (TCE)	experimental	1.26
			Tetrachloroethylene (TeCE)		1.42
			Total organic carbon (TOC)		1.01
			Chemical oxygen demand (COD)		1.01
			Toluene		1.07
			TCE		1.11
			TeCE		1.72
			TOC		1.00
			COD		1.00
			TOC		1.05
			COD		1.09
			TOC		1.03
			COD		1.08
			Toluene	Rd	2.31
			TCE	theroretical	1.82
			TeCE		2.64
			Toluene		2.38
			TCE		1.87
			TeCE		2.73
			Toluene	Kd (ml/g)	0.046
			TCE	experimental	0.070
			TeCE		0.114
			TOC		0.003
			COD		0.003
			Toluene		0.018
			TCE		0.028
			TeCE		0.107
			TOC		0.013
			COD		0.024
			TOC		0.008
			COD		0.023
			Toluene	Kd (ml/g)	0.355
			TCE	theroretical	0.223
			TeCE		0.445
			Toluene		0.355
			TCE		0.223
			TeCE		0.445

Table 3.13: Transport parameters ascertained by various researchers using different tracers and sandstones (continued).

Reference	Sandstone	Test	Tracer	Parameter	Value
Thornton et al. (2000b)	West Midlands	Column	COD	Rd -	1.21
			Benzene	experimental	1.56
			Toluene		1.03
			DCB		1.68
			TCB		2.99
			TCA		1.65
			TeCA		1.114
			TCE		1.65
			TeCE		1.42
			Naphthalene		3.04
			Benzene	Rd -	1.09
			Toluene	theroretical	1.24
			DCB		1.34
			TCB		2.09
			HCB		4.95
			TCA		1.15
			TeCA		1.09
			TCE		1.15
			TeCE		1.3
			Naphthalene		2.31
			Hexachlorobutadiene (HCBD)		5.36
			Lindrane		3.74
			Dieldrin		26.3
			COD	Kd (ml/g)	0.054
			Benzene	experimental	0.144
			Toluene		0.0077
			DCB		0.175
			TCB		0.514
			TCA		0.168
			TeCA		0.038
			TCE		0.08
			TeCE		0.108
			Naphthalene		0.527
			Benzene	Kd (ml/g)	0.025
			Toluene	theroretical	0.063
			DCB		0.089
			TCB		0.281
			HCB		1.02
			TCA		0.04
			TeCA		0.023
			TCE		0.039
			TeCE		0.078
			Naphthalene		0.338
			HCBD		1.126
			Lindrane		0.966
			Dieldrin		6.531

Table 3.14: Transport parameters ascertained by various researchers using different tracers and sandstones (continued).

Reference	Sandstone	Test	Tracer	Parameter	Value
Shepherd et al. (2002)	Birmingham Triassic	Batch equilibrium	Artificial Triassic groundwater	Rd Kd (ml/g)	1.70 - 9.00 0.15 - 1.45
Streetly et al. (2002)	Triassic	In situ slug injection	Amino-G-acid Fluorescein	α (m) - test 1 Rd - test 1 Rd - test 2	2.00×10^{-2} - 3.00×10^{-2} 1.00 1.40
			Amino-G-acid Fluorescein	α (m) - test 3 Rd - test 3 Rd - test 3	1×10^{-2} - 2.00 1.00 1.00 - 1.50
Neukum et al. (2014)	Herzogenrather Obernkirchner Solling	Column	Silver nanoparticles (AgNP) $NaNO_3$ $Ca(NO_3)_2$	α (m) α (m) α (m)	6.90×10^{-4} - $9.80 \times 10{-}3$ 1.33×10^{-3} 6.88×10^{-4} - 5.82×10^{-3}
Honari et al. (2016)	Berea Donnybrook	Core flood apparatus	$CH_4{-}CO_2$	α (m) α (m)	3.60×10^{-4} - 2.63×10^{-3} 8.50×10^{-4} - 5.20×10^{-3}
Malov (2016)	Upper part of the Vendian strata	In situ	Uranium	Rd	20.00 - 28.00
Pini et al. (2016)	Berea	Pulse-tracer with X-ray computed tomography (CT) and Positron emission tomography (PET)	$[11C]NaHCO_3$	α_L (m) 1D α_L (m) - multilayer model α_L (m) - tuned streamtubes	1.24×10^{-3} - 1.68×10^{-3} 1.04×10^{-3} - 1.41×10^{-3} 7.90×10^{-4} - 1.15×10^{-3}
Malov & Zykov (2020)	Upper part of the Vendian strata	Extraction by centrifuge	Uranium	Rd	10.73
Latrille et al. (2021)	Clayey	Column	H, I, Cl Sr	α (m) Kd (ml/g)	2.40×10^{-3} - $3.30\times^{-3}$ 6.44

3.4 Conclusions

This study conducted column tests to determine hydraulic and contaminant transport parameters in materials commonly found in tropical environments. Through a non-reactive saline tracer (NaCl) in a sandy tropical soil with low clay content and a sandstone utilizing NaCl, Mn, Ni, and Pb. Remarkable points include:

(i) The hydraulic conductivity decreased with depth and with increased confinement due to the reduction in porosity. Using a saline tracer in the soil reduced its permeability and had little effect on the sandstone.

(ii) Permeability, tortuosity, flow lines, and interconnected pores significantly influenced the determination of dispersivity and hydrodynamic dispersion, essential parameters in advective-dispersive transport.

(iii) The retardation factor indicates that the velocity of the center of mass of the contamination plume moves closely aligns with the water flow, with a slight delay evidenced by $1 < \mathrm{Rd} < 2.7$, indicating slight sorption of the tracer by the soil and sandstone, the former due to laterization and the latter due to the presence of clay minerals from the smectite group. Nevertheless, the partition coefficient, approaching zero, implies that nearly all tracers are dissolved in the percolating fluid.

(iv) Ni and especially Mg demonstrated an ability to spread even in alkaline environments, unlike Pb, which did not demonstrate mobile. This highlights the risk to which the environment is exposed due to heavy metals.

3.5 Supplementary material A – Data validation

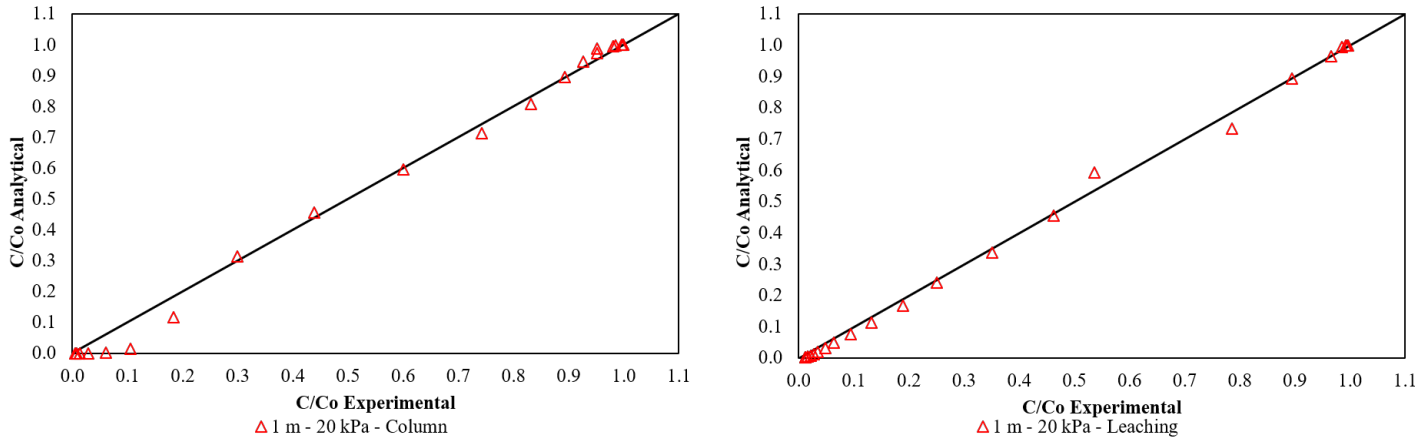

Figure 3.67: Validation of the fit of the analytical curve with the experimental column and leaching data from the soil at 1 m depth consolidated at 20 kPa.

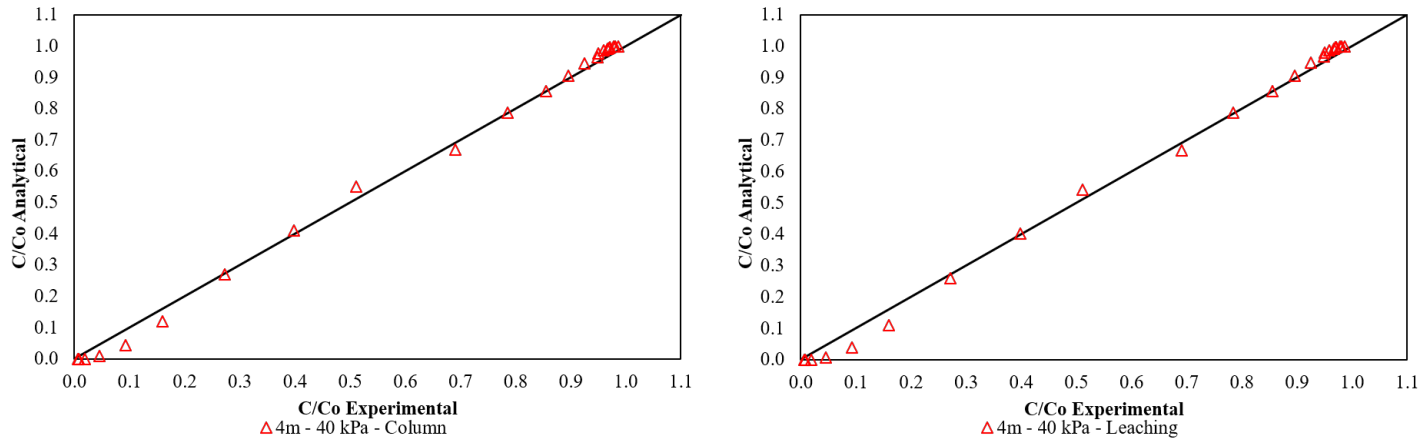

Figure 3.68: Validation of the fit of the analytical curve with the experimental column and leaching data from the soil at 4 m depth consolidated at 40 kPa.

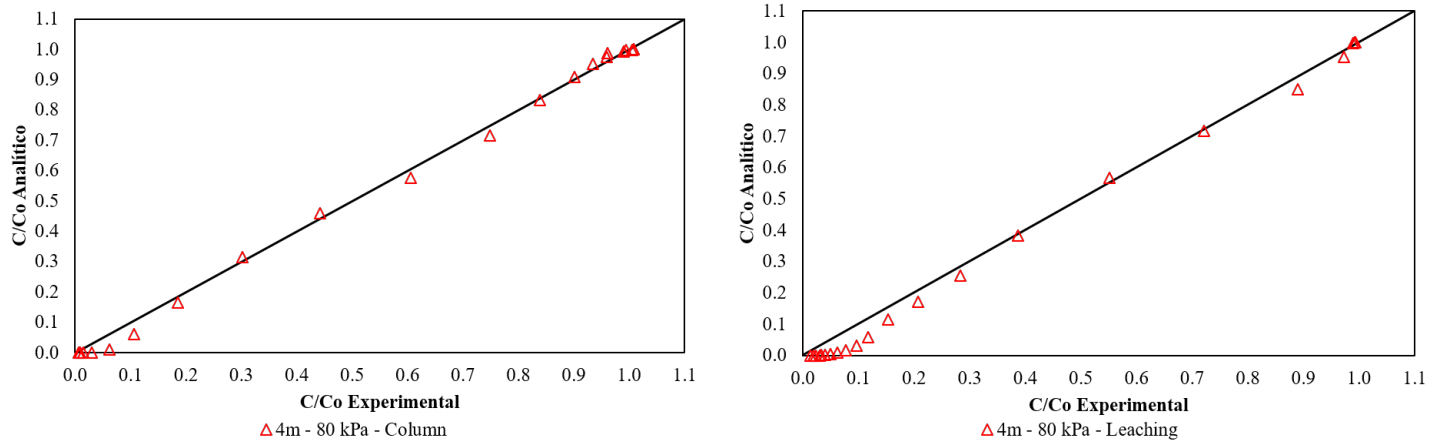

Figure 3.69: Validation of the fit of the analytical curve with the experimental column and leaching data from the soil at 4 m depth consolidated at 80 kPa.

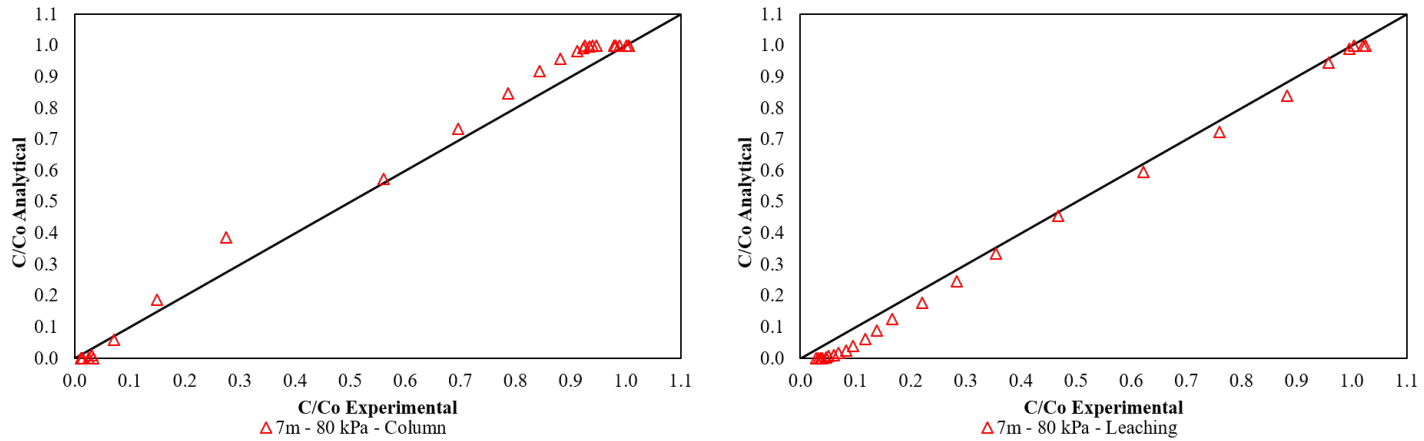

Figure 3.70: Validation of the fit of the analytical curve with the experimental column and leaching data from the soil at 7 m depth consolidated at 80 kPa.

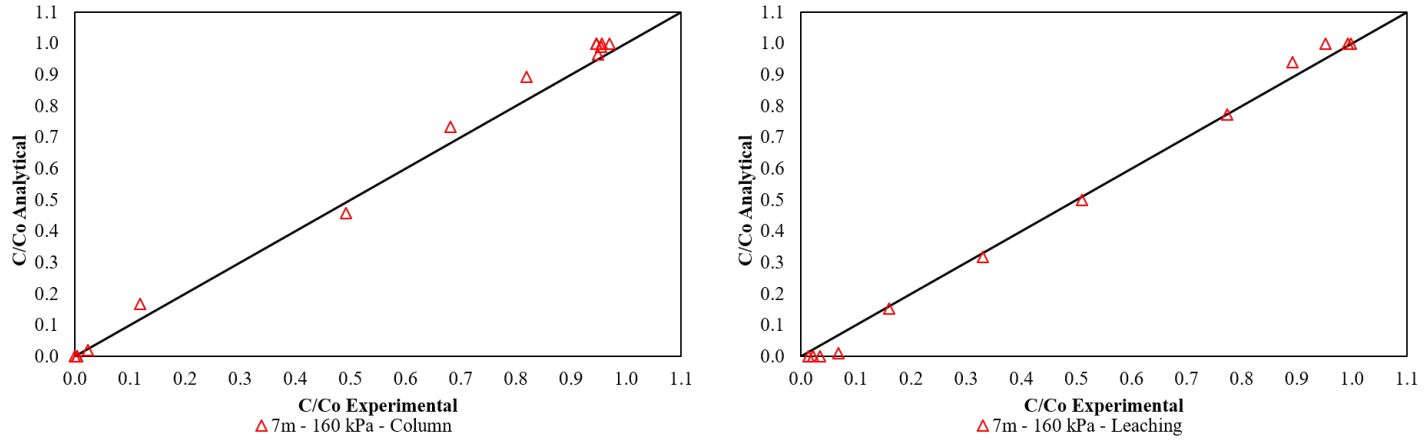

Figure 3.71: Validation of the fit of the analytical curve with the experimental column and leaching data from the soil at 7 m depth consolidated at 160 kPa.

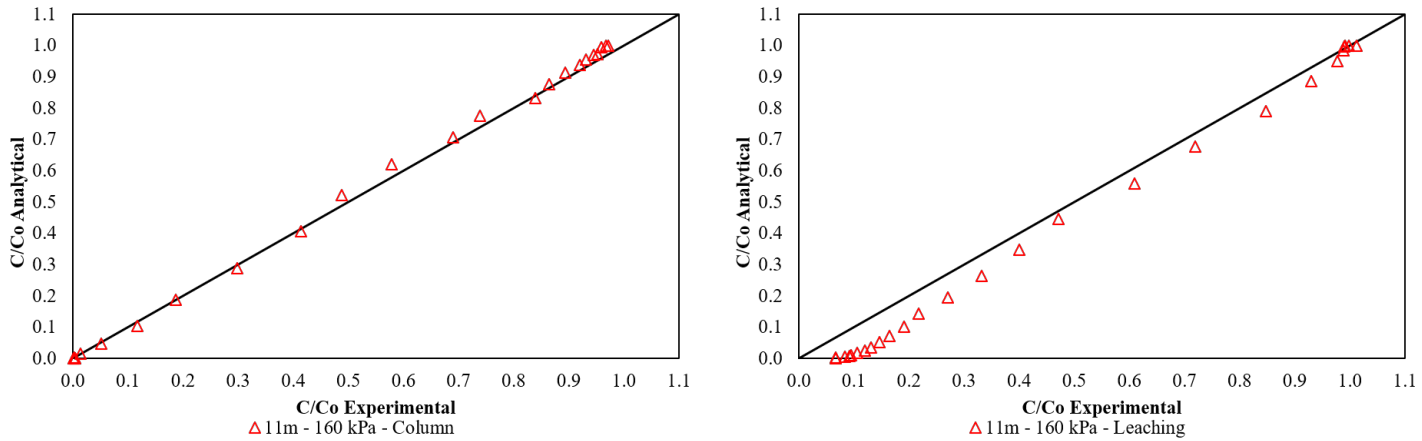

Figure 3.72: Validation of the fit of the analytical curve with the experimental column and leaching data from the soil at 11 m depth consolidated at 160 kPa.

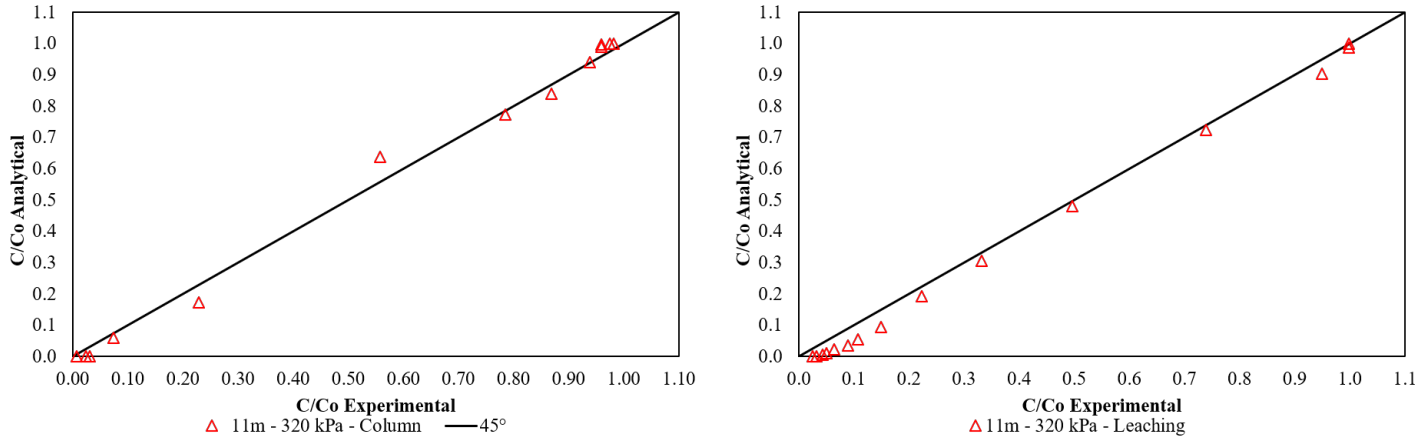

Figure 3.73: Validation of the fit of the analytical curve with the experimental column and leaching data from the soil at 11 m depth consolidated at 320 kPa.

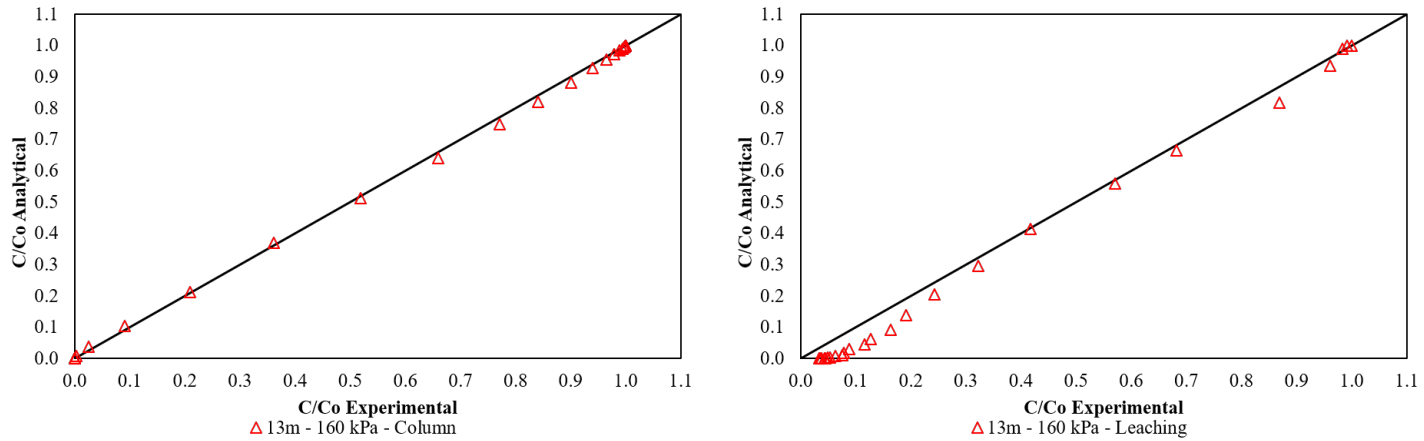

Figure 3.74: Validation of the fit of the analytical curve with the experimental column and leaching data from the soil at 13 m depth consolidated at 160 kPa.

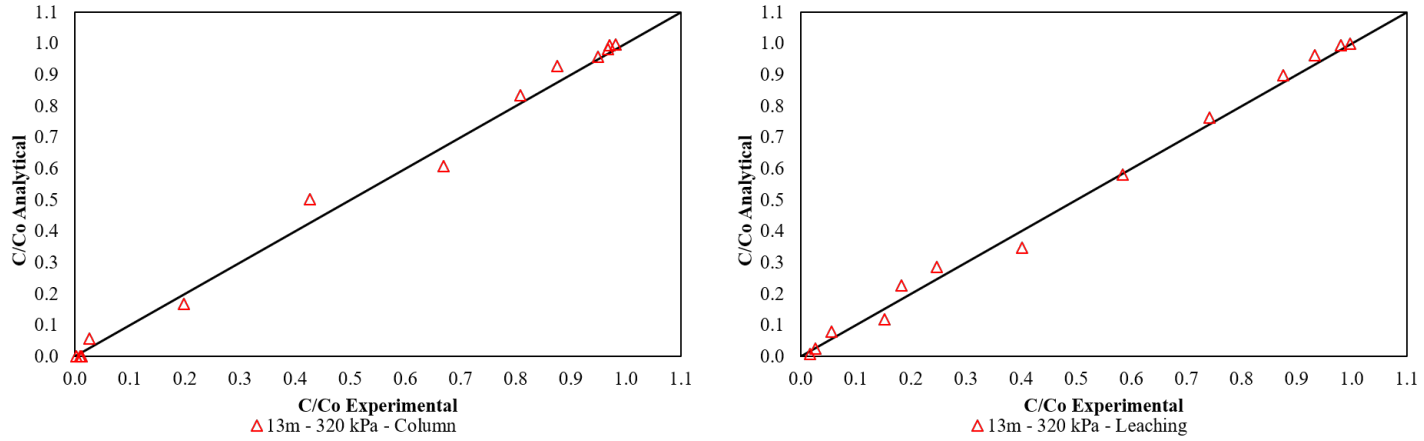

Figure 3.75: Validation of the fit of the analytical curve with the experimental column and leaching data from the soil at 13 m depth consolidated at 320 kPa.

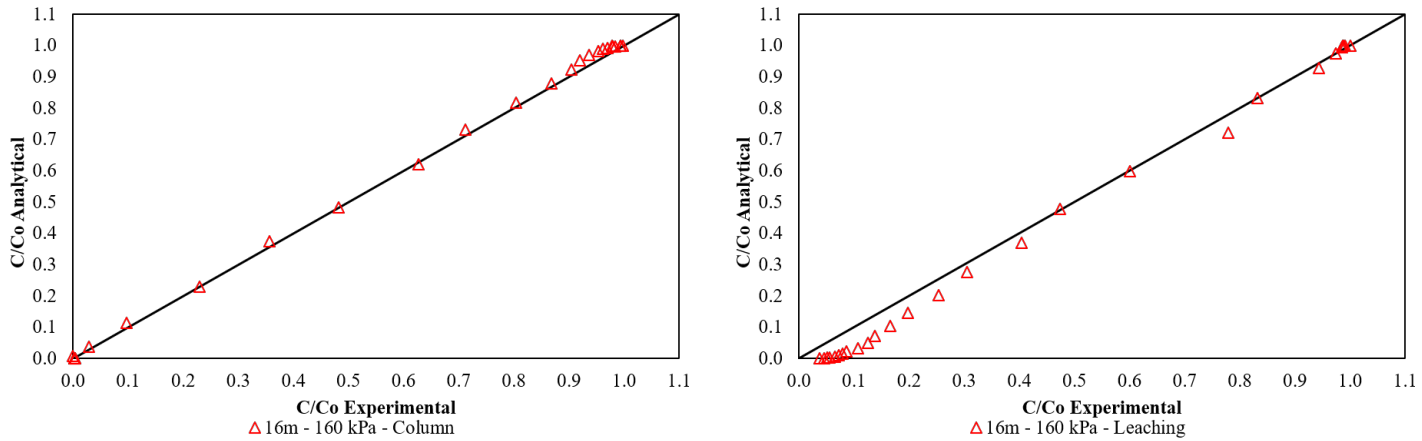

Figure 3.76: Validation of the fit of the analytical curve with the experimental column and leaching data from the soil at 16 m depth consolidated at 160 kPa.

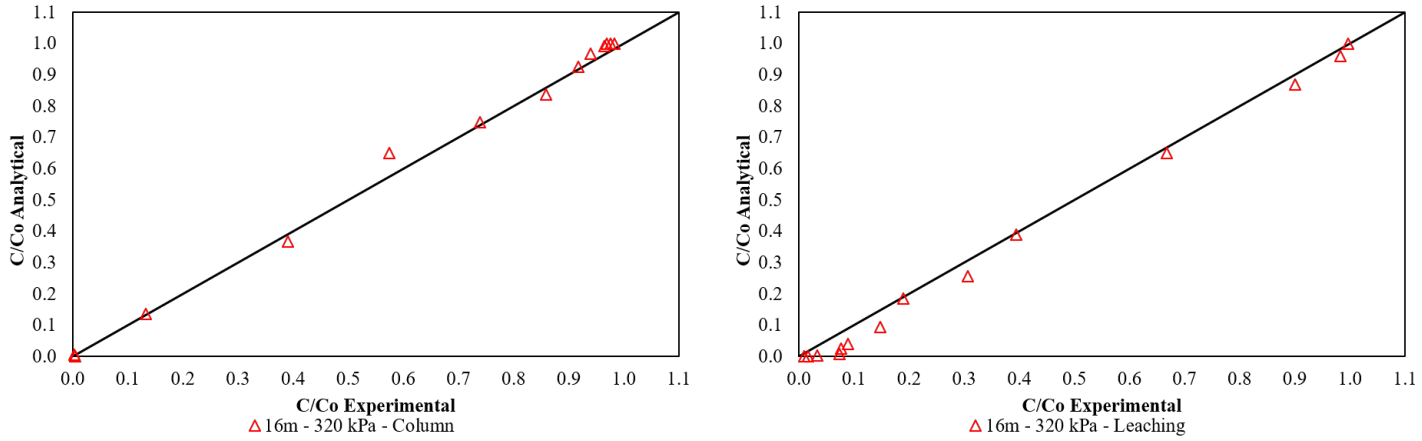

Figure 3.77: Validation of the fit of the analytical curve with the experimental column and leaching data from the soil at 7 m depth consolidated at 320 kPa.

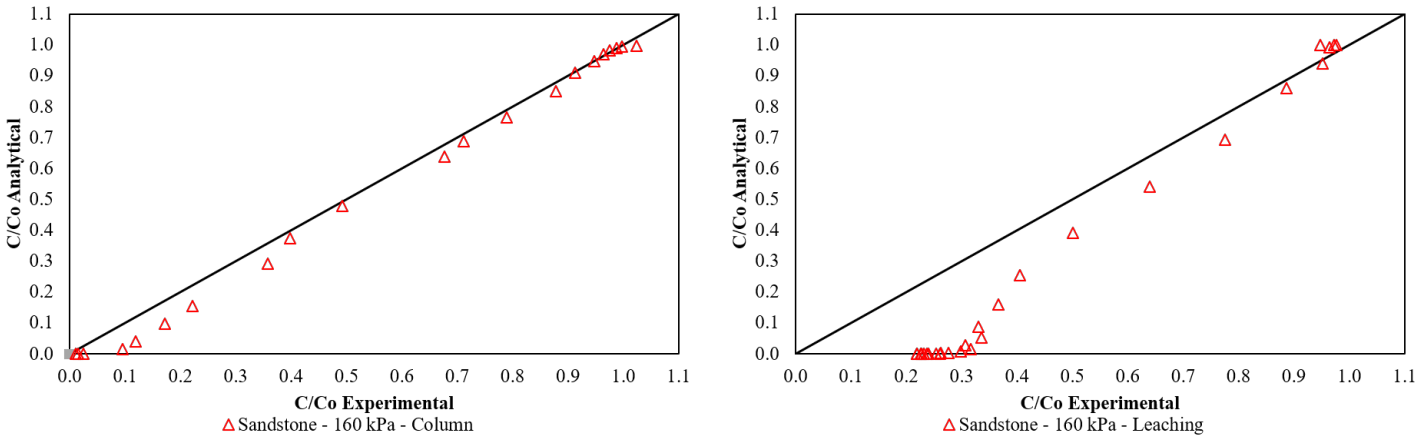

Figure 3.78: Validation of the fit of the analytical curve with the experimental column and leaching data from the sandstone consolidated at 160 kPa.

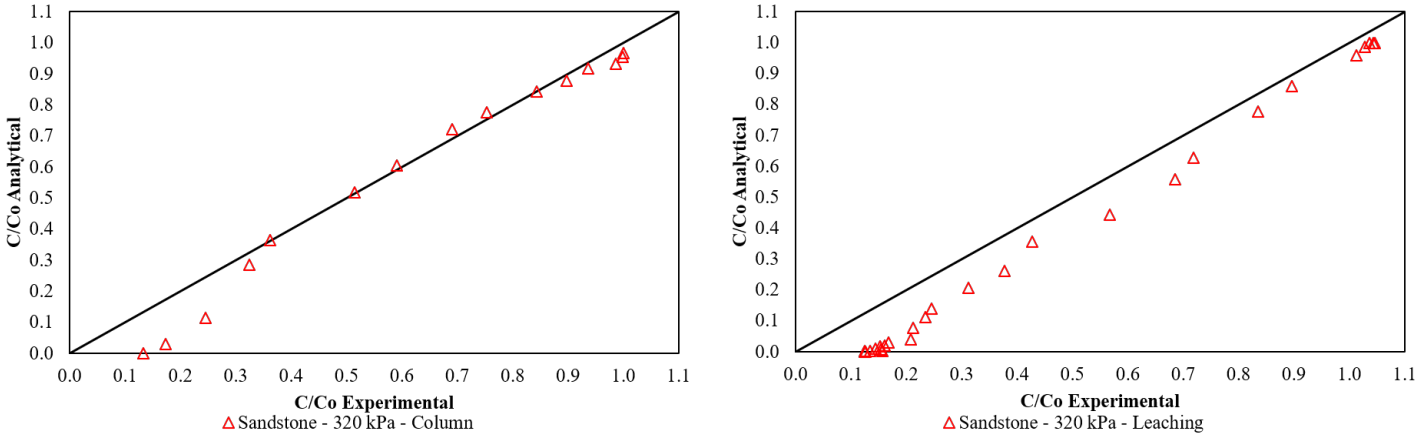

Figure 3.79: Validation of the fit of the analytical curve with the experimental column and leaching data from the sandstone consolidated at 320 kPa.

3.6 Supplementary material B – Box plot data

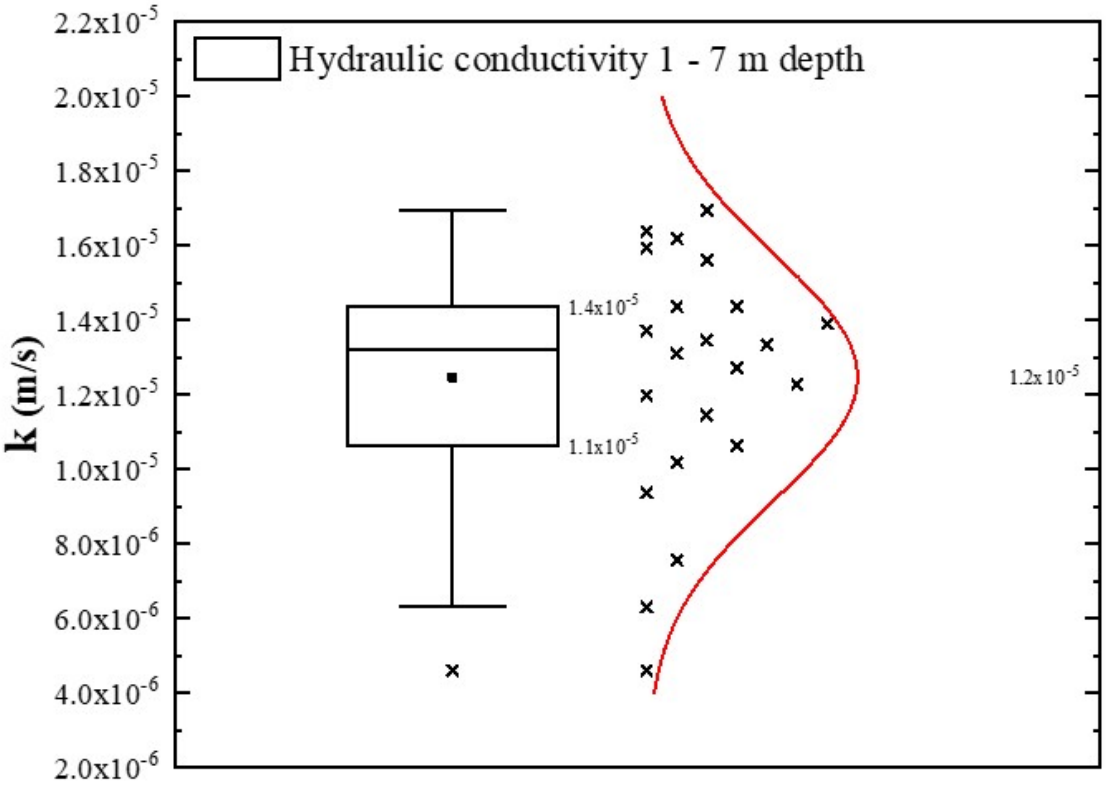

Figure 3.80: Box plot with soil hydraulic conductivity values at 1, 4 and 7 m depth.

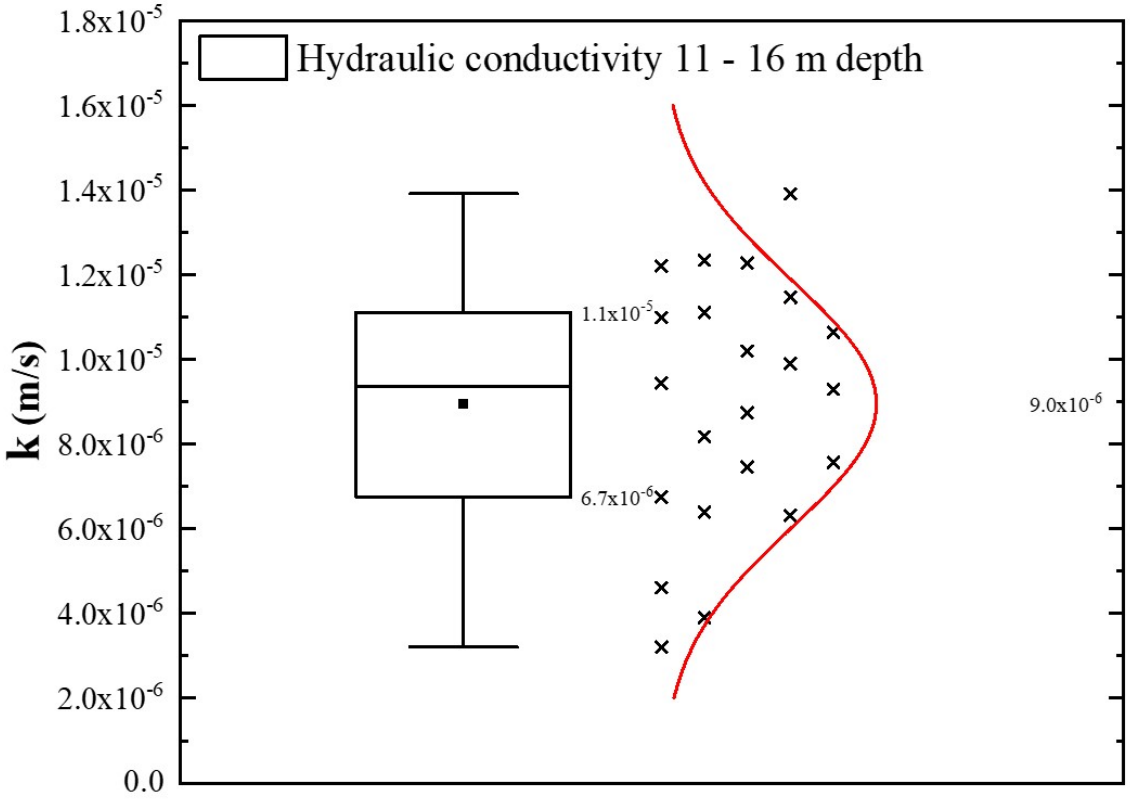

Figure 3.81: Box plot with soil hydraulic conductivity values at 11, 13 and 16 m depth.

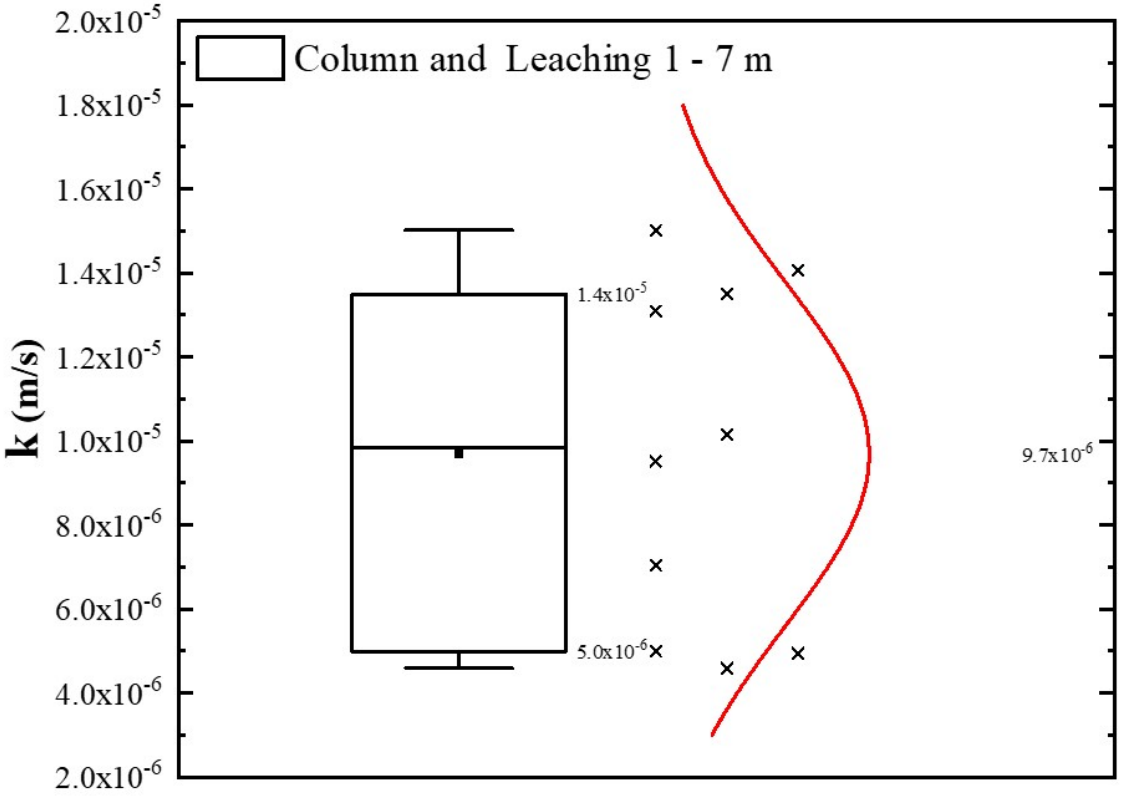

Figure 3.82: Box plot of the hydraulic conductivity of the soil from 1 to 7 m depth, considering the column and leaching tests.

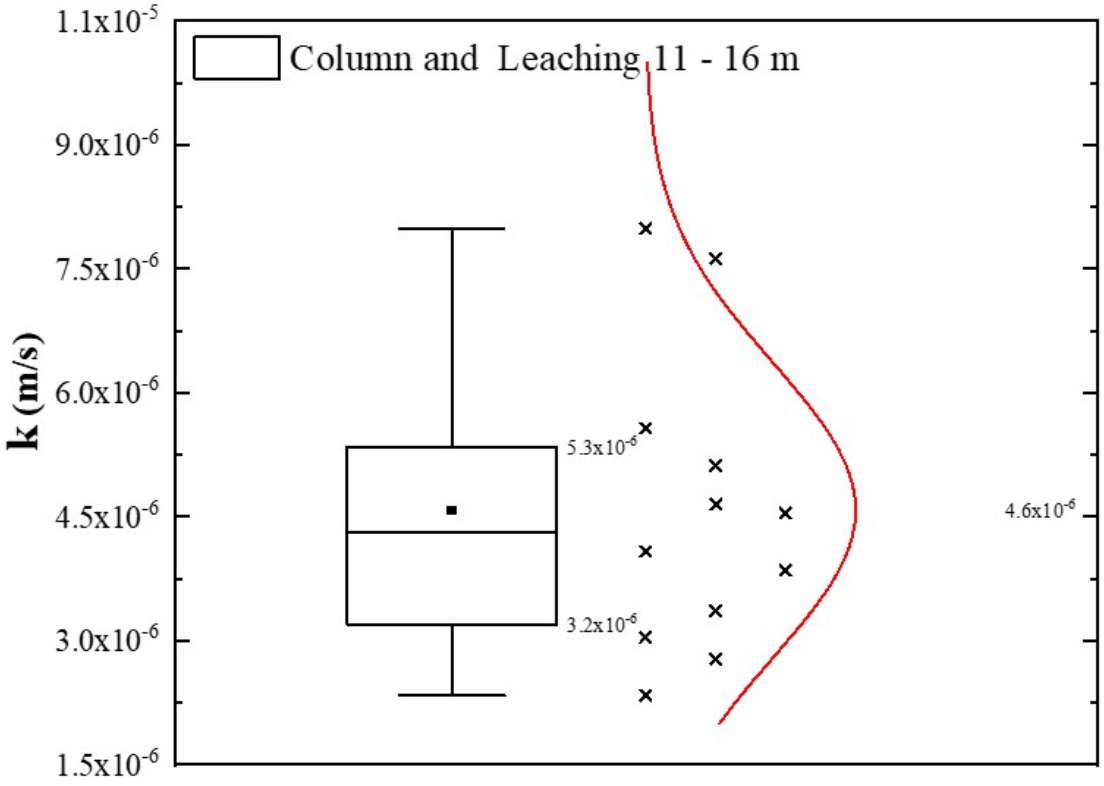

Figure 3.83: Box plot of the hydraulic conductivity of the soil from 11 to 16 m depth, considering the column and leaching tests.

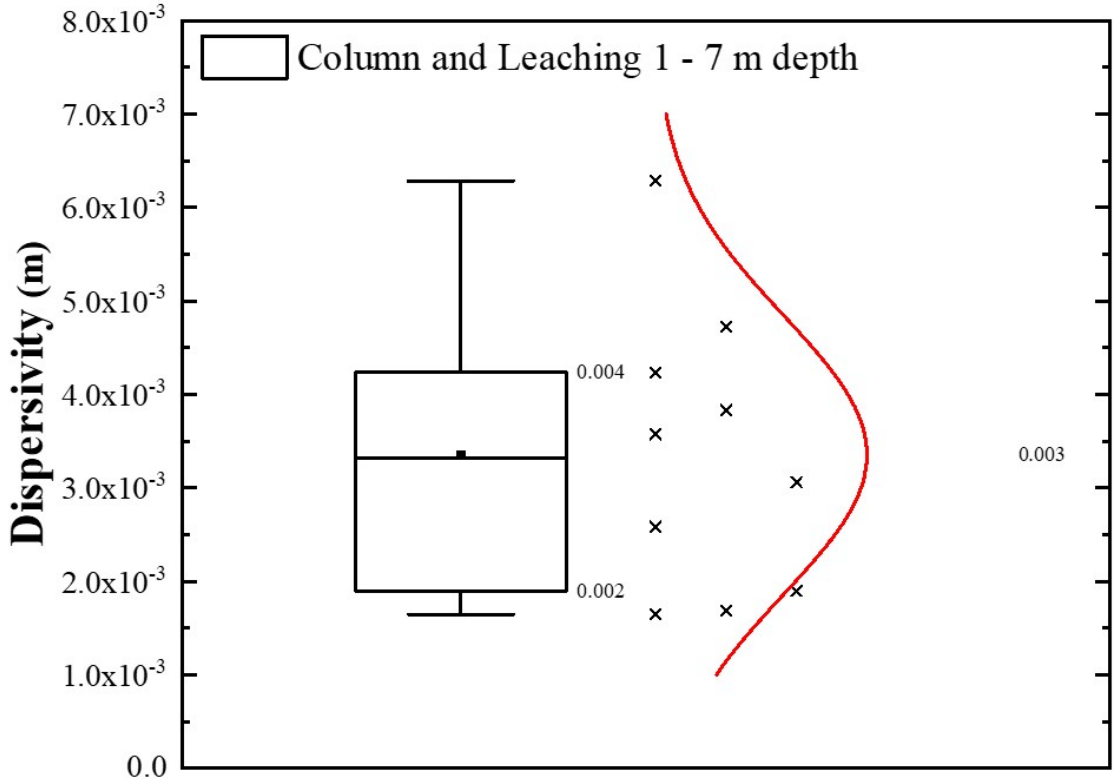

Figure 3.84: Box plot with soil dispersivity values from 1 to 7 m depth using column and leaching data.

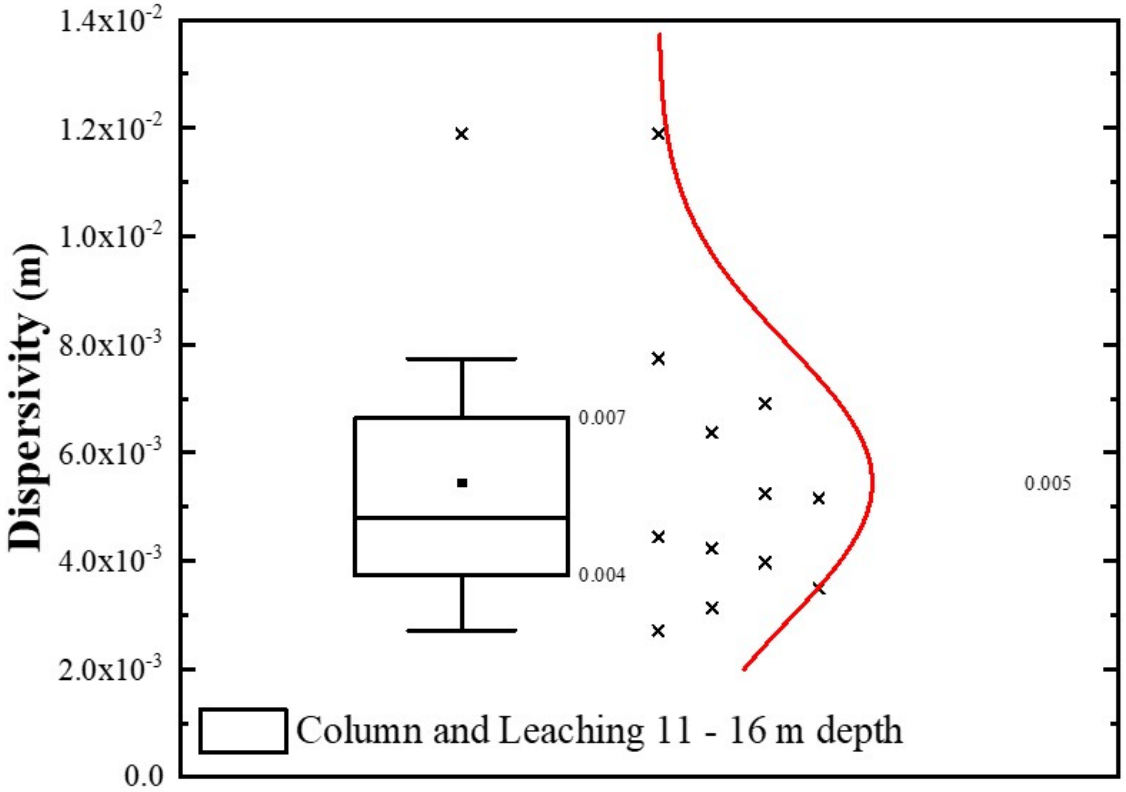

Figure 3.85: Box plot with soil dispersivity values from 11 to 16 m depth using column and leaching data.

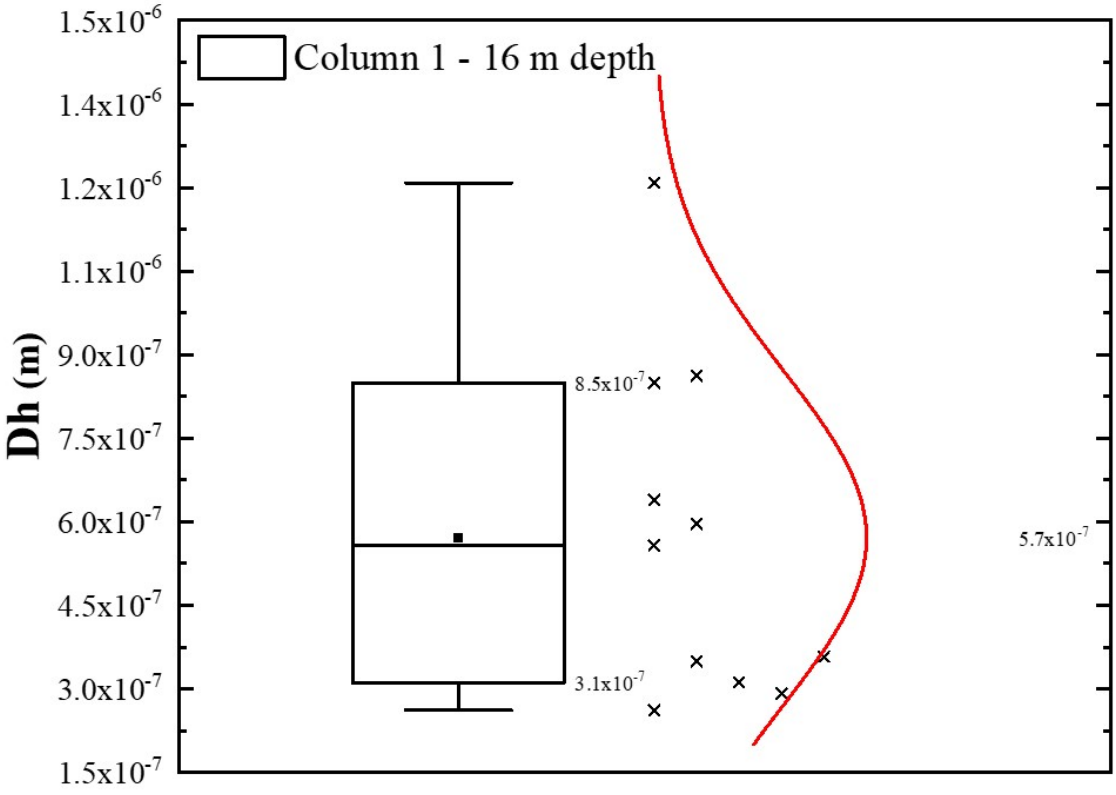

Figure 3.86: Box plot of the soil profile's hydrodynamic dispersion values considering the column test.

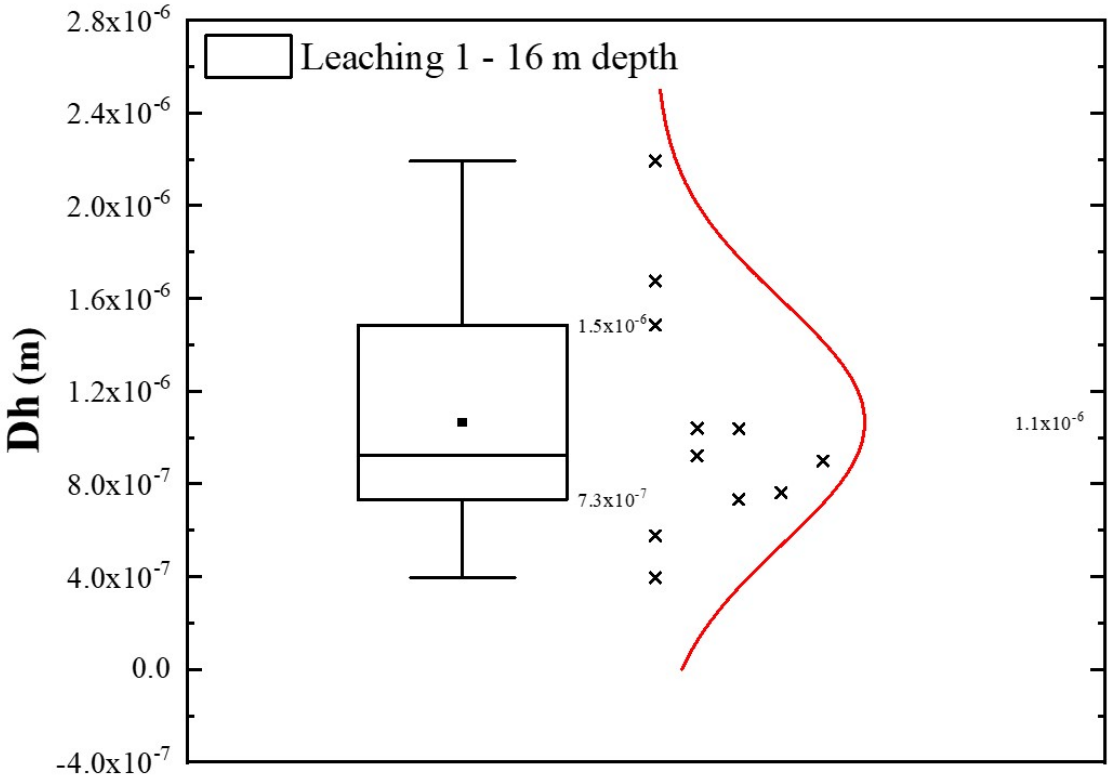

Figure 3.87: Box plot of the soil profile's hydrodynamic dispersion values considering the leaching test.

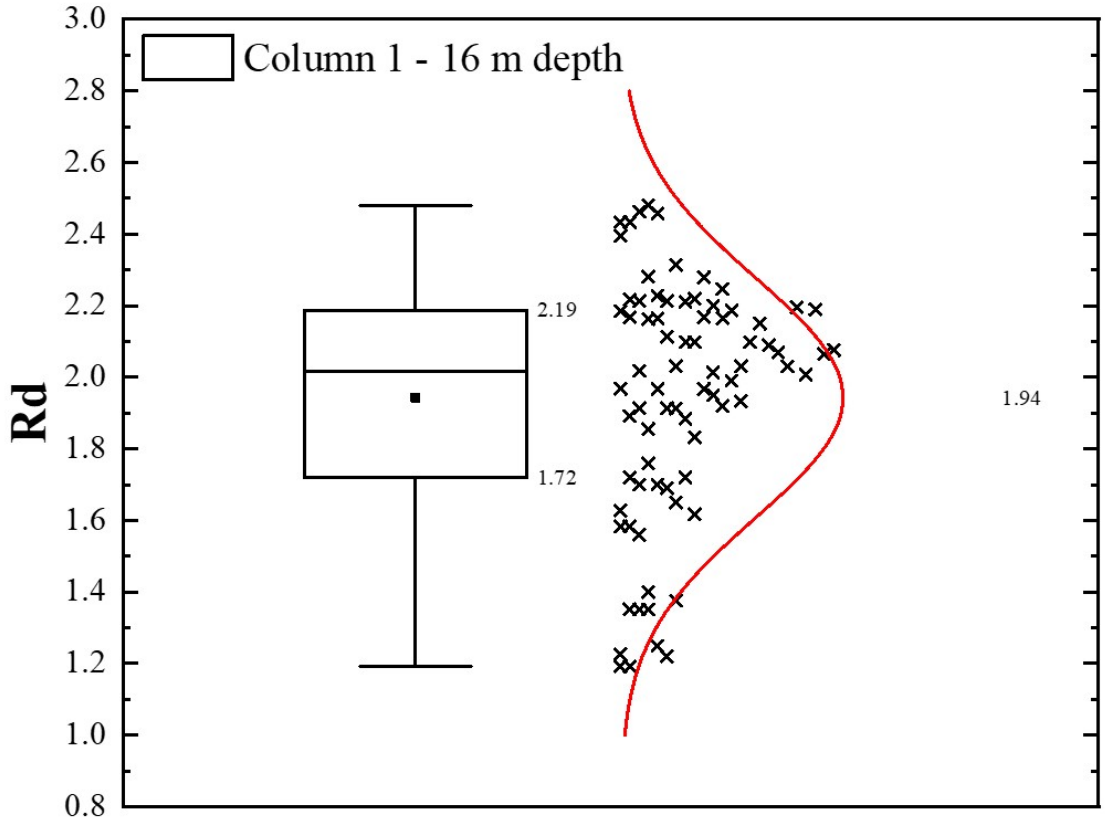

Figure 3.88: Box plot with the retardation factor values from the column test for the soil profile.

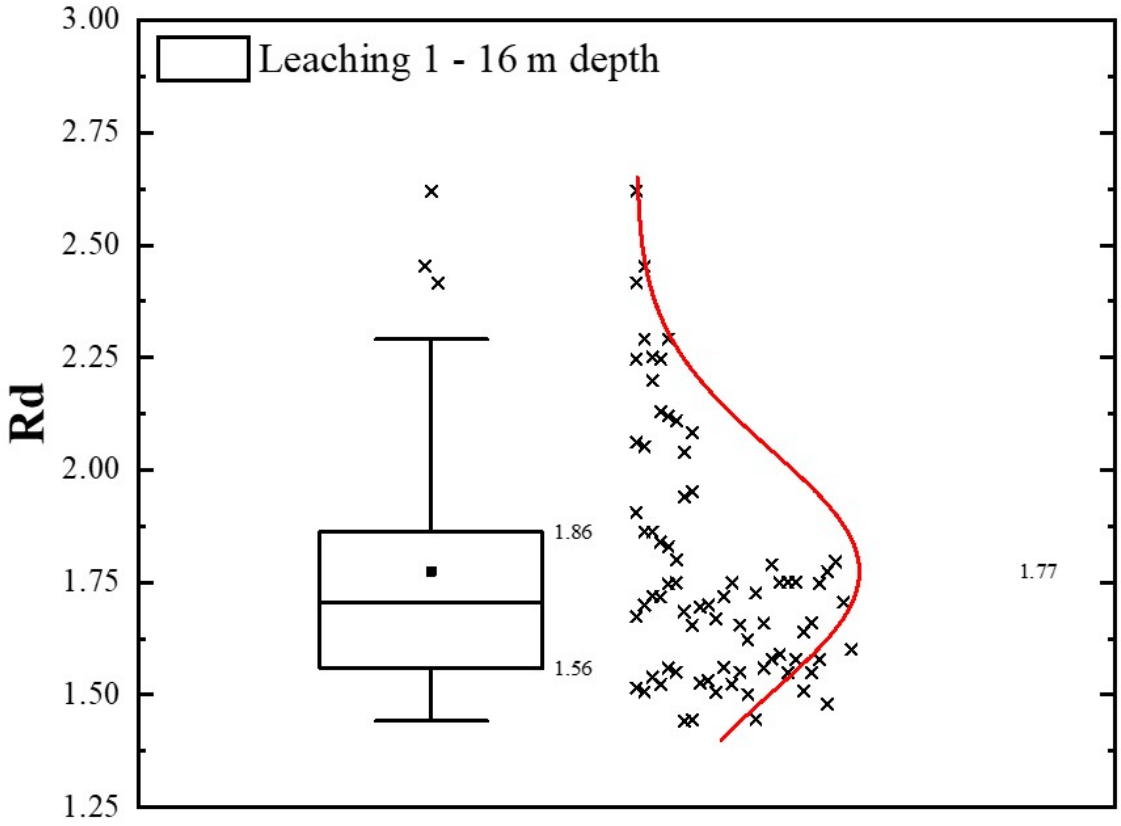

Figure 3.89: Box plot with the retardation factor values from the leaching test for the soil profile.

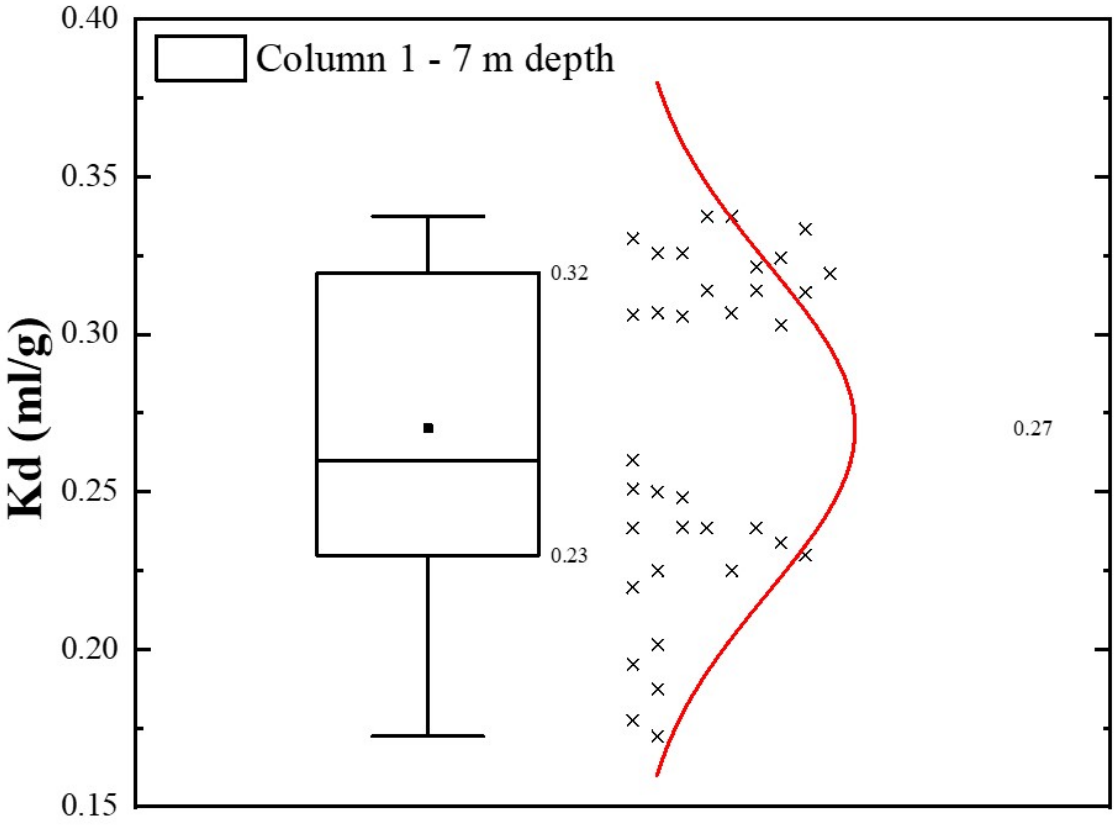

Figure 3.90: Box plot with the partition coefficient values considering the column test for soil from 1 to 7 m depth.

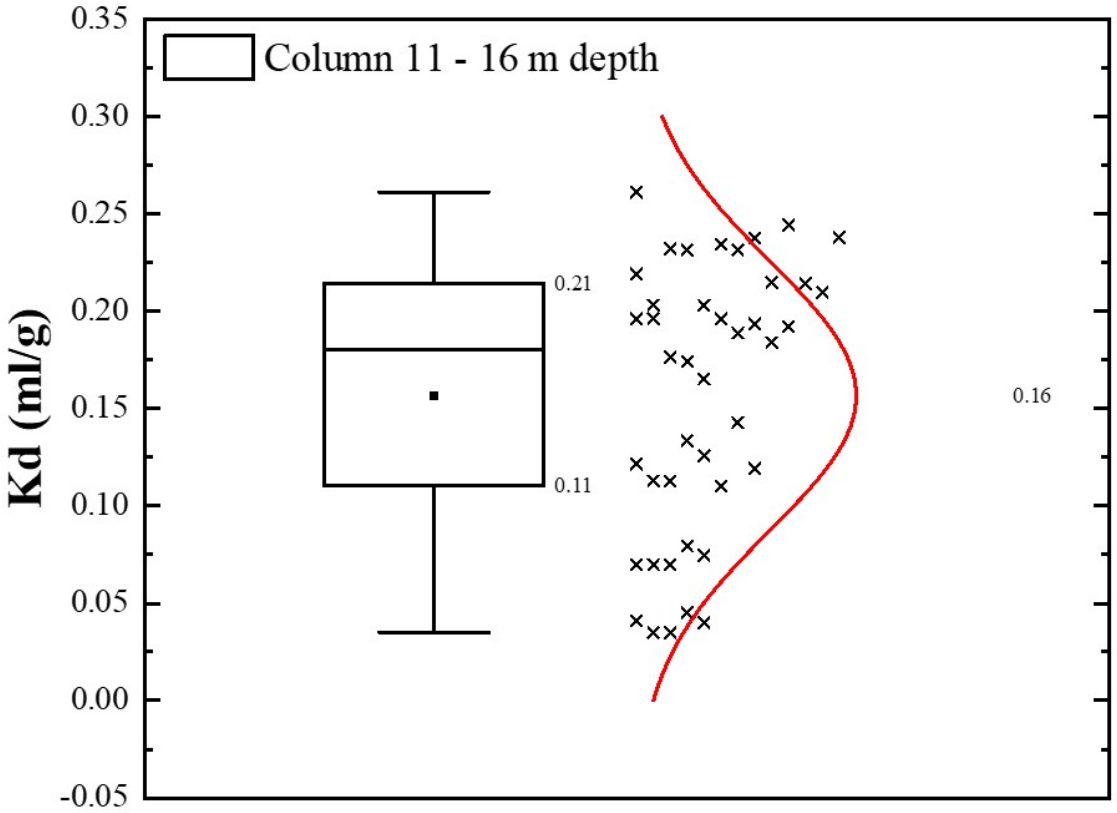

Figure 3.91: Box plot with the partition coefficient values considering the column test for soil from 11 to 16 m depth

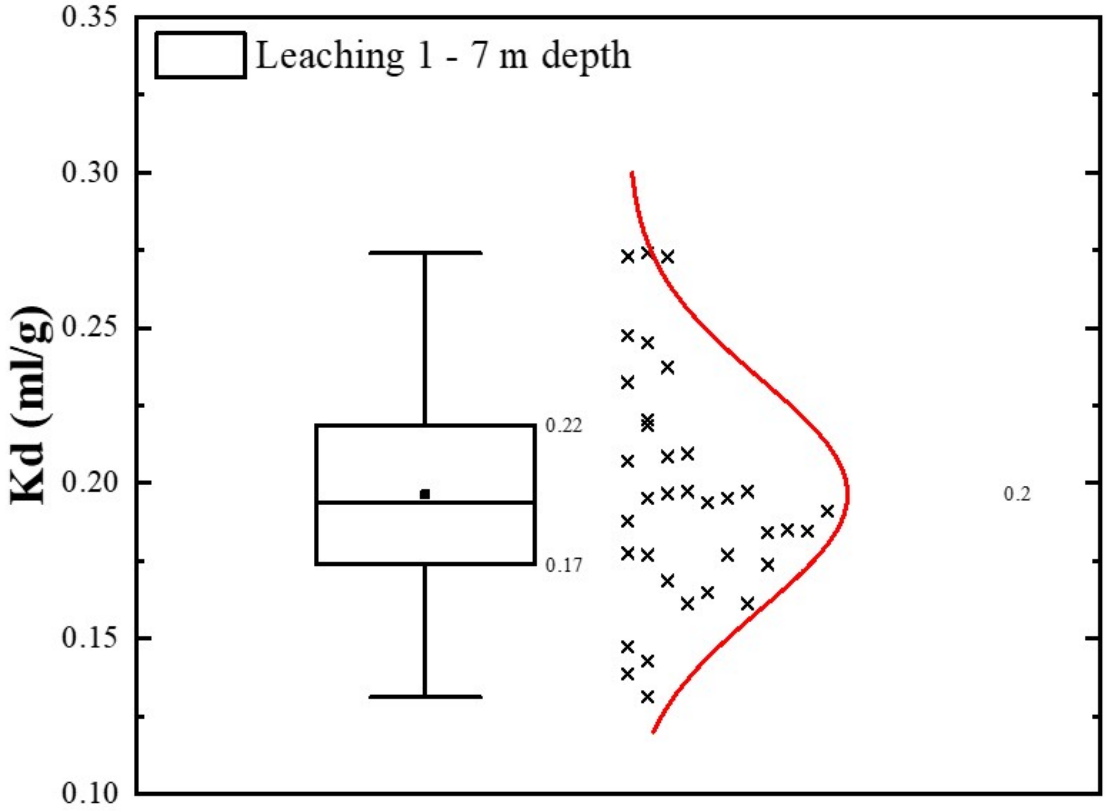

Figure 3.92: Box plot with the partition coefficient values considering the leaching test for soil from 1 to 7 m depth.

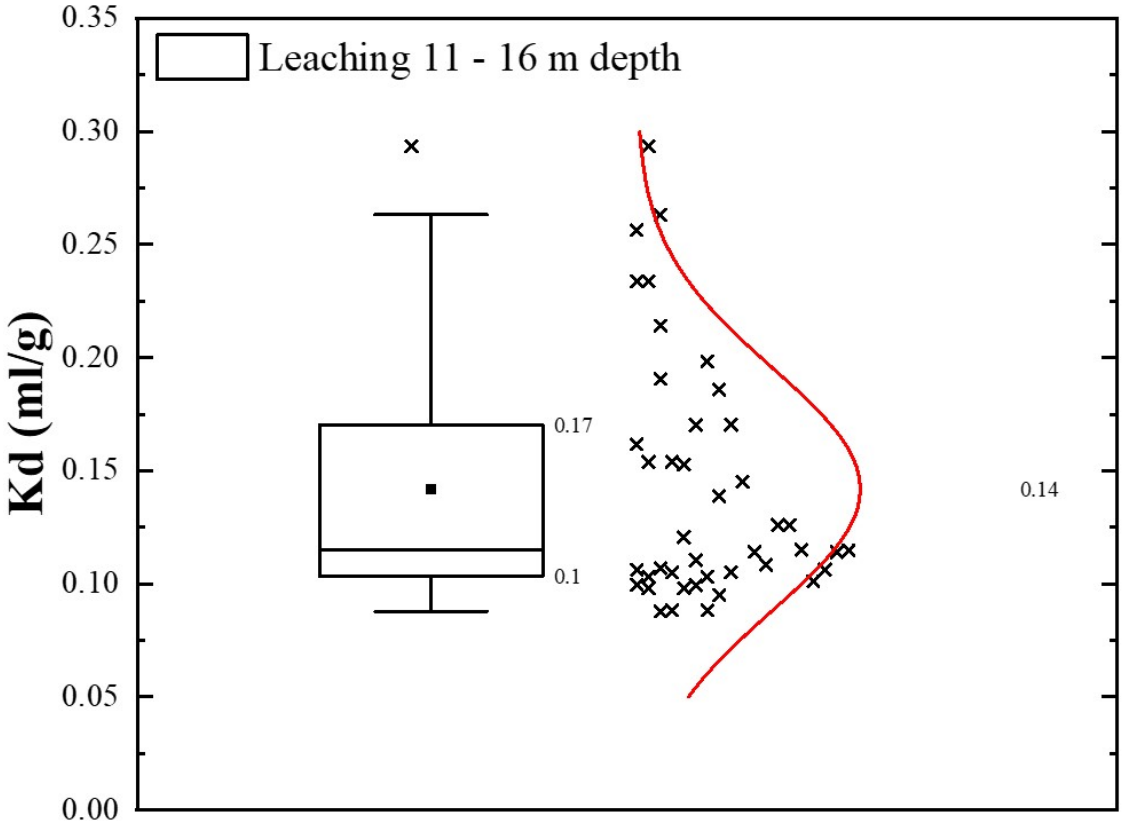

Figure 3.93: Box plot with the partition coefficient values considering the leaching test for soil from 11 to 16 m depth.

References

ABREMA (2023). Panorama dos Resíduos Sólidos no Brasil 2023. *Associação Brasileira de Resíduos e Meio Ambiente*.

Abunama, T., Moodley, T., Abualqumboz, M., Kumari, S., & Bux, F. (2021). Variability of leachate quality and polluting potentials in light of leachate pollution index (LPI) – A global perspective. *Chemosphere*, 282(June), 131119.

Amadi, A. & Odedede, O. (2021). Attenuation of contaminants in landfill leachate by lateritic soil enhanced with bentonite. *Geomechanics and Geoengineering*, 16(5), 348–358.

Appelo, C. & Postma, D. (2004). *Geochemistry, groundwater and pollution*. Taylor & Francis, 2 edition.

Aral, M. M. & Liao, B. (1996). Analytical solutions for two-dimensional transport equation with time-dependent dispersion coefficients. *Journal of Hydrologic Engineering*, 1(1), 20–32.

ASTM D4874 (2014). Standard test method for leaching solid material in a column apparatus. *ASTM International, West Conshohocken, PA*, (Reapproved 2014), 1–8.

ASTM D5084 (2016). Standard test methods for measurement of hydraulic conductivity of saturated porous materials using a flexible wall permeameter. *ASTM International, West Conshohocken, PA*, (pp. 1–24).

ASTM D7100 (2011). Standard test method for hydraulic conductivity compatibility testing of soils with aqueous solutions. *ASTM International, West Conshohocken, PA*, (Reapproved 2020), 1–17.

Basilici, G., Bo, P. F. D., & de Oliveira, E. F. (2016). Distribution of palaeosols and deposits in the temporal evolution of a semiarid fluvial distributary system (Bauru Group, Upper Cretaceous, SE Brazil). *Sedimentary Geology*, 341, 245–264.

Batta, R. & Murty, V. (1982). In situ determination of the hydrodynamic dispersion coefficient and its correlation under laboratory and field conditions. *Journal of Hydrology*, 59(1-2), 139–147.

Bear, J. & Cheng, A. H.-D. (2010). *Modeling groundwater flow and contaminant transport*. Springer Science & Business Media.

Blackwell, R., Rayne, J., & Terry, W. (1959). Factors Influencing the Efficiency of Miscible Displacement. *Transactions of the AIME*, 217(01), 1–8.

Bohnsack, D., Potten, M., Freitag, S., Einsiedl, F., & Zosseder, K. (2021). Stress sensitivity of porosity and permeability under varying hydrostatic stress conditions for different carbonate rock types of the geothermal Malm reservoir in Southern Germany. *Geothermal Energy*, 9(1), 15.

Bourg, A. C., Degranges, P., Mouvet, C., & Sauty, J. P. (1993). Migration of chlorinated hydrocarbon solvents through Coventry sandstone rock columns. *Journal of Hydrology*, 149(1-4), 183–207.

Boving, T. B. & Grathwohl, P. (2001). Tracer diffusion coefficients in sedimentary rocks: correlation to porosity and hydraulic conductivity. *Journal of Contaminant Hydrology*, 53, 85–100.

Bruderer, C. & Bernabé, Y. (2001). Network modeling of dispersion: Transition from Taylor dispersion in homogeneous networks to mechanical dispersion in very heterogeneous ones. *Water Resources Research*, 37(4), 897–908.

Brusseau, M., Rao, P., Jessup, R., & Davidson, J. (1989). Flow interruption: a method for investigating sorption nonequilibrium. *Journal of Contaminant Hydrology*, 4(3), 223–240.

Brusseau, M. L., Hu, Q., & Srivastava, R. (1997). Using flow interruption to identify factors causing nonideal contaminant transport. *Journal of Contaminant Hydrology*, 24(3-4), 205–219.

Carberry, J. J. & Bretton, R. H. (1958). Axial dispersion of mass in flow through fixed beds. *AIChE Journal*, 4(3), 367–375.

Carey, G. R., McBean, E. A., & Feenstra, S. (2018). Estimating transverse dispersivity based on hydraulic conductivity. *Environmental Technology and Innovation*, 10, 36–45.

Ceazan, M. L., Thurman, E. M., & Smith, R. L. (1989). Retardation of ammonium and potassium transport through a contaminated sand and gravel aquifer: the role of cation exchange. *Environmental Science and Technology*, 23(11), 1402–1408.

CETESB (2014). Valores orientadores para solo e água subterrânea no estado de São Paulo 2014. *Companhia Ambiental do Estado de São Paulo*.

Chapuis, R. P. (2012). Predicting the saturated hydraulic conductivity of soils: a review. *Bulletin of Engineering Geology and the Environment*, 71(3), 401–434.

Chotpantarat, S., Ong, S. K., Sutthirat, C., & Osathaphan, K. (2011). Competitive sorption and transport of Pb2+, Ni2+, Mn2+, and Zn2+ in lateritic soil columns. *Journal of Hazardous Materials*, 190(1-3), 391–396.

Christensen, T. H., Kjeldsen, P., Bjerg, P. L., Jensen, D. L., Christensen, J. B., Baun, A., Albrechtsen, H. J., & Heron, G. (2001). Biogeochemistry of landfill leachate plumes. *Applied Geochemistry*, 16(7-8), 659–718.

Chrysikopoulos, C. V., Lee, K. Y., & Harmon, T. C. (2000). Dissolution of a well-defined trichloroethylene pool in saturated porous media: Experimental design and aquifer characterization. *Water Resources Research*, 36(7), 1687–1696.

CONAMA 420/09 (2009). Resolução CONAMA N° 420 de 28 de Dezembro de 2009. *Conselho Nacional do Meio Ambiente*.

Copenhaver, S. A., Krishnaswami, S., Turekian, K. K., Epler, N., & Cochran, J. (1993). Retardation of 238U and 232Th decay chain radionuclides in Long Island and Connecticut aquifers. *Geochimica et Cosmochimica Acta*, 57(3), 597–603.

Dafalla, M., Shaker, A. A., Elkady, T., Al-Shamrani, M., & Dhowian, A. (2015). Effects of confining pressure and effective stress on hydraulic conductivity of sand-clay mixtures. *Arabian Journal of Geosciences*, 8(11), 9993–10001.

Dal' Bó, P. F. F., Basilici, G., & Angélica, R. S. (2010). Factors of paleosol formation in a Late Cretaceous eolian sand sheet paleoenvironment, Marília Formation, Southeastern Brazil. *Palaeogeography, Palaeoclimatology, Palaeoecology*, 292(1-2), 349–365.

Ding, X. H., Feng, S. J., & Zheng, Q. T. (2021). A two-dimensional analytical model for contaminant transport in a finite domain subjected to multiple arbitrary time-dependent point injection sources. *Journal of Hydrology*, 597(March), 126318.

Divya, A., Shrihari, S., & Ramesh, H. (2020). Predictive simulation of leachate transport in a coastal lateritic aquifer when remediated with reactive barrier of nano iron. *Groundwater for Sustainable Development*, 11(March), 100382.

Fagundes, J. R. T. & Zuquette, L. V. (2011). Sorption behavior of the sandy residual unconsolidated materials from the sandstones of the Botucatu Formation, the main aquifer of Brazil. *Environmental Earth Sciences*, 62(4), 831–845.

Faria, G. M. M. & Mondelli, G. (2017). Interaction between municipal solid waste leachate and Bauru aquifer system: a study case in Brazil. *Environmental Science and Pollution Research*, 24(35), 27553–27572.

Faria, G. M. M. & Mondelli, G. (2018). Proposal for MSW contaminant classification applied to a tropical aquifer. *Environmental Science and Pollution Research*, 25(10), 9771–9796.

Feng, Y. & Jin, X. (2019). Studies on effects of traffic tunnels on the migration of the contaminants under landfill sites. *Environmental Science and Pollution Research*, 26(34), 34801–34817.

Fernandes, Saab, A., Rocha, B., Rodrigues, R., Lodi, P., & Giacheti, H. (2022). Geomechanical parameters in the active zone of an unsaturated tropical soil site via laboratory tests. *Soils and Rocks*, 45(4), 1–15.

Fetter, C. W., Boving, T., & Kreamer, D. (2017). *Contaminant Hydrogeology*. Prentice hall Upper Saddle River, NJ.

Francisca, F. M. & Glatstein, D. A. (2020). Environmental application of basic oxygen furnace slag for the removal of heavy metals from leachates. *Journal of Hazardous Materials*, 384(September 2019), 121294.

Freeze, R. A. & Cherry, J. A. (1979). *Groundwater*. New Jersey: PrenticeHall Inc Englewood cliffs.

Freyberg, L. (1986). A natural gradient experiment on solute transport in a sand aquifer: 2. Spatial moments and the advection and dispersion of nonreactive tracers. *Water Resources*, 22(13), 2031–2046.

Fujii, Y., Saito, S., Oshima, T., ichi Kodama, J., Fukuda, D., Sakata, S., Uchida, K., Matsumoto, H., & Dassanayake, A. B. (2020). Complete slaking collapse of dike sandstones by fresh water and prevention of the collapse by salt water. *International Journal of Rock Mechanics and Mining Sciences*, 131(January), 104378.

Gaganis, P., Skouras, E., Theodoropoulou, M., Tsakiroglou, C., & Burganos, V. (2005). On the evaluation of dispersion coefficients from visualization experiments in artificial porous media. *Journal of Hydrology*, 307(1-4), 79–91.

Giacheti, H. L., Bezerra, R. C., Rocha, B. P., & Rodrigues, R. A. (2019). Seasonal influence on cone penetration test: An unsaturated soil site example. *Journal of Rock Mechanics and Geotechnical Engineering*, 11(2), 361–368.

Godoy, V. A., Zuquette, L. V., & Gómez-Hernández, J. J. (2018). Scale effect on hydraulic conductivity and solute transport: small and large-scale laboratory experiments and field experiments. *Engineering Geology*, 243(March), 196–205.

Grathwohl, P. & Susset, B. (2009). Comparison of percolation to batch and sequential leaching tests: theory and data. *Waste Management*, 29(10), 2681–2688.

Gworek, B., Dmuchowski, W., Koda, E., Marecka, M., Baczewska, A., Brągoszewska, P., Sieczka, A., & Osiński, P. (2016). Impact of the municipal solid waste Łubna landfill on wnvironmental pollution by heavy metals. *Water*, 8(10), 470.

Harleman, D. R. & Rumer, R. R. (1963). Longitudinal and lateral dispersion in an isotropic porous medium. *Journal of Fluid Mechanics*, 16(3), 385–394.

Hassanzadeh, Y., Marofi, S., & Vahabian, M. (2020). Three-Dimensional Modeling of Contaminant Transport in Subsurface Soil Media Using UFV Approach. *International Journal of Geomechanics*, 20(4), 1–15.

Hazen, A. (1911). Dams on sand formations: discussion. *Trans ASCE*, 73, 199–203.

Head, K. H. (1994). *Manual of Soil Laboratory Testing. Volume 2: Permeability, Shear Strength and Compressibility Tests*. New York: John Wiley & Sons, second edition.

Honari, A., Zecca, M., Vogt, S. J., Iglauer, S., Bijeljic, B., Johns, M. L., & May, E. F. (2016). The impact of residual water on CH4-CO2 dispersion in consolidated rock cores. *International Journal of Greenhouse Gas Control*, 50, 100–111.

Hong, C. S. & Shackelford, C. D. (2017). Long-term column testing of zeolite-amended backfills. II: solute transport properties. *Journal of Geotechnical and Geoenvironmental Engineering*, 143(9), 04017051.

Horn, R., Taubner, H., Wuttke, M., & Baumgartl, T. (1994). Soil physical properties related to soil structure. *Soil and Tillage Research*, 30(2-4), 187–216.

Huesemann, M. H., Hausmann, T. S., & Fortman, T. J. (2005). Leaching of BTEX from aged crude oil contaminated model soils: experimental and modeling results. *Soil and Sediment Contamination: An International Journal*, 14(6), 545–558.

Huggett, J. M. & Uwins, P. J. (1994). Observations of water-clay reactions in water-sensitive sandstone and mudrocks using an environmental scanning electron microscope. *Journal of Petroleum Science and Engineering*, 10(3), 211–222.

Jellali, S., Diamantopoulos, E., Kallali, H., Bennaceur, S., Anane, M., & Jedidi, N. (2010). Dynamic sorption of ammonium by sandy soil in fixed bed columns : Evaluation of equilibrium and non-equilibrium transport processes. *Journal of Environmental Management*, 91(4), 897–905.

Jesus, L. S., Fernandes, J. B., & Giacheti, H. L. (2013). Investigação da condutividade hidráulica dos solos de uma área de aterro de resíduos sólidos urbanos através de ensaios de campo e laboratório. *Ciencia y Engenharia/ Science and Engineering Journal*, 22(1), 21–28.

Khayyun, T. S. (2018). Simulation of groundwater flow and migration of the radioactive Cobalt-60 from LAMA Nuclear Facility-Iraq. *Water (Switzerland)*, 10(2).

Kjeidsen, P. & Christensen, T. H. (1984). Soil attenuation of acid phase landfill leachate. *Waste Management & Research*, 2(1), 247–263.

Kjeldsen, P., Barlaz, M. A., Rooker, A. P., Baun, A., Ledin, A., & Christensen, T. H. (2002). Present and long-term composition of MSW landfill leachate: a review. *Critical Reviews in Environmental Science and Technology*, 32(4), 297–336.

Koch, S. & Flühler, H. (1993). Non-reactive solute transport with micropore diffusion in aggregated porous media determined by a flow-interruption method. *Journal of Contaminant Hydrology*, 14(1), 39–54.

Kozeny, J. (1927). Via capillary conduction of water in the soil (in German). *Sitzungsberichte der Akademie der Wissenschaften in Wien*, 136, 271.

Kulikowska, D. & Klimiuk, E. (2008). The effect of landfill age on municipal leachate composition. *Bioresource Technology*, 99(13), 5981–5985.

Labrecque, S. P. & Blanford, W. J. (2021). Fate and transport of bromide and mononuclear aromatic hydrocarbons in aqueous solutions through Berea Sandstone. *Science of the Total Environment*, 766, 141714.

Laidlaw, M. A. & Taylor, M. P. (2011). Potential for childhood lead poisoning in the inner cities of Australia due to exposure to lead in soil dust. *Environmental Pollution*, 159(1), 1–9.

Lapidus, L. & Amundson, N. R. (1952). Mathematics of adsorption in beds. VI. The effect of longitudinal diffusion in ion exchange and chromatographic columns. *The Journal of Physical Chemistry*, 56(8), 984–988.

Latrille, C., Wissocq, A., Beaucaire, C., & Bildstein, O. (2021). Reactive transport of strontium in two laboratory-scale columns: Experiments and modelling. *Journal of Contaminant Hydrology*, 242(June).

Levy, J. & Chesters, G. (1995). Simulation of atrazine and metabolite transport and fate in a sandy-till aquifer. *Journal of Contaminant Hydrology*, 20(1-2), 67–88.

Lu, C., Chen, Y., Zhang, C., & Luo, J. (2013). Steady-state freshwater-seawater mixing zone in stratified coastal aquifers. *Journal of Hydrology*, 505, 24–34.

Malov, A. I. (2016). Estimation of uranium migration parameters in sandstone aquifers. *Journal of Environmental Radioactivity*, 153, 61–67.

Malov, A. I. & Zykov, S. B. (2020). Study of the mobilization of Uranium isotopes in a sandstone aquifer in combination with groundwater data. *Water (Switzerland)*, 12(1).

Miretzky, P., Muñoz, C., & Carrillo-Chávez, A. (2006). Experimental Zn(II) retention in a sandy loam soil by very small columns. *Chemosphere*, 65(11), 2082–2089.

Mishra, S., Tiwary, D., & Ohri, A. (2018). Leachate characterisation and evaluation of leachate pollution potential of urban municipal landfill sites. *International Journal of Environment and Waste Management*, 21(4), 217.

Mondelli, G., Giacheti, H. L., Boscov, M. E. G., Elis, V. R., & Hamada, J. (2007). Geoenvironmental site investigation using different techniques in a municipal solid waste disposal site in Brazil. *Environmental Geology*, 52(5), 871–887.

Mondelli, G., Giacheti, H. L., & Howie, J. A. (2010). Geo-environmental investigation: A brief review and a few suggestions for Brazilian contaminated sites. *Soils and Rocks*, 33(3), 171–182.

Moody, C. M. & Townsend, T. G. (2017). A comparison of landfill leachates based on waste composition. *Waste Management*, 63, 267–274.

Mouvet, C., Barberis, D., & Bourg, A. C. (1993). Adsorption isotherms of tri- and tetrachloroethylene by various natural solids. *Journal of Hydrology*, 149(1-4), 163–182.

Naka, A., Yasutaka, T., Sakanakura, H., Kalbe, U., Watanabe, Y., Inoba, S., Takeo, M., Inui, T., Katsumi, T., Fujikawa, T., Sato, K., Higashino, K., & Someya, M. (2016). Column percolation test for contaminated soils: key factors for standardization. *Journal of Hazardous Materials*, 320, 326–340.

Needleman, H. L. (1990). The future challenge of lead toxicity. *Environmental Health Perspectives*, 89(15), 85–89.

Neukum, C., Braun, A., & Azzam, R. (2014). Transport of stabilized engineered silver (Ag) nanoparticles through porous sandstones. *Journal of Contaminant Hydrology*, 158, 1–13.

Ng, C. W. & Pang, Y. (2000). Experimental investigations of the soil-water characteristics of a volcanic soil. *Canadian Geotechnical Journal*, 37(6), 1252–1264.

Ng, C. W., So, P. S., Lau, S. Y., Zhou, C., Coo, J. L., & Ni, J. J. (2020). Influence of biopolymer on gas permeability in compacted clay at different densities and water contents. *Engineering Geology*, 272(March).

Ng, C. W. W., So, P. S., Coo, J. L., Zhou, C., & Lau, S. Y. (2019). Effects of biofilm on gas permeability of unsaturated sand. *Geotechnique*, 69(10), 917–923.

Nguyen, V. & Papavassiliou, D. V. (2020). Hydrodynamic dispersion in porous media and the significance of lagrangian time and space scales. *Fluids*, 5(2), 79.

Odling, N. W., Elphick, S. C., Meredith, P., Main, I., & Ngwenya, B. T. (2007). Laboratory measurement of hydrodynamic saline dispersion within a micro-fracture network induced in granite. *Earth and Planetary Science Letters*, 260(3-4), 407–418.

Ogata, A. & Banks, R. B. (1961). *A solution of the differential equation of longitudinal dispersion in porous media*. US Government Printing Office.

Ojuri, O. O. & Ola, S. A. (2010). Estimation of contaminant transport parameters for a tropical sand in a sand tank model. *International Journal of Environmental Science & Technology*, 7(2), 385–394.

Oostrom, M., Dane, J. H., Güven, O., & Hayworth, J. S. (1992). Experimental investigation of dense solute plumes in an unconfined aquifer model. *Water Resources Research*, 28(9), 2315–2326.

Pang, L., Close, M., Greenfield, H., & Stanton, G. (2004). Adsorption and transport of cadmium and rhodamine WT in pumice sand columns. *New Zealand Journal of Marine and Freshwater Research*, 38(2), 367–378.

Pearce, A. E., Voudrias, E. A., & Whelan, M. P. (1994). Dissolution of TCE and TCA Pools in Saturated Subsurface Systems. *Journal of Environmental Engineering*, 120(5), 1191–1206.

Perkins, T. & Johnston, O. (1963). A review of diffusion and dispersion in porous media. *Society of Petroleum Engineers Journal*, 3(01), 70–84.

Pini, R., Vandehey, N. T., Druhan, J., O'Neil, J. P., & Benson, S. M. (2016). Quantifying solute spreading and mixing in reservoir rocks using 3-D PET imaging. *Journal of Fluid Mechanics*, 796, 558–587.

Plassard, F., Winiarski, T., & Petit-Ramel, M. (2000). Retention and distribution of three heavy metals in a carbonated soil: comparison between batch and unsaturated column studies. *Journal of Contaminant Hydrology*, 42(2-4), 99–111.

Podlasek, A., Bujakowski, F., & Koda, E. (2020). The spread of nitrogen compounds in an active groundwater exchange zone within a valuable natural ecosystem. *Ecological Engineering*, 146(January), 105746.

Puranik, R. & Patil, P. (2021). A Study on Contaminant Transport Through Soil. In *Lecture Notes in Civil Engineering*, volume 134 (pp. 63–73). Singapore: Springer.

Reedy, O. C., Jardine, P. M., Wilson, G. V., & Selim, H. M. (1996). Quantifying the diffusive mass transfer of nonreactive solutes in columns of fractured saprolite using flow interruption. *Soil Science Society of America Journal*, 60(5), 1376–1384.

Rhino, K., Iyer, J., Walsh, S., Carroll, S., & Smith, M. (2021). Influence of effective stress and transport on mechanical and chemical alteration processes at the Cement-Caprock interface. *International Journal of Greenhouse Gas Control*, 109, 103340.

Rixey, W. G., Garg, S., & Nie, Y. (1999). Comparison of the fixed-bed and batch leaching characteristics of aromatic compounds in residually trapped crude oils and oily wastes. *Journal of Hazardous Materials*, 64(2), 137–156.

Robbins, G. A. (1989). Methods for determining transverse dispersion coefficients of porous media in laboratory column experiments. *Water Resources Research*, 25(6), 1249–1258.

Rowe, R. K. & Abdelrazek, A. Y. (2019). Effect of interface transmissivity and hydraulic conductivity on contaminant migration through composite liners with wrinkles or failed seams. *Canadian Geotechnical Journal*, 56(11), 1650–1667.

Rowe, R. K., Quigley, R. M., Richard, Brachman, R. W., & Brooker, J. R. (2004). *Barrier systems for waste disposal facilities*. London, UK: Taylor & Francis.

Saab, A. L., Rodrigues, A. L. d. C., Rocha, B. P., Rodrigues, R. A., & Giacheti, H. L. (2023). Suction influence on load-settlement curves predicted by DMT in a collapsible sandy soil. *Sensors*, 23(3), 1429.

Santos, A., Domínguez, C. M., Lorenzo, D., García-Cervilla, R., Lominchar, M. A., Fernández, J., Gómez, J., & Guadaño, J. (2019). Soil flushing pilot test in a landfill polluted with liquid organic wastes from lindane production. *Heliyon*, 5(11).

Schmittner, K. E. & Giresse, P. (1999). The impact of atmospheric sodium on erodibility of clay in a coastal Mediterranean region. *Environmental Geology*, 37(3), 195–206.

Schulze-Makuch, D. (1997). A permeameter designed to measure both hydraulic conductivity and dispersivity of consolidated rocks. *Canadian Geotechnical Journal*, 34(4), 615–620.

Seagren, E. A., Rittmann, B. E., & Valocchi, A. J. (1999). An experimental investigation of NAPL pool dissolution enhancement by flushing. *Journal of Contaminant Hydrology*, 37(1-2), 111–137.

Sebastián, E., Cultrone, G., Benavente, D., Linares Fernandez, L., Elert, K., & Rodriguez-Navarro, C. (2008). Swelling damage in clay-rich sandstones used in the church of San Mateo in Tarifa (Spain). *Journal of Cultural Heritage*, 9(1), 66–76.

Shackelford, C. D. (1990). Transit-time design of earthen barriers. *Engineering Geology*, 29(1), 79–94.

Shackelford, C. D. (1993). Contaminant transport. In D. E. Daniel (Ed.), *Geotechnical Practice for Waste Disposal* chapter 3, (pp. 33–65). Boston, MA: Springer US.

Shackelford, C. D. (1995). Cumulative mass approach for column testing. *Journal of Geotechnical Engineering*, 121(10), 696–703.

Shackelford, C. D. (2021). Fundamental considerations for column testing of engineered, clay-based barriers. *Japanese Geotechnical Society Special Publication*, 9(10), 441–460.

Shackelford, C. D. & Hong, C. S. (2020). Comparative analyses of alternative breakthrough curves from cumulative mass column testing of soil-bentonite backfills. *Canadian Geotechnical Journal*, 57(8), 1197–1214.

Shackelford, C. D. & Redmond, P. L. (1995). Solute breakthrough curves for processed kaolin at low flow rates. *Journal of Geotechnical Engineering*, 121(1), 17–32.

Shepherd, K. A., Rivett, M. O., & Mitchener, R. G. (2002). Organic contaminant sorption in Triassic sandstone deposits, Birmingham, UK. *IAHS-AISH Publication*, (275), 193–198.

Silva, M. L., Batezelli, A., & Ladeira, F. S. B. (2019). Genesis and evolution of paleosols of the Marília Formation, Maastrichtian of the Bauru Basin, Brazil. *CATENA*, 182(October 2018), 104108.

Skempton, A. W. (1954). The pore-pressure coefficients A and B. *Geotechnique*, 4(4), 143–147.

Slavinskienė, G., Jurevičius, A., Satkūnas, J., & Šimanauskienė, R. (2019). Landfill leachate quantity and attenuation distance of inorganic contaminants in the groundwater of different hydrogeological systems: A case study of Lithuania. *Baltica*, 32(2), 127–138.

Sousa, R. G. U., de Oliveira, I. B., Machado, S. L., & de Fátima Carvalho, M. (2020). Solute dispersion of organic compounds on undisturbed soil columns. *Transport in Porous Media*, 132(2), 267–282.

Streetly, H. R., Hamilton, A. C. L., Betts, C., Tellam, J. H., & Herbert, A. W. (2002). Reconnaissance tracer tests in the Triassic sandstone aquifer north of Liverpool, UK. *Quarterly Journal of Engineering Geology and Hydrogeology*, 35(2), 167–178.

Studds, P. G. (1998). The effects of salt solutions on the properties of bentonite-sand mixtures. *Clay Minerals*, 33(4), 651–660.

Sutton, O. F., Kessel, E. D., Gharedaghloo, B., & Price, J. S. (2022). Characterizing the hydraulic and transport properties of a constructed coarse tailings sand aquifer. *Journal of Contaminant Hydrology*, 249(November 2021), 104047.

Szecsody, J. E., Brockman, F. J., Wood, B. D., Streile, G. P., & Truex, M. J. (1994). Transport and biodegradation of quinoline in horizontally stratified porous media. *Journal of Contaminant Hydrology*, 15(4), 277–304.

Taylor, D. W. (1948). *Fundamentals of soil mechanics*, volume 66. John Wiley & Sons.

Terzaghi, K. (1925). Principles of soil mechanics: III. Determination of permeability of clay. *Engineering news record*, 95(21), 832–836.

Theodoropoulou, M. A., Karoutsos, V., Kaspiris, C., & Tsakiroglou, C. D. (2003). A new visualization technique for the study of solute dispersion in model porous media. *Journal of Hydrology*, 274(1-4), 176–197.

Thornton, S. F., Tellam, J. H., & Lerner, D. N. (2000a). Attenuation of landfill leachate by UK Triassic sandstone aquifer materials: 1. Fate of inorganic pollutants in laboratory columns. *Journal of Contaminant Hydrology*, 43(3-4), 327–354.

Thornton, S. F., Tellam, J. H., & Lerner, D. N. (2000b). Attenuation of landfill leachate by UK Triassic sandstone aquifer materials 2. Sorption and degradation of organic pollutants in laboratory columns. *Journal of Contaminant Hydrology*, 43(3-4), 327–354.

Thu, H. H. T., Van, S. L., Trong, H. T., Viet, H. L., Huu, Q. N., & Thi, L. P. (2023). Determination of the pore water velocity using a walt tracer combined with self-potential measurements. *Journal of Geoscience and Environment Protection*, 11(01), 15–27.

US EPA (1999). Understanding variation in partition coefficient, Kd, values. Volume I: the Kd Model, methods of measurement, and application of chemical reaction codes. *US EPA - United States Environmental Protection Agency*, (pp. 1–212).

US EPA (2008). Fate, transport and transformation test guidelines - OPPTS 835.1240 leaching studies. *US EPA - United States Environmental Protection Agency*, (pp. 1–16).

US EPA Method 1314 (2017). Liquid-solid partitioning as a function of liquid-solid ratio for constituents in solid materials using an up-flow percolation column procedure. *US EPA - United States Environmental Protection Agency*, (pp. 1–30).

van Breukelen, B. M., Griffioen, J., Röling, W. F., & van Verseveld, H. W. (2004). Reactive

transport modelling of biogeochemical processes and carbon isotope geochemistry inside a landfill leachate plume. *Journal of Contaminant Hydrology*, 70(3-4), 249–269.

van Genuchten, M. T. & Parker, J. C. (1984). Boundary conditions for displacement experiments through short laboratory soil columns. *Soil Science Society of America Journal*, 48(4), 703–708.

Von Rosenberg, D. U. (1956). Mechanics of steady state single-phase fluid displacement from porous media. *AIChE Journal*, 2(1), 55–58.

Voudrias, E. A. & Yeh, M.-F. (1994). Dissolution of a toluene pool under constant and variable hydraulic gradients with implications for aquifer remediation. *Groundwater*, 32(2), 305–311.

Wehrer, M. & Totsche, K. U. (2008). Effective rates of heavy metal release from alkaline wastes — Quantified by column outflow experiments and inverse simulations. *Journal of Contaminant Hydrology*, 101(1-4), 53–66.

Whitehead, P. G., Pye, V. I., Patrick, R., & Quarles, J. (1985). *Groundwater Contamination in the United States*, volume 22.

Wilson, J., Bateman, K., & Tachi, Y. (2021). The impact of cement on argillaceous rocks in radioactive waste disposal systems: A review focusing on key processes and remaining issues. *Applied Geochemistry*, 130(May), 104979.

Wood, W. W. & Ehrlich, G. G. (1978). Use of Baker's Yeast to Trace Microbial Movement in Ground Water.

Woodman, N. D., Rees-White, T. C., Stringfellow, A. M., Beaven, R. P., & Hudson, A. P. (2015). Multiple-tracer tests for contaminant transport process identification in saturated municipal solid waste. *Waste Management*, 38(1), 250–262.

Woumeni, R. S. & Vauclin, M. (2006). A field study of the coupled effects of aquifer

stratification, fluid density, and groundwater fluctuations on dispersivity assessments. *Advances in Water Resources*, 29(7), 1037–1055.

Yu, C., Yang, Y., xiang Wu, Z., fang Jiang, J., ping Liao, R., & feng Deng, Y. (2021). Experimental study on the permeability and self-healing capacity of geosynthetic clay liners in heavy metal solutions. *Geotextiles and Geomembranes*, 49(2), 413–419.

Zhao, X., Dong, D., Hua, X., & Dong, S. (2009). Investigation of the transport and fate of Pb, Cd, Cr(VI) and As(V) in soil zones derived from moderately contaminated farmland in Northeast, China. *Journal of Hazardous Materials*, 170(2-3), 570–577.

Chapter 4

Study of pollutant transport at a municipal solid waste disposal site using the CODE_BRIGHT program

Abstract

Although municipal solid waste (MSW) disposal sites constitute significant environmental risks due to the potential for contaminant transport into surrounding soil and groundwater, they are widely used to dispose of MSW. Over time, the leachate generated from waste decomposition can migrate through the soil, carrying harmful contaminants that may threaten local ecosystems and water resources. Understanding the contaminant transport in heterogeneous geological-geotechnical environments such as tropical soil and sandstone formations is crucial for effective environmental management and remediation strategies. This study investigates the fate and transport of contaminants from an MSW disposal site in Brazil, focusing on breakthrough times to reach undesirable contamination levels in the subsoil. We conducted numerical simulations employing the CODE_BRIGHT program, analyzing two representative MSW disposal site profiles (North-South and East-West) in both vertical and horizontal contaminant flow. The simulations used parameters from column tests previously collected in the laboratory with sodium chloride (NaCl) as a tracer and projected the migration of contaminants over 1, 10, and 100 years under different hydraulic leaching heights (0.3, 0.6, and 1.2 m). The findings revealed that increased leachate head significantly reduced breakthrough time (BTt), with horizontal flow prevalent in permeable soil horizons. The East-West profile was more vulnerable to contaminant spread, while sandstone layers exhibited some capacity for attenuation. Both profiles reached critical contamination levels for the tracer after 100 years, suggesting long-term environmental risk without intervention.

Keywords: MSW disposal site; Contaminant transport; Breakthrough time; CODE_BRIGHT; Natural attenuation.

4.1 Introduction

The increasing consumption and resulting industrial activity have resulted in significant annual volumes of municipal solid waste, posing a global challenge for disposal. Inadequate disposal methods persist in Brazil. Even facilities employing sanitary landfill techniques frequently encounter design, implementation, upkeep, and closure issues.

Soil and groundwater contamination can be attributed to human activities, particularly waste disposal in MSW disposal sites, which poses significant environmental pollution potential (Mor et al., 2006; Butt et al., 2008; Teh et al., 2016; Ahmed et al., 2019; Zhang et al., 2021).

In this context, the MSW disposal site in Bauru, state of São Paulo, Brazil, has been identified as a source of contamination, with evidence of contaminated soil and groundwater, as previously observed by Mondelli et al. (2007, 2010) and Faria & Mondelli (2017).

Furthermore, the Gabiroba stream, situated within the subbasin of Bauru's MSW disposal site, has been under monitoring since 2005, revealing indicators of declining water quality. Additionally, the Gabiroba stream feeds into the Ribeirão Água Parada, recognized as a potential future water source for municipalities in Bauru (Leal, 2011). Groundwater extraction for water supply has also increased in the city (Cavaguti & Paula e Silva, 1992). Given these factors, it is imperative to study and monitor Bauru's MSW disposal site to prevent further environmental deterioration in its vicinity and the consequent high costs associated with remediation efforts.

Among remediation methods, natural attenuation is frequently utilized in developing countries. It involves several physical, chemical, and biological processes that can reduce the concentration of contaminants in soil, water, and air (van Breukelen et al., 2004; Young, 2006; Mahallei & Badv, 2020). Effective implementation requires monitoring contaminant levels and assessing the time needed to bring them within acceptable limits set by environmental agencies. Thus, integrating laboratory tests, in situ data and numerical modeling is crucial in the decision-making before, during, and after the monitored natural attenuation process.

The CODE_BRIGHT program is well-established in the scientific community. Its

applications in the context of MSW disposal sites include deformation and development of cracks in landfill covers (Jamei et al., 2024), simulation of cracking in the clay layer of a flume model system with a 3-layer landfill cover system under rainfall conditions (Ng et al., 2015b), transport and permeability of gases in landfill cover with compacted unsaturated clays due to the biodegradation of waste (Ng et al., 2015a), and investigating the rehydration of geosynthetic clay liners due to defects in geomembranes (Ghavam-Nasiri & El-Zein, 2016).

Although there are numerical simulations with CODE_BRIGHT involving waste, its use is mainly aimed at nuclear waste (Guimarães et al., 2006; Zandarin et al., 2011; Li et al., 2013; Gaus et al., 2014; Rodriguez-Dono et al., 2020; Ibrahim et al., 2022; Kim et al., 2022; Khadivipanah et al., 2022; Friedenberg et al., 2023). Thus, its use in the transportation and disposal of pollutants in MSW disposal sites is still in its incipient compared to other applications (Olivella & Gens, 2000; Jacinto et al., 2009; Nowamooz et al., 2009; Guo & Dixon, 2010; Mokni et al., 2011; Trabelsi et al., 2012; Zandarin et al., 2013; Pujades et al., 2017; Yubero et al., 2021; Song et al., 2022; Zhou et al., 2024).

However, Olivella et al. (1996) demonstrated the potential for simulating the transport of solutes using this computational program. To the best of the authors' knowledge, no previous studies have been reported on CODE_BRIGHT simulations concerning MSW disposal sites and the migration of the contamination plume.

Therefore, this work aims to investigate the flow of contaminants in two typical profiles of Bauru's MSW disposal site using the CODE_BRIGHT program, with pre and post-processing by the GID software, to simulate and verify solute concentrations and their variations with depth and time. To contribute to decision-making regarding similar MSW disposal sites in developing countries and demonstrate the use of the CODE_BRIGHT computer program to analyze the spread of contamination plumes.

4.2 Materials and Methods

4.2.1 Study site

The Bauru MSW disposal site (22°15'S 49°08'W) is near km 353 of the Marechal Rondon Highway. Managed by the Municipal Company of Bauru's Urban and Rural Development (EMDURB), it has a total area of around 270000 m^2 and used to receive 220 to 250 tons of waste deposited daily. The MSW disposal area started operations in 1993 and closed in 2016. Initially designed as a sanitary landfill, it has been reclassified as a controlled landfill in response to increasingly stringent environmental regulations. Four compacted soil layers cover the landfill base, each measuring 20 centimeters thick, with compaction 3% above the optimum water content. A bituminous primer has been applied to the surface of this layer. The base excavations were conducted until reaching the sandstone's altered soil, approximately 5 meters from the water table (Mondelli et al., 2007; Jesus et al., 2013). Figure 4.1 overviews Bauru's MSW disposal area. Figure 4.2 details the sections defined by Mondelli (2008), simulated here, and the section studied by Lago et al. (2006), which is used for comparison with this work. This point will be addressed later.

The geological formations in Bauru include the Marília and Adamantina Formations, which overlay the São Bento Group. This group belongs to the transition of the Cretaceous and Triassic–Jurassic periods and encompasses the Serra Geral, Botucatu, and Piramboia Formations (Dal' Bó et al., 2010; Basilici et al., 2016; Silva et al., 2019).

The soil presents in the experimental site from Unesp-Bauru has been widely studied, and corresponds to the middle profile found in the city of Bauru, thereby, red fine clayey sand, classified as SM-SC by USCS and A-2-4 by HRB, with lateritic behavior up to 13 m depth (Giacheti et al., 2019; Fernandes et al., 2022; Saab et al., 2023).

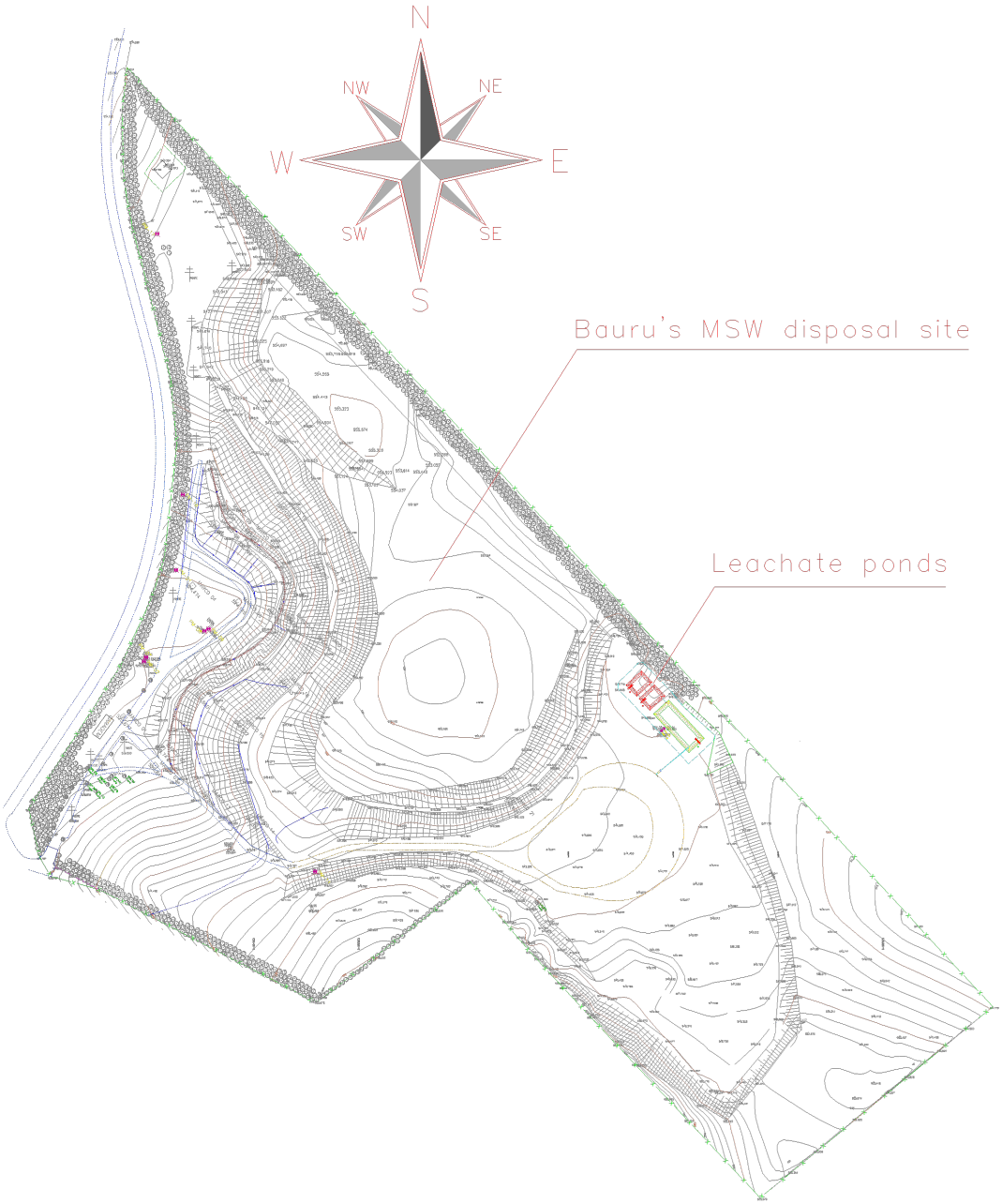

Figure 4.1: Overview of Bauru's MSW disposal site.

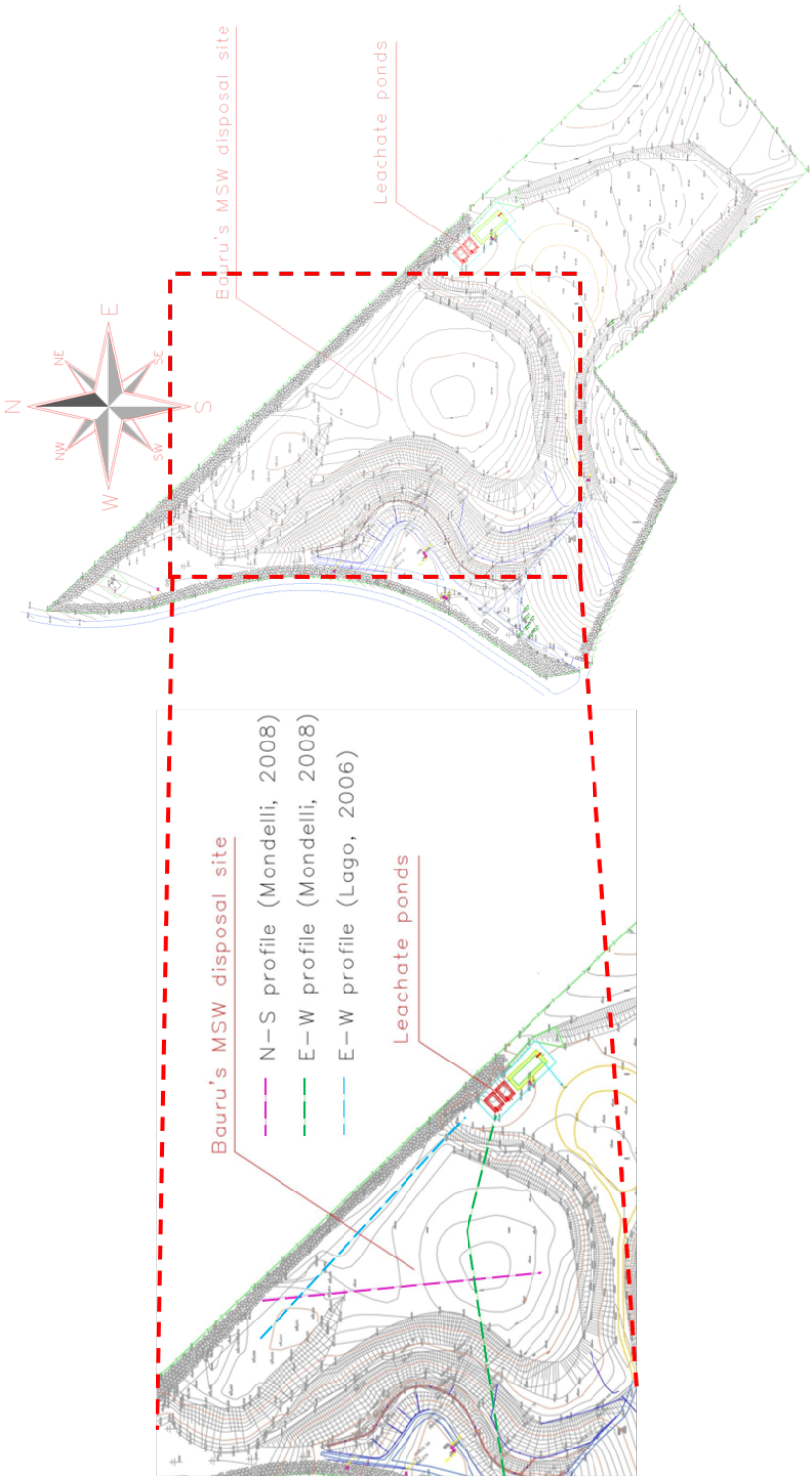

Figure 4.2: Analyzed sections of Bauru's MSW disposal site.

4.2.2 Experimental data

The experimental data in this research's simulations was previously gathered in the laboratory. As detailed in Chapters 2 and 3, there is a predominance of advective-dispersive transport through the soil and advective-dispersive-diffusive transport through the sandstone. The parameters previously determined and used in the simulations were hydraulic conductivity, porosity, dispersivity, and Young's modulus (during the validation stage). Additionally, the van Genuchten (1980) fit parameters from the soil water retention curve (SWRC) of Fernandes et al. (2022) and those collected here in Chapter 2 using the filter paper technique for sandstone were taken into account, even though the position of the water table (WT) is close to the waste pit.

Based on the previously determined parameters from the column and leaching tests with NaCl, the values were adjusted until a good fit was established with the breakthrough curves (BTCs) for depths of 1, 4, 7, 11, 13, and 16 m of the soil profile and the sandstone under confining pressures close to the in situ geostatic stress, i.e., 20 kPa for 1 m depth; 40 and 80 kPa for 4 m depth; 80 and 160 kPa for 7 m depth; and finally 160 and 320 kPa for depths of 11, 13, and 16 m, as well as for the sandstone. The latter showed experimental results indicating the presence and contribution of clay minerals from the smectite group, albeit minor. During the data validation stage, it was necessary to include the diffusion parameter initially with the default value suggested by CODE_BRIGHT and then adjust until there was good agreement between the breakthrough curves.

NaCl was chosen as a tracer, in addition to its use in preliminary laboratory determination of the parameters of interest, because it is a non-reactive tracer that aligns well with the local stratigraphic profile. Furthermore, it can be used as an initial indicator of the spread of the contamination plume in the field, directing research on relevant substances and locations (Rowe, 2012; Feng & Jin, 2019; Thu et al., 2023).

The soil was divided by its genesis. The colluvial soil was attributed to a depth of 1 to 5 meters depth, residual sandstone from 5 to 10 meters depth, and sandstone from 10 meters to the lower limit of the sections. The analysis assumed homogeneous and isotropic

media. The position of the water table was defined based on the site profiles (see Figures 4.4 and 4.5) outlined by Mondelli (2008), that is, 20 m deep for the N-S profile and 30 m deep for the E-W profile. The analysis did not include underground flow, contaminant attenuation or decay, and rainfall.

Table 4.1 presents Young's moduli used to validate the simulation with soil and sandstone specimens. Table 4.2 shows the values of the material properties used in the simulations.

Table 4.1: Young's moduli used to validate the simulation with previous tests on soil and sandstone.

Material	**Young's modulus (MPa)**
Colluvium	2.9 - 15.0
Residual	10.0 - 11.3
Sandstone	10.0 - 20.0

Table 4.2: Properties of the materials used in the simulations.

Layer	K (m²)	n	α (m)	Po (kPa)	σ (N/m)	λ	Srl	Srs	D (m²/s)	Q (J/mol)	τ
Colluvium	1.5×10^{-12}	0.41	2×10^{-3}	50.00	0.072	0.70	0.22	1.00			
Residual	3.0×10^{-13}	0.33	3×10^{-3}	50.00	0.072	0.80	0.50	1.00			
Sandstone	1.0×10^{-15}	0.23	8×10^{-3}	50.00	0.072	0.20	0.00	1.00	1.0×10^{-5}	24530	1.00

where K is the intrinsic permeability, n is the porosity, α the dispersivity, here used the same in the longitudinal and transverse directions, Po represents the pressure at a specific temperature, σ is the surface tension at which Po was measured, with the value used by default, λ is the shape function of the retention curve, i.e., parameter m of the van Genuchten (1980) fit, Srl the degree of residual saturation, Srs the degree of saturation when saturated, D diffusion, Q activation energy, and τ the tortuosity coefficient.

4.2.3 Numerical model

The CODE_BRIGHT program used the following equations to solve flux and transport problems. Equation 4.1 shows the equation that describes the flow in porous media of the liquid and gaseous phases and the mass transport of solutes.

Although the simulation did not use mechanical parameters, it was validated using data from the column and leaching tests carried out in Chapter 3, which were subjected to different confining stresses.

Equation 4.2 describes the stresses involved in the sample consolidation process. Equation 4.3 shows the permeability of materials described by Darcy's law in its generalized form, with transport by diffusion and advection elucidated by Equations 4.4 to 4.7.

Governing equations

Mass balance equation

$$\frac{\partial}{\partial t}(\omega_l^w \rho_l S_l \phi + \omega_g^w \rho_g S_g \phi) \nabla \cdot (\mathbf{j}_l^w + \mathbf{j}_g^w) = f^w \tag{4.1}$$

where subindex l and g refer respectively to liquid and gas phase, overwritten w refers to water, ω is the mass fraction, S is the degree of saturation, ϕ is the porosity, $\mathbf{j}$ energy fluxes due to mass motion, and f^w is a external supply of water.

Momentum balance for the medium

$$\nabla \cdot \boldsymbol{\sigma} + \mathbf{b} = 0 \tag{4.2}$$

where $\boldsymbol{\sigma}$ is the stress tensor and $\mathbf{b}$ is the vector of body forces.

Darcy's generalized law

$$\mathbf{q}_l = -\frac{\mathbf{K}\mathrm{k}_{rl}}{\mu_l}(\nabla P_l - \rho_l \mathbf{g}) \tag{4.3}$$

where $\mathbf{q}$ is the Darcy's flux, $\mathbf{K}$ is the tensor of intrinsic permeability, μ is the dynamic viscosity, ρ is the liquid density, and $\mathbf{g}$ is a vector of gravity forces.

Fick's law for molecular diffusion

$$\mathbf{i}_\alpha^i = -(\tau\phi\rho_\alpha S_\alpha D_\alpha^i \mathbf{I})\nabla\omega_\alpha^i \tag{4.4}$$

where $\mathbf{i}$ is the matrix non-advective fluxes, i and α stand for species i in phase α. The molecular diffusion D is defined as

$$D_\alpha^i = D\exp\left(-\frac{Q}{R(273.15+T)}\right) \tag{4.5}$$

where R is the ideal gas constant

Fick's law for mechanical dispersion

$$\mathbf{i}_\alpha^i = -(\rho_\alpha \mathbf{D'}_\alpha)\nabla\omega_\alpha^i \tag{4.6}$$

where the mechanical dispersion tensor $\mathbf{D'}$ is

$$\mathbf{D'} = d_t \mid \mathbf{q}_\alpha \mid \mathbf{I} + (d_l - d_t)\frac{\mathbf{q}_\alpha \mathbf{q}_\alpha^t}{\mid \mathbf{q}_\alpha \mid} \tag{4.7}$$

where d_t is the transversal dispersivity, d_l is the longitudianl dispersivity, and $\mathbf{I}$ is the identity matrix.

Geometry

For the simulation, the geometry depicted in Figures 4.4 and 4.5 was derived from a previous study by Mondelli (2008). Figure 4.3 presents an illustrative section of the waste pit with the elements that will be analyzed (right and left slopes, center pit, and longitudinal

profile). Simulations with a 2D section were carried out as suggested by Ding et al. (2020), who infer the critical role of modeling in two dimensions when there is a predominance of transport by advection.

The finite element mesh for the North-South (N-S) section consisted of 16480 elements with 8682 nodes, while the East-West (E-W) section consisted of 7882 triangles and 4372 nodes. The mesh was refined at the base of the waste pit, with less refinement as you moved away from the top of the sections towards the bottom.

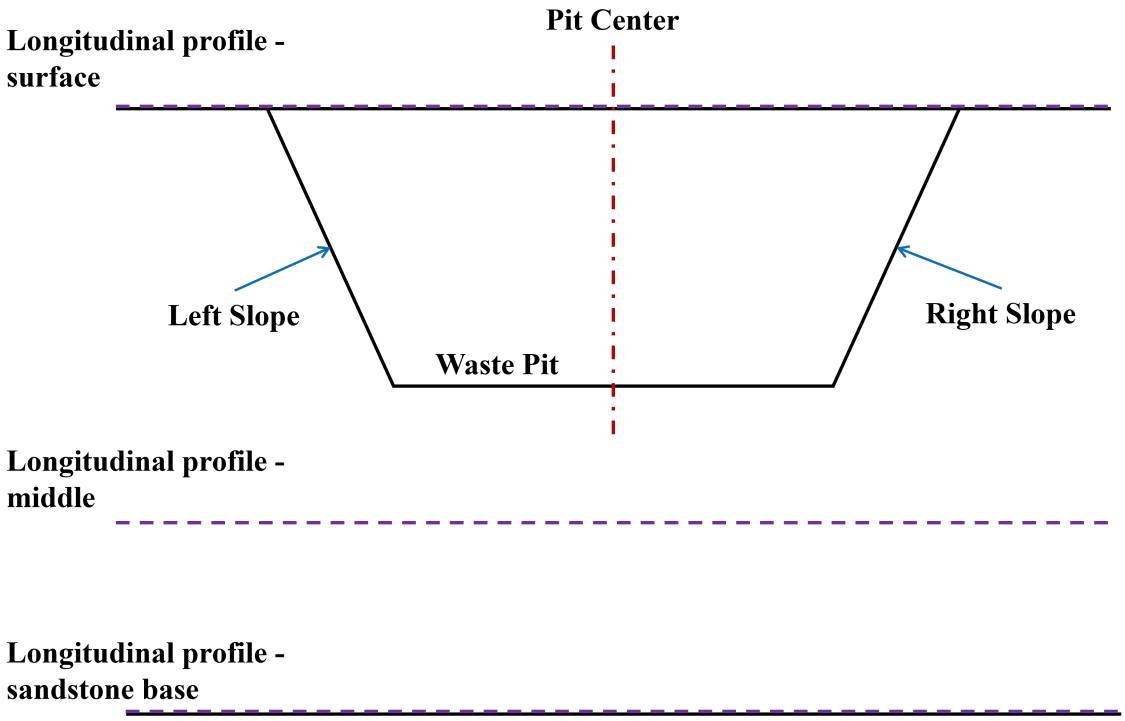

Figure 4.3: Illustrative section of the solid waste pit, highlighting the elements analyzed throughout the work.

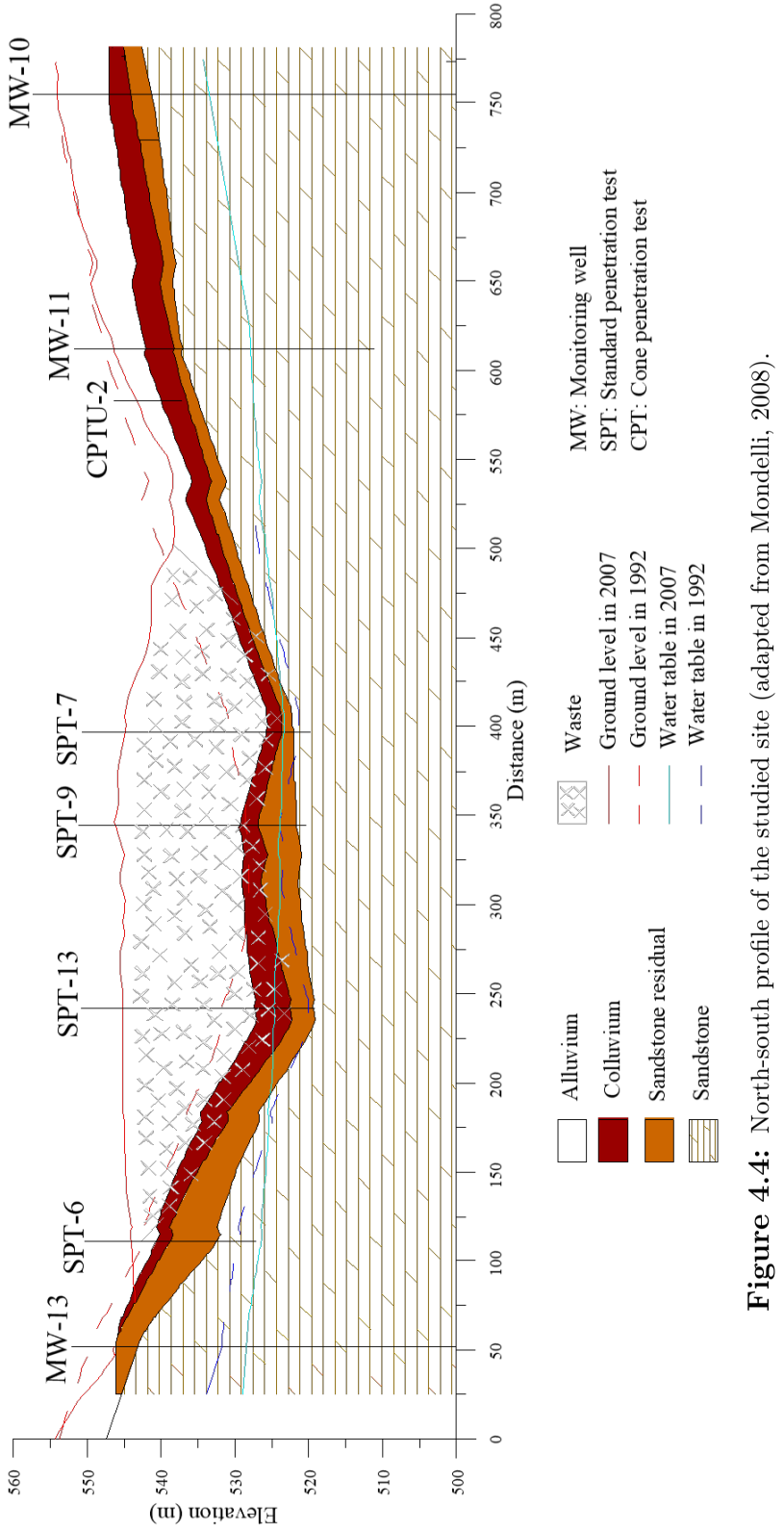

Figure 4.4: North-south profile of the studied site (adapted from Mondelli, 2008).

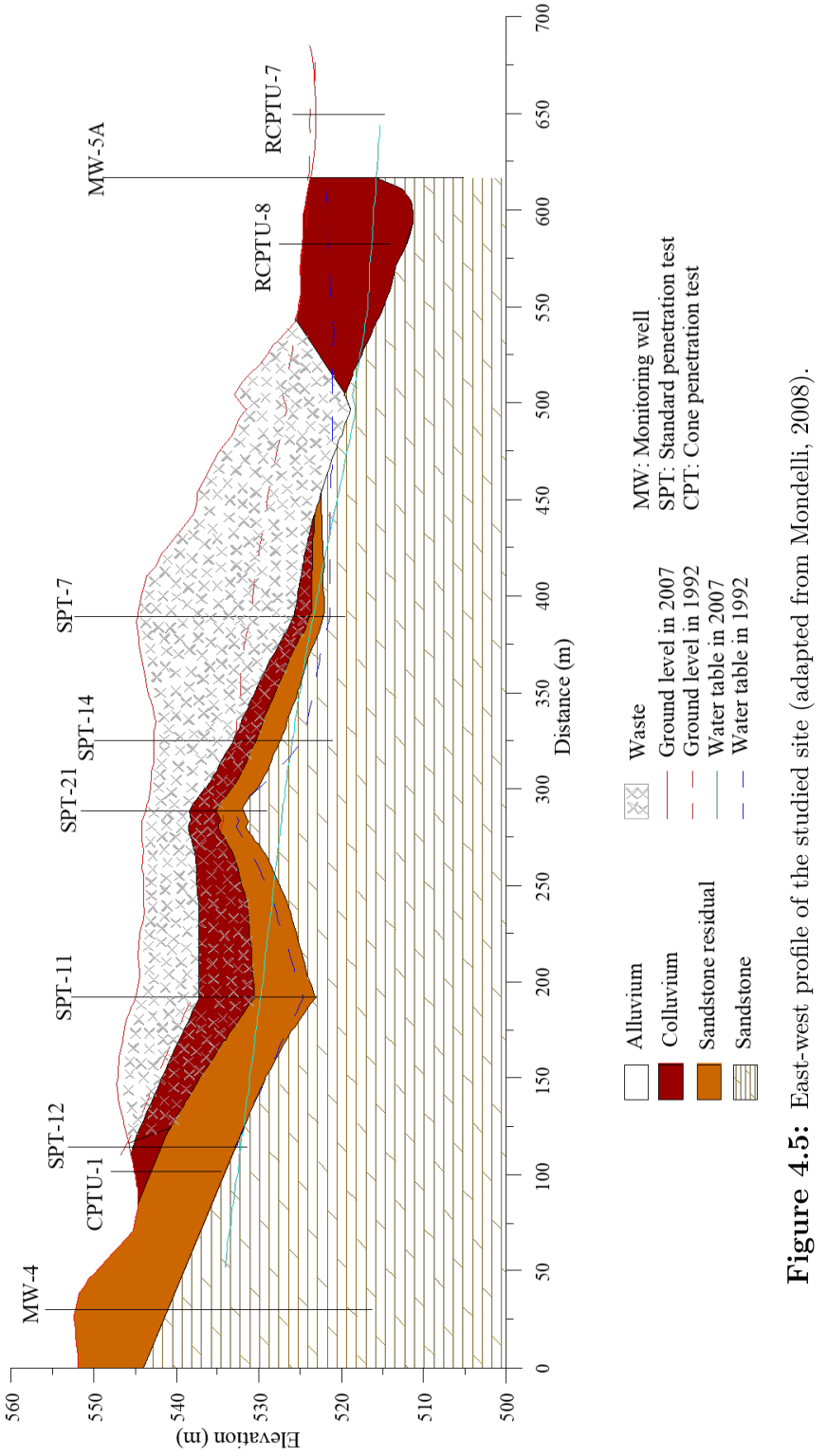

Figure 4.5: East-west profile of the studied site (adapted from Mondelli, 2008).

Initial and boundary conditions

The initial conditions of the simulations assumed the phreatic position, background concentration, and initial soil and sandstone suction. The boundary conditions used the background concentration in the sandstone and NaCl based on laboratory studies, which were kept constant, with a hydraulic leachate head of 0.3 m for the initial simulations since this is the maximum value recommended by Shu et al. (2019) and Rowe & Barakat (2021). The position of the water table was set based on the profiles defined by Mondelli (2008), i.e., 20 m deep for the N-S profile and 30 m deep for the E-W profile.

Since this is an MSW disposal site in a developing country, whose waste has high organic matter and consequently high humidity and leachate generation, higher hydraulic heads of 0.6 and 1.2 m were analyzed, keeping the other parameters constant, to compare the breakthrough curves and predict the spread of the contamination plume, as well as the moment when the concentration reached the limit value of 200 mg/L of sodium stipulated by the CONAMA 420/09 (2009) during the initial periods of use, that is, 1 and 10 years, and in the long term after the closure of the MSW disposal site with 100-year. Tables 4.3 and 4.4 display the values assigned in the initial and boundary conditions.

Table 4.3: Initial conditions for the simulations.

Profile	Water table depth (m)	Concentration (kg/kg)	Surface suction (kPa)
N-S	20	2×10^{-5}	10
E-W	30	2×10^{-5}	10

Table 4.4: Simulation boundary conditions.

Position	Concentration (kg/kg)	Leachate head (m)
Sandstone base	2×10^{-5}	
Pit surface	1×10^{-3}	0.3 0.6* 1.2*

*Values assumed in the sensitivity analysis of the hydraulic leachate head.

Figures 4.6 and 4.7 depict the initial conditions for the N-S and E-W sections, and Figures 4.8 and 4.9 illustrate the N-S and E-W boundary conditions used in the simulations.

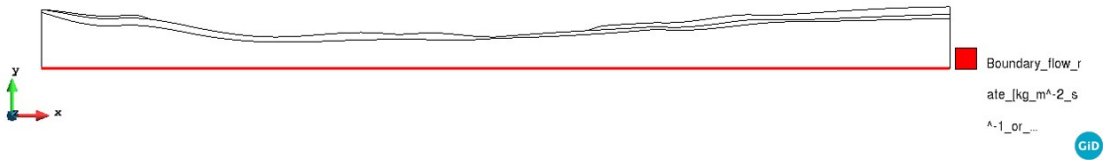

Figure 4.6: Initial conditions of the N-S section.

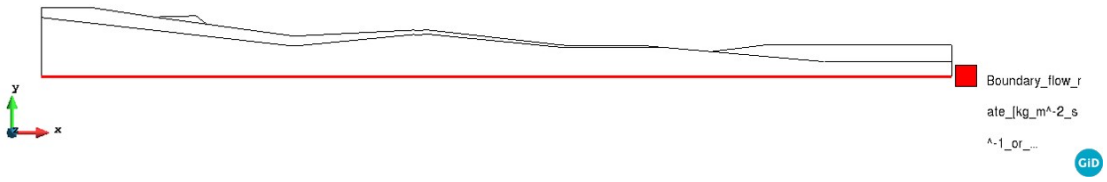

Figure 4.7: Initial conditions of the E-W section.

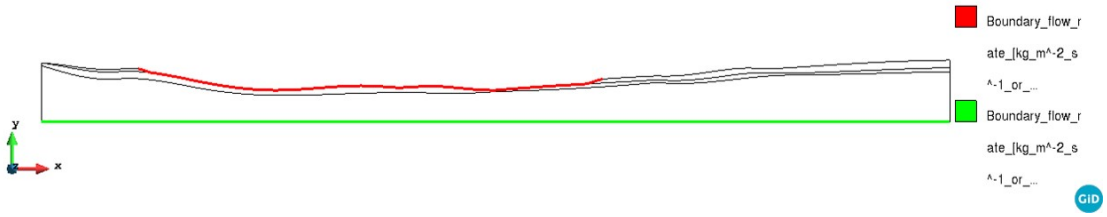

Figure 4.8: N-S section boundary conditions.

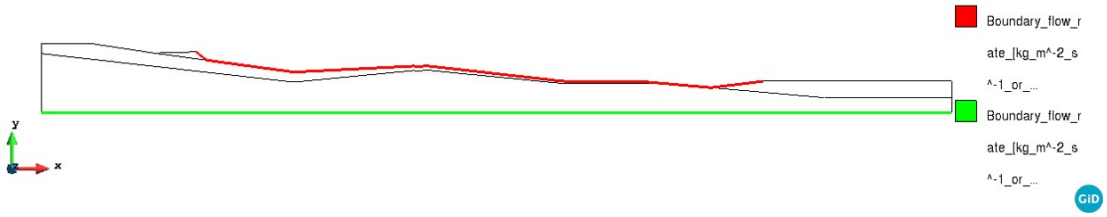

Figure 4.9: E-W section boundary conditions.

4.3 Results and Discussion

4.3.1 Model validation

The model was validated by comparing the experimental and analytical results of the breakthrough curves of the soil and sandstone samples presented in Chapter 3.

Figures 4.10 to 4.22 illustrate the modeling results along with the experimental and analytical results. From these, we can infer a good fit with an R^2 above 0.98 compared to the experimental data and above 0.99 compared to the analytical data. The relationship between the experimental and analytical results and the modeling results is available in the supplementary material.

With the breakthrough curves via modeling, the parameters that had previously been determined experimentally and analytically could be compared with the results of the specimen modeling.

Thus, for the column test simulations, arrival time (At), breakthrough time (BTt), and pick time (Pt), as well as first leaching time (FLt), leaching breakthrough time (LBTt), and leaching time (Lt) for the leaching test simulations were determined.

In general, the parameters of the analytical and numerical solutions were very close, given the higher R^2 between the two. It can be seen that the numerical values slightly underestimated the parameters, i.e., the times determined were lower than the experimental and numerical data, especially at the beginning and end of the breakthrough curves, similar to what occurred between the experimental and analytical results. These results align with those observed by Ding et al. (2020), in which the cut-off wall breakthrough time from 1D simulations was also underestimated. The authors attributed this phenomenon to the fact that they had not used the contribution of dilution in the vertical direction.

Since this topic aimed to validate the results and, given the proximity between the analytical and numerical values, Chapter 3 further discusses the pollutant arrival parameters.

In this way, the results provided confidence for the simulations' representative profiles of the North-South and East-West sections of Bauru's MSW disposal site.

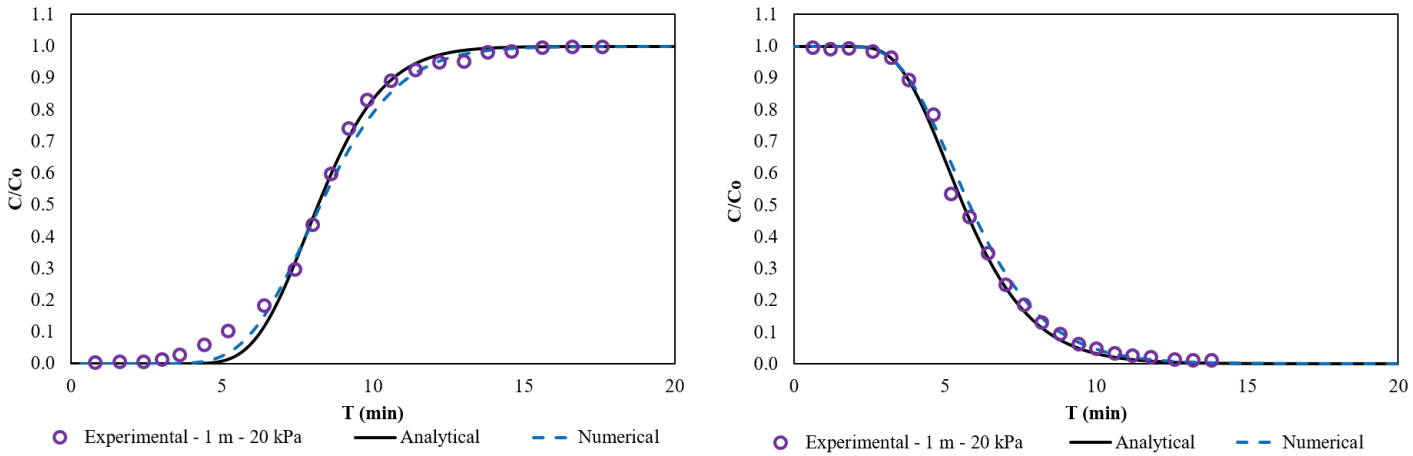

Figure 4.10: Numerical fitting with the experimental and analytical data from column and leaching tests from the soil at 1 m depth consolidated at 20 kPa.

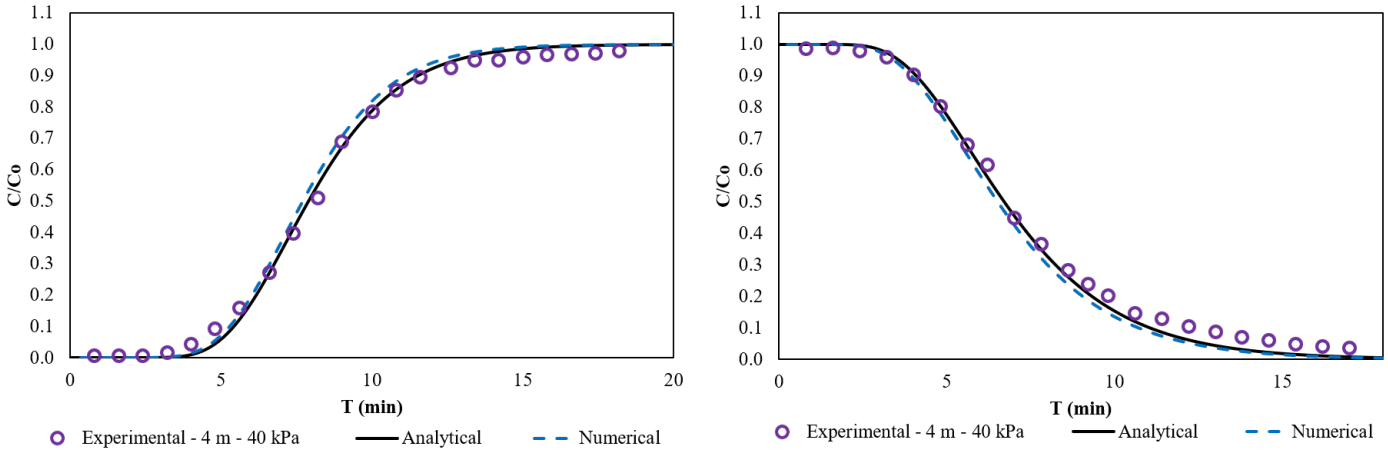

Figure 4.11: Numerical fitting with the experimental and analytical data from column and leaching tests from the soil at 4 m depth consolidated at 40 kPa.

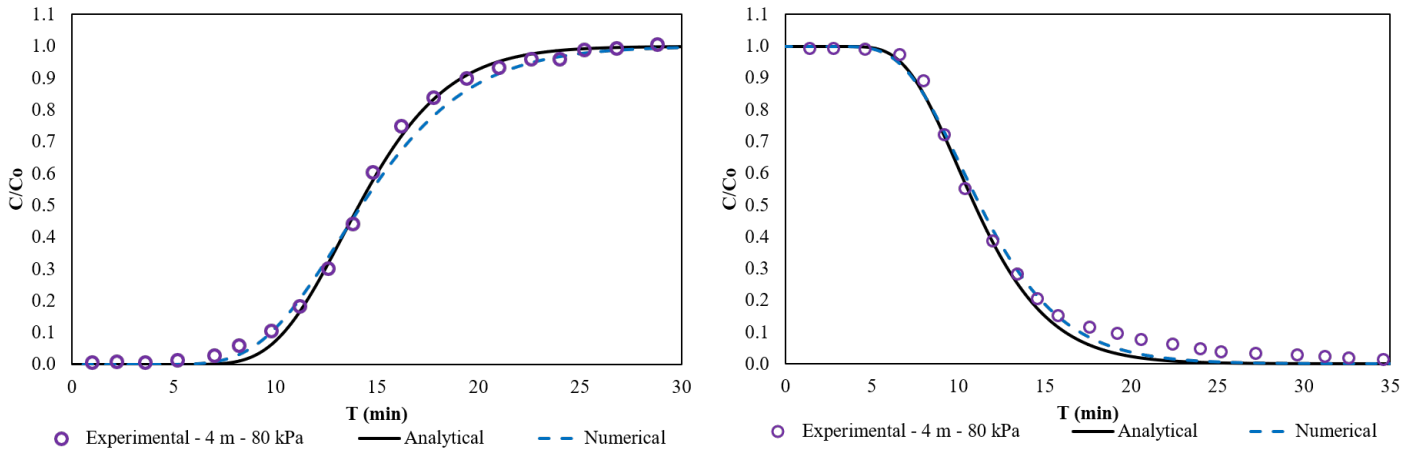

Figure 4.12: Numerical fitting with the experimental and analytical data from column and leaching tests from the soil at 4 m depth consolidated at 80 kPa.

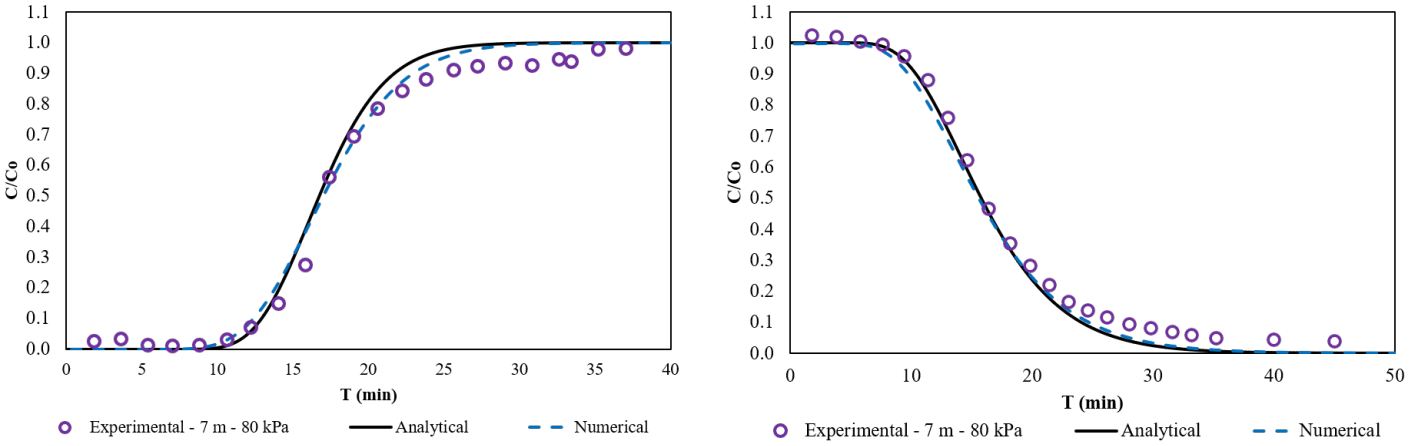

Figure 4.13: Numerical fitting with the experimental and analytical data from column and leaching tests from the soil at 7 m depth consolidated at 80 kPa.

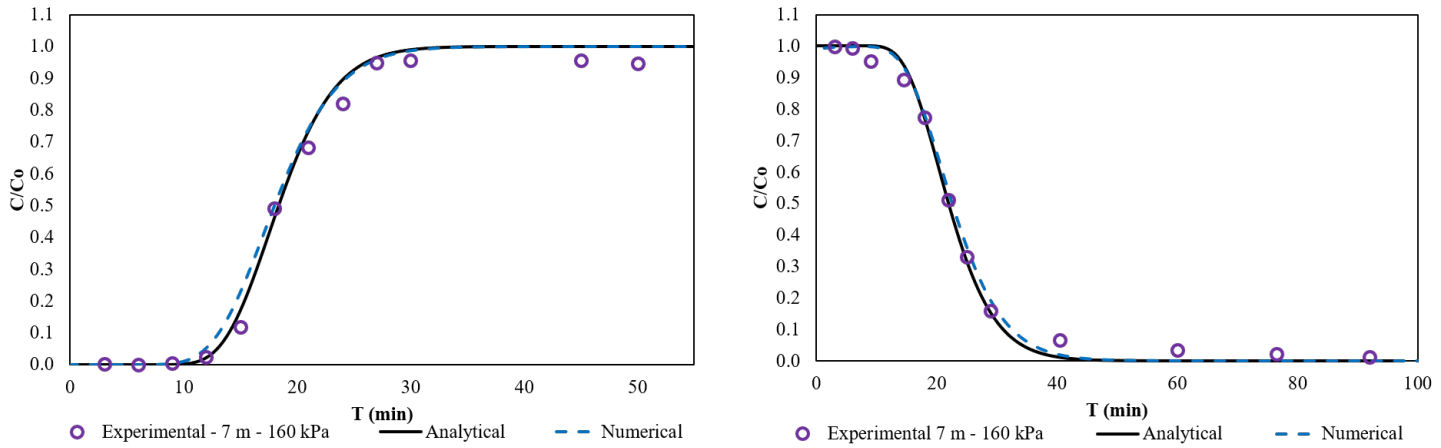

Figure 4.14: Numerical fitting with the experimental and analytical data from column and leaching tests from the soil at 7 m depth consolidated at 160 kPa.

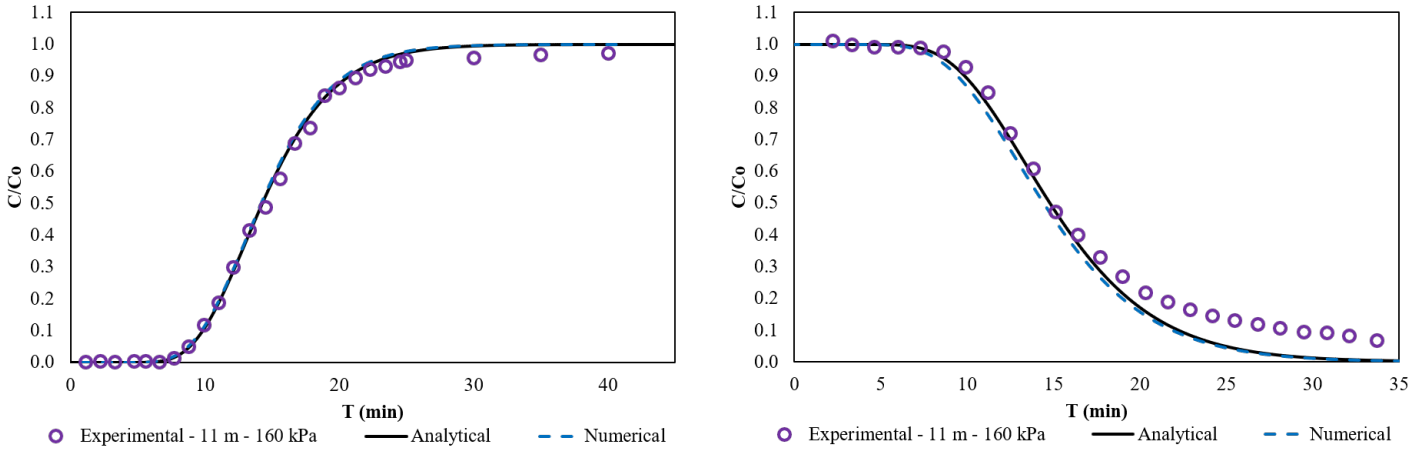

Figure 4.15: Numerical fitting with the experimental and analytical data from column and leaching tests from the soil at 11 m depth consolidated at 160 kPa.

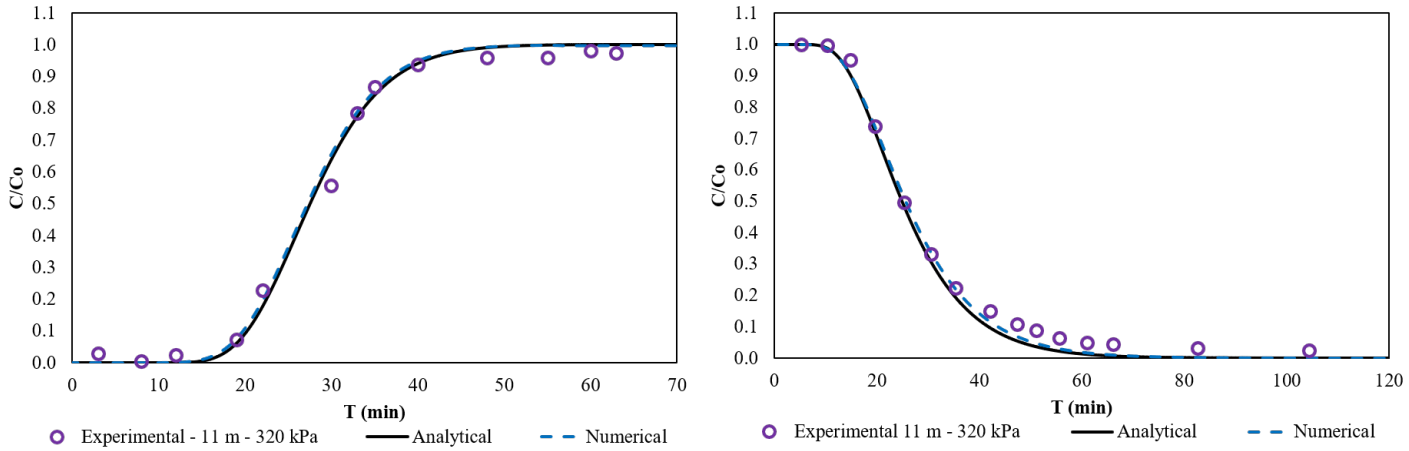

Figure 4.16: Numerical fitting with the experimental and analytical data from column and leaching tests from the soil at 11 m depth consolidated at 320 kPa.

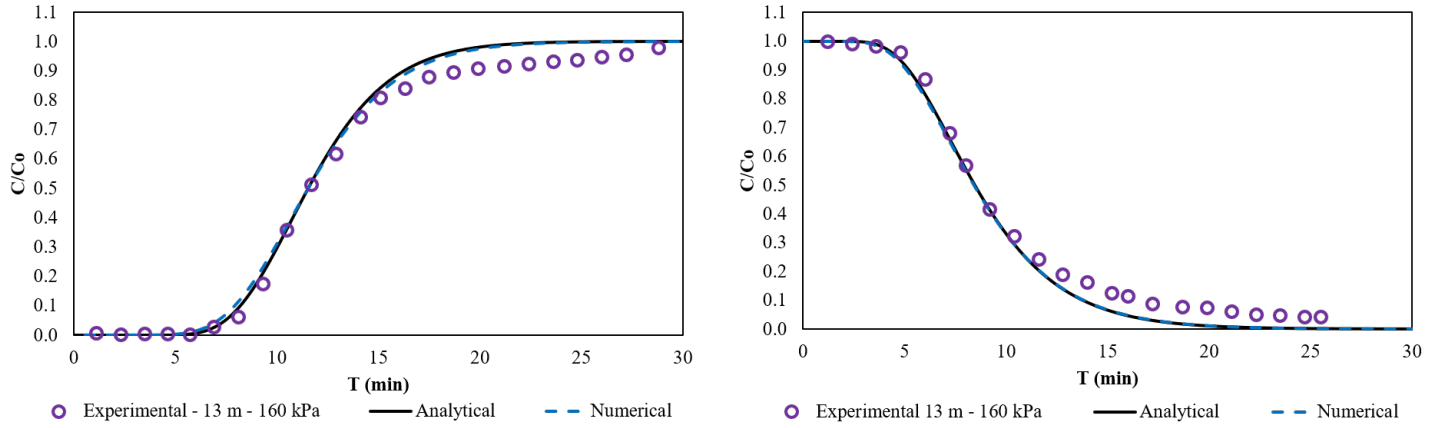

Figure 4.17: Numerical fitting with the experimental and analytical data from column and leaching tests from the soil at 13 m depth consolidated at 160 kPa.

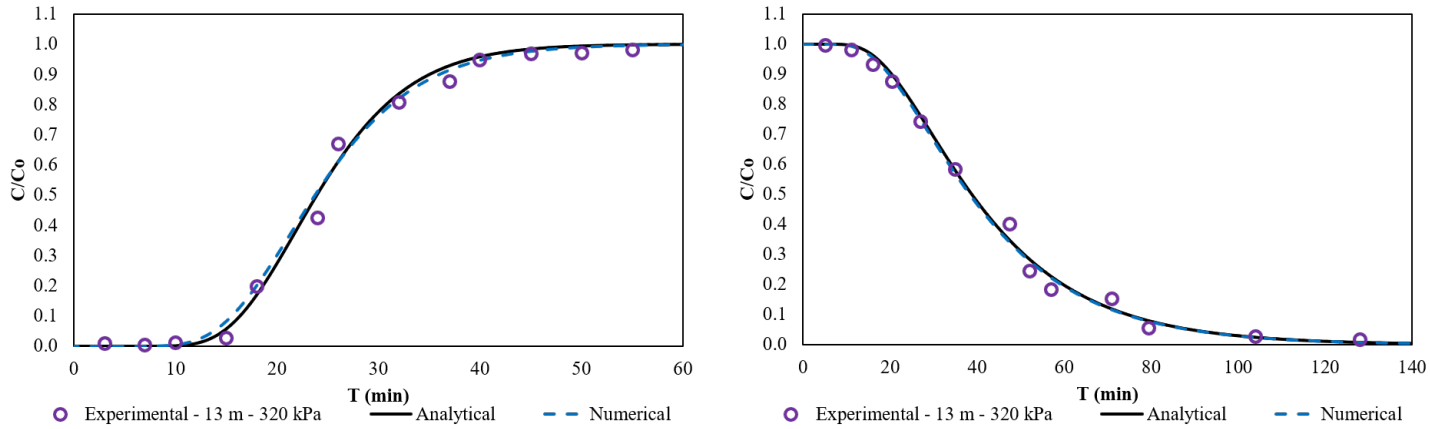

Figure 4.18: Numerical fitting with the experimental and analytical data from column and leaching tests from the soil at 13 m depth consolidated at 320 kPa.

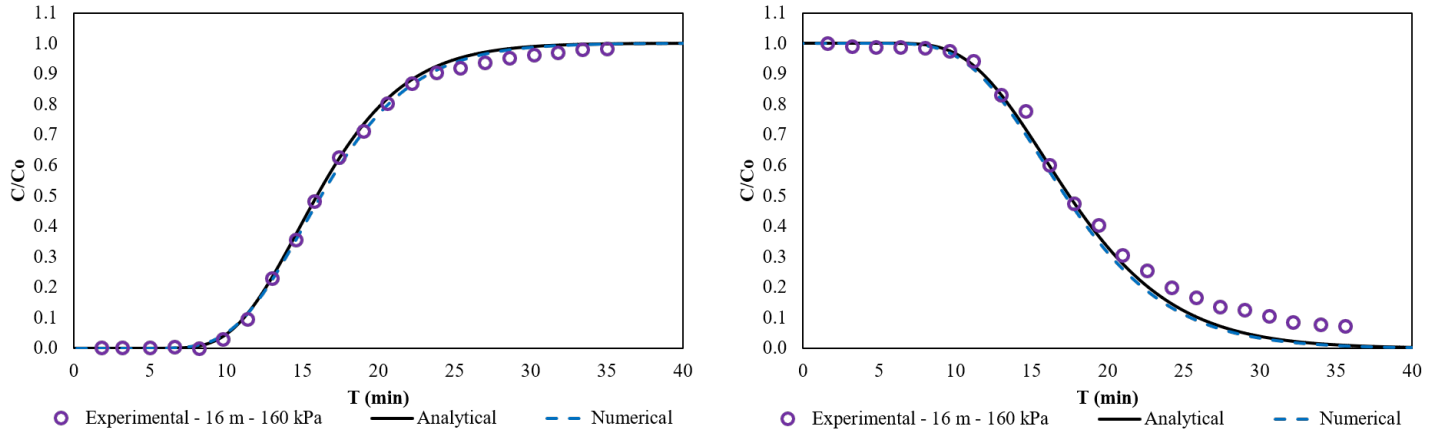

Figure 4.19: Numerical fitting with the experimental and analytical data from column and leaching tests from the soil at 16 m depth consolidated at 160 kPa.

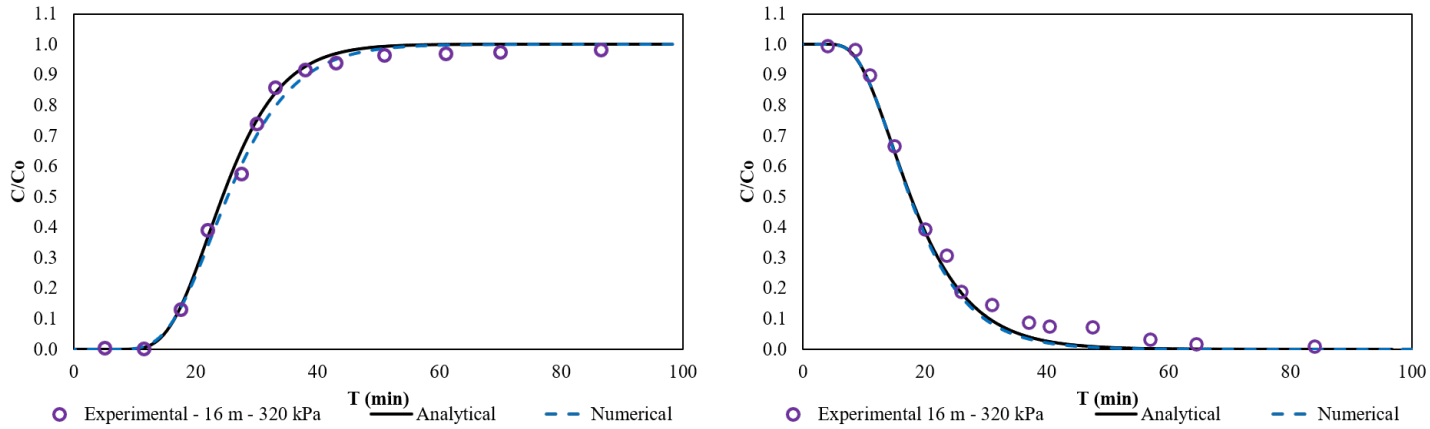

Figure 4.20: Numerical fitting with the experimental and analytical data from column and leaching tests from the soil at 16 m depth consolidated at 320 kPa.

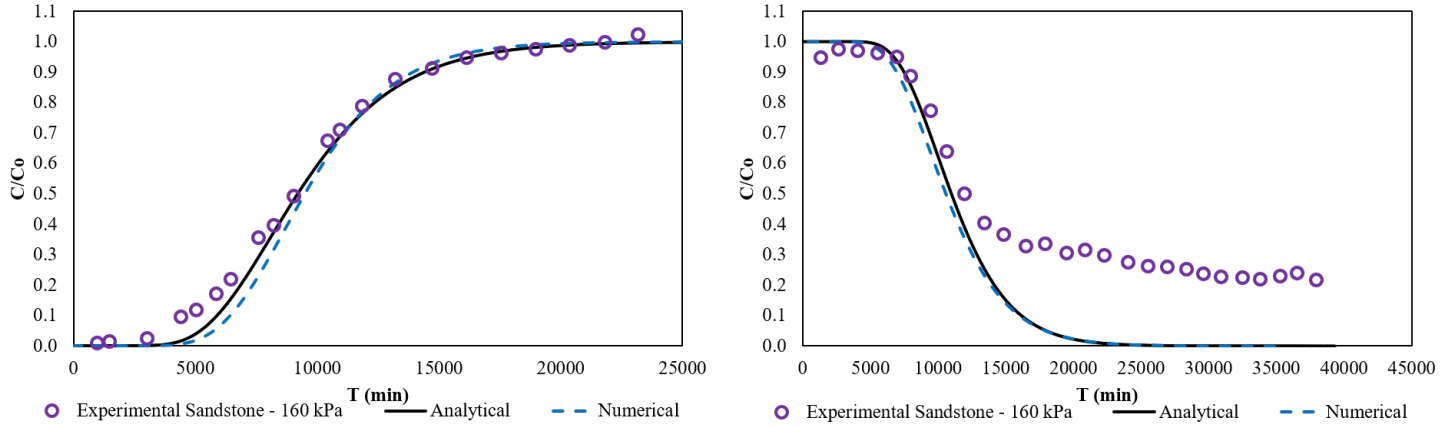

Figure 4.21: Numerical fitting with the experimental and analytical data from column and leaching tests from the sandstone consolidated at 160 kPa.

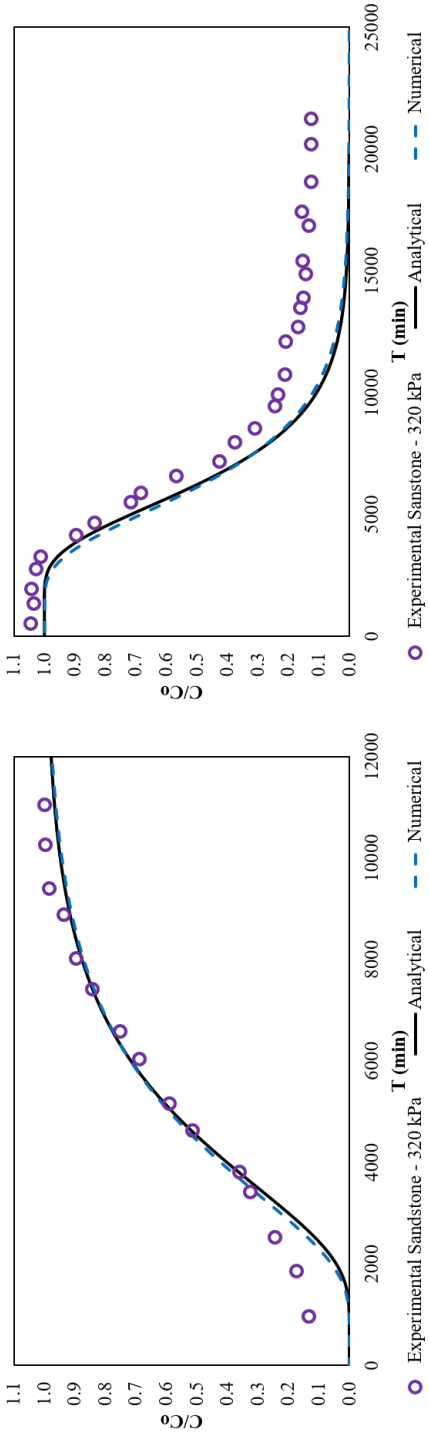

Figure 4.22: Numerical fitting with the experimental and analytical data from column and leaching tests from the sandstone consolidated at 320 kPa.

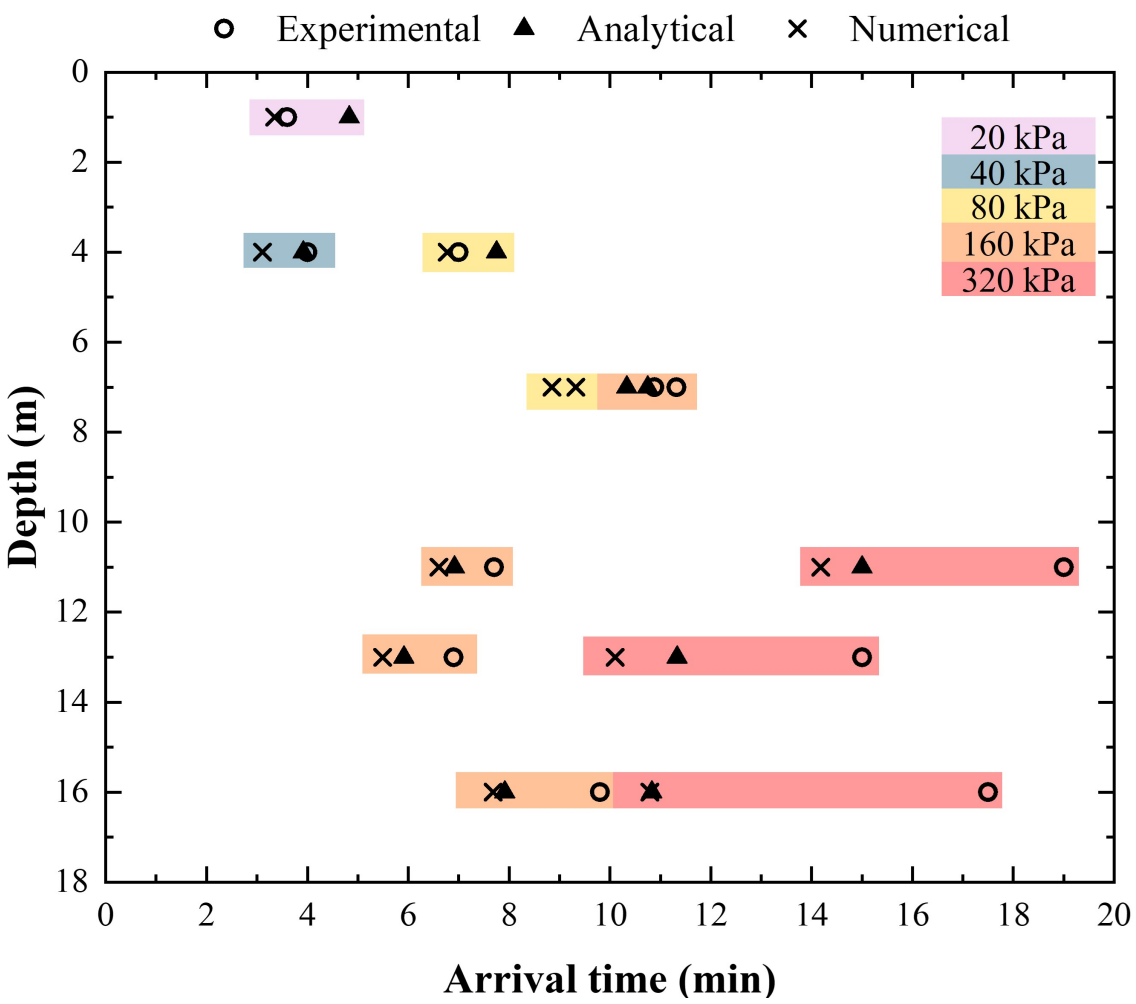

Figure 4.23: Experimental, analytical, and numerical arrival times.

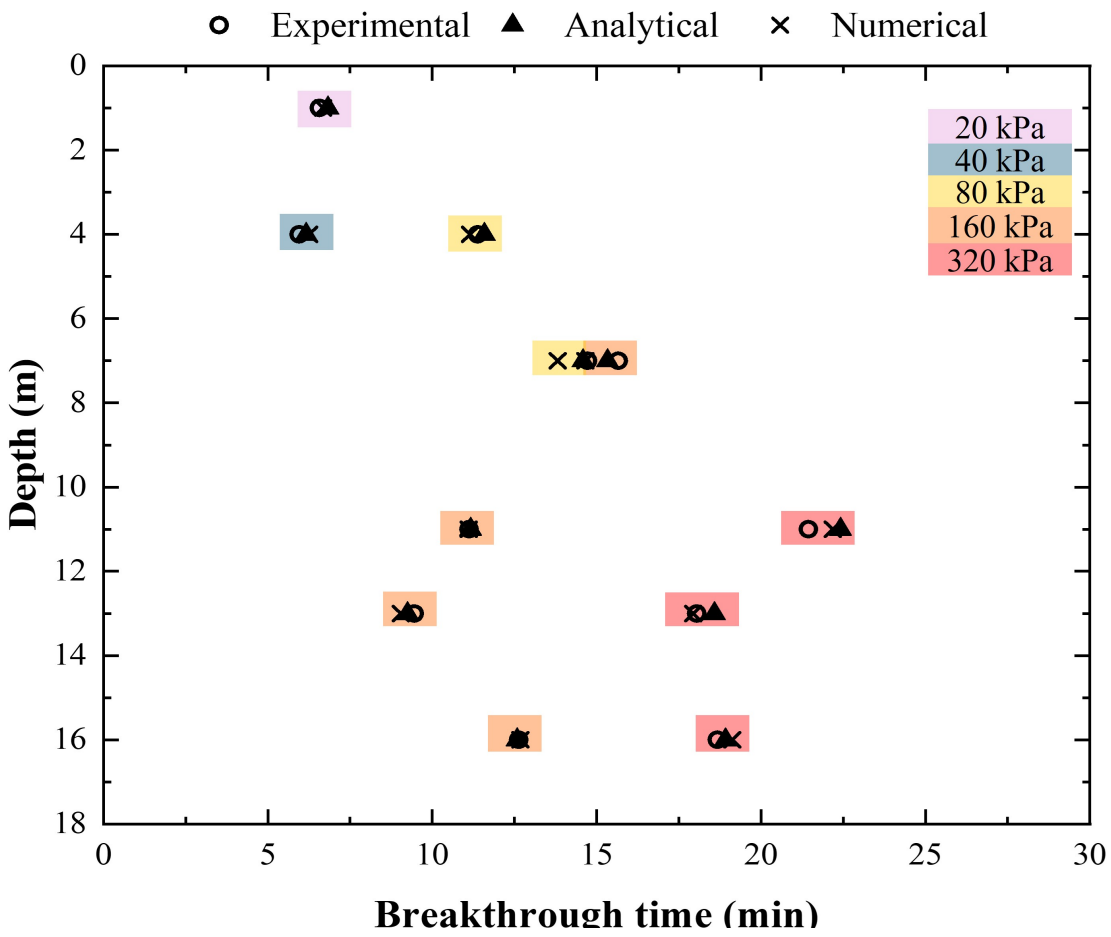

Figure 4.24: Experimental, analytical, and numerical breakthrough times.

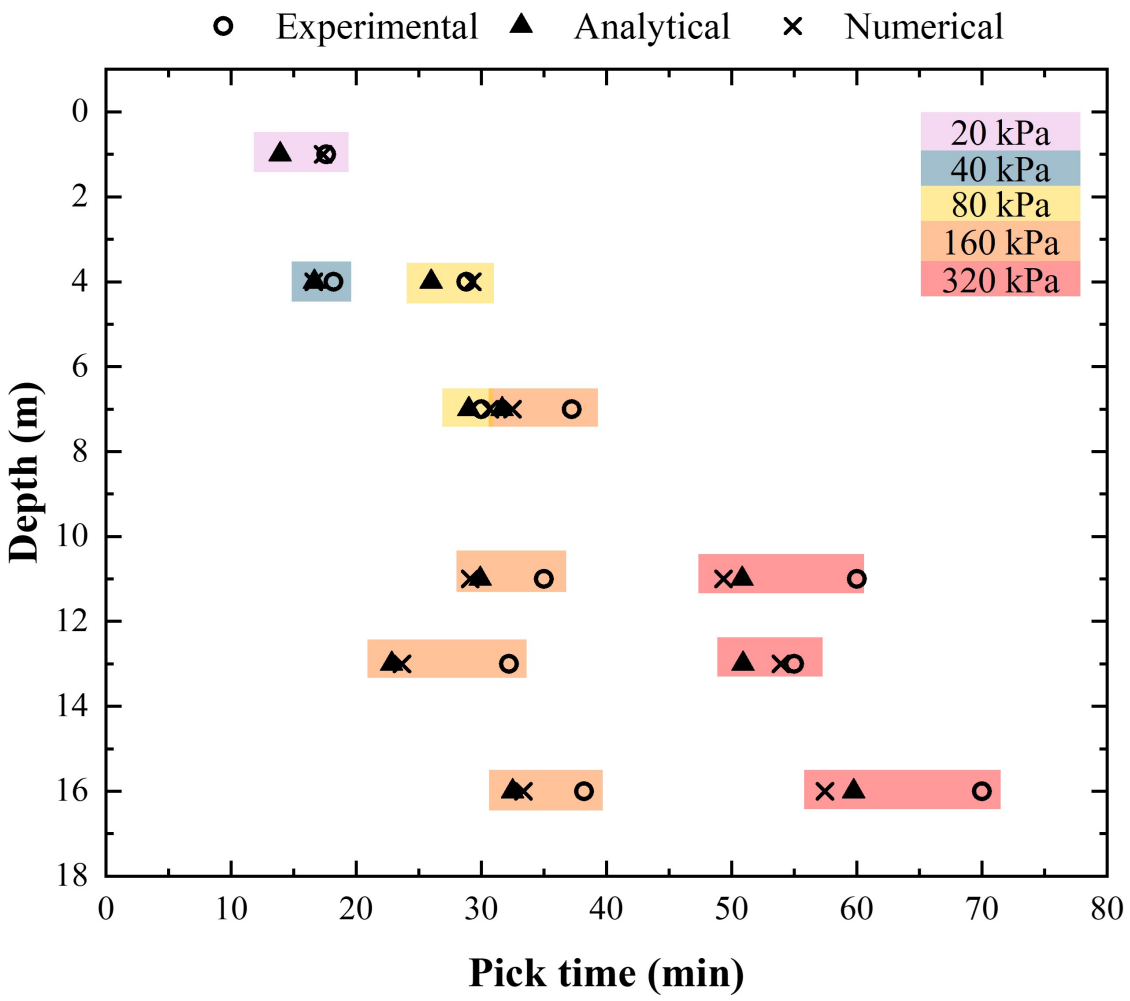

Figure 4.25: Experimental, analytical, and numerical pick times.

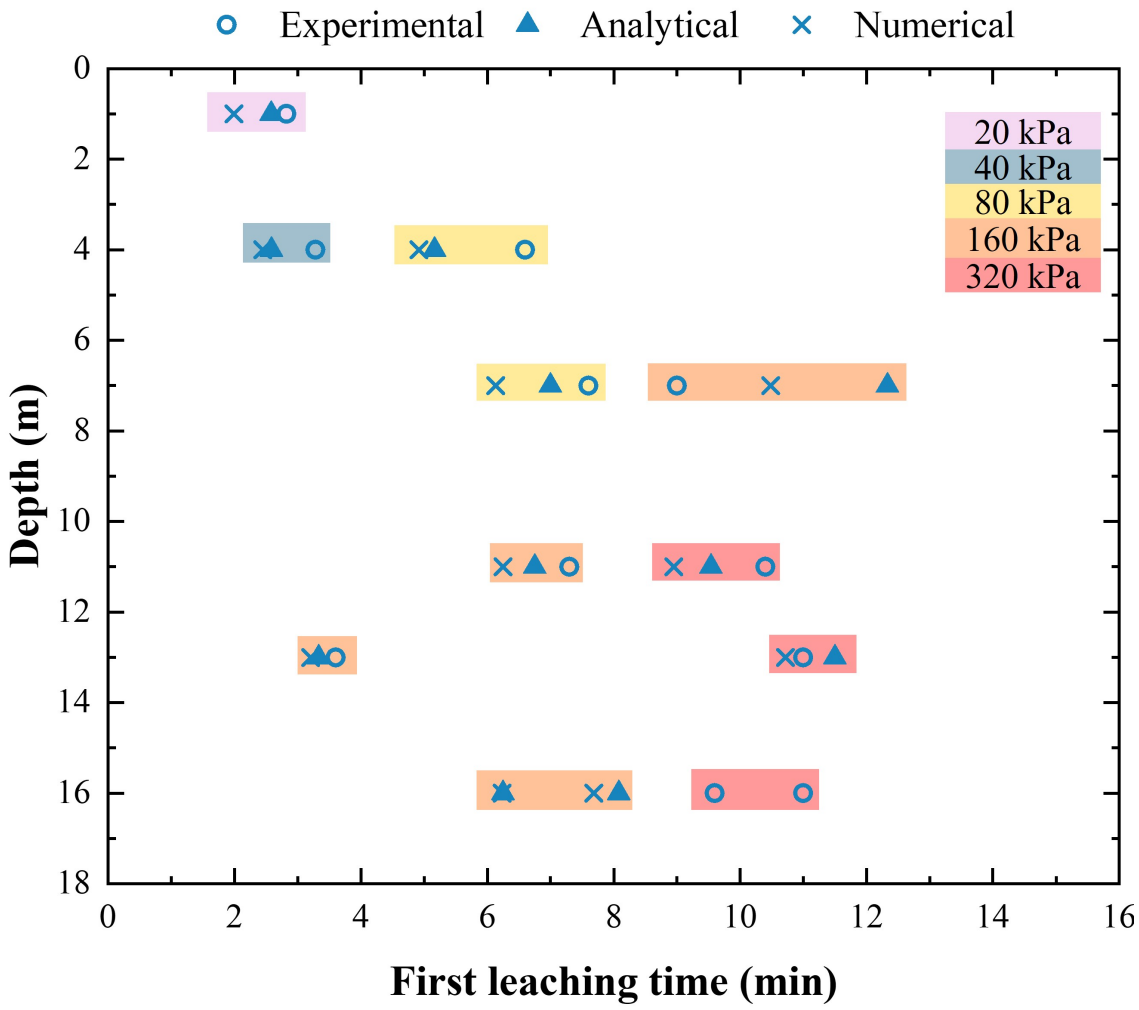

Figure 4.26: Experimental, analytical, and numerical first leaching times.

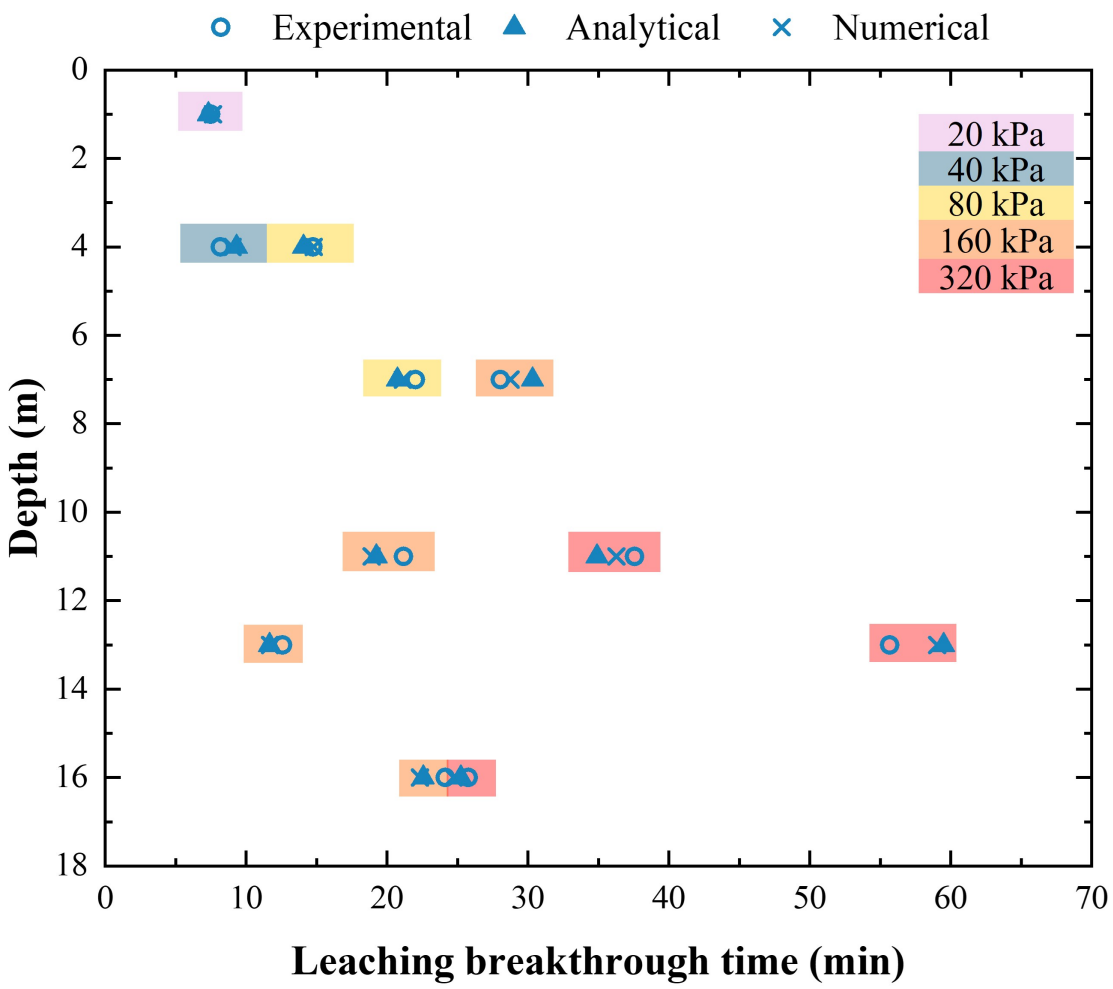

Figure 4.27: Experimental, analytical, and numerical leaching breakthrough times.

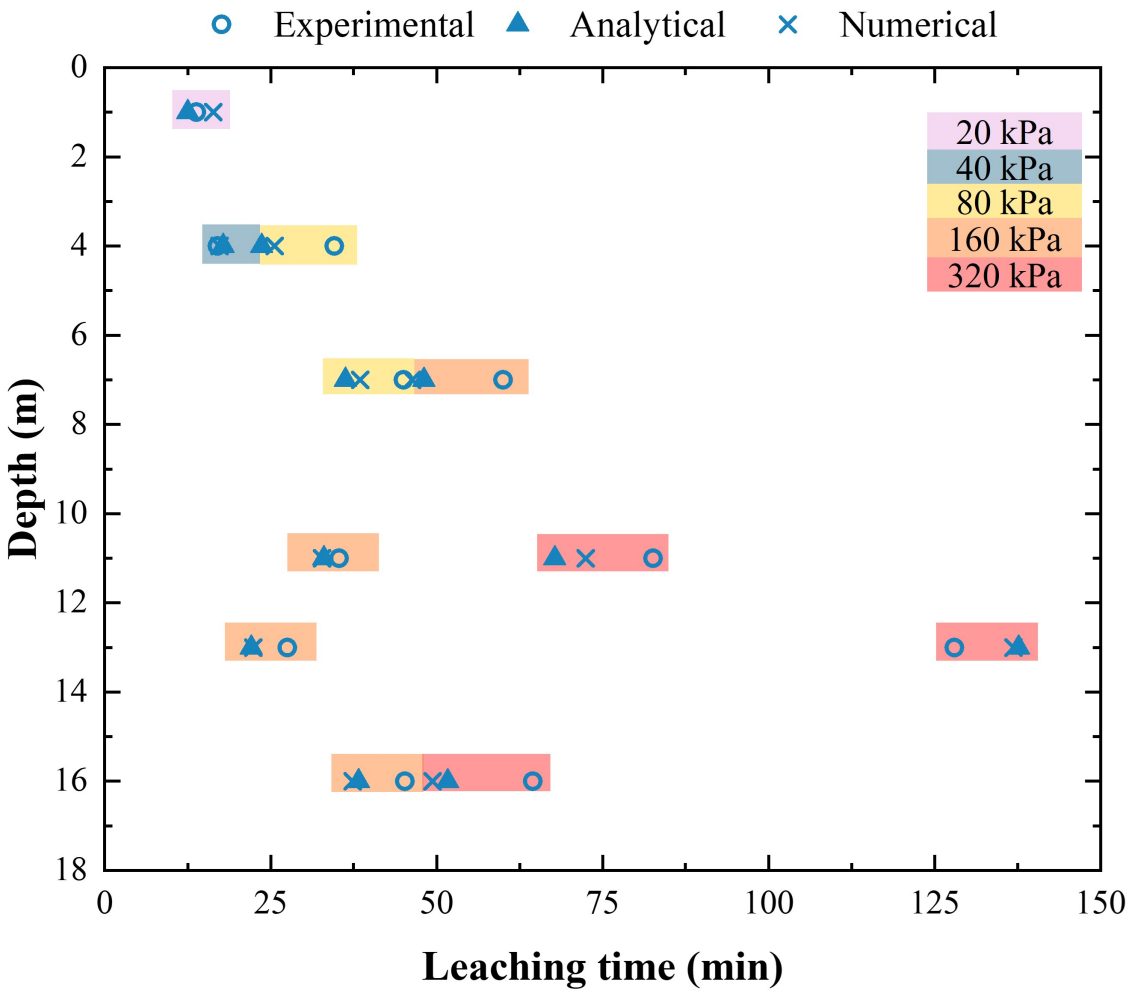

Figure 4.28: Experimental, analytical, and numerical leaching times.

4.3.2 N-S – 0.3 m

Longitudinal profile

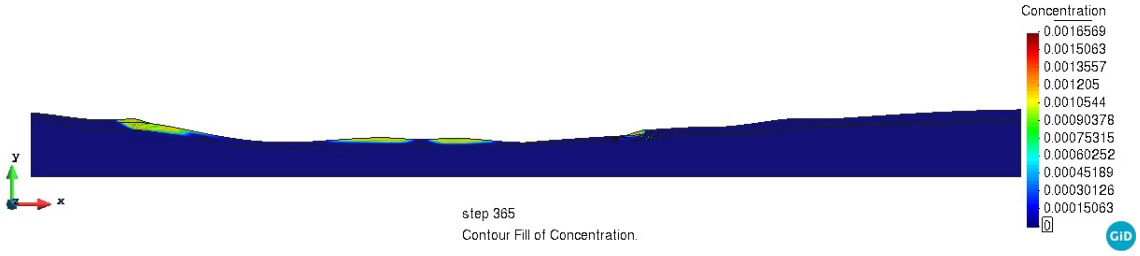

Figure 4.29: Results of the 1-year simulation with a 0.3 m leachate head for the representative north-south profile.

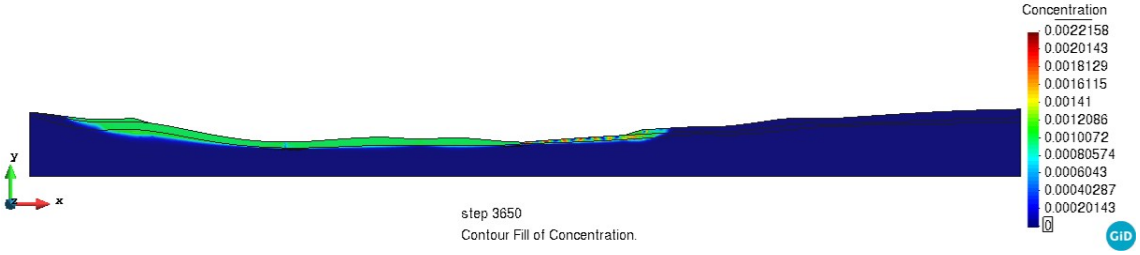

Figure 4.30: Results of the 10-year simulation with a 0.3 m leachate head for the representative north-south profile.

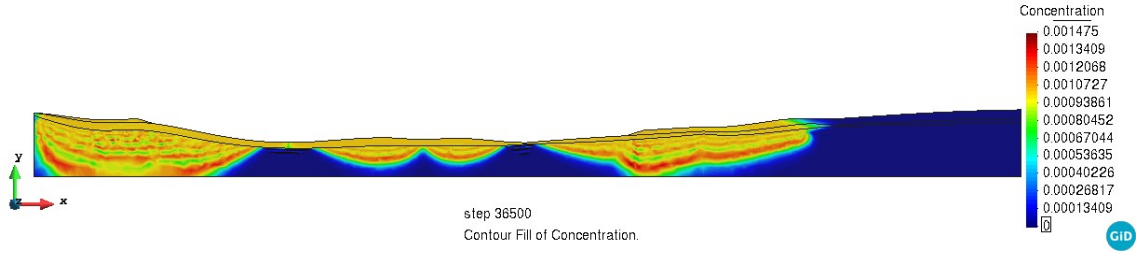

Figure 4.31: Results of the 100-year simulation with a 0.3 m leachate head for the representative north-south profile.

The results of the N-S profile simulations are depicted in Figures 4.29, 4.30, and 4.31 for 1, 10, and 100 years of simulation with a hydraulic leachate head of 0.3 m, illustrating the contamination plume's fate. The results show that up to the tenth year, the plume spread homogeneously. Still, in the transition between soil and sandstone, there was a preference for flow through the residual soil due to its higher permeability compared to sandstone, a result

reflected in the 100-year simulation in which the center of the pit was not entirely affected by the contaminant, unlike the edges of the section.

Figure 4.32 depicts the horizontal spread profile of the contaminant at depths of 21, 33, and 45 m over 1, 10, and 100 years of simulation. At a depth of 21 m, the plume initially showed concentration in the central area of the waste pit within the first year, reaching maximum concentration in 10 years and ultimately extending across the entire profile after 100 years. Conversely, relative concentration remained negligible at a depth of 33 m in the first year but exhibited lateral spread after a decade, intensifying over 100 years.

Notably, between 10 to 100 years, at a depth reflecting the sandstone's center just under 200 m horizontally, the pollutant propagated laterally, reducing its concentration in this specific area while intensifying between 200 and 300 m horizontally. Subsequently, zero concentrations after 100 years in the horizontal positions between 150 and 200 m and between 225 and 275 m exemplify the dominance of horizontal migration over vertical migration.

For the base of the sandstone, in this profile defined at 45 m depth, there is no evidence of the contamination plume in the center of the waste pit in any of the periods analyzed. Maximum relative concentrations after 100 years were between 25 and 100 m from the origin of the profile, and 80% of the maximum concentration was at 450 m horizontal distance.

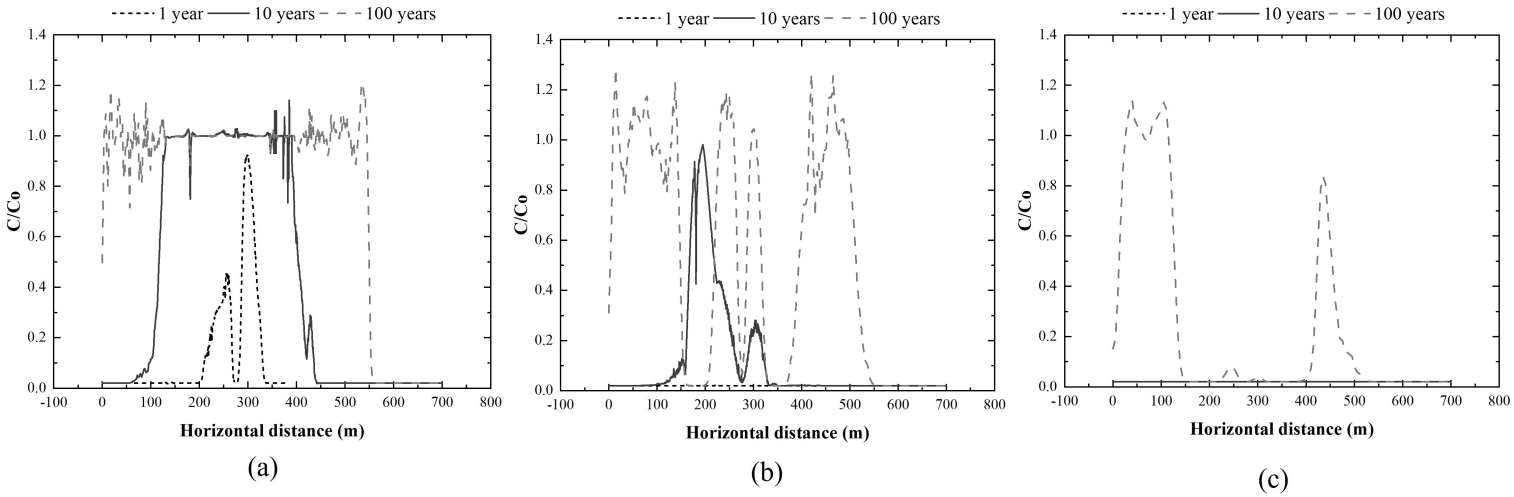

Figure 4.32: Variation of the relative concentration with the horizontal distance for 0.3 m of leachate head, considering 1, 10, and 100 years in a study of the (a) surface, (b) middle, and (c) the base of the north-south profile.

Left slope

Concerning the vertical spread of the contamination plume, Figure 4.33 illustrates the section corresponding to the left slope located 75 m from the source. At 250 m from the origin, the center of the pit is shown in Figure 4.34, while Figure 4.35 shows the slope to the right of the waste pit at a distance of 430 m from the origin. Figure 4.33 reveals that the horizons formed by colluvium and residual sandstone were saturated with a maximum relative concentration in the first year, reducing to zero when encountering the sandstone at 1 year and, after 10 years, the concentration remained maximum up to a depth of around 15 m in the sandstone. After 100 years, the concentration varied along the profile but was consistently above 80% of the maximum value.

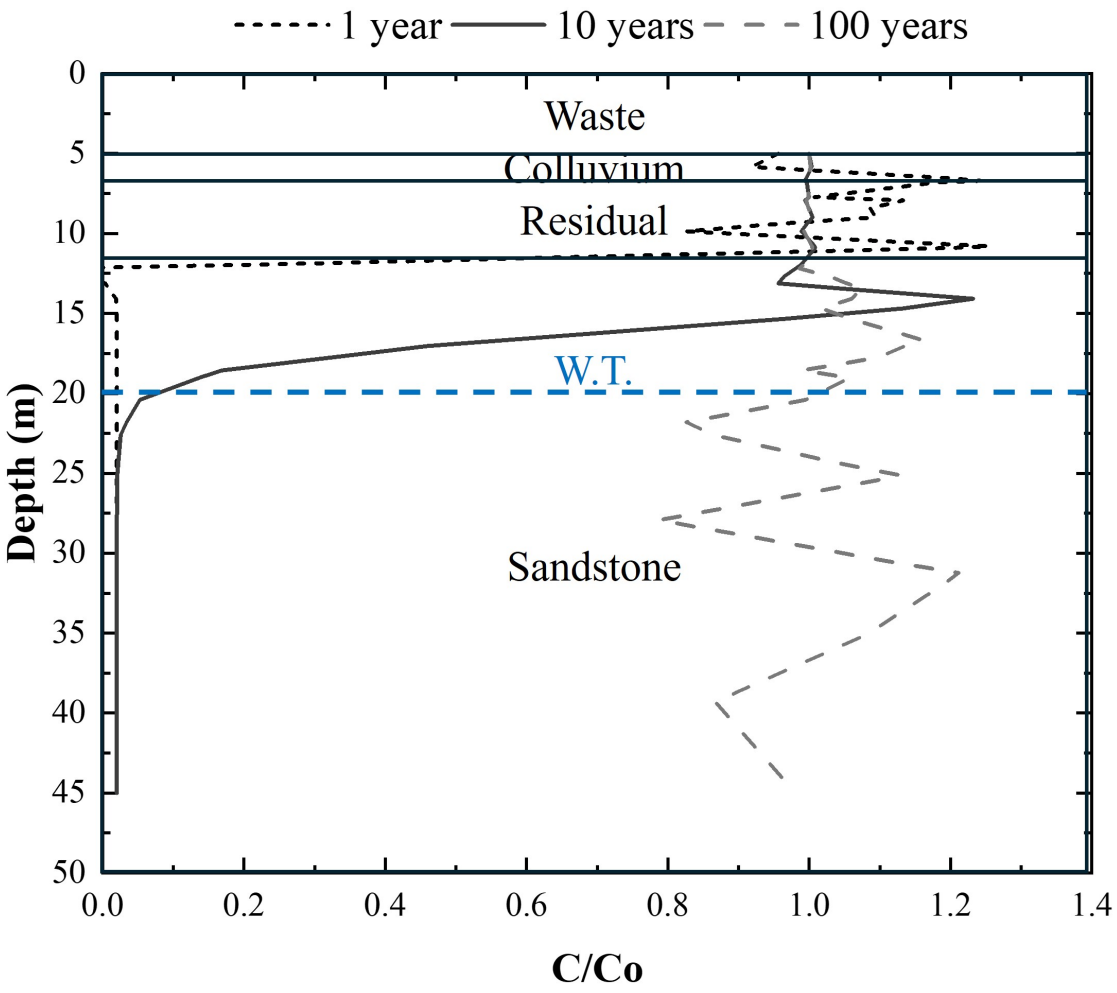

Figure 4.33: Relative concentration with depth for 1, 10, and 100 years of simulation of the left waste pit of the north-south profile, considering 0.3 m of leachate head.

Pit center

The concentration profile along the depth in the middle of the investigated section is depicted in Figure 4.34. In this section, colluvium is absent, and the waste mass closely aligns with the water table. At this position, the concentration peaks in the first year, gradually decreasing as it crosses the WT and diminishing to zero at the interface of the residual soil with the sandstone. After a decade, the contaminant saturates the soil layer, and once it encounters the sandstone, the concentration dramatically reduces, reaching zero at a depth of approximately 5 m. Over a century, the concentration peaks at the base of the residue with minor fluctuations. Upon reaching a depth of 32.5 m, it declines to 10% of the concentration at a depth of 45 m.

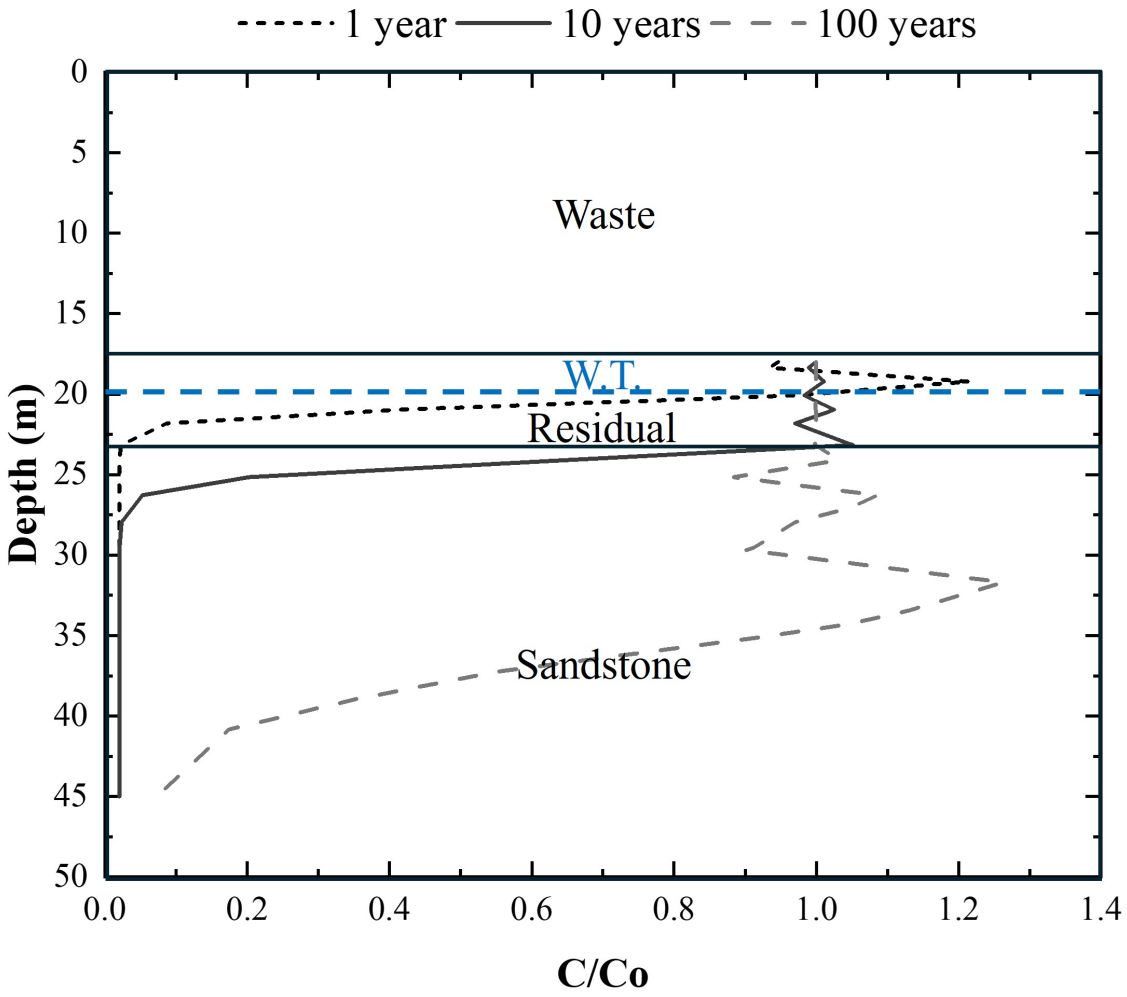

Figure 4.34: Relative concentration with depth for 1, 10, and 100 years of simulation of the middle waste pit of the north-south profile, considering 0.3 m of leachate head.

Right slope

The representative section of the slope to the right of the waste pit, 430 m from the origin coordinate, is shown in Figure 4.35 , and it shows a similar behavior to the slope to the left of the pit. In 10 years, the horizons with colluvium and residual soil reached maximum concentration. Still, in the first year, only the colluvium showed a similar condition. Even before approaching the residual soil horizon, its concentration reduced to zero when percolating less than 5 m in depth, reaching half of the maximum concentration at 2.5 m below the base of the residual soil. Over 100 years, both slopes demonstrated analogous behavior, exhibiting oscillations along the profile. Throughout this time, the relative concentration consistently remained above 80%.

The supplementary material for this chapter contains the data on the variation in c/co versus horizontal distances and depth for hydraulic leachate heads of 0.6 and 1.2 m. To compare the results, they were grouped by year and hydraulic head, with exclusions for the 21 m depth, the first year for the section at 33 m depth, and the tenth year for the section at 45 m depth due to negligible differences.

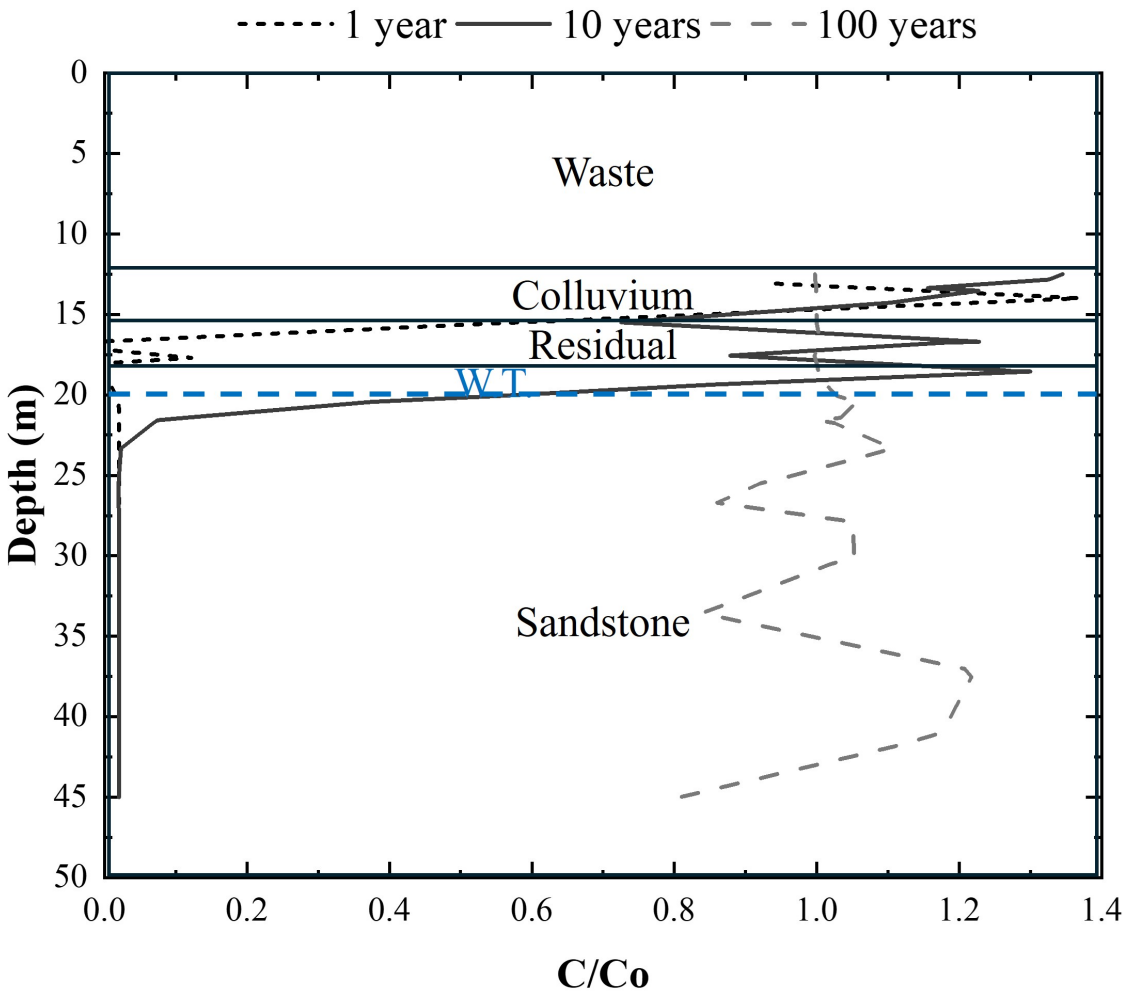

Figure 4.35: Relative concentration with depth for 1, 10, and 100 years of simulation of the right waste pit of the north-south profile, considering 0.3 m of leachate head.

4.3.3 N-S – Same layer, different heads and years

Therefore, Figure 4.36 (a) shows the longitudinal profile at 33 m depth after 10 years for the three simulated hydraulic heads. The increase in hydraulic heads triggered the rise in concentration peaks in the center of the waste pit, with a noticeable increase to 1.2 m of leachate at 300 m from the origin of the section, in which the relative concentration increased by 5% about the other hydraulic heads.

After 100 years for the same section shown in Figure 4.36 (b), the relative concentration was high and, as described in the previous section for 0.3 m of leachate, there was a tendency for it to migrate to the sides of the profile, denoted by the zero concentration between 150 and 200 m, as well as at 325 and 375 m from the origin and close to zero at 275 m. The increase in the hydraulic head of leachate filled the gaps between 150 and 200 m and at 275 m, mainly at 1.2 m, with the interior of the pit being taken over by the maximum concentration, excluding only the interval from 325 to 375 m of horizontal distance, which was practically narrowed to a point value of zero concentration at 350 m from the origin of the section.

The data covering the section located at the base of the sandstone at a depth of 45 m displays the results for the simulated hydraulic heads, as depicted in Figure 4.36 (c). Like the findings for the section above, the increase in hydraulic head resulted in heightened concentration peaks, revealing that the projection of the waste pit's center at 45 m depth, specifically between 150 and 400 m from the simulation's origin, did not exhibit a notable relative concentration for leachate heads of 0.3 and 0.6 m. Only with a 1.2 m leachate head and between 225 and 260 m from the origin was c/co found to be equal to or greater than 0.2, surpassing the acceptable concentration for the tracer analyzed. This aspect concerning breakthrough curves will be further elaborated in a dedicated section.

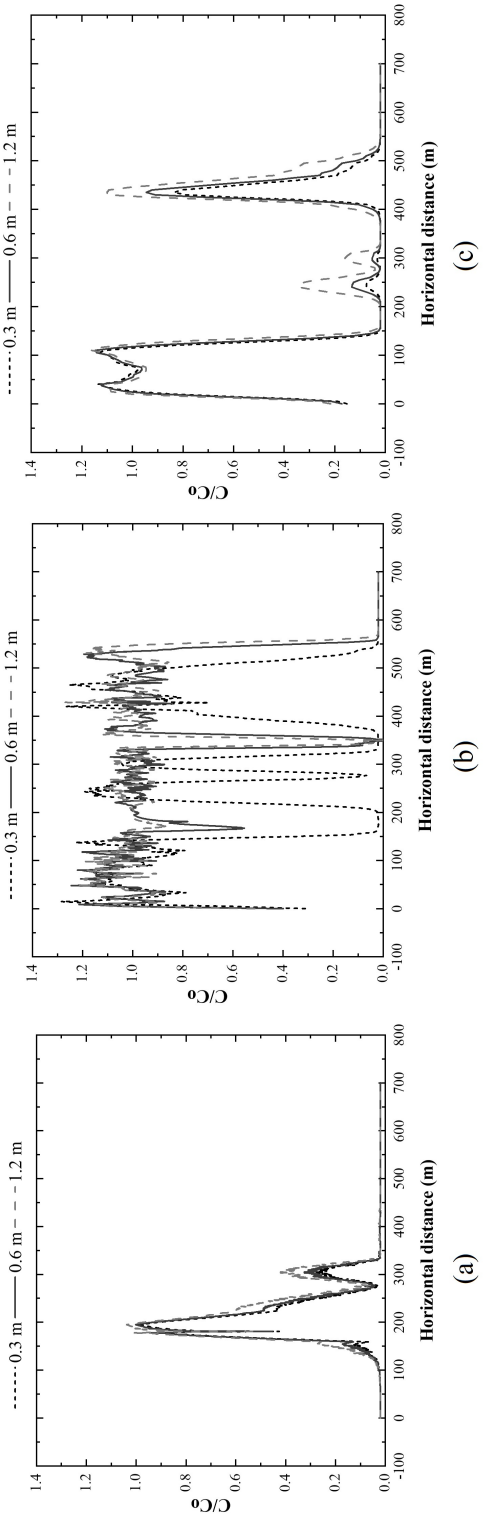

Figure 4.36: Variation of relative concentration with horizontal distance for 0.3, 0.6, and 1.2 m leachate height (a) in the middle of the N-S pit after 10 years of simulation, (b) in the middle of the N-S pit after 100 years of simulation, and (c) at the base of the N-S pit after 100 years of simulation.

Left slope

The cross-section representing the slope to the left of the waste pit, 75 m from the origin of the section, includes the data for the variation in concentration by depth at 10 and 100 years of simulation, which are illustrated in Figure 4.37. According to the findings, the variation in the hydraulic head of leachate did not exhibit notable changes in the initial scenario, with the concentration attenuating from a depth of 15 m from the maximum concentration to nearly zero after percolating 7.5 m vertically. The concentration remained below 20% of the peak concentration upon reaching the water table.

The increase in the leachate column in the 100-year simulation led to a greater spread of concentration in-depth, albeit with variations, but always at values higher than 0.8 c/co at any of the simulated hydraulic heads. Therefore, at 100 years, the entire profile was contaminated by the maximum concentration stipulated in the simulation, regardless of the hydraulic heads considered.

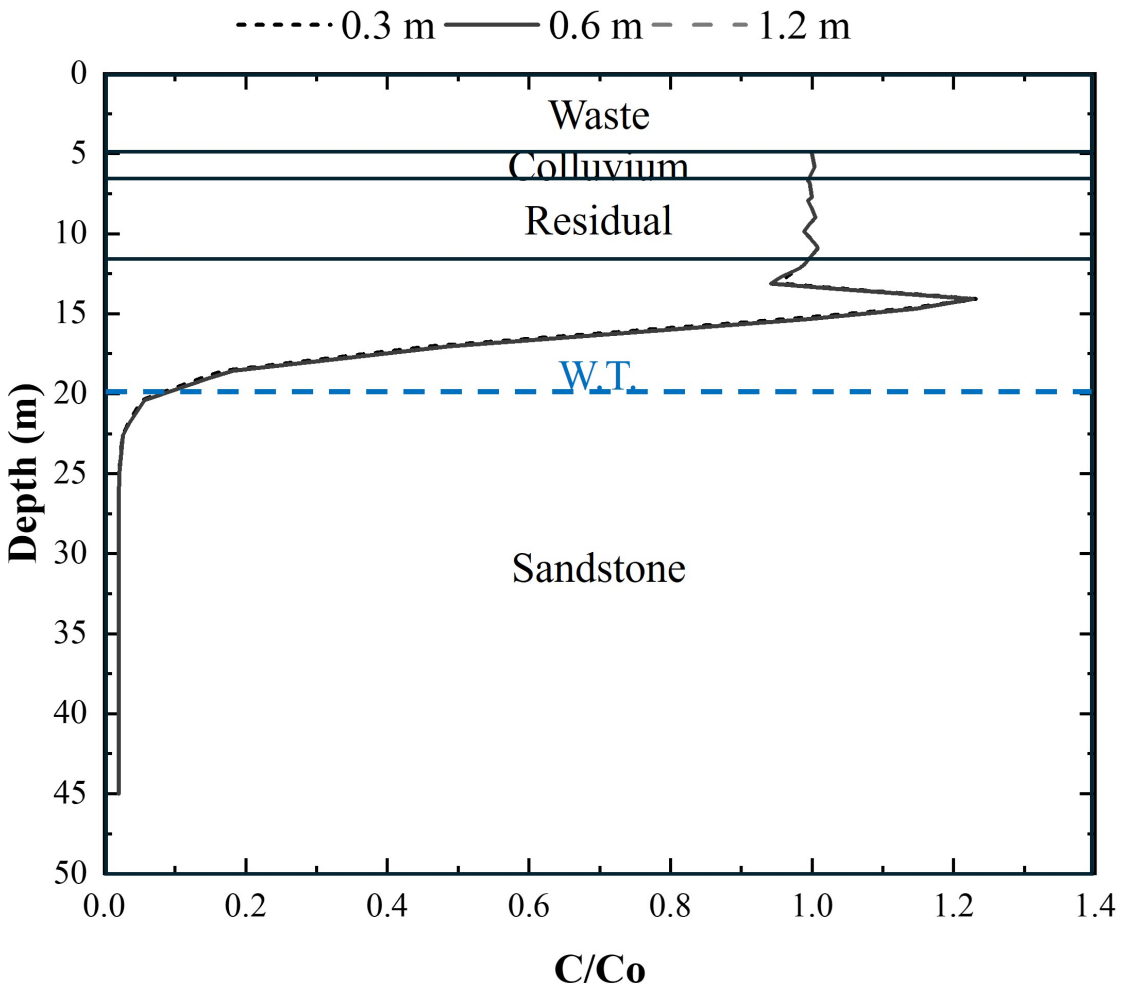

Figure 4.37: Relative concentration with depth resulting of the left waste pit N-S profile for leachate heads of 0.3, 0.6, and 1.2 m from (a) a 10-year simulation, and (b) a 100-year simulation.

Pit center

The simulation results, depicting the impact of increasing hydraulic head in the central section located 250 m from the source, are illustrated in Figure 4.38 for 10- and 100-year simulation periods. Following the 10-year mark, a slight difference in concentration can be seen, which at 0.3 m reduced rapidly from the peak concentration when it reached the sandstone. The maximum concentration with increased leachate head occurred in the same position. However, the reduction was less pronounced, showing a more remarkable advance of the contamination in the vertical direction toward the interior of the sandstone. Thus, the sandstone could attenuate the plume in the three simulated conditions even at peak concentration when reaching the WT.

Similarly, after 100 years, the trend of the contamination plume with increasing leachate head was to extend vertically and be less attenuated, e.g., with 0.3, 0.6, and 1.2 m of leachate column, the concentration at 40 m depth was respectively 23.5%, 38.5%, and 74% of the maximum concentration. The water table is highly vulnerable, given the proximity to the waste pit and the boundary condition that initiates at c/co=1 at the pit's base. Although the sandstone possesses attenuating capabilities, after a century, the profile displayed concentrations exceeding the permissible limits under the three simulation conditions. It closely approached the peak concentration with a 1.2 m leachate head.

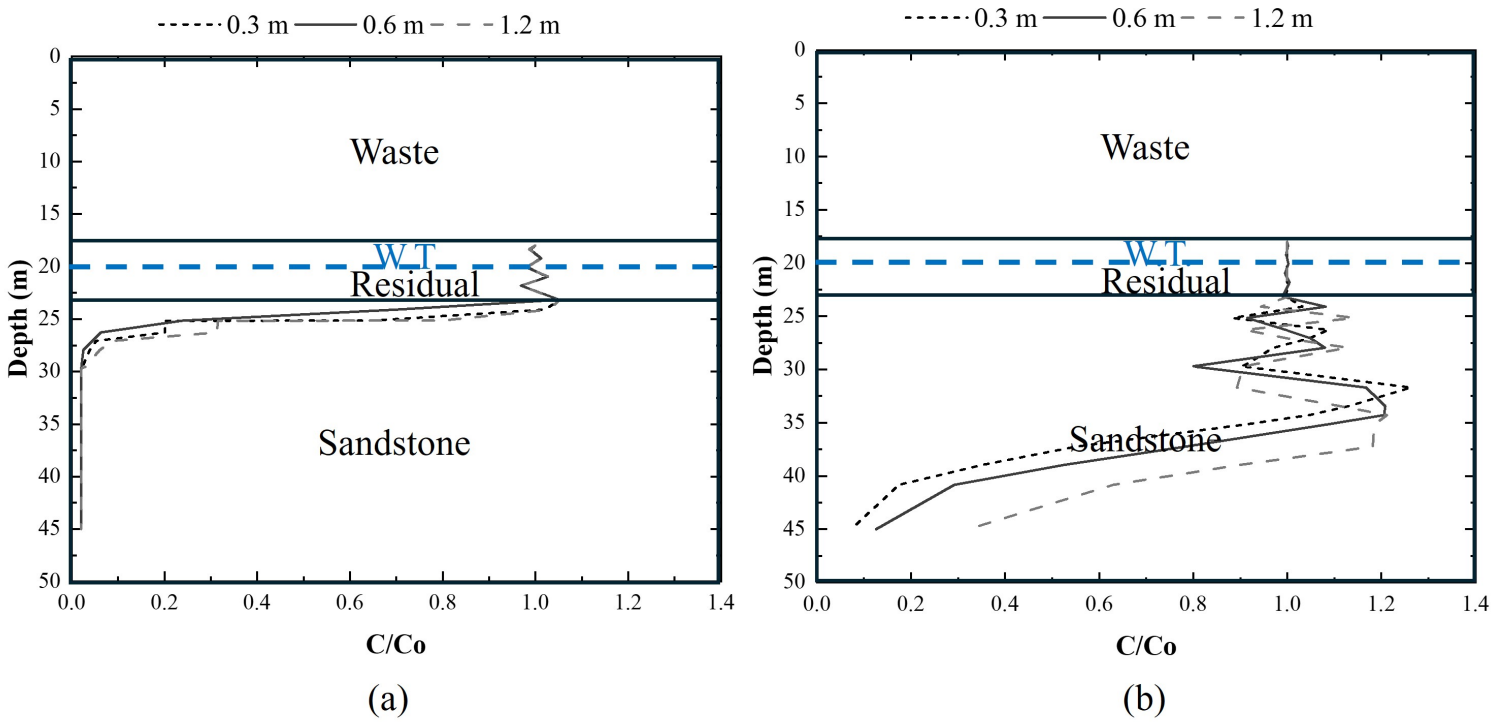

Figure 4.38: Relative concentration with depth resulting in (a) a 10-year simulation and (b) a 100-year simulation in the middle waste pit N-S profile for leachate heads of 0.3, 0.6, and 1.2 m.

Right slope

The representative section of the slope to the right of the waste pit, located 430 m from the simulation's origin, shows the results for 10 and 100 years, as shown in Figure 4.39. As with the previous sections, there were no significant variations in concentration with depth after a decade. It is interesting to note that with 0.3 m of leachate, the concentration in the colluvium and residual horizons differed from the heads at 0.6 and 1.2 m, starting with a higher concentration than the previous two. Still, when they met the sandstone horizon, the three heads reduced their concentration to zero when they percolated 5 m in depth.

After a century, the profile had become saturated with the contaminant. Despite fluctuations along the depth, the concentration consistently exceeded 80%. Moreover, increased hydraulic head resulted in higher concentrations at greater depths, with less apparent evidence of attenuation.

In both instances, the plume exceeded 0.2 c/co when it reached the water table. However, its impact diminished upon reaching the sandstone during the 10-year simulation. Nevertheless, after 100 years, the contaminant plume fully occupied the entire profile.

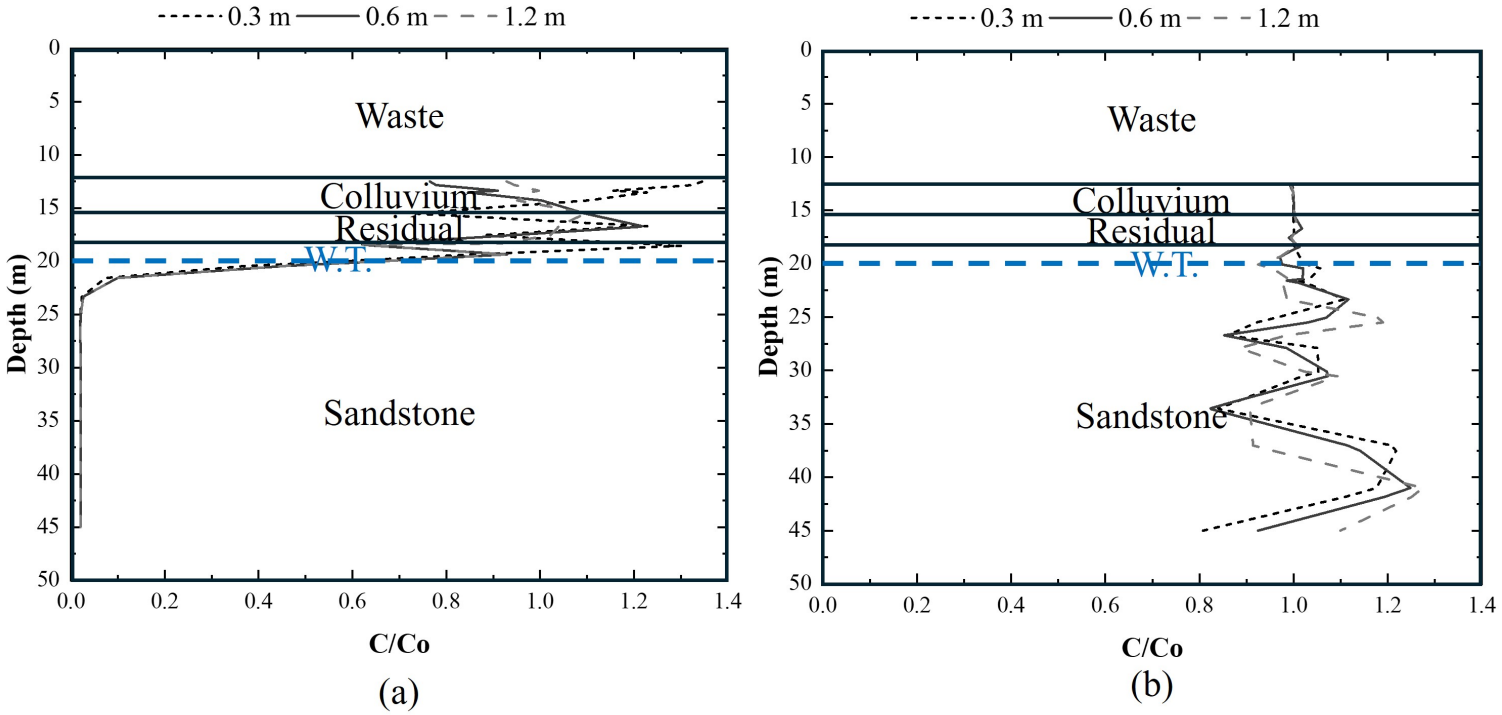

Figure 4.39: Relative concentration with depth resulting from (a) a 10-year simulation and (b) a 100-year simulation of the right waste pit N-S profile for leachate heads of 0.3, 0.6, and 1.2 m.

4.3.4 N-S – BTCs

The data from the NaCl transport in Chapter 3 was used as a reference for the failure in the system related to Na concentrations above 200 mg/L, which formed the basis for the simulations in the current chapter. Therefore, Figure 4.40 (a) depicts the breakthrough curves for the colluvium horizon of the slope to the left of the waste pit at 75 m horizontal from the origin and 6.70 m deep at the base of this soil for 0.3, 0.6, and 1.2 m of leachate. The BTCs were consistent for the three simulated situations, indicating that the colluvium is at a limiting relative concentration at 103 days at this position in the profile.

Figure 4.40 (b) shows the boundary of the residual soil with the sandstone for the same slope but at a depth of 11.95 m. The findings indicate a rapid spreading of the contamination plume, which reached its maximum value after 4.5 years and reached BTt at 1.07 years.

The longitudinal section at a depth of 28.45 m reveals the findings depicted in Figure 4.40 (c). The leachate head increase from this depth led to temporal shifts in the BTC. Consequently, the arrival times of the concentration of interest were shortened, and as a result, the time to BTt decreased from 20.20 years at 0.3 m to 19.85 years and 19.15 years at 0.6 m and 1.2 m of head, respectively.

The data presented in Figure 4.40 (d) illustrates the BTCs from the base of the sandstone for the same slope. The curves suggest that the contamination plume required approximately 35 years to surpass the reference value for the three analyzed scenarios. Additionally, it is noteworthy that the curves corresponding to the highest hydraulic heads yielded the shortest breakthrough time (BTts). The threshold values for distances of 0.3, 0.6, and 1.2 m were respectively 50.93, 49.92, and 47.97 years.

In light of the similar results obtained for the colluvium and residual sandstone horizons across all longitudinal and cross sections in the various scenarios under investigation, it is deemed beneficial to direct greater attention to the depths corresponding to the center and base of the sandstone in the N-S section. Thus, BTCs of the colluvial soils situated to the right of the pit slope and at a depth of 15.5 m, residual at 250 m from the origin with a

depth of 23.15 m, and residual at a distance of 430 m from the origin with a depth of 18.4 m are accessible in the supplementary materials.

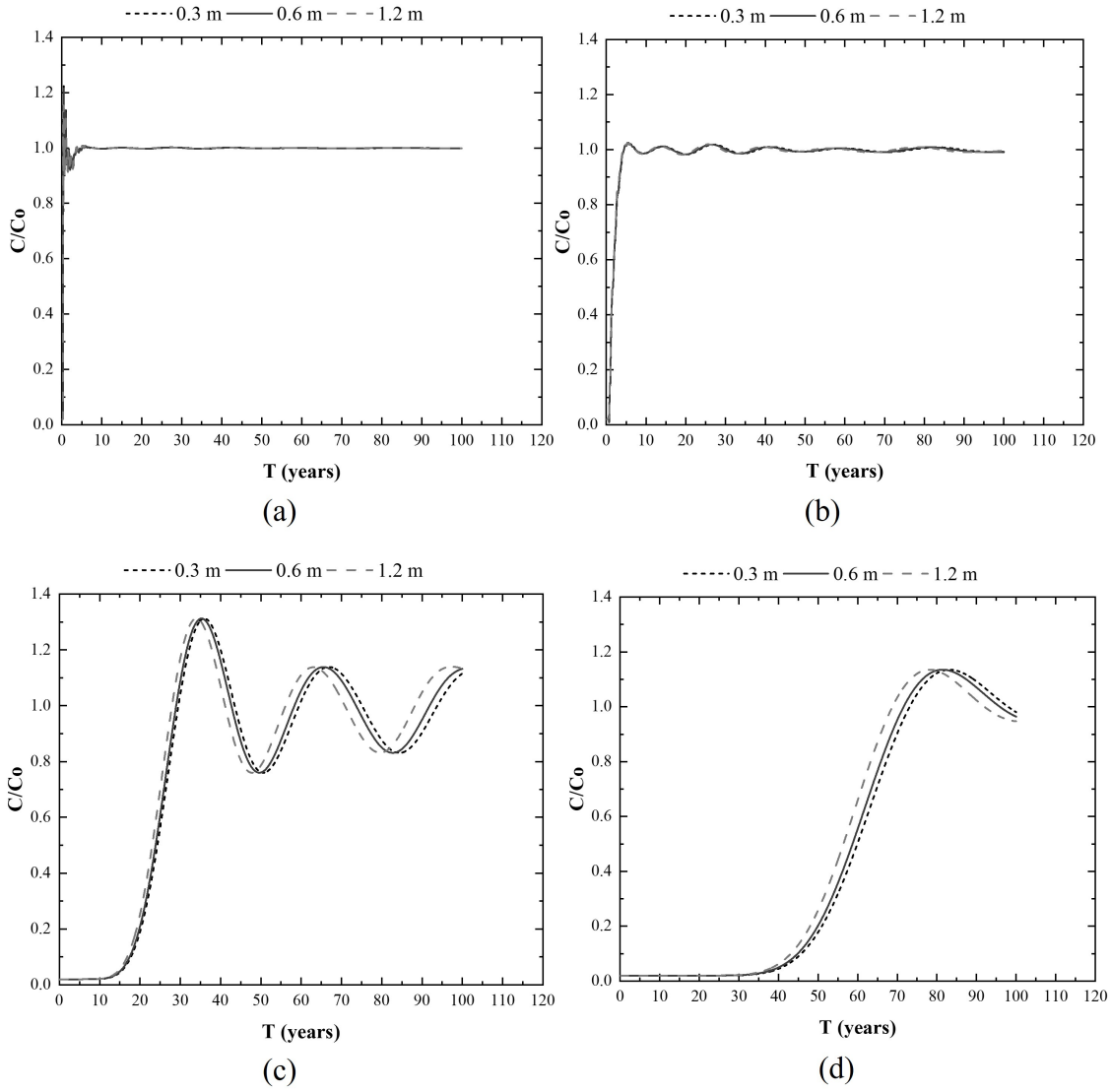

Figure 4.40: Breakthrough curve for the N-S waste pit at the left slope, with leachate heads of 0.3, 0.6, and 1.2 m at horizons (a) colluvium, (b) residual soil, (c) in the middle of the sandstone, and (d) in the sandstone base.

Therefore, Figure 4.41 (a) describes the BTCs representative of the sandstone situated beneath the center of the waste pit at 250 m from the origin and a depth of 34.1 m. The increase in the hydraulic head of the leachate resulted in the tracer's earlier arrival times, as evident from the simulations for this position, with limit concentrations reaching after 25 years. Specifically, the limit concentration was achieved at 47.03, 42.83, and 36.43 years for the 0.3, 0.6, and 1.2 m leachate columns.

In Figure 4.41 (b), the results from the base of the sandstone at a depth of 45 m in the same section are shown. The breakthrough curves indicate the absence of a contamination plume in this specific section. It is noteworthy that the 0.3 and 0.6 m leachate columns did not attain the limit concentration. However, upon increasing the leachate head to 1.2 m, the breakthrough time was observed to be 90.84 years.

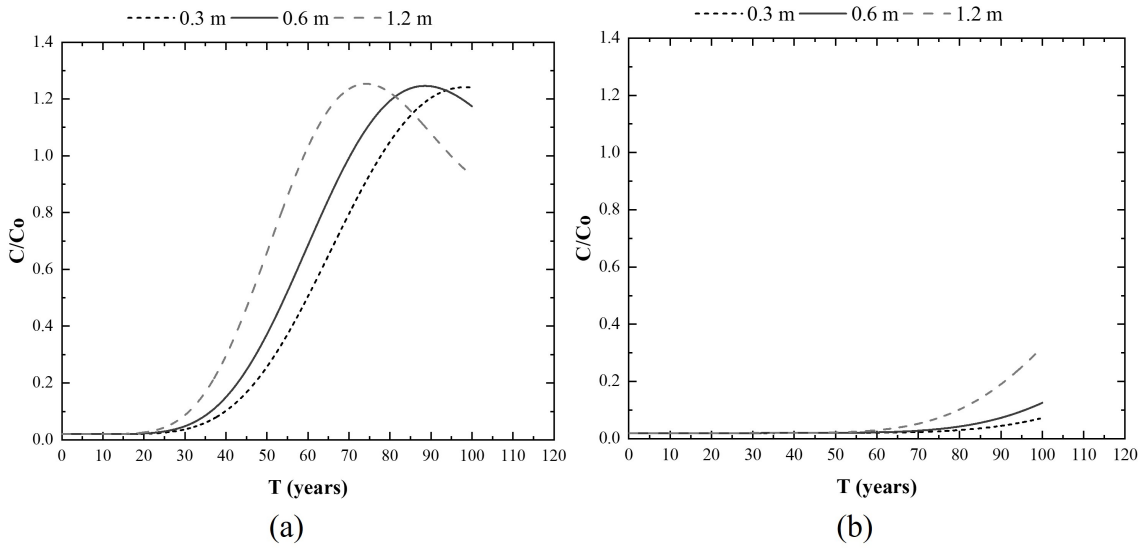

Figure 4.41: Breakthrough curve (a) in the middle of the sandstone and (b) in the sandstone base at the center of the N-S waste pit with leachate heads of 0.3, 0.6, and 1.2 m.

The BTCs results about the right-hand slope of the waste pit in the N-S profile, located 430 m from the origin and with depths of 31.7 m and 45 m, are illustrated in Figure 4.42. At a depth of 31.7 m, the BTCs exhibited behavior like others in the analyzed profile, indicating reduced arrival times with increased hydraulic head. Specifically, the BTt of 35.99 years with a 0.3 m leachate column was observed to shift to 34.45 and 31.71 years with hydraulic heads of 0.6 m and 1.2 m, respectively.

The findings obtained at a depth of 45 m for the rightward slope indicate that the contaminant penetrated the base of the sandstone, with its peak concentration occurring under a hydraulic head of 1.2 m. However, these results also illustrate the sandstone's ability to attenuate, as it exhibited signs of contamination after 50 years of simulation. Regarding BTts with leachate columns of 0.3, 0.6, and 1.2 m, the threshold concentration was attained after respectively 74.93, 71.61, and 65.75 years.

Tables 4.5 to 4.7 present the durations required to achieve the threshold concentrations in the soil and rock profiles examined in this section.

The tables demonstrate a decrease in breakthrough time as the hydraulic head of leachate increases and highlight the differential impact of the contamination plume on the left and right slopes of the waste pit as compared to the center, particularly the left slope. The findings also indicate diminished contaminant migration through the sandstone, particularly at the base in the central area of the pit, which was minimally affected by the tracer. The results suggest lateral flow, primarily through the more permeable layers, directed towards the left slope of the pit, namely, towards the northern part of the MSW disposal site.

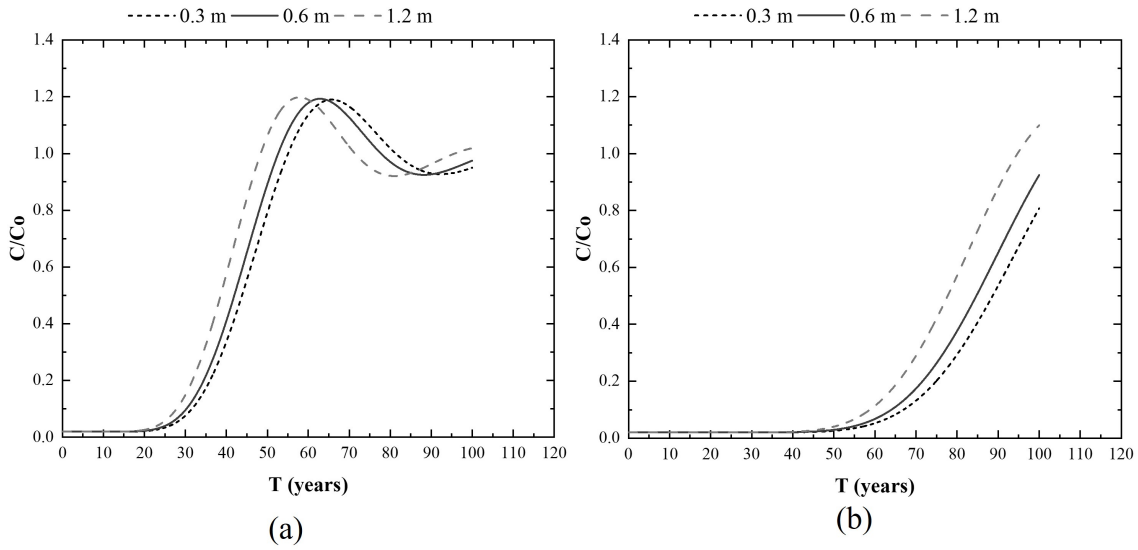

Figure 4.42: Breakthrough curve (a) in the middle of the sandstone and (b) in the sandstone base at the right slope of the N-S waste pit with leachate heads of 0.3, 0.6, and 1.2 m.

Table 4.5: An overview of the breakthrough curve results from the N-S colluvium horizon.

Layer	Depth (m)	Position	Distance from the origin (m)	Head (m)	BTt (days)
Colluvium base	6.70	Left slope	75.00	0.30	103
				0.60	103
				1.20	103
Colluvium base	15.50	Right slope	430.00	0.30	356
				0.60	342
				1.20	310

Table 4.6: An overview of the breakthrough curve results from the N-S residual horizon.

Layer	Depth (m)	Position	Distance from the origin (m)	Head (m)	BTt (years)
Residual base	11.95	Left slope	75.00	0.30	1.07
				0.60	1.07
				1.20	1.05
Residual base	23.15	Middle	250.00	0.30	1.85
				0.60	2.21
				1.20	1.82
Residual base	18.40	Right slope	430.00	0.30	1.79
				0.60	1.67
				1.20	1.37

Table 4.7: An overview of the breakthrough curve results from the N-S sandstone.

Layer	Depth (m)	Position	Distance from the origin (m)	Head (m)	BTt (years)
In the middle of the sandstone	28.45	Left slope	75.00	0.30	20.20
				0.60	19.85
				1.20	19.15
In the middle of the sandstone	34.10	Middle	250.00	0.30	47.03
				0.60	42.83
				1.20	36.43
In the middle of the sandstone	31.70	Right slope	430.00	0.30	35.99
				0.60	34.45
				1.20	31.71
Sandstone base	45.00	Left slope	75.00	0.30	50.93
				0.60	49.92
				1.20	47.97
Sandstone base	45.00	Middle	250.00	0.30	N.R.
				0.60	N.R.
				1.20	90.84
Sandstone base	45.00	Right slope	430.00	0.30	74.93
				0.60	71.61
				1.20	65.75

4.3.5 E-W – 0.3 m

Longitudinal profile

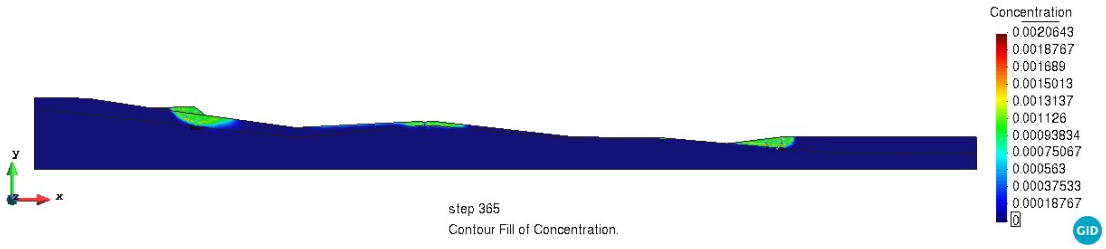

Figure 4.43: Results of the 1-year simulation with a 0.3 m leachate head for the representative east-west profile.

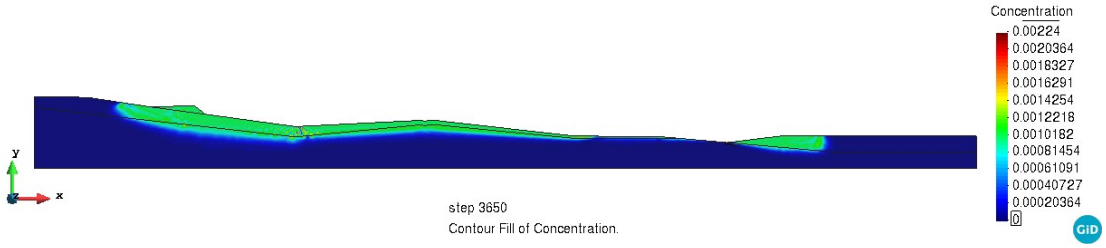

Figure 4.44: Results of the 10-year simulation with a 0.3 m leachate head for the representative east-west profile.

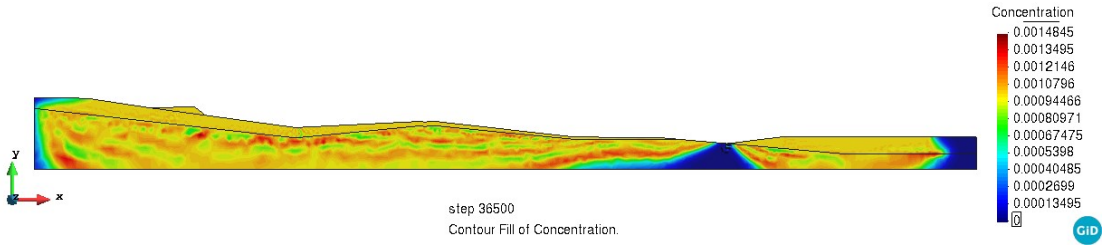

Figure 4.45: Results of the 100-year simulation with a 0.3 m leachate head for the representative east-west profile.

Analogously to the North-South profile, the East-West profile depicted in Figures 4.43, 4.44, and 4.45 illustrates the contamination plume migration simulation outcomes along the longitudinal profile over 1, 10, and 100 years, with a leachate head of 0.3 m. Initially, the simulations of the N-S and E-W sections were comparable up to the tenth year. However, unlike the previously analyzed section, the contaminant had largely spread across the E-W

section after 100 years of simulation, except the right-hand slope, which demonstrated a comparable behavior to the center of the pit in the N-S section, indicating a predominantly horizontal flow.

Given the steepness of the slope, it was determined that an analysis of two longitudinal sections would be beneficial: one at a depth of 31.5 m and the other at a depth of 50 m. Consequently, Figure 4.46 (a) displays the findings regarding the variation in relative concentration with horizontal distance, specifically for a 0.3 m leachate column at 31.5 m and 50 m depths.

The concentration profile along the longitudinal axis at a depth of 31.5 m primarily occurs within the sandstone. However, approximately 500 m from the source, the profile emerges at the surface. Beyond this point, it encounters colluvial soil, resulting in a bottleneck formation due to the presence of the sandstone outcrop. Under these conditions, the concentration at this juncture exhibits a peak following the problem's boundary conditions. Nonetheless, the pollutant tends to disperse laterally through the soil, capitalizing on its higher permeability. This lateral spread is evident between the horizontal distances of 500 and 550 m. It is observed to extend over the investigated period, reaching 570 m at the 10-year mark and extending to the simulation's lateral boundary over 100 years.

Similarly, the section explored at a depth of 31.5 m displayed an elevation in relative concentration, surpassing 40% of the maximum value, within a horizontal range of 100 to 250 m. This signifies that, over a decade, the plume had reached this position. However, it had not extended to the 250 to 500 m horizontal range, which the contaminant occupied after 100 years. As we discussed before, these concentration spikes could be attributed to the topography of the section and the variances in the permeabilities of the profile under analysis.

An examination at a depth of 50 m revealed that the pit located 500 m down displayed zero relative concentration in all the observed periods, as illustrated in Figure 4.46 (b). The low permeability of the outcropping sandstone at this specific point on the surface caused the plume to disperse laterally, resulting in a 500 m horizontal cross-section with no contaminants, even after 100 years.

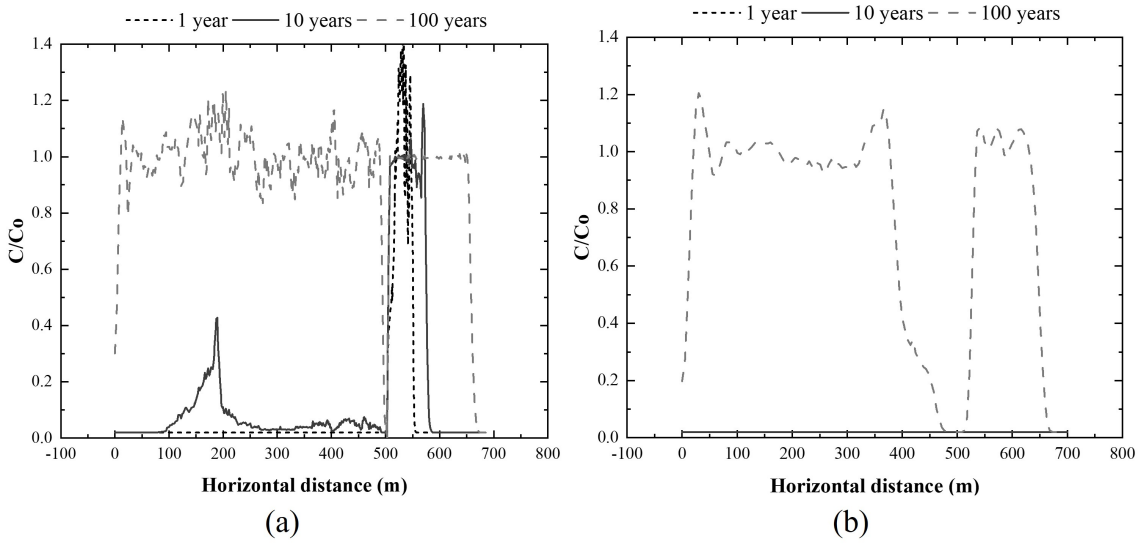

Figure 4.46: Variation of the relative concentration with the horizontal distance for 0.3 m of leachate head, considering 1, 10, and 100 years in a study of (a) the surface, (b) the middle, and (c) the base of the north-south profile.

Left slope

The data shown in Figure 4.47 depict the concentration profile along the depth of the E-W section for the slope situated to the left of the waste pit, precisely 116.5 m from the section's origin. The findings highlight the boundary condition implemented immediately following the waste layer with the highest relative concentration. It is also noted that, upon encountering the more permeable layers composed of colluvium and residual materials, the concentration levels remained consistently high across all scenarios examined.

Considering the first year of the same section, the concentration decreased at around 16 m depth, reaching zero upon encountering the sandstone after seeping 2.5 m vertically. After a decade, the concentration was maximum until it reached the boundary between the residual soil and the sandstone. The concentration was attenuated at this point, with a value below 0.2 c/co when it reached the water level. After 100 years, the relative concentration had a similar profile to a decade's. Still, the reduction in concentration when reaching the sandstone was restricted to values above 0.7 c/co, with a further increase to the maximum concentration when percolating about 3 m vertically.

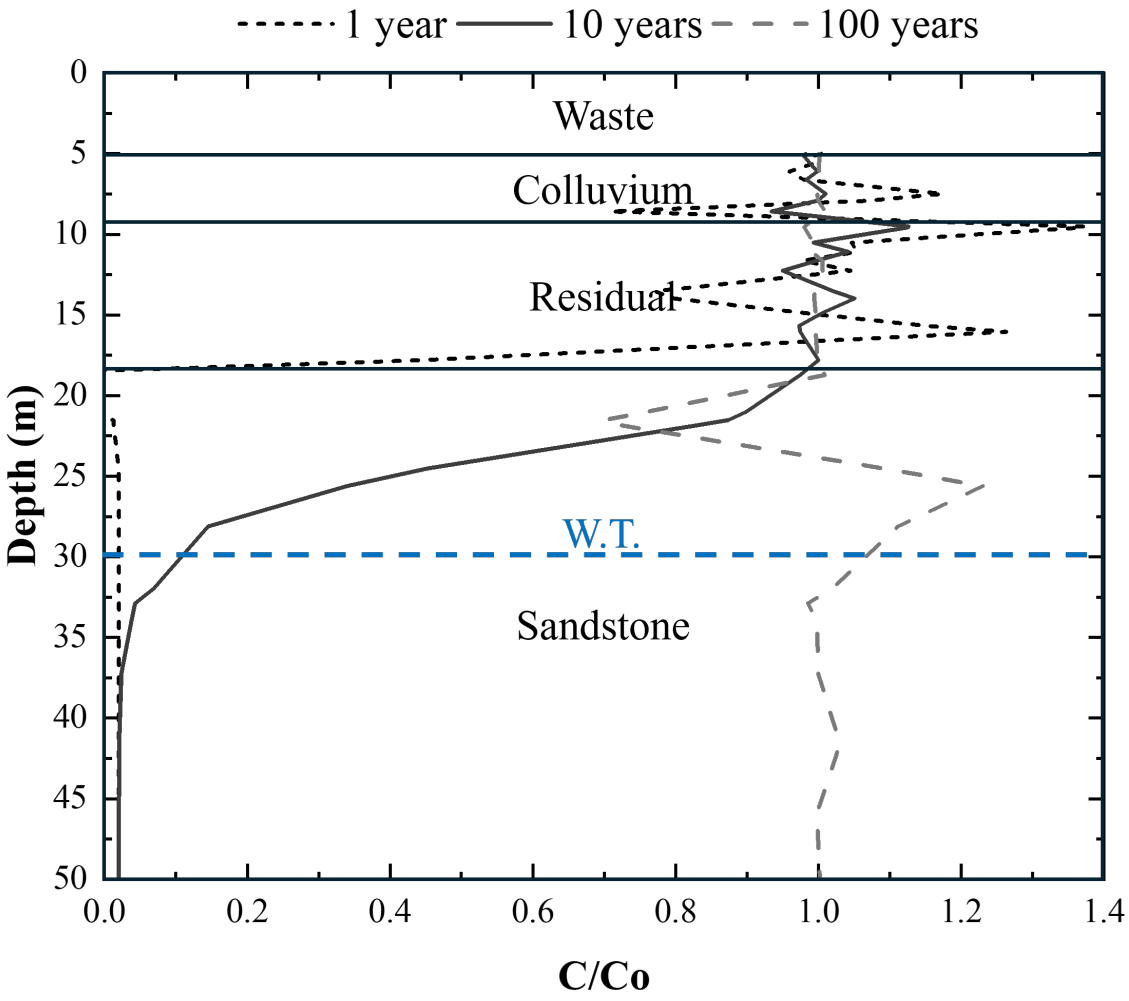

Figure 4.47: Relative concentration with depth for 1, 10, and 100 years of simulation of the left waste pit of the east-west profile, considering 0.3 m of leachate head.

Pit center

In relation to the cross-section located in the center of the pit 330 m from the origin, Figure 4.48 shows the variation in relative concentration along the depth, where it can be seen that due to the slope of the section and the cut made to install the waste pit, the residual soil horizon has narrowed to just over 2 m, with the sandstone quite close to the waste. At one year into the simulation, the relative concentration was zero, indicating that, even when starting from the boundary condition of maximum concentration, it shifted horizontally at the beginning of the simulation, probably due to the proximity of the sandstone horizon, which acted as a barrier to the vertical spread of the contaminant. In contrast, after 10 years of simulation, the relative concentration was maximum in the residual soil and extended around 1.5 m vertically in the sandstone. From this point, the concentration fell to less than 10% of the maximum value when it met the WT after percolating just over 10 m in depth. At 100 years, the relative concentration fluctuated but always at values equal to or greater than 90% of the maximum value, demonstrating that the contamination plume had wholly filled the section.

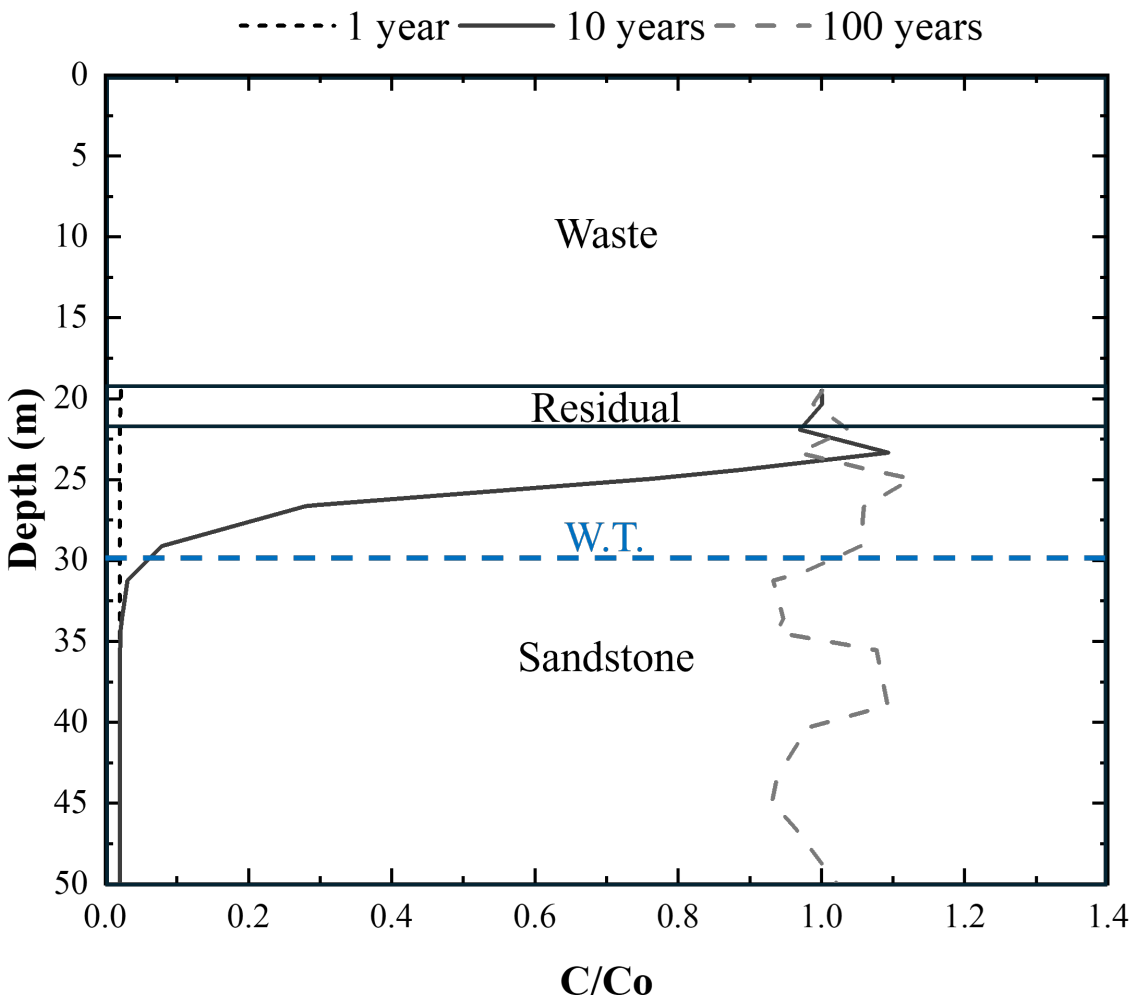

Figure 4.48: Relative concentration with depth for 1, 10, and 100 years of simulation of the middle waste pit of the east-west profile, considering 0.3 m of leachate head.

Right slope

The slope located 543 m from the section's origin exhibits a relative concentration of waste as a function of depth, shown in Figure 4.49. The significant layer of waste results from the slope's inclination, which tends to be predominantly occupied by MSW and is close to the groundwater. Consequently, there is no residual soil horizon, and the sandstone is again near the pit.

One year into the simulation, relative concentration within the colluvium horizon varied significantly. This variability decreased upon encountering the sandstone, leading to more consistent concentration values. The scenarios simulated at 10 and 100 years revealed less variability in the relative concentration values, possibly because they reached the steady state more quickly. At 10 years, the c/co=1 value was constant up to a depth of around 1.5 m in the sandstone, regressing to zero after percolating down to a depth of 40 m.

After running a 100-year simulation, it was found that the entire section was contaminated, displaying varying concentrations. The concentration decreased to 70% of the maximum value in the sandstone. Subsequently, it increased to the maximum value after percolating 2 m deep, maintaining this level to the analyzed depth limit.

Due to the WT's close position in relation to the waste, the tracer saturated the groundwater at 1 and 10 years of simulation, with attenuation generated by the sandstone. As previously mentioned, the sandstone was unable to reduce the concentration after a century of constant contamination.

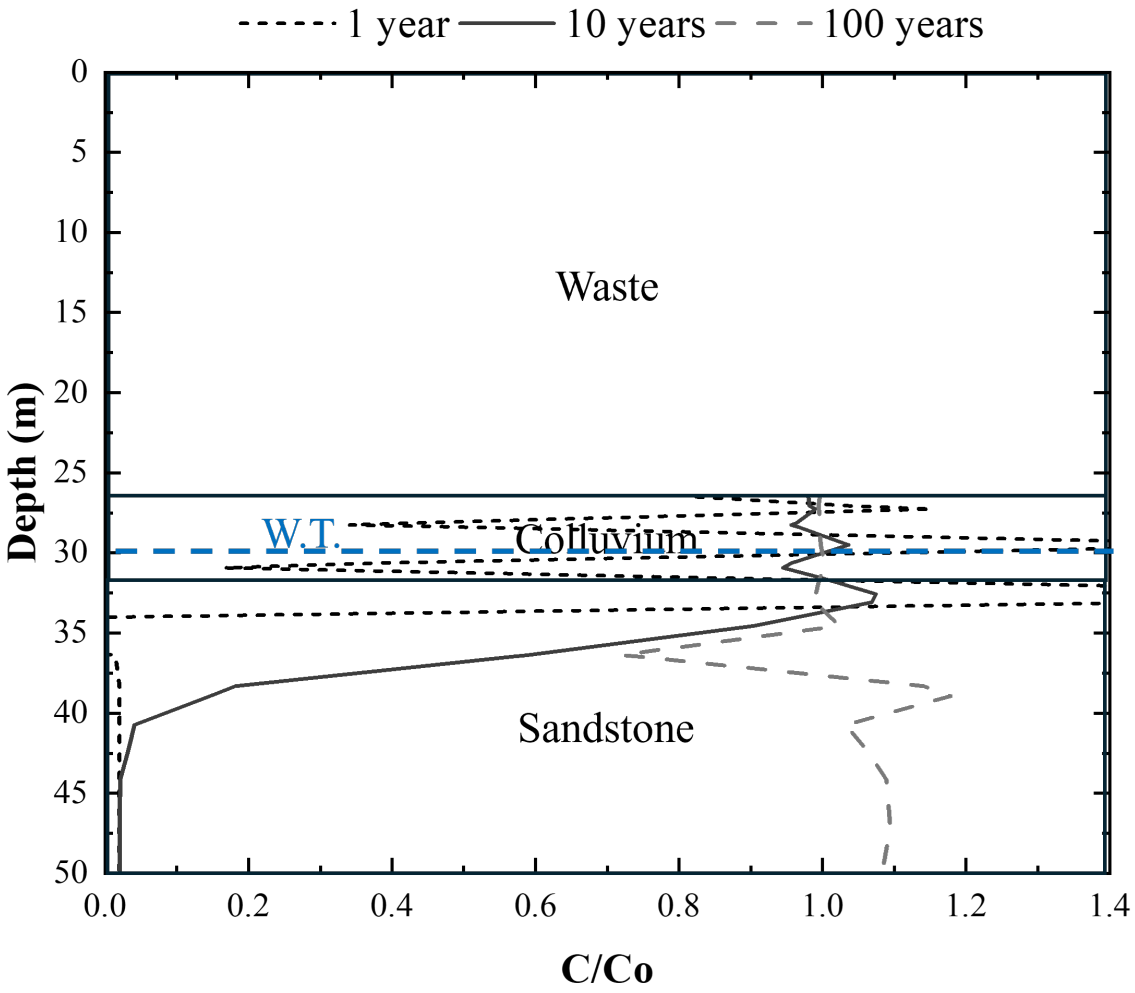

Figure 4.49: Relative concentration with depth for 1, 10, and 100 years of simulation of the right waste pit of the east-west profile, considering 0.3 m of leachate head.

4.3.6 E-W – Same layer, different heads and years

In the same way as the N-S section, the findings regarding the variation in relative concentration with horizontal distance and depth for leachate heads of 0.6 and 1.2 m in the E-W section closely resembled those observed for 0.3 m. Therefore, these particular outcomes are available for reference in the supplementary material. However, disparities become apparent when comparing the results for 10 and 100 years.

Thus, Figure 4.50 (a) illustrates the outcomes for a depth of 31.5 m, located 116.5 m away from the section's origin, after 10 years. The results indicate that the three simulated hydraulic heads produced similar findings, with a slight concentration increase observed between 400 and 500 m horizontally and a peak concentration occurring between 500 and 570 m. Additionally, there was a concentration peak exceeding 0.4 c/co between 100 m and 250 m from the origin, which remained consistent despite variations in the leachate column.

After a century, the simulation in the same section has the results shown in Figure 4.50 (b). From this, it can be inferred that the entire contamination plume has spread horizontally, with only one point differing at 500 m from the origin with zero concentration. This occurrence may be attributed to the outcropping sandstone next to two more permeable horizons, which have turned into preferred seepage paths.

For the same 100 years, but at the base of the sandstone, Figure 4.50 (c) shows the results for the three leachate head scenarios, from which it can be seen that the increase in the column was reflected in an increase in the relative concentration with a notable reflection at 400 m horizontally, not only with an increase in concentration but also with the horizontal spread of the plume which, even with the increase in the leachate column, still showed a gap around 500 m from the origin without the presence of the contamination plume.

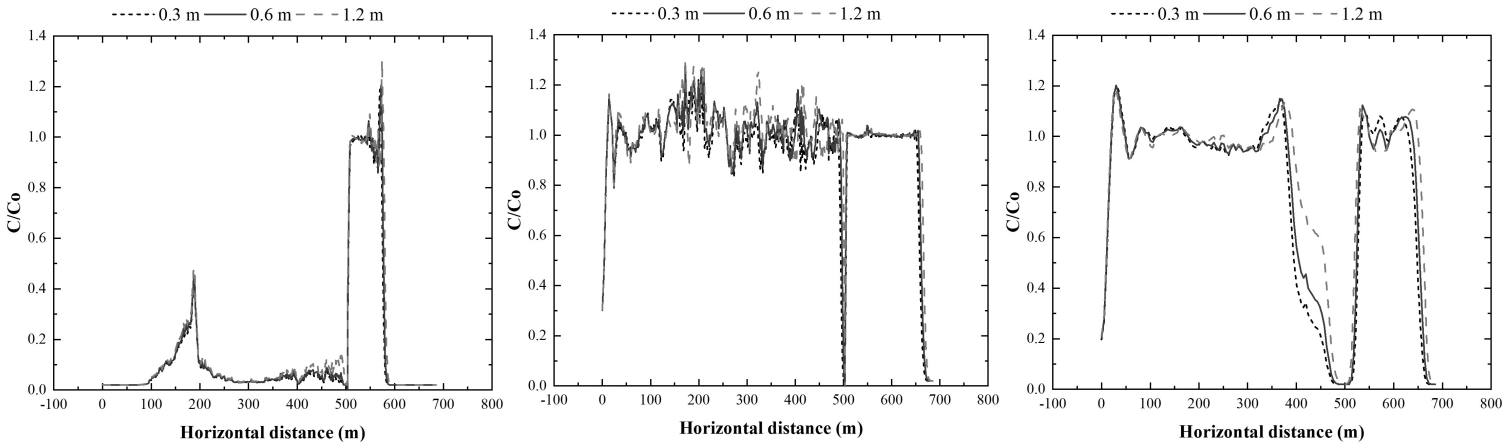

Figure 4.50: Variation of relative concentration with horizontal distance for 0.3, 0.6, and 1.2 m leachate height in the middle of the E-W pit after (a) 10 years of simulation, (b) 100 years of simulation, and (c) at the base of the E-W pit after 100 years of simulation.

Left slope

Figure 4.51 illustrates the three hydraulic heads simulated for the slope to the left, 116.5 m from the start of the section. The results show that the different leachate columns did not result in significant differences. The profile proved to be saturated by the contaminant in the more superficial horizons formed by the colluvium and residual, and the concentration was reduced at the boundary with the sandstone, again underscoring the sandstone's capacity for attenuation, reducing the relative concentration of the interface with the residual soil by 90% up to the WT.

After 100 years, the same profile exhibited in Figure 4.52 had a maximum relative concentration until the residual soil met the sandstone, at which point the concentration was reduced to 70% of the maximum value at a depth of 22 m and increased again to a maximum level at a depth of around 27.5 m. The influence of leachate head increase was observed from the concentration attenuation point at a depth of 18 m. Notably, the 0.6 and 1.2 m hydraulic heads led to lower concentrations at the same depth. This fact has no reasonable explanation.

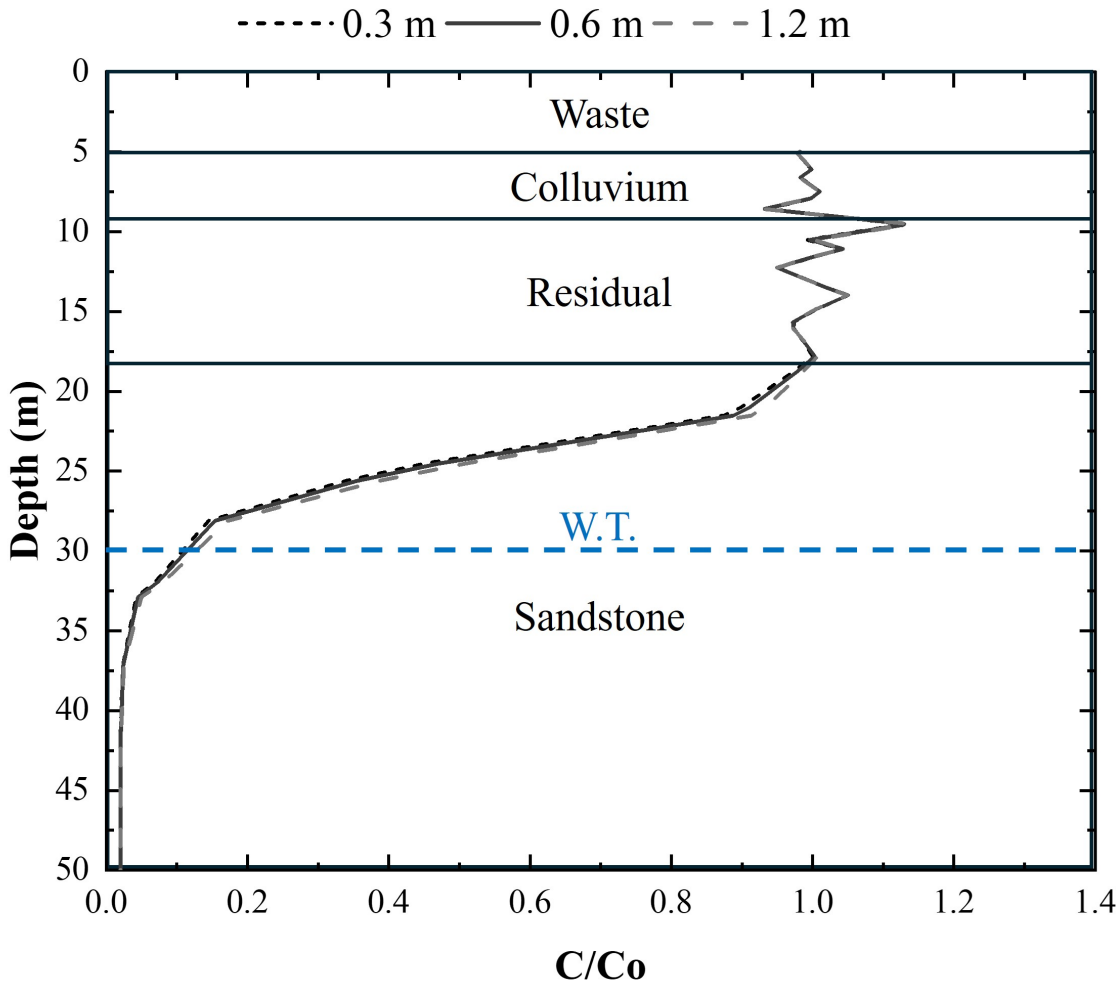

Figure 4.51: Relative concentration with depth resulting from a 10-year simulation of the left waste pit E-W profile for leachate heads of 0.3, 0.6, and 1.2 m.

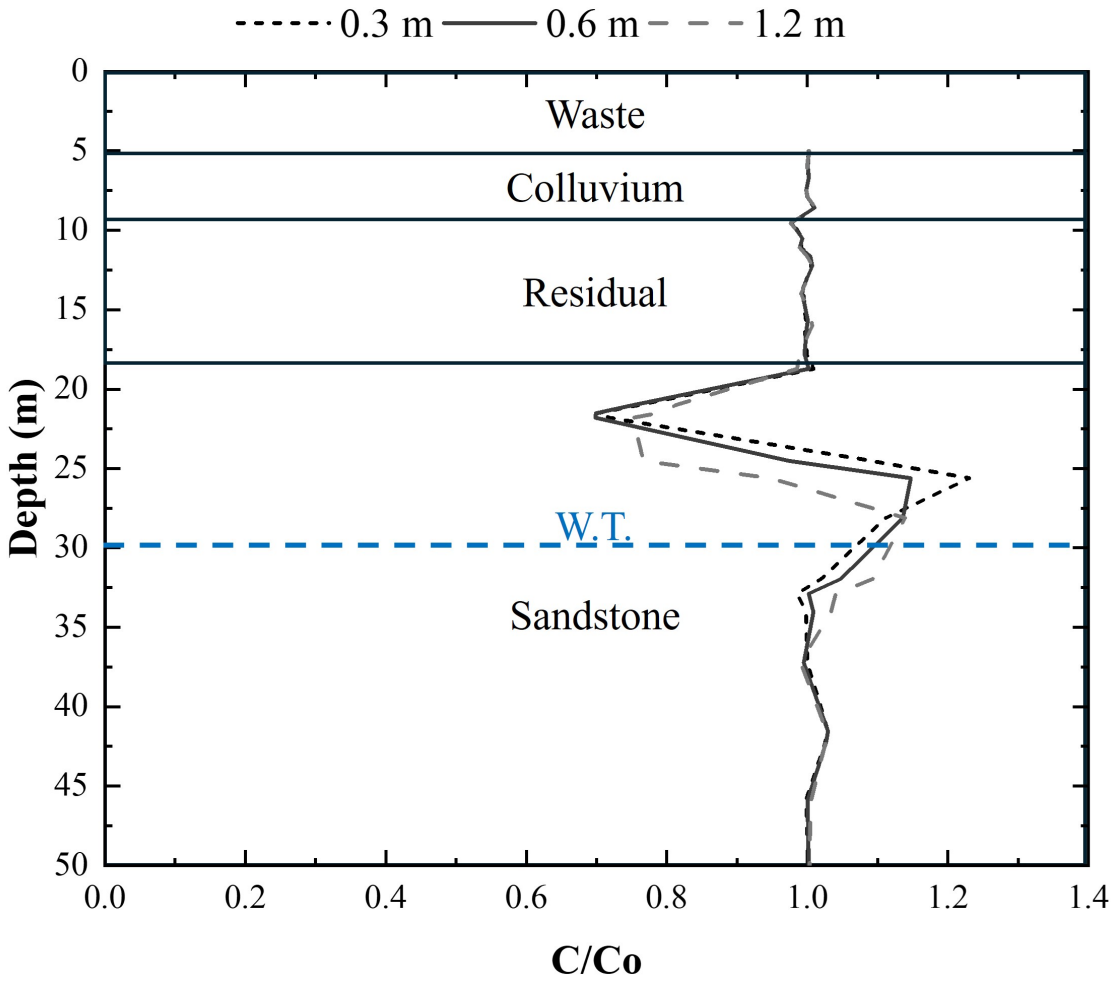

Figure 4.52: Relative concentration with depth resulting from a 100-year simulation of the left waste pit E-W profile for leachate heads of 0.3, 0.6, and 1.2 m.

Central pit

In Figure 4.53, the depiction shows the center of the pit, which is situated 330 m from the initial E-W section coordinate. Despite its proximity to the waste layer, the concentration was effectively reduced to 10% of the peak value after a 10-year simulation, as it seeped 7.5 m through the sandstone. The maximum relative concentration initially concentrated at the base of the MSW remained consistent as it percolated through the residual soil and permeated the sandstone to a depth of approximately 2.5 m. Notably, the concentration profile was unaffected by an increase in the leachate column for the simulated scenario.

Figure 4.54 illustrates the same section that, after a century of simulation, was taken over by the contamination plume, which varied but was consistently above 80% of the maximum concentration. The hydraulic heads of 0.3, 0.6, and 1.2 m did not result in significant differences along the profile. However, at specific depths, the increase in the leachate column resulted in a reduction in the relative concentration in a similar way to that simulated for the left of the waste pit after 100 years.

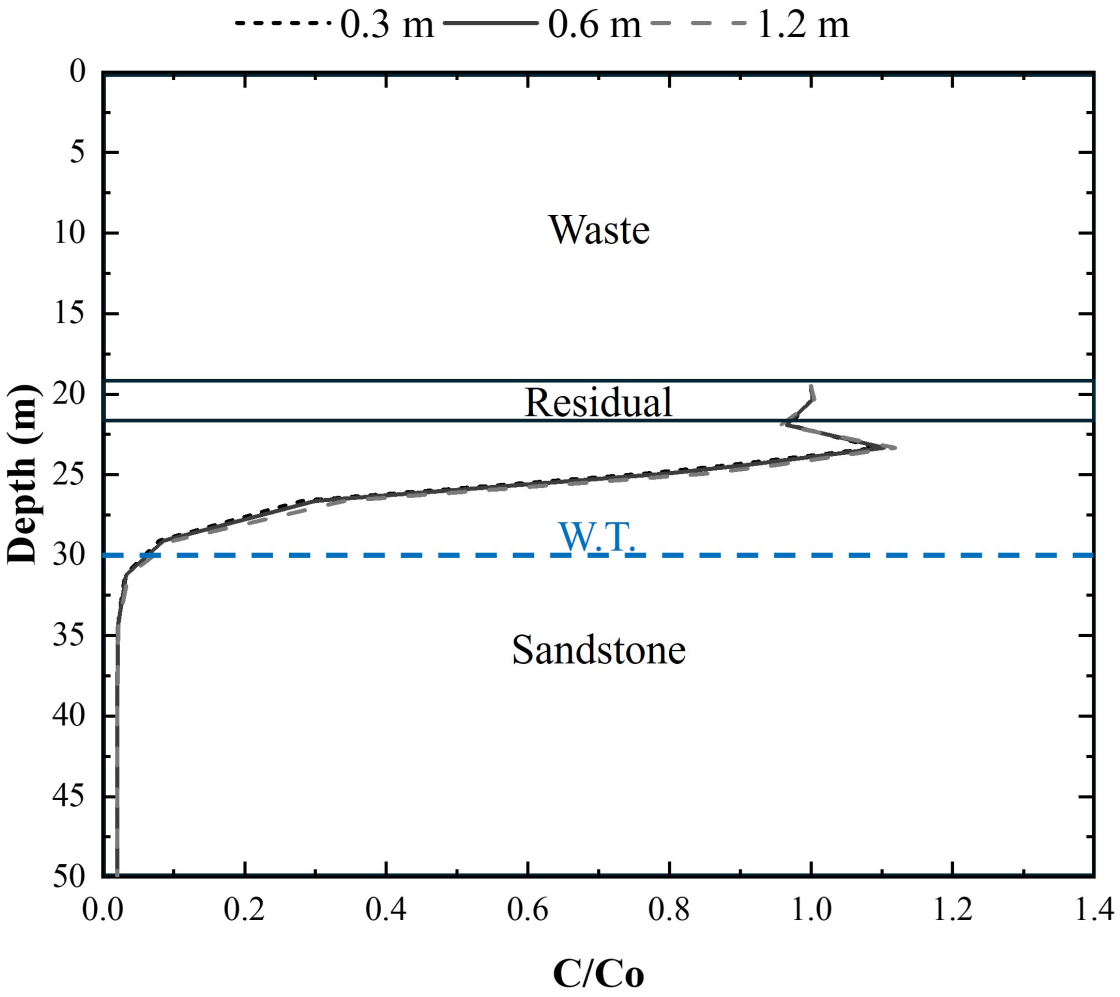

Figure 4.53: Relative concentration with depth resulting from a 10-year simulation in the middle waste pit E-W profile for leachate heads of 0.3, 0.6, and 1.2 m.

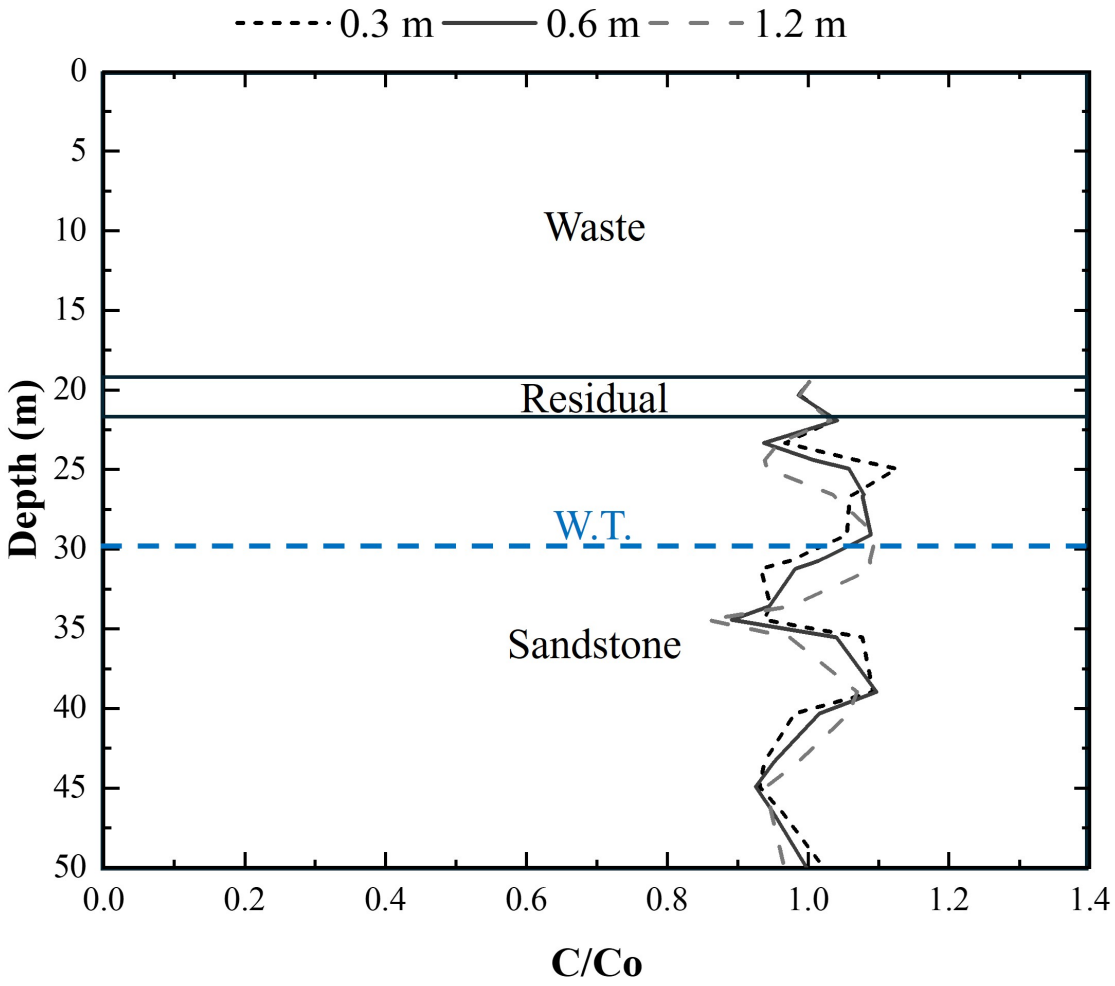

Figure 4.54: Relative concentration with depth resulting from a 100-year simulation in the middle waste pit E-W profile for leachate heads of 0.3, 0.6, and 1.2 m.

Right slope

The waste pit, situated 543 m from the simulation's origin, exhibits a ten-year trend in the right-side slope detailed in Figure 4.55. Correspondingly, like the outcomes for other slopes after a decade, the relative concentration profile commences from a peak just below the waste. It then sustains this concentration up to a depth of 34.55 m in the sandstone. After approximately 12.5 m of vertical percolation, the plume diminishes to less than 2% of the highest concentration at a depth of 44.15 m. In contrast, hydraulic head variances were minimal over the ten-year simulation period, unlike the disparities noted over a century, illustrated in Figure 4.56.

In addition to the contamination profiles throughout a century of simulation, the findings in Figure 4.56 indicate that approximately 30% of the highest concentration was reduced between elevations 34.55 and 38.32 m in this scenario. Subsequently, the concentration returned to its peak value. Consistent with previous similar outcomes, a definitive explanation for this occurrence remains elusive.

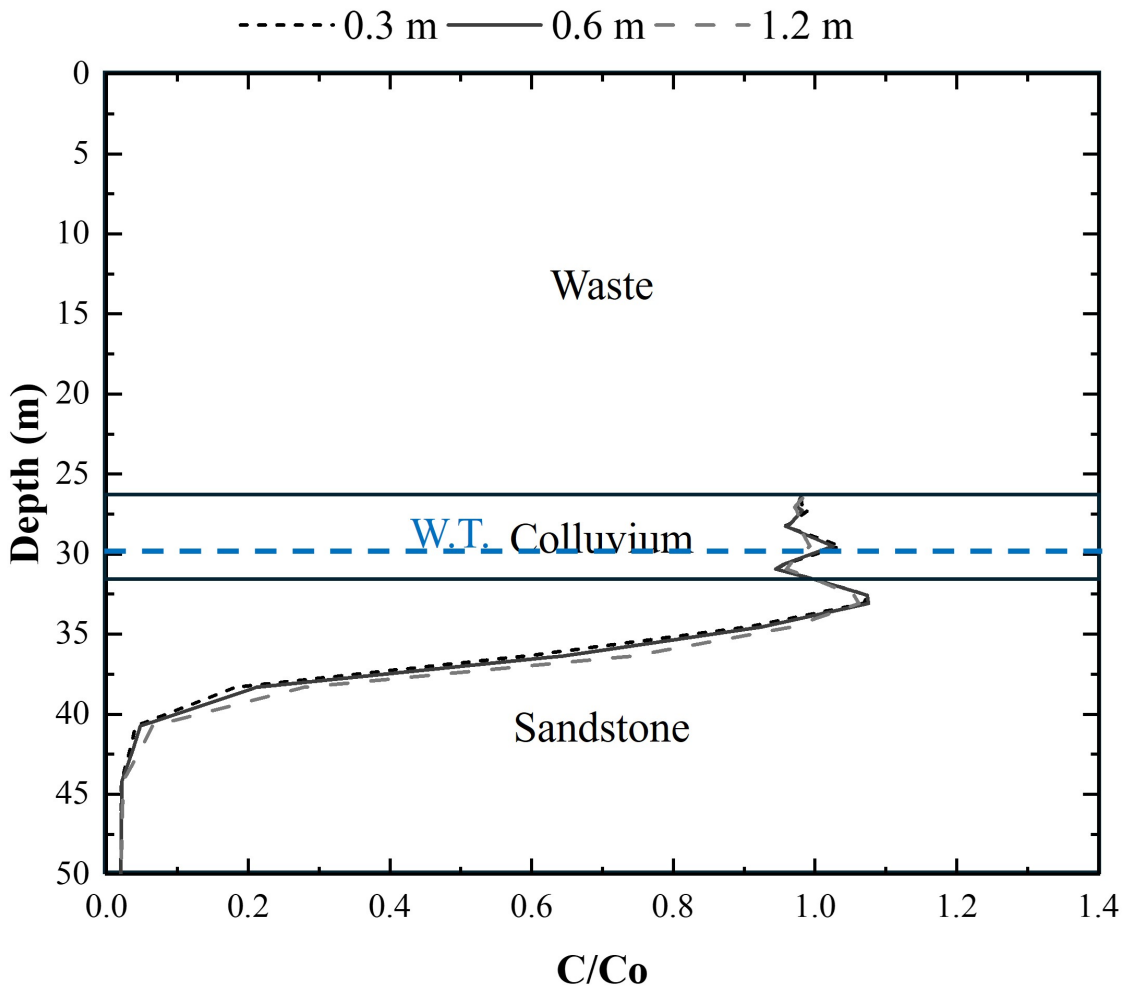

Figure 4.55: Relative concentration with depth resulting from a 10-year simulation of the right waste pit E-W profile for leachate heads of 0.3, 0.6, and 1.2 m.

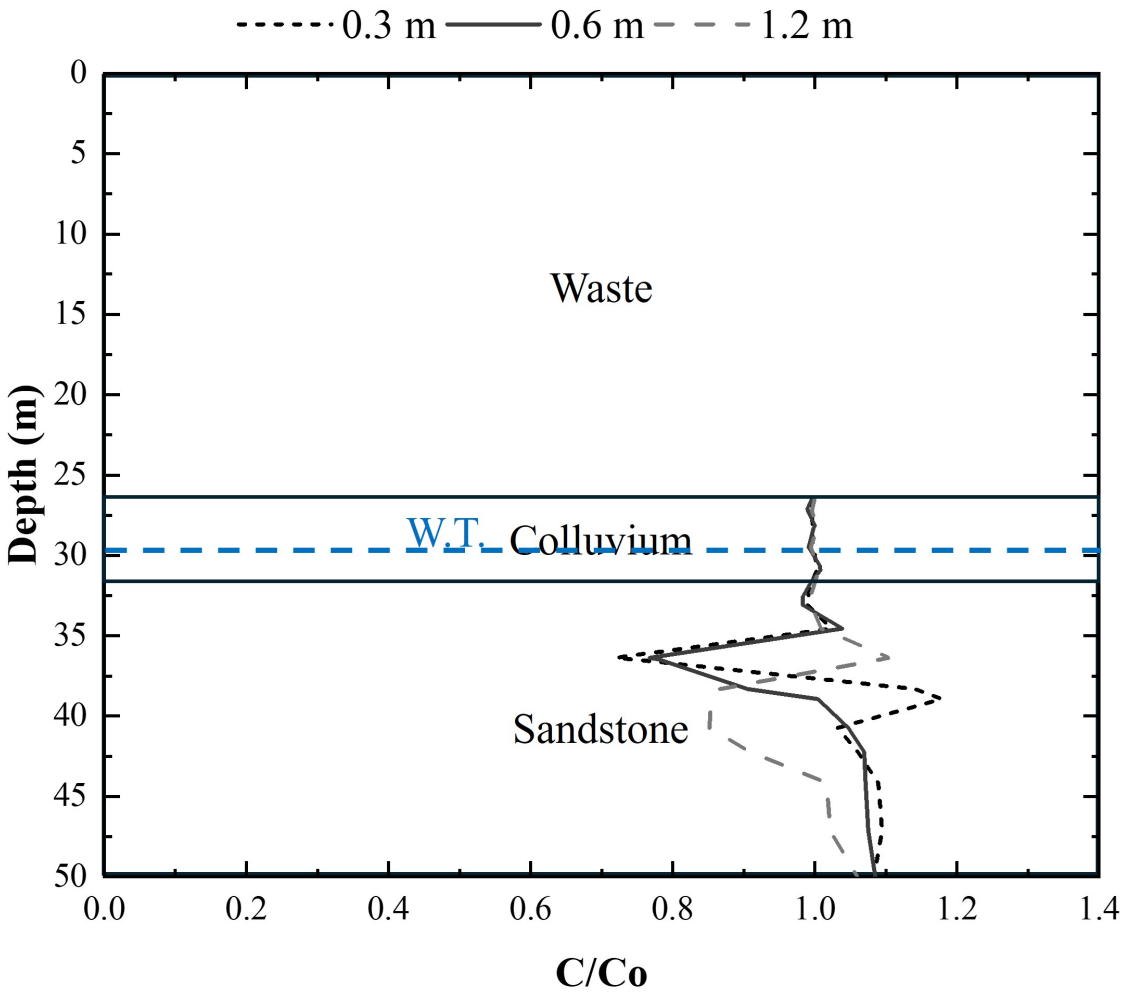

Figure 4.56: Relative concentration with depth resulting from a 100-year simulation of the right waste pit E-W profile for leachate heads of 0.3, 0.6, and 1.2 m.

4.3.7 E-W – BTCs

The BTCs corresponding to leachate columns of 0.3, 0.6, and 1.2 m, evaluated at the base of the colluvium horizon situated 116.5 m from the origin coordinate and at a depth of 9.5 m, are depicted in Figure 4.57 (a). The analysis reveals a significant oscillation at the onset of the curve. With a breakthrough time of 106 simulation days, it was observed that the colluvium exceeded the maximum concentration permitted for the tracer parameters, which is 0.2 c/co. This outcome was consistent across all three simulated hydraulic heads.

When analyzing the residual soil base at a depth of 18.70 m, BTCs shown in Figure 4.57 (b) from the three leachate columns indicated no significant differences. The breakthrough time (BTt) was 1.67 years at 0.3 m, 1.66 years at 0.6 m, and 1.63 years at 1.2 m hydraulic head.

At the midpoint of the sandstone, located at a depth of 34.35 m and a distance of 116.5 m from the section's origin, BTCs for this point are shown in Figure 4.57 (c). These BTCs illustrate a decrease in breakthrough times as the leachate head increases. It is important to note that the evaluated site endured a 10-year simulation period without being impacted by the contamination plume. Furthermore, the rise in the head from 0.3 to 1.2 m reduced the breakthrough time from 16.33 years to 15.6 years, or 262 days, to reach the same limit concentration. An intermediate time of 16.13 years was achieved when considering a leachate column of 0.6 m, bridging the gap between the two previous hydraulic heads.

Figure 4.57 (d) shows the same section as previously analyzed. Still, at the base of the sandstone at a depth of 50 m, the contamination plume reached the sandstone at 15.65 m above the base in double the time; in other words, it reached the lower limit of the simulated section after 20 years. The BTCs were anticipated with an increase in a hydraulic head of leachate, as can be seen by the BTt of 32.21, 31.73, and 30.84 years as a result, respectively, of 0.3, 0.6, and 1.2 m of leachate column. The increase from 0.3 m to 0.6 m resulted in a reduction of 173 days, and when comparing 0.3 m with 1.2 m, there was a reduction of 493 days.

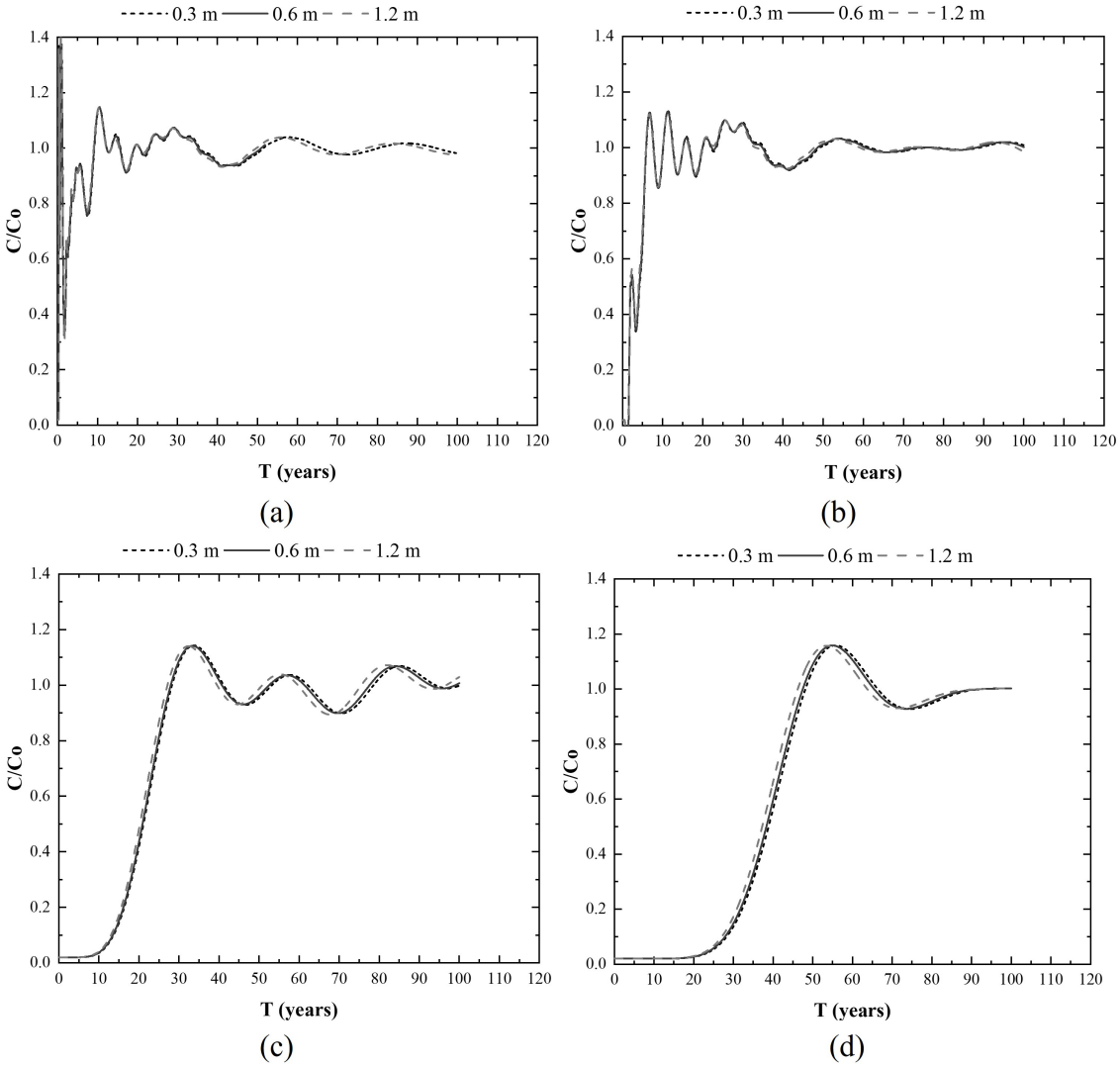

Figure 4.57: Breakthrough curve on the left slope of the E-W waste with leachate heads of 0.3, 0.6, and 1.2 m for (a) colluvium, (b) residual soil, (c) the middle of sandstone, and (d) the sandstone base.

Considering the base of the residual soil located in the center of the waste pit at coordinates 330 m horizontal and 21.9 m vertical, Figure 4.58 (a) illustrates the BTCs for the three simulated hydraulic heads. Again, the increase in the leachate column reduced the BTCs, slightly anticipating the BTts from 1.67 years at 0.3 m hydraulic head to 1.66 and 1.63 years at 0.6 and 1.2 m. The proximity to the waste and the small thickness of the residual horizon led to a rapid breach of the concentration limit and a rapid reach of the steady state.

Figure 4.58 (b) presents the outcomes for the identical horizontal position at a depth of 35.95 m. The hydraulic pressures of 0.6 and 1.2 m reduced the BTCs and, consequently, the BTts to 24.46 years for the former and 23.29 years for the latter. Initially, a simulation with a 0.3 m leachate head indicated a BTt of 25.10 years, indicating an advancement of the limit concentration by up to 1.8 years.

The concentration migration took approximately 15 years to reach the specified coordinates of the analyzed section and about 35 years to reach a depth of 50 m, as indicated in Figure 4.58 (c). This figure also illustrates the decrease in the arrival time of the plume as the hydraulic head increased. The system failed after 48.85 years with a 0.3 m column, 47.58 years with a 0.6 m column, and 45.21 years with a 1.2 m column. Consequently, the system failed 1.27 years earlier with a 0.6 m leachate column and 3.64 years earlier with a 1.2 m column, compared to a 0.3 m column.

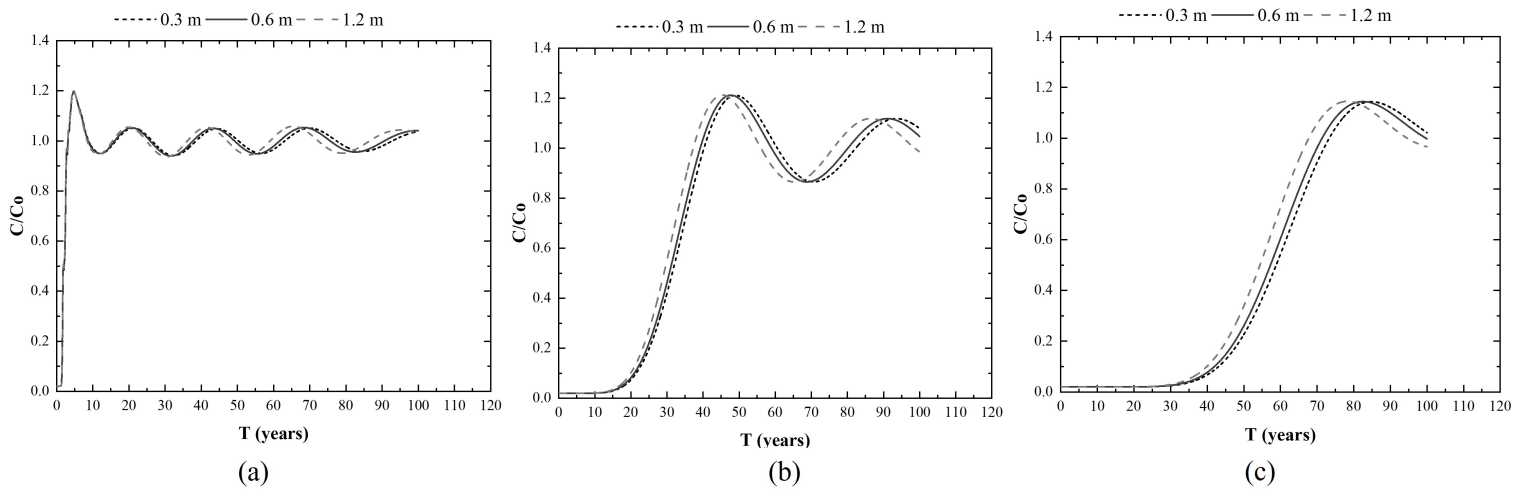

Figure 4.58: Breakthrough curve (a) in the residual soil in the center, (b) in the middle of the sandstone, and (c) in the sandstone base of the E-W waste pit with leaching heights of 0.3, 0.6, and 1.2 m.

Analogous to the preceding sections, the cross-sectional points evaluated on the slope to the right of the waste pit and 543 m from the origin, as depicted in Figure 4.59 (a), present the findings for the base of the shallowest horizon formed by the colluvium. The analysis revealed significant variability in results during the initial 15 years until reaching a steady-state. The breakthrough times were 208 days with 0.3 m of leachate and 210 days for 0.6 and 1.2 m. At this juncture, the limit concentration was attained. Thus, the escalation in the hydraulic head had no discernible impact at the specified point, contrary to the outcomes shown in Figure 4.59 (b), corresponding to a depth of 42.3 m, which signifies the center of the sandstone within the same section. This coordinate demonstrates a decline in BTCs with an increase in the leachate column, with 1.5 and 4 years less time required to attain BTt compared to the 0.3 m leachate head, which necessitated 21.25 years for achievement.

Finally, for the base of the section under study, Figure 4.59 (c) illustrates the results for the 50 m depth. The increase in leachate head noticeably reduced the BTCs, a position that again was around 20 years without contact with the contamination plume. Once in contact with the simulated contaminant, 43.08 years were required to reach 20% of the maximum concentration when utilizing 0.3 m leachate. This duration decreased to 39.69 and 34.35 years when employing 0.6 and 1.2 m hydraulic head.

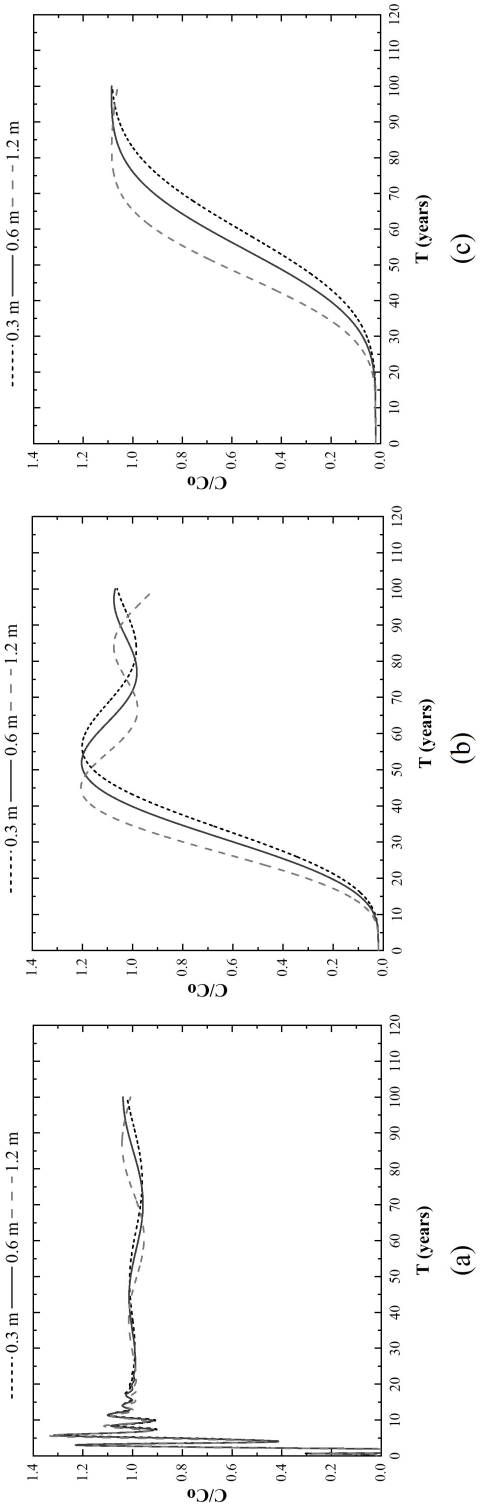

Figure 4.59: Breakthrough curve at the right slope of the E-W waste pit, with leaching heights of 0.3, 0.6, and 1.2 m in (a) colluvium, (b) the middle of sandstone, and (c) the sandstone base.

The data in Tables 4.8 to 4.10 provide a comprehensive overview of the breakthrough times for the various sections within the E-W profile. The analysis indicates a correlation between the increase in the leachate column and a reduction in breakthrough curves, with closer times observed in more permeable layers and more significant disparities in less permeable horizons. The areas primarily impacted by the contaminant are the slopes flanking the waste pit, followed by the pit's center, indicating a preference for horizontal percolation. Comparatively, the sandstone played an essential role in attenuating the plume, except for the E-W profile, where the contaminant entirely permeated, except for the 570 m horizontal due to the rocky outcrop. At this point, percolation occurred in its vicinity and did not include vertical flow.

It was possible to notice that in some of the breakthrough curves generated, concentration was reduced after reaching the peak concentration, particularly in the sandstone curves. As inferred by Shackelford (2021), this curve shape is related to the sum of transport by advection, dispersion, and decay, or advection, dispersion, sorption, and decay. In contrast, Kjeidsen & Christensen (1984) mentions advection, dispersion, and degradation or dilution. Given the conditions imposed on the sandstone and the simulation, and the fact that NaCl is a conservative tracer and is not subject to sorption, precipitation, and degradation reactions, dilution was the only attenuation mechanism (Lake & Rowe, 2000; Naveen et al., 2019; Rowe & Abdelrazek, 2019).

From the N-S and E-W profiles, the results indicated rapid contamination of the colluvium and residual horizons, with attenuation of the plume when it encountered the sandstone. Hydraulic conductivity was a key parameter driving the plume through the most permeable materials and deserves special attention in future sensitivity analyses. The E-W section proved to be more susceptible to the simulated plume, e.g., the sandstone base of the N-S profile in the central region was not affected by the plume for the leachate hydraulic heads of 0.3 and 0.6 m, while the contamination completely took over the E-W profile. This may be related to the more rugged E-W relief , with a steeper slope. Furthermore, the results indicated that the sandstone exhibited a notable capacity to attenuate the simulated contaminant. However, under conditions of constant leachate head, both profiles were projected to reach

the maximum contamination levels stipulated for the tracer after a century, except the base of the.

Table 4.8: An overview of the breakthrough curve results from the E-W colluvium horizon.

Layer	Depth (m)	Position	Distance from the origin (m)	Head (m)	BTt (days)
Colluvium base	9.50	Left slope	116.50	0.30	106
				0.60	106
				1.20	106
Colluvium base	34.55	Right slope	543.00	0.30	208
				0.60	210
				1.20	210

Table 4.9: An overview of the breakthrough curve results from the E-W residual horizon.

Layer	Depth (m)	Position	Distance from the origin (m)	Head (m)	BTt (days)
Residual base	18.70	Left slope	116.50	0.30	1.67
				0.60	1.66
				1.20	1.63
Residual base	21.90	Middle	330.00	0.30	1.59
				0.60	1.59
				1.20	1.59

Table 4.10: An overview of the breakthrough curve results from the E-W sandstone.

Layer	Depth (m)	Position	Distance from the origin (m)	Head (m)	BTt (days)
In the middle of the sandstone	34.35	Left slope	116.50	0.30	16.33
				0.60	16.13
				1.20	15.60
In the middle of the sandstone	35.95	Middle	330.00	0.30	25.10
				0.60	24.46
				1.20	23.29
In the middle of the sandstone	42.30	Right slope	543.00	0.30	21.25
				0.60	19.68
				1.20	17.18
Sandstone base	50.00	Left slope	116.50	0.30	32.21
				0.60	31.73
				1.20	30.84
Sandstone base	50.00	Middle	330.00	0.30	48.85
				0.60	47.58
				1.20	45.21
Sandstone base	50.00	Right slope	543.00	0.30	43.08
				0.60	39.69
				1.20	34.35

For the purpose of comparison, Figures 4.60 and 4.61 illustrate, respectively, the field results of Mondelli et al. (2007) and Lago et al. (2006) from the N-S and E-W sections based on resistivity tests using the electrical resistance survey. The N-S profile corresponds to the one utilized in this study, while the E-W profile is derived from a nearby section. It should be noted that both images are at different scales, and the E-W resistivity profile comprises a 360 m horizontal section, whereas the one simulated here is 700 m.

Based on the commencement of operations of the Bauru MSW in 1993 and the publication dates of the aforementioned authors, the research periods for the study conducted by Mondelli et al. (2007) were estimated to cover 15 years of operation, equivalent to 5475 days. Similarly, the investigation performed by Lago et al. (2006) spanned 11 years, encompassing 4015 days. Therefore, the simulation profiles provide an overview of the estimated time frames along with the analysis of the electrical resistivity findings.

The longitudinal profiles depicted in Figure 4.36 reveal intriguing similarities to the results observed at a depth of 33 m between 350 and 425 m horizontal distance. Over a ten-year simulation period, relative concentration increases noticeably between 150 and 200 m horizontally, while the 100-year simulation shows no concentration at 350 m.

A similar comparison becomes more challenging for the E-W section since they correspond to different profiles. However, both results showed a tendency for the plume to spread in an easterly direction (left of the image) when the result was conceived. In Figure 4.50, which represents the plume's spread at a depth of 31.5 m, considering 10 years of simulation, concentrations close to zero are observed between 250 and 500 m, contrary to the in situ results. On the other hand, the findings from Lago et al. (2006) for a depth of 24.5 m reveal that the contamination plume had already reached a lower depth than the simulated one.

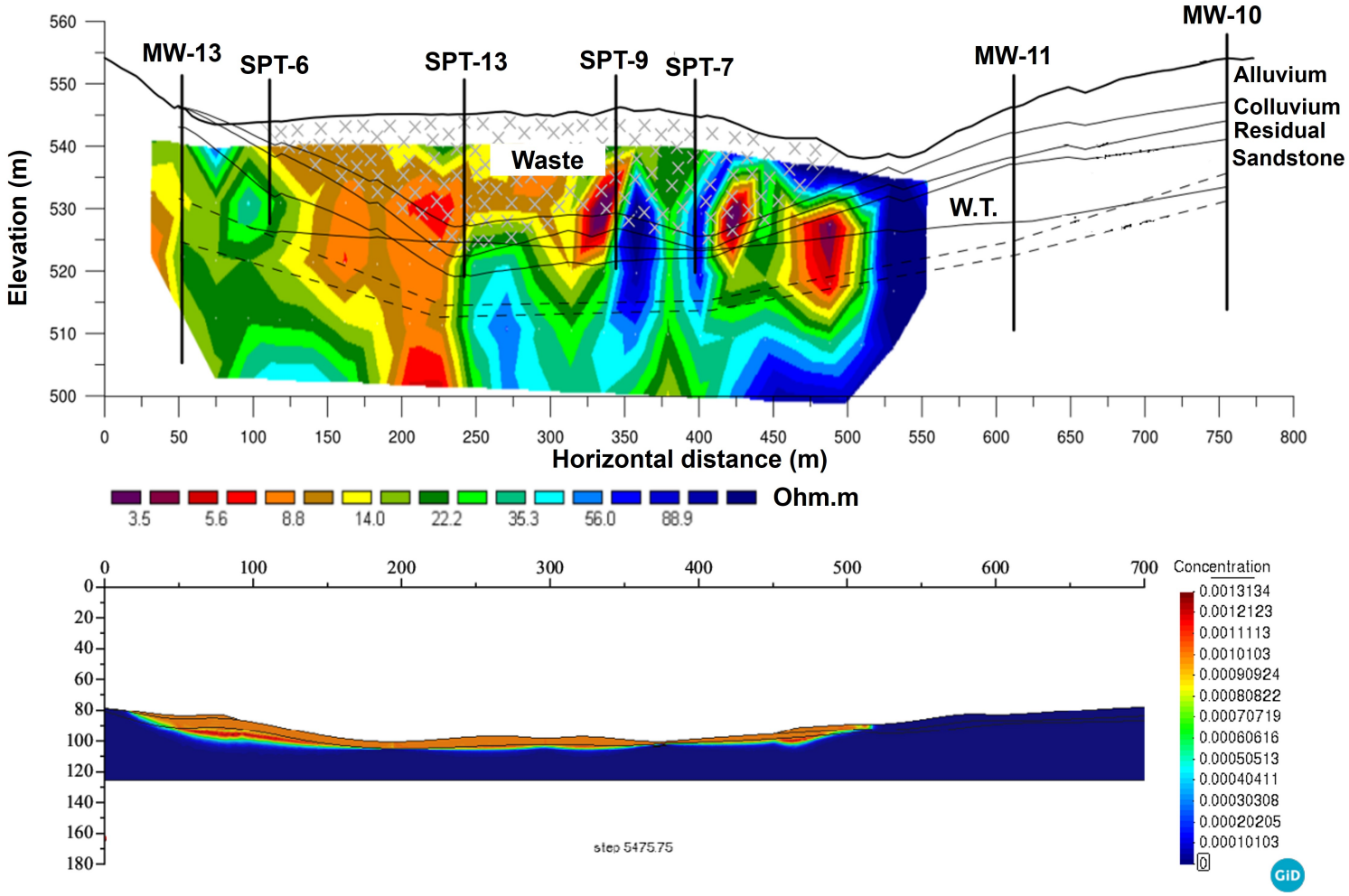

Figure 4.60: Comparison of the resistivity results adapted from Mondelli et al. (2007) (above) and simulated profiles (below) with a 1.2 m leachate head in the N-S section.

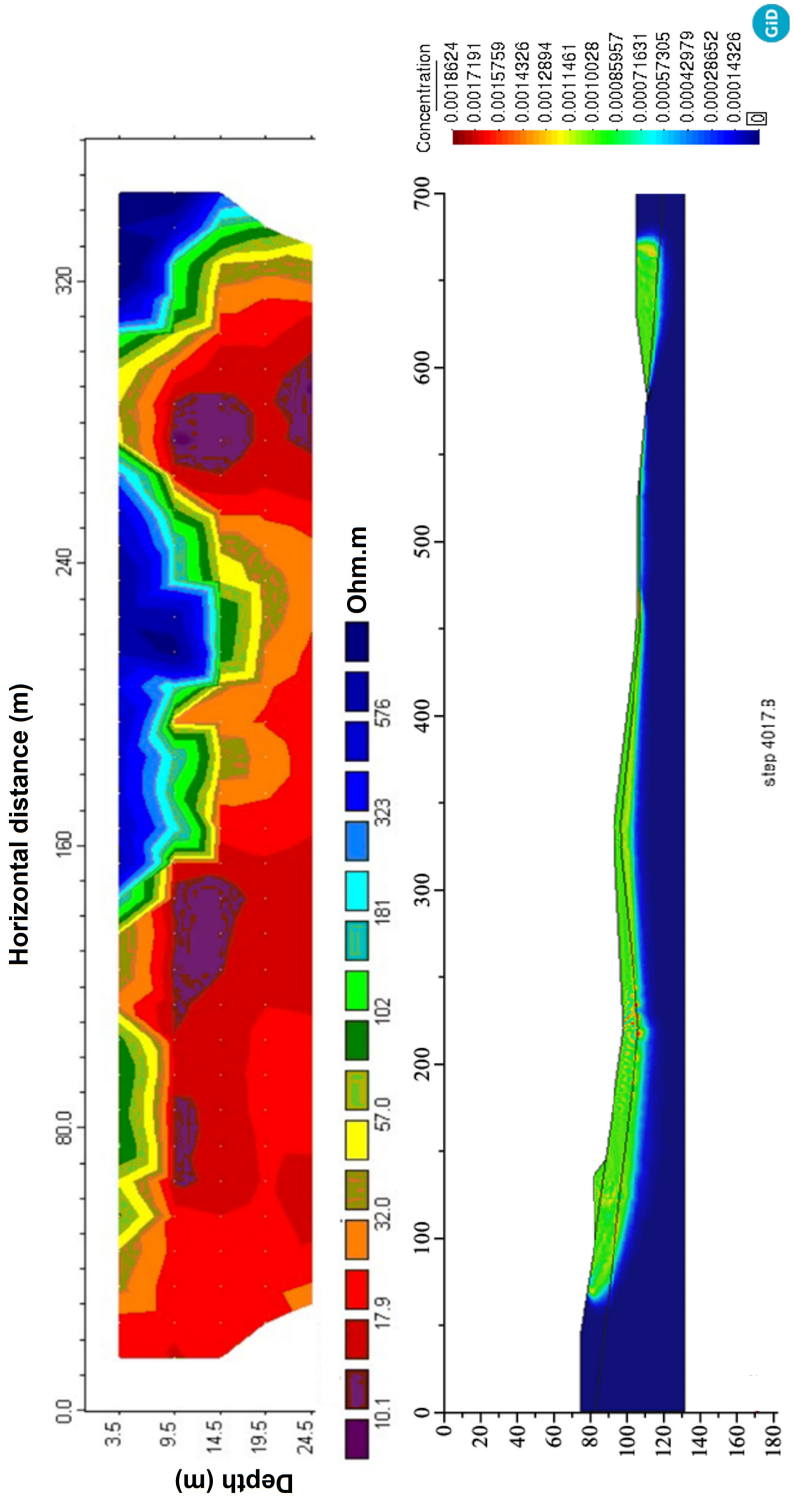

Figure 4.61: Comparison of the resistivity results adapted from Lago et al. (2006) (above) and simulated profiles (below) with a 1.2 m leachate head in the E-W section.

As previously inferred, the above observations were only for comparison purposes but reflect essential information worth highlighting. The simulation underestimated the electrical resistivity results, even though the former did not take into account considerations that would mitigate the fate of the contamination plume, such as constructive aspects, e.g., diluted asphalt applied to the base of the MSW disposal site along with 0.20 m of soil compacted 3% above optimum humidity with a 95% degree of compaction. This information indicates a concern about the state of the MSW disposal site.

Furthermore, the in situ results of previous research have more accurately reflected, among other aspects, the operational history of the MSW disposal site, a factor that was not accounted for in the simulations. As highlighted in the work of Mondelli et al. (2007), health waste was disposed of between 450 and 500 m horizontally (Figure 4.60). Additionally, between 180 and 240 m, leachate ponds, such peculiarities, should be considered when comparing and assessing the contamination plume spreading profiles generated here.

Feng et al. (2019) explain in their work that high leachate heads, exceeding 5 m for the reported case, caused a vertical concentration profile for times above 10 years, indicating that the presence of a protection layer of 0.75 m was unable to impede the contamination plume. Moreover, Ding et al. (2020) reiterate the importance of the hydraulic gradient, which is directly related to the breakthrough of contaminants, endorsing the importance of the volume of leachate generated.

Thus, Bauru's MSW disposal site is in a situation of vulnerability, aggravated by the proximity of the water level and the time elapsed between the results of Mondelli et al. (2007) and Lago et al. (2006) to the present date, even though the MSW disposal site closed its activities in 2016, the trend, as shown by the results of the simulations, is for the geoenvironmental conditions of the MSW disposal site, its surroundings, as well as groundwater and surface water to worsen, as shown in Table 4.11 which shows the Pb, Mn, Ni and Na concentration data evaluated in Chapter 3 from the monitoring wells in the sections analyzed, as well as from the Gabiroba stream, near Bauru's MSW disposal site.

The results of this research expose the risk to which human health, local fauna, and flora are exposed, taking into account that the process of natural attenuation can take decades

or even centuries (Baun et al., 2003; van Breukelen et al., 2004; Mahallei & Badv, 2020). Han et al. (2016) emphasize that the natural attenuation process and hydrogeological conditions are not solely responsible for altering groundwater contamination, in view of the significant contribution of leachate quality to the contamination process.

It is advisable to consistently monitor the water quality of the wells and tributary rivers surrounding the MSW disposal site, both upstream and downstream. This monitoring is crucial in identifying any necessary adjustments to mitigate leachate generation. For instance, improving rainwater drainage can help reduce the leachate column, affecting the hydraulic gradient and the contamination plume. It is important to note that elevated leachate levels can also impact the stability of the MSW disposal site by increasing the pore pressure.

Other measures, such as implementing cut-off walls or reactive barriers as proposed by Xie et al. (2009) in a Chinese MSW disposal site, are similar to the one studied here. This approach could be valuable when protective liners are absent, and advection and mechanical dispersion are the primary means of transport. However, it is notorious that natural attenuation is the primary tool in developing countries, as the additional expenses associated with barrier construction are frequently deemed impractical.

Besides the above, the simulations carried out here have the limitation of considering the position of the fixed water level and not considering underground flow. The soil and rock masses were supposed to be homogeneous, isotropic, and without the occurrence of fractures that give rise to preferential percolation. The process of attenuation by degradation was not considered, as well as deformations due to the waste layer and the self-weight of the soil and rock, in addition to critical environmental factors such as rainfall. Furthermore, leachate is a complex compound with which the competition between its constituents was not taken into account, and data from a saline tracer was used to infer the input parameters for the analyses.

In this study, despite its limitations, we conducted simulations incorporating key parameters previously determined in laboratory experiments for geomaterials found at Bauru's MSW disposal site. These parameters include suction, hydraulic conductivity, and advection, with the latter two being particularly crucial for understanding contaminant transport, especially in areas lacking clay or similar materials to delay the spread of the contamination

plume. The 2D simulations, along with 1D analyses divided into longitudinal and transverse profiles, have enhanced our understanding and prediction of plume spread in a geologically complex site, mainly due to the presence of rock formations in a tropical environment.

The study conducted here sought to portray a case study. It should be considered that the definition of profiles, choice of parameters, boundary conditions, and the use of 1D, 2D, or 3D simulations must be accompanied by an appropriate field investigation in conjunction with the laboratory aimed at local geological-geotechnical understanding. For example, dispersivity and hydrodynamic dispersion values tend to increase in the field (Levy & Chesters, 1995; Woumeni & Vauclin, 2006; Odling et al., 2007; Ojuri & Ola, 2010). Additionally, as illustrated by Rowe & Abdelrazek (2019), anisotropy plays a crucial role, with longitudinal dispersivity influencing flow direction and transverse dispersivity affecting uniform distribution within the aquifer.

The selection of simulation type is a critical factor in drawing inferences, as noted by Yan et al. (2021), who reported that 1D findings reduced 2D BTCs by ten years. Konikow (2011) suggests that modeling in complex locations should begin with simple scenarios, gradually increasing in complexity. Furthermore, the author stresses that 3D simulations enhance the quality of result visualization and analysis. However, this enhancement necessitates a more critical assessment, as one should more than merely assume that the simplifications adopted during the model validation stage are sufficient and meaningful.

This work endorses that new contributions from the research group with updates on the current stage of migration of the contamination plume have been conducted.

Table 4.11: Concentration of heavy metals in monitoring wells near the sections under study.

Site	Profile	MW	Pb (µg/L)	Mn (µg/L)	Ni (µg/L)	Na* (µg/L)
Bauru MSW	N-S	10	<10	<10	<10	2750
		11	10	1242	<10	1600
		13*	92.5	300	<10	1400
	E-W	4*	<10	589.8	32.8	1550
		5-A	14.5	<10	<10	1000
Gabiroba stream	Upstream		<10	47	<10	
	Downstream		<10	127	<10	

4.4 Conclusions

This work analyzed the fate and transport of contaminants from Bauru's MSW disposal site in Brazil and the breakthrough time to reach undesirable contamination levels in the local subsoil profile through numerical simulation using the CODE_BRIGHT program. From this study, we can draw the key points:

(i) Increasing leachate head reduced the time it takes for contaminants to reach undesirable levels.

(ii) The slopes to the left and right of the waste pit were most affected by the contamination plume, followed by the center of the pit, indicating a tendency for horizontal flow, especially in the more permeable soil horizons above the sandstone.

(iii) The East-West section has a higher susceptibility to the percolation of contaminants, with findings indicating rapid contamination of the colluvium and residual horizons and attenuation of the plume upon encountering the sandstone.

(iv) After a century of constant leachate head conditions, the North-South and East-West profiles reached the maximum contamination level for the tracer, increasing concerns about long-term environmental risks without intervention.

(v) The simulations for Bauru's MSW disposal site underestimated in situ electrical resistivity results, raising concerns about contaminants' behavior, spread, and fate.

4.5 Supplementary material

4.5.1 Model validation

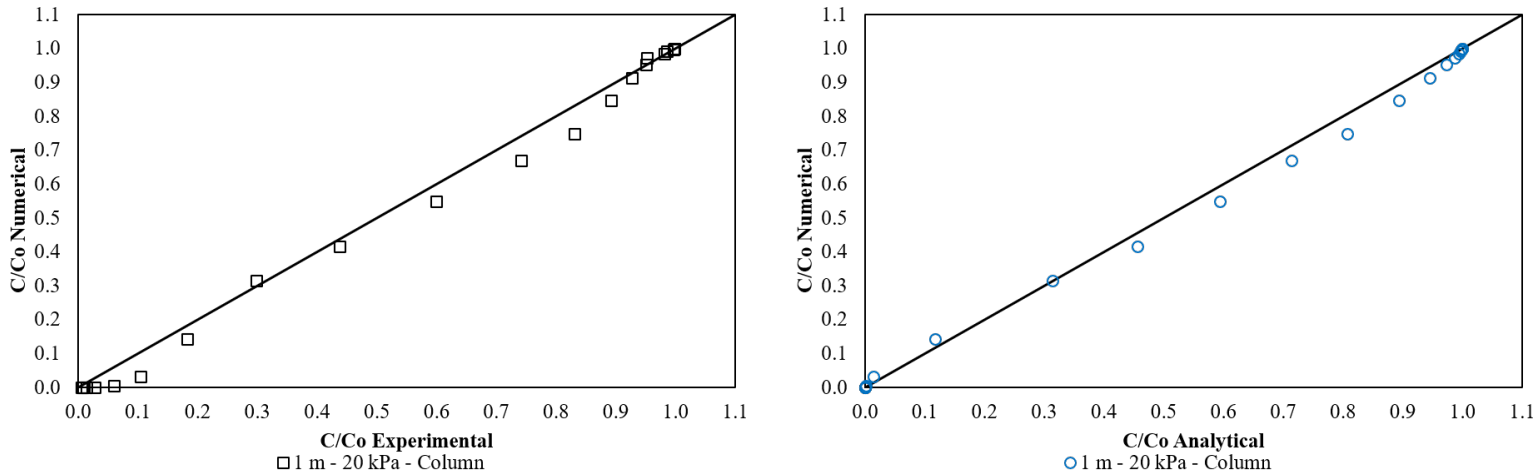

Figure 4.62: Numerical validation with column test through experimental data (left) and analytical (right) from the soil at 1 m depth consolidated at 20 kPa.

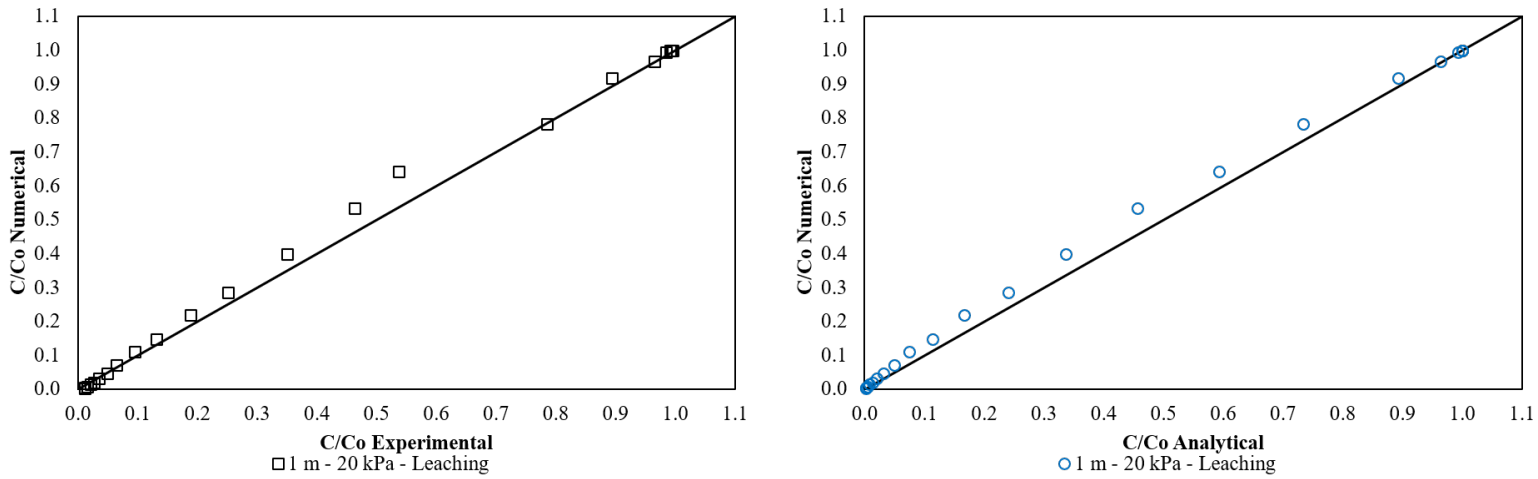

Figure 4.63: Numerical validation with leaching test through experimental data (left) and analytical (right) from the soil at 1 m depth consolidated at 20 kPa.

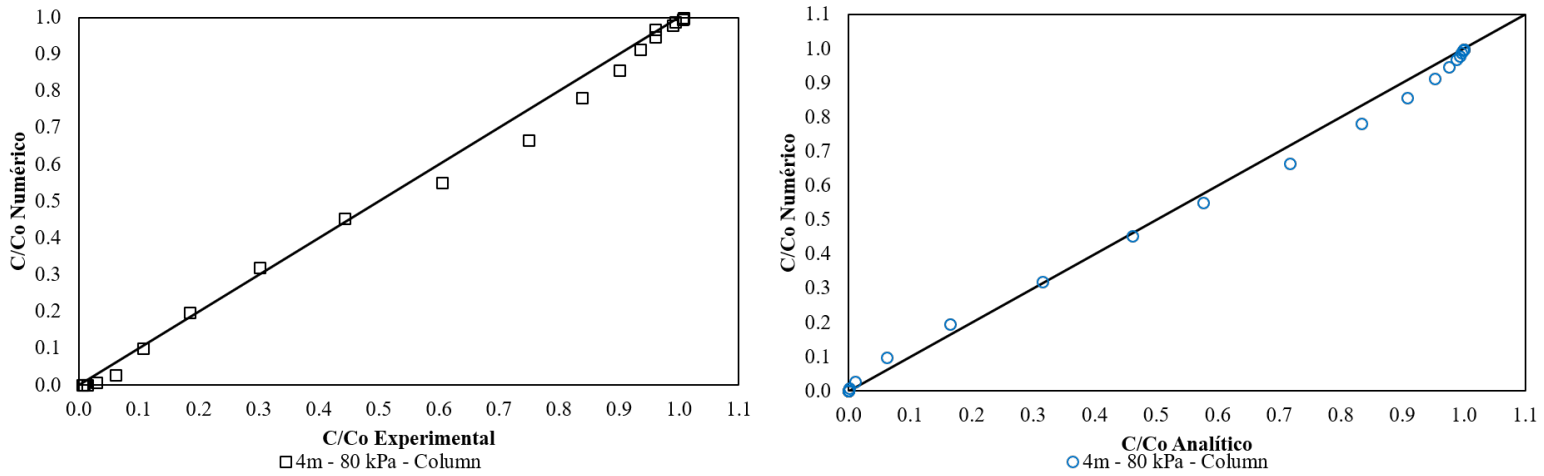

Figure 4.64: Numerical validation with column test through experimental data (left) and analytical (right) from the soil at 4 m depth consolidated at 40 kPa.

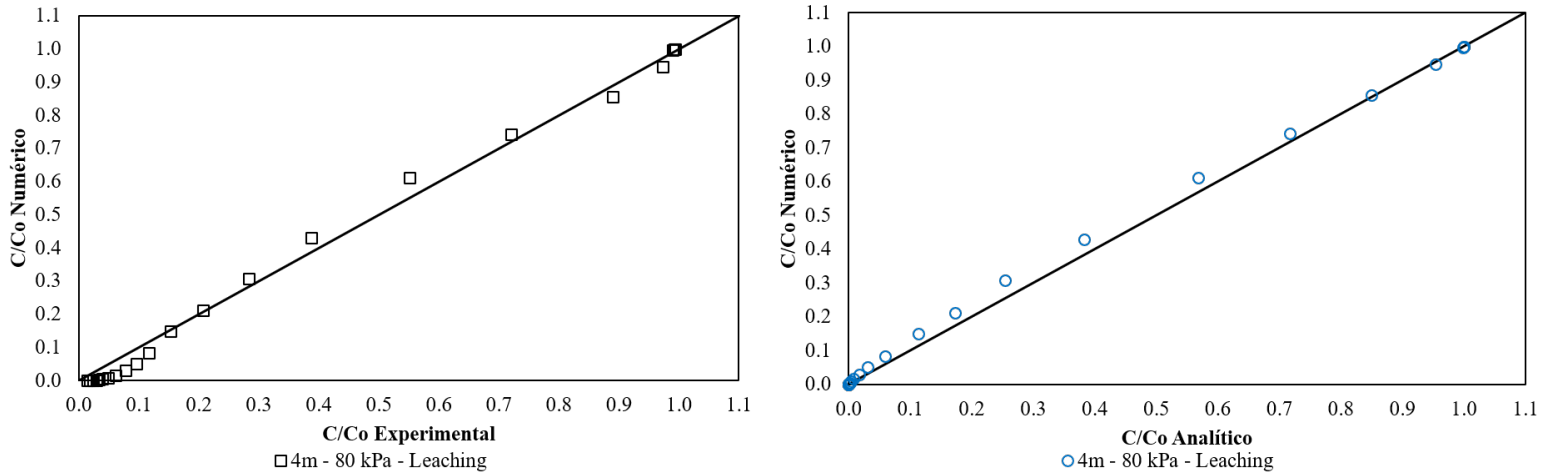

Figure 4.65: Numerical validation with leaching test through experimental data (left) and analytical (right) from the soil at 4 m depth consolidated at 40 kPa.

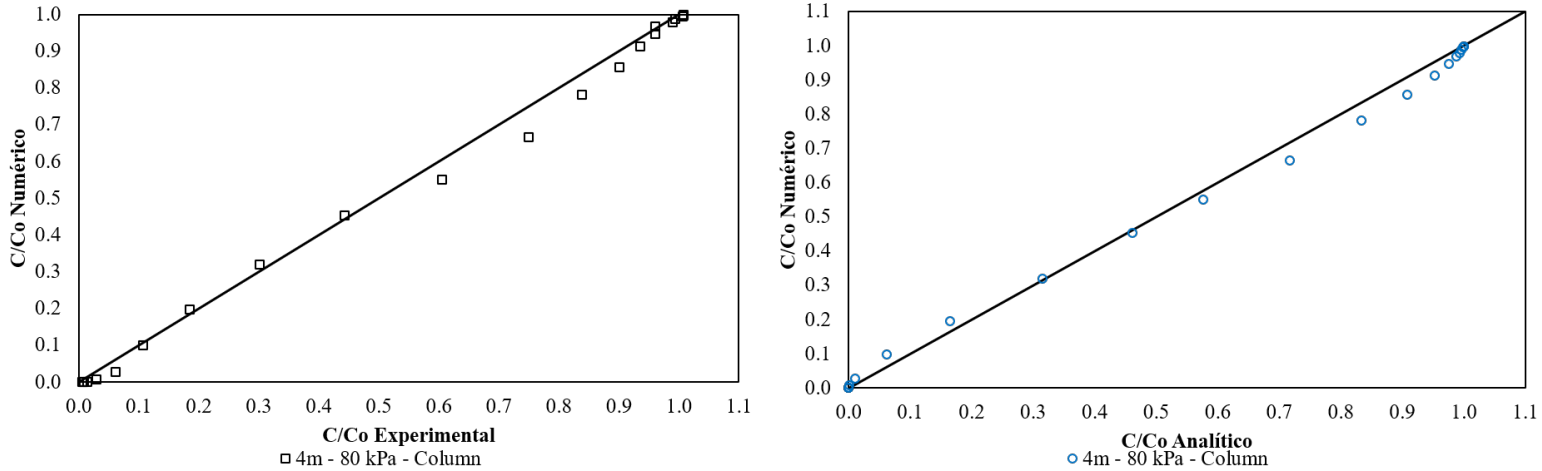

Figure 4.66: Numerical validation with column test through experimental data (left) and analytical (right) from the soil at 4 m depth consolidated at 80 kPa.

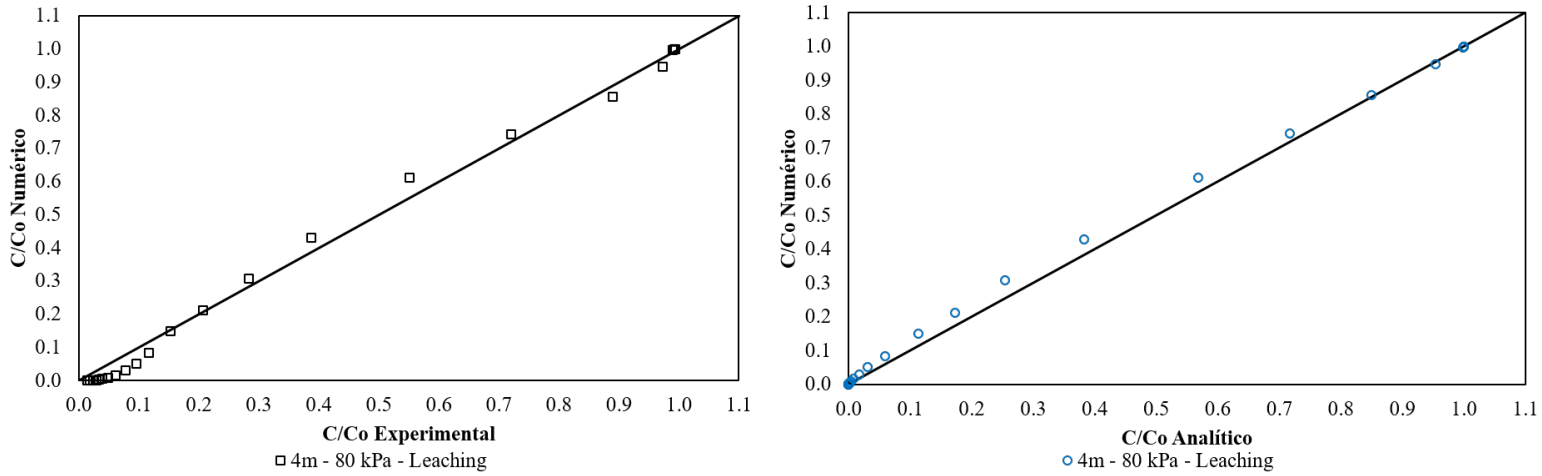

Figure 4.67: Numerical validation with leaching test through experimental data (left) and analytical (right) from the soil at 4 m depth consolidated at 80 kPa.

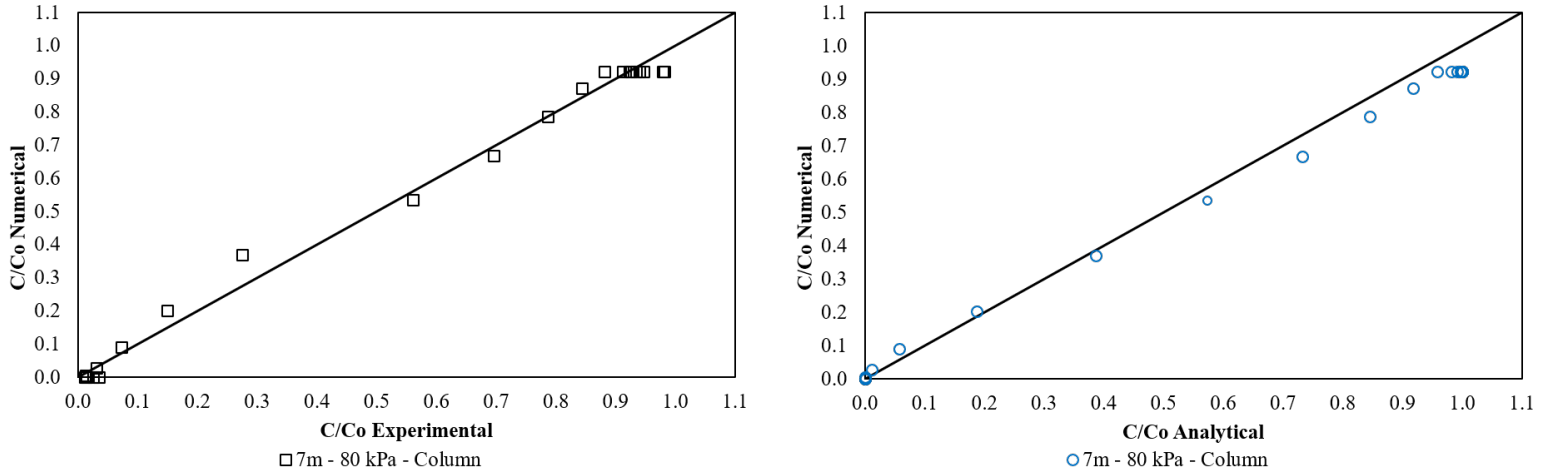

Figure 4.68: Numerical validation with column test through experimental data (left) and analytical (right) from the soil at 7 m depth consolidated at 80 kPa.

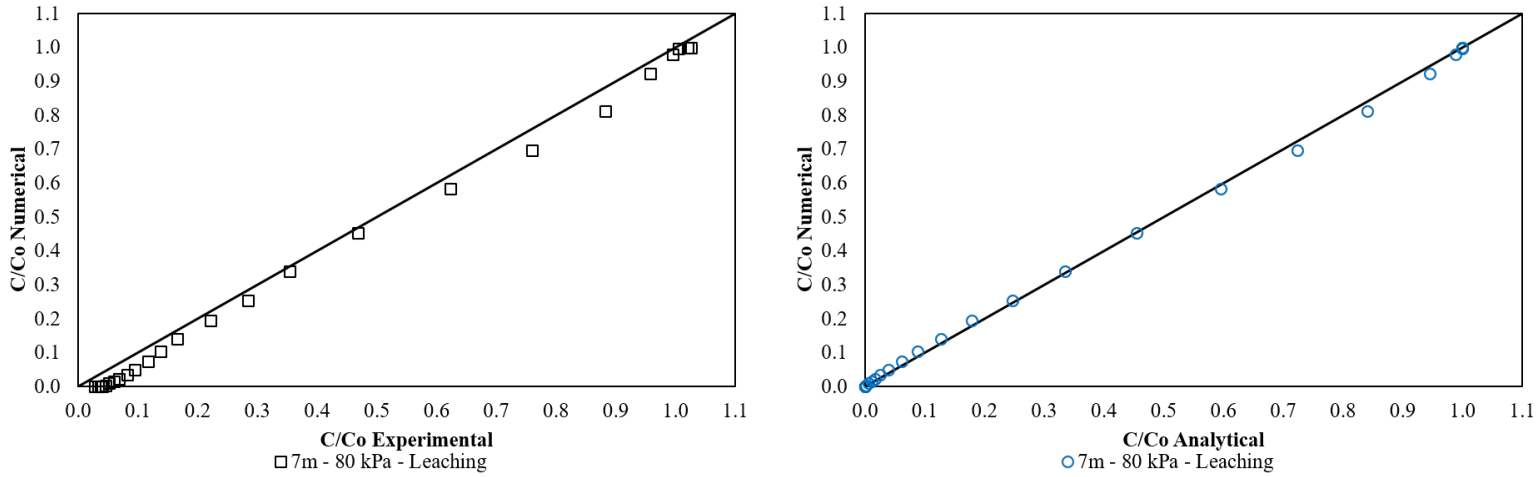

Figure 4.69: Numerical validation with leaching test through experimental data (left) and analytical (right) from the soil at 7 m depth consolidated at 80 kPa.

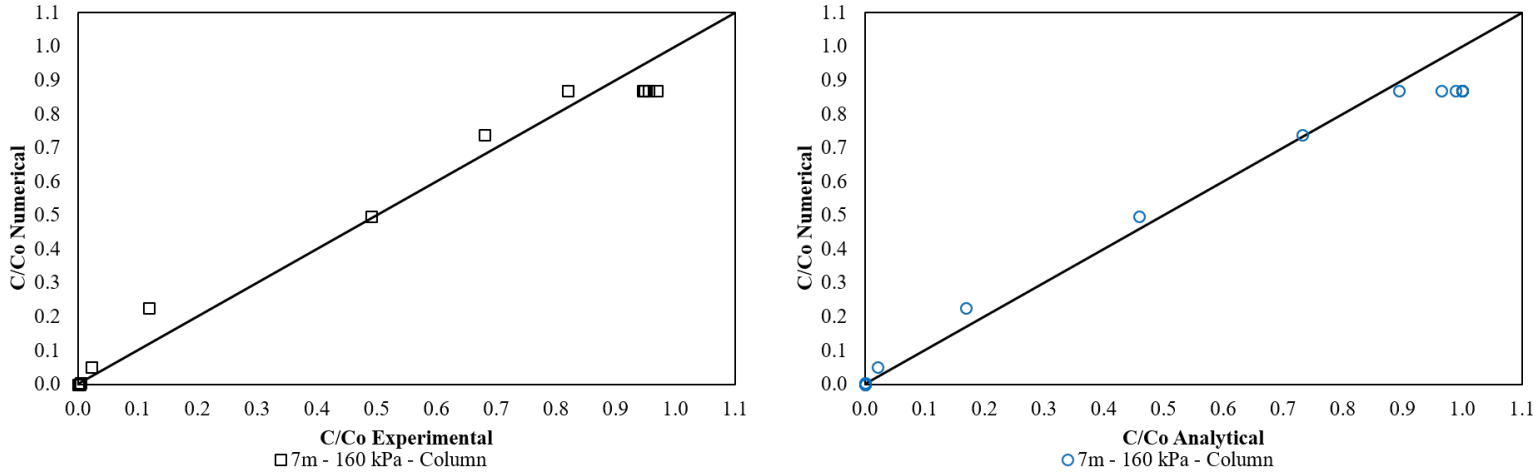

Figure 4.70: Numerical validation with column test through experimental data (left) and analytical (right) from the soil at 7 m depth consolidated at 160 kPa.

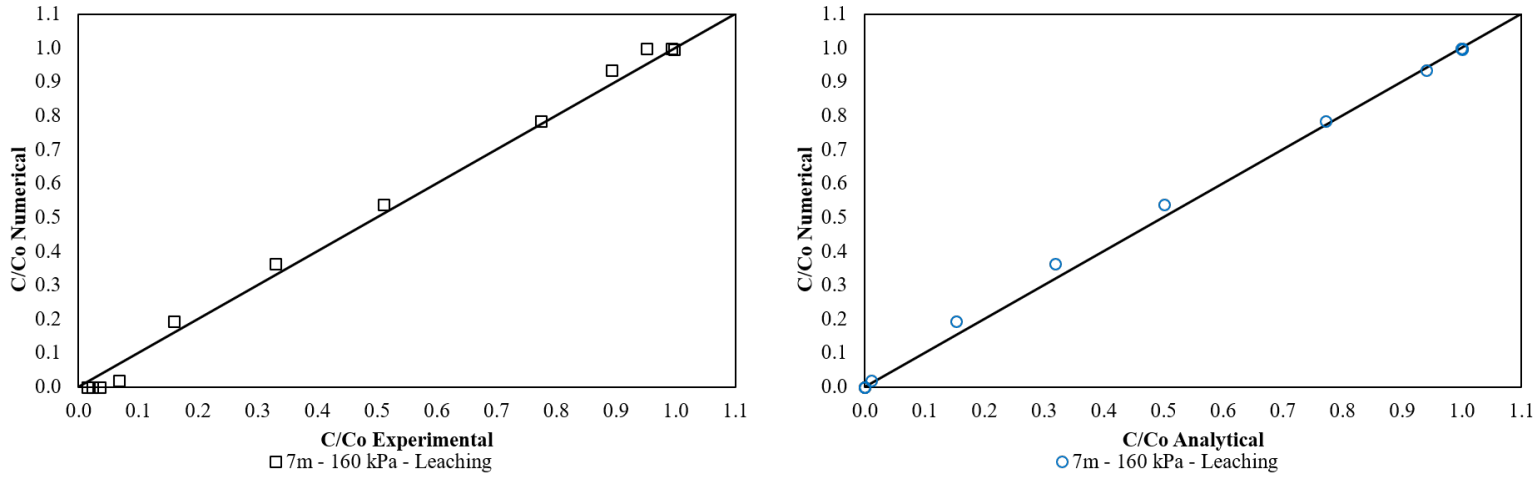

Figure 4.71: Numerical validation with leaching test through experimental data (left) and analytical (right) from the soil at 7 m depth consolidated at 160 kPa.

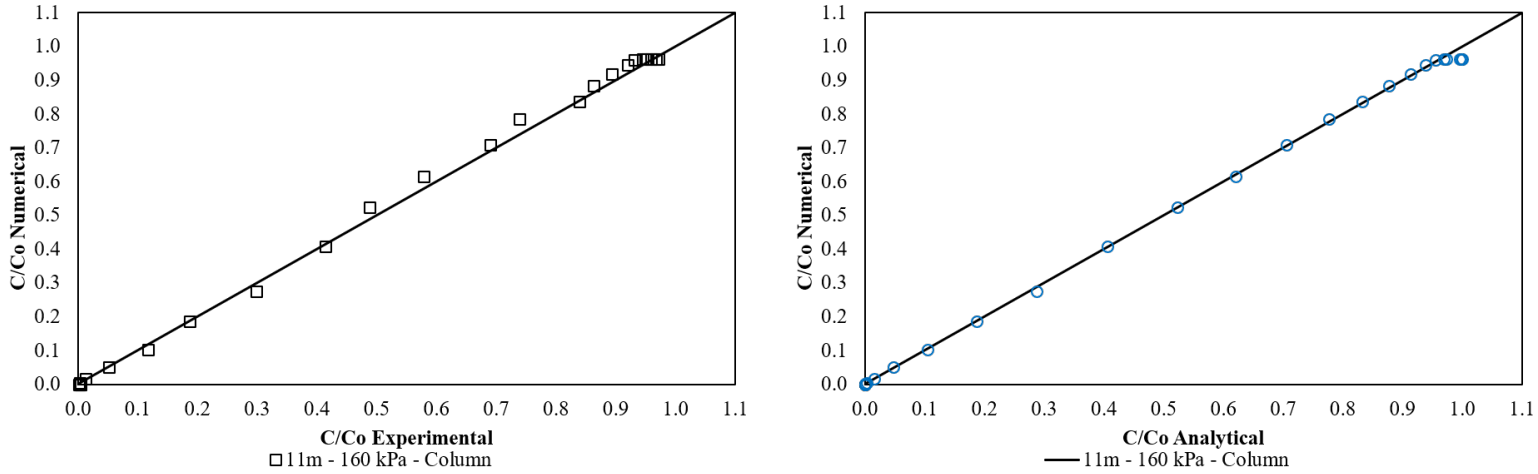

Figure 4.72: Numerical validation with column test through experimental data (left) and analytical (right) from the soil at 11 m depth consolidated at 160 kPa.

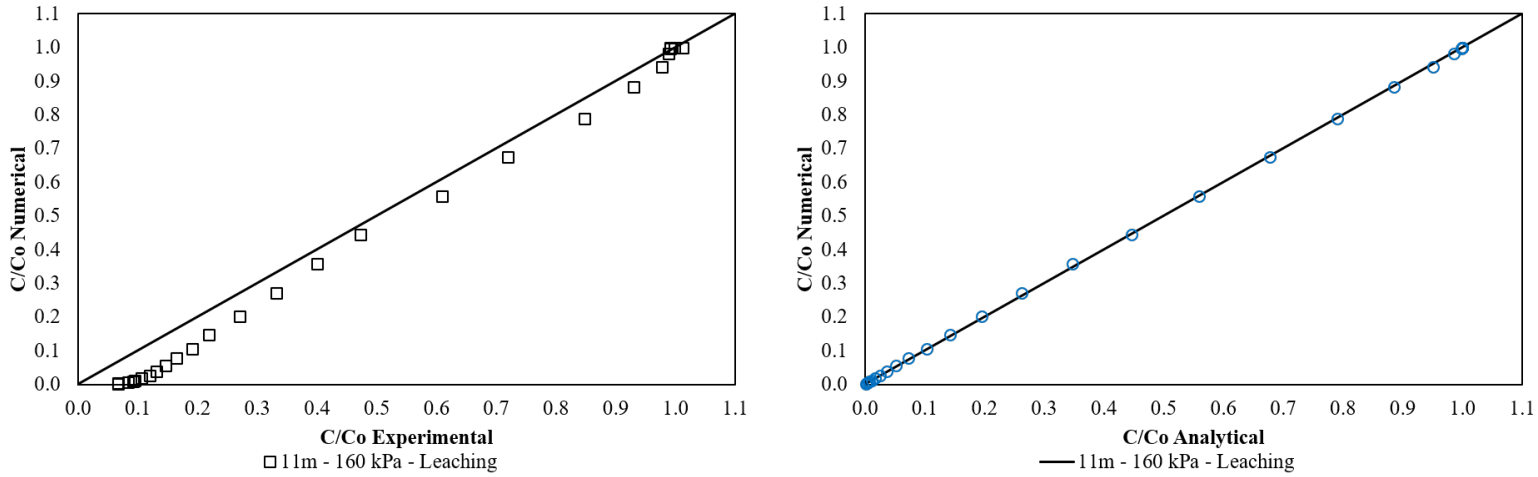

Figure 4.73: Numerical validation with leaching test through experimental data (left) and analytical (right) from the soil at 11 m depth consolidated at 160 kPa.

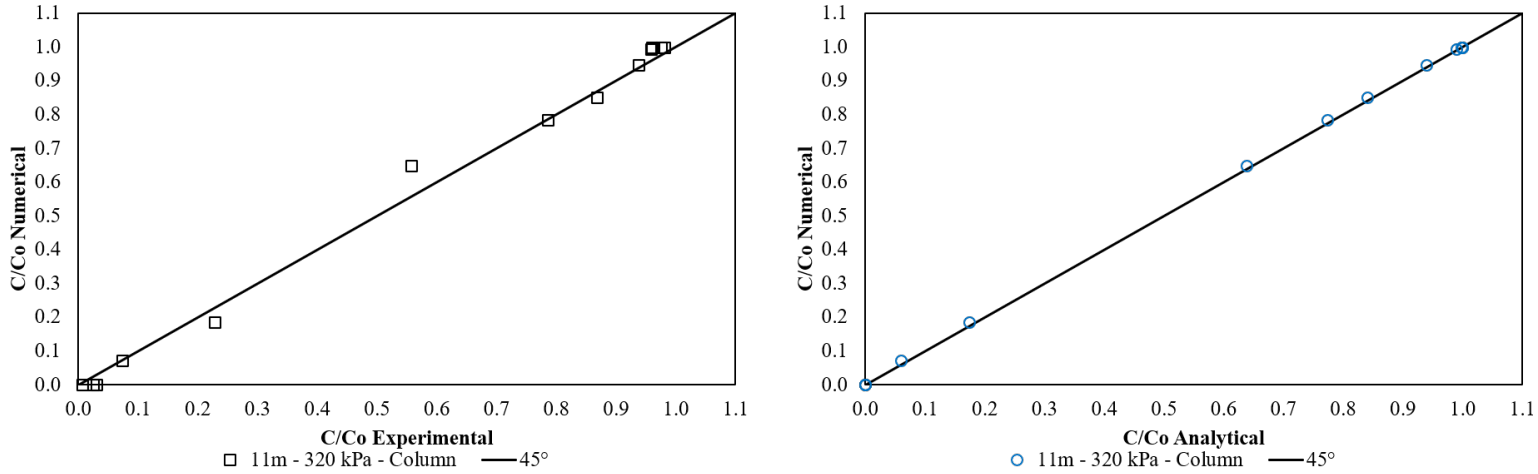

Figure 4.74: Numerical validation with column test through experimental data (left) and analytical (right) from the soil at 11 m depth consolidated at 320 kPa.

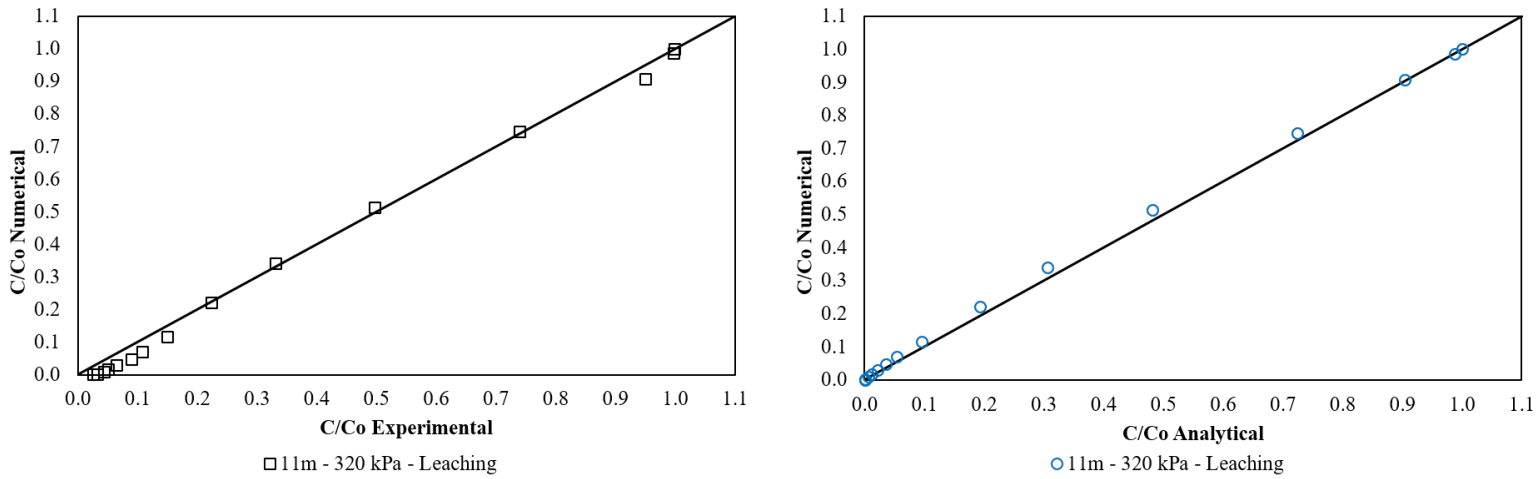

Figure 4.75: Numerical validation with leaching test through experimental data (left) and analytical (right) from the soil at 11 m depth consolidated at 320 kPa.

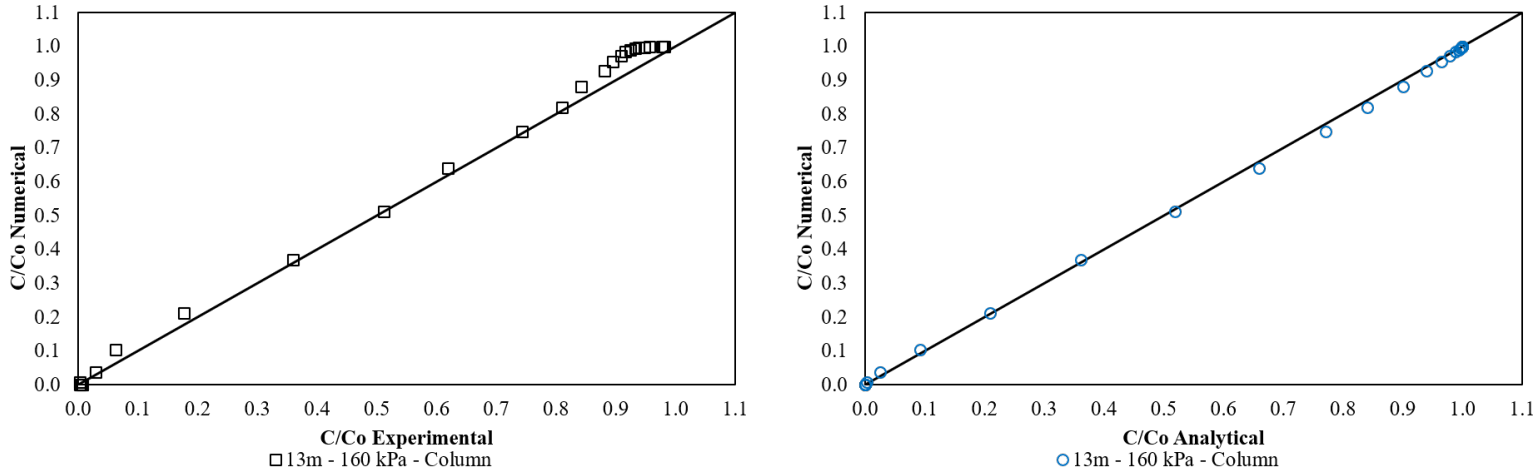

Figure 4.76: Numerical validation with column test through experimental data (left) and analytical (right) from the soil at 13 m depth consolidated at 160 kPa.

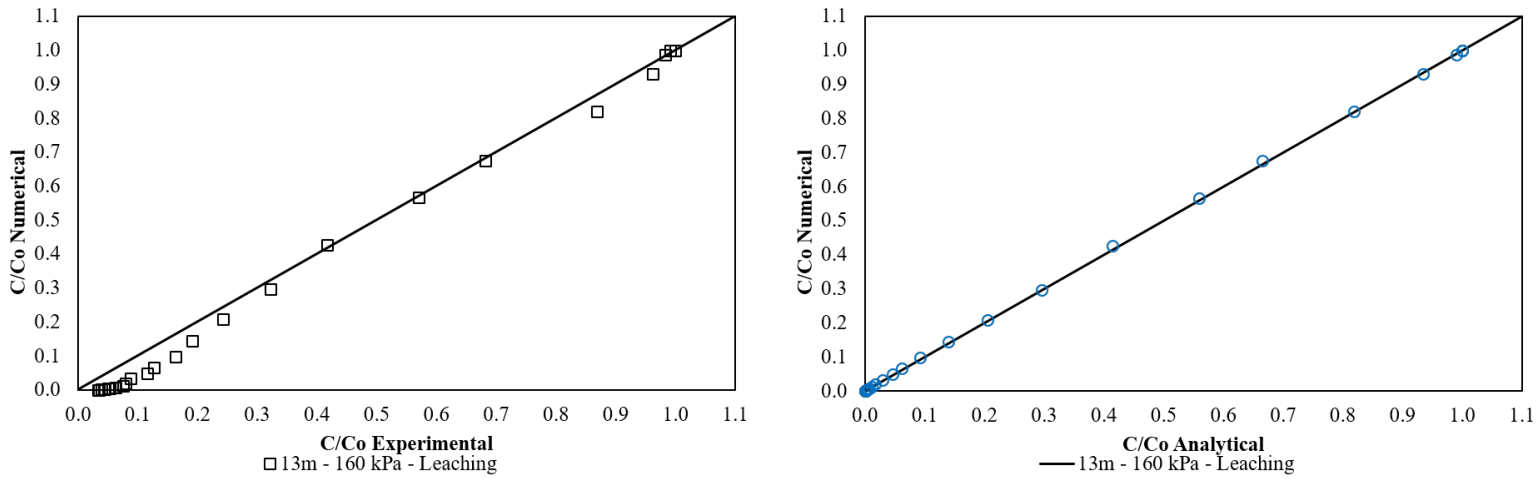

Figure 4.77: Numerical validation with leaching test through experimental data (left) and analytical (right) from the soil at 13 m depth consolidated at 160 kPa.

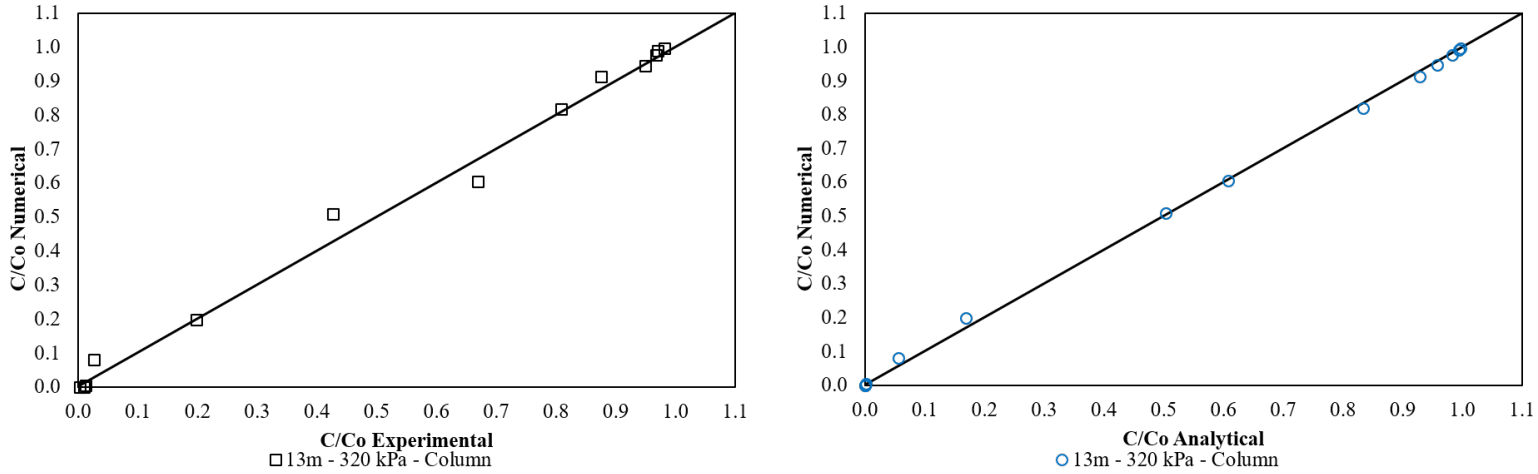

Figure 4.78: Numerical validation with column test through experimental data (left) and analytical (right) from the soil at 13 m depth consolidated at 320 kPa.

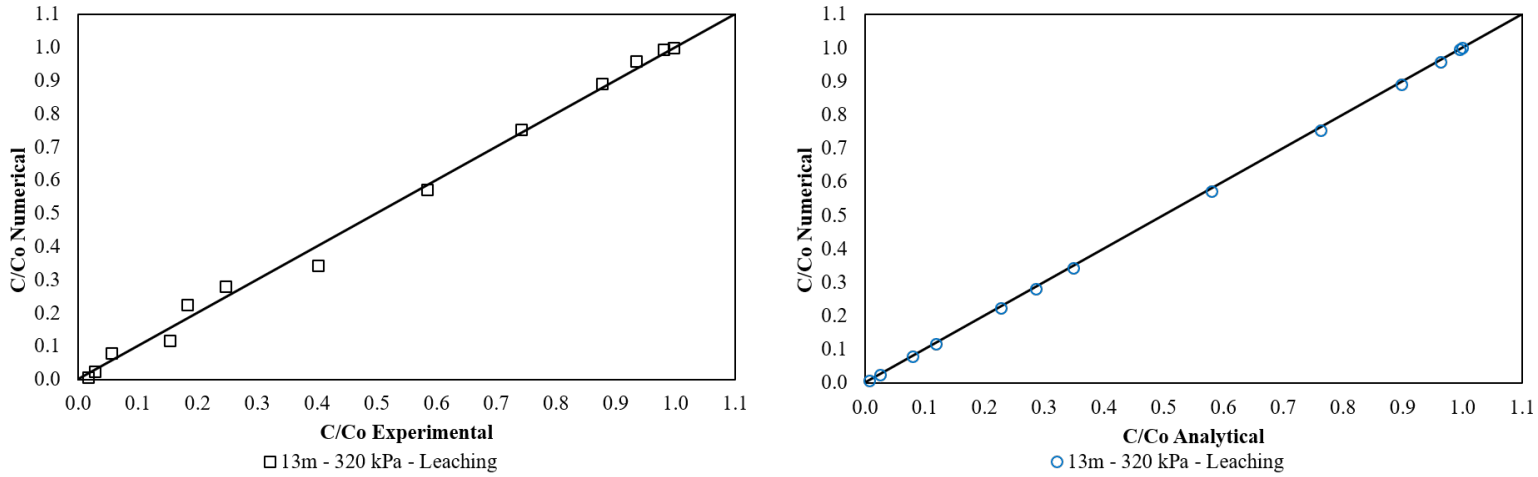

Figure 4.79: Numerical validation with leaching test through experimental data (left) and analytical (right) from the soil at 13 m depth consolidated at 320 kPa.

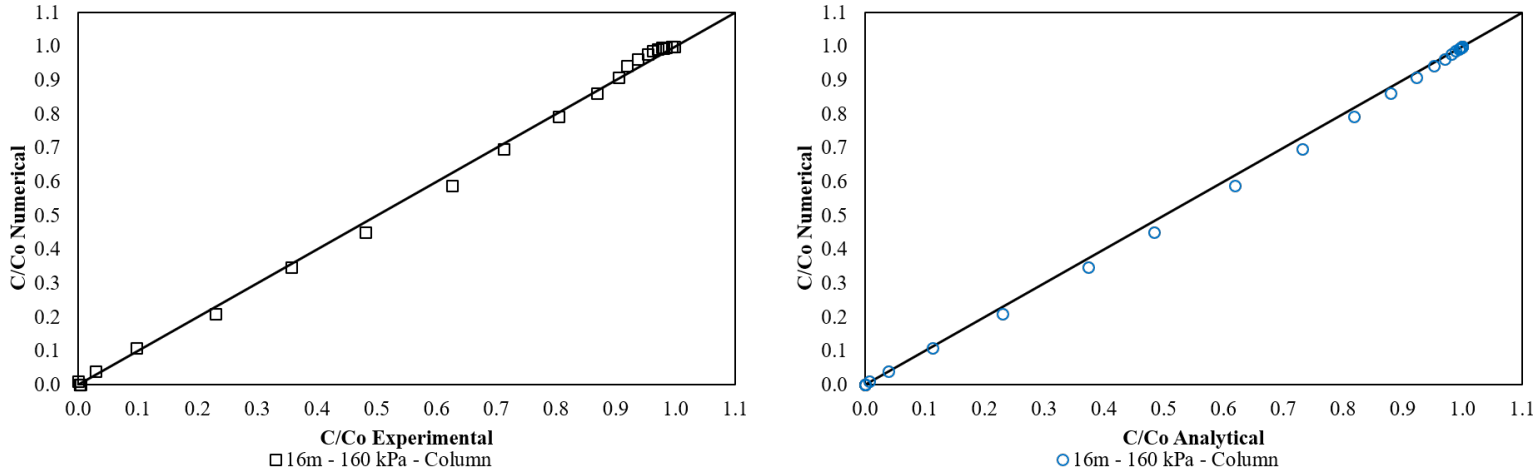

Figure 4.80: Numerical validation with column test through experimental data (left) and analytical (right) from the soil at 16 m depth consolidated at 160 kPa.

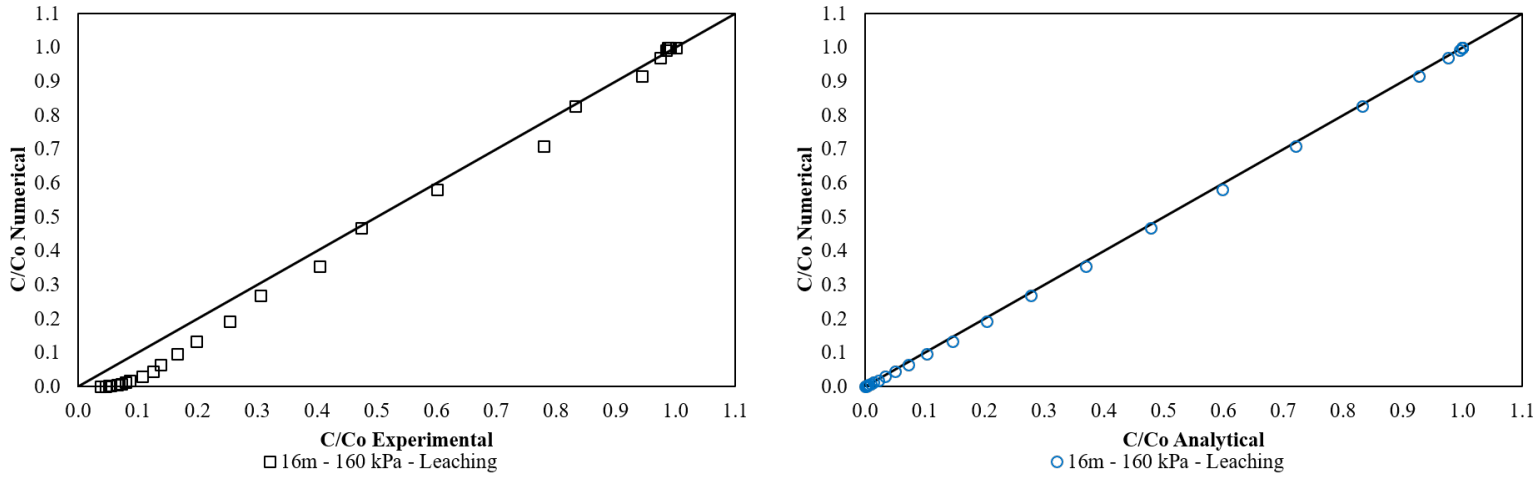

Figure 4.81: Numerical validation with leaching test through experimental data (left) and analytical (right) from the soil at 16 m depth consolidated at 160 kPa.

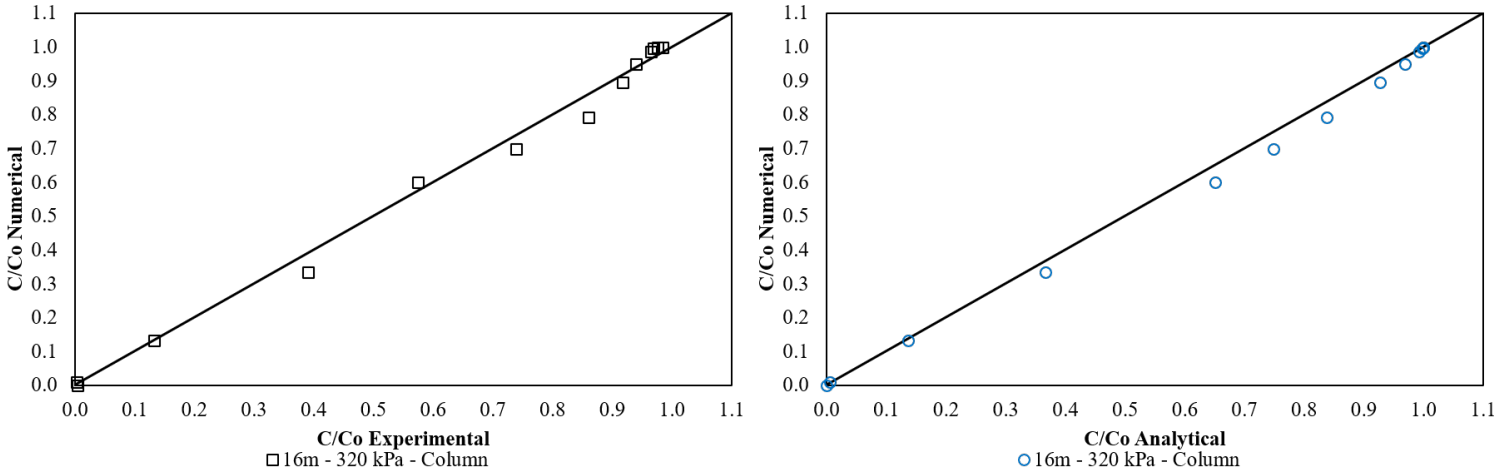

Figure 4.82: Numerical validation with column test through experimental data (left) and analytical (right) from the soil at 16 m depth consolidated at 320 kPa.

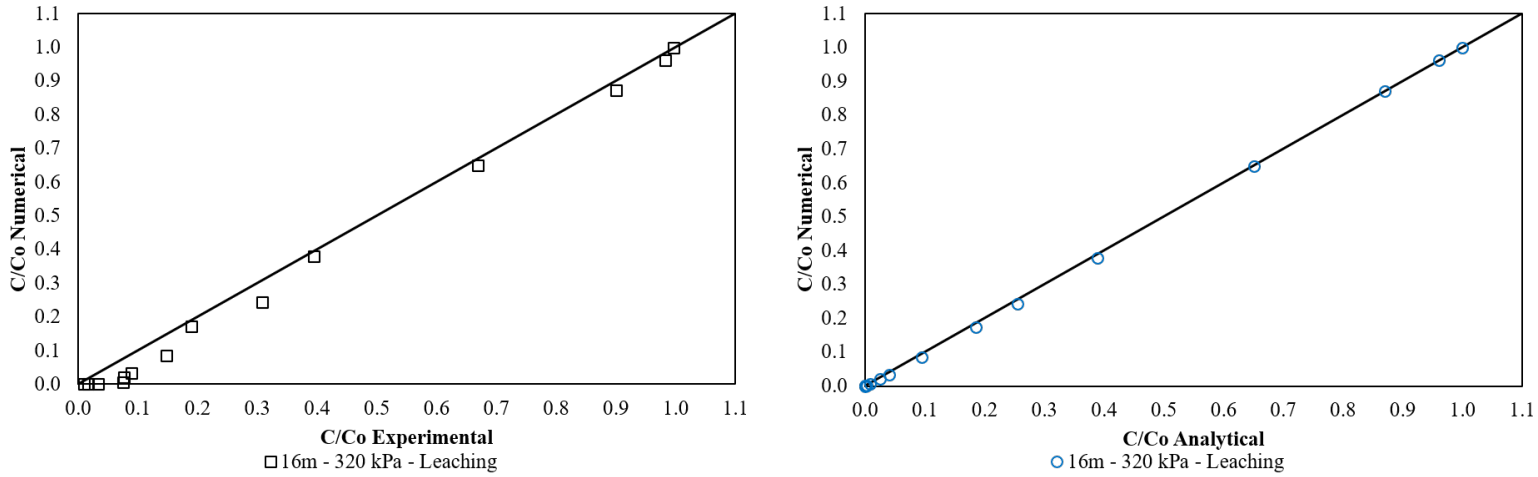

Figure 4.83: Numerical validation with leaching test through experimental data (left) and analytical (right) from the soil at 16 m depth consolidated at 320 kPa.

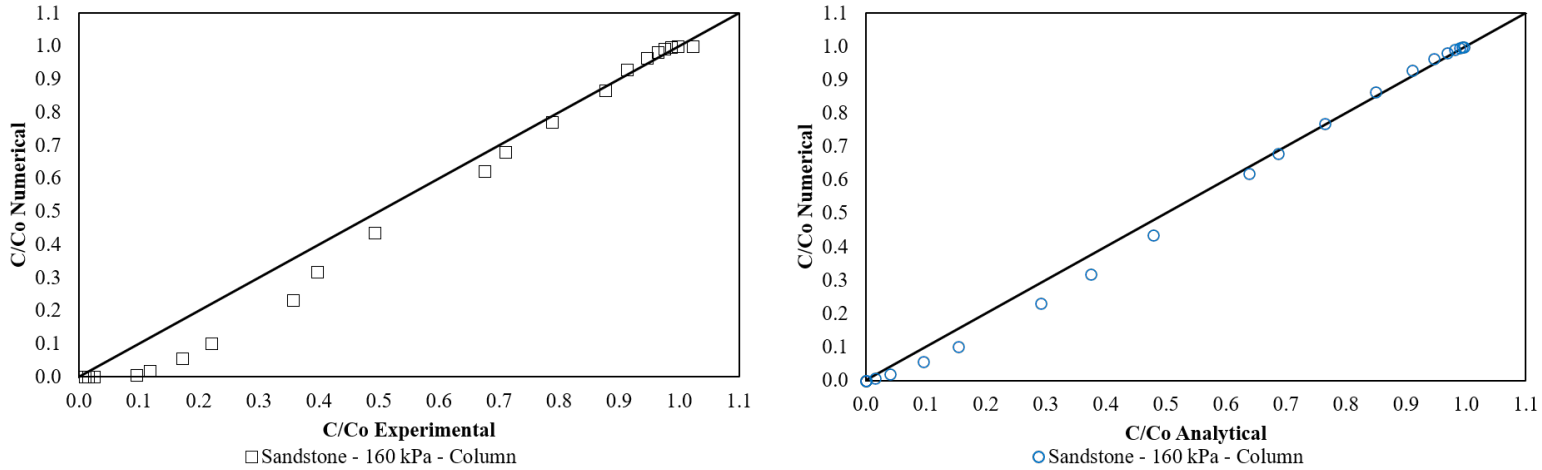

Figure 4.84: Numerical validation with column test through experimental data (left) and analytical (right) from the sandstone consolidated at 160 kPa.

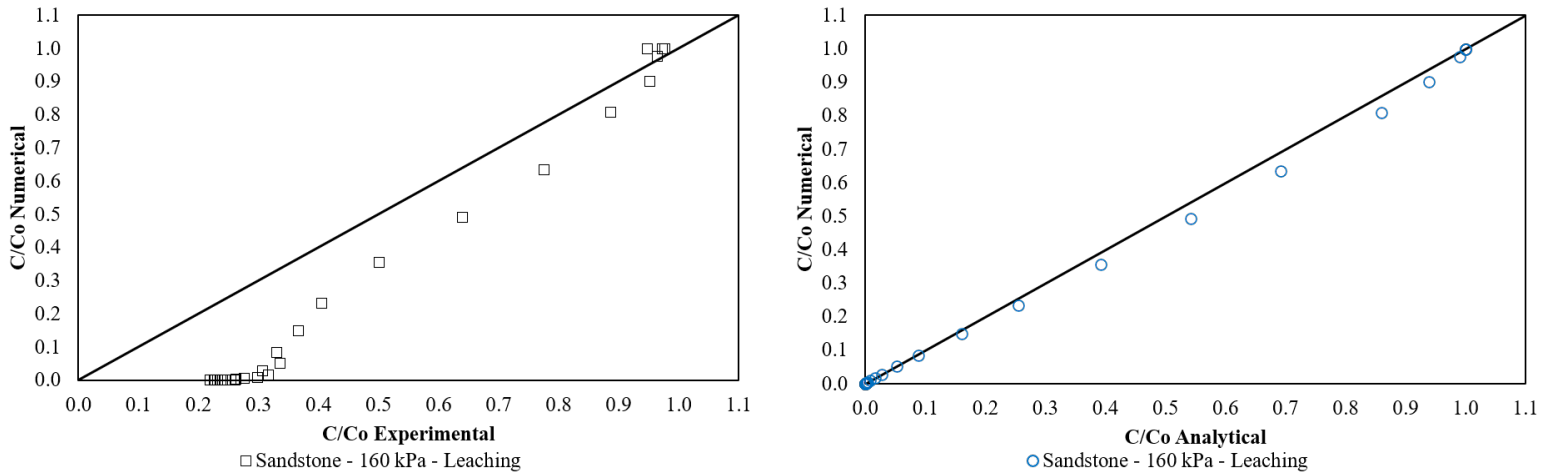

Figure 4.85: Numerical validation with leaching test through experimental data (left) and analytical (right) from the sandstone consolidated at 160 kPa.

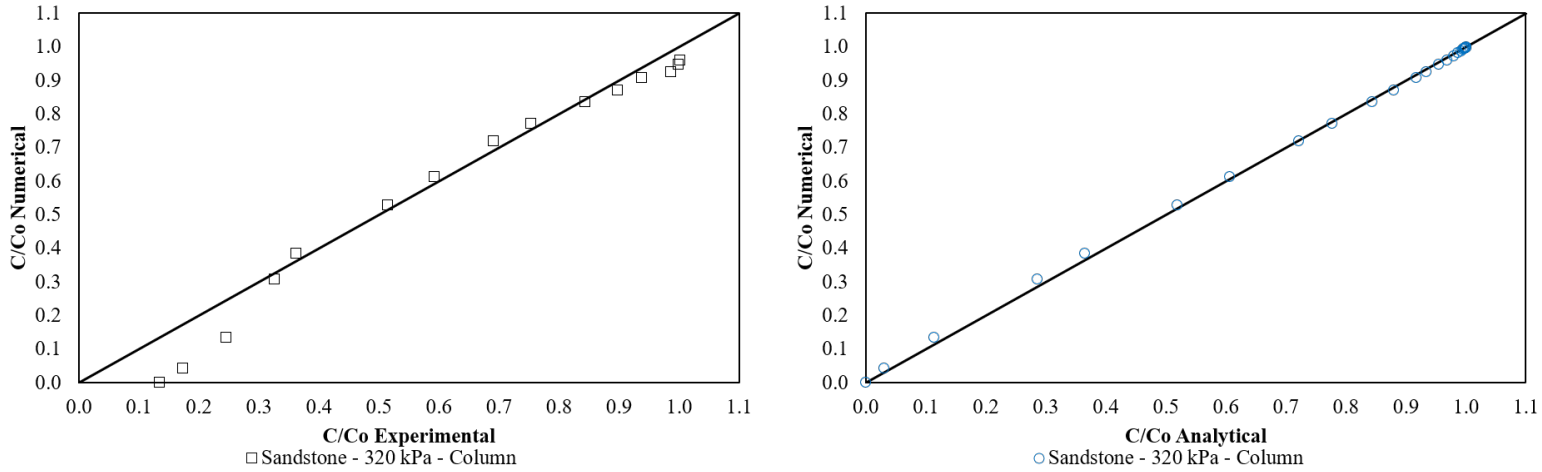

Figure 4.86: Numerical validation with column test through experimental data (left) and analytical (right) from the sandstone consolidated at 320 kPa.

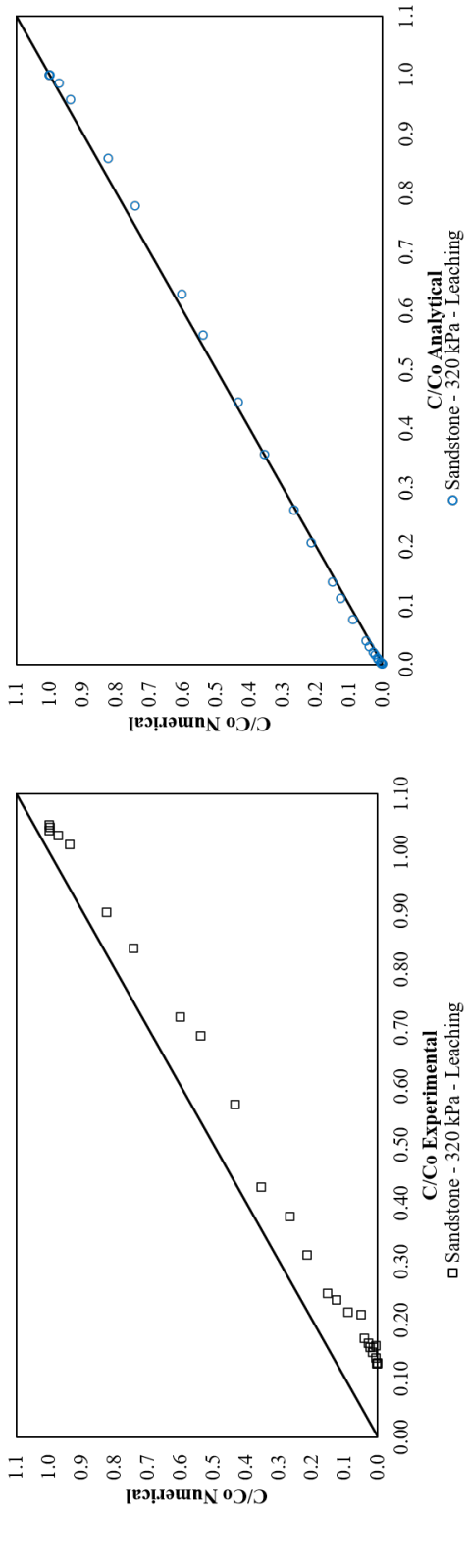

Figure 4.87: Numerical validation with leaching test through experimental data (left) and analytical (right) from the sandstone consolidated at 320 kPa.

4.5.2 N-S – 0.6 m

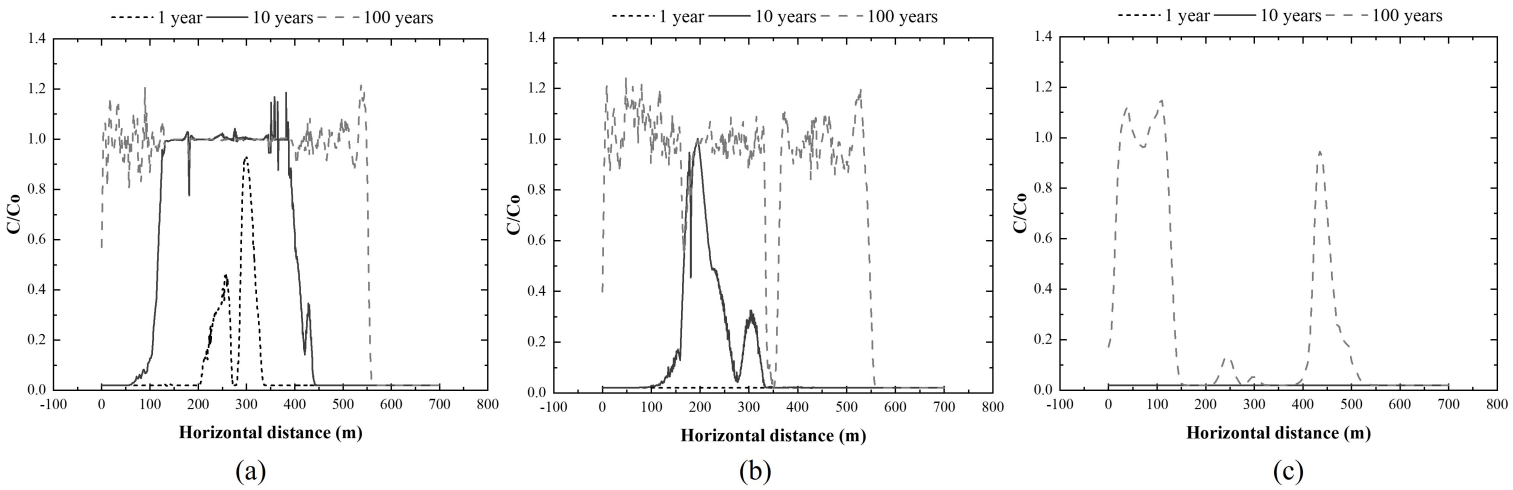

Figure 4.88: Variation of the relative concentration with the horizontal distance for 0.6 m of leachate head, considering 1, 10, and 100 years in a study of (a) the surface, (b) the middle, and (c) the base of the N-S profile.

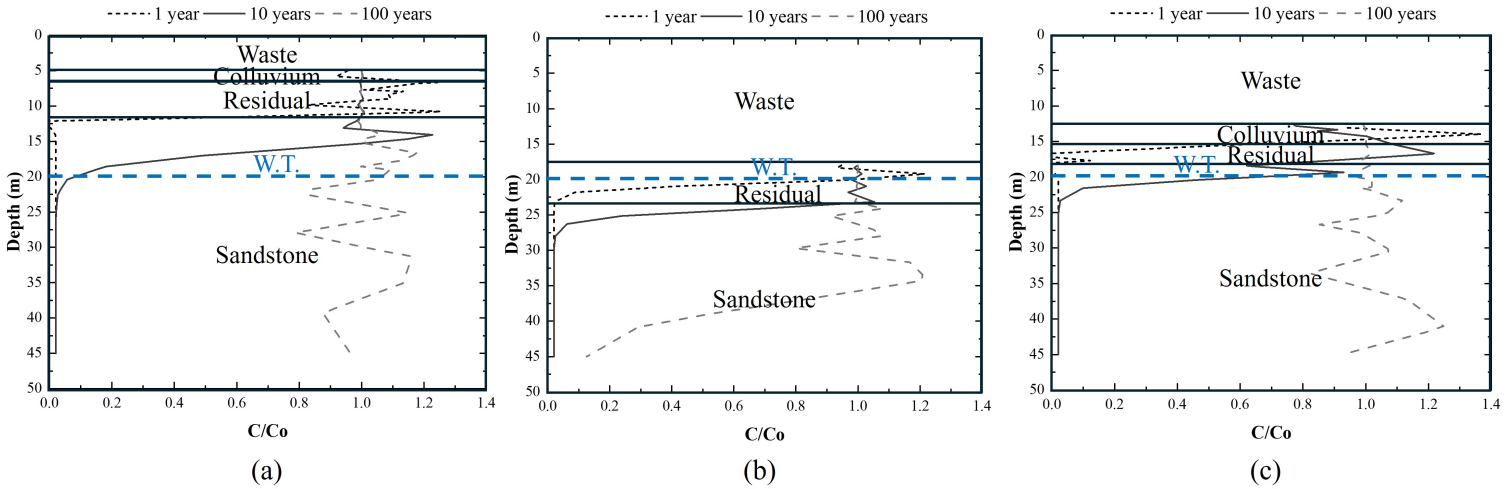

Figure 4.89: Relative concentration with depth for 1, 10, and 100 years of simulation of (a) the left, (b) the middle, and (c) the right waste pit of the N-S profile, considering 0.6 m of leachate head.

4.5.3 N-S – 1.2 m

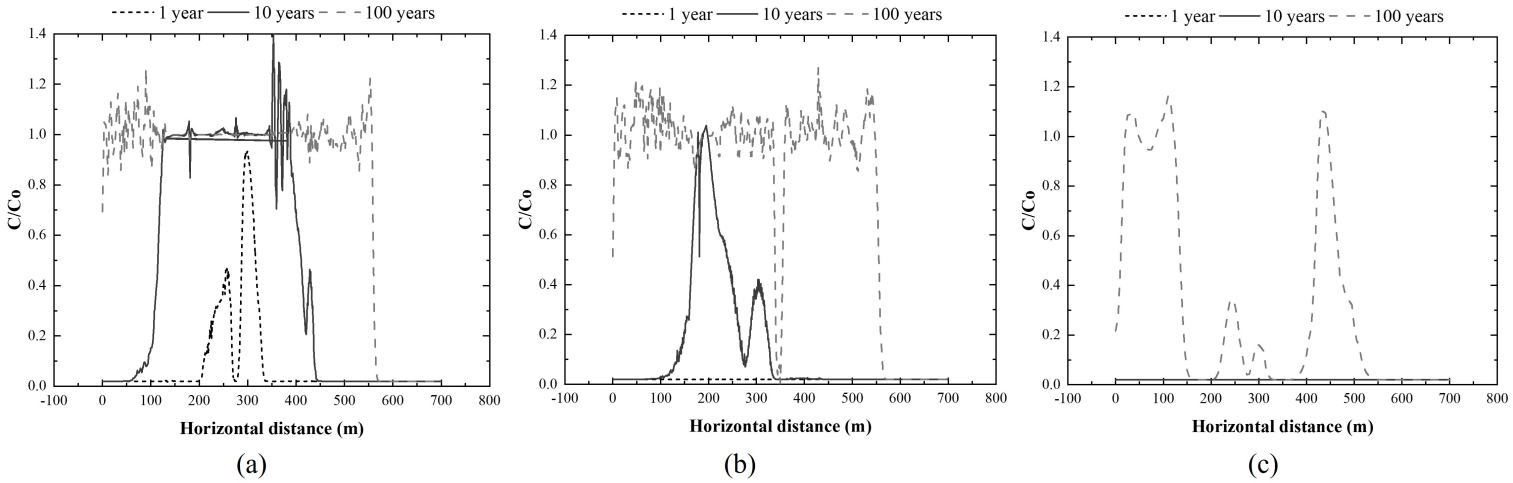

Figure 4.90: Variation of the relative concentration with the horizontal distance for 1.2 m of leachate head, considering 1, 10, and 100 years in a study of (a) the surface, (b) the middle, and (c) the base of the N-S profile.

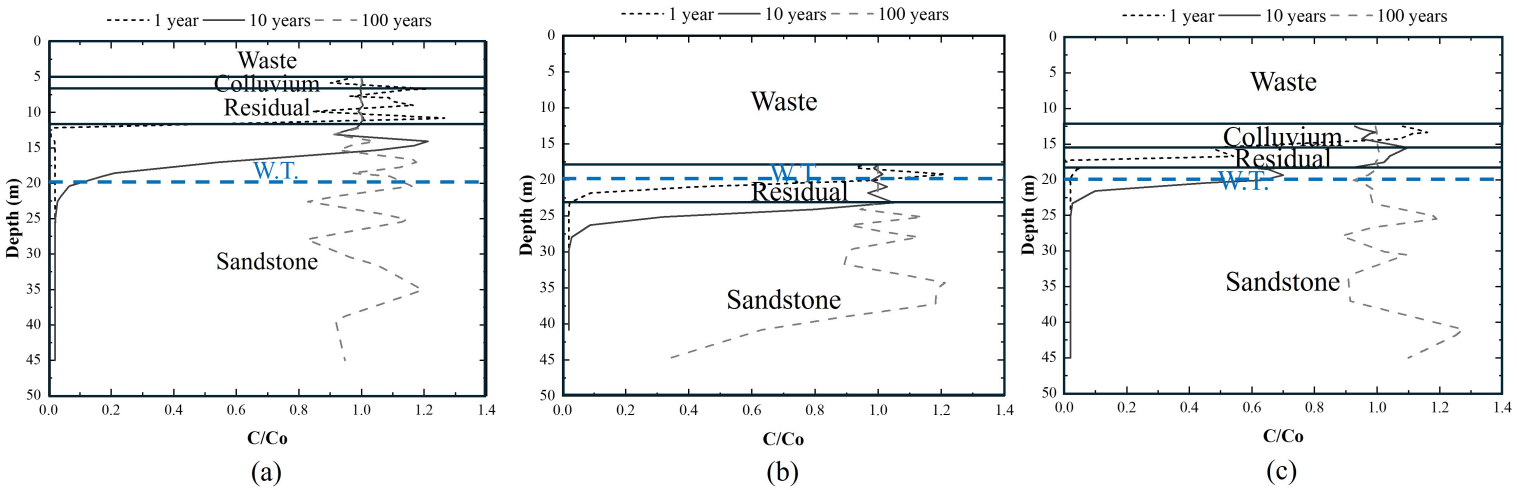

Figure 4.91: Relative concentration with depth for 1, 10, and 100 years of simulation of (a) the left, (b) the middle, and (c) the right waste pit of the N-S profile, considering 1.2 m of leachate head.

4.5.4 N-S – Colluvium and residual BTCs

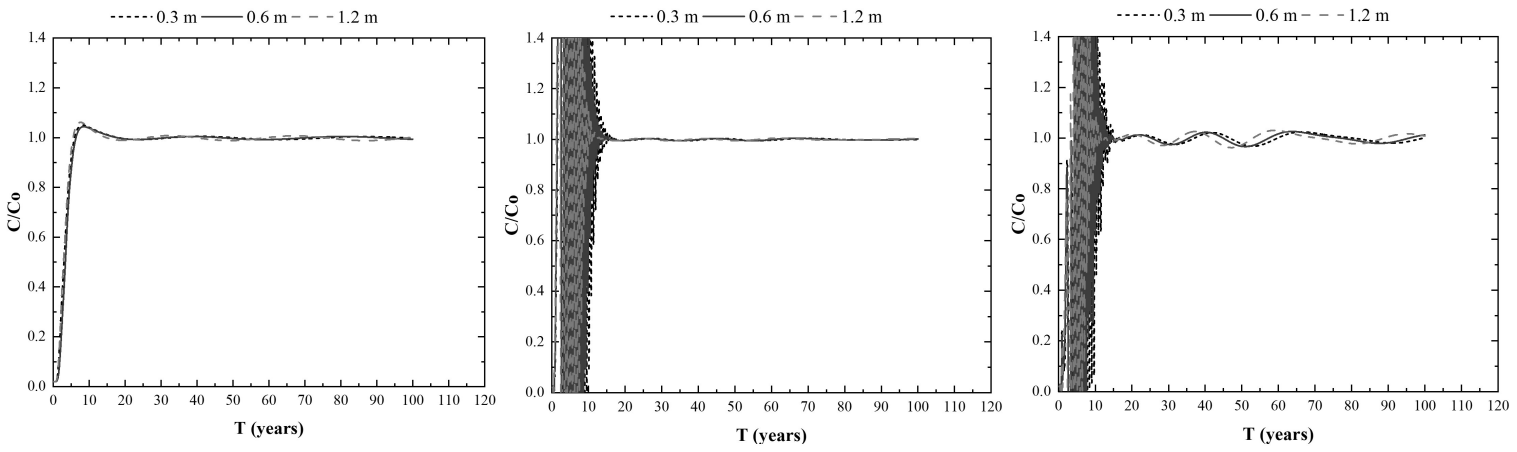

Figure 4.92: Breakthrough curves (a) in the middle of the residual at the center, (b) in the colluvium on the right slope, and (c) in the residual on the right slope of the N-S waste pit, with leachate heads of 0.3, 0.6, and 1.2 m.

4.5.5 E-W – 0.6 m

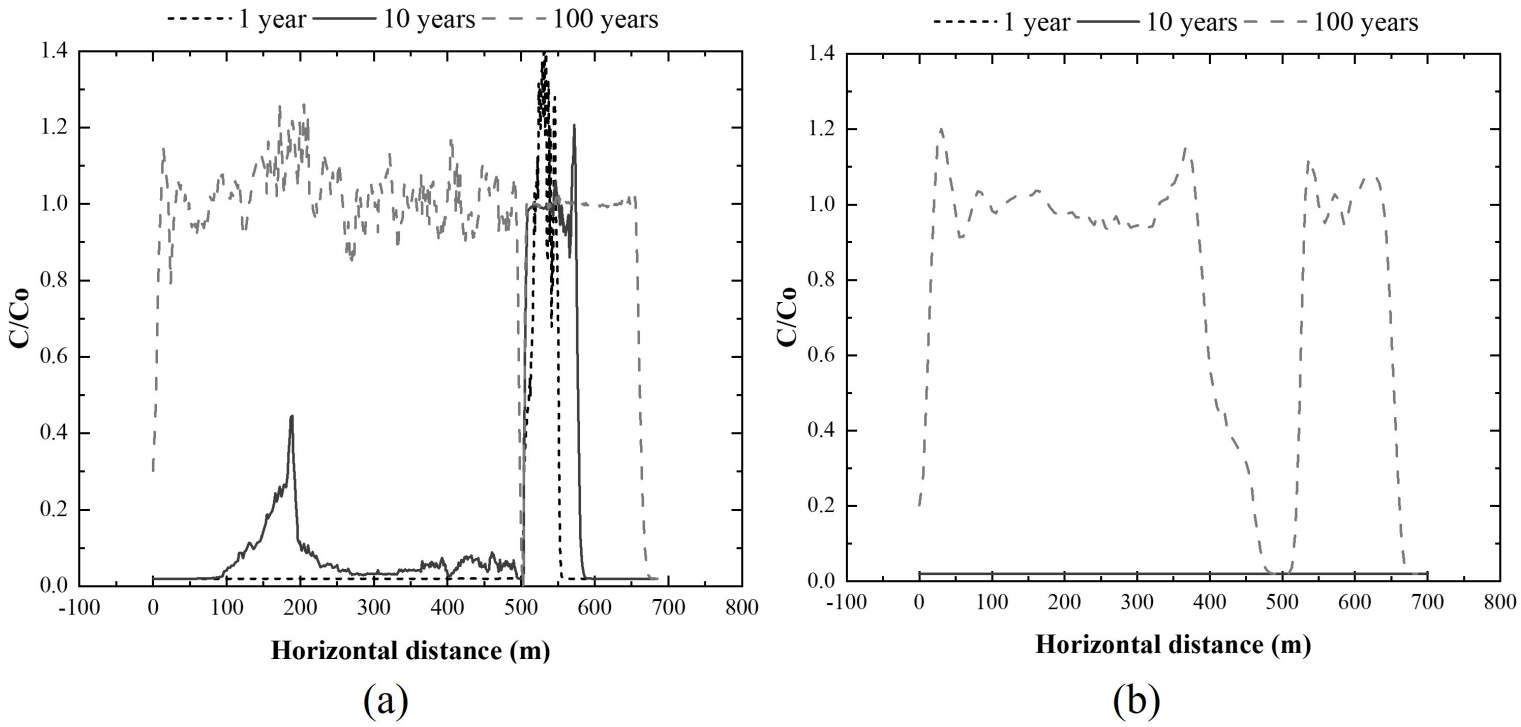

Figure 4.93: Variation of the relative concentration with the horizontal distance for 0.6 m of leachate head, considering 1, 10, and 100 years in a study (a) of the middle and (b) profile base of the E-W profile.

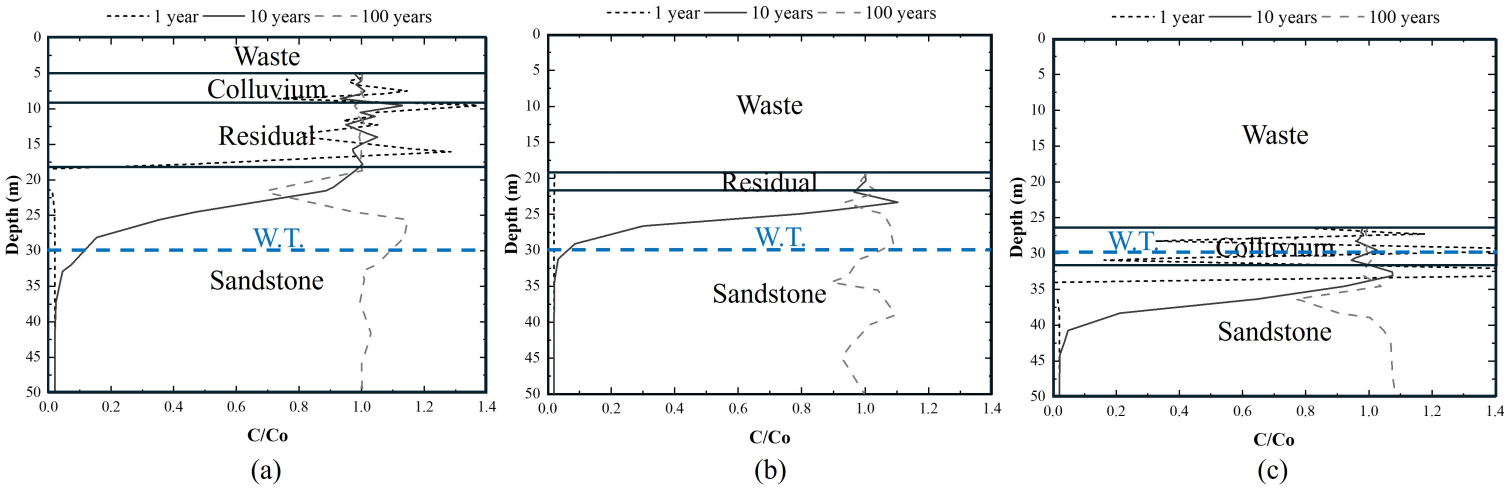

Figure 4.94: Relative concentration with depth for 1, 10, and 100 years of simulation of (a) the left, (b) the middle, and (c) the right waste pit of the E-W profile, considering 0.6 m of leachate head.

4.5.6 E-W – 1.2 m

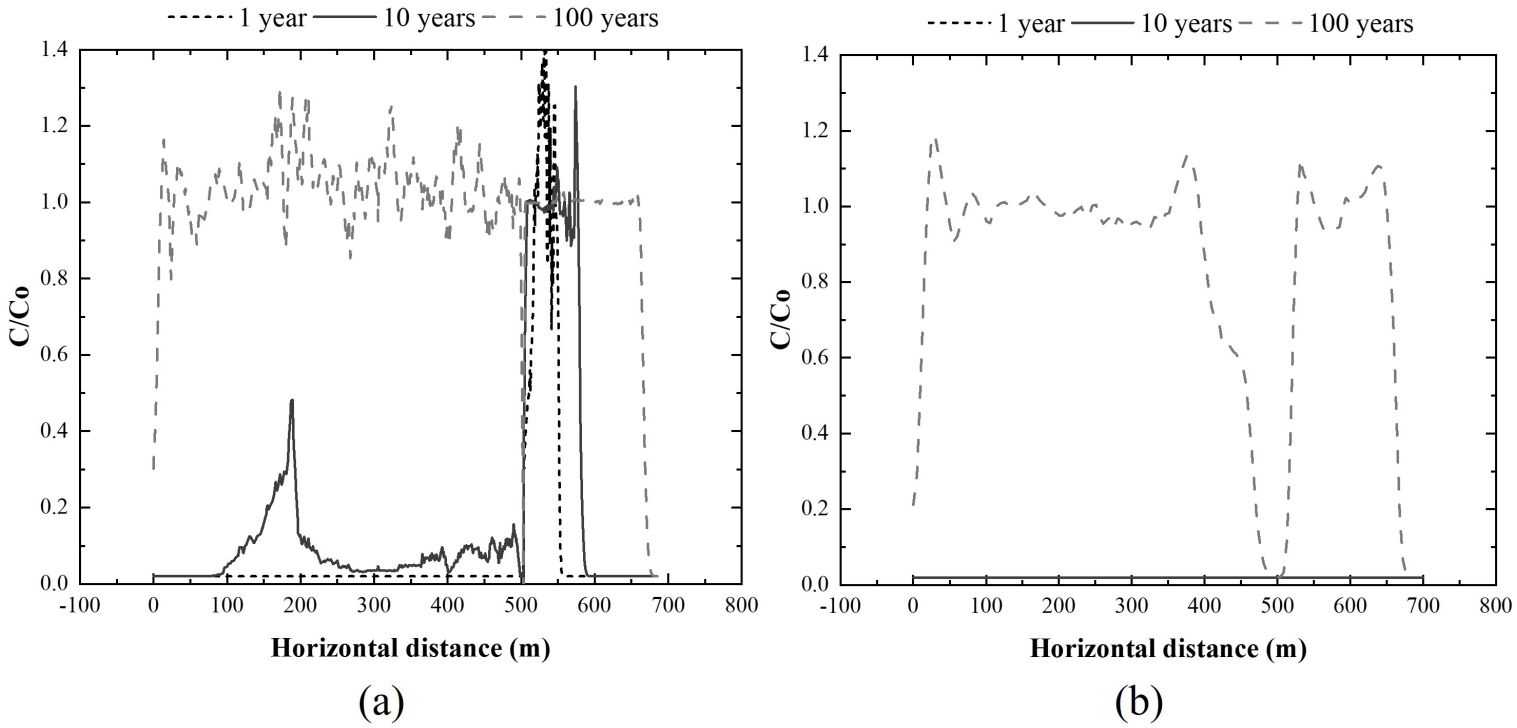

Figure 4.95: Variation of the relative concentration with the horizontal distance for 1.2 m of leachate head, considering 1, 10, and 100 years in a study of (a) the middle and (b) the base of the E-W profile.

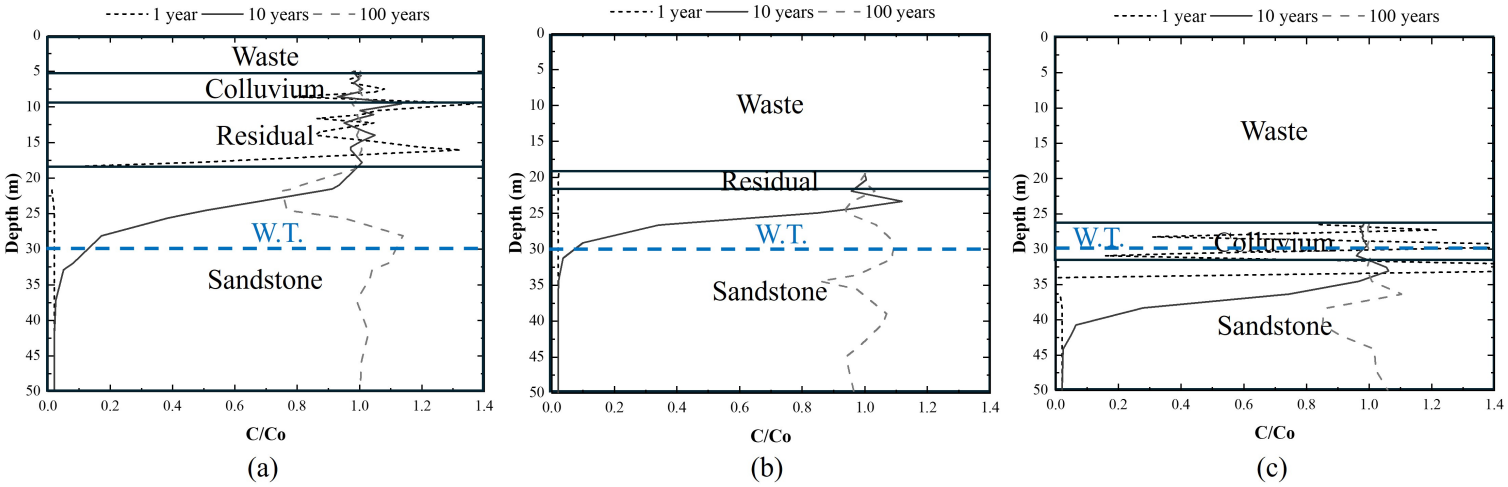

Figure 4.96: Relative concentration with depth for 1, 10, and 100 years of simulation of (a) the left, (b) the middle, and (c) the right waste pit of the E-W profile, considering 1.2 m of leachate head.

References

Ahmed, A. T., Alluqmani, A. E., & Shafiquzzaman, M. (2019). Impacts of landfill leachate on groundwater quality in desert climate regions. *International Journal of Environmental Science and Technology*, 16(11), 6753–6762.

Basilici, G., Bo, P. F. D., & de Oliveira, E. F. (2016). Distribution of palaeosols and deposits in the temporal evolution of a semiarid fluvial distributary system (Bauru Group, Upper Cretaceous, SE Brazil). *Sedimentary Geology*, 341, 245–264.

Baun, A., Reitzel, L. A., Ledin, A., Christensen, T. H., & Bjerg, P. L. (2003). Natural attenuation of xenobiotic organic compounds in a landfill leachate plume (Vejen, Denmark). *Journal of Contaminant Hydrology*, 65(3-4), 269–291.

Butt, T. E., Lockley, E., & Oduyemi, K. O. (2008). Risk assessment of landfill disposal sites - State of the art. *Waste Management*, 28(6), 952–964.

Cavaguti, N. & Paula e Silva, F. (1992). Management of groundwater resources in the city of Bauru - SP, given the special hydrogeological characteristics of the region (in Portuguese). In *VII Congresso Brasileiro de Águas Subterrâneas*.

CONAMA 420/09 (2009). Resolução CONAMA N° 420 de 28 de Dezembro de 2009. *Conselho Nacional do Meio Ambiente*.

Dal' Bó, P. F. F., Basilici, G., & Angélica, R. S. (2010). Factors of paleosol formation in a Late Cretaceous eolian sand sheet paleoenvironment, Marília Formation, Southeastern Brazil. *Palaeogeography, Palaeoclimatology, Palaeoecology*, 292(1-2), 349–365.

Ding, X.-H., Feng, S.-J., Zheng, Q.-T., & Peng, C.-H. (2020). A two-dimensional analytical model for organic contaminants transport in a transition layer-cutoff wall-aquifer system. *Computers and Geotechnics*, 128(May), 103816.

Faria, G. M. M. & Mondelli, G. (2017). Interaction between municipal solid waste leachate

and Bauru aquifer system: a study case in Brazil. *Environmental Science and Pollution Research*, 24(35), 27553–27572.

Feng, S. J., Peng, M. Q., Chen, Z. L., & Chen, H. X. (2019). Transient analytical solution for one-dimensional transport of organic contaminants through GM/GCL/SL composite liner. *Science of the Total Environment*, 650, 479–492.

Feng, Y. & Jin, X. (2019). Studies on effects of traffic tunnels on the migration of the contaminants under landfill sites. *Environmental Science and Pollution Research*, 26(34), 34801–34817.

Fernandes, Saab, A., Rocha, B., Rodrigues, R., Lodi, P., & Giacheti, H. (2022). Geomechanical parameters in the active zone of an unsaturated tropical soil site via laboratory tests. *Soils and Rocks*, 45(4), 1–15.

Friedenberg, L., Olivella, S., & Düsterloh, U. (2023). Numerical analysis for the simulation of crushed salt compaction behavior. In *All Days*: ARMA.

Gaus, I., Wieczorek, K., Schuster, K., Garitte, B., Senger, R., Vasconcelos, R., & Mayor, J. C. (2014). EBS behaviour immediately after repository closure in a clay host rock: HE-E experiment (Mont Terri URL). *Geological Society, London, Special Publications*, 400(1), 71–91.

Ghavam-Nasiri, A. & El-Zein, A. (2016). Effects of defects in geomembranes on reducing desiccation potential of geosynthetics clay liners. *Japanese Geotechnical Society Special Publication*, 2(70), 2418–2422.

Giacheti, H. L., Bezerra, R. C., Rocha, B. P., & Rodrigues, R. A. (2019). Seasonal influence on cone penetration test: An unsaturated soil site example. *Journal of Rock Mechanics and Geotechnical Engineering*, 11(2), 361–368.

Guimarães, L. d. N., Gens, A., Sánchez, M., & Olivella, S. (2006). THM and reactive transport analysis of expansive clay barrier in radioactive waste isolation. *Communications in Numerical Methods in Engineering*, 22(8), 849–859.

Guo, R. & Dixon, D. (2010). Effectiveness and limitations of the existing modelling in application for thermohydromechanical evolution of clay bulkhead in tunnel. *Applied Clay Science*, 47(1-2), 16–22.

Han, Z., Ma, H., Shi, G., He, L., Wei, L., & Shi, Q. (2016). A review of groundwater contamination near municipal solid waste landfill sites in China. *Science of the Total Environment*, 569-570(1), 1255–1264.

Ibrahim, R., Buijs, A., & Luxat, J. (2022). Evaluation of the canister spacing and criticality safety of spent plutonium-thorium nuclear fuel. *Annals of Nuclear Energy*, 172, 109056.

Jacinto, A. C., Villar, M. V., Gómez-Espina, R., & Ledesma, A. (2009). Adaptation of the van Genuchten expression to the effects of temperature and density for compacted bentonites. *Applied Clay Science*, 42(3-4), 575–582.

Jamei, M., Mabrouk, A., & Alassaf, Y. (2024). Influence of deflection deformations on the sustainability of the landfill cover: analysis and recommendations. *Engineering, Technology & Applied Science Research*, 14(3), 14387–14394.

Jesus, L. S., Fernandes, J. B., & Giacheti, H. L. (2013). Investigação da condutividade hidráulica dos solos de uma área de aterro de resíduos sólidos urbanos através de ensaios de campo e laboratório. *Ciencia y Engenharia/ Science and Engineering Journal*, 22(1), 21–28.

Khadivipanah, P., Olivella, S., Pintado, X., & Vaunat, J. (2022). Analysis of shear mock-up tests in a canister-clay system for spent nuclear fuel isolation. *Geomechanics for Energy and the Environment*, 32, 100361.

Kim, C. S., Alfaro, M. C., Blatz, J., & Graham, J. (2022). Swelling pressures and hydration times in a clay seal. *Environmental Geotechnics*, 9(5), 298–309.

Kjeidsen, P. & Christensen, T. H. (1984). Soil attenuation of acid phase landfill leachate. *Waste Management & Research*, 2(1), 247–263.

Konikow, L. F. (2011). The secret to successful solute-transport modeling. *Ground Water*, 49(2), 144–159.

Lago, A. L., Elis, V. R., & Giacheti, H. L. (2006). Aplicação integrada de métodos geofísicos em uma área de disposição de resíduos sólidos urbanos em Bauru-SP. *Revista Brasileira de Geofísica*, 24(3), 357–374.

Lake, C. B. & Rowe, R. K. (2000). Diffusion of sodium and chloride through geosynthetic clay liners. *Geotextiles and Geomembranes*, 18(2-4), 103–131.

Leal, K. R. D. (2011). *Análise ambiental de uma terro sanitário e sua influência relativa sobre a qualidade das águas superficiais do entorno*. Dissertação (mestrado), Universidade Estadual Paulista (Unesp).

Levy, J. & Chesters, G. (1995). Simulation of atrazine and metabolite transport and fate in a sandy-till aquifer. *Journal of Contaminant Hydrology*, 20(1-2), 67–88.

Li, X., Zhang, C., & Röhlig, K. J. (2013). Simulations of THM processes in buffer-rock barriers of high-level waste disposal in an argillaceous formation. *Journal of Rock Mechanics and Geotechnical Engineering*, 5(4), 277–286.

Mahallei, H. & Badv, K. (2020). The study of diffusion characteristics of soil bentonite to control contaminant transport. *World Journal of Engineering*, 18(3), 379–388.

Mokni, N., Olivella, S., Valcke, E., Mariën, A., Smets, S., & Li, X. (2011). Deformation and flow driven by osmotic processes in porous materials: application to bituminised waste materials. *Transport in Porous Media*, 86(2), 635–662.

Mondelli, G. (2008). *Integração de diferentes técnicas de investigação para avaliação da poluição e contaminação de uma área de disposição de resíduos sólidos urbanos*. Tese (doutorado), Escola de Engenharia de São Carlos - Universidade de São Paulo (USP).

Mondelli, G., Giacheti, H. L., Boscov, M. E. G., Elis, V. R., & Hamada, J. (2007). Geoenvironmental site investigation using different techniques in a municipal solid waste disposal site in Brazil. *Environmental Geology*, 52(5), 871–887.

Mondelli, G., Giacheti, H. L., & Howie, J. A. (2010). Geo-environmental investigation: A brief review and a few suggestions for Brazilian contaminated sites. *Soils and Rocks*, 33(3), 171–182.

Mor, S., Ravindra, K., Dahiya, R. P., & Chandra, A. (2006). Leachate characterization and assessment of groundwater pollution near municipal solid waste landfill site. *Environmental Monitoring and Assessment*, 118(1-3), 435–456.

Naveen, B. P., Sumalatha, J., & Malik, R. K. (2019). Numerical modelling of leachate transport into water bodies at a landfill site. *Journal of Environmental Engineering and Science*, 15(1), 6–15.

Ng, C., Chen, Z., Coo, J., Chen, R., & Zhou, C. (2015a). Gas breakthrough and emission through unsaturated compacted clay in landfill final cover. *Waste Management*, 44, 155–163.

Ng, C. W., Liu, J., Chen, R., & Xu, J. (2015b). Physical and numerical modeling of an inclined three-layer (silt/gravelly sand/clay) capillary barrier cover system under extreme rainfall. *Waste Management*, 38(1), 210–221.

Nowamooz, H., Mrad, M., Abdallah, A., & Masrouri, F. (2009). Experimental and numerical studies of the hydromechanical behaviour of a natural unsaturated swelling soil. *Canadian Geotechnical Journal*, 46(4), 393–410.

Odling, N. W., Elphick, S. C., Meredith, P., Main, I., & Ngwenya, B. T. (2007). Laboratory measurement of hydrodynamic saline dispersion within a micro-fracture network induced in granite. *Earth and Planetary Science Letters*, 260(3-4), 407–418.

Ojuri, O. O. & Ola, S. A. (2010). Estimation of contaminant transport parameters for a tropical sand in a sand tank model. *International Journal of Environmental Science & Technology*, 7(2), 385–394.

Olivella, S. & Gens, A. (2000). Vapour transport in low permeability unsaturated soils with capillary effects. *Transport in Porous Media*, 40(2), 219–241.

Olivella, S., Gens, A., Carrera, J., & Alonso, E. (1996). Numerical formulation for a simulator (CODE_BRIGHT) for the coupled analysis of saline media. *Engineering Computations*, 13(7), 87–112.

Pujades, E., De Simone, S., Carrera, J., Vázquez-Suñé, E., & Jurado, A. (2017). Settlements around pumping wells: Analysis of influential factors and a simple calculation procedure. *Journal of Hydrology*, 548, 225–236.

Rodriguez-Dono, A., Olivella, S., & Mokni, N. (2020). Assessment of a high-level spent nuclear fuel disposal model. *Environmental Geotechnics*, 7(1), 42–58.

Rowe, R. K. (2012). Third Indian Geotechnical Society: Ferroco Terzaghi oration design and construction of barrier systems to minimize environmental impacts due to municipal solid waste leachate and gas. *Indian Geotechnical Journal*, 42(4), 223–256.

Rowe, R. K. & Abdelrazek, A. Y. (2019). Effect of interface transmissivity and hydraulic conductivity on contaminant migration through composite liners with wrinkles or failed seams. *Canadian Geotechnical Journal*, 56(11), 1650–1667.

Rowe, R. K. & Barakat, F. B. (2021). Modelling the transport of PFOS from single lined municipal solid waste landfill. *Computers and Geotechnics*, 137(June), 104280.

Saab, A. L., Rodrigues, A. L. d. C., Rocha, B. P., Rodrigues, R. A., & Giacheti, H. L. (2023). Suction influence on load-settlement curves predicted by DMT in a collapsible sandy soil. *Sensors*, 23(3), 1429.

Shackelford, C. D. (2021). Fundamental considerations for column testing of engineered, clay-based barriers. *Japanese Geotechnical Society Special Publication*, 9(10), 441–460.

Shu, S., Zhu, W., & Shi, J. (2019). A new simplified method to calculate breakthrough time of municipal solid waste landfill liners. *Journal of Cleaner Production*, 219, 649–654.

Silva, M. L., Batezelli, A., & Ladeira, F. S. B. (2019). Genesis and evolution of paleosols of the Marília Formation, Maastrichtian of the Bauru Basin, Brazil. *CATENA*, 182(October 2018), 104108.

Song, F., Rodriguez-Dono, A., & Sanchez Farfan, P. (2022). Modelling underground excavations in rock masses with anisotropic time-dependent behaviour. *Geomechanics and Geophysics for Geo-Energy and Geo-Resources*, 8(5), 146.

Teh, T., Nik Norulaini, N. A. R., Shahadat, M., Wong, Y., & Mohd Omar, A. K. (2016). Risk assessment of metal contamination in soil and groundwater in Asia: a review of recent trends as well as existing environmental laws and regulations. *Pedosphere*, 26(4), 431–450.

Thu, H. H. T., Van, S. L., Trong, H. T., Viet, H. L., Huu, Q. N., & Thi, L. P. (2023). Determination of the pore water velocity using a walt tracer combined with self-potential measurements. *Journal of Geoscience and Environment Protection*, 11(01), 15–27.

Trabelsi, H., Jamei, M., Zenzri, H., & Olivella, S. (2012). Crack patterns in clayey soils: Experiments and modeling. *International Journal for Numerical and Analytical Methods in Geomechanics*, 36(11), 1410–1433.

van Breukelen, B. M., Griffioen, J., Röling, W. F., & van Verseveld, H. W. (2004). Reactive transport modelling of biogeochemical processes and carbon isotope geochemistry inside a landfill leachate plume. *Journal of Contaminant Hydrology*, 70(3-4), 249–269.

van Genuchten, M. T. (1980). A closed-form equation for predicting the hydraulic conductivity of unsaturated soils. *Soil Science Society of America Journal*, 44(5), 892–898.

Woumeni, R. S. & Vauclin, M. (2006). A field study of the coupled effects of aquifer stratification, fluid density, and groundwater fluctuations on dispersivity assessments. *Advances in Water Resources*, 29(7), 1037–1055.

Xie, H.-j., Chen, Y.-m., Zhan, L.-t., Chen, R.-p., Tang, X.-w., Chen, R.-h., & Ke, H. (2009). Investigation of migration of pollutant at the base of Suzhou Qizishan landfill without a liner system. *Journal of Zhejiang University-SCIENCE A*, 10(3), 439–449.

Yan, H., Xie, H., Wang, S., & Zheng, Z. (2021). A two-dimensional analytical model for organic contaminant transport in cutoff wall and aquifer system. *International Journal for Numerical and Analytical Methods in Geomechanics*, 45(5), 631–647.

Young, T. M. (2006). Natural attenuation of contaminants in soils. *Vadose Zone Journal*, 5(3), 913–914.

Yubero, M. T., Olivella, S., Gens, A., Bonet, E., Lloret, A., & Alfonso, P. (2021). Analysis of the process of compaction movements of deposits of crushed salt tailings. *Engineering Geology*, 293(November 2019), 106290.

Zandarin, M., Gens, A., Olivella, S., & Alonso, E. (2011). Thermo-hydro-mechanical model of the Canister Retrieval Test. *Physics and Chemistry of the Earth, Parts A/B/C*, 36(17-18), 1806–1816.

Zandarin, M. T., Alonso, E., & Olivella, S. (2013). A constitutive law for rock joints considering the effects of suction and roughness on strength parameters. *International Journal of Rock Mechanics and Mining Sciences*, 60, 333–344.

Zhang, J., min Zhang, J., Xing, B., dong Liu, G., & Liang, Y. (2021). Study on the effect of municipal solid landfills on groundwater by combining the models of variable leakage rate, leachate concentration, and contaminant solute transport. *Journal of Environmental Management*, 292(May), 112815.

Zhou, Y., Rodriguez-Dono, A., & Olivella, S. (2024). A spatially correlated heterogeneous anisotropic model for simulation of gas flow in Callovo-Oxfordian claystone. *Computers and Geotechnics*, 173(December 2023), 106570.

Final considerations

Overall conclusions

This thesis presents significant findings regarding the behavior of contaminants in subsurface environments, focusing on the Bauru landfill in Brazil. The study highlights the impact of clay minerals from the smectite group on the expansive characteristics of sandstone, particularly its hydromechanical behavior. Both gray and brown sandstones exhibited similar properties in terms of uniaxial compressive strength (UCS), Young's modulus, and shear strength, indicating brittle failure with low resistance but intermediate to high modulus. However, these materials showed distinct compressibility and expansion behaviors under dry and saturated conditions.

The research also revealed permeability anisotropy, with the brown sandstone demonstrating higher horizontal hydraulic conductivity than the gray sandstone. Moreover, hydraulic conductivity decreased with depth and increased confinement pressure, influenced by a reduction in porosity. Introducing a saline tracer reduced soil permeability but had minimal impact on the sandstone. Key transport parameters such as dispersivity and hydrodynamic dispersion were significantly influenced by permeability, tortuosity, flow lines, and interconnected pores, which are crucial for advective-dispersive transport.

Tracer movement was closely aligned with water flow, as evidenced by a retardation factor (Rd), indicating slight sorption of tracers by the soil and sandstone. Thereby, most tracers were dissolved. Notably, heavy metals Ni and Mg exhibited mobility even in alkaline environments, while Pb remained immobile, raising concerns about environmental exposure

to heavy metals.

Laboratory column tests validated simulations performed using CODE_BRIGHT, which analyzed the Bauru landfill's two profiles (North-South and East-West). The simulations revealed that the slopes adjacent to the waste pit were the most affected by the contamination plume, primarily due to horizontal flow in the more permeable soil horizons above the sandstone. The East-West section demonstrated a higher susceptibility to contaminant percolation, with rapid contamination of the colluvium and residual horizons, followed by plume attenuation upon reaching the sandstone.

Under constant leachate head conditions, both profiles reached maximum contamination levels after a century, raising significant concerns about long-term environmental risks if no interventions are implemented. Additionally, increased leachate head reduced the time for contaminants to reach critical levels. Furthermore, the simulations suggested a potential for more severe impacts from the landfill's contaminants than initially predicted, as they underestimated the contamination spread compared to field results from previous electrical resistivity investigations.